UNIVERSIDAD AUTÓNOMA DE QUERÉTARO

CONIIN

LIBRO DE POSTERS

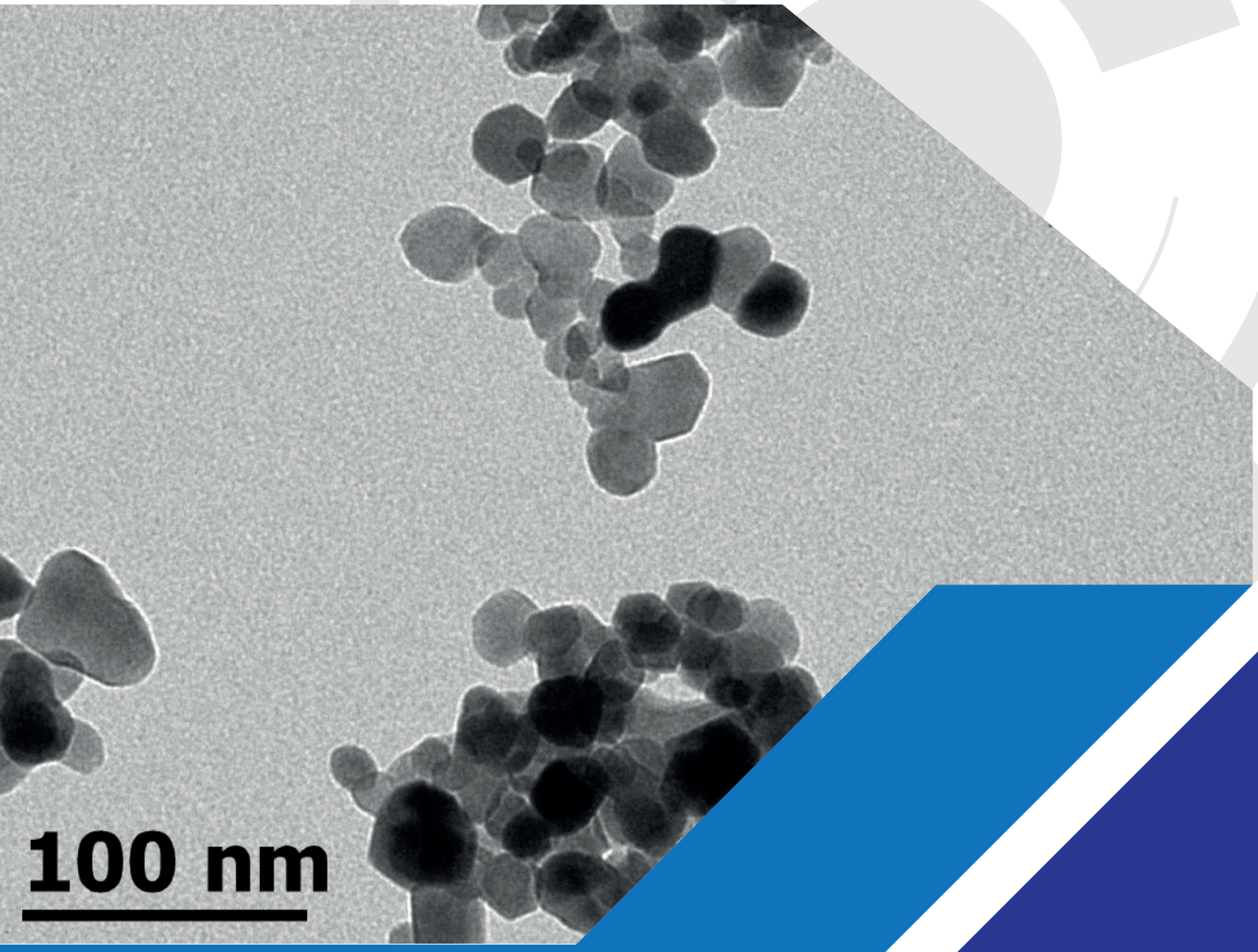

FACULTAD DE INGENIERÍA

CONCYTEQ

CONIIN

LIBRO DE POSTERS

CONACYT
Consejo Nacional de Ciencia y Tecnología

UNIVERSIDAD AUTÓNOMA DE QUERÉTARO

CONIIN

LIBRO DE POSTERS

Fracture as a critical failure in the solder joint of an electronic asembly generated by accelerated life tests.

M.I. Mariana Culebro Pérez
Universidad Autónoma de Querétaro, Facultad de Ingeniería, Departamento de Realidad Virtual y Aplicaciones Inmersivas.
maculebrop@live.com.mx, 442 592 96 93, Cerro de Las Campanas, s/n, Las Campanas, 76010 Santiago de Querétaro, Qro.

M.C. Oswaldo Mendoza-Herbert
Universidad Autónoma de Querétaro, Facultad de Ingeniería, Departamento de Realidad Virtual y Aplicaciones Inmersivas.
oswaldo.herbert@uaq.mx, 442 435 65 90, Cerro de Las Campanas, s/n, Las Campanas, 76010 Santiago de Querétaro,

***Abstract*—the accelerated life tests are used to measure the reliability of a system, in this research tests were realized to find fractures in the solder joint of electronic assemblies. This research is focused to find fractures in the solder joint because these will not allow the current flow in electronic assemblies and are considered critical failures in a system. With the obtained results, failures occasioned for fractures were find in the solder joint.**

Keywords— linear regression model, failure, fracture, accelerated life test, solder joint.

I. Introduction

An electronic assembly is a system that realizes functions as the power control, communication protocols and telemetry systems in the industry, it could be used as a conveyor belt, a welder arm or a packer; most of the industrial process have one or more electronic systems. A solder alloy is an important element for an electronic assembly because the components that form the assembly are joined with it to the motherboard allowing the conduction of electrons. Due to this, a failure in the solder joint is a critical problem because it will not allow the current flow and the function of the system will not work. Some of the failures are open circuit, short circuit, cold weld, splash, weld bridges, pores or reflux and could be originated by human errors, random system or material wear.

An open circuit could be caused by both thermal and mechanical stress, propitiating a ductile fracture in the solder alloy. Mattila [1] indicates that a fracture appears because the impurities or phenomena originated in the process of weld, for example the nucleation of microhollows or fractures for intergranularity. These impurities, scratches or tensions located in the surface of the weld propitiate places for the appearance of fractures. Therefore, it is important that the surface of the welding could be prepared in agreement to the normatives.

A ductile fracture occurs when the solder alloy is exposed to a plastic deformation due to the damage that excessive tensions as thermal variations or mechanical efforts cause. In some research is mentioned that mechanical efforts cause parallel fissures and thermal variation generates a net of multiple fissures. Moreover, it has been realized a fracture analysis using measures of the resistance and the visual inspection. Karppinen et al. [2] realized a microstructural analysis of a circuit that allow to identify visually the propagation route of fractures through micrographics obtained with a microscope of high resolution. Besides, numerous authors have been analyzed the different failures originated in the solder alloy, Laurila et al. [3] observed that the temperature fluctuations cause expansions in the solder alloy generating its degradation, therefore it has been development tests that allow to determine the capacity to resist thermal fatigue. Chen et al. [4] mentions that the electronic systems are dynamic object of charges like vibration, their investigation demonstrated that the solder alloy is a place of failures caused because of the vibrations. These authors utilized a criterion of failures for the identification of the fractures propagation, which was a consecutive increase of 20% of the initial resistance.

II. SOLDER ALLOY

In the process of welding different metals like stain (Sn), lead (Pb), antimony (Sb), copper (Cu), silver (Ag), cadmium

(Cd) and zinc (Zn) are used. The metal with major application in the industry is the laid because it is economic and its fusion point is low. The disadvantage of the laid is that it has a high grade of toxicity and due to this metals are mixed with other metals obtaining alloys and reducing the toxicity. Another reason to obtain a solder alloy is to improve the characteristics of the metals, such as thermal and mechanical resistance. The solder alloy most used is stain with lead, which has different compositions, that is the percentage of stain with lead and the variation of the fusion point. The most common composition used in electronic applications is 60% of stain and 40% of lead with a fusion point of 188ºC. The figure 1 shows a hypoeutectic microstructure of SnPb alloy.

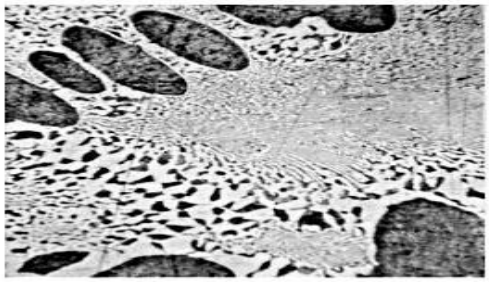

Figure 1. Hypoeutectic microstructure of SnPb alloy.

III. EXPERIMENTATION.

In the development of this research 17 electronic assemblies with measures of 2 cm per 2 cm were fabricated, where components such as leds and resistance were utilized, this with the objective of analyze the characteristics of the solder alloy. Besides, five control factor were selected, which are solder alloy, path width, temperature levels, pretreatment and vibration levels. The levels of the solder alloy are Sn40Pb60 and Sn0.3Cu0.5Ag3.5, of the path 0.38 and 0.56, of the temperature 90ºC and 125ºC, of the pretreatment with thermal shock (0ºC) and without thermal shock, of the vibration with resonance (40Hz) and without resonance.

The accelerated life test were divided in two stages, in the first stage the fundaments of the design of the test were established. In this stage four tools were used, which are the functional block diagram, the fault tree analysis (FTA), the failure mode and effects analysis (FMEA) and the parameters diagram. To elaborate this tools, field information, terms of use and technical sheet were utilized. On the other hand, the stage two consisted in the test design, where the failure modes, the stress variables and the test conditions were established. In the failure mode effect analysis, the fracture in the solder alloy was the failure mode with major grade of severity with a NPR of 300, this due to the solder alloy is found in the pines of each component allowing the current flow. With the fault tree analysis the causes of the failure were found; which are the temperature and vibration. The figures 2 and 3 show the equipment used in the accelerated life tests.

Figure 2. Drying oven used for experimentation.

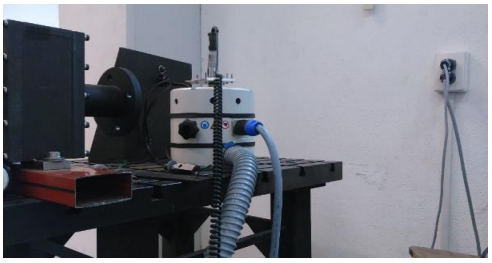

Figure 3. Phase two for the simulation of vibrations.

To calculate the accelerated factor of the temperature test, the Arrhenius equation were used (equation 1). This mathematical equation allow to escalate the time of the test with the time of use.

$$A_f = \left[\frac{\ddot{E_a}}{k}\left(\frac{1}{T_u} - \frac{1}{T_c}\right)\right] \quad (1)$$

Af is the accelerated factor.
Ea is the activation energy or the typical valor for a mechanism of failure derivative of empirical data.
K is the Boltzmann's constant ($8.6171\ x\ 10{-}5\ eV$).
Tu is the temperature of use in ºK.
Tt is the temperature of the test in ºK.

To calculate the equivalence on days of the test to a year in terms of use, the days of the year were divided by the acceleration factor.

III. RESULTS.

The table 1, shows the results obtained in the lineal regression, where it can be observed that the high level of the temperature is significant with a p value of 0.001 and the stain lead alloy is significant with a p value of 4.74e-07. The coefficients R^2 y R^2 adjusted have a value of 86% and 84% respectively and the p value of the model is 8.014e-07 indicating that this is a significant model.

TABLE 1. LINEAL REGRESSION OF THE DATA.

Lineal regresssion.				
Coeficientes	Estimate std.	Error	T value	Pr(>|T|)
(Intercepto)	653.24	37.28	17.521	6.41e-11
Aleasnpb	-370.03	42.28	-8.753	4.74e-07
temp+	-174.97	42.28	-4.139	0.001
Residual standard error: 86.87 on 7 degrees of freedomMultiple R-squared: 0.8654, Adjusted R-squared: 0.8461 F-statistic: 45 on 2 and 14 DF, p-value: 8.014e-07				

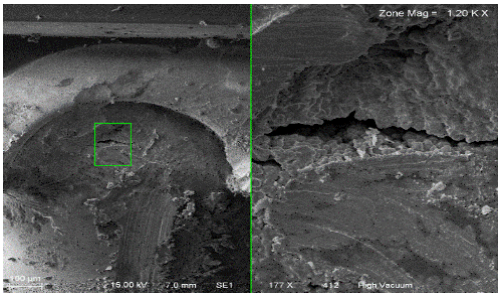

Figure 4. Fracture in a solder alloy of SnPb.

The figure 4 shows a fracture in a solder alloy was found by an image obtained with a scanning microscope.

IV. DISCUSSION.

It is observed that the data adjusted to the regression analysis and the weibull reliability distribution. The data indicated that they can represented the failure phenomena in the electronic assembly. This because the R values are high and close between them. The results show that a fracture is a critical cause of failure in a solder joint.

REFERENCES

[1] Mattila, T., Li, J., and Kivilahti, J. ”On the effects of temperature on the drop reliability of electronic component boards”. *Microelectronics Reliability*, *52*(1), 165–179, 2012.

[2] Karppinen, J., and Li, J. The Effects of Concurrent Power and Vibration Loads on the Reliability of Board-Level Interconnections in Power Electronic Assemblies, *13*(1), 167–176, 2013.

[3] Laurila, T., Karppinen, J., Li, J., Vuorinen, V., and Paulasto-Kröckel, M. ”Effect of isothermal annealing and electromigration pre-treatments on the reliability of solder interconnections under vibration loading”. *Journal of Materials Science: Materials in Electronics*, *24*(2), 644–653, 2012.

[4] Chen, H., Han, J., Li, J., and Li, M. ”Inhomogeneous deformation and microstructure evolution of Sn-Ag-based solder interconnects during thermal cycling and shear testing”. *Microelectronics Reliability*, *52*(6), 1112–1120, 2012.

Rainwater harvesting for household use.

F. Colom-R, A. Soriano-G, J.M. Hernández-Martínez, G. J Ríos Moreno, O. Chávez Alegría, M. Trejo-Perea*

Abstract
Now a days, water expenditure in households has increased due to the improper use of water in various activities such as: gardening, car washing or household cleaning. This causes water scarcity and an increase in household economic expenditure.
In order to deal with this problem, a mathematical model was established, in which the amount of water collected during the year is calculated in order to carry out all the aforementioned activities, in which variables such as catchment area, Rainfall, expenditure on a house-room and the size of the tank.
The calculations were made for a house-room made up of 5 people, which gave us an expense of 600 liters per day (120 liters per person), distributed as follows: 240 WC, 120 shower, 60 clothes, 30 kitchen and 150 irrigation (all in liters).

Key words — *Rain water, waste, reuse, system, drainage, home room.*

I. *INTRODUCTION*

The reuse of rainwater today is fundamental for domestic use, however, it is not exploited in any way. Currently there is a water loss of approximately 72.5% that could be used in various daily activities essential for the home. There is no doubt that water is the main and most important component of the planet, could be considered as an essential resource, which is granted by land. It is a shame that human beings do not even realize the role that this resource has for human development and no reaction on their part to promote the care and use of water.

The proposal that has to solve the problem, is the implementation of a mathematical model, which having a catchment area could be clearly observed in what aspects can be used rainwater. All this as previously said is according to the area of catchment that has, which is applied an efficiency factor of 80% because of losses. In the same way you have certain filters through which the water passes to make it more useful and of better quality. This model is different in each place, because it is done according to the precipitation of rain that has month to month in order to be able to perform the necessary calculations and to know how much you have and never need.

Water uses are classified into two types, consumptive and non-consumptive. Consumption is one in which there is water loss, that is, the quantity that comes out is less than the quantity that is returned to the supply. On the other hand, non-consumptive is one in which there are no minimum losses or losses that can be considered null (Stealth Survival, "Rainwater collection" RIVERWALKER, 2009).

Most sustainable building codes force or recommend the installation of rainwater harvesting systems (RHS) in buildings to achieve sustainable development goals. The widespread perception of RHS as an environmentally friendly initiative stems from its benefits for integrated water management strategies, including but not limited to: saving potable water; Mitigation of floods in urban watersheds and extensive impermeable areas; Reduction of nutrient loads to waterways; And the increase in the useful life of the centralized water distribution infrastructure restricted due to reductions in demand (Abel S. Vieiraa, 2014).

The success of rainwater harvesting systems depends to a large extent on the identification of suitable sites and their technical design (Ahmad, 2013). Several methodologies have been developed for selecting sites and techniques suitable for RWH (Oberle, 1998; Han, 2012). Field surveys are the most common method for selecting appropriate sites and RWH techniques for small areas. Selecting appropriate sites for different RWH technologies in larger areas is a major challenge. (Mun y Han, 2012).

This article focuses on the development of an optimal design for a rainwater reuse system in the domestic environment; with the objective of designing an effective rainwater capture and processing system for home-room use based on a previously studied physical model, in order to economize and promote a conscious and responsible behavior of the care of the environment. As well as making the best use of water resources through the collection of rainwater and the rational

use of water, differentiated in pure, rainwater, residual and recycled water.

II. THEORETICAL CONSIDERATIONS

Initially, an investigation was made of the annual precipitation of rainfall in the state of Querétaro (Comisión Nacional del Agua. Registro Mensual de Precipitación Pluvial en mm.), but that data were given month by month, in order to perform the calculations Necessary to know the amount of water stored in the cistern.

For more accurate results, the monthly average rainfall (Pmn) from 1921 to 2013 was taken into account. As a next step, the total catchment area (AT) was calculated, after finishing the channel in which it would be obtained Greater amount of catchment area, to later apply an efficiency factor of 80% due to losses of different types.

$$A = 0.8 * A_T \tag{1}$$

Once the actual catchment area has been calculated, the next step is to multiply the area (in square decimeters) by the monthly precipitation (in decimeters) to calculate the amount of water (W_n) in the storage tank (in liters), the n depends on the month of the year to be calculated. In the same way, it is necessary to subtract the amount of water that is used in this case is for irrigation (R), as is done the project for simple gardens, it is considered that 4 liters of water per square meter of the garden area (A_j), To calculate the amount of irrigation (R) a multiplication of these variables would be performed for the days of irrigation needed according to the precipitation of the month (the result would be obtained in liters). It should be mentioned that the amount for irrigation in the months of June, July, August and September are equal to zero, because it is not necessary to use what is stored by the rains.

$$W_n = A * Pm_n - R \tag{2}$$

Where:

$$R = 4 * A_j * d \tag{3}$$

$$si\ n = 6,7,8\ y\ 9\ ; d = 0;\ \therefore R = 0$$

As in June (n = 6) is when the rainy season begins in that month to calculate the amount of water that begins to accumulate in the cistern, where the equation would be as follows:

$$\therefore W_6 = A * Pm_6 \tag{4}$$

This operation will be done month by month adding the amount of water you have and subtracting the amount of water that is used for what in this case is irrigation:

$$W_7 = W_6 + A * Pm_7 \tag{5}$$

This would be successively without taking into account the R, until the month of October where R would take a value of 1 since the precipitation begins to fall so that later in the months of November, December, January, February, March and April take a Value of 5 and finally in May it would take a value of 2.

$$si\ n = 10\ ; d = 1;\ R = 4 * A_j$$

$$\therefore W_{10} = W_9 + A * Pm_{10} - 4 * A_j \tag{6}$$

$$si\ n = 11,12,1,2,3,4\ ; d = 5;\ R = 20 * A_j$$

$$\therefore W_n = W_{n-1} + A * Pm_n - 20 * A_j \tag{7}$$

* When it reaches 12 that would be the month of December the next month would be January and n would take value of 1 and its n-1 would take the value of 12.

$$si\ n = 5\ ; d = 2;\ R = 8 * A_j$$

$$\therefore W_5 = W_4 + A * Pm_5 - 8 * A_j \tag{8}$$

III. METODOLOGÍA

The Universidad Autónoma de Querétaro provided us with a catchment area located in the same, a cistern, part of the channel and pipeline (Figure 1) and some of the missing materials for the system.

The next step was the completion of the channel, this in order to have a larger catchment area and avoid greater losses of water. This was done with partitions, cement, sand and water (Figure 2).

Likewise, the pipeline was connected to the cistern and to a device called "tlaloque" which serves to store the first rains that, due to dirt from the roof, is the most contaminated water that is during the year. For this, a 200-liter drum and tubes, elbows, reducers and T-connections of sanitary grade PVC were used.

Figure 1- catchment area

As a next step a natural waterproofing made of nopal slime was made. For this, cactus nopal pieces were first cut into small pieces, placed in the middle of a 20-liter bucket and filled with water to leave it standing for one day (Figure 3). After rest, 5 kg of lime and a half kilo of salt were placed and

subsequently painted and waterproofed on the outside of the tank.

Finally, a blacksmith was hired to take care of the construction and installation of a 60x40 cm cover, which served as protection for the interior of the cistern (Figure 4).

Figure 2-Channer termination

Figure 3-Preparation of waterproofing

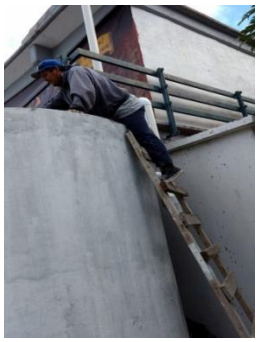

Figure 4- Placement of tank lid

IV. RESULTS

First, the previously mentioned data of the annual precipitation of rainfall in the state of Querétaro (National Water Commission, Monthly Rainfall Precipitation Register in millimeters) were obtained, which can be seen in Table 1.

For purposes of this article we worked with a smaller catchment area and instead of requiring to satisfy a house with 5 members, the goal was a small garden of 23.2 m^2.

In addition to that, it was not necessary to build a new catchment area since there was already one previously, so only the catchment system and pipes were adapted.

What was sought was that when entering the data of both catchment area and water that would be used, the data from the program were never negative, which was initially not achieved (Figure 5).

This was when introducing a catchment area of 41.2m^2. So we proceeded to cast a wall a little longer and higher to have a larger area.

For trial number two, a catchment area of 83,842 m^2 was obtained and an area of 23.2 m^2 was required, and once it was introduced in the previously mentioned program, it showed favorable results, all positive (figure 6), which means That in all months of the year the cistern adapted to the catchment system will have water, it will never be empty.

These calculations were the first part of the project, so the next step is the operation of the system for domestic use, it was decided to split into two parts to facilitate the work.

The first part is the connection of the system for an irrigation use only, then with the necessary filters, the connection could be made to be distributed as if it were in a house-room, all this always taking into account the amount of water in the tank so that our system is always self-sufficient.

Table 1. Monthly precipitation in Querétaro.

Monthly precipitation in Querétaro, Querétaro.													
Season	**Period**	**Mes**											
Concept		***Jan***	***Feb***	***Mar***	***Apr***	***May***	***Jun***	***Jul***	***Aug***	***Sept***	***Oct***	***Nov***	***Dic***
Querétaro	2013	3.1	0	4.1	0.7	64.9	62	110.2	42	172.3	30.4	25.3	24.5
Average	De 1921 a 2013	11	7.4	6.3	16.3	34.7	103.3	128	91.3	94.6	38.2	11.3	8.3
Drier year	2000	0	0	0	3.5	11.9	35.1	42.4	41.5	34.5	0.5	18.3	0
Rainier year	1933	9.7	3.6	6.5	15.8	4	21	401	250.6	269	18	0	0

Calculo de almacenamiento de agua pluvial en casa habitacion TABACHINES															ducha	0%	0
														Consumos :	ropa	0%	0
															cocina	0%	0
Area de azoteas		41.2	m2												riego patio	100%	92.92
(factor de eficiencia del 80%)		3296	dm2												tot lt/dia	100%	92.92
Precipitacion media mensual			mm														
		Ene		Feb	Mar	Abr	May	Jun	Jul	Ago	Sep	Oct	Nov	Dic			
dias por mes		31		28	31	30	31	30	31	31	30	31	30	31			
precipitacion/mes mm		11		7.4	6.3	16.3	34.7	103.3	128.8	91.3	94.6	38.2	11.3	8.3			
En dm		0.11		0.074	0.063	0.163	0.347	1.033	1.288	0.913	0.946	0.382	0.113	0.083			
Precipitacion en azoteas Lt:		363		244	208	537	1,144	3,405	4,245	3,009	3,118	1,259	372	274			
de Reciclado Pluvial																	
0	*lt/dia*																
Consumo/mes WC.(s/lf 81)		0		0	0	0	0	0	0	0	0	0	0	0			
92.92	*lt/dia*																
Consumo/mes patio limpieza		2880.52		2601.76	2880.52	2787.6	2880.52	2787.6	2880.52	2880.52	2787.6	2880.52	2787.6	2880.52			
jardin A		*23.23*	*m2*		*4*	*lt/m2/dia*											
dias de riego por mes:		5		5	5	5	2	0	0	0	0	1	5	5			
Consumo riego A (sobrante)		464.6		464.6	464.6	464.6	185.84	0	0	0	0	92.92	464.6	464.6			
Consumo total de Pluvial:		3345.12		3066.36	3345.12	3252.2	3066.36	2787.6	2880.52	2880.52	2787.6	2973.44	3252.2	3345.12			
Acumulado de Pluvial							0	617	1,982	2,111	2,441	**727**	- 2,153	- 5,225			
		- 8,207		- 11,030	- 14,167	- 16,882	- 18,805										

Figura 5-Datos negativos acumulados

Figura 6-Datos positivos acumulados

Calculo de almacenamiento de agua pluvial en casa habitacion TABACHINES															ducha	0%	0
														Consumos :	ropa	0%	0
															cocina	0%	0
Area de azoteas		83.842	m2												riego patio	100%	92.92
(factor de eficiencia del 80%)		6707.36	dm2												tot lt/dia	100%	92.92
Precipitacion media mensual			mm														
		Ene		Feb	Mar	Abr	May	Jun	Jul	Ago	Sep	Oct	Nov	Dic			
dias por mes		31		28	31	30	31	30	31	31	30	31	30	31			
precipitacion/mes mm		11		7.4	6.3	16.3	34.7	103.3	128.8	91.3	94.6	38.2	11.3	8.3			
En dm		0.11		0.074	0.063	0.163	0.347	1.033	1.288	0.913	0.946	0.382	0.113	0.083			
Precipitacion en azoteas Lt:		738		496	423	1,093	2,327	6,929	8,639	6,124	6,345	2,562	758	557			
de Reciclado Pluvial																	
0	*lt/dia*																
Consumo/mes WC.(s/lf 81)		0		0	0	0	0	0	0	0	0	0	0	0			
92.92	*lt/dia*																
Consumo/mes patio limpieza		2880.52		2601.76	2880.52	2787.6	2880.52	2787.6	2880.52	2880.52	2787.6	2880.52	2787.6	2880.52			
jardin A		*23.23*	*m2*		*4*	*lt/m2/dia*											
dias de riego por mes:		5		5	5	5	2	0	0	0	0	1	5	5			
Consumo riego A (sobrante)		464.6		464.6	464.6	464.6	185.84	0	0	0	0	92.92	464.6	464.6			
Consumo total de Pluvial:		3345.12		3066.36	3345.12	3252.2	3066.36	2787.6	2880.52	2880.52	2787.6	2973.44	3252.2	3345.12			
Acumulado de Pluvial							0	4,141	9,900	13,143	16,701	**16,289**	13,795	11,007			
		8,399		5,829	2,907	748	9										

V. CONCLUSIONS

This project was done for a good cause in our university since this system of water collection is a very viable option to feed an irrigation system, thanks to the calculations made, we obtained that the capacity of our cistern is adequate and that this will be Capable of supplying the entire irrigation system covering the entire garden area without the need to extract water from any other source.

In addition, we leave a water outlet without connecting yet, this in order to work in the future connecting it to other pipes that will be destined to applications like the water supply for the bathrooms of the faculty.

As we are not in the rainy season for the time being it will be difficult to obtain results of our project immediately, so it is advisable to mention that the physical results that we obtain in terms of our project will take about a year to manifest, since it

is a system designed To work throughout the year according to the variations that occur during this year.

VI. REFERENCES

[1] Stealth Survival, "Rainwater collection" RIVERWALKER. stealthsurvival.blogspot.mx/2009/05/rainwater-collection-advantages-and.html

[2] Abel S. Vieiraa, Cara D. Bealb, Enedir Ghisia, Rodney A. Stewart. Renewable and Sustainable Energy Reviews 34 (2014) 225-242.

[3] Ahmad (2013), I. Ahmad, Investigating of potential water harvesting sites at Potohar using modeling approach, Pakistan Journal of Agricultural Sciences, 50 (4) (2013), pp. 723–729

[4] Mun and Han, 2012, J.S. Muna, M.Y. Hanb, Design and operational parameters of a rooftop rainwater harvesting system: definition, sensitivity and verification, Journal of Environmental Management, 93 (2012), pp. 147–153

[5] J. S. Muna, M.Y. Han, Design and operational parameters of a rooftop rainwater harvesting system: Definition, sensitivity and verification, Journal of Environmental Management, 2012.

[6] Ahmad (2013), I. Ahmad, Investigating of potential water harvesting sites at Potohar using modeling approach, Pakistan Journal of Agricultural Sciences, 50 (4) (2013), pp. 723–729

[7] Farreny (2011), X. Gabarrell, Cost-efficiency of rainwater harvesting strategies in dense Mediterranean neighbourhoods, Resources, Conservation and Recycling, Elsevier, 9.

[8] Han, M.Y., Mun, J.S., 2008. Particle behaviour consideration to maximize the settling capacity of rainwater storage tanks. Water Science & Technology 56 (11), 73e79.

[9] Helmreich (2009), H. Horn, Opporunities in rainwater harvesting, Elsevier, 7.

[10] Vieira (2014), D. Beal, Energy intensity of rainwater harvesting systems: A review, Elsevier, 18.

[11] A. Campisano, C. Modica, Selecting time scale resolution to evaluate water saving and retention potential of rainwater harvesting tanks. Procedia Engineering, Elsevier 70 (2014) 218 – 227.

[12] B. Kus, J. Kandasamy, S. Vigneswaran, H.K. Shon, Water quality in rainwater tanks in rural and metropolitan areas of New South Wales, Australia. Journal of water Sustainability 1 (2011), 33-43.

[13] EF Conserve Energy Future, Be Green Stay Green. http://www.conserve-energy-future.com/Advantages_Disadvantages_Rainwater_Harvesting.php

[14] Gupta, Deelstra, & Sharma (1997), Gupta, K. K., Deelstra, J., & Sharma, K. D. (1997). Estimation of water harvesting potential for a semiarid area using GIS and remote sensing. IAHS Publications-Series of Proceedings and Reports-Intern, Assoc Hydrological Sciences, (pp. 63), 242.

[15] Gupta, Deelstra, & Sharma (1997), Gupta, K. K., Deelstra, J., & Sharma, K. D. (1997). Estimation of water harvesting potential for a semiarid area using GIS and remote sensing. IAHS Publications-Series of Proceedings and Reports-Intern, Assoc Hydrological Sciences, (pp. 63), 242.

Development of a hybrid base solar cell PTB7 doped with CdS and FeS_2 nanoparticles.

Ing. Jorge Cruz Gómez
Student of Energy Science Master
Autonomous University of Queretaro
Queretaro, México
jorge_jcg@icloud.com

Dr José Santos Cruz
Coordinator of Energy Science Master
Autonomous University of Queretaro
Queretaro, México.
j.santos@uaq.edu.com

***Abstract*—the need for clean energy is undoubtedly to cover the decline in the availability of fossil fuels and maintain the level of well-being achieved by the current civilization; and as a main objective reduce the emission of carbon dioxide to the environment. Within these efforts is the use of photovoltaic cells and in particular those of organic type. This project focuses on these cells, which have desirable advantages such as cost, flexibility and easy processing, but also present very important challenges such as increasing their efficiency and increasing their life cycle; these challenges are the focus of much research. In particular, this project proposes a way to improve its effectiveness by the doping with the inorganic nanoparticles of CdS and FeS the semiconductor polymer PTB7. It is expected to obtain efficiency higher than 7% and to determine the effect of doping level with these nanoparticles on the properties of this polymer.**

Keywords—organic cells; inorganic nano-particles; photovoltaic cells; doping

I. INTRODUCTION

So far, efficiencies have been reported in solar cells (of research) close to the theoretical limits, particularly in those cells composed of inorganic materials; However they have drawbacks such as the cost of manufacture [1], that their origin process generates carbon dioxide and also at the end of their useful life, which are approximately 20 years, their final destination must be in confinement due to the materials used. A viable option are cells based on organic materials, which in contrast, have a low cost of production and do not generate hazardous waste, other important advantages are ease of processing, flexibility and lightness that allow new technological applications. However there is still a gap, between the efficiency and the life time that have been achieved with these devices and that obtained from inorganic cells.

The electric field in an organic cell can be generated by the union of two layers, one with an electron-accepting compound and the other with a donor compound. An acceptor is a compound that due to large electro negativity draws electrons from a chemical system. On the other hand, a donor is a compound that gives electrons to the system. The donor in the solar cell is the light absorbing material, a polymer or a small molecule, in which an electron is excited and transferred to the acceptor. In order to increase the efficiency in organic cells it is necessary to avoid the recombination of the exciton (electron-hole pair) formed after the absorption of the photon of light, since the dissociation of the exciton is what generates that the free loads are directed to the respective electrodes thus generating the electric current. The problem experienced by organic materials is that the energy difference between the two layers is very high and the dissociation of the exciton in two free charges is very poor, in addition the required energy would enter the ultraviolet range, which is also a problem because this type of light is not the most intense in the solar spectrum that we receive, besides it generates free radicals inside the polymer, which interfere with the efficiency of the cell and cause its degradation.

For the development of organic photovoltaic structures of better PCE (Potency Conversion Efficiency) and useful life, the correct choice and mixing of materials is of fundamental importance for the reasons mentioned above. The PTB7, to date is one of the most promising semiconductor polymers, can be synthesized in 3 or 4 very short steps depending on the method chosen, easy to process, relatively stable, inexpensive and affordable. But despite all the above advantages, the challenge with PTB7 is to overcome the poor overlap with the solar spectrum, due to which the efficiency (PCE) achieved so far is 7.62% for an organic ternary solar cell [2].

The method to be used to increase the potency of the organic cell is through the doping process, using the CdS and FeS_2, the added or extracted charge of the polymer generates "islands" of load (solitons, polarons or bipolarons), around the Ions of the doping substance. Polymers having conjugated aromatic rings do not form solitons, but polarons (cationic radicals) or bipolarons (polaron pair with opposite spin). When a high degree of doping of the polymer chains is achieved, the "islands" begin to overlap, resulting in semi-filled bands, through which the electrons can flow freely, see Figure 1. Therefore, the generation of charges in the polymer chains leads to the formation of intermediate energy bands between the HOMO and LUMO levels of the material. The polymer thus becomes conductor of electricity.

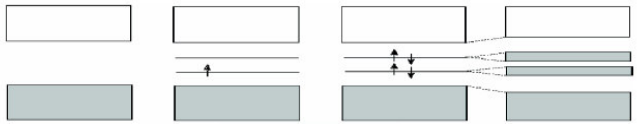

Figure 1.Diagram of evolution of the bands during the doping process by introduction of positive ions

PTB7, Figure 2, gives some of the highest reported efficiencies for polymer: fullerene solar cells due to its extended absorption into the near infra-red and lower HOMO level. PTB7 becomes a quick and easy way to improve device efficiencies and represents a cost effective method to increase performance and impact of devices and data for a wide range of OPV related research.

The high solubility in a wide range of solvents makes ink preparation simple and PTB7 one of the easiest materials to work with. This also makes it an excellent candidate for a variety of coating techniques including ink-jet printing, spray coating and blade coating.

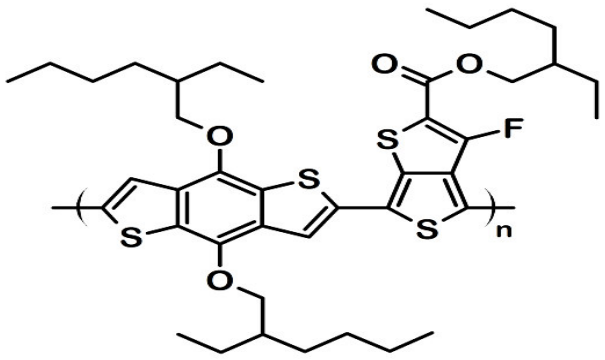

Figure 2.PTB7 Polymer semiconductor molecule.

R. Sharma, S. Bhalerao, and D. Gupta [3], show that with the slightly elongated and highly crystalline synthesized CdS nanoparticles with their absorption in the visible region, the experimental results for devices in an inverted geometry with an ITO / ZnO structure / PTB7: CdS: PCBM / MoO_3 / Ag have shown an increase in PCE by almost 10%. However, it was observed that this increase is only when the nano-particles were added at the low concentration in the active layer.

The use of FeS_2 as an active layer is recommended in photovoltaic solar cells because pyrite has a suitable band gap (Eg = 0.95 eV), strong light absorption (R> 105 cm -1 for hν> 1, 3 eV), a suitable minor carrier diffusion length (100-1000 nm), and essentially infinite elemental abundance [4].

With the addition of FeS_2 nano-particles in polymer solar cells, improved light harvesting was achieved, resulting in an apparent increase of Jsc, whereas too many FeS_2 nano particles brought the electron transmission loss defects. The solid solar cell reached its optimum PCE of 3.0% at an FeS_2 concentration of 1.25 mg / ml [5].

Work on solar cells based on PTB7: PCBM: ICBA of high population level in excited states means that the separation of charge is significantly reduced in such systems. In addition, the polar-ionic states are also very populated, implying that the dissociation of charge is also very affected. The authors consider that the results of this study will provide information on which material can be appropriately designed and selected for high efficiency organic solar cells [3]

The low conductivity in the polymers is a challenge since the exciton generated by the solar radiation depends on the diffusion length or excitation energy of the electrons in order to be able to transport greater lengths inside the semiconductor volume and thus the load carriers are not lost, Through annihilation processes, they need to be collected at the anode and cathode of the solar cell. To solve this situation, the use of hybrid materials (organic inorganic, PTB7-CdS, FeS_2) is proposed to combine the properties of both, where the inorganic material is introduced as a nano particle and impurified to the organic. By properly combining the properties of nano particles, the diffusion lengths of the charge carriers are favored, as well as the electrical properties.

Efficiency of a solar cell can be calculated from its characteristic voltage density curves (J-V). From such curves, the Open Circuit Voltage (Voc), the Closed Circuit Current Density (Jsc) and the Fill Factor (FF) can be obtained. Thus the Potency Conversion Efficiency (PCE, in the formula ŋ) can be determined according to the following equation:

$$\eta = \frac{Jsc\ Voc\ FF}{P_s} \qquad (1)$$

Where Ps is the energy density of the incident light [6].

II. METODOLOGY.

The development of the hybrid solar cell requires synthesizing nano particles of CdS, FeS_2 and TiO_2, cadmium sulfide by chemical bath and iron disulfide by colloidal chemical synthesis[4] and titanium dioxide by sol-gel process.

Synthesis of CdS. At room temperature and under constant stirring, 50 ml of 0.1 M solution of cadmium acetate in

methanol are slowly added dropwise to 50 ml of a 0.1 M solution of sodium sulfide in methanol. The resultant CdS, figure 3, nanoparticles are filtered, washed and dried.

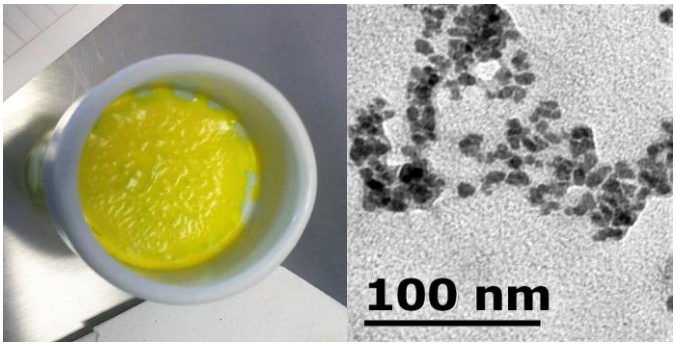

Figure 3. CdS particles before dry and TEM image.

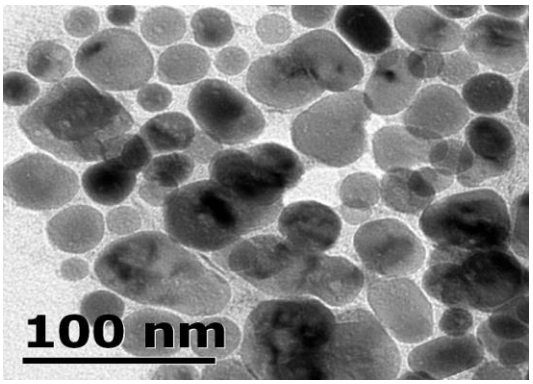

Figure 5. TEM image of FeS_2 nano particles

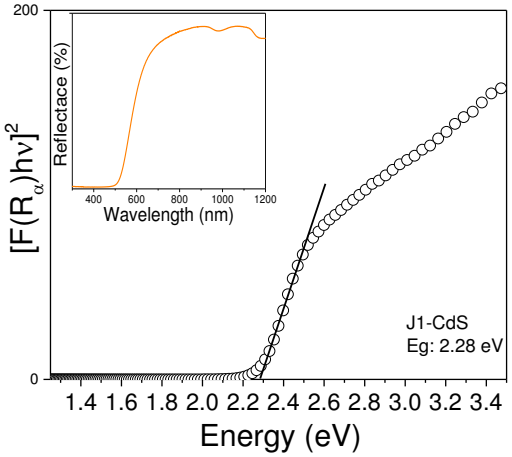

Figure 4. Difuse reflectance of CdS.

Figure 6.Laboratory synthesis equipment and wet FeS_2.

Synthesis of FeS_2. Needs the following precursors: Diphenyl ether ($C_{12}H_{100}$) and sulfur, and on the other hand Iron Chloride ($FeCl_2$) and Octadecylamine ($C_{18}H_{39}N$), the precursors are introduced into a three-necked flask, Figure 5, in an inert environment (Argon gas) . The solutions are heated for one hour at 70 and 120 ° C respectively. Subsequently, the two solutions that were formed are put together and held for three hours at a temperature of 220 ° C, time required to form the desired compound. Finally, the solution is allowed to cool to room temperature and 20 ml of methanol and 10 ml of chloroform are added in a beaker, which is allowed to settle for 24 hours. The solution with the nano particles is cleaned by extracting the excess solution of methanol and chloroform and adding 15 ml of methanol and 10 ml of chloroform, leaving it in an ultrasonic bath for 5 minutes and letting the nano particles settle, all of this is repeated for a week, to observe that the solution is transparent. The precipitate is then dried in a hot dish at 75 ° C. The obtained nano crystals (FeS_2), figure 4, are redispersed in a suitable solvent (chloroform or di-chlorobenzene)

Synthesis of TiO_2. The reagents that were used for the preparation of the sol-gel solution of TiO_2 are:

30 ml. of $H_3CHCOHCH_3$, J.Tbaker 99.9%.
4 ml of Ti {OCH $(CH_3)_2\}_4$, 97%.
120 µl. HCl J. Tbaker 70%.
730 µl deionized water.

In a vial add 15 ml of ethanol (all in relation to the ml of titanium isopropoxide). On the other hand, 730 µl of water, 120 µl of hydrochloric acid and 15 ml of ethanol are mixed in a beaker. The ethanol flask, the vessel with the above mixture and the titanium isopropoxide will be placed inside a glove box (with nitrogen atmosphere), a nitrogen gas flow will be allowed to pass for fifteen minutes, to ensure that it has complete moved through all the air contained inside the box. Subsequently, 4 ml of titanium isopropoxide will be added to the bottle with ethanol and mixed manually. The contents of the beaker will be slowly added to the bottle under slow stirring. Finally, the bottle will close tightly and the solution can be used immediately. The TiO_2 solution will be poured

into a vessel suitable for deposition of the films, using a dipping / removing apparatus / system, according with step II of the development of the hybrid cell.

Hybrid Cell Development

Step I. This stage must be carried out in a glove box with a nitrogen atmosphere, for which, after putting all materials and equipment, open valves and regulates the flow, after 15 minutes can be started to work. Find the mixture of CdS and FeS_2 nanoparticles with better photoelectric properties for electrical generation. In this stage it is necessary to perform tests with different concentrations of each nano particle, for which a solution is made with the polymer PTB7 and by means of spin counter a film is deposited in glass substrate, all this process must be in an environment of gaseous nitrogen to avoid polymer oxidation, and after heat treatment the photoelectric properties are reviewed to correlate the concentration effect on the film properties.

Step II. After the analysis of the data of step I we can decide for the best mixture of nano particle / polymer PTB7 and to include it in the development of the cell. The cell is started with ITO glass conductive, to which four films of nano particles TiO_2 obtained by sol-gel are deposited by insertion remotion technique. Between each deposit requires gentle heat treatment and at the end heat treatment for one hour at 550° C.

Step III. This stage must be carried out in a glove box with a nitrogen atmosphere, for which, after putting all materials and equipment, open valves and regulates the flow, after 15 minutes can be started to work. The next step is to deposit the polymer PTB7 / NanoP in the concentration found in stage I, this is done under a nitrogen atmosphere, and then heat treatment is performed.

Step IV. At the end the MoO_3 / Ag electrode is deposited by electro deposition under vacuum.

III. CHARACTERIZATION.

Characterization is necessary to be sure that our results are repeatable and to obtain the efficiency of the cell developed, for this we have the following equipment:

• UV-Vis spectrophotometer, 190-1100nm, transmission and absorption UV-Vis; Genesys 10S Thermo Scientific. Ideal for basic assurance, quality control, routine analysis, training and educational laboratories.
Precision electronics and simple single-beam optical geometry provide accurate measurements.

•Quantum Efficiency. QEPVSI-b System, Newport Corporation. Is a way to measure External Quantum Efficiency (QE or EQE), also known as Incident Photon to Charge Carrier Efficiency (IPCE).

• Morphological characterization by AFM, Nanosurf 2. Is an atomic force microscope system that can make nanometer scale resolution measurements of topography and several other properties of a sample?

• X-ray diffraction, Rigaku Miniflex, copper radiation, 2 theta, 15KV. It is a general purpose X-ray diffract-meter that can perform a qualitative and quantitative analysis of polycrystalline materials.

• Electrical characterization of the devices by curves J-V, Solar simulator Oriel 68820 Universal Power Supply (400-1000W). Solar simulators are intended for researchers requiring the performance of a certified system over a small area of illumination.

• Profiler, KLA Tencor, D-100. Measures 2D topography of surfaces

• Hall Effect, Ecopia, HMS-3000. Is a complete system for measuring the resistivity, carrier concentration, P/N type, and mobility of various materials including semiconductors (N Type & P Type) such as Si, Ge, SiGe, SiC, GaAs, InGaAs, InP, GaN, ZnO, TCOs, metals, oxides, etc., at both 300K and 77K

IV. EXPECTED RESULTS

It is projected to obtain efficiency greater than 7% and to determine the effect of nano-particles doping level in properties of this polymer.

V. REFERENCES

[1] M. Martínez Bogado, “Materiales y materias primas,” p. 33, 2011.

[2] Q. An *et al.*, “Efficient organic ternary solar cells with the third component as energy acceptor,” *Nano Energy*, vol. 26, pp. 180–191, 2016.

[3] R. Sharma, S. Bhalerao, and D. Gupta, “Effect of incorporation of CdS NPs on performance of PTB7: PCBM organic solar cells,” *Org. Electron. physics, Mater. Appl.*, vol. 33, pp. 274–280, 2016.

[4] J. Puthussery, S. Seefeld, N. Berry, M. Gibbs, and M. Law, “Supporting Information for Colloidal Iron Pyrite (FeS_2) Nanocrystal Inks for Thin Film Photovoltaics,” *J. Am. Chem. Soc.*, vol. 133, no. 4, pp. S1–S9, 2011.

[5] L. Luo, W. Luan, B. Yuan, C. Zhang, and L. Jin, “High Efficient and Stable Solid Solar Cell: Based on FeS_2 Nanocrystals and P3HT: PCBM,” *Energy Procedia*, vol. 75, pp. 2181–2186, 2015.

[6] T. Xu and Q. Qiao, “Conjugated polymer–inorganic semiconductor hybrid solar cells,” *Energy Environ. Sci.*, vol. 4, no. 8, p. 2700, 2011.

Biodiesel production from waste cooking oil over MgO/SBA-16 catalysts and ultrasonic radiation

Vázquez-Maya N. [#1], Nava-Mendoza R. [#1]

[#1] *División de Investigación y Posgrado, Facultad de Ingeniería, Universidad Autónoma de Querétaro (UAQ), Cerro de las Campanas s/n, C.P. 76000 Querétaro, Qro., México*

[1] naancyvm5@gmail.com

[2] rufino@uaq.edu

***Abstract*—Heterogeneous alkali catalysts MgO-SBA-16 type were prepared and applied for the biodiesel transesterification reaction of waste cooking oil. Transesterification reactions were performed by high frequency ultrasonic radiation. MgO particles were deposited in the SBA-16 mesoporous material, with different percentages by weight of MgO (5, 10 and 20%). The catalysts were characterized by Chemical analysis by Inductively Coupled Plasma Atomic Emission Spectroscopy (ICP-AES), N_2 physisorption (SBET), X-ray diffraction (XRD), high-resolution transmission electron microscopy (HRTEM), scanning electron microscopy (SEM), diffuse reflectance spectroscopy in the ultraviolet-visible range (DRS uv-vis) and Thermogravimetric analysis (TGA). The quality and chemical composition of waste cooking oil, as well as quality, chemical composition and yield of biodiesel obtained were determined by different physicochemical techniques. In accordance to experiments, the catalyst that showed the highest catalytic activity was 20% by weight of MgO in the SBA-16 and the best reaction conditions that were obtained were a molar ratio 3:1 (methanol/oil), reaction temperature of 60°C and 1% of catalyst loading. The time for the ultrasonic radiation method was of 5 minutes and amplitude in the sonotrode of the 50%. The conventional method had a yield (90-93%). The ultrasonic radiation helped transesterification with a high yield (93-95%).**

***Keywords*—transesterification; biodiesel; MgO; SBA-16, sonochemistry**

I. Introduction (*Heading 1*)

Many of the world energy needs are supplied from petrochemical sources, natural gas and coal. These sources are nonrenewable and finite and will be consumed shortly at current usage rates [1].

The pollution problems caused by the use of fossil fuels and the high demand for energy in the industrialized world have made necessary the development of alternative renewable energy sources. One of the particular alternatives considered is the use of biodiesel. Biodiesel is a well known alternative, renewable fuel which produces fewer harmful emissions than conventional fossil-based diesel fuel [2,3].

There are different oil raw materials which can be used to produce biodiesel, including mainly vegetable edible oils like palm, soybean, jatropha, sunflower, etc. [4-6] The animal fats are also another source of raw material for the production of biodiesel [7]. Currently not only vegetable oils and animal fats are excellent sources of triglycerides for biodiesel production, also the waste cooking oils that are discarded by the food industry and generate an environmental problem, are raw materials used for this purpose [8].

The general production process of biodiesel is performed by transesterification reaction, which consists of triglyceride oil to react with methanol in the presence of a catalyst. Conventional catalysts used are alkali homogeneous catalysts such as sodium hidroxide or potassium hydroxide; and acid homogeneous catalysts, as hydrochloric acid and sulfuric acid [9]. However, this process presents some disadvantages, as it requires the use of high amounts of catalyst (which cannot be recovered), the production of different streams which might be treated (neutralization step and wash step), and the purification of glycerine to reuse it. These aspects also play important roles in the economy of the process [10].

An alternative has been studied to counteract the disadvantages of the use of traditional homogeneous catalysts, is the use of heterogeneous basic catalysts [1,11], because these can minimize the risk of side reactions and the catalyst can be removed by physical methods when the reaction is complete, thereby decreasing subsequent washing and drying processes, and the generation of polluting effluents. Furthermore, heterogeneous catalysts have excellent catalytic effects and prolonged lifetime [12].

On the other hand, the low mass transfer due to immiscible nature of reactants is the main weakness of the transesterification reaction [13, 14]. Recently, ultrasound assisted transesterification, used in this study, has been set as a green synthesis method that is fast and energy-efficient [15]. It is due to the ultrasound ability to enhance mass transfer between the immiscible reactants [16].

In this sense, this investigation is about the biodiesel production by the transesterification reaction from wasting

cooking oil using heterogeneous catalysts such as MgO supported on a SBA-16 mesoporous silica. The main idea consisted on synthesize small particles of MgO highly dispersed inside the SBA-16 pores, and examine their influence on the catalytic efficiency of the different percentage of catalysts. Then, four influence factors were investigated to get the best reaction conditions, which were MgO wt % loaded into a SBA-16 substrate, molar ratio of methanol:used cooking oil, reaction temperature and reaction time.

II. Experimental

A. Preparation of the SBA-16 support.

Siliceous SBA-16 mesoporous material was synthesized according to the procedure described by Zhao et al. [17]. The Pluronic triblock copolymer (BASF, EO106–PO70–EO106, F127) was used as the structure-directing agent and tetraethylorthosilicate (TEOS, 98%, Aldrich) as a source of silica. In a typical synthesis, the triblock copolymer was dissolved in a mixture of deionized water and 2 M hydrochloric acid solution stirred for 1 h, after which the required amount of TEOS was added to the solution at 308 K and kept under stirring conditions for 24 h. The mixture was heated for 24 h. After synthesis, the obtained solid was filtered, washed, dried, and finally was calcined to remove the organic template [17].

B. Modification of mesoporous material SBA-16 with MgO particles.

The incorporation of the nanoparticles of MgO on the inner surface of the pores of SBA-16 was made by the impregnation method by pore filling, using as a precursor of MgO, magnesium acetate (Mg(CH3COO)2). 5%, 10% and 20% by weight of MgO were incorporated into the SBA-16, using aqueous solutions of magnesium acetate with different concentrations.

An appropriate concentration of magnesium acetate diluted in water was prepared in each of the catalysts. The catalyst was deposited inside the SBA-16 support drop wise with a syringe, stirring constantly to form a muddy solution which is stirred again. Finally it allowed to dry for 3 hours in order to evaporate gently, and achieve a deposition of solutes on the support.

C. Ultrasonic mechanism

Ultrasonic radiation diverges from other energy sources (such as heat, light, or ionizing radiation) in duration, pressure and energy per molecule. The immense local temperatures and pressures and the extraordinary heating and cooling rates generated by cavitation bubble collapse provide and unusual mechanism for generating high-energy chemistry. Similar to photochemistry, very large amounts of energy are introduced in a short period of time, but it is thermal, not electronic, excitation.

D. Characterization Methods.

1) Chemical analysis: The MgO loadings of the MgO/SBA-16 matrices were determined by Inductively Coupled Plasma Atomic Emission Spectroscopy (ICP-AES), Perkin Elmer Optima 3300DV. The solid samples were first digested (in a mixture of HF, HCl, and HNO_3) in a microwave oven for 2 h. Then, aliquots of solution were diluted to 50 mL using deionized water (18.2 mΩ quality).

2) X-ray diffraction (XRD): X-ray diffraction (XRD) measurements of the samples in powder were carried out using the Cu Kα radiation with a wavelength of 1.54 Å in two ranges: 0.5°-3° (low-angle) and 10°-80° (wide-angle) on a Bruker D8 Advance diffractometer. Particle size calculation was made using the Scherrer equation.

3) N_2 adsorption–desorption isotherms: The textural properties of the mesoporous matrices were determined from the nitrogen adsorption isotherms recorded at 77 K with a Quanthachrome iQ^2 apparatus. The samples were previously degassed at 423 K for 24 h under a vacuum (10^{-4} mbar) to ensure a clean, dry surface, free of any loosely bound adsorbed species. The specific areas of the samples were calculated according to standard BET procedure using nitrogen adsorption data collected in the relative equilibrium pressure interval of $0.03 < P/P_0 < 0.3$. Pore size distributions were calculated from the desorption branches of the corresponding nitrogen isotherm using the BJH method. The total pore volume (V_{total}) was estimated from the amount of nitrogen adsorbed at a relative pressure of 0.99.

4) Transmision electron microscopy (TEM): TEM images of our mesoporous silica materials SBA16 and MgO/SBA-16 were obtained on a JEOL JEM-2000FX FASTEM microscope operating at 200 kV with very low illumination to avoid destruction of the material under the electron beam.

5) *Diffuse reflectance spectroscopy (DRS)*: The UV–Vis diffuse reflectance spectra of the mesoporous matrices were recorded at room temperature using an Ocean Optics Inc. spectrometer First in Photonics (Mini-DT 2) in the 200-400 nm range. The respective support of each mesoporous matrix was used as a reference.

6) Thermogravimetric analysis (TGA/DTG): Thermogravimetric analysis (TGA/DTG) data was obtained with TA Instruments Model TGA-Q500 thermobalance with a quartz furnace tube, with a constant heating rate of 10 C/min, starting the race in 25°C, employing a dynamic atmosphere of nitrogen with the flow 50 mL/min. Each experiment was conducted at constant pressure so that temperature dependence of transitions could be measured. Five milligram samples were used in platinum pans of 20 μL in each analysis, with an approximately 0.5 mm hole in the lid. TGA curves, as well as derivate thermogravimetric (DTGA) curves were used in the study.

III. Results and Discussion

A. *Physicochemical properties of SBA-16 and modified SBA-16 materials.*

The quantification of MgO (by chemical analysis) is presented

Catalysts	MgO (% weight)
5 MgO-SBA-16	4.0
10 MgO-SBA-16	9.0
20 MgO-SBA-16	18.0

in the samples synthesized x% MgO-SBA-16. As seen in Table 1, the MgO content of the materials is in the range of 4.0-19.0% by weight.

Table 1. Chemical analysis of the catalysts MgO/SBA-16

Figure 1 shows XRD patterns in low angles of the materials 5%MgO/SBA16, 10%MgO/SBA16, 20%MgO/SBA16, and SBA-16. As seen in this figure, all SBA-16-based samples show three well-resolved typical diffraction peaks, which are associated with a symmetry cubic (*Im 3m*) cage-structured mesoporous silica material (SBA-16) [19]: one intense reflection centered approximately at 0.88º in 2θ, and two very low- intensity peaks at about 1.22° y 1.50° in 2θ, which can be indexed as the (100), (110) and (200) *khl* reflections, respectively [19]. Thus, one might infer that the mesoporous structure of SBA16 adsorbent did not suffer modification upon MgO addition. However, it can be observed that the position of the reflection corresponding to SBA16 (1.22º 2*θ*) moves slightly to higher angles (1.30º in 2*θ*) when the SBA-16 is modified superficially. This result indicated that the SBA-16 modification occurs inside of their mesoporous structure, so that the MgO is bonding on the internal surface of the SBA-16 substrate.

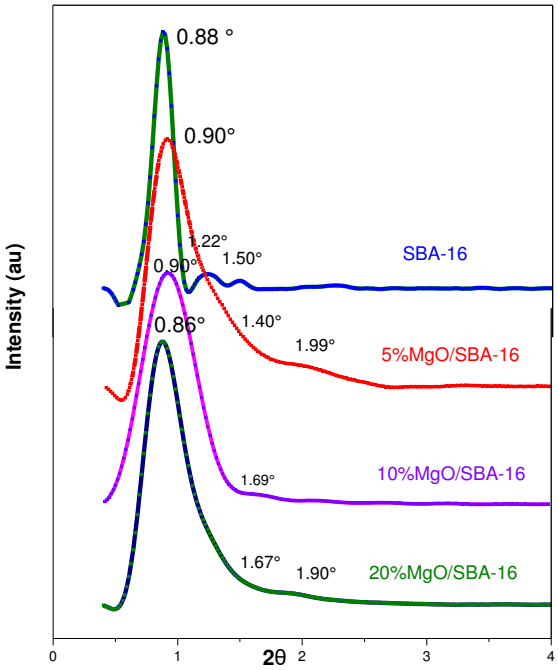

Figure1. Small-angle XRD patterns of of 5%MgO/SBA-16, 10%MgO/SBA-16, 20%MgO/SBA-16, and SBA-16 materials.

Figure 2 shows XRD patterns of the materials 5%MgO/SBA-16, 10%MgO/SBA16, and 20%MgO/SBA16. As seen in this figure, all SBA-16-based samples show three well-resolved typical diffraction peaks, which are associated with a symmetry cubic (*Im 3m*) cage-structured mesoporous silica material (SBA-16) [19]: one intense reflection centered approximately at 22º in 2θ, which can be indexed as the (100), (110) and (200) *khl* reflections, respectively [19]. Thus, one might infer that the mesoporous structure of SBA16 adsorbent did not suffer modification upon MgO addition. However, it can be observed that the position of the reflection corresponding to SBA16 moves slightly to higher angles when the SBA-16 is modified superficially. This result indicated that the SBA-16 modification occurs inside of their mesoporous structure, so that the MgO is bonding on the internal surface of the SBA-16 substrate.

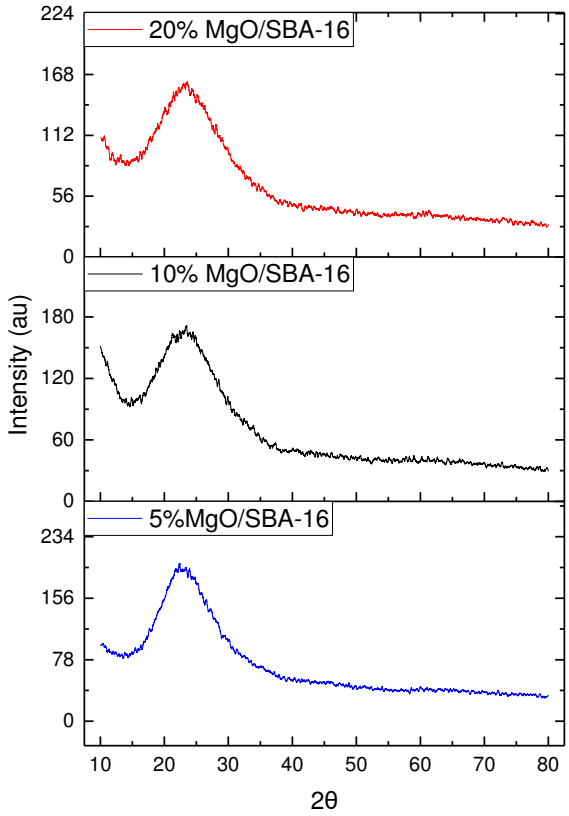

Figure 2. XRD patterns of 5%, 10% and 20% MgO/SBA-16

The transmission electron micrograph (TEM) images further verified the results of the low-angle XRD patterns. As example, Figure 3 shows the TEM images of the 20%MgO/SBA-16 sample. A well-ordered cubic array of mesopores can be seen when the electron beam is parallel to the main axis of the cylindrical pores.

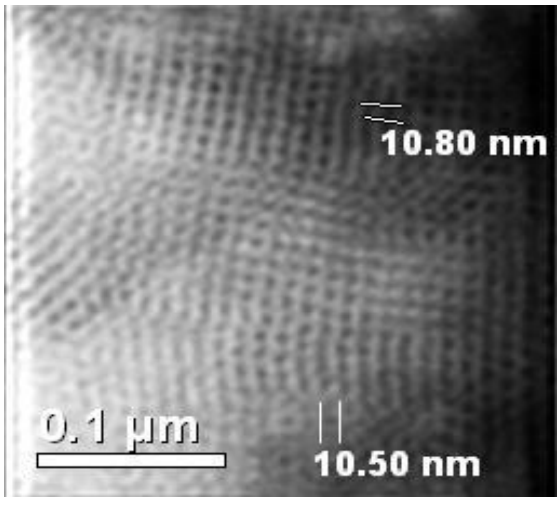

Figure 3. TEM image of the 20%MgO/SBA-16 adsorbent showing well-oedered cubic array of mesopores.

Figure 4 shows N2 adsorption-desorption isotherms at 77 K for determine the textural properties, the isotherms of SBA-16 and 20%MgO/SBA-16 having maximum concentration of MgO, exhibited irreversible type IV adsorption-desorption isotherms with a H2 hysteresis loop in the partial pressure range from 0.4 to 0.6 p/p0, characteristic of materials with 3-6 nm pore diameter [20]. These results are typical for materials with cubic pores and pore network connectivity like SBA-16 and reveals that the mesoporous nature of the material is preserved even though the grafting has occurred, as shown in the material MgO/SBA-16 with the mayor concentration of MgO. A well-defined step occurs approximately at P/P0 ≈ 0.4, which is associated with the filling of the mesopores due to capillary condensation. In the material after modification with MgO, the amount of adsorbed nitrogen increases and the inflection point of the step shifts from 0.4 to 0.41 value of relative pressure. The minimum value of adsorbed nitrogen suggests the modification in the pores with MgO, while the shift of the step to a higher value of relative pressure is indicative of mesopore sizes. The pore size distributions of SBA-16 and 20%MgO/SBA-16 material, as calculated from the adsorption branch of N2 isotherm by using the Barrett-Joyner-Halenda (BJH) model [21], are shown in both samples Fig. 3 (inlet). It should be noted that SBA-16 and 20%MgO/SBA16 show a uniform, narrow pore size distributions centered at about 3.39 and 3.4 nm, respectively, confirming that the modification of the SBA-16 with maximum concentration of MgO does not damage the cubic structure of this mesoporous material.

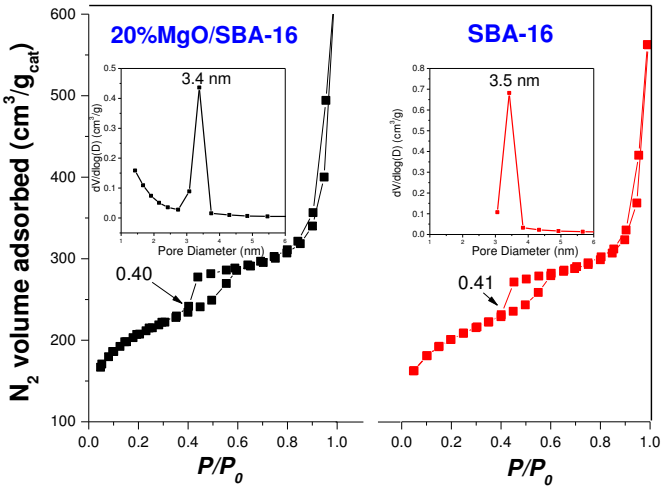

Figure 4. N2 adsorption-desorption isotherms and pore size distribution (inlets) of 20%MgO/SBA-16 and SBA-16 materials.

Table 2 lists some textural properties of SBA-16 before and after the modification, which were calculated from nitrogen sorption studies by applying the BET equation for specific surface area [20] and the BJH formula for pore size distribution [21]. For the modified SBA-16 the BET surface and volume were standardized versus pure silica weights. As expected, the BET surface area and the mesoporous volume strongly decreased after modification, according to the sequence SBA-16 > 20%MgO/SBA-16, suggesting that the grafted species are

located inside the mesoporous structure of the SBA-16 substrate and not only on its outer surface.

Table 2. Textural Properties of SBA-16 before and after of modification with MgO particles.

Sample	S_{BET} (m^2/g)	V_{pmeso} (cm^3/g)	dp (nm)
SBA-16	650	0.64	3.4
5%MgO/SBA-16	507	0.45	3.34
10%MgO/SBA-16	500	0.42	3.2
20%MgO/SBA-16	494	0.43	3.1

a Specific BET surface area (SBET), total volume of mesopores (Vpmeso) and average pore diameter (dp) as determined by N2 physisorption at 473 K.

Figure 5 shows the absorption spectra of the MgO/SBA-6 catalysts (5, 10, and 20%wt MgO). In the spectra can be observed an absorption band in the UV 200 range to 300 nm, according to literature this absorption is assigned to Mg^{2+} in the magnesium oxide (MgO) The intensity of this band increases with increasing in wt% MgO. Therefore this result confirms the presence of MgO in the synthesized catalysts.

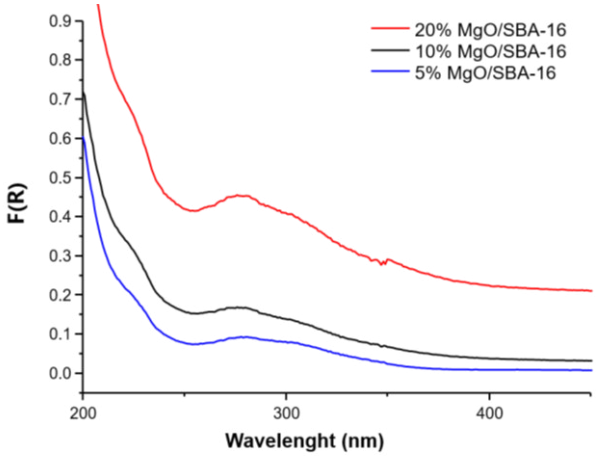

Figure 5. Uv-vis of 5, 10 and 20% MgO/SBA-16

On Figure 6, percentage variation is shown by weight of the catalysts according to the temperature. There is a mass loss of the catalysts at 100°C due to a water loss; after this degradation, there is a little decreasing on temperature at 80°C. It can be seen as increasing the percentage will by weight MgO in the catalysts, they require more temperature to decrease its total weight percent. What this indicates that the MgO deposited on our support.

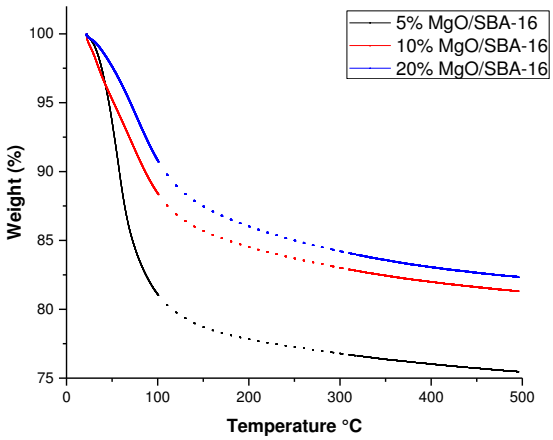

Figure 6. Thermogravimetric analysis of 5%, 10%, and 20% MgO/SBA-16 catalysts.

B. *Thermogravimetric Analysis of Used Cooking Oil and Biodiesel (TG curves).*

Thermogravimetric analysis (TGA) is a technique for characterizing a material (element, compound, or mixture) by measuring changes in its physicochemical properties expressed as weight change as a function of increasing temperature [22]. Therefore, the change in mass of a substance is measured as a function of increasing temperature and it is correlated to the thermal stability of a material that is directly related to the material's volatility or thermal degradation to gaseous products. The boiling point is an important property of the biodiesel and is a parameter that relates to the quality of the biodiesel, as determined by ANP [22]. Thermogravimetric analysis is a fast, easy, cheap, and very useful technique to measure the biodiesel boiling point [23]. Besides, thermogravimetric analysis can confirm the occurrence of the transesterification reaction because the boiling points of the triglycerides and esters (biodiesel) are very different.

The used cooking oil (initial material) and biodiesel produced in this work were analyzed by TGA. The thermogravimetric curve of the initial material (Figure 7) presented a loss of mass was equivalent to 100 %, with an onset temperature of 421°C, and it was attributed to the boiling point of triglycerides that formed the used cooking oil.

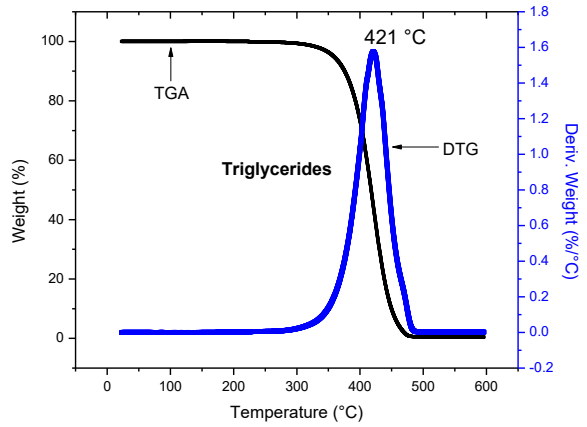

Figure 7. TGA and DTG curves of used cooking oil.

The TGA/DTGA curve of biodiesel (Figure 8) presented three events: the first one has a mass loss of 80 % and onset temperature of 225°C, which refer to the boiling point of saturated fatty acids esters; the second had an onset temperature of 316°C and a mass loss of 4 %, which was attributed to the boiling point of unsaturated fatty acid esters; and the third with an onset temperature of 384°C had a mass loss of 16.0 %, and it was assigned to volatilization of saturated fatty acid esters C20:0 and carbonization [23].

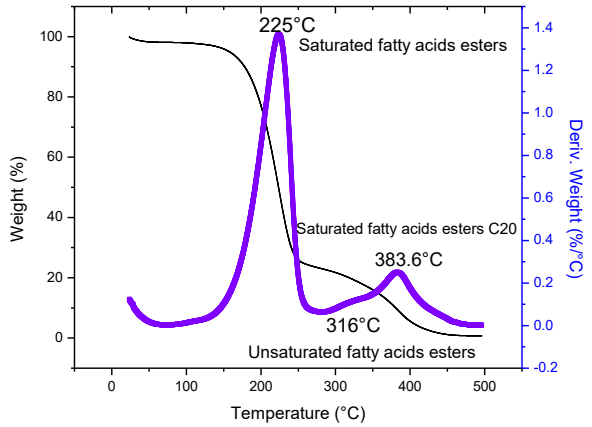

Figure 8. TGA and DTG curves of biodiesel fuel. Reaction conditions: molar ratio of methanol:oil was 6:1; reaction temperature was 65°C; MgO loaded into SBA-16 was 20 wt %; and reaction time was 5 minutes.

The use of thermal analyses in the industry of biodiesel is highly consistent because this technique provides high precision and sensitivity, small sampling, and speed in analytical quality control. TGA peaks of biodiesel can be attributed to mixtures of saturated and unsaturated methyl esters and the results have been correlated to the technique of GC-MS.

C. *Transesterification reactions of used cooking oil over the MgO/SBA-16 catalysts.*

Parameters that influenced the transesterification reaction are the molar ratio of methanol:used cooking oil, the amount of MgO species located within porous structure of the SBA-16 substrate, temperature and reaction time. The biodiesel was prepared with amplitude of 50% corresponding to approximately 40 W of power.

Effect of the MgO loaded into a SBA-16 substrate is shown in Figure 9. As it could be seen, the yield of FAMEs increased linearly with an increase of the MgO content of the catalysts. This is because the increase of MgO content led to an increase of the basicity of the catalyst. Besides this factor, other factors such as crystal phase, surface area, crystalline size and the localization of the MgO clusters, etc. also play an important role on catalyst'activity. Furthermore, a stable measoporous network of SBA-16 [17-19] might facilitate the diffusion of reactants and products, enhancing the activity by facilitating access to reactive sites of MgO [20, 21].

The yield reached 93 % when the MgO content of the catalyst was 20 wt %. More basic centers formed with the increase of MgO content; this brought stronger catalytic activity before the MgO content was 20 wt %.

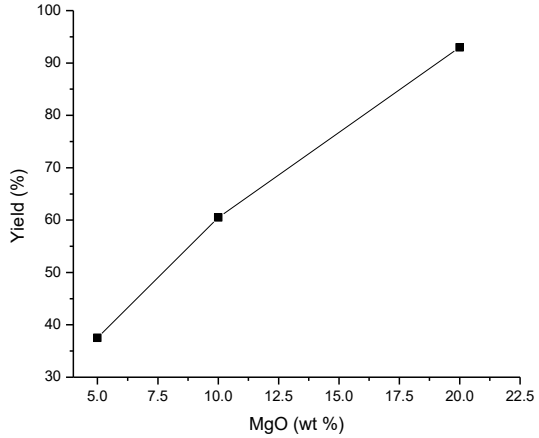

Figure 9. Effect of the MgO loaded into a SBA-16 substrate on the yield of FAMEs. Reaction conditions: molar ratio of methanol:used cooking oil was 6:1; temperature was 60°C; and time was5 minutes.

Figure 10 shows the effect of molar ratio methanol:used cooking oil on the yield of FAMEs. From 3:1 to 6:1 of molar ratio of metahol to used cooking oil, yield of FAMEs increased. The maximum FAMEs yield was 93 %, when molar ratio was 6:1. After the molar ratio was over 6:1, the FAMEs yield commenced to descend tempestuously with molar ratio mounting up. This might be because from 3:1 to 6:1 of molar ratio, increase of methanol engendered augment of FAMEs yield. However, with molar ratio amounting up, higher molar ratio lowered the relative concentration of used cooking oil in mixture. Low concentration of used cooking oil brought out low reaction rate, which also changed the equilibrium of reaction. Thus, 6:1 was accepted as the best molar ratio.

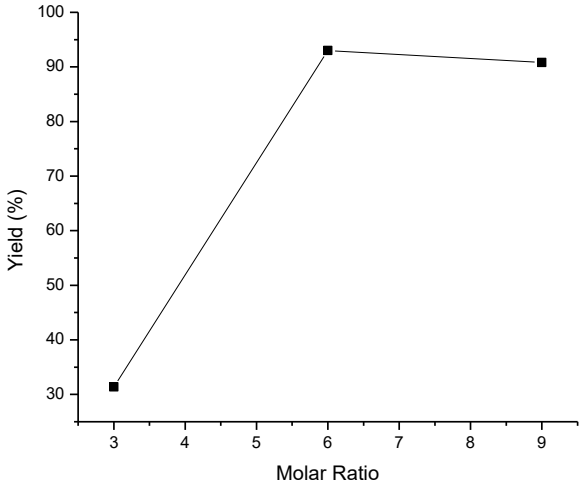

Figure 10. Effect of molar ratio of methanol:used cooking oil on the yield of FAMEs. Reaction conditions: 20%MgO/SBA-16; temperature was 60°C; and time was 5 minutes.

In Figure 11, it is shown that effect of reaction temperature on the yield of FAMEs. Obviously, yield of FAMEs increased as temperature rose. The FAMEs yield was just about 58% when reaction temperature was 40°C, and it even reached 93 % when the temperature was 65°C. Higher temperature made molecules move more actively, which increased the collision probability of molecules of oil and methanol, then accelerated the reaction more fleetly and more easily. Therefore, yield of FAMEs increased with temperature, as Figure 8 shows. However, much higher temperature was not suggested. Because the boiling point of methanol was 64.5°C, methanol volatilized and became less involved when temperature was greater than 65°C. Thus, 65°C was selected as the best reaction temperature here.

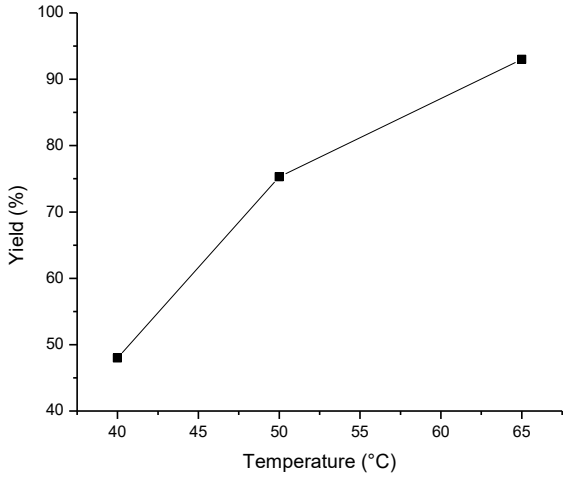

Figure 11. Effect of reaction temperature on the yield of FAMEs. Reaction conditions: 20%MgO/SBA-16; molar ratio of methanol:used cooking oil was 6:1; and time was 5 minutes..

IV. Conclusions

Biodiesel of good quality can be prepared from used cooking oil by one step heterogeneous base catalyzed reaction. This method can be easily adapted to a continuous process. TGA instrument, which gave the same results as chromatographic techniques, can be used to determine the yield of methyl esters instead of GC or any other chromatographic method. MgO/SBA-16 was an active catalyst to prepare biodiesel from used cooking oil. The optimal conditions according to the experiments realized for the transesterification reaction were as followed: the MgO loaded into a SBA-16 substrate was 20 wt. %, molar ratio was 6:1, reaction temperature was 65°C, and reaction time was 5 min. Under these conditions, yield of FAMEs could reach over 93 %.

Acknowledgment

The authors express their gratitude to the following persons for the catalyst's characterization by different techniques: R. Velázquez Castillo (FI-UAQ, México); and J. L. Garcia Fierro (ICP-CSIC, Spain). Financial support by PROMEP (Project UAQ-PTC-190) and FOFI-UAQ-2012 is gratefully acknowledged.

References

[1] M.R. Avhad, J.M. Marchetti, "A review on recent advancement in catalytic materials for biodiesel production", Renewable and Sustainable Energy Reviews, vol. 50, October 2015, Pages 696-718

[2] G. L. Maddikeri, A. B. Pandit, and P. R. Gogate, "Intensification Approaches for Biodiesel Synthesis from Waste Cooking Oil: A review", *Ind. Eng. Chem. Res.*; 51 (45), pp 14610-14628, Oct. 2012.

[3] N.L. Panwar, S.C. Kaushik, Surendra Kothari, "Role of renewable energy sources in environmental protection: A review", Renewable and Sustainable Energy Reviews, Volume 15, Issue 3, April 2011, Pages 1513-1524

[4] W. Xie, L. Zhao, "Heterogeneous CaO–MoO3–SBA-15 catalysts for biodiesel production from soybean oil", Energy Conversion and Management, Volume 79, March 2014, Pages 34-42

[5] S. L. Martínez, R. Romero, R. Natividad, J. González, "Optimization of biodiesel production from sunflower oil by transesterification using Na_2O/NaX and methanol", Catalysis Today, Volumes 220–222, March 2014, Pages 12-20

[6] W. Xie, L. Zhao, "Heterogeneous CaO–MoO3–SBA-15 catalysts for biodiesel production from soybean oil", Energy Conversion and Management, Volume 79, March 2014, Pages 34-42

[7] L.S. Teixeira, J. C Assis, D. R. Mendonça, I.T. Santos, P.R. Guimarães, L.A. Pontes, J.S. Teixeira, "Comparison between conventional and ultrasonic preparation of beef tallow biodiesel", Fuel Processing Technology, Volume 90, Issue 9, September 2009, Pages 1164-1166

[8] Z. Al-Hamamre, J. Yamin, "Parametric study of the alkali catalyzed transesterification of waste frying oil for Biodiesel production", Energy Conversion and Management, Volume 79, March 2014, Pages 246-254

[9] J.M. Marchetti, V.U. Miguel, A.F. Errazu, "Possible methods for biodiesel production", Renewable and Sustainable Energy Reviews, Volume 11, Issue 6, August 2007, Pages 1300-1311

[10] J.M. Marchetti, "Influence of economical variables on a supercritical biodiesel production process", Energy Conversion and Management, Volume 75, November 2013, Pages 658-663

[11] S.P. Singh, D. Singh. “Biodiesel production through the use of different sources and characterization of oils and their esters as the substitute of diesel: a review”. Renewable and Sustainable Energy Reviews 2010;14(1):200–16. [5] Lapuerta M, Armas O, Rodrı´guez FJ. Effect of biodiesel fuels on diesel engine emissions. Progress in Energy and Combustion Science 2008;34(2): 198–223.

[12] A. F. Lee, J. A. Bennett, J. C. Manayil, K. Wilson, “Heterogeneous catalysis for sustainable biodiesel production via esterification and transesterification” Chem Soc Rev., 2014, 43, 7887

[13] B. Sajjadi, A.A. Abdul, S. Baroutian, S. Ibrahim, “Investigation of convection and diffusion during biodiesel production in packed membrane reactor using 3D simulation”, Journal of Industrial and Engineering Chemistry, Volume 20, Issue 4, 25 July 2014, Pages 1493-1504

[14] B. Sajjadi, A. A. Abdul, S. Baroutian, S. Ibrahim, R. Shah, “3D Simulation of fatty acid methyl ester production in a packed membrane reactor”, Fuel Processing Technology, Volume 118, February 2014, Pages 7-19

[15] S. M. Hingu, P. R. Gogate, V. K. Rathod, “Synthesis of biodiesel from waste cooking oil using sonochemical reactors”, Ultrasonics Sonochemistry, Volume 17, Issue 5, June 2010, Pages 827-832

[16] B. Sajjadi, A.R. Abdul, S. Ibrahim, “Mechanistic analysis of cavitation assisted transesterification on biodiesel characteristics, Ultrasonics Sonochemistry, Volume 22, January 2015, Pages 463-473

[17] D.Y. Zhao, J.L. Feng, Q.S. Huo, N. Melosh, G.H. Fredrickson, B.F. Chmelka, G.D. Stucky, “Triblock copolymer syntheses of mesoporous silica with periodic 50 to 300 angstrom pores”. Science 279, (1998) 548–552.

[18] C.L. Peza, L. Escamilla, R. Nava, B. Pawelec, J.L.G. Fierro, “Supported gold catalysts in SBA-15 modified with TiO2 for oxidation of carbon monoxide” Appl. Catal. A: Gen. 375 (2010) 37-48.

[19] Y. Sakamoto, M. Kaneda, O. Teresaki, D. Zhao, J.M. Kim, G.D. Stucky, H.J. Shin, R. Ryoo, Nature 408, (2000) 449-453.

[20] P.I. Ravikovitch, A.V. Neimark, Langmuir, Unified approach to pore size characterization of microporous carbonaceous materials from N2, Ar, and CO2 adsorption isotherms18, (2002) 9830–9837.

[21] E.P. Barrett, L.G. Joyner, P.P. Halenda, “The determination of pore volume and area distributions in porous substances. I. Computations from nitrogen isotherms”. J. Am. Chem. Soc. 73, (1951) 373-380.

[22] Knothe, G. Fuel Process. Technol. 2007, 88, 669–677. Resoluc-~ao ANP Number 7, March 19, 2008; Brazilian National Agency for Petroleum, Natural Gas and Biofuels.

[23] Coats, A. W.; Redfern, J. P. Thermogravimetric analysis. Analyst1963, 88, 906–924.

CONACYT
Consejo Nacional de Ciencia y Tecnología

CONCYTEQ

UNIVERSIDAD AUTÓNOMA DE QUERÉTARO
13° CONGRESO INTERNACIONAL DE INGENIERÍA
15th-19th MAY 2017

Neuro-Fuzzy controller for a Fuel Cell Hybrid Vehicle

Osuna Castro Héctor Manuel
Departamento de Investigación y Posgrado de la Facultad de Ingeniería
Universidad Autónoma de Querétaro
Santiago de Querétaro, Querétaro
Hector_hec8@hotmail.com

Rivas Araiza Edgar Alejandro
Departamento de Investigación y Posgrado de la Facultad de Ingeniería
Universidad Autónoma de Querétaro
Santiago de Querétaro, Querétaro
erivas@uaq.mx

***Abstract*—This paper is about a proposal for a hybrid intelligent controller for a fuel cell hybrid vehicle that will decrease the amount of fuel consumed in a driving cycle**

Keywords—fuel cell; fuzzy; controller; neural network; hydrogen; FCHV.

I. INTRODUCTION

Is well known that the non-renewable resources has an important impact in the ecosystem [1], the transport's sector has a big environmental impact, approximate a 15% of the global pollution, in the urbans sector the produced gases by the internal combustion engines(ICE) vehicles are the main source of pollution, recent studies lead to the attempt of replace these ICE's for a cleaner ones [2] .

In the recent years the Industry and the academic institutions have put attention in the fuel cell vehicles, the hybrid vehicles based con fuel cells seems to be the best option for the future transportation thanks to their high efficiency and their low emissions [3]. The result of these researches lead to the challenge of new low and null pollution vehicles designs[1].

PEMFC.

"A Fuel Cell is defined as a electric-chemical device in which the chemical energy stored in a fuel is directly converted into electricity.", the low operating temperature proton exchange membrane fuel cells (PEMFC) are the promising devices for the decentralized production of energy for vehicular use [4].

A Fuel Cell is constituted by an stack of independent fuel cell type cells having 3 basics components; an anode and a cathode separated by a membrane[5]. A Fuel Cell can reach a 60% of efficiency, higher than an ICE with a 25-30% of efficiency [4].

FCHV's

The electric vehicles are moved through an electric motor powered by batteries(BEV's), the batteries require high amount of charging time and the self-sufficiency is much less compared with a ICE [1], a fuel cell hybrid vehicle (FCHV) is like a BEV but the fuel cell provide the electric energy for the engine and the battery. The hydrogen is used as main fuel but other gases can be used such as: natural gas and alcohol, methanol as an example [5]. Toyota has been working to reach new compression's levels of H2, their goal is to pass the 35MPa to 70MPa in order to extend the driving range up to 500km, to do this is necessary find new materials and designs for the storage tank [6].
A Sweden study classified the types of the vehicles and the distances in which they are used respectively as follows:
-Battery Electric Vehicles for short distances
-Hydrogen and Methane vehicles for medium distances
-Liquid Biofuel, synthetic fuel and liquid methane for longer distances.
The goal is to develop the technology in hardware and software so the FCHV's can extend their distances like fossil fuels do [7].

1.4 ENERGY MANAGEMENT SYSTEMS

Modern Engineering has increased the performance of the existing systems helping itself with computational software and a variety of resources that allow it to simulate the systems that are required. The use of auxiliary sources in hybrid vehicles (HV's) leads to energy management systems (EMS) with more degrees of freedom , doing this the performance rest greatly in the hands of the implemented EMS, then it becomes in a minimization problem where the function to minimize it's the hydrogen consumption [8].

II. CONTROL STRATEGIES FOR ENERGY MANAGEMENT SYSTEMS

Many control strategies have been implemented, some of them will be listed here: a fault tolerant control strategy using an ultra-capacitor as storage device in a FCHV and a PID controller [9], an energy management system was develop and implemented for a FCHV despite of they did not mentioned what control technique they used they mention the importance of measure and control the individual voltage of each cell separately in the fuel cell stack [10], control strategies based on duty cycles previously established and their logic relation between the power demand and the power of the fuel cell in its optimal point of efficiency to decrease the consumption of fuel [11], Multi-Mode control strategy for fuel cell electric vehicles(FCEV's) minimizing the battery's high charge and discharge state prolonging its useful life [12].

Tolj hybridized a light electric vehicle (golf car) in which he added a FC+UC and a EMS achieving extend the driving range (<63%) and other benefits such as smoother and repetitious accelerations, the amount of energy that can be subtract and recover also increased 61% thanks to the fast dynamic of the ultra-capacitor [13].

H. Hemi also used a FC+UC for their fast dynamic, FCHV's demand power peaks during acceleration since the cell is slow it can't follow these types of demand so the cell can't be the only source of energy. The driving cycles in reality are unknown so they proposed an EMS strategy based on *"Pontryagin's minimun principle"* with 3 parameters and a Fuzzy Logic Controller with 10 parameters, a genetic algorithm and a quadratic programming are responsible for improve the fuel economy [14].

In 2014 Ravey A. designed an EMS in which the device to control was the FC, a couple of batteries directly connected to a CD bus, the control strategy lead to control the FC in its optimal point of operation while keep the batteries SOC in their optimal zone, he implemented a Fuzzy Logic Controller for this job[15]. Other job with a Fuzzy Logic Controller for a EMS was the work of Q. Li , he said that as the FCHV is a non-lineal multivariable system, a Fuzzy Logic Controller is more convenient for a EMS [16].

III. CONTROLLER'S PROPOSAL

The proposal consist in a fuzzy logic controller in charge of the estimation of the hydrogen flow through the fuel cell and a neural recurrent network that will maintain the flow rate with a minimum of variation.

IV. APPLICATION

This controller will be implemented in a solar powered golf car that was rescued for the Universidad Autónoma de Querétaro and used in others projects before.

V. NEURAL NETWORK

we are using a one hidden layer recurrent neural network as shown on the fig 1.

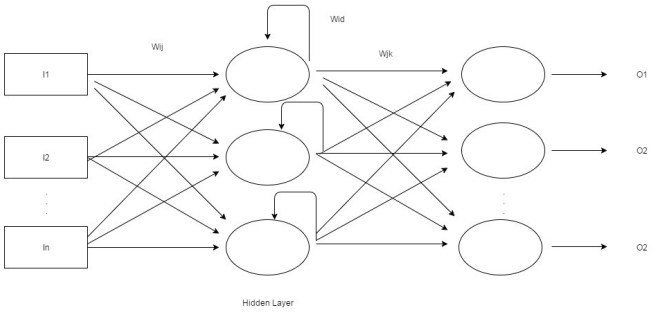

Fig. 1) Recurrent Neural Network(RNN)

Where i=1,2…,n , j =1,2…,l and k=1,2,…,m

Given the structure of the RNN we can calculate the output and the equations to adjust the weights as is shown below.

The excitation function for the j neuron of the hidden layer in t:

$$Sj(t) = \sum_{i=i}^{n} Ii(t)W_{ij}(t) + X_j(t-1)W_{jd}$$

For the output of the hidden layer we passed the excitation function trough a non-linear function called "bias":

$$\mathrm{Xj(t)} = \frac{1}{1 + e^{-Sj(t)}}$$

The output of the neural network will be given by a linear function:

$$r_k(t) = \sum_{j=1}^{l} X_j(t)W_{jk}$$

For convenience, we put the E function as shown to avoid some local minimums and the error is the difference between the output of the RNN and the output of the plant.

$$E = \frac{1}{2}e^2, where\ e = Y_k - O_k$$

We used a method named "steepest descent" to minimize the E function, that means we need to move in the direction of the gradient negative, the gradient is a three dimension vector which consists of the partial derivates of E with respect to the weights.

$$\nabla E = \begin{bmatrix} \frac{\partial E}{\partial W_{jk}} \\ \frac{\partial E}{\partial W_j} \\ \frac{\partial E}{\partial W_{ij}} \end{bmatrix}$$

Using the method of the fastest descent the resulting equations for the adjustment of weights are the following:

$$W_{jk} = W_{jk}(t-1) + \eta e X_j$$
$$W_j = W_j(t-1) + \eta W_{jk} X_j(t-1) e X_j(1-X_j)$$
$$W_{ij} = W_{ij}(t-1) + \eta W_{jk} X_j(1-X_j) I_i(t)$$

VI. Fuzzy Logic Controller

The fuzzy logic controller is a three input one output design (Fig. 2).

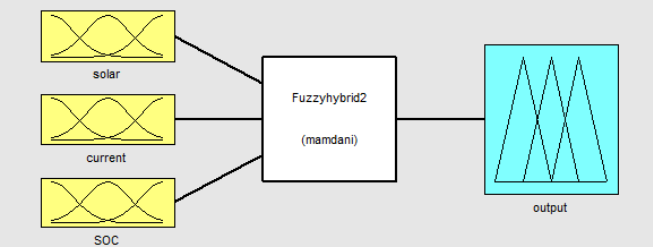

Fig. 2) Fuzzy logic controller design

Inputs and output both were designed on a normalized 0-100% universe. Membership functions and their dimensions were proposed initially as triangular.

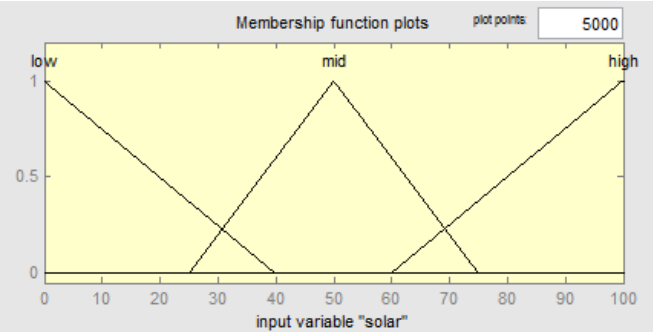

Fig. 3) Solar Input Universe and Membership Functions.

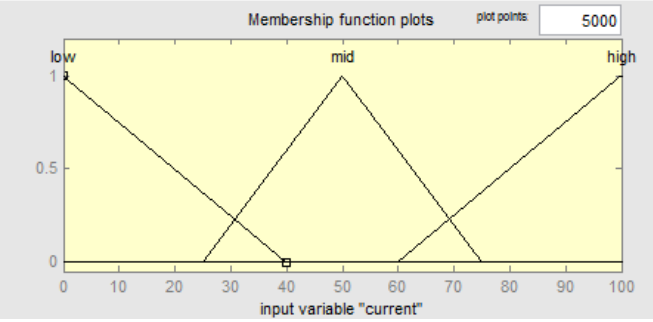

Fig. 4) Current Input Universe and Membership Functions.

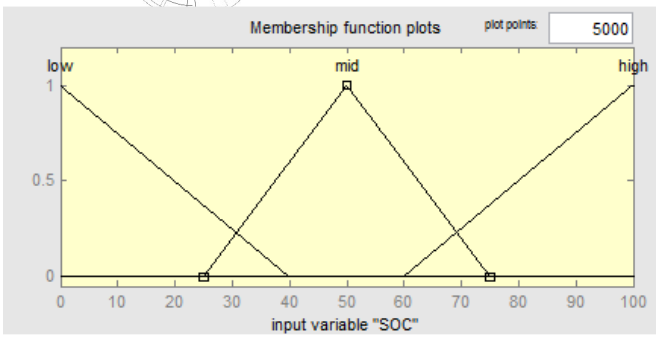

Fig. 5) SOC Input Universe and Membership Functions.

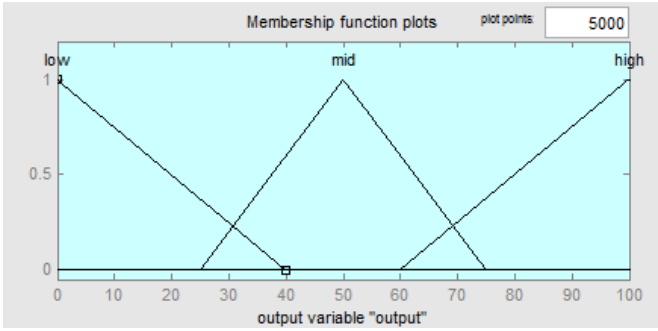

Fig. 6) Output Universe and Membership Functions.

The rules of the fuzzy were designed to regulate the H2 consumption based on demand, solar incidence and the SOC of the batteries, example:

[If current is low & SOC is high & solar is high then output is low].

As we can see in the example the controller can reduce the H2 consumption and take advantage of solar energy in some cases.

VII. RESULTS.

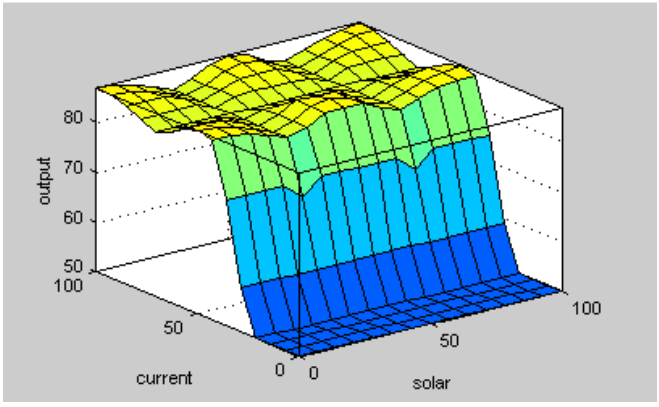

Fig. 7) Fuzzy solar-current surface.

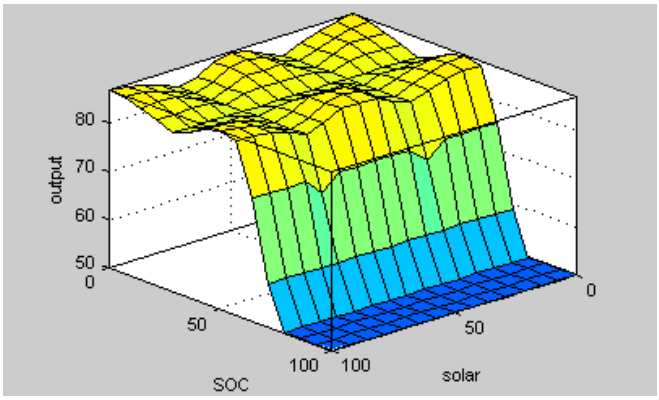

Fig. 8) Fuzzy solar-SOC surface.

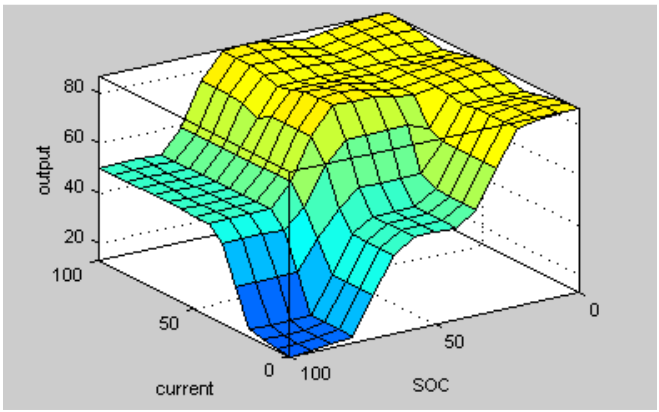

Fig. 9) Fuzzy current-SOC surface.

On the figures 7,8 and 9 we can see how the variables interact with the output signal, as we observe the output is inversely proportional. The figure 9 is the most significant surface, the output reacts more dynamically to the inputs because of the rules design.

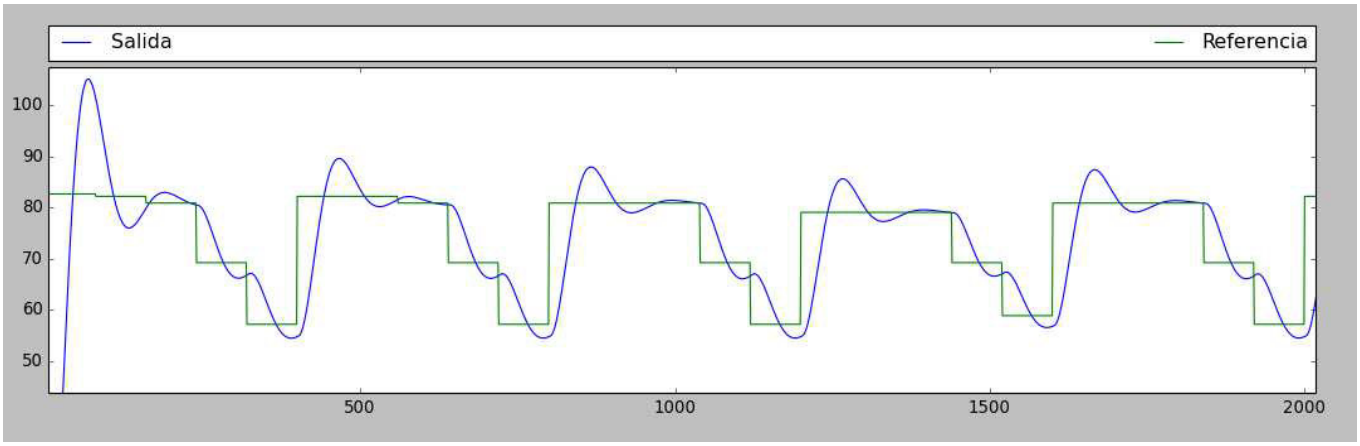

Fig. 10) Output of the RNN.

We Tested the RNN variating abruptly the parameters of the fuzzy logic in a linear plant to see how the controller follows the reference.

VIII. Conclusions

We can see on the surfaces that we have the expected behavior on the fuzzy logic controller, on the other hand the RNN showed that can follow well the variations in the output of the FLC.

The next step is using this neuro-fuzzy controller with an EMS, which will do the disconnections of the sources, and the electromechanical parts.

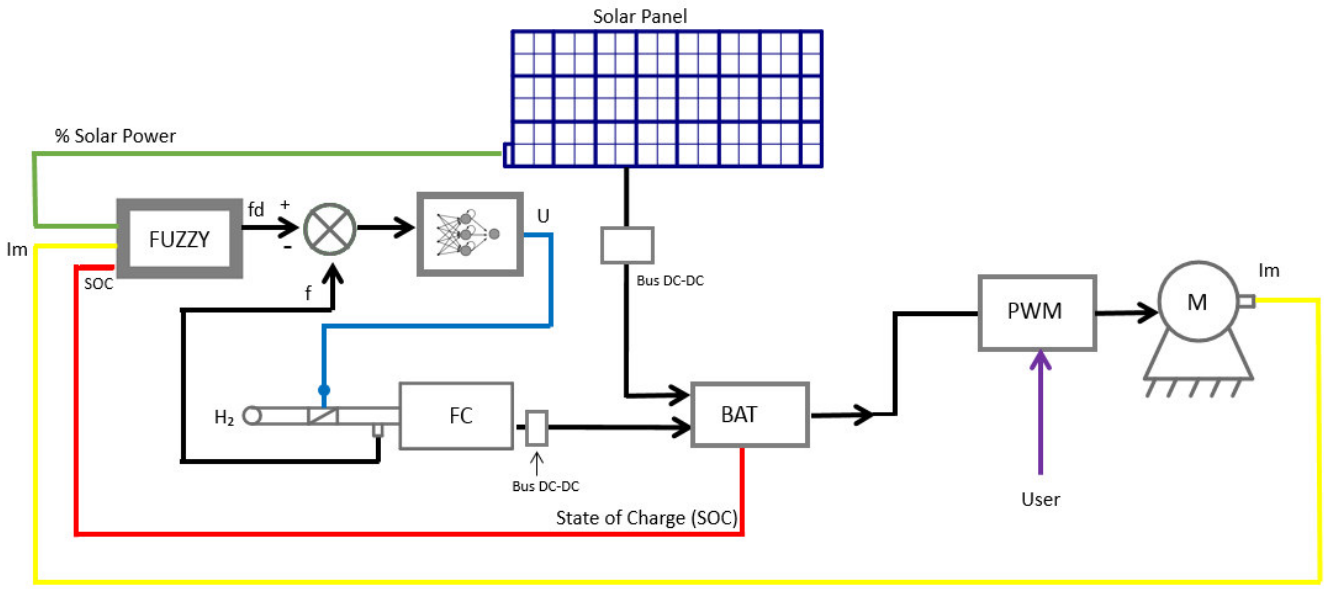

Fig. 11) Neuro-Fuzzy controller proposal

REFERENCES

[1] J.-J. Hwang, J.-S. Hu, and C.-H. Lin, "Design of a range extension strategy for power decentralized fuel cell/battery electric vehicles," *Int. J. Hydrogen Energy*, vol. 40, no. 35, pp. 1–9, 2015.

[2] M. Abu Mallouh, E. Abdelhafez, M. Salah, M. Hamdan, B. Surgenor, and M. Youssef, "Model development and analysis of a mid-sized hybrid fuel cell/battery vehicle with a representative driving cycle," *J. Power Sources*, vol. 260, pp. 62–71, 2014.

[3] S. Ahmadi and S. M. T. Bathaee, "Multi-objective genetic optimization of the fuel cell hybrid vehicle supervisory system: Fuzzy logic and operating mode control strategies," *Int. J. Hydrogen Energy*, vol. 40, pp. 12512–12521, 2015.

[4] L. Salemme, L. Menna, and M. Simeone, "Energy efficiency of Fuel Processor – PEM Fuel Cell systems," pp. 157–181, 2002.

[5] A. Colmenar-Santos, L. Alberdi-Jiménez, L. Nasarre-Cortés, and J. Mora-Larramona, "Residual heat use generated by a 12 kW fuel cell in an electric vehicle heating system," *Energy*, vol. 68, pp. 182–190, 2014.

[6] S. Aso, M. Kizaki, and Y. Nonobe, "Development of fuel cell hybrid vehicles in Toyota," *Power Convers. Conf. ...*, vol. 223, pp. 366–370, 2007.

[7] M. Larsson, F. Mohseni, C. Wallmark, S. Grönkvist, and P. Alvfors, "Energy system analysis of the implications of hydrogen fuel cell vehicles in the Swedish road transport system," *Int. J. Hydrogen Energy*, vol. 0, pp. 1–8, 2015.

[8] M. Ansarey, M. Shariat Panahi, H. Ziarati, and M. Mahjoob, "Optimal energy management in a dual-storage fuel-cell hybrid vehicle using multi-dimensional dynamic programming," *J. Power Sources*, vol. 250, pp. 359–371, 2014.

[9] H. Aouzellag, K. Ghedamsi, and D. Aouzellag, "Energy management and fault tolerant control strategies for fuel cell/ultra-capacitor hybrid electric vehicles to enhance autonomy, efficiency and life time of the fuel cell system," *Int. J. Hydrogen Energy*, vol. 40, no. 22, pp. 7204–7213, 2015.

[10] F. Barreras, M. Maza, A. Lozano, S. Báscones, V. Roda, J. E. Barranco, M. Cerqueira, and A. Vergés, "Design and development of a multipurpose utility AWD electric vehicle with a hybrid powertrain based on PEM fuel cells and batteries," *Int. J. Hydrogen Energy*, vol. 37, pp. 15367–15379, 2012.

[11] H. Yun, S. Liu, Y. Zhao, J. Xie, C. Liu, Z. Hou, and K. Wang, "Energy management for fuel cell hybrid vehicles based on a stiffness coefficient model," *Int. J. Hydrogen Energy*, vol. 40, no. 1, pp. 633–641, 2015.

[12] L. Xu, J. Li, M. Ouyang, J. Hua, and G. Yang, "Multi-mode control strategy for fuel cell electric vehicles regarding fuel economy and durability," *Int. J. Hydrogen Energy*, vol. 39, no. 5, pp. 2374–2389, 2014.

[13] I. Tolj, M. V. Lototskyy, M. W. Davids, S. Pasupathi, G. Swart, and B. G. Pollet, "Fuel cell-battery hybrid powered light electric vehicle (golf cart): Influence of fuel cell on the driving performance," *Int. J. Hydrogen Energy*, vol. 38, no. 25, pp. 10630–10639, 2013.

[14] H. Hemi, J. Ghouili, and A. Cheriti, "Combination of Markov chain and optimal control solved by Pontryagin's Minimum Principle for a fuel cell/supercapacitor vehicle," *Energy Convers. Manag.*, vol. 91, pp. 387–393, 2015.

[15] A. Ravey, S. Faivre, C. Higel, F. Harel, and A. Djerdir, "Energy management of fuel cell electric vehicle with hydrid tanks," 2014.

[16] Q. Li, W. Chen, Y. Li, S. Liu, and J. Huang, "Energy management strategy for fuel cell/battery/ultracapacitor hybrid vehicle based on fuzzy logic," *Int. J. Electr. Power Energy Syst.*, vol. 43, pp. 514–525, 2012.

Synthesis of the precursors for the double perovskite Sr_2FeMoO_6 formation.

Ing. Jesús Valdés Hernández, Dra. Angeles Cuán, Dr. Rufino Nava Mendoza
Dirección de investigación y posgrados, Facultad de ingeniería.
Universidad Autónoma de Querétaro (UAQ)
Santiago de Queretaro, Queretaro, Mexico
jesvalher@hotmail.com

Dra. Bertha Oliva Aguilar, Dr. Oracio Navarro
Unidad Morelia del Instituto de Investigaciones en Materiales
Universidad Nacional Autónoma de México (UNAM)
Morelia, Michoacán, México

***Abstract*— The $SrMoO_4$ and $SrFeO_{3-x}$ precursors of the double perovskite Sr_2FeMoO_6 were synthesized by sol-gel technique. The resulting powder from the sol-gel synthesis was analyzed by X-Ray technique and SEM microscopy. Its micrographs showed microstructures consisting of very fine grains with different sizes (with average of 5µm) and the Bragg reflections correspond to a perovskite crystalline structure type. The gel was dried at 90°C and then it was sintered at 900°C in an oxidant atmosphere. This is the first attempt of future experiments that intend to improve the synthesis process of the Sr_2FeMoO_6.**

Keywords— Precursors formation, double perovskite Sr_2FeMoO_6; sol-gel synthesis.

I. INTRODUCTION

$A_2B'B''O_6$ is the formula unit of an ideal double perovskite, where A denotes an alkaline-earth or rare-earth ion, B' and B'' are transition-metal sites occupied alternately, there are oxygen bridges every B' and B'' atom pair give-alternating $B'O_6$ and $B''O_6$ octahedral form [1]. The double perovskite has a particular interest because ferromagnetic and half-metallic behavior. The ordered lattice structure of Sr_2FeMoO_6 (SFMO) consist of body centered cubic lattice with alternating FeO_6 and MoO_6 octahedral forms at the corners where the strontium atom in its center [2]. In particular, the half–metallic behavior, in which only one-spin direction is present at the Fermi energy, has been investigated due to its attractive properties for spintronics applications [3]. Then double perovskite SFMO is very attractive for applications in magnetic recording devices [2] caused by the grate low-field magnetoresistance in granular form [4] and a relatively high Curie temperature (410-450K) [1] .

The synthesis of SFMO is traditionally prepared with the solid state method by mixing the $SrMoO_4$ and $SrFeO_{3-x}$ precursors to form double perovskite Sr_2FeMoO_6 by calcination and reduction of the precursors to obtain the target product [5]. This method requires a high temperature (1270°C) and the grain size is in the micron scale, reducing its magnetoresistance [5].

The intergrain magnetoresistance of polycrystalline Sr_2FeMoO_6 is known to depend on its grain size [6] and the amount of insulating nonmagnetic $SrMoO_4$ impurity formed during fabrication caused [4]. Therefore, the method and synthesis conditions must be chosen carefully [7], it is a reason why a new techniques of synthesis have to be development to find a better crystalline phase of the SFMO.

II. EXPERIMENTAL PROCEDURE.

The precursor phases $SrMoO_4$ and $SrFeO_{3-x}$ were prepared by sol-gel method, starting from strontium nitrate $Sr(NO_3)_2$ (99.995%), iron (III) nitrate nonahydrate $Fe(NO_3)_3$-$9H_2O$ (99.95%), molybdenum (IV) oxide MoO_2 (99.99%) and citric acid Monohydrate (99%) and ammonium hydroxide solution (28.0-30.0%) to form Ammonium molibdate $(NH_4)_2$ MoO_4. All reagents are provided by Sigma-Aldrich. The reagents were weighted according to their stoichiometric amount. Molar ratio citric acid: ($Sr^{2+}Fe^{3+}Mo^{6+}$) salts used were 4.3:1. The amount of citric acid was added under magnetic stirring to the mixture of strontium nitrate, iron (III) nitrate and ammonium molibdate, and a stable sol was obtained at 80°C. The sol was maintained under continuous stirring at this temperature for 4 h, to achieve the gelification process. After drying the gel at 90°C, the resulting powder was calcined at 900°C, 3 h in air to obtain the precursor phases of SFMO.

A. Characterization.

The structure and microstructure of the precursors phase of Sr_2FeMoO_6 powders were investigated by X-ray diffraction

(XRD) and scanning electron microscopy (SEM). The XRD patterns of Sr_2FeMoO_6 and its precursor phases were recorded with a D8 ADVANCE diffractometer form Bruker-AXS. For the powder diffraction, CuKα1 radiation (wavelength 1.5406 Å), LiF crystal monochromator and Bragg-Brentano diffraction geometry were used. The data were acquired at 25°C, with a step-scan interval of 0.020° and step time of 5s. The SEM was carried out using a JSM-IT300 operated at 10.0KeV.

III. Results and Discussion.

A. *Sol gel.*

The approach used to make SFMO it is by hydrolysis and policondensation of a nitrate precursors followed by aging and drying under ambient atmosphere[7]. In this method nitrates precursors in aqueous solution, are hydrolyzed by mixing with citric acid (eq 1).

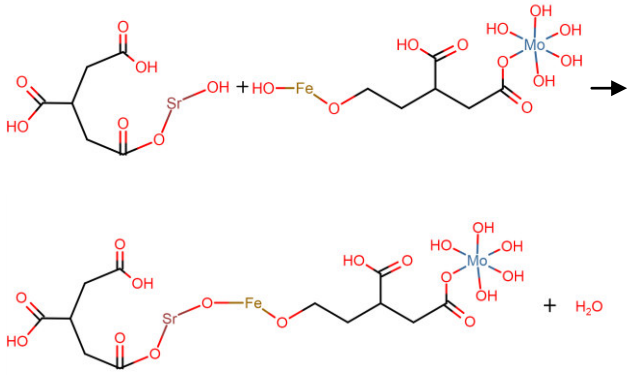

(1)

One of the roles for the citric acid it's to control the growth of the network, favoring the creation of a colloidal system[7], the hydroxides can interact with the carboxyl groups in the citric acid, this interaction generates a protection around strontium, iron and molybdenum as shown in figure 1, it is evident that this protection can be created not only for one atom, eq 1 shows one possibility of the interaction between the atoms in the net, the hydrolysis and policondensation reactions initiate at numerous sites with the hydroxides of strontium, iron, and molybdenum, forming a complex network[7].

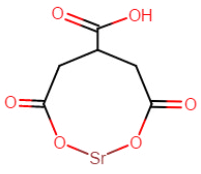

Fig. 1. Strontium atom interacting with the carboxyl groups of the citric acid, this interaction reduces the reaction with other elements.

B. *X-ray diffraction.*

The XRD pattern of the precursors obtained after pre-sintering is shown in Fig 2. It can be seen that the precursor is composed mainly by Tetragonal $SrMoO_4$ (PDF: 01-072-6394) for the most intense peaks in 2theta axis: 27.68°, 45.14° and 56.99°, that corresponds to the indexes hkl (103), (204) and (312) respectively, and Cubic Hexoctahedral $SrFeO_{3-x}$ (PDF: 01-034-0638) for the most intense peaks in 2theta axis: 32.36°, 46.42° and 57.72°, that corresponds to the indexes hkl (103), (200) and (321) respectively. It is well known that the valence state of Mo is 6+ in $SrMoO_4$ and that of Mo is 5+ in SFMO [8]. In order to obtain the target products SFMO the precursor must be reduced.

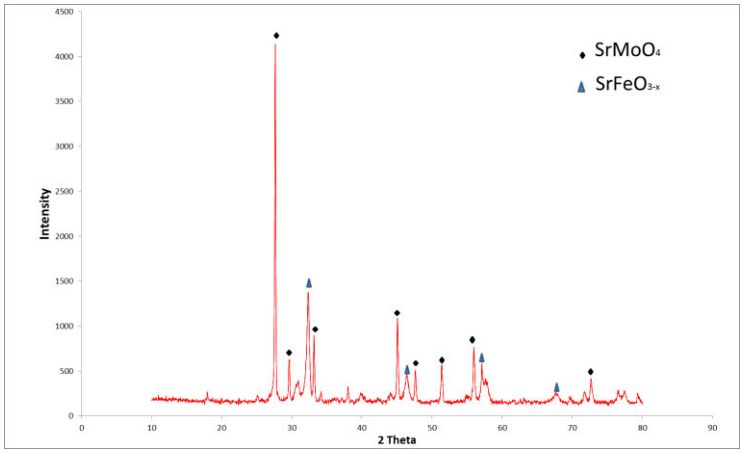

Fig. 2. The XRD pattern matches with the tetragonal $SrMoO_4$ and cubic hexoctahedral $SrFeO_{3-x}$ according to the data base.

C. *Scanning electron microscopy.*

Fig. 3 presents the SEM micrographs of Sr_2FeMoO_6 precursor gel powder calcined at 900°C during 3 h in air. In Fig. 2(a) and (b) a conglomeration of cumulus and pores formation is observed, this arrangement was expected since it is characteristic of the material morphology [9]. The result corroborate that synthesis for the precursors was successfully done.

The gel-powder has an average grain size about 0.5 µm. The dense microstructure of the ceramic samples can be attributed to the homogeneous and fine morphology of the powder prepared by sol-gel method.

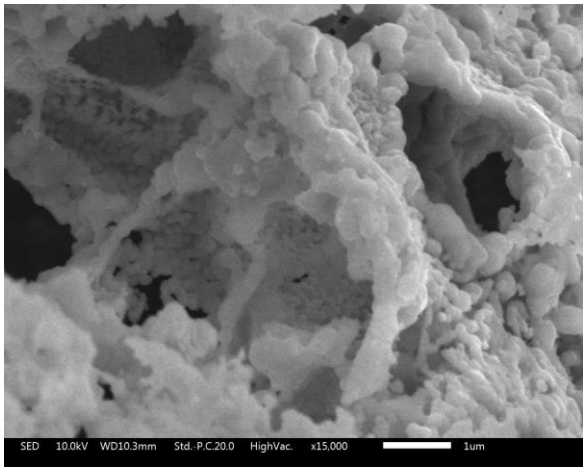

(a)

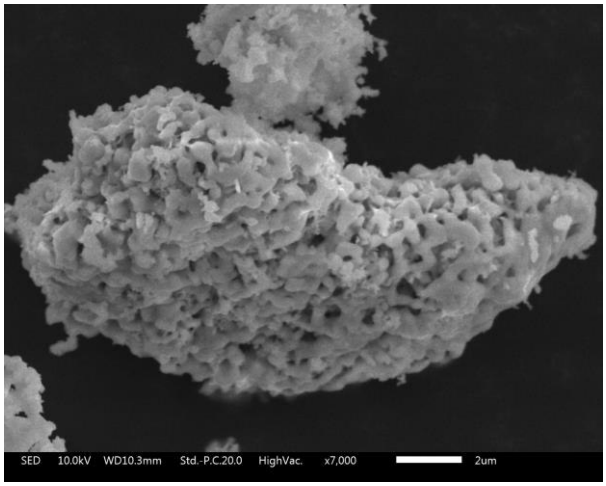

(b)

Fig. 3. SEM micrographs for Sr_2FeMoO_6 precursor gel powder ($SrMoO_4$ and $SrFeO_{3-x}$), it was calcined at 900°C for 3 h in air.

IV. CONCLUSION.

The synthesis of the $SrMoO_4$ and $SrFeO_{3-x}$ by the sol-gel methodology as a precursors of the double perovskite Sr_2FeMoO_6 was succeed, this was corroborated by the X-Ray technique and SEM microscopy, where the micrographs showed microstructures consisting of very fine grains with different sizes (with average of 5µm) and the Bragg reflections correspond to a perovskite crystalline structure type. Specifically tetragonal for $SrMoO_4$ and cubic hexoctahedral for $SrFeO_{3-x}$, which match with the data base and the previously reported [3]. This first step was essential to gain insight and better understanding about the behavior of the synthesis when the mixed of the reactive interacts to form the precursors of the double perovskite Sr_2FeMoO_6. Because, our interest is to improve the quality of the crystal form, not only in morphology but also in the crystalline phase, the future goal will probe different routes of synthesis to achieve this goal.

ACKNOWLEDGMENTS: This work was partially supported by grants No. 252677 from Conacyt and PAPIIT-IN104616 from UNAM México.

REFERENCES

[1] K.-I. Kobayashi, T. Kimura, H. Sawada, K. Terakura, and Y. Tokura, "Room-temperature magnetoresistance in an oxide material with an ordered double-perovskite structure," *Nature*, vol. 395, no. 6703, pp. 677–680, 1998.

[2] J. L. Valenzuela, T. E. Soto, J. Lemus, O. Navarro, and R. Morales, "Reaction kinetics of the double perovskite Sr2FeMoO6 by gas-solid reactions," *Phys. B Condens. Matter*, vol. 455, pp. 10–13, 2014.

[3] T. E. Soto, J. L. Valenzuela, R. Mondragón, R. Morales, J. Lemus-Ruíz, and O. Navarro, "Synthesis of the off-stoichiometric oxide system $Sr_2Fe_{1+x}Mo_{1-x}O_6$ with 1<x<0.25," *Phys. B Condens. Matter*, vol. 455, pp. 6–9, 2014.

[4] M. Cernea *et al.*, "Preparation by sol-gel and solid state reaction methods and properties investigation of double perovskite Sr2FeMoO6," *J. Eur. Ceram. Soc.*, vol. 33, no. 13–14, pp. 2483–2490, 2013.

[5] Y. Zhai, J. Qiao, G. Huo, and S. Han, "Synthesis, magnetic and electrical transport properties of magnetoresistance material Sr2FeMoO6 by microwave sintering," *J. Magn. Magn. Mater.*, vol. 324, no. 13, pp. 2006–2010, 2012.

[6] X. H. Li *et al.*, "Size dependence of electronic and magnetic properties of double- perovskite Sr 2 FeMoO 6," vol. 145, pp. 98–102, 2008.

[7] L. L. Hench and J. K. West, "The sol-gel process," *Chem. Rev.*, vol. 90, no. 1, pp. 33–72, 1990.

[8] Y. Zhai, J. Qiao, and Z. Zhang, "Magnetic and Electrical Transport Properties of Double Perovskite Sr 2 FeMoO 6 Prepared by Sol-Gel Method," vol. 8, pp. 189–195, 2011.

[9] M. Cernea, F. Vasiliu, C. Bartha, C. Plapcianu, and I. Mercioniu, "Characterization of ferromagnetic double perovskite Sr2FeMoO6 prepared by various methods," *Ceram. Int.*, vol. 40, no. 8, pp. 1–9, 2014.

Nanoencapsulation of Lauric Acid with Chitosan for the control of bacteria Propionibacterium Acne.

Dr. Arturo Eduardo Elizalde Peña.
Laboratory of nanostructured and functional materials.
Autonomous University of Querétaro.
Querétaro, México.

Frida Yeliana Soto Nájera.
Laboratory of nanostructured and functional materials.
Autonomous University of Querétaro.
Querétaro, México.

***Abstract*— This work has studied the preparation of chitosan(CS) particles to nanoscale for loaded and released drugs which were synthesized by ionic gelation method, using in CS particles crosslinked with sodium tripolyphosphate (TPP). Different samples were prepared (CS) with different proportions of modifier agents: crosslinker (TPP) and lauric acid (LA) for the control of bacteria propionibacterium acne (PA).**

Keywords*— Nanoparticles, chitosan, lauric acid, ionic gelation, encapsulation.

I. INTRODUCTION

In last decades, the implementation of new pharmaceutical forms of loaded and released drugs, have had great interest in representing a promising platform for the optimization of medical treatments. They are devices that provide better properties, such as stability, high ability to associate, bioadhesivity and reduction of adverse effects, improving the speed, time and place of drug release [1]. Currently, in the development of controlled release systems, a large number of polymers are used. Among them, there are two major groups: Natural polymers and Synthetic polymers [2].

Nowadays, the natural polymers are used as biomaterials. These are biodegradable, non-toxic and biocompatible. They are also abundant in nature and their extraction processes are inexpensive. From the various natural polymers, the chitosan has stood out for its characteristics and great potential. The chitosan is a linear cationic biopolymer obtained by the partial deacetylation of the chitin which is found in the shell of the shrimp, the second most abundant polysaccharide on earth [3]. Some of the functional properties of CS are biodegradability, biocompatibility, mucoadhesivity, absorption promoter, antimicrobial activity, anticholesterolemy and antioxidant. Chitosan has pharmaceutical applications as an extended drug release matrix and it has biomedical applications. From a physicochemical point of view, CS has the special quality of gelling upon contact with anions thus allowing the formation of beads under very mild conditions [4].

The ionotropic gelation method is commonly used to prepare nanoparticles of polysaccharides. This technique has attracted considerable attention due to the fact that this process is non-toxic, organic solvent free, convenient and controllable [5]. This method allows the cross-linking of polymer chains that are ordered in nanostructures by interactions that may be intermolecular of the covalent or non-covalent type, behaving as a metastable thermodynamic system which is highly sensitive to variations in ionic strength [6].

Propionibacterium acnes is a gram-positive human skin commensal that prefers anaerobic growth conditions and is involved in the pathogenesis of acne, the most common skin disease, affecting up to 80% of all teenagers [7]. Wound materials and other puncture fluids are considered as contaminants in the blood. Causal agents of inflammatory acne can also be the cause of endocarditis, discitis, osteomyelitis and diseases of the central nervous system [8]. PA bacteria are becoming increasingly resistant to some of the common antibiotics used to treat acne. One of the most frequently applications that have been reported include erythema, scaling, burning [9].

Early studies suggest that medium-chain fatty acids, commonly found in tropical oils such as coconut oil, are bactericidal for gram-positive bacteria, even more than gram-negative bacteria, fungi, protozoa, and viruses [10].

Lauric acid is a medium chain saturated fatty acid, present in lauric oils up to 50%. Its systematic name is dodecanoic acid. It

doesn't induce any cytotoxicity to human sebocytes. It has a greater antiviral and antibacterial activity than other medium-chain triglycerides. The antibacterial activity mechanism of LA suggests that membrane lipids are solubilized as the LA fatty acids integrate into the membrane, causing lysis of bacteria [11].

II. Materials and Methods

A. Materials

Chitosan medium molecular weight with a 75–85% degree of deacetylation came from Sigma–Aldrich, Sodium tripolyphosphate technical grade 85% , Glacial acetic acid, Acetone, Lauric acid ≥98% from Sigma–Aldrich, Inoculo of P. Acne and P. aeruginosa with 16hr growth, PBS/Tween 1%, Agar LB.

B. Chitosan–tripolyphosphate nanoparticle production

CS-TPP nanoparticles were produced using a modified ionic gelation method [12]. CS was disolved in acetic acid (the concentration was, 1.75 times higher than that of CS) aqueous solutions at various CS concentrations: 0.05%, 0.2% and 0.3% (w/v). Later, TPP was dissolved in purified water at the same concentration as CS. In 10 ml of the CS solution was added a variable volume of the TPP solution (2ml, 4ml and 6ml) under magnetic stirring, drop by drop with the aid of an insulin syringe.

	2ML	4ML	6ML
CS 0.05%	TPP 0.05%	TPP 0.05%	TPP 0.05%
CS 0.2%	TPP 0.2%	TPP 0.2%	TPP 0.2%
CS 0.3%	TPP 0.3%	TPP 0.3%	TPP 0.3%

Table 1 Preparation of solutions at different concentrations of chitosan and TPP.

C. Preparation of CS/TPP/LA-loaded nanoparticles

LA-loaded were formed spontaneously after the incorporation of TPP aqueous solution of 10 ml of the CS acidic solution, containing various concentrations of LA (1ml, 2ml, and 4ml), the LA was dissolved in acetone at the same concentration as CS, under magnetic stirring.

	2ML TPP	4ML TPP	6ML TPP
CS 0.2%	0ml LA	0ml LA	0ml LA
CS 0.2%	1ml LA	1ml LA	1ml LA
CS 0.2%	2ml LA	2ml LA	2ml LA
CS 0.2%	4ml LA	4ml LA	4ml LA

Table 2 Preparation of solutions at different concentrations of TPP and LA.

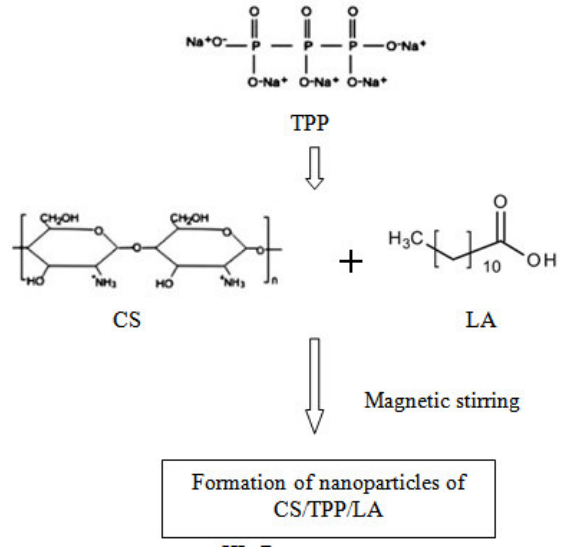

Figure 1 Preparation of nanoparticles. [6, 12, 13]

D. Preparation of QS/TPP/LA films.

Was placed 30 ml of the previously selected solution of Qs/TPP and Qs/TPP/LA on a Teflon surface of 10cm in diameter X 1cm, to avoid the adhesion of the film on any other surface, it continued with storage in a desiccator for evaporation and obtaining od the film required.

E. Preparation of working inoculum.

- Place 5 ml of LB / PBS solution in culture tube with 250 µl of bacteria suspension.
- Make a 1:10 dilution (500 ul of 10^8 + 4.5 ml of LB: PBS).
- Make a 1:02 dilution (2.5 ul of 10^7 + 2.5 ml of LB: PBS).

F. Antimicrobial evaluation of samples.

The first is the neutralization of films, take a small samples of 2cm diameter, and wash films with NaOH solution after wash films with distilled water until the pH of the solution reaches 7. Leave films in distilled water for 2 h for complete hydration. After sterilization of samples placing them in light UV during 30min.

Put 25 µl of the bacterial suspension on the surface of the films, put a coverslip on the sample with bacteria making sure that it is completely covered, incubate samples at 37º C, at different times. Wash films, take 100 ul of the washing solution and put them in an agar box. Incubate during 14hrs. Finally count the colonies to get the percentage of control of the bacteria.

III. RESULTS

The nanoparticle of CS/TPP was visually analyzed at different concentrations, and three main systems were identified: conglomerate, opalescent suspension and clear solution. Based on Table 1, a comparison graphic of the present systems was made. In Graphic 1 the three systems formed, according to the established concentrations, were observed. According to previous research [12], the sample of the opalescent suspension, which should correspond to a solution with very small particles, is illustrated (only visually) in figure 2 (b, c). These opalescent solutions are in the range of 1.5 to 3 mg / m as shown in Graphic 1.

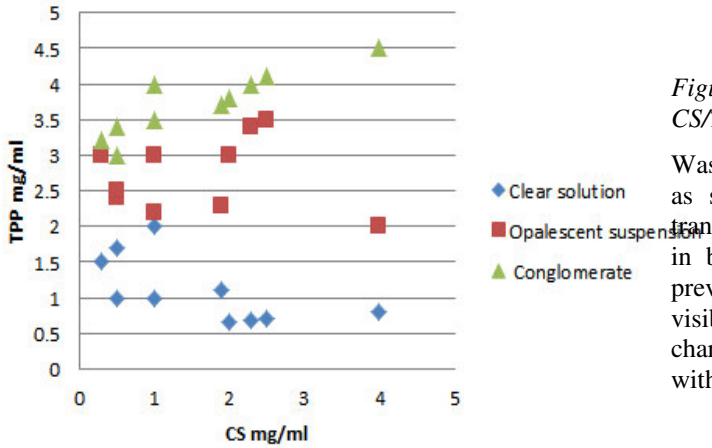

Graphic 1 Comparative analysis of chitosan particles in respect to their concentration.

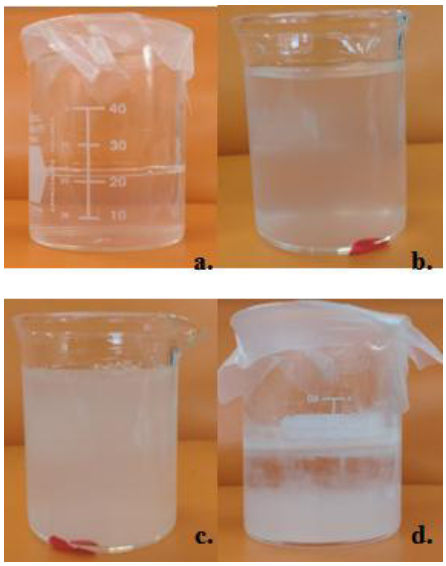

Figure 2 Solutions of nanoparticles with different concentrations of TPP, a) clear solution, b) and c) Opalescent suspension, d) Conglomerate.

The solution with concentration of 2 mg/ml was used to incorporate LA. More opaque solutions were obtained, without separation of phases or conglomerates as show in Figure 3 (a, b).

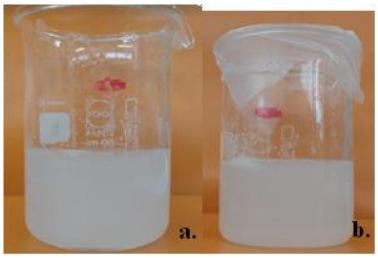

Figure 3 Solutions of nanoparticles of CS/TPP/LA, a). 0.2% CS/TPP 2ml LA, b) 0.2%CS/TPP 4ml LA.

Was obtained thin films with a coloration opaque translucent as shown in figure 4. In a) is a Qs/TPP film which is translucent with limited flexibility and without visible clusters, in b) is Qs/TPP/LA film which is more opaque than the previous film without flexibility apparent and with some visible clusters, this film also presents a slight odor to soap characteristic of LA deducting the presence and interaction with Qs.

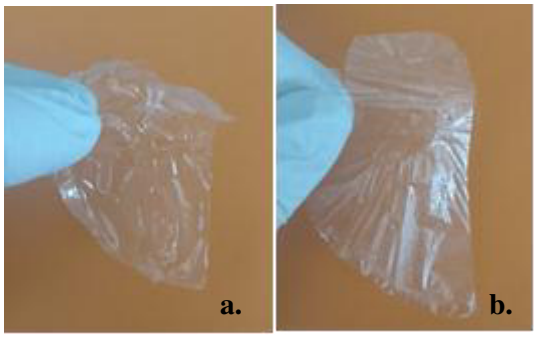

Figure 4 a). Qs/TPP film, b). Qs/TPP/LA film.

IV.CONCLUSIONS

Chitosan colloidal particles were recognized as an opalescent suspension, which was used for the preparation of nanoparticles loaded with lauric acid (obtaining a stable solution) with this solution was obtained a film which will be neutralized applied in an inoculum of P. acne for release of acid lauric which will keep the growth control of PA bacteria.

REFERENCES

[1] N.G.M. Schipper, K.M. Varum, P. Artursson, Chitosans of absorption enhancers of poorly absorbable drugs: Influence of molecular weight and degree of acetylation, Eur. J. Pharm. Sci. 4 (1996) S153-S153.

[2] Cerchiara T., Abruzzo A., Di Cagno M., Bigucci F., Bauer-Brandl A., Parolin C., Vitali B., Gallucci M. y Luppi B.(2015) Chitosan based micro and nanoparticles for colon targeted delivery of vacomycin prepared by alternative processing methods. European Journal of Pharmaceutics and Biopharmaceutics, 92, mayo, pp. 112-119.

[3] Yang J., Han H., Zheng H., Dong H. y Liu J. (2015), Preparation and application of micro/nanoparticles based on natural polysaccharides. Carbohydrate Polymers, 123, junio, pp. 53-66.

[4] Chen M., Liu Y., Yang W., Li X., Liu L., Zhou Z., Wang Y., Li R. y Zhang Q. (2011), Preparation and characterization of self-assembled nanoparticles of 6-O-cholesterol-modified chitosan for drug delivery. Carbohydrate Polymers, 84, abril, pp. 1244-1251.

[5] Dong Y., Kiong Ng W., Shen S., Kim S. y Tan R. (2013), Scalable ionic gelation synthesis of chitosan nanoparticles for drug delivery in static mixers. Carbohydrate Polymers, 94(2), mayo, pp. 940-945.

[6] J. Berger, M. Reist, J.M. Mayer, O. Felt, N.A. Peppas, R. Gurny. Structure and interactions in covalently and ionically crosslinked. 57 (2004) 19–34.

[7] Bruggemann H (2005) Insights in the pathogenic potential ofPropionibacter-ium acnesfrom its complete genome.Semin Cutan Med Surg24:67–72.

[8] Bruggemann H, Henne A, Hoster F, Liesegang H, Wiezer A, Strittmatter Aet al.(2004) The complete genome sequence ofPropionibacteriumacnes, a commensal of human skin.Science305:671–3.

[9] Coenye T, Peeters E, Nelis HJ (2007) Biofilm formation byPropionibacteriumacnesis associated with increased resistance to antimicrobial agents andincreased production of putative virulence factors.Res Microbiol158:386–92.

[10] Georgel P, Crozat K, Lauth X, Makrantonaki E, Seltmann H, Sovath Setal.(2005) A toll-like receptor 2-responsive lipid effector pathway protectsmammals against skin infections with gram-positive bacteria.InfectImmun73:4512–21

[11] abara JJ, Swieczkowski DM, Conley AJ, Truant JP (1972) Fatty acids andderivatives as antimicrobial agents.Antimicrob Agents Chemother2:23–8

[12] Calvo, P., Remuñan –López, C., Vila-Jato, J.L., Alonso, M.J., Novel hydrophilic chitosan-polyethylene oxide nanoparticles as protein carriers. 63(1997b) 125-132.

[13] Lauric acid for synthesis. CAS 143-07-7, EC Number 205-582-1, chemical formula $CH_3(CH_2)_{10}COOH$. Sigma-Aldrich.

CONACYT
Consejo Nacional de Ciencia y Tecnología

CONCYTEQ

Types of Controllers for Application of Paintwork in a Plane X-Y

Jose Manuel Flores Juarez
Engineering school
UAQ
Queretaro, Mexico

Abstract*— The application of paintwork over a plane x-y consists in deposit a chemical substance over a plane surface, for this process has been used a controller for a table x-y. The pressures in the application process are different with respect to application distances over table x-y. So it was necessary to have en consideration it this factor to have a uniform finish in the application surface. Others important factors for application are velocity and position of application device of paintwork. The principal objective this work is show different types of controllers that have been used for automation of paintwork in plane x-y.

***Keywords—Application of paintwork*, control x-y, table x-y,**

I. INTRODUCCIÓN

Nowadays the automation of the industrial process is very important because enhance quality in products and also reduce production time. For application of paintwork in the plane x-y is necessary that the application device of paintwork it move through both axes uniformly as shown in the Fig 1.

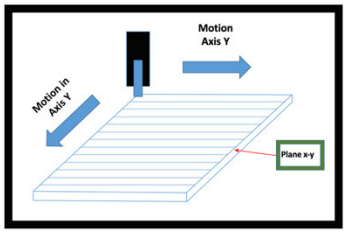

Figure 1. Device for application of paintwork.

The displacement through both axes must be of smoothly for applications of paintwork, taking into consideration principally the velocity and normal distance of application. For this application be used a table x-y with ball screw as shown in Fig. 2. For any paint application process in an x-y plane, one must take into consideration the type of finish and the quality required in the application of the paint in order to be able select a type of controller. Nowadays there are very exact controllers for the x-y tables, most of these controllers reach very high precisions and are very expensive for their manufacture, however in the applications of painting it has not been necessary attain such precision for this reason in this article they are shown several types of controller that can be used for this application but with a lower cost in its development.

For automation of this process it was necessary first know the plant dynamic model as shown coming up next.

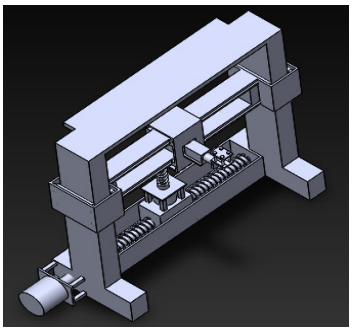

Figure 2. Table X-Y with ball screw.

II. MODELLING OF 2-AXIS SYSTEM.

X-Y table is moved to a straight line and is connected by a right angle. X-Y table, which is using right angle coordinates, is two dimensional position system. This X-Y table is simply separated from each independent moving. So general mechanical equation of each axis is represented equation (1), (2).

$$J_x \frac{dV_X}{dt} + B_x V_x = u_x(t) \quad (1)$$

$$J_y \frac{dV_y}{dt} + B_y V_y = u_y(t) \quad (2)$$

where, J_x, and J_y are inertia of each axis, $u_x(t)$, $u_y(t)$ are input torque which is moving motor of each axis, and B, and B_y are viscous-friction coefficient of each axis.
State equation of total system is described by equation (3).

$$\begin{bmatrix}\dot{\theta}_x\\ \dot{V}_x\\ \dot{\theta}_y\\ \dot{V}_y\end{bmatrix}=\begin{bmatrix}0 & 1 & 0 & 0\\ 0 & -\frac{B_x}{J_x} & 0 & 0\\ 0 & 0 & 0 & 1\\ 0 & 0 & 0 & -\frac{B_y}{J_y}\end{bmatrix}\begin{bmatrix}\theta_x\\ V_x\\ \theta_y\\ V_y\end{bmatrix}+\begin{bmatrix}0 & 0\\ \frac{K_x}{J_x} & 0\\ 0 & 0\\ 0 & \frac{K_y}{J_y}\end{bmatrix}\begin{bmatrix}u_x\\ u_y\end{bmatrix} \quad (3)$$

For automation of process of paintworks does not is necessary a high precision in the position, however it is totally important than velocity and displacement of application dispositive be smoothly into axes x-y for this occasion is very important have in count the nonlinearities or disturbances which may happens in the system due to friction in each axis.

The older controllers can be more simple and easy to use for application of paintworks.

III. Literature Review

In this section, we have presented a literature review of different authors in various domains. We have ordered the articles in chronological order regardless of the technique used to perform the pitch control, for this reason it is possible to present in several sections the work of several authors even when they use similar techniques.

Such as PD and PID controllers, are widely used in industrial applications. Such controllers exhibit poor performance when applied to systems containing nonlinearities arising from unknown deadzones

Schmidt, and Lorenz (1992), presented a work with the title following Design Principles and Implementation of Acceleration Feedback to Improve Performance of DC Drives. These work consist in a implementation of acceleration feedback to substantially improve the performance of DC servo drives It will explain the first principles on what acceleration feedback is, and why it improves the system performance compared to conventional position-, velocity-, and current feedback techniques. Acceleration feedback increases the effective inertia of the system for disturbance rejection purposes. This allows higher overall stiffness to be achieved without increasing position and velocity loop bandwidths. The effect is analogous to an electronic gear reduction [1].

Habetler *el al*., (1992) presented a work with the title following Direct Torque Control of Induction Machines using Space Vector Modulation. These work consist in Control scheme for direct torque and flux control of induction machines based on the stator flux field-orientation method. With the proposed predictive control scheme, an inverter duty cycle has directly calculated each fixed switching period based on the torque and flux errors, the transient reactance of the machine, and an estimated value of the voltage behind the transient reactance. The inverter duty cycle can then be calculated using the space vector PWM technique. With this scheme, the requirement of a separate current regulator and proportional-integral (PI) control of the flux, torque, and/or current error is eliminated, thereby improving transient performance [2].

Kim *et al*., (1993) presented a work with the title following Control of Systems with Dead zones using PD Controllers with Fuzzy Precompensation. These work consist in a novel fuzzy logic-based precompensation approach for controlling systems with dead zones. The control structure consists of a fuzzy logic-based precompensator followed by a conventional PD controller. Our proposed control scheme shows superior transient and steady-state performance compared to conventional PD and PID controllers. In addition, the scheme is robust to variations in dead zone nonlinearities, as well as the steady-state gain of the plant [3].

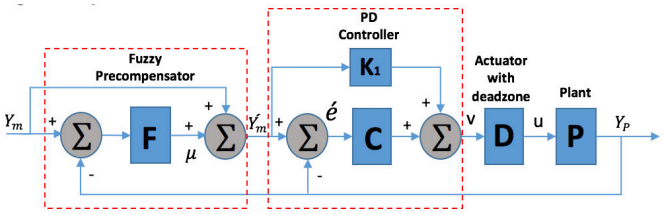

Figure 3. Proposed control structure.

Utkin (1993) presented a work with the title following Sliding Mode Control Design Principles and Applications to Electric Drive**.** These work consist in shown that the dominant role in variable structure systems (VSS) theory is played by sliding modes, VSS consist of a set of continuous subsystems with a proper switching logic and, as a result, control actions are discontinuous functions of system state, disturbances (if they are accessible for measurement), and reference inputs. Also shown that the dominant role in VSS theory is played by sliding modes, and the core idea of designing VSS control algorithms consists of enforcing this type of motion in some manifolds in system state spaces. Implementation of sliding mode control implies high frequency's witching. It does not cause any difficulties when electric drives are controlled since the "on-off" operation mode is the only admissible one for power converters. The mathematical background and sliding mode control design philosophy oriented to high-dimensional nonlinear systems operating under uncertainty conditions and has demonstrated its applicability to control of different types of electric motors [4].

Kim *et al.,* (1994) presented a work with the title following A Two-Layered Fuzzy Logic Controller for Systems with Dead zones.These work consist in a novel two-layered fuzzy logic controller for controlling systems with dead zones. The two-layered control structure consists of a fuzzy logic-

based precompensator followed by a usual fuzzy PD controller. Our proposed controller exhibits superior transient and steady-state performance compared to usual fuzzy PD controllers. In addition, the controller is robust to variations in dead zone nonlinearities [5] .

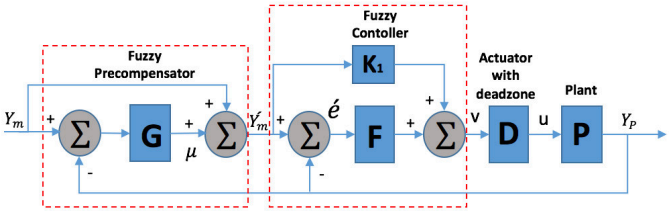

Figure 4. Proposed two-layered fuzzy logic control structure.

Lee and Kim, (1995) presented a work with the title following CMAC Network-Based Robust Controller for Systems with Friction. These work consist in a robust tracking control scheme is proposed for compensation of the friction in a mechanical system. The friction forces are identified by a CMAC network whose weights are adjusted by an adaptation algorithm derived from Lyapunov function. Experimental result demonstrates the effectiveness of the proposed [6].

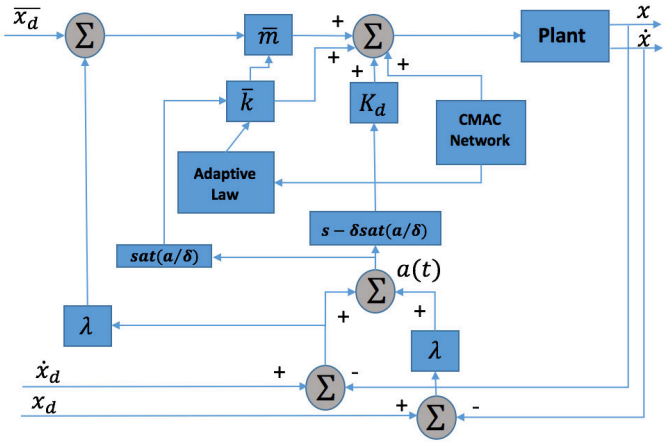

Figure 5. The block diagram of the control scheme

Fischer and Tomizuka (1996) presented a work with the title following Application and Comparison of Alternative Position Sensors in High-Accuracy Control of an X-Y Table. These work consist in High-accuracy positioning that is applied in a variety of modern computer-controlled machines The achievable precision is not only determined by the mechanical properties of the systems but strongly depends on the utilized control algorithms and the quality of the sensor signals. The alternative position sensors influence the performance of a robust digital tracking controller that consisting of a disturbance observer in the velocity loop, a feedback controller in the position loop, and a zero phase error tracking controller as feedforward controller [7].

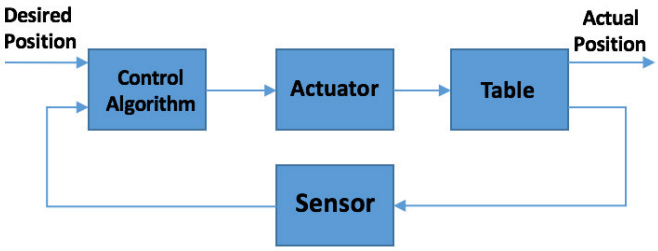

Figure 6. Principle scheme of a positioning system.

Jeon *et al.*, (1996) presented a work with the title following High-Precision Control of X-Y Table Using Experimental Evolutionary Programming-Based Scheme. These work consist in a high precision control scheme for a precise point to point positioning system under the influence of nonsmooth nonlinearities is proposed. The proposed scheme consists of two controller modes: a tracking controller mode and a two-layered controller mode. The tracking controller is composed of a friction compensator, a linear feedback controller and a sliding control. The friction compensator is designed based on identified friction model by using evolution strategies. The two-layered controller consists of a fuzzy precompensator and a PD controller. The fuzzy precompensator is employed to improve the performance of the PD controller. The fuzzy rules of the two-layered controller were tuned to minimize the output error and eliminate the steady state error by EEP [8].

Tomita *et al.,* (1996) presented a work with the title following High response X-Y Stage System Driven by In-Parallel Linear Motors. These work consist in described operational principles. associated mechanical and control system design based on analysis of stage dynamics, and typical results of system performance experiments Stepping motion with high- response and accurate positioning was obtained by incorporating a force disturbance observer and jerk- continuous trajectory generation into a conventional control system operated under PID and acceleration feedforward compensation Measurements of stage stepping motion demonstrate a highly suitable design [9].

Wang and Chen (1996) presented a work with the title following Fuzzy Logic Control of a Positioning Table with DSP Real-Time Implementation. These work consist in develop a rule-based fuzzy logic controller (FLC) for trajectory tracking control of an x-y axis positioning table. Compared to the conventional PI controller, the proposed FLC resulted in better control performances at both low-speed motion and high-speed motion, especially in the latter case. In the presence of payload variations, the experiments confirmed that the proposed FLC provides more robustness than the PI controller for high-speed trajectory tracking [10].

Figure 7. Fuzzy logic control system

Lee and Tomizuka (1996) presented a work with the title following Robust Motion Controller for High-Accuracy Positioning System. These work consist in a controller structure for robust high-speed high-accuracy motion control systems. The overall control system consists of four elements: a friction compensator, a disturbance observer for the velocity loop, a position loop feedback controller, and a feedforward controller acting on the desired output. A parameter estimation technique coupled with friction compensation is used as the first step in the design process. The friction compensator is based on the experimental friction model and it compensates for unmodeled nonlinear friction. Stability of the closed-loop is provided by the feedback controller. The robust feedback controller based on the disturbance observer compensates for external disturbances and plant uncertainties. Precise tracking is achieved by the zero phase error tracking controller. Experimental results are presented to demonstrate performance improvement obtained by each element in the proposed robust control structure [11].

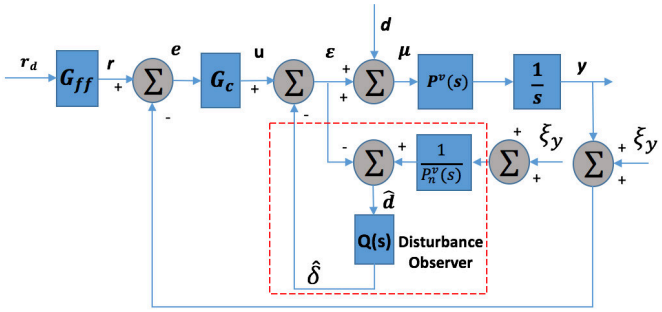

Figura 8. Robust digital tracking control based on a disturbance observer.

Endo *et al*., (1996) presented a work with the title following Robust Digital Tracking Controller Design for High Speed Positioning Systems. These work consist in the combination of a feedforward controller and a robust feedback controller is desirable, because the feedforward controller anticipates and compensates for closed loop dynamics and the feedback controller compensates mechanical nonlinearities, parameter variations, and disturbances. A disturbance observer and PD compensation was used as a robust feedback controller and a zero phase error tracking controller was used as the feedforward controller. A controller which combines the disturbance observer as an inner loop, a PD controller as an outer loop, and ZPETC as a feedforward controller is a highly effective method of addressing these problems [12].

Kim *et al*., (1996) presented a work with the title following High-Precision Control of Positioning Systems with Nonsmooth Nonlinearities. These work consist in a high precision control scheme for a precise point to point positioning system under the influence of nonsmooth nonlinearities is proposed. The proposed scheme consists of two controller modes: a tracking controller mode and a two layered controller mode. The tracking controller is composed of a friction compensator, a linear feedback controller and a sliding control. The friction compensator is designed based on identified friction model by using evolution strategies. The two-layered controller consists of a fuzzy precompensator and a PD controller. The fuzzy precompensator is employed to improve the performance of the PD controller. The fuzzy rules of the two-layered controller were tuned to minimize the output error and eliminate the steady state error by EEP [13].

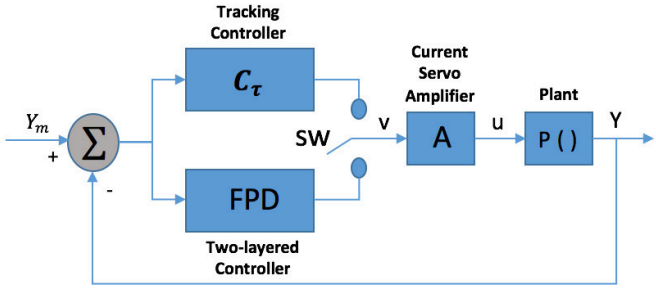

Figure 9. Block diagram of the overall control system.

Chiu and Yao (1997) presented a work with the title following Adaptive Robust Contour Tracking of Machine Tool Feed Drive Systems a Task Coordinate Frame Approach. These work consist in show that contouring performance can be viewed as a regulation problem in a curvilinear task coordinate frame that is attached to the desired contour. By transforming the machine tool feed drive dynamics to this task coordinate frame, an adaptive robust control (ARC) law is derived to improve the contouring performance under system parameter variation and bounded disturbances. The resulting control law is in essence a time varying PID control law with build in integral anti windup. The effectiveness of the proposed control law is demonstrated through the simulated control of an industrial CNC machine tool feed drive system [14].

Huang y Chen, (1997) presented a work with the title following Design of PID Controller for Precision Positioning Table Using Genetic Algorithms. These work consist in demonstrate a PID controller design for high precision positioning table using a real coded genetic algorithm, In order to show the ability of this algorithm, a precision ball screw table are used for evaluation. a real coded genetic algorithm is proposed and tested by implementation on three different examples successfully. The PID gains found in these examples perform well in point to point (PTP) precision positioning. The friction effect is eliminated through the genetic algorithm and zero steady state error is achieved [15].

Lee *et al*., (1997) presented a work with the title following Improved Contouring Control for Multi Axis System

with Two Degrees of Freedom Structure. These work consist in show an position controller with the disturbance observer for multi axis servo system. The overall control system consists of three parts: the position controller, the disturbance observer with free parameters and cross coupled controller which enhances contouring performance by reducing errors. Using two degrees of freedom conception, we design the command input response and the closed loop characteristics independently. The servo system can improve the closed loop characteristics without affecting the command input response. The characteristics of the closed loop system is improved by suppressing disturbance torque effectively with the disturbance observer. Moreover, the cross coupled controller enhances tracking performance. Thus total position control performance is improved o improves tracking performance and contour performance, disturbance observer which influence outer disturbance and uncertainty of modeling and *CCC* which influence contour error are used [16].

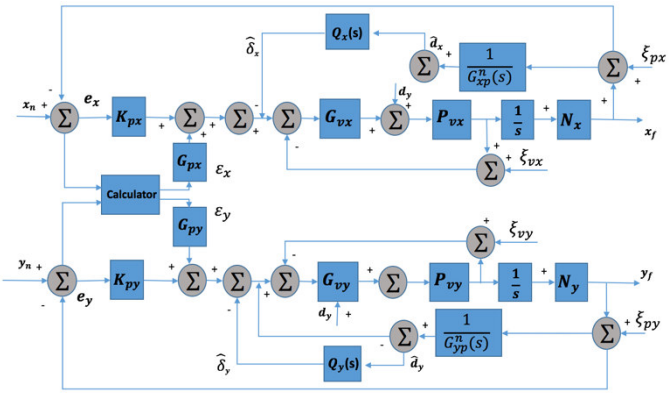

Figure 10. Whole system structure.

Huang *et al.,* (1998) presented a work with the title following Real Coded Genetic Algorithm Based Fuzzy Sliding Mode Control Design for Precision Positioning. These work consist in a fuzzy sliding mode controller was optimized through real coded genetic algorithms and successfully implemented on an industrial XY table. The fuzzy sliding-mode controller is special type of fuzzy controller. By using the sliding surface, the fuzzy rule is simpler and the entire rule base is more compact. Thus, more easily for applying self-learning schemes. The real coded genetic algorithm uses the internal floating point representation of the computer system. With this advantage, the finite resolution problem of traditional genetic algorithm has been solved. The fuzzy sliding mode controller (FSMC) is a special type of fuzzy controller. The fuzzy rule is simpler and the entire rule base is more compact, the speed of fuzzy inference of FSMC therefore is faster than that of conventional FLC. A FSMC with automatic knowledge acquisition through Real Coded Genetic Algorithm (RGA) is applied to solve this nonlinear compensation problem through repetitive learning process. Good parameter patterns are collected and combined step by step, to cope with real parameter changing, floating- point coding other than fix-point coding is employed to resolve the coding resolution problem [17].

Kim *et al.*, (1998) presented a work with the title following Contour Control of Mechatronic Servo Systems using Chaotic Neural Networks. These work consist in contour control of mechatronic servo systems using chaotic neural networks(CNNs). For controlling the trajectories of a X-Y table, control system uses direct adaptive control strategy with modified chaotic neural networks. The proposed controller demonstrates accurate tracking of the planned contour path and also shows excellent performance on convergence and final error comparing with recurrent neural network (RNN) controller. Chaotic neural networks have efficient structure for realizing dynamic characteristics, modified chaotic neural networks are applied to the contour control of servo X-Y table system by direct adaptive control method. To apply dynamic control system, the learning strategy and structure of CNN were modified by error back- propagation algorithm. As results, designed chaotic neural network controller for X-Y table shows excellent characteristics on the final error and learning speed comparing with recurrent neural networks [18].

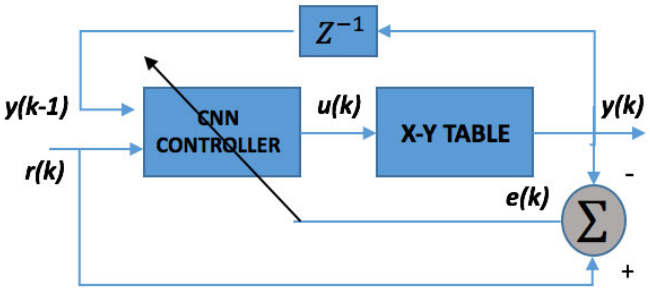

Figure 11. Table X-Y contour control by chaotic neural network.

Mir *et al* (1999) presented a work with the title following Torque Ripple Minimization in Switched Reluctance Motors Using Adaptive Fuzzy Control. These work consist in an adaptive fuzzy control scheme for torque-ripple minimization of switched reluctance machines (SRM) is presented. The fuzzy parameters are initially chosen randomly and then adjusted to optimize the control. The controller produces smooth torque up to the motor base speed. The torque is generated over the maximum positive torque-producing region of a phase. This increases the torque density and avoids high current peaks. The controller is robust toward errors in the rotor position information, which means inexpensive crude position sensors can be used. results are presented [19].

Patino and Liu (2000) presented a work with the title following Neural Network-Based Model Reference Adaptive Control System. These work consist in an approach to model reference adaptive control based on neural networks is proposed and analyzed for a class of first order continuous-time nonlinear dynamical systems. The controller structure can employ either a radial basis function network or a feedforward

neural network to compensate adaptively the nonlinearities in the plant. A stable controller parameter adjustment mechanism, which is determined using the Lyapunov theory, is constructed using a σ modification type updating law. The control error converges asymptotically to a neighborhood of zero, whose size is evaluated and depends on the approximation error of the neural network. In the design and analysis of neural network-based control systems, it is important to take into account the neural network learning error and its influence on the control error of the plant [20].

Yang *et al*., (2001) presented a work with the title following A Reliable H∞ controller design for linear systems. These work consist in procedures for designing reliable controllers are presented for the case of sensor failures and actuator failures that can be modeled by a scaling factor and a disturbance. The resulting control systems are reliable in that they provide guaranteed asymptotic stability and H∞ performance when all control components (sensors and actuators) are operational as well as when some control components experience failures [21].

Cheng *et al*., (2002) presented a work with the title following Real Time NURBS Command Generators for CNC Servo Controllers. These work consist in At first, the engineers have to design molds using CAD, and then the cutter contact (CC) path is converted to the cutter location (CL) path by CAM. In order to guide the CNC machine to perform cutting along the CL path, the CL paths usually are divided into a set of line or circular segments (also called NC codes). These segments will approximate the original CL path to a desired accuracy if sufficient numbers of segments are used. To obtain a more accurate approximation and to reduce the contour error, the size of the NC code should be increased. Based on the above observation and analysis, it is evident that accurate high-speed manufacturing is hard to achieve if the conventional line and circular command generators are used. Therefore, developing a new type of command generator for CNC machines is of importance. It is proposed a real-time Non Uniform Rational B-Spline (NURBS) motion command generator for computer numerical control (CNC) machines to achieve the goal of high speed and highly accurate machining. Different numerical algorithms for implementing the NURBS motion command generator are compared on the basis of both the computation time and the precision of geometric representation. In addition, to reduce the computation time such that the corresponding servo control laws can be executed in real time, both the NURBS motion command generator and the servo control laws are realized using a digital signal processor. This indicates that the NURBS machining approach has significant advantages over the conventional approach [22].

Park *et al.,* (2002) presented a work with the title following Design of a Dual-Drive Mechanism for Precision Gantry. These work consist in Gantry mechanisms have been widely used for precision manufacturing and material handling in electronics, nuclear, and automotive industries. Dual drive servo mechanism is a way to increase control bandwidth, in which two primary axes aligned in parallel are synchronously driven by identical servo motors. With this mechanism, a flexible coupling (compliance mechanism) is often introduced in order to avoid the damage by the servo mismatch between the primary drives located at each side of gantry. This paper describes the design guidelines of the dual-drive servo mechanism with focus on its dynamic characteristics and control ramifications. The error and torque in case of servo mismatch, and the driving force required at each axis to overcome friction forces. In general, it is concluded that the frequency bandwidth can be greatly increased by adopting the dual drive mechanism but once the compliance mechanism is chosen, the curtailment of the frequency band is inevitable. However, the shortening of the band can be reduced up to 20% with slightly controlling the stiffness [23].

Tsai *et al*., (2003) presented a work with the title following A Real Time NURBS Surface Interpolator for Precision Three Axis CNC Machining. These work consist in Due to the fact that the cutting occurs around the cutter contact (CC) point, the efficiency and quality of CNC machining can be improved significantly if the CC velocity along the surface is kept constant. Conventional approaches to machining mainly maintain a constant cutter location (CL) velocity, so that the CC velocity along the surface is often not constant and usually results in non uniform machining and unsatisfactory quality. To overcome this difficulty, this paper presents a novel NURBS surface interpolator that is capable of real time generation of CL motion command for ball end milling of NURBS surfaces and maintaining a constant CC velocity along the CC path and its intervals. For performance evaluation, a three-axis servomechanism driven by three servo motors is controlled to track segments represented by NURBS surfaces. This paper has developed a novel NURBS surface interpolator for real time CL motion command generation of parts represented in NURBS surface forms. The central idea of the proposed method is to maintain a constant CC velocity rather than a constant CL velocity, in which a constant CC velocity along a NURBS surface can improve the machining efficiency and quality significantly. Experimental results have indicated that the proposed NURBS surface interpolator is capable of real time generation of CL motion commands for the servo controller and maintains the desired feed rate (CC velocity) along the CC paths and CC path intervals. Accordingly, the machining efficiency and quality can be much improved through the use of the proposed novel NURBS surface interpolator [24].

Wang *et al.*, (2003) presented a work with the title following Positioning and Tracking Control of an X-Y Table with Sliding Mode Control. These work consist in the sliding-mode control (SMC) technique shows more robust performance than H_∞ control. Some feedforward compensation of the motor ripple and friction may further improve the tracking performance, Van den Braembussche (1998). The discrete-time sliding-mode controller (DSMC) in combination with feedforward, Wang et al. (2003) are designed for an x-y sliding

table driven directly by linear motors. The controllers are designed using an integrated reaching law method, based on a simplified model of the current control loop of these motors. To achieve high bandwidth tracking performance, a feedforward controller is added. Although the sliding table is operating in the presence of friction, no friction compensation is applied [25].

Jang *et al.,* (2004) presented a work with the title following Modeling and Positioning Control of a Ball Screw Driven Stage. These work consist in the ball screw driven systems, the friction behavior dominates the resulting performance and is usually known as the stick-slip phenomenon, friction models are introduced to describe the dynamic behavior of a conventional ball screw driven x-y stage. Two sets of controllers corresponding to the static and the dynamic fiction models are proposed based on the integral type sliding mode control law. The controller designs are carried out by the sliding mode control (SMC) method to reject system disturbances and uncertainties. To provide the system robustness, two integral sliding mode controllers were proposed based on different characteristics of the model dynamics. Comparing with the conventional SMC, the actuator chattering was eliminated by introducing an integral action The controllers were activated according to the friction regimes to fulfill long range operation [26].

Cheng (2005) presented a work with the title following A Novel NURBS Surface Motion Command Generator. These work consist in This study presents a novel real-time NURBS surface motion command generator which ensures a constant CC velocity along the CC paths and its intervals. The advantage is that the machining performance can be improved significantly. To achieve the goal of multi-axis synchronous motion, this study develops a PC based real time motion control network utilizing SSCNET (servo system control network). The experimental results confirm that the proposed real time NURBS surface motion command generator is capable of achieving a satisfactory performance [27].

Hwang *et al*., (2005) presented a work with the title following A Trajectory Tracking of Piezo-Driven X-Y Table System Using Fuzzy T-S Model-Based Variable Structure Decentralized Control. These work is based on a preload design and a suitable feedback gain for the piezo-driven x-y table system (PD-XY-TS), the system response was improved. It was called "enhanced piezo-driven x-y table system (EPD-XY-TS)." Each subsystem of the EPD-XY-TS was then approximated by a weighted combination of *L* linear pulse transfer function systems (LPTFSs). For every nominal LPTFS of the *ith* subsystem, a dead beat to its switching surface was first designed. The output disturbance of the *mth* LPTFS included the interconnections coming from the other subsystems, the approximation error of the *ith* subsystem, and the interactions resulting from the other LPTFSs. In general, this output disturbance was not small and contains various frequencies. In this situation, the *H* norm of the weighted sensitivity function between the *mth* switching surface and its corresponding output disturbance was minimized. In addition, an appropriate selection of the weighted function could reject the corresponding mode of the output disturbance. Although the effect of the output disturbance is attenuated and partially rejected, a better performance could be improved by a switching control [28].

Jang and Kim (2005) presented a work with the title following Optimal Tuning of a Biaxial Servomechanism using a Cross Coupled Controller and Disturbance Observers. These work consist in order to improve the contouring accuracy of a biaxial servomechanism and the robustness against disturbance, a cross coupled controller with a disturbance observer is studied, as well as the optimal tuning based on the integrated design methodology is proposed. Strict mathematical modeling and identification process of a servomechanism are performed first. An optimal tuning problem is formulated as a nonlinear constrained optimization problem including the relevant controller parameters of a servomechanism. The objective of the optimal tuning procedure is to minimize both contour error and settling time while satisfying constraints, such as relative stability and overshoots, etc. Experiments show that the contour error of the system with the optimal tuning results applied to it was smaller than any other systems. Combining the cross-coupled controller and the disturbance observer better performance is obtained in various types of motion [29].

Yau *et al*., (2005) presented a work with the title following Design and Implementation of Real Time NURBS Interpolator using a FPGA Based Motion Controller. These work consist in a novel field programmable gate array based (FPGA-Based) motion controller is proposed to realize real time non uniform rational B-spline (NURBS) interpolator and CNC controller in a FPGA chip. Motion controller expands most computation time on the calculation of basis functions of NURBS curves. For serial computation under PC and nsp architectures, the computation time is proportional to the degree of NURBS curve and the number of motion axis. In contrast to serial computation, the proposed fast Cox de Boor algorithm improves computation performance significantly via parallel computation for multi-axes NURBS interpolation; it is also compatible with B-spline and Bezier interpolations without changing the algorithm architecture. It is shown that, the novel FPGA Based controller can replace the traditional motion controller to execute Cox de Boor algorithms and infinite impulse response (IIR) algorithms in several ten clock cycles. Finally, analytical simulations and experimental results for a X-V table verify the feasibility and computation performance of the novel FPGA-Based motion controller [30].

Yan *et al.,* (2005) presented a work with the title following Research of a Novel XY-table Based on Error Compensation. These work consist in with the increasing demand of high speed high precision positioners in industrial applications, a novel high speed high precision x-y table based on error compensation is presented in the paper. According to

the theory of yaw error compensation (While the x-y table moving on high speed or there be a impulsive force on it, the endpoint will offset from its theoretical position which brings out the yaw error), four inductive sensors were used to measure the yaw error and a micro table used to compensate the error while the macro table moving in high speed mode. Based on theoretical calculation and finite element analysis, the micro table based on piezoelectric actuator (PZT) driven was designed. The cross coupling controller (CCC) took the whole system as the control target to reduce contour error. Experimental results proved that the contour accuracy of the x-y table was improved by applied the error compensation combined with CCC [31].

Chen *et al.,* (2006) presented a work with the title following Adaptive Contouring Control for High Accuracy Tracking. Systems these work consist in the desired performance of the mechanical system is specified in terms of contouring error instead of traditional method which specifies a task as a desired timed trajectory tracking problem. By defining the task frame, a simplified contouring error model is obtained through projecting tracking error to this new frame. Then a novel adaptive contouring controller is developed directly in the task frame to handle bounded external disturbances and system model uncertainties while maintaining superior contouring tracking performance. The algorithm effectively exploits the the structure of manipulator dynamics to reduce the computation complexity [32].

Lin et al., (2006) presented a work with the title following An Adaptive Recurrent Neural Network Motion Controller for X–Y Table in CNC Machine. These work consist in an adaptive recurrent neural network (ARNN) motion control system for a biaxial motion mechanism driven by two field oriented control permanent magnet synchronous motors (PMSMs) in the computer numerical control (CNC) machine is proposed. In the proposed ARNN control system, a RNN with accurate approximation capability is employed to approximate an unknown dynamic function, and the adaptive learning algorithms that can learn the parameters of the RNN on line are derived using Lyapunov stability theorem. Moreover, a robust controller is proposed to confront the uncertainties including approximation error, optimal parameter vectors, higher order terms in Taylor series, external disturbances, cross coupled interference and friction torque of the system. To relax the requirement for the value of lumped uncertainty in the robust controller, an adaptive lumped uncertainty estimation law is investigated. Using the proposed control, the position tracking performance is substantially improved and the robustness to uncertainties including cross coupled interference and friction torque can be obtained as well [33].

Chen *et al*., (2007) presented a work with the title following A Synchronous Drive Control Scheme Based on Neural Networks for a Novel XY-table. These work consist in an adaptive recurrent-neural-network (ARNN) motion control system for a biaxial motion mechanism driven by two field-oriented control permanent magnet synchronous motors (PMSMs) in the computer numerical control (CNC) machine is proposed. In the proposed ARNN control system, a RNN with accurate approximation capability is employed to approximate an unknown dynamic function, and the adaptive learning algorithms that can learn the parameters of the RNN on line are derived using Lyapunov stability theorem. Moreover, a robust controller is proposed to confront the uncertainties including approximation error, optimal parameter vectors, higher order terms in Taylor series, external disturbances, cross-coupled interference and friction torque of the system. To relax the requirement for the value of lumped uncertainty in the robust controller, an adaptive lumped uncertainty estimation law is investigated. Using the proposed control, the position tracking performance is substantially improved and the robustness to uncertainties including cross-coupled interference and friction torque can be obtained as well [34].

IV. CONCLUSION

There is a great variety of controllers for a table x-y that have as purpose to make smooth movements through axes x-y and to obtain the quality necessary in the coating by paint, in this work several types of controllers were presented that can produce smooth movements through the axes x-y and make to face nonlinearities such as delays to reach the desired position, mechanical wear, inertia, etc. It was necessary by take into consideration the main working factors for selecting the controller which are the speed and position with which application device moves of paint. In order to avoid any change in the control parameters of the table x-y that may cause any possible failure within the system, It was necessary that the controller can absorb these changes by performing a compensation of errors in the system. Over time controllers have evolved to obtain high accuracy at the tables x-y and newer controllers can give higher accuracy like the numerical control (CNC) machines in very pronounced trajectories and non uniform geometry, In the application of paint it is not necessary have such high accuracy. So it can be concluded that any of the controllers mentioned in the article can do a good job for this type of activities. Depending of selection of controller can obtain better results in the quality of the product but in some occasions can be very expensive your manufacture.

REFERENCES

[1] P. B. Schmidt and R. D. Lorenz, “Design Principles and Implementation of Acceleration Feedback to Improve Performance of DC Drives.”

[2] T. G. Habetler, F. Profumo, S. Member, M. Pastorelli, and L. M. Tolbert, “Modulation,” vol. 28, no. 5, pp. 1045–1053, 1992.

[3] J. Kim, J. Park, S. Lee, and E. K. P. Chong, “Fa3 10:40,” pp. 451–456.

[4] V. I. Utkin, “Sliding Mode Control Design Principles and Applications to Electric Drives,” vol. 40, no. 1, pp. 23–36, 1993.

[5] J. Kim, J. Park, S. Lee, E. K. P. Chong, and M. Ieee, “A Two-Layered Fuzzy Logic Controller for Systems with Deadzones,” vol. 41, no. 2,

pp. 155–162, 1994.

[6] S. Lee and J. Kim, “CMAC Network-Based Robust Controller for Systems with Friction,” no. December, pp. 2938–2939, 1995.

[7] M. Fischer, “Application and Comparison of Alternative Position Sensors in High-Accuracy Control of an X-Y Table,” pp. 494–499, 1996.

[8] J. Jeon and J. Kim, “High-Precision Control of X-Y Table Using Experimental Evolutionary Programming-Based Scheme,” no. April, 1996.

[9] I. L. Motors, “X-Y by,” vol. 45, no. 1, 1996.

[10] M. Wang and Y. Chen, “Fuzzy Logic Control of a Positioning Table with DSP Real-Time Implementation,” 1996.

[11] M. Tomizuka, “otion Controller for High-Accuracy Positionin,” vol. 43, no. 1, pp. 48–55, 1996.

[12] S. Endo, H. Kobayashi, C. J. Kempf, S. Kobayashi, M. Tomizuka, and Y. Hori, “HIGH-SPEED POSITIONING SYSTEMS,” vol. 4, no. 4, pp. 527–536, 1996.

[13] J. K. J. Jeon and S. L. K. Koht, “High-Precision Control of Positioning Systems with Nonsmooth Nonlinearities,” no. December, pp. 4375–4380, 1996.

[14] G. T. C. Chiu and W. Lafayette, “ADAPTIVE ROBUST CONTOUR TRACKING OF MACHINE TOOL FEED SYSTEMS - A TASK COORDINATE FRAME APPROACH,” no. June, pp. 2731–2735, 1997.

[15] P. Huang and Y. Chen, “Design of PID Controller for Precision Positioning Table Using Genetic Algorithms,” no. December, pp. 3–4, 1997.

[16] J. Lee and H. Park, “Improved Contouring Control for Multi-Axis System with Two-Degrees-of-Freedom Structure,” pp. 901–905.

[17] P. Huang, S. Lin, and Y. Chen, “Real-Coded Genetic Algorithm Based Fuzzy Sliding-Mode Control Design For Precision Positioning,” pp. 1247–1252.

[18] S. Kim, W. Choi, C. Chai, S. Lee, and H. Choi, “Contour Control of Mechatronic Servo Systems using Chaotic Neural Networks,” pp. 2122–2125.

[19] M. E. Elbuluk and I. Husain, “Torque-Ripple Minimization in Switched,” vol. 35, no. 2, pp. 461–468, 1999.

[20] D. Liu, “Neural Network-Based Model Reference Adaptive Control System,” vol. 30, no. 1, pp. 198–204, 2000.

[21] G. Yang, J. L. Wang, and Y. C. Soh, “Reliable H controller design for linear systems ☙,” vol. 37, pp. 717–725, 2001.

[22] M. Cheng, M. Tsai, and J. Kuo, “Real-time NURBS command generators for CNC servo controllers,” vol. 42, pp. 801–813, 2002.

[23] L. Td, “Design of a Dual-Drive Mechanism for Precision Gantry,” vol. 16, no. 12, pp. 1664–1672, 2002.

[24] M. Tsai, C. Cheng, and M. Cheng, “A real-time NURBS surface interpolator for precision three-axis CNC machining,” vol. 43, pp. 1217–1227, 2003.

[25] “OF AN X-Y TABLE WITH SLIDING MODE.”

[26] M. J. Jang, “Modeling and Positioning Control of a Ball Screw Driven Stage,” pp. 943–948, 2004.

[27] C. Cheng and W. Tseng, “Novel Surface Command,” pp. 593–598.

[28] C. Hwang, M. Hsieh, and S. Han, “A Trajectory Tracking of Piezo-Driven X-Y Table System Using Fuzzy T-S Model-Based Variable Structure Decentralized Control,” pp. 49–54, 2005.

[29] M. Jang, S. Kim, S. Chung, and H. S. Design, “OPTIMAL TUNING OF A BIAXIAL SERVOMECHANISM USING A CROSS-COUPLED CONTROLLER AND DISTURBANCE OBSERVERS.”

[30] H. Yau, M. Lin, Y. Chan, and K. Yuan, “Design and Implementation of Real-time NURBS Interpolator using a FPGA-Based Motion Controller - J,” pp. 56–61, 2005.

[31] Z. Yan, L. Sun, and B. Huang, “Research of a Novel XY-table Based on Error Compensation,” no. July, pp. 61–64, 2005.

[32] N. Chen, Y. Lou, and Z. Li, “Adaptive Contouring Control for High-Accuracy Tracking Systems,” 2006.

[33] F. Lin, S. Member, H. Shieh, P. Shieh, and P. Shen, “An Adaptive Recurrent-Neural-Network Motion Controller for X – Y Table in CNC Machine,” vol. 36, no. 2, pp. 286–299, 2006.

[34] J. Chen, Q. Liu, and C. Qi, “A Synchronous Drive Control Scheme Based on Neural Networks for a Novel XY-table *,” pp. 2355–2360, 2007.

Thermo acoustic panels based on mortar with added magnesium oxide.

Ing. Raúl Herrera Vega

Estudiante de la maestría en ciencias (Construcción)
Facultad de Ingeniería de la Universidad Autónoma de Querétaro, Santiago de Querétaro, Qro
raulheve@gmail.com

Dr.Juan Bosco Hernández Zaragoza; Dr. Jose Luis Reyes Araiza
Docente investigador Facultad de Ingeniería.
Facultad de Ingeniería Universidad Autónoma de Querétaro, Santiago de Querétaro, Qro.

ABSTRACT- The objective of the present work is the development of an alternative constructive component (panel) based on sand-cement mortar and magnesium oxide (MgO) addition in percentage of cement; for its application in housing construction for the purpose of its use as a thermo-acoustic material, compared to the main commercial materials. The mechanical properties are measured by destructive tests: axial compression, flexing; and non-destructive such as: density, moisture. To analyze the thermal behavior the hot plate method [1] will be used: placing panel on a constant temperature plate and measuring the time and temperature that the material acquires; For the acoustic properties the speaker method will be applied [2]: the panel will be placed in the opening of a wood box with a sound intensity to the interior and with a sonometer to measure the reduction of the sound to the outside.

Keywords: Slim panel; Mortar; Magnesium oxide.

I. INTRODUCTION

In Mexico, the construction of housing of social interest predominates in a traditional system. These types of housing lack architectural design, materials and construction processes. This leads to constant maintenance or adjustments to achieve comfort (acoustic and thermal).

It is necessary to experimentally determine the thermal and acoustic properties of building materials with more use in the country, as well as those characteristic of each region and whose properties can be improved to help comfort.

Despite the use of appropriate materials and construction processes, there are external agents to the work, which can not be modified at times, such as variations in temperature caused by the urban spot, noise and sounds greater than comfort guidelines for certain activities. For example, INEGI says that climate change (CC) will have serious repercussions in Mexico, since the average annual temperature is projected to increase between 0.5 and 4.8 ° C in the period 2020-2100 [3], this will cause service changes in Existing structures.

That is why it is necessary to develop an alternative material suitable for construction, with the capacity to improve the service conditions, of small thickness, using MgO and evaluating its acoustic and thermal behavior.

Noise causes a wide variety of effects, as well as response, it is perhaps this great variability which makes it difficult to predict the degree of annoyance caused by a noise to a group of people.

The degree of discomfort depends on the task; It is a noise that is more annoying the more it interferes with the task and the more complex it is.

Table. 1 Selection criterion acoustic margins for the development of activities

Tipo de interior Type of interior	Acoustic Margins DB (a)
Libraries and classrooms.	35-45
Laboratories	40-50
Housing (rural)	25-35
Housing (urban)	30-40
Kitchens and dry cleaners	45-55

1.1 Mortar

It is a homogeneous mixture of a cementing material (Portland cement), a filling material (fine aggregate or sand), water and sometimes additives. It is considered a concrete without the coarse aggregate.

The history of mortar is a fundamental chapter in the history of construction. When the man chose to build buildings using clay or stone materials, the need arose to obtain pulps or mortars that will allow joining said masonry to be able to form stable structures. Initially pasta made with clay, gypsum or lime was used, but deteriorated rapidly in the inclement weather [4].

With the development of technology and like many materials used in construction have evolved to obtain the mixture we know today, the mortar consists of cement and / or lime, fine aggregate (sands) and water. In some cases it is necessary the placement of some additives, to give with this certain characteristics that alone does not contain [5].

Mortars are classified in the types indicated in Table 1 [6].

Table 2. Classification of lightweight concrete

types	Parts of Portland cement.	Parts of lime.	Parts of sand.
l	1	0 a ¼	Not less than 2.25 and not more than 4 times the sum of volume cementants.
	1	0	
ll	1	¼ a ½	
	1	0	
lll	1	0 a 1 1/4	
	1		

1.2 Magnesium oxide (MgO)

It is the result of the combination of magnesium with oxygen; this is obtained by a controlled process of calcination of magnetite, also known as magnesia carbonate.

Magnesium oxide (MgO / magnesia) is the most important industrial component of magnesium and is mainly used in the steel and refractory sectors, but also in many other industrial sectors.

1.3 Prefabricated Panels.

Nowadays there are new industrialized systems of construction like the system of panels formed by sheets with polyurethane core or other material, W panel, tablaroca, etc., which are generated for the mass production of housing.

The types of prefabricated panels most used in the construction industry are:

- Lightweight panel: Lightweight interior material covered by mortar or material inlaid with air bubbles or lightweight material, asbestos cement.
- Construction panel: Material entirely made of concrete and steel, for example ferrocement.

1.4 Research work.

For the following work, it is sought to develop a material of physical and mechanical conditions in similarity to a conventional cement-sand mortar, which is apt to be the matrix of production of a panel of thin thickness to be used as wall cladding or as Part of non-structural dividing walls, in order to evaluate its capacity of thermal and acoustic material inside the place of placement.

1.5 Background.

Magnesium oxide (MgO) has been used previously in concrete mixtures in other countries within the last 30 years. However, their uses, and the subsequent benefits of its use, are not anticipated. Engineers working on the arc of gravity of the Baishan bow dam in northeastern China did not observe any significant cracking in concrete dam despite extremely harsh conditions. They found that the content of MgO in the cement was very high, and that this was the only possible reason for so little cracking [7].

When added to concrete mixtures in the correct proportions, magnesium oxide can lead to autogenous expansion of the concrete. This expansion may compensate for part or all of the contraction that would occur in concrete mixtures without higher MgO contents, but the type and amount of added MgO powder may have different effects.

ASTM specifies a maximum MgO content in cement of 6% to avoid this undue expansion. Therefore, it is the supplemental administration of additional, controlled amounts of MgO which helps to mitigate the concrete contraction [8].

II. METHODOLOGY

2.1 Collection and characterization of the raw material.

Magnesium oxide will be obtained with some distributor or distributor of mineral products or raw materials and chemical inputs, having as data of the product: its characterization and technical specifications.

Purchase of base materials for the manufacture of conventional mortar (cement-sand), in order to identify and classify according to provenance and physical properties.

2.2 Moisture content

Based on standard [9], constant weight method, the amount of water that a sand sample has, relative to the dry weight of the sample, shall be determined. This test is carried out before making a concrete mix, in order to make adjustments in the amount of mixing water.

$$\omega = \frac{Ww}{Ws} X100 = \frac{Peso\ de\ agua}{Peso\ de\ arena\ seca} X100 \quad (1)$$

2.3 Granulometry.

The standard [10] allow a relatively wide range in the granulometry of the fine aggregate.

For this project will obtain the material that passes through the sieve No. 4 (4.75 mm) and the percentage of composition will be determined by total volume of particles.

2.4 Experimental test.

For the experimental tests will be made on the basis of a Mix Design, by comparing the means of the response variables, in the different proportions.

The specimens shall be composed of cement, sands, and MgO concentrations of 2% and 4% of the total weight of cement.

The water-cement ratio remains constant.

Table 3. Proportions for test specimens.

Mixture	Cement	Cement Water Ratio	MgO
1	100%	0.45	0%
2	100%	0.45	2%
3	100%	0.45	4%

Once the blends are designed, specimens are fabricated to determine the compressive and flexural strength, with tests in the materials mechanics laboratory of the UAQ, through the use of a universal machine [11].

a) Compression test.

Applying the standard [11] for compression test of mortar for structural use; where the use of 50x50 mm cubic specimens for compressive strength (Rc) in MPa is specified:

$$R_c = \frac{F_c}{S} \quad (2)$$

where:
Fc = maximum applied load (N)
S = surface of load planes = 50x50 mm

Figure 2. Samples and compression test method for mortars.

b) Bending test.

From standard [12], each 40x40x160 mm test piece is flexed by applying a load centered at a speed of 50 N / s on the specimen with two supports at 100 mm clear, determining its flexural strength (Rf) in MPa According to the equation:

$$R_f = \frac{(1.5)(F_f)(l)}{h^3} \quad (3)$$

where:
Ff = applied load (N)
L = distance between supports = 100 mm
B = side of square section

Figure 1. Samples and bending test method for mortars.

2.5 Elaboration of panels.

The previous laboratory tests determine the best mortar mix, in order to use it as a matrix in the production of the desired precast.

The dosage and measurements of all the elements will be unified by weight.

To determine the physical, thermal, acoustic and mechanical behavior of the panels, the number of test pieces will be similar based on the design of the mixtures.

2.6 Physical and mechanical tests.

Once the specimens have been obtained, the corresponding tests will be carried out, mainly those that determine the thermal and acoustic properties.

2.7 Density.

It is obtained by the weight ratio of its occupied volume.

2.8 Moisture content.

It consists in determining the moisture content in hygroscopic equilibrium of the test pieces (representative sample of each type of mixture). It is performed by comparing the weight of a panel under humidity conditions (curing room) and the same panel subjected to oven drying at 105 ° C.

2.9 Thermal behavior.

It consists in determining the moisture content in hygroscopic equilibrium of the test pieces (representative sample of each type of mixture). It is performed by comparing

the weight of a panel under humidity conditions (curing room) and the same panel subjected to oven drying at 105 ° C.

The primary method used will be the guarded hot plate apparatus operating in a steady state condition of heat flow, since it is the method closest to ideal conditions.

If a material is placed between two sources with temperatures TA and TB and TA> TB, then a heat flux is established through the material. If the heat source is uniform (without gradients) the heat flux flows only through the material (there is no loss of heat) and the material is uniform, then the heat flux is uniform anywhere in the material and the conductivity Thermal properties of the material can be calculated by Fourier law

$$k = \frac{qL}{A\Delta T} \tag{4}$$

Where q is the heat flux through the sample, k is the thermal conductivity of the sample, ΔT is the temperature difference across the sample, L is the thickness of the sample and A is the area of the sample. Cross section of the sample.

Experimentally there are gradients in the heat sources and heat losses in the surroundings, this fact causes that the heat flow is not uniform [1].

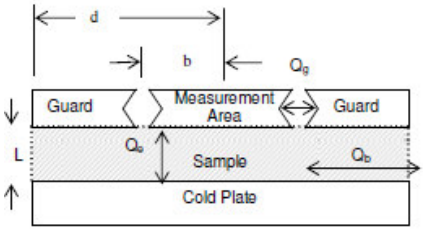

Figure 3. Schematic of the hot plate apparatus [1].

2.10 Acoustic Behavior.

A box, such as an acoustic bench with an open face the size of the prefabricated panels, will be made to perform acoustic reduction tests.

The acoustic behavior is based on determining the "Sound reduction compensated index" Rw, for this the test consists of generating the sound inside the speaker with the panel located in the mouth of the box and measuring the sound difference in dB decibels abroad.

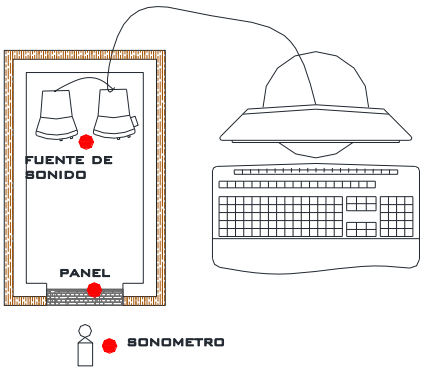

Figure 3. Schematic of the test method.

$$Rw = i1(dB) - i2(dB) \tag{5}$$

where:

I1 = Volume of air, in cm^3

I2 = Total volume, in cm^3

To measure decibels dB a digital sound level meter (figure 12), with a range (35-100 dB), with a sensitivity of 0.5 dB, will be used.

Figure 4. Type of digital sound level meter.

III. EXPECTED RESULTS

When evaluating the density is expected very close to that of the base sample. This will influence the ease of manipulation of the final panel.

Because magnesium oxide has a very high melting point, it will influence the thermal insulation behavior of the material.

The acoustic part of the absorption behavior will be affected by the porosity and the thickness of the final panel.

REFERENCES

[1] Lira, L. (2007). Medición de la Conductividad Térmica de Materiales Aislantes en CENAM ., 1–11.

[2] IRAM 4074 Medidor del nivel sonoro, especificaciones generales.

[3] Sosa-rodríguez, F. S. (2015). Política del cambio climático en México : avances, obstáculos y retos, 4–23.

[4] Hernández C, A (1998) NTP 503, confort acústico, el ruido en las oficinas.

[5] Villalvilla, R., Mont, J. & Agulles, E. (2003). Homogenization Documental, impartición de las Enseñanzas de Contenidos Prácticos. Veracruz, México: Grupo Vitruvio.

[6] Norma N-CTM-2-01-004/02 Cactericticas de los materiales, materiales para mamposteria

[7] Chongjiang Du. (2005). A Review of Magnesium Oxide in Concrete. Concrete International-Detroit, (December), 45–50.

[8] [7] Joy, W. T. (2011). Scoping Study on New Technologies to Halt Concrete Shrinkage and Cracking, (September), 5. Retrieved from http://www.usbr.gov/research/projects/download_product.cfm?id=31

[9] ASTM C 70 – 94 (reaprobada en 2001). Método de ensayo para la humedad superficial en agregado fino.

[10] ASTM C33 – 07 Historical Standard: Especificación Normalizada de Agregados para Concreto.

[11] NMX-C-486-ONNCCE-2014 Mortero para uso estructural

[12] ASTM C348 - 14 Standard Test Method for Flexural Strength of Hydraulic-Cement Mortars

.

CONACYT
Consejo Nacional de Ciencia y Tecnología

CONCYTEQ

Aspects of the implementation of the critical state model in soil mechanics, proposing an improvement for preconsolidated soils

Paulina Lizeth Talamantes Carrillo
"Autonomous University of Queretaro"
Faculty of Engineering
Santiago de Querétaro, Querétaro, México.
pao.talamantesc@gmail.com

***Abstract*— The behavior of the soil depends on many factors and parameters. The critical state model is used as a reference to obtain several special cases and it has come to the deduction that is a presiso model and useful for soils, with some special features. One of the great disadvantages is that when analyzing a preconsolidated soil the model is no longer accurate and varies considerably. Therefore, this document focuses on the proposition of the adaptation of the critical state model for preconsolidated soils.**

Keywords—The critical state model, Preconsolidated soils, model clam-clay.

I. INTRODUCTION

The behavior of soils subjected to external loads or other phenomena can be simulated using constitutive models. A model can integrate and simulate the responses of a soil. The mechanical behavior of the geotechnical materials presents phenomena of creep, irrecoverable deformations and dilatancy induced by shear forces (Gens and D.M., 1988).

These characteristics immediately suggest that the plasticity theory could be very suitable for describing the behavior of soils and rocks.
These models are based on stress-deformation relationships that are normally established by elastoplastic theories. However, the constitutive models can be established considering the main phenomena that occur during the application of loads and are sufficiently precise for different engineering purposes.

The constituent models that are used in geotechnics are mainly based on the hypothesis that is a continuous medium. Thus we start from the three constitutive equations of the mechanics of the continuous medium:

- Equilibration of stresses
- Compatibility of deformations
- Constitutive relation that relates tensions and deformations.

Based on the elastoplastic models, the mechanics of soils have been able to develop, and to respond to phenomena of creep, irrecoverable deformations and dilatance produced by cutting tensions, therefore it is proposed that the application of the theory of pasticity may be adequate, for The explanation of their behavior.

With the criterion of Coulomb (1776), which is known as breaking criterion, which is tested in the analysis of land pressures on walls, which subsequently adapts to several problems in the breakage of soil and the pressures generated by it, However the delimitation of this criterion is that we cannot achieve the complete stress-strain state in the soil, because these methods are restricted to obtaining the tensional state at break.. The critical state models were developed at the University of Cambridge (Drucker 1957), which improves the prediction of soil behavior with a qualitative approach.

The first model that was developed was the Cam-Clay, of which several authors will be based to make improvements or to change them for different special cases.

The critical state model is used as a reference to obtain several parameters in soils, it is an accurate model, its disadvantage is that when working with preconsolidated soils the model varies a lot, and is not precise, which is why an improvement is proposed for This type of soil.

II. MODEL CLAM-CLAY

A. *Elastic state to plastic state in soils*

When the deformation of the material recovers completely after eliminating the applied load, it is said to have an elastic behavior.

$$K = \frac{E}{3(1-2\mu)} \qquad G = \frac{E}{2(1+\mu)} \tag{1}$$

K and G are the elastic behavior is divided into a size change without change of shape (volumetric behavior).

Considering the linear isotropic elasticity (G = constant and K = constant) is a simple way of obtaining the tenso-deformational behavior of soils subjected to loads.

The classical theory of plasticity, its main foundation is the behavior in this case of a soil after a point of fluence, when a load is applied, which is obtained by consequent a decrease of the resistance as the deformation increases.

This is called plastic softening.

B. *Critical Status Line*

Critical line of state depends on the type of soil being studied, because it does not have the same behavior. In agreement with the model of Clam-Clay which is focused on clay is represented as follows.

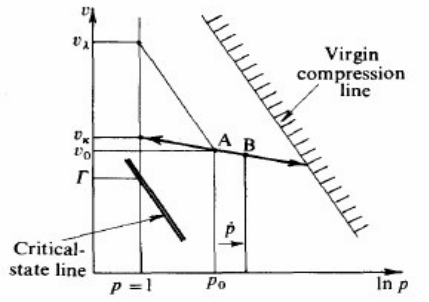

Fig.1 Elastic Change of State (Andrew Schofield)

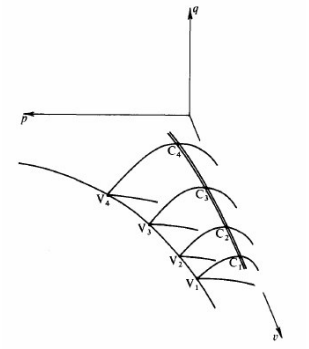

Fig.2 Upper Half of State Boundary Surface for Cam-clay (Andrew Schofield)

The concept of critical state to represent the relationship between the relative density, or index of pores and the pressure of confinement.

C. *Plastic Compressibility and the Tests*

If we have a simple laboratory with only a water supply, a drying oven, a balance and a simple indentation test equipment (such as the falling cone test widely used in Scandinavia), we can find a value of λ for a silty clay soil. We mix the soil with water and remould it into a soft paste: we continually remould the soil and as it dries in the air it becomes increasingly strong. There will be a surface tension in the water of the menisci in the wet soil surface that naturally compresses the effective soil structure as water evaporates. As long as the soil is continually being remoulded it must remain at the critical state (Andrew Schofield).

D. *The Unconfined Compression Strength*

. The critical state model is the natural basis for interpretation of the unconfined compression test. It is a simple test in which a cylindrical specimen of saturated clayey soil sustains no total radial stress $\sigma r = 0$, and the total axial stress σ_1 is rapidly increased until the specimen yields and fails. The unconfined compressive strength qu is defined to equal the ultimate total axial stress σ_1. No attempt is made to measure pore-pressure, and no sheath is used to envelop the specimen, but the whole operation is so rapid relative to the. (Andrew Schofield).

III. HVORSLEV AREA

Hvorslev found a straight line, which is a good approximation for the rupture envelope for preconsolidated soils. Adapting a straight line as a surface of fluence on the supercritical side using numerical applications of the Cam-clay models, which is often called Hvorslev surface, if associated plasticity is adopted, the result is a high dilatancy.

The flow surface itself moves according to changes in plastic volumetric deformation, but the surface of rupture (supercritical) is fixed. Therefore, softening is not predicted. The model implies associated plasticity.

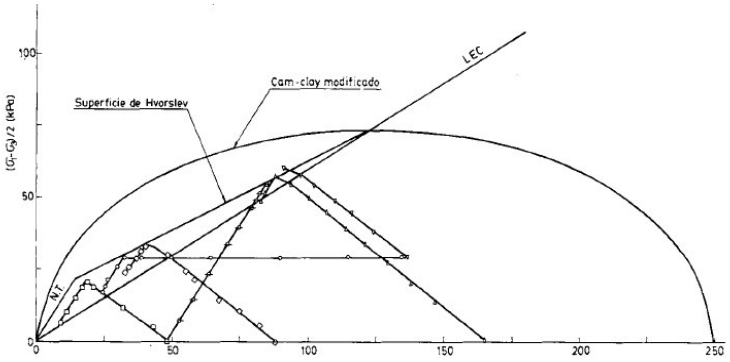

Fig.3 Comparison of the Hvorslev surface and the modified Cam-clay model as a surface of creep on the supercritical side for the Lower Cromer clay.

IV. LIMIT SURFACE MODEL FOR PRECONSOLIDATED CLAYS

The model of preconsolidated clays has a long history. The critical state model provides a broad framework for describing the stress-strain relationships of preconsolidated and normally consolidated soil and represents a starting point for developing constitutive models (Vukic, 2017).

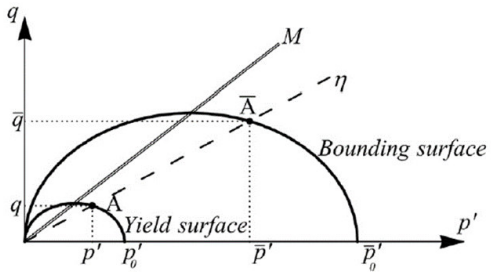

Fig.4 Concept of boundary surface and radial mapping. Hardening State Parameter (HASP)

The Hardening State Parameter (HASP) overcomes many shortcomings of the modified Clam-clay model, while retaining its simplicity and the same set of parameters.
The Hardening State Parameter (HASP) model takes into account the behavior of preconsolidated clays, based on the concept of boundary surface.

V. EXPERIMENTATION TO BE CARRIED OUT

Based on the existing critical state models it is intended to improve, in order to obtain a correlation of the parameters of the critical state model, it is intended to perform triaxial tests.

A. *Experimentation*

It is expected to perform 6 triaxial tests with the same deflector effort but different confining efforts. In addition to performing several consolidation tests.

B. *Explanation of the experimentation to obtain parameters*

First make different test pieces using the same soil, which in this case will be a non-expansive soil.

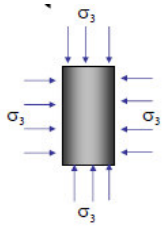

Fig.5 Representation of the soil test piece in the triaxial chamber where (σ_1) diverting effort, confining effort(σ_3).

The confining effort is the one that represents the consolidation of the soil and is the one that will be varied.

C. *Expected results*

With the accomplishment of these tests, to different efforts of confinement, we will obtain the behavior of the same soil, besides obtaining the volumetric changes, obtaining the different slopes and the different points of origin or critical state.

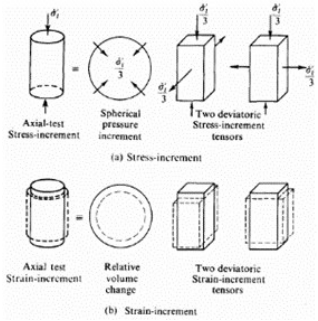

Fig.6 Unconfined Axial Compression of Elastic Specimen

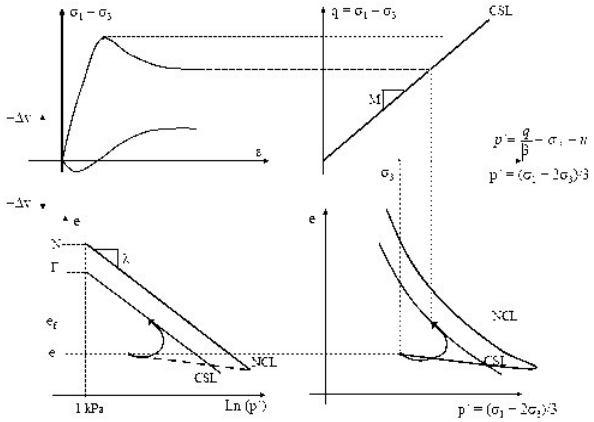

Fig.7 Representation of a consolidated floor drained preconsolidated.

D. *Equations*

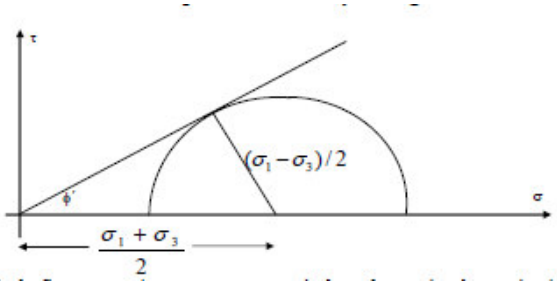

Fig.8 It represents a circle in terms of effective pressures containing the point of failure.

$$(\sigma_1 - \sigma_3) = q \quad (2)$$

$$(\sigma_1 + \sigma_3) = \frac{6p' + q}{3} \quad (3)$$

$$q = Mp \quad (4)$$

$$\Gamma = v + \lambda \ln p. \quad (5)$$

The constants M, Γ, and λ represent basic soil-material properties, and the parameters q, v, and p are defined in due course.

With these equations we can implement a relationship of soil behavior with different confinement efforts.

VI. CONCLUSIONS

The critical states become our base of reference. We combine the effective pressure and specific volume of soil in any state to plot a single point: when we are looking at a problem we begin by asking ourselves if the soil is looser than the critical states. In such states we call the soil 'wet', with the thought that during deformation the effective soil structure will give way and throw some pressure into the pore-water (the amount will depend on how far the initial state is from the critical state), this positive porepressure will cause water to bleed out of the soil, and in remoulding soil in that state our hands would get wet. In contrast, if the soil is denser than the critical states then we call the soil 'dry', with the thought that during deformation the effective soil structure will expand (this expansion may be resisted by negative pore-pressures) and the soil would tend to suck up water and dry our hands when we remoulded it. (Andrew Schofield).

With the planned experimentation it is tried to find an improvement for preconsolidated soils in models of critical state, with that to raise a relation and adaptation of the model of the critical state.

There are different constitutive models, which predict the behavior of soils, but each one focuses on specific phenomena.

Some constitutive models that have been developed only apply under certain conditions and with certain types of soils. However, there are many problems where different states and different types of soils are required.

The constitutive models that exist use parameters that were obtained by performing triaxial tests using expansive soils.

Existing models applied to highly preconsolidated soils have important shortcomings.

As mentioned above, we intend to make a constitutive model with non-expansive soil, in triaxial drained tests, with preconsolidated and normally consolidated soils.

REFERENCES

[1] Roscoe, K. H. and Schofield, A. N. Mechanical Behaviour of an Idealised Wet

[2] Roscoe, K. H., Schofield, A. N. and Thurairajah, A. Yielding of Clays in States

[3] Burland, J. B. Correspondence on 'The Yielding and Dilation of Clay',

[4] Géotechnique 15, 211 – 214, 1965.K. Elissa, "Title of paper if known," unpublished.

[5] Bishop, A. W., Webb, D. L. and Lewin, P. I. Undisturbed Samples of London Clay from the Ashford Common Shaft: Strength Effective Stress Relationships, Géotechnique 15, 1 – 31, 1965..

[6] Casagrande, A. Characteristics of Cohesionless Soils affecting the Stability of Slopes and Earth Fills, J. Boston Soc. Civ. Eng., pp 257 – 276, 1936.

[7] Andrew Schofield and Peter Wroth, Critical Satate Soil Mechanics.

CONACYT
Consejo Nacional de Ciencia y Tecnología

CONCYTEQ

Development of sustainable framework by sawdust and plastic as aggregates in support of bioclimatics

José Pablo Balderas Rojas
Maestría en Ciencias, Departamento de Posgrado
Universidad Autónoma de Querétaro
Querétaro, México

Dr. José Luis Reyes Araiza
Maestría en Ciencias, Departamento de Posgrado
Universidad Autónoma de Querétaro
Querétaro, México

***Abstract*— Sustainable formwork for concrete molding through the use of sawdust and plastic as aggregates in a way that is practical, economical and ecological, which with its physical and mechanical characteristics will contribute to be more efficient than the current formwork and its application will be simpler , all in contribution to bioclimatics problems**

Keywords—formwork; sawdust; plastic; sustainable;

I. INTRODUCTION (*HEADING 1*)

Actually the formwork in Mexico and a lot of countries hasn´t been developed in a productive, sustainable, economical or practical way. Actually we´re using new wood, this is a big problem because of the deforestation, then we apply it used oil for nonsticking to the concrete, and then we throw away this wood with used oil to the closest landfill, this is a huge problem for our soils and oceans. So it's a need that we have to find a sustainable way to do formwork

Actually exists a new material called WPC(wood plastic composite) made with wood, plastic and additives. These material it's made by mixing these three materials and then melting them. These material its sustainable because we could make it with recycled plastic, with waste sawdust, also this materials in the market are very cheap so, if the process it´s not expensive, it wouldn´t be a problem to introduce it to the actual market.

II. PROBLEMS IN THE ACTUAL PROCESS OF FRAMEWORK

A. *Deforestation*

Changes in land cover, including high deforestation rates, are considered to be the main drivers leading to environmental degradation, land fragmentation and loss of biodiversity at a global scale (Lambin et al., 2001). Global deforestation in the tropics is a consequence of changes in land cover at local and regional scales, due to socio-economic, demographic and biophysical factors that explain the spatial land-use patterns in this ecosystem (Pan et al., 2004; Lambin y Mayfroidt, 2011). Spatial differences in the patterns of land use emerge because not all uses are equally profitable; soil quality, access and distance induce revenue losses and differ in each case (Bakker y Veldkamp 2012).

B. *Used oil*

The pollutant potential is enormous if we consider that with only two liters are able to contaminate all the water of an Olympic pool and a single liter can contaminate the surface of a football field.

This substance contains a series of hydrocarbons that are not biologically degradable and that destroy the humus vegetal and end with the fertility of the soil. The used oil also contains toxic substances such as lead, cadmium and chlorine compounds, which seriously pollute the earth. Its contaminating action is also reinforced by the action of some additives that are added and that favor its penetration in the ground, being able to be contaminated the groundwater.

If they are discharged into the waters, either directly or through the sewage system, the used oil has a great capacity for environmental deterioration. It produces a film impermeable,

that prevents the proper oxygenation and that can asphyxia to the living beings that inhabit there. For example, only one liter of oil contaminates one million liters of water.

Also, the oil used, due to its low biodegradability, seriously affects the biological treatment of water treatment plants, even disabling them. If used oil is burned, only or mixed with fuel oil, without proper treatment and control, it causes significant pollution problems and emits very toxic gases due to the presence of lead, chlorine, phosphorus and sulfur compounds. Five liters of oil burned in a stove pollute, with lead and other harmful substances, 1,000,000 m3 of air, which is the amount of air breathed by a person for three years. Pouring five liters of used oil into the sea, creates a thin film of grease of 5,000 m2 that hinders and contaminates marine life

C. Non practical formwork

Currently in Mexico, the cimbra has not had a refinement process, the most "novel" systems are the steel frame, and in other countries is already occupied with plastic-modulated formwork.

If there is a process in which the frame is already prefabricated and will simply be placed on site, without having to do it on site, it would be a more efficient and therefore economic process.

Also if the material to be cut was a material that does not adhere to concrete, there would be no need to spend on a nonstick, which in this case is the used oil, so there would be a saving in materials and in manufacturing.

III. OBJECTIVE

Development of sustainable framing for concrete molding through the use of sawdust and plastic as aggregates, which with its physical and mechanical characteristics will contribute to be more efficient in terms of time of laying on site and more economical than a wooden frame

IV. WPC

Wood plastic composite (WPC) is a composite material made from sawdust and plastic as polymer bonding, that´s used in a variety of structural and nos-structural applications. Nowadays is made from sawdust and recycled HDPE plastic.

Thermoplastic composites with sawdust (WPC) have some advantages over the conventional mineral material. They are lighter in compared to the fiber glass = 2.5 kg/m3, CaCO3 or talc = 2.8 kg/m3. Moreover, these materials are less abrasive and not wear the equipment (CAMARGO, 2006). Consumption of composite is very significant in the USA - about 1,170,000 ton of wood-profile extruded plastic was produced. In Europe, consumption was approximately 1,200,000 ton each in 2007. The consumer sectors are furniture, packaging (pallets) and construction (manufacture of terraces, balconies, ceilings, etc.). In the other countries, like Brazil and Chile, consumption still comes up in the cultural barrier that can be broken through an appeal of environmental issues facing marketing (OMEGA, 2007).

An important factor in the quality of the material is the use of polymer HDPE – High Density Polyethylene. Thanks to this the material gets the wishing properties and still looks like wood. Composite materials have been enlarged thanks to mastering of the technology since the start of the production in the 90s of the last century and its popularity is growing ever since.

Generally, there are four main factors that make the use of natural fibres and wood in plastics attractive: (1) they enhance specific properties e.g. stiffness and thermal behaviour (2) they reduce the price of the material (3) they heavily improve the bio-based share and (4) they are better recyclable when compared to glass fibres. When compared with glass fibre, wood fibre offers a weight reduction for the composite, which can be an important factor in transport costs. After more than 30 years of market development, in 2010 global wood-plastic composite production reached 1.5 million extruded tonnes, which would mean, with an average wood share of 50%, 750,000 tonnes of wood - which is still only a fragment of the total timber market. WPC is predominantly extruded worldwide to hollow or solid decking boards and is predominately replacing tropical wood. The oldest market can be found in North America where a few big companies make the running.

Today’s major production growth rates of WPC can be found in the Chinese WPC-extrusion (25% p.a.) and also Chinese domestic demand for WPC is growing. China’s WPC industry is the second largest in the world after the United States. According to the forecast (Fig. 1) China will reach 33% of the global WPC production in 2015, following the USA, which produces almost half of the total global market share. After China, South East Asia, Russia, South America and India are rapidly emerging WPC markets. Decking continues to be the most common field of application for WPCs, also in Europe, where sales of solid profiles are rising compared to hollow ones, but injection moulded decking tiles are also produced. In Europe the WPC decking market has reached the mature stage, which means lower growth rates for the companies involved. This development is driving producers to look for new areas of application. Initially this was in the field of garden fencing and siding.

TABLE I. Production of WPC in the World

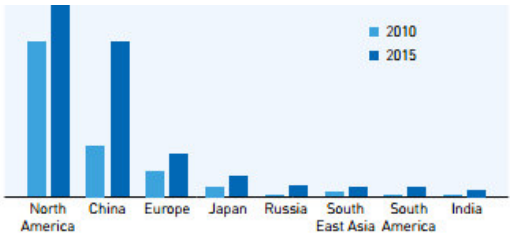

	2010	2015	growth % p.a	global share in 2015
North America	900000	1300000	8	48%
China	300000	900000	25	33%
Europe	150000	250000	11	9%
Japan	60000	120000	15	4%
Russia	10000	70000	48	3%
South East Asia	30000	55000	13	2%
South America	10000	50000	38	2%
India	5000	40000	52	1%
Total	1450000	2695000	13	103%

A. *Benefits of using WPC*

1) **Low maintenance**: WPC can stand up against the elements without the need to seal, stain or paint it, which are burdens associated with traditional building materials. Also, it is resistant to bugs so you may not face the need to replace insect damaged, uneven or rotting WPC boards.

2) **Safe**: As opposed to traditional wooden building material, WPC boards are slip-resistant and splinter free

3) **Durable**: Wood boards and decks look good but do not last long. Frigid winters, rainy springs and scalding summers make wooden material warped, splintered and faded. WPC is not much affected by these factors and come with assured warranties for durability. WPC does not corrode, rot or decay.

4) **Cuts expenses**: In the short term, the wood material may seem cheaper but in the long run, WPC is the better cost saving material as it avoids costs like cleaning and sealing. Wood tends to splinter and warp over time.

5) **Easily mold-able**: WPC has great work-ability and can be fashioned using traditional woodworking tools

In the next picture we can see the tensile strength in wpc, according to a experiment done in Indonesia

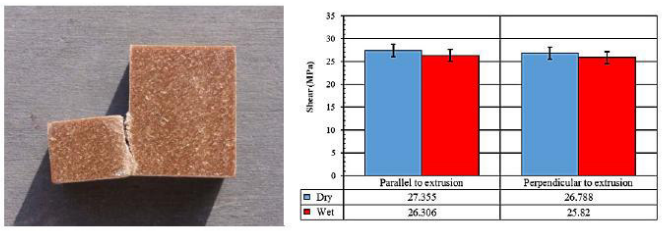

Fig. 1. Tensile strength in WPC made in Indonesia

.

V. Results

By means of a thermoforming process, a very practical sample was made, which can be seen in the following figures:

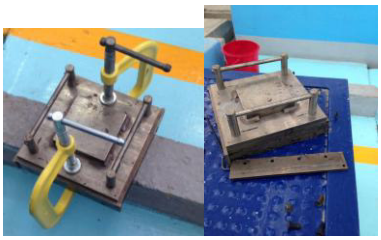

Fig. 2. Proccess of WPC made in UAQ

Fig. 3. Sample of WPC made in UAQ

As we see in the picture the sample has a lot of strength and it seems that in one side has te qualities of plastic, so it would be ideal as a formwork as it doesn´t stick to the concrete.

VI. Conclussion

These article explains the importance of using new materials in the formwork for construction of concrete structures. It´s important because we have already being using these material in other areas and these studio shows the possibility to use the WPC in formwork and it´s benefits. It´s very important to stop using new wood in the process of formwork because of the deforestation and also to stop using used oil because it´s a hazardous waste. Also it´s important to

do these investigation because as we read in the article it could be a economical benefit for the constructors.

We also have to consider that the wpc has to be improved, and after that we have improved the best, we need to consider to do tests of tensile strength, toxicity of the process and the adhesion to concrete.

ACKNOWLEDGMENT

The authors wish to express their appreciation to the researcher José Luis Reyes Araiza and Ruben Ramírez Jiménez for for his helpful advises and his kind help during the writing and experimental process.

[1] O. Faruk, A. Bledzki, H. Fink, M. Sain, Bio-composites reinforced with natural fibers: 2000-2010, Progress in Polymer Science, 37, 1552-1596, 2012

[2] K. Wuttke, Preparation of raw materials for extrusion process in wood plastic composite industry, 5th Global Wood and Natural Fibre Composites, Kassel, 2004

[3] R. Kozlowski, M. Wladyka-Przybylak, A.K. Jakubowska, State of the art in the research on nat-ural fibers and their properties used in composites, 7th Global WPC and Natural Fiber Composites Congress and Exhibition, June, 2008, Kassel Ger-many

.

[4] W. Fung, M. Hardcastle, Textiles in automotive engineering, Woodhead Publishing Ltd, Cambridge, England, 2001

.

[5] A. Bledzki, O. Faruk, A. Jaszkiewicz. Cars from renewable materials, COMPOSITES 10: 3, 282-288, 2010

[6] A.K. Bledzki, O. Faruk, Woodfibre reinforced polypropylene composites in an injaction moulding process. Polymer Plastics Technology and Engineering, 42(2004) 3

[7] O. Faruk, A. Bledzki, H. Fink, M. Sain, Bio-composites reinforced with natural fibers: 2000-2010, Progress in Polymer Science, 37, 1552-1596, 2012

CONACYT
Consejo Nacional de Ciencia y Tecnología

CONCYTEQ

Falsework made of cellulose cardboard for use in plinth and columns.

Ing. José Guadalupe Martínez Pérez
Universidad Autónoma de Querétaro
Facultad de Ingenieria
Querétaro, México
jose.gpe.mtz.27@hotmail.com

Dr. Juan Bosco Hernández Zaragoza
Universidad Autónoma de Querétaro
Facultad de Ingenieria
Querétaro, México
bosco@uaq.mx

***Abstract*— The following work consists of the elaboration of a material made of cardboard cellulose. This cellulose will be made from recycled cardboard and periodic material, the latter will be processed to obtain paper pulp which will be placed in molds to manufacture elements of falsework. The paperboard cellulose elements will replace the wood, steel, plastic and other materials used to make falsework. It is expected to obtain a more economical material than wood, but with the same characteristics of resistance to compression and of water absorption.**

Keywords—cardboard cellulose; recycled material; paper pulp; falsework; economical.

I. INTRODUCTION

Many of the problems currently studied and discussed at the global level are those related to global warming and pollution; This is due to the little interest of the different companies that refuse to develop sustainable materials that do not endanger the development of future generations, for this reason it is important to implement the recycling of materials and give them a new or second use [1]. This article presents a new material made of cardboard cellulose, which will be used to replace wood, steel, plastic and other materials in the concrete falsework.

The falsework is a system composed of generally wooden forms and their supports, whose function is to contain the concrete until it has reached at least the necessary resistance to self support

1.1 Classification of the falsework

a) Contact falsework

b) False play

The contact falsework is the one that is in direct contact with the concrete, its main function is to contain and configure the concrete according to the design of the structure; Is made up of panels, pallets, prefabricated molds among others.

The false play is constituted by the elements that support the contact falsework, among them are used beams, feet rights and others [2].

The falsework are used to create different concrete structures as they are [3].

- Falsework for foundations.
- Falsework for columns.
- Falsework for walls.
- Falsework for slabs and beams

They can be classified as plinth for walls and plinth for columns. A wall plinth consists of a strip of reinforced concrete wider than the wall and distributing its pressure. Column plinth are usually square, representing the simplest and most economical type of foundation [4].

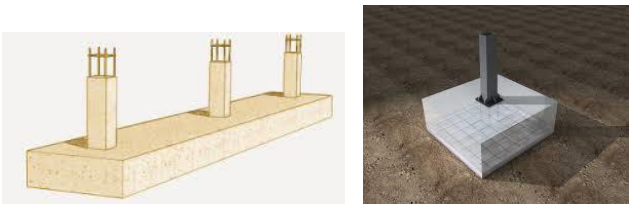

Figure 1. Wall and column plinth.

The columns are elements that hold mainly charges to compression. In general, they also support bending moments with respect to one or both axes of the cross-section and this bending action can produce stresses on a part of the cross-section.

Figure 2. Falsework of concrete columns.

1.2 Falsework materials

The materials of the falsework are established by the economy, the need, or by a combination of both factors.

Among the most common materials are wood, steel and aluminum, if the falsework can be made in boards or other forms that allow them to be used as many times, as this can make the cost lower by each operation.

The following can be used as a falsework material:

Tabla 1. Some materials for falsework and form of use [5].

Material	*Primary use*
Steel	Heavy falsework, columns, scaffolding, struts.
Aluminum	Lightweight panels
Pressed paper	Columns, slabs.
Corrugated cardboard	Beams, slabs.
Fiberglass and plastic	Reticular slab, apparent finishes.
Wood	Various finishes, scaffolding.
Wood chipboard	Apparent finishes.

1.3 Paper pulp

The paper consists of a fabric or structure of vegetable fibers with a high content of cellulose, this cellulose is present in plants or vegetables such as: cotton, wood, cereal straw, sugar cane among others. At present most of the world's paper production comes from wood, the largest proportion of pulp is made from wood pulp, approximately 89% of total production, the remainder is made from other fibers [6].

The main objective of carton cellulose is to create an ecological, economic and safe material.

In the civil work, a very important aspect is related to money, both for the contractor and the builder, and the creation of new materials will benefit both parties.

The cost of the falsework for a concrete work, can represent between 35 and 60% of the total cost for concrete, so the design and construction of structures requires good planning and good judgment, which guarantees economy and safety.

It should be taken into account that to produce a ton of virgin paper requires about 2 to 3.5 tons of trees to be processed in a pulp mill. This involves using large amounts of water, energy and chemicals, and generates large amounts of gaseous and liquid pollutants and solid waste.

II. MATERIALS

A. Cardboard and paper

The paper is obtained from a paste of vegetable fibers which is subjected to processes such as refining, gluing or coloring. To this are adhered a series of substances that as final product will form a thin sheet which is the sheet itself.

The fundamental raw material used in papermaking is cellulose; Derived mainly from wood from trees, from non-timber plant fibers from shrubs such as cotton or flax, and *fibers recovered through the recycling of paper and paperboard.*

B. Wood

The wood is formed by 4 main constituents: The cellulose fibers represent approximately 40 to 50% of the wood. Approximately 25 to 35% of a tree is hemicellulose, another 20 to 30% is lignin, a low molecular weight organic cement that binds the various constituents of the wood. Finally, the extractives, the latter represent up to 10% of the total wood [7].

C. Glue

It is a product that is used as a binder and achieve adhesion from one object to another. Its purpose is to get things together once their surfaces come into contact.

III. METHODOLOGY

The methodology will be divided into stages:

A) Procurement of materials:

In this will be obtained the materials for the development of the investigation, as they are, cardboard, newspaper, wood and glue.

The cardboard and the newspaper will be obtained from the product of the recycling, in order to reduce the price of the new material.

The wood will be used to make the molds for the elements of falsework, will be joined with hinges for their better detachment.

The glue will serve to join the pulp of paper and paper that is obtained.

B) Mold making

Molds will be manufactured for the molding elements with specified dimensions, in order to join the corners, hinges will be used, so that when the element is removed from the mold, it is easier to remove them.

Figure 3. Mold making

C) Preparation of cellulose

Strips of both paperboard and newspaper, about 2 cm thick, shall be cut and placed in a container.

Figure 4. Material cut

Water will be heated and poured into the vessel with the strips of material, while the water will cool, circular movements with a stick.

Figure 5. Pulp paper

Subsequently the material to be ground in a blender is passed and the excess moisture is subsequently removed.

Then the pulp will be placed in the molds and expected to be completely dried. Then a cast of a shoe and a column will be made.

IV. Expected Results

It is hoped to obtain a new material that can substitute mainly wood in elements of falsework.

Being a material made from recycling products is cheaper and will help reduce the pollution generated by such materials.

Compressive, bending and absorption resistances similar to those of wood are expected to allow the elements made of cellulose to successfully replace the wood and other materials used to manufacture falsework.

A material with minimum strengths as follows:

Compression perpendicular to the fiber: 0.3 - 0.4 N/mm^2.

Compression parallel to the fiber: 8 - 18 N/mm^2.

References

[1] Omer, A.M. 2008. Energy, environment and sustainable development. Renew. Sustain. Energy Rev. 12:2265-2300.

[2] Alcaraz, F. 1990. Diseño de cimbras de madera. Ed. Fundec A.C. México.

[3] Díaz-Infante, L.A. 2009. Curso de edificación. Ed. Trillas. México..

[4] Nilson, A. 2001. Diseño de estructuras de concreto. Ed. Mc Graw Hill..

[5] PEMEX, 2000. Especificación técnica para construcción de obras. Cimbras para concreto. Norma P.3.0135.01.

[6] Greenpeace. 2006. El futuro de la producción de celulosa y técnicas de producción más desfavorables para el medio ambiente. Febrero. USA.

[7] Askeland, D. y Phulé, P. 2005. Ciencia e ingeniería de los materiales (4ta edición). Ed Thomson. México.

Effect of several acids on the photocatalytic performance of TiO_2 powders obtained by Sol-Gel

A. Velasco-Hernández, S. A. Mayén-Hernández
Departamento de Materiales-Energía
Facultad de Química, Universidad Autónoma de Querétaro, UAQ.
Querétaro, Qro., México.
rexarturo93@gmail.com

M. Sánchez-Domínguez
Centro de Investigación en Materiales Avanzados, Unidad Monterrey.
Apodaca, N.L., México

***Abstract*—Nanocrystalline titanium dioxide (TiO_2) powder was synthesized by using a simple sol–gel technique. By hydrolyzing titanium tetraisopropoxide in a mixture of ethanol, deionized water and some catalyst acid (HBr, HCl, HF, HI), TiO_2 nanopowder was obtained. The nanopowders were characterized by diffuse reflectance spectroscopy, X-ray diffraction and Scanning Electron Microscopy (SEM). The photocatalytic performance was determined by the photodegradation of methylene blue in aqueous solution and quantified by UV-Vis spectroscopy.**

Keywords*— *Titanium dioxide; Sol-gel; Nanopowder; Synthesis; Photocatalytic performance

I. INTRODUCTION

For the degradation and mineralization of many aqueous pollutants, including some that are very difficult to remove by conventional methods, the heterogeneous photocatalysis with Titanium dioxide is a promising technique [1].

Titanium dioxide (TiO_2) ceramic is used in a variety of applications in industry and in our daily life [2]. As for many oxides, properties of TiO_2 are directly determined by its polymorphs. TiO_2 occurs in nature in three different phases, namely, rutile, anatase and brookite. The rutile is the most stable structure of TiO_2, whereas the anatase and brookite are considered as metastable forms. Nevertheless, the highest photocatalytic activity is attributed to the anatase phase [3].

Photocatalytic processes in polluted air and water through the use of UV irradiated inorganic oxides degrade the concentration of contaminants [4]. Photocatalysis is widely used to describe the process in which the acceleration of a reaction occurs when a material, usually a semiconductor, interacts with light of sufficient energy (or of a certain wavelength) to produce reactive oxidizing species which can lead to the photocatalytic transformation of a pollutant. It must be noted that during the photocatalytic reaction, at least two events must occur simultaneously in order for the successful production of reactive oxidizing species to occur. Typically, the first involves the oxidation of dissociative adsorbed H_2O by photogenerated holes, the second involves reduction of an electron acceptor (typically dissolved oxygen) by photoexcited electrons; these reactions lead to the production of a hydroxyl and superoxide radical anion, respectively [5].

II. EXPERIMENTAL PROCEDURE

A. *Synthesis of nanocristalline TiO_2 powders*

Nanocristalline TiO_2 powders were synthesized via a sol-gel method using titanium tetraisopropoxide (TTIP, Sigma Aldrich, USA, 97%, solution), Ethanol (J. T. Baker, USA, 99.8%) and deionized water as starting materials. TTIP was added into the half of volume of Ethanol, the deionized water and the catalyst acid were mixture with the other half volume of Ethanol. The first solution was added in drops in the second solution while stirring was applied at the same time. The reactant ratios were as follows; $M_{TTIP} : M_{ethanol} : M_{H2O} : M_{acid}$ = 1:36:A:B, where A is 0, 1, 3 and 5 and B is 0.1, 0.3 and 0.5 for the acids: HB, HCl, HF and HI. The preparation of these solutions required an inert atmosphere. The samples were allowed to stand and dry in the environment until the material was completely free of liquids. Once the samples were dry, they were ground in an agate mortar. No washes were performed to remove the remaining acid in the samples.

B. Photocalytic activity

Photocatalytic activity of TiO_2 samples was evaluated in a reactor equipped with magnetic stirring and PL-S lamp (8 W/cm^2) placed into the reactor. Reaction mixture consisted of 400 mL of methylene blue solution (6.397 ppm in water), 0.5 g/L of TiO_2. The photolysis experiment was done for 5 h and the adsorption experiment in dark achieved the adsorption equilibrium in 30 minutes. After the adsorption equilibrium was reached, the lamp was turn on and samples were taken every certain time period. The methylene blue concentration was followed by UV-Vis spectroscopy in the range from 500 nm to 750 nm.

C. Powders Characterization

Phase characterization and calculation of average crystallite size of the powders were studied by XRD technique. XRD patterns were recorded in the 2θ range of 10° to 90° with an automated X-ray diffractometer (Panalytical Empyream) using Cu Kα radiation (λ = 1.5418A°) in the step scanning mode, with tube voltage of 45 kV and tube current of 40 mA. The 2θ step size was 0.033°and 29.845 s per step. Crystallite size was further verified from XRD patterns using the Sherrer equation:

$$\beta = 0.9\lambda / [\langle d \rangle \text{ Cos } \theta] \qquad (1)$$

where λ is the wavelength of X-rays, θ the Bragg angle, ⟨d⟩ the average crystallite size, and β is the full width at half maximum.

UV-Vis measurements were performed on a spectrometer (Ocean Optics) with optical fiber. The integration time was 2.2 s. The spectrum was measured in transmission mode and the band gap was calculated from Kubelka-Munk model.

The morphology of the synthesized TiO_2 powders were studied using SEM(Model Nova NanoSEM200, FEI Co., Hillsboro, OR). Results and discussion

III. RESULTS AND DISCUSSION

Fig. 1 shows the results obtained by X-Ray diffraction for the different samples of TiO_2 prepared by sol-gel method. According to this, in the interval 2θ = 20° - 90° the four samples prepared with different hydrolysis catalyst are polycrystalline materials since they have reflection characteristic of TiO_2 in anatase phase, according to card ICDD PDF 21-1272 and rutile phase, according to card ICDD PDF 78 – 1509. In order to obtain an average particle size, the Scherrer's equation was applied to two of the samples with well-defined peaks. Table 1 lists the calculated values, corresponding to the samples prepared with HF and HBr. Therefore an outstanding influence in crystallinity can be detected during the synthesis due to hydrolysis catalyst.

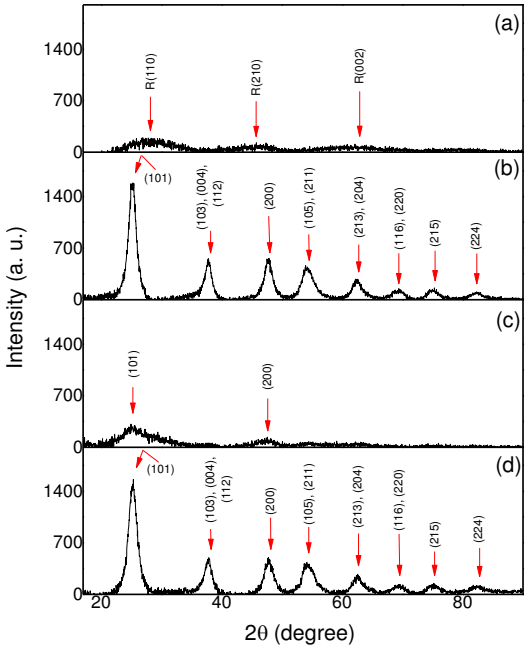

Fig.1. XRD of various TiO_2 powders synthesized with different hydrolysis catalyst, (a) HI, (b) HF, (c) HCl and (d) HBr.

Determination of band gap energy was essential for identification of changes in the electronic structure of TiO_2 powders obtained with different acids during the synthesis. The band gap values for the different samples can be seen in Table 1, these values were obtained using reflectance technique by applying the Kubelka-Munk theory and estimated from the intercept with x-axis.

The analysis showed a band gap value of 3.33 eV (using HCl) < 3.42 eV (using HBr) < 3.46 eV (using HF) < 3.66 eV (using HI). This behavior can be explained by the presence of vacancies of titanium in the crystalline structure as a result of the hydrolysis catalyst, suggesting that protons and oxygen interact to form OH ions that are liberated [6].

Table 1. Main physicochemical properties of TiO_2 prepared by sol-gel route using different hydrolysis catalysts.

Hydrolysis catalysts	**M_{TTIP} : M_{acid}**	**M_{TTIP} : M_{H2O}**	**Particle size (nm)**	**Band gap (eV)**
HI	1:0.5	1:1	-	3.66
HF			6.34	3.46
HCl			-	3.33
HBr			5.55	3.42

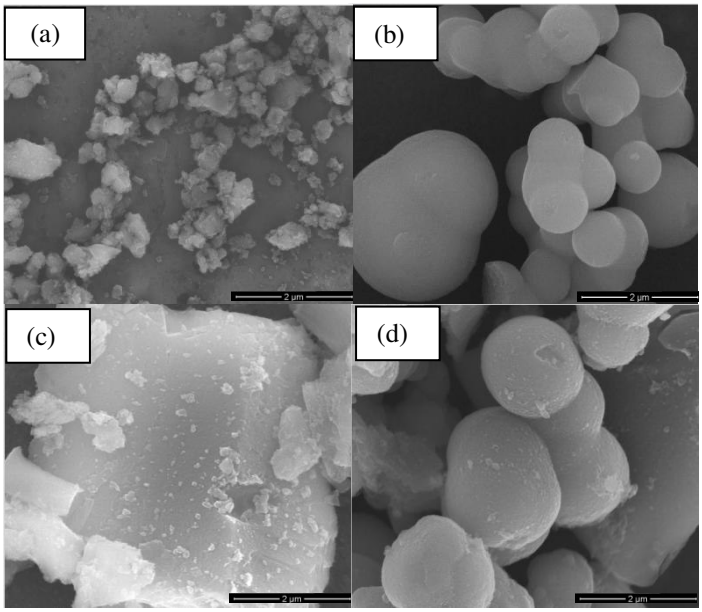

Fig.2. Scanning electron micrographs of various TiO_2 powders synthesized with different hydrolysis catalyst, all to 50000 X, (a) TiO_2 (using HI), (b) TiO_2 (using HF), (c) TiO_2 (using HCl) and (d) TiO_2 (using HBr).

Fig. 2 shows the scanning electron microscopy (SEM) images for the samples in study. These micrographs clearly show that there are changes in the surface morphology of the TiO_2 with the adding of the hydrolysis catalyst.

The shape of the aggregates of the TiO_2 powders using HF and HBr as hydrolysis catalysts have a near-spherical morphology with well-defined coatings, while the sample using HCl as a hydrolysis catalyst has almost parallelepiped aggregates.

The photocatalytic activity was studied by the bleaching of a water diluted methylene blue (MB) solution. The MB residual normalized concentration [MB] was determined indirectly from the absorbance spectra. The Fig. 3 shows the [MB] normalized as a function of the exposure time for the samples of TiO_2 prepared with different hydrolysis catalysts.

It can be observed from these graphs that the sample prepared with HBr as catalyst has a better photocatalytic performance, which presents high crystallinity compared to the other samples and its morphology and the aggregates is almost spherical. The other samples show similar behavior between them; however, the results obtained for other syntheses show that for TiO_2 powders prepared with HF as catalyst show a competitive behavior with the samples prepared with HBr. These two acids as catalysts, promote the formation of planes (101) that can be related to their photocatalytic efficiency.

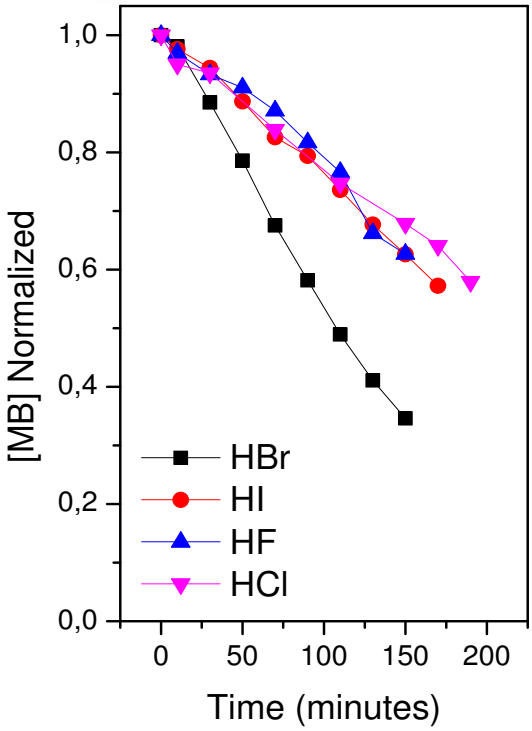

Fig.3. Photodecomposition of MB for the TiO2 powders synthesized with different hydrolysis catalyst, HI, HF, HCl and HBr.

The samples prepared with HI have a very irregular morphology, and their photocatalytic activity is low, possibly related to the formation of the rutile phase, although of low crystallinity. The lowest photocatalytic activity corresponds to the samples prepared with HCl as a catalyst, its surface morphology is similar to the parallelepiped and its crystallinity is very low, but with an anatase phase.

In order to understand the behavior of TiO_2 powders, it is necessary to apply other techniques to determine the adsorption of the material and its surface composition.

IV. Conclusions

TiO_2 particles were synthesized by sol-gel method using different acids as hydrolysis precursors. It was founded that the physicochemical properties of the as-prepared materials are linked with the acid employed. The morphology of the aggregates as well as the crystallinity, are related to the photocatalytic efficiency of the powders, being found that those of almost spherical form present better results. The bang gap of the samples show values similar to those reported in the literature, with a small increase of energy due to the acids used as hydrolysis catalysts.

ACKNOWLEDGMENT

The authors acknowledge financial support for this work from Universidad Autónoma de Querétaro, Facultad de Química and the area of Materials and Energy.

REFERENCES

[1] Valencia, S., Vargas, X., Rios, L., Restropo, G., and M. Marín, J., Sol-gel and low-temperature solvothermal synthesis of photoactive nano-titanium dioxide. J. Photochem. Photobiol., B. 251: 175-181.

[2] Qiu, S., and S. J. Kalita. 2006. Synthesis , processing and characterization of nanocrystalline titanium dioxide. 436:327–332.

[3] Praveen, P., G. Viruthagiri, S. Mugundan, and N. Shanmugam. 2014. Spectrochimica Acta Part A : Molecular and Biomolecular Spectroscopy Structural , optical and morphological analyses of pristine titanium di-oxide nanoparticles – Synthesized via sol – gel route. Spectrochim. Acta Part A Mol. Biomol. Spectrosc. 117:622–629.

[4] Guillén-santiago, A., S. A. Mayén, G. Torres-delgado, and R. Castanedo-pérez. 2010. Photocatalytic degradation of methylene blue using undoped and Ag-doped TiO 2 thin films deposited by a sol – gel process : Effect of the ageing time of the starting solution and the film thickness. 174:84–87.

[5] Pelaez, M., N. T. Nolan, S. C. Pillai, M. K. Seery, P. Falaras, A. G. Kontos, P. S. M. Dunlop, J. W. J. Hamilton, J. A. Byrne, K. O'Shea, M. H. Entezari, and D. D. Dionysiou. 2012. A review on the visible light active titanium dioxide photocatalysts for environmental applications. Appl. Catal. B Environ. 125:331–349.

[6] Manzo-Robledo, A., Cruz-Lopez, A., Flores Caballero, A.A., Zaldívar Cadena, A.A., Máximo López, and Vázquez-Cuchillo, O., Photochemical properties of sol-gel aynthesized titanium dioxide nano-particles using different acids: X-ray photoelectron spectroscopy reveals the induced effect of hydrolysis precursor. Mater. Sci. Semicond. Process. 31: 94-99.

CONACYT
Consejo Nacional de Ciencia y Tecnología

CONCYTEQ

Review of Use and Production of Polyethylene Terephthalate Fibers for Soil Stabilization

Juan Roberto Muñoz Solís
Autonomous University of Querétaro
Querétaro, México
betos_900@hotmail.com

Teresa López Lara
Professor, Autonomous University of Querétaro
Querétaro, México
lopezlarat@gmail.com

***Abstract*— Materials that constitute the ground on which it is built must be evaluated to ensure that their properties are appropriate to obtain an acceptable project performance, it is therefore that the improvement of the mechanical properties of the soil can assure that performance. The infrastructure projects represent a social and economic benefit, improving the quality of life and promoting the population development. However, this causes negative effects on the environment. With the application of methodologies that involve recycling or the use of materials that do not fragment the environment, may be offset some significant impacts that generated the ancient techniques and materials commonly used. In addition, most recently reviews are focused on determining a way to eliminate waste by using it as an alternative material in the civil and industrial engineering implementation. The reuse of waste materials, such as: polyethylene terephthalate and textile waste fibers, is a great importance issue in terms of sustainability, adding them to the soil to improve its resistance. Availability, economic benefits, ease of work, fast handling and the quality of use in any weather condition are the advantages of soil-fiber composites.**

Keywords*— *soil stabilization; soil reinforcement; polyester fibers; PET extrusion; recycling.

INTRODUCTION

In recent years, the environmental and economic issues have stimulated interest in the development of alternative materials that can satisfy the design specifications [1]. Large quantities of waste are generated daily from various industries and human activities. The waste materials are defined as any type of by-product material of human and industrial activity that has no lasting value [2]. In addition, Foti [3] said that the problem of recycling waste materials of various types is, and will be, without a doubt, one of the issues that most afflict to society in future and that we must address and resolve in all possible ways.

Therefore, one of the most promising approaches in this area is the use of fiber form waste materials in the composite material. Materials such as polyethylene terephthalate (PET) or plastic bottles are profuse and widely produced. However, these materials have been little used for engineering purposes and the overwhelming majority of them have been placed in storage or disposal sites. Then, everything that goes to landfills is considered useless material, since it is the surplus of construction works. However, the use of recycled materials instead of virgin, helps to relieve the landfill pressures and reduce the extraction demand. This is a way in which the roads construction industry is set on the road to the practice of sustainable construction. As outlined in [4] recent research focuses on the use of waste materials in lower grades (base, sub-base, etc.) of the road as they absorb greater quantities of materials that the upper grades.

DEFINITION AND WASTE SITUATION

In geotechnical engineering applications, such as load bearing construction, erosion control and vegetation support, the engineering properties of the soil can have a significant influence on site reclamation and development operations, transportation infrastructure construction, and general construction costs and configurations [5]. The components of the soil can influence the soil's load bearing capability, stability, resistance to lateral movement, drainage and settling characteristics. Desirable soil characteristics include high shear strength, low compressibility, good compatibility, high permeability, high ductility, low Weight and high density.

Jones [6] pointed out that the reinforcement consists in the incorporation of a material with the desired properties that the other material does not possess. This is how to the soil reinforcement have been introduced the geosynthetics, such as geotextiles, geogrid, among others, and even more recently natural and synthetic fibers, which have been able to avoid the formation of tension cracks and contraction cracks, besides

increasing the resistance and producing a ductile behavior in brittle soils as reported in [7] and [8].

The polyethylene terephthalate is the most common thermoplastic polyester and is often called "polyester", this often causes confusion with the other polyesters [9]. The polyethylene terephthalate exists both as amorphous (transparent) and as semi-crystalline (opaque and white) thermoplastic material. The semi-crystalline has good resistance, ductility, stiffness and hardness. The amorphous has better ductility but less stiffness and hardness. Absorbs very little water.

Among the most widespread uses of this polymer emphasizes the production of bottles for soft drinks and water, as well as for cosmetics, medicines, oils and jars of all kinds. Besides to these products, are also used to manufacture geotextiles, and fiber for the textile industry.

In Mexico, consumes close to 800 thousand tons of polyethylene terephthalate per year (Table 1) and 50.4% of this total is collected for later recycling 40% abroad and 60% within the Mexican Republic (Figure 2), positioning itself as a leading country in America in PET collection and recycling [10]. There are about 100 Mexican companies dedicated to the production, collection, washing and recycling of polyethylene terephthalate, activity from which live 27 thousand workers in a direct way and employs other 150 thousand indirectly. This tells us about the great importance of this activity in the lives of thousands of Mexicans and that not only helps to alleviate the impact that the human causes to the environment, but also provides sustenance and a better quality of life to the worker.

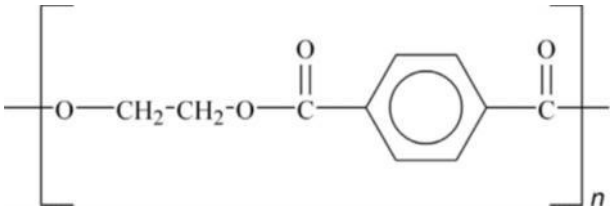

Figure 1. Chemical structure of polyethylene terephthalate polyester.

TABLE 1. MATERIALS USED FOR CONTAINERS AND PACKAGING (ECOCE, 2015)

Thousands of Tons/Base year 20013

Material	*Average ANC*	*Packing Use*	*Collected*	*Collected vs Packing*
PET	799	709	428	60%
PEAD	820	363	182	50%
PVC	512	4	2	50%
PEBD	574	254	16	6%
LLDPE	412	183	146	80%
PP	1138	504	61	12%
PS	487	216	2	1%
Cardboard	588	250	74	30%
Laminated Cardboard	190	190	20	11%
Aluminium	317	317	308	97%
Steel	21874	490	-	-
Glass	3782	3414	57	2%
Total	31493	6894	1296	18.8%

Average ANC=average Apparent National Consumption

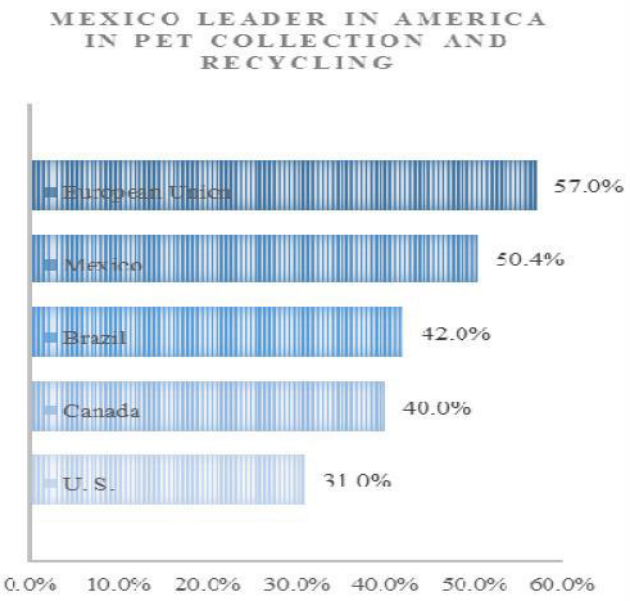

Figure 2. Mexico leader in America in PET collection and recycling (ECOCE, 2015)

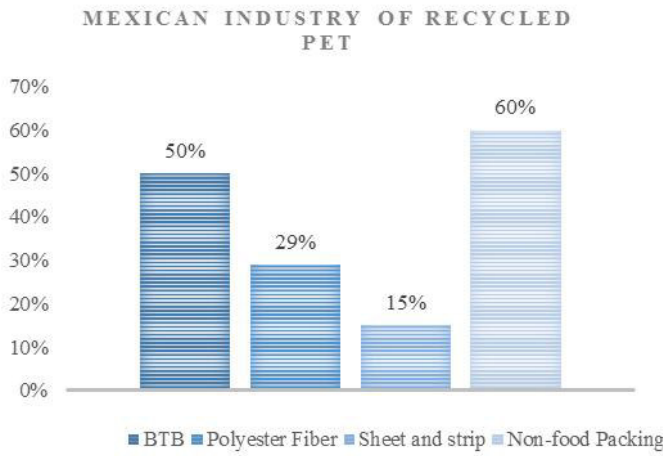

Figure 4. Mexican industry of recycled PET (ECOCE, 2015)

Despite the above, the consumption of polyethylene terephthalate increases by 7% each year and although recycling in Mexico amounts to 10% is far from the work which done in other countries. Thus, promoting the recycling culture among citizens and businesses would avoid excessive waste by promoting the use of alternatives for the reuse and recycling of the polymer.

AREA OF STUDY

All the techniques of soil improvement seek to improve those soil characteristics that do not match the desired results of a project, such as increasing their density and shear strength, soil compressibility reduction, influence the soil permeability to reduce and control the soil water flow or to increase the range of consolidation, or to improve the soil homogeneity.

In the soils improvement, the distinction is made between methods of compaction or densification and methods of soil reinforcement through the introduction of an additional material into the soil.

Due to the above, the properties of the soil can increase dramatically through the addition (or subtraction) of materials to (or from) soil. In many cases, the changes are permanent. This method is usually called soil stabilization, since in many cases turns out to be more stable the ground in question, with fewer fluctuations in their mechanical properties.

In addition, a variety of inclusions have been used ranging from low modulus polymer materials to relatively rigid high strength metal inclusions to reinforce the soils [11]. Further, these inclusions come in many forms ranging from strips and grids to discrete fibers and woven and non-woven fabrics. Availability, economic benefits, ease of working, fast handling and the quality of use in all weather conditions are the advantages of fiber composite soils. Nguyen [12] assert that the resistance and the stiffness of composite soil are enhanced by fiber reinforcement. These properties are in function of the characteristics of the fiber and the characteristics of the soil.

Several researchers like [13], [14] and [15] have performed resistance test on sand samples reinforced with fabric inclusions. Gray, ASCE and Al-Refeai [11] ensures that in general the results have shown that the final strength increased with increasing layers of fabric and the axial deformation tended to increase with decreasing separation between layers of fabric (increase in the number of layers). In addition to the above, it has also been shown that the deformation required to reach the maximum strength is increased and the tendency towards the fragile behavior after the peak was significantly reduced by the presence of reinforcement.

Therefore, authors such as Hejazy, Sheikhzadeh, Abtahi and Zadhoush [8] and Nguyen, Hrubešová and Voltr [12] analyze the behavior of several fibers, including those of polyester, mixed with different soils. This investigations perform shear strength tests and Standard Proctor compaction tests with different percentages of fiber aggregate. In addition the inclusion of the materials was done randomly, but mention is made of three different methods of mixing: i) mixed with plowman, ii) concrete mixer or iii) mixing by falling. This results in favor of the use of synthetic fibers such as polyester, since with this type of fibers the maximum strength of the soil increases and greater length of the fiber the greater the resistance to the unconfined compression (UCS). Meanwhile, Yetimoghu and Salbas [16] affirm that in comparison with the systematically reinforced soils, the soils reinforced with randomly distributed fiber have some advantages. The preparation of such reinforced soils imitates soil stabilization by mixing, since the discrete fibers are simply added and mixed with the soil, like cement, lime and other additives. The randomly distributed fibers provide isotropy of force and limit the potential planes of weakness that can be developed in parallel with the oriented reinforcement.

Similar research, as in [17], [18] and [19] speak in favor of the use of synthetic fibers or derivatives thereof (liquid polystyrene fluid, geogrids, polystyrene spheres, among others), that have been shown to improve the mechanical properties of different composite soils. In addition, a number of factors such as the fiber characteristics (content, length, thickness, module, tensile strength and failure) and soil characteristics, grain size distribution and average piece size, influence in the behavior of the soil-fiber composite [20]. However, these documents are focused only in some very specific cases, so it is not possible to accurately predict the behavior of the aggregates in each type of soil.

PRODUCTION AND IMPLEMENTATION OF THE FIBER

McKeen [21] mentions that polyester is formed by a condensation reaction which is very similar to the one used to produce polyamide or nylon. The polyester resins can be formulated to be fragile and hard, resistant and resilient, or soft and flexible. The three dominant materials in this family of plastics are polycarbonate (PC), polyethylene terephthalate (PET) and polybutylene terephthalate (PBT).

Within the research, some authors that implement a useful method to obtain short-fiber through the use of recycled polyethylene terephthalate were found, these were carried out

by [22] and [23]. Both methods use an extruder to form the fiber.

Listed below are the synthesized steps of the fiber production process.

1. Inspection. The fiber production depends on an appropriate choice of the scrap quality. Therefore, it is necessary the inspection and cleaning of the material; avoiding the presence of non-plastic or metal waste, debris, paper or cardboard compounds, among others.

2. Washing. The scrap is subjected to washing with pressurized water mixed with industrial detergent for a more effective process. Subsequently, it is rinsed with pure water and deposited in mesh-based containers to allow the water to flow.

3. Drying. The material is dried out at a constant temperature. This process can be in vacuum or with a simple hot air flow system.

4. Casting, filtration and extrusion for spinning. A viscous solution is obtained by melting the material at a temperature between 250°C and 260°C, which will be then filtered to make sure the absence of some other polymers that affect the performance. It is necessary to pump the viscous solution through small holes in a row and thus obtain the fibers. The product cools and hardens after getting out of the row.

5. Elongation. Before the fibers are elongated, there is a previous bath in a water and oil emulsion. This increases the crystallinity and the ordered-internal distribution, reduces the diameter and groups the molecules. The process is carried out hot for an effective molecular alignment.

6. Crimping and drying. The fiber crimp refers to the waves, breaks, curls or bends along its length. Its application increases the cohesion, resilience, resistance to abrasion, elasticity, volume and heat conservation. The curl is made by passing the fiber by stamped rollers, twisting or flattening one of its sides. After curling, the product is passed through a drying tunnel to fix the curl to the fiber and making it ready to obtain short fiber, giving it the desired cut length.

7. Cut. Finally, the product is cut into predetermined lengths.

Ibrahim and Fourmont [24] further mention that experimental results have shown that fiber reinforcement causes a significant improvement in compressive strength and, especially, linearly in relation to the amount of fiber added. The above, demonstrates the efficiency of the polymeric fibers used for the reinforcement of the soils; affirming that the greater the fiber length and/or fiber content, the greater the resistance to compression, making this material an excellent additive to create soil and fiber compounds that help the use of poor soils, as well as increasing the quality of those considered good ones.

Experimentation by researchers such as [8], [26], [27] and [28], show results in favor of polyester short fiber, especially pointing out the use of lengths between 12 mm and 36 mm for the application in fine and coarse sands for its stabilization and improvement of mechanical properties. The randomly inclusion of the fiber shown to be the best option to perform the soil-fiber mixture as mentioned in [16] and [26].

CONCLUSION

The recycling theme has increased in importance over the years due to the creation of new techniques in the use of waste materials. In addition, rules and laws around the world support recycling and punish those companies that do not meet the minimum requirements in the fight against the environmental impact that they cause.

One of the most consumed and wasted materials is the polyethylene terephthalate. It is possible to recycle this plastic and reuse it in its entirety through the implementation of a recycling culture and methodologies that give new and different uses than those already commonly known (bottles, packaging, cosmetics, among others). This type of waste material, has a wide range of applications after being collected and Mexico is a leader in the polymer collection topic.

Among the recycled polyethylene terephthalate forms there is the production of polyester fibers. The fiber has been studied and analyzed in the soils stabilization, yielding positive results in favor of its implementation. Several researchers ([8], [12], [16], [25], [26], [27] and [28]) state that the random inclusion of polyester fibers to a soil, increases significantly its maximum strength. That is why, the use of such material as soil stabilizer is recommended and by analyzing the project status, the total fiber amount that will be used, can be obtained, as well as its size. In addition, polyester fiber offers great resistance to weather changes, it is not absorbent, it is extremely strong, it has high elasticity, it is not attacked by microorganisms, and something of great importance to the industry, it is obtained at low cost. With the above, recycled polyethylene terephthalate fibers implementation alleviates the environmental impact generated by making use of new and different variants of this material.

However, the several investigations that have been consulted refer to very specific cases of soil type, as well as the amount and size of the fiber that is implemented in the stabilization. It is important that both the soil and the fiber are tested before their application to verify their effectiveness, as well as to perform a cost-benefit analysis. The above is mentioned since it is at the engineers discretion to decide if it is the right choice, and if the costs of the fiber production and material hauling are suitable for the project.

ACKNOWLEDGMENT

The review described in this paper was supported by scholarship from the Consejo Nacional de Ciencia y Tecnologia and the Autonomous University of Querétaro. This support is gratefully acknowledged.

REFERENCES

[1] B. E. Novich, A. Maher & J. A. Neubauer (2000). Fiber-reinforced Soil Mixtures.

[2] N. C. Consoli, J. P. Montardo, P. D. Marques P. & G. S. Pasa (2002). Engineering Behavior of Sand Reinforced with Plastic Waste. Journal of Geotechnical and Geoenvironmental Engineering Vol. 128. Pp. 462, 463, 470, 471.

[3] A. Serpell & L. Alarcon (1998) Construction process improvement methodology for construction projects. International Journal of Project Management.

[4] D. Foti (2012). Use of recycled waste pet bottles fibers for the reinforcement of concrete. Composite Structures Vol. 96. Pp. 396, 397, 404.

[5] Y. Huang, R. Bird & O. Heidrich (2007) A review of the use of recycled solid waste materials in asphalt pavements. Resources Conservation & Recycling Vol. 52. Pp. 58, 67, 68.

[6] R. M. Jones (1999) Mechanics of Composite Materials 2ª Edición. Taylor and Francis. Pp. 1-14.

[7] Ch. Tang, B. Shi & L. Zhao (2010). Interfacial shear strength of fiber reinforced soil. Geotextiles and Geomembranes Vol. 28. Pp. 54-61.

[8] S. M. Hejazi, M. Sheikhzadeh, S. M. Abtahi & A. Zadhoush (2012) A simple review of soil reinforcement by using natural and synthetic fibers. Construction and Building Materials Vol. 30. Pp. 1, 2, 7.

[9] L. McKeen (2016). Fatigue and Tribological Properties of Plastics and Elastomers. William Andrew. Pp. 149-156.

[10] ECOCE (2015). Ecología y Compromiso Empresarial: Datos Estadísticos. Disponible en: http://www.ecoce.mx/datos-estadisticos.php

[11] D. H. Gray, A. M. ASCE & T. Al-Refeai (1986). Behavior of Fabric versus Fiber-Reinforced Sand. Journal of Geotechnical Engineering. Vol. 112. Pp. 1, 2, 8, 9.

[12] G. Nguyen, E. Hrubešová & A. Voltr (2015). Soil improvement using polyester fibers. Procedia Engineering. Vol. 111. Pp. 596-599.

[13] J. P. Giroud, (1984). Geotextiles and Geomembranes. Geotextiles and Geomembranes Journal. Vol. 1. Pp. 5-40.

[14] M. R. Madhav & P. P. Vitkar (1978). Strip Footing on Weak Clay Stabilized with a Granular Trench or Pile. Canadian Geotechnical Journal. Vol. 15. Pp. 605-609.

[15] A. McGown & K. Z.Andrawes (1977). The Influence of Non-Woven Fabric Inclusions on the Stress-Strain Behavior of a Soil Mass. Proceedings, International Conference on the Use of Fabrics in Geotechnics, L'Ecole des Ponts et Chaussees, Vol. 1. Pp. 161-166.

[16] T. Yetimoglu & O. Salbas (2003). A study on shear strength of sands reinforced with randomly distributed discrete fibers. Geotextiles and Geomembranes 21. Pp. 104, 108, 109.

[17] M.T. Isa, A.S. Ahmed, B.O. Aderemi, R.M. Taib & I.A. Mohammed (2013) Effect of fiber type and combinations on the mechanical, physical and thermal stability properties of polyester hybrid composites. Composites Part B: Engineering Vol. 52. Pp. 217-222.

[18] S.M. Haeri, R. Noorzad & A.M. Oskoorouchi (2000) Effect of geotextile reinforcement on the mechanical behavior of sand. Geotextiles and Geomembranes Vol. 18. Pp. 385-400.

[19] K.J. Mun, N.W. Choi, S.Y. So & Y.S. Soh (2007). Influence of fine tailings on polyester mortar properties. Construction and Building Materials Vol. 21. Pp. 1335-1341.

[20] N. C. Consoli, M. T. Casagrande & M. R. Coop (2005). Effect of Fiber Reinforcement on the Isotropic Compression Behavior of a Sand. Journal of Geotechnical and Geoenvironmental Engineering Vol. 131. Pp. 1434, 1437.

[21] L. W. McKeen (2012). Polyesters. Permeability Properties of Plastics and Elastomers 3a Edic. Pp. 89, 100.

[22] L. Mansilla & M. Ruíz (2009). Reciclaje de botellas de PET para obtener fibra de poliéster. Ingeniería Industrial. Pp. 123-137.

[23] J. C. Tapia, A. García, R. Gonzalez, A. Bonilla, G. Luna, A. Champión & A. Alvarez (2014). Performance of a Modified Extruder for Polyester Fiber Production Using Recycled PET. Revista Mexicana de Ingeniería Química. Vol. 13. Pp. 337-344.

[24] E. Ibraim & S. Fourmont (2006). Behaviour of Sand Reinforced with Fibers. Soil Stress-Strain Behavior: Measurament, Modeling and Analysis. Geotechnical Symposium in Roma. Pp. 807, 808, 817.

[25] S. R. Kaniraj & V.G. Havanagi (2001). Behavior of Cement-Stabilized Fiber-reinforced Fly Ash-soil Mixtures. Journal of Geotechnical and Geoenvironmental Engineering. Vol. 127. Pp. 574-584.

[26] R. L. Santoni, J. S. Tingle & S. L. Webster (2001). Engineering Properties of Sand-fiber Mixtures for Road Construction. Journal of Geotechnical and Geoenvironmental Engineering. Vol. 127. Pp. 258-268.

[27] A. Kumar, B. S. Walia & A. Bajaj (2007). Influence of Fly Ash, Lime, and Polyester Fibers on Compaction and Strength Properties of Expansive Soil. Journal of Materials in Civil Enfineering. Vol. 19. Pp. 242-248.

[28] N. C. Consoli, J. P. Montardo, M. Donato & P. D. M. Prietto (2004) Effect of Material Properties on the Behaviour of sand-cement-fibre composites. Proceedings of the Institution of Civil Engineers Ground Improvement. No. 2. Pp. 77-90.

Digital Filter-Amplifier for the Detection of Scattered Laser Light

Anuar Jassen Morales[1], Iván Domínguez López[2], Julio Cesar Sosa Savedra[3], Adrián García García[4]
Materials processing and manufacturing department, Instituto Politécnico Nacional, CICATA-Qro, Querétaro, México.
anuar_jassen@hotmail.com[1], idominguezl@ipn.mx[2], jcsosa@ipn.mx[3], agarciag@ipn.mx[4]

Abstract— **Laser light scattering is an optical technique, which is widely used in the determination of the structural properties of materials, this because it does not require physical contact between probe and sample, and it does not produce modifications on the surface. One inconvenient with this technique is that the signal of interest is immerse in ambient light noise thousands of times larger. For this reason, a prototype was designed with the purpose of acquiring and filtering the laser light scattered by rough surfaces. This prototype uses a microcontroller and active filters based on operational amplifiers. The acquired signal was then compared with the signal output from a commercial Lock-in amplifier. The results prove the capacity of the in-house system for filtering and amplifying the signal of interest with comparable quality. The design of this filter is a low cost alternative that will help with the study of the wear phenomena of surfaces in a pin on disk tribometer. Eventually, it will be implemented in a linear array of photo detectors, which will allow obtaining the angular distribution of the scattered laser light by rotating surfaces.**

Keywords—Lock-in amplifier, Roughness, Tribometer, LLS

I. Introduction

Tribological tests are used to study wear between two surfaces that are in contact, this tests are made under the ASTM G-99-05 standard [1], which recommends not to make contact measurements during the test; therefore, in order to study what happens during the transition wear phenomena, new non-contact probes need to be developed.

An innocuous technique that can be used in parallel with wear measurements in a pin-on-disc tribometer is laser light scattering (LLS), which consists on observing the scattered light produced by the interaction of a laser beam, with a solid surface. In an ideally flat surface the light will be reflected specularly; however, in real surfaces, the laser beam is scattered, as shown schematically in figure 1.

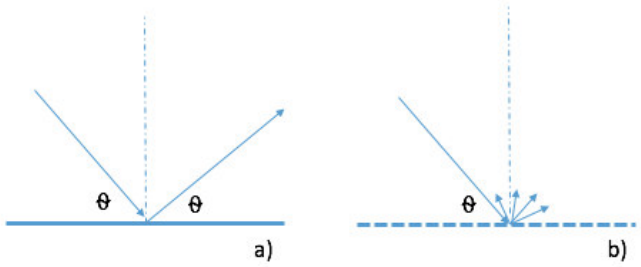

Fig. 1. a) LLS in ideal flat surface b) LLS in rough surface.

There have been previous attempts of measuring the roughness based on the LLS signal, for example Rong-Sheng in [2] a device was implemented in which with the use of a charged coupled device (CCD) sensor and with the use of a 2D Gaussian low-pass filter it was able to detect changes in roughness with one-dimensional manufacturing marks.

Martinez-Fuentes in [3] show that the LLS technique can be implemented in a pin on disk tribometer, the laser beam was pointed towards the wear-track and a silicon sensor was placed in some position outside the reflected plane, the signal was then filtered and amplified with the use of a commercial lock-in amplifier, the results conclude that the LLS signal can be related with the wear caused in the surface of the material.

Finally, in [4] present an experimental-theorical study in which the LLS pattern formed when the laser beam is pointed in the direction of the radius of the wear-track is compared to the Monte Carlo method used for the modeling of the scattered light intensity, it´s important to mention that when the laser is placed in this configuration with respect to the wear track a linear scattered pattern is formed as it will be shown after.

The LLS technique has been used previously in the materials processing and manufacturing group in CICATA-Querétaro, until now it has been observed that in the initial phase, while the surface is under wear test in the pin on disk tribometer, the LLS signal increases [3][4] There exist interest in the mentioned technique because at having such a weak interaction with the sample it is possible to perform in-situ measurements without causing a structural change in the material properties, hence the disadvantage is that the signal of

interest is immerse in noise which comes from natural and artificial sources of light, this noise can be thousands of times larger than the LLS signal and has to be removed so the desired signal can be studied.

In this paper a digital filtering technique named phase sensitive filtering was used, the algorithm was programmed in a low cost microcontroller of the PIC family and with the use of active filters and amplifiers based on operational amplifiers it was able to extract and amplify the desired signal from a noisy environment.

II. Theorical Background

Even tough the purpose of this paper is far from explaining in detail the theory behind the filtering technique it is important to mention some aspects of it, the reader who would like to go deeper can search in other references [5] only the most important aspects of the technique will be mentioned here which are: the signal of interest must be modulated at a known frequency, the modulation signal can also be named reference signal, once that the unprocessed signal is obtained it is multiplied by the reference signal, by doing this the signal of interest stays near to zero Hertz hence it is easy to get rid of the noise with a well tuned low-pass filter.

III. Circuit Design

In recent years there have been an increase in applications based on embedded systems, this increase has taken us to the creation of new design methodologies in order to reduce the design time, the risk of a failure and the scrap. One of this is the V methodology [6], which is especially suited for software and hardware development in embedded systems.

This work will make use of the previous mentioned methodology, which has seven steps, of which the first three steps are for design and goes from the general to the particular and the least three steps are for test and they go from the particular to the general, the middle step is the implementation, and is where the conceived design is built, the diagram of this methodology is shown in figure 2.

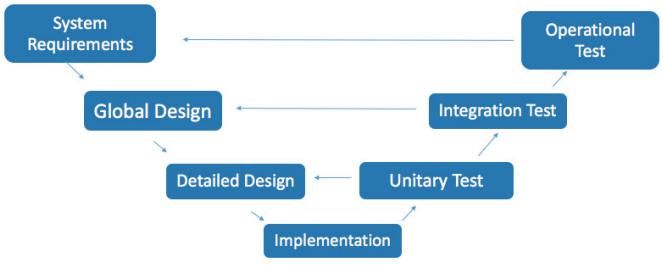

Fig. 2. V Methodology.

Following the first step of the methodology and as it was mentioned previously the laser beam must be modulated, to use this technique hence it is necessary to have a sensor which responds quickly to the light changes, knowing this the SFH206K photodiode will be used [7] this sensor is specially suited for wavelengths between 400 to 1100 nm, the laser used here was the LTG6504A5 from Lasermate [8] this laser emits in a wavelength of 650 nm.

The photodiodes allow the flow of a current when they are connected in inverse mode which is proportional to the amount of light present in the sensor in that moment, this current is so tiny that has to be amplified and transformed into voltage in order to be used by a microcontroller, to perform this a transimpedance amplifier was used, this amplifier was built using the operational amplifier TL082 from Texas Instruments [9], the architecture that was used is shown in figure 3.

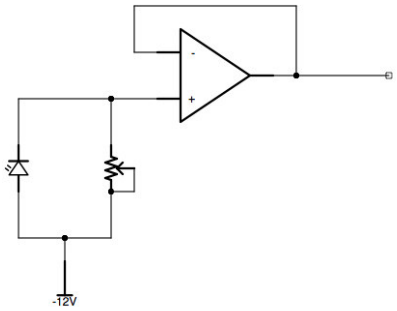

Fig. 3. Transimpedance Amplifier.

This circuit amplifies the current from the photodiode and transform it into voltage, it is posible to tune the amplifing factor from zero to one million by use of the variable resistance of 1 MΩ which is shown in figure 1, even though this resistance can input noise into the circuit it is not a big concern since the signal will then pass by other filtering steps.

As it is expected the photodiode does not detect exclusively the light from the laser, it also detects the light from the ambient which comes from natural sources like the sun and artificial sources like the lamps, it is for this reason that a pre-filtering step was designed using the second operational amplifier of the TL082 integrated circuit, the connection diagram of this filter is shown in figure 4.

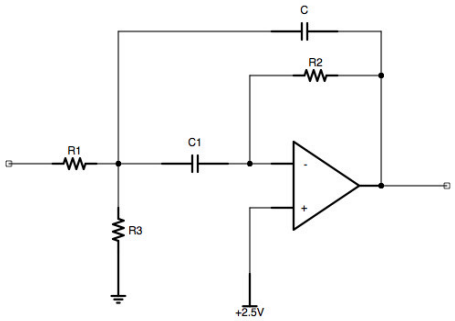

Fig. 4. Multiple Feedback Band-Pass Filter.

The selected topology is a band-pass filter of multiple feedback (MFB), it was designed to be centered at 50 Hertz, which is also the frequency at which the laser will be modulated, this frequency is named middle frequency (m_f), the shown filter has an amplification rate in middle frequency

(A_m) of 4.1 and a quality factor (Q) of 9.3, this values can be calculated using the equations (1) to (3).

$$m_f = \frac{1}{2\pi C}\sqrt{\frac{R_1+R_3}{R_1R_2R_3}} \quad (1)$$

$$A_m = \frac{-R_2}{2R_1} \quad (2)$$

$$Q = \frac{1}{\pi R_2 C} \quad (3)$$

IV. Microcontroller Programming

Once the signal has left the band-pass filter is digitalized by the analog to digital converter (ADC) of the PIC16F88 microcontroller from Microchip [10], this is a 10-bit resolution converter which gives up to 1024 different values, but since the microcontroller has an 8 bit processor the use of the 10 bits will cause a considerably increase in processing time, for this reason and with the purpose of optimizing the code only the 8 most significant bits were used, which provides 256 different values, some of the other reasons why this pic was used was the native UART port, which is easy to work at different Baud rates by the use of some configuration registers that can be found in the datasheet, also this port is able to send up to 8 bits, using a ninth bit as parity check, which is another reason for working only with the eight most significant bits.

The microcontroller was programmed in C language with the use of the XC8 compiler and the MP-Lab software, it was configured to send an interruption every 10 ms, this interruption changes the state of one of the microcontroller pins, which is the one used to modulate the laser at 50 Hz., the analog measurement is then made, once it is ready it is multiplied by -1 if the laser state is "down" and stored in a twenty position vector which is named "In Phase Vector" (IPV), if the state of the laser is "high" the measure is only stored in the vector without being multiplied.

Every new cycle the vector is shifted, this drops the oldest measurement and the newest measurement is stored in the first position of the vector. There`s also another 20 position vector which is called "In Quadrature Vector" (IQV), which is constructed with the equation shown in (4).

$$IQV = -IFV \quad (4)$$

Both vectors then are filtered with a low-pass finite impulse response filter (FIR), the outputs of this filtering are named IFO and IQO respectively for the in phase vector and the in quadrature vector, having this information it is possible to reconstruct the laser light scattered signal with the equation shown in (5).

$$LLS = \sqrt{IPO^2 + IQO^2} \quad (5)$$

At the end the filtered data is send by the UART module of the microcontroller, the block diagram of the programming is shown in figure 5.

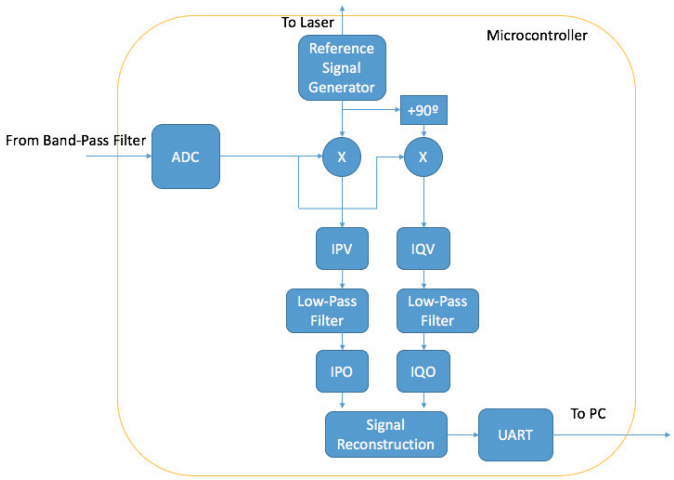

Fig. 5. Block Diagram of the Microcontroller Program.

And the block diagram of the complete phase sensitive filter is shown in figure 6.

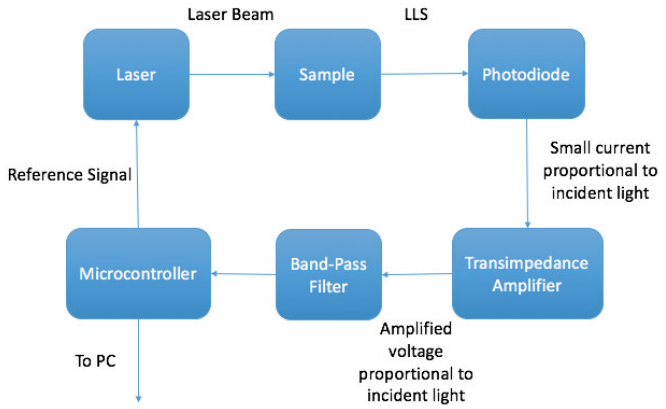

Fig. 6. Phase Sensitive Filter Block Diagram.

As it can be seen the process starts with the change of state of the reference signal and ends when the data is sent from the UART port.

V. Test and Comparative

In order to perform the validation of the constructed system, measurements were taken sending the signal directly from the output of the photodiode to a commercial SR830DSP Stanford Research lock in amplifier [11] and to the built system.

The measurements were made by sending the laser light to the metallic surface at an angle of 45º making the incident plane be aligned in the direction of the radius of the wear track, doing this a scattered linear pattern like the one shown in figure 7 was obtained.

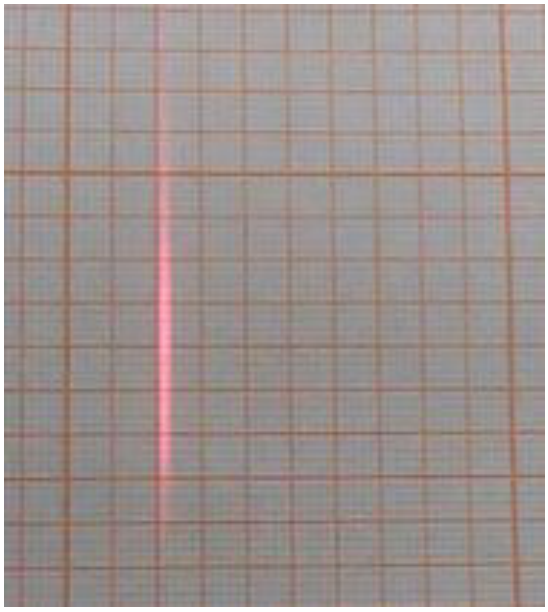

Fig. 7. Linear Scattered Pattern.

The photodiode was placed in this line with the use of a goniometer, specially suited for this aplication, which can be seen in [12], the laser was placed in one of the arms at an angle of fourtyfive degrees with respect to the sample and the sensor was placed in the other one. The angular distribution was obtained making a rotation of the sensor of seventy degrees with the use of stepper motors which are incorporated in the experimental setup, the configuration of the experiment is shown in figure 8 and a picture of the circuit can be seen in figure 9.

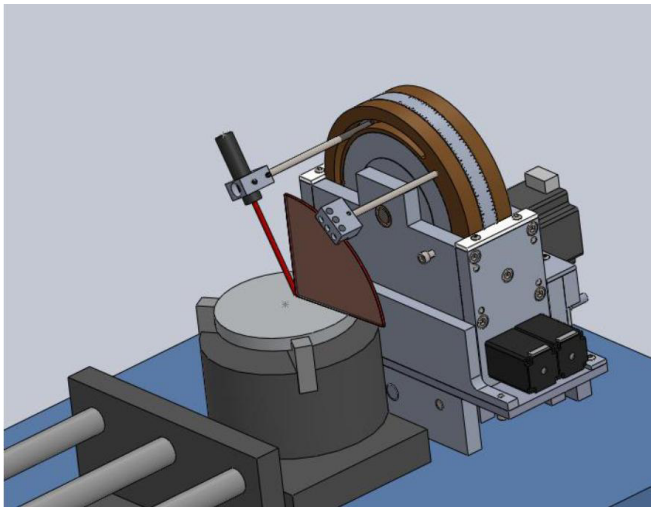

Fig. 8. Configuration of the Experiment.

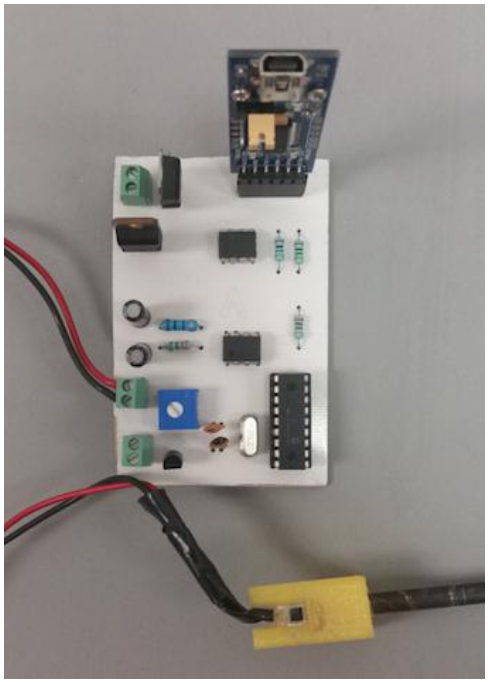

Fig. 9. Picture of the Built Circuit.

Three replicates were made for each surface, the mean of this replicates are shown in figure 10.

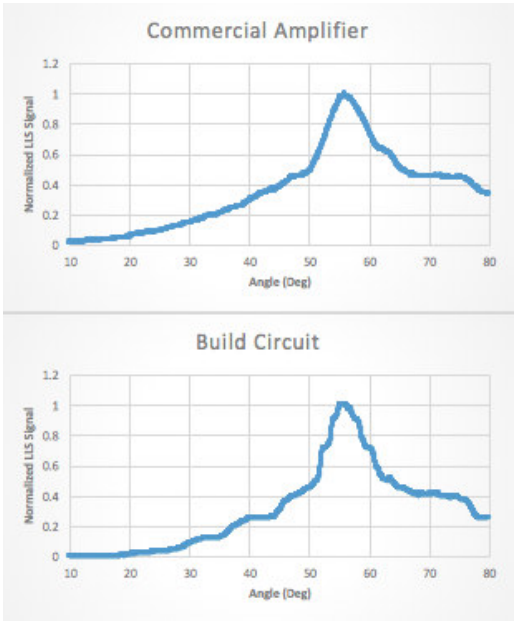

Fig. 10. Plot comparative between (a) built circuit and (b) comercial lock in.

In the plots is evident that both systems are detecting the same shape of the laser light scattered pattern, hence there is more variation in the signal obtained by the developed circuit in this work.

Measurements were also made in the same surface with different light conditions in the laboratory, this conditions were a) ambient light on and b) ambient light off, the results of both measurements are shown in figure 11.

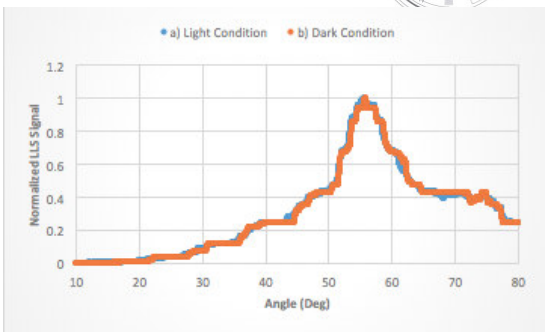

Fig. 11. Comparative of the builded circuit: with and with out noise.

The residual of the data shown in figure 11 were calculated and can be seen in figure 12.

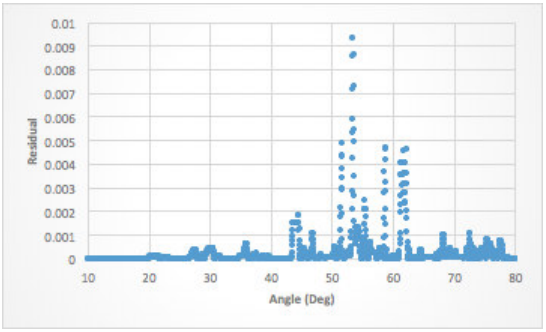

Fig. 12. Residuals of light vs dark conditions in circuit.

As it can be seen the difference in the ambient light caused just small residuals, the root mean square error (RMSE) was calculated and it is of a value equal to 0.016, with this information it can be concluded that the designed circuit is filtering successfully the noise.

VI. Conclusion and Future Work

The obtained results showed that the laser light scattered signal outputed by the built system is comparable with the one obtained with a commercial equipmment, hence it has the following restrictions: the operation frequency is fixed at 50 Hertz, the signal that is inputed to the microcontroller has to be in a range from 0 to 5 Volts.

The system architecture makes it possible to implement a large quantity of sensors, this will make it possible to use the system in different applications for the acquisition of small signals in noisy environments.

The cost of the materials used in this work represent a 0.24% of the cost of the commercial lock in used.

As future work it is planned to make the modifications to implement the phase sensitive filter in a linear array of photo detectors which contain some thousands of individual detectors, this will allow the quick acquisition of the angular distribution of scattered laser light while the surface is under a wear test in a pin on disk tribometer.

VII. Bibliography

[1] ASTM International, "Standard Test Method for Wear Testing with a Pin-on-Disk Apparatus".

[2] Tian, Rong-Sheng Lu and Gui Yun, “On-line measurement of surface roughness by laser light scattering.” *IOP Science*, May 2006.

[3] V. Martinez-Fuentes, I. Dominguez-Lopez, A.L. Garcia-Garcia, “Surface texture changes followed-up in real time during the initial wear transient of dry sliding of steel against several metals using laser light scattering” *Wear*, Jan 2011.

[4] V. Martínez Fuentes, I. Domínguez López, A. L. García García. “Estudio teórico-experimental del esparcimiento de luz láser por superficies sometidas a desgaste.” *CIINDET*, 2008.

[5] Ivanov, E. Marín and R. “LIA in a Nut Shell: How can Trigonometry help to understand Lock-in Amplifier operation?” Sep 2009.

[6] A. Perez, O. Berreteaga, A. Ruiz de Olano,A. Urkidi, J. Perez. “Una metodología para el desarrollo de hardware y software embebidos en sistemas críticos de seguridad.” 2006.

[7] OSRAM. “SFH206K Datasheet.” Datasheet, 2017.

[8] Lasermate Goup, Inc. “*Specifications of LTG-Series Laser Diode Modules with TTL Modulation*”, May 2017.

[9] Texas Instruments. “TL08xx JFET-Input Operational Amplifiers.” Datasheet, 2015.

[10] Microchip. “PIC16F87/88.” Datasheet, 2017.

[11] Standford Research. “MODEL SR830 DSP Lock-In Amplifier.” Datasheet, 2011.

[12] J. Vázquez Pérez, I. Domínguez López, A.L. García García, J.D.O. Barceinas Sánchez,. “Diseño y construcción de un goniómetro para aplicaciones tribológicas.” *SOMIM*, Sep 2014.

Water safety plans for hydroarsenicism and its effects on public health: A review

Raúl Bautista Camacho, Marcela Susana Duhne Ramírez
Facultad de Ingeniería.
Universidad Autónoma de Querétaro (UAQ)
Querétaro, Mexico
rbautista05@alumnos.uaq.mx, marcela.duhne@uaq.mx

Abstract— The access to safe drinking water is an important issue in health and development at international, national, regional and local levels. In order to generate a more prepared and safer society, in addition, to a less vulnerable country, it is necessary to move from a reactive to a preventive scheme. Strategies that allow the population to provide biological, chemical, physical and radiologically safe drinking water need to be established. As well as water security plans that take into account the economic, social, legal, political, scientific and technological aspects. This must allow evaluating and managing adequately the risk, which the population is exposed to. This research seeks to collect the most relevant information about hydroarsenicism and its public health effects, as a mean to understand the next steps required to implement a preventing scheme.

Keywords— Water hazard; water quality; sources of pollution; disaster risk reduction and management; water safety plans.

I. INTRODUCTION

The World Health Organization (WHO) considers Arsenic (As) one of the ten most concerning chemicals for public health because it is found in contaminated groundwater (inorganic As) in many countries, including Argentina, Bangladesh, Brazil, Chile, China, India, Mexico, Mongolia, and the United States [1-9]. Ground water is used for crop irrigation, food preparation or direct consumption. The inorganic form of As is present in the air, water and earth, since it is a natural element of the terrestrial crust [10-16]. This can be found as inorganic salts of arsenite (As III) and arsenate (As V), having no taste or odor. Therefore, when in drinking water, it can be inadvertently consumed and cause the so-called chronic hydroarsenicism [17-20].

In developing countries, deaths due to related diseases to inadequate quality or lack of safe drinking water rises to approximately 5 million people, of whom about 2 million die from diarrheal diseases [21-22]. Due to lack of water disinfection and other contaminants present in water, such as As.

The presence of As in drinking water is a problem that happens in the aquifers of Durango, Coahuila, Zacatecas, Morelos, Aguascalientes, Chihuahua, Puebla, Nuevo León, Guanajuato, San Luis Potosí, Sonora, and Torreón, Mexico [24-25]. In all these states, concentrations higher than the reported by NOM-127-SSA1-1994 [25] have been detected. A total of about 450,000 inhabitants are estimated to consume water with As concentrations above 0.025 mgL^{-1}.

In order to generate a more prepared and safer society, and a less vulnerable country to potentially destructive phenomena, whether by natural or anthropogenic causes, we must go from a reactive to a preventive scheme [26]. This would allow providing safe drinking water coverage for human consumption with concentrations of contaminants (biological, chemical, physical and radiological) below the permissible limits [25]. This research, seeks to collect the most relevant information about hydroarsenicism and its effects on public health.

II. ARSENIC TOXICOLOGY.

Ingestion and inhalation of As are the main causes of exposure of people to this pollutant. This accumulates in the body by chronic exposure and causes various conditions depending on the concentration. Some examples are: skin disorders, side effects in the nervous system, irritation of organs of the respiratory, gastrointestinal and hematopoietic apparatus, and accumulation in the bones, muscles, skin, liver and kidneys.

The toxicity of As depends on the state of oxidation, chemical structure, and solubility in the biological environment, according to [50] the toxicity of As (III) is ten times greater than As (V), with As concentrations 1-4 $mgkg^{-1}$ being the lethal dose for adults.

Studies by [51] show that As contained in drinking water is in the form of arsenate and is easily absorbed from 40 to 100% by the gastrointestinal tract. Ingested inorganic arsenic passes into the bloodstream, where it binds to hemoglobin and in 24 hours it can be found in the liver, kidneys, lungs, spleen and

skin. When it is found in tissues, arsenic exerts its toxic effects by binding to sulfhydryl groups of various enzymatic systems, which inhibits its activity [52-54].

Ingested inorganic As is absorbed by tissues and then progressively eliminated by mutilation; its excretion occurs in the urine through the kidneys. When ingestion is greater than excretion, it tends to accumulate in the hair and nails. Normal levels of arsenic in urine, hair, and nails are 5-40 $\mu g day^{-1}$, 80-250 $\mu g kg^{-1}$ and 430-1080 $\mu g kg^{-1}$, respectively [50].

The sensitivity of people to the toxic effects of As varies according to genetics, metabolism, diet, health status, and sex. Studies have determined that urine is the best biomarker to measure the absorbed dose of As since blood, hair, and nails are less sensitive to exposure [50].

Consumption of water with As does not lead to cases with acute but chronic effects, because small amounts are ingested in the water in the long term.

Four stages are recognized in As ingestion:

- Preclinical: The patient does not show symptoms, but arsenic can be detected in tissue and urine samples.
- Clinical: Stage with effects on the skin. Darkening of the skin (melanosis) commonly on the palm of the hand. Dark spots on the chest, back, limbs, and gums may also occur. A more serious symptom is keratosis, or hardening of the skin in the form of nodules on the palms and soles of the hands and feet. WHO estimates that when this stage has been reached, there has been exposure to arsenic for 5 to 10 years.
- Complications: More pronounced clinical symptoms and affectations of the internal organs. There is involvement in this stage with conjunctivitis, bronchitis, and diabetes.
- Malignancy: Development of tumors or cancers that affect the skin and other organs. At this stage, the person may develop gangrene or skin, lung or bladder cancer.

In the first two stages, if the patient replaces the source of drinking water with an arsenic-free one, his recovery is almost complete. In the third stage, it may be reversible, but in the fourth stage, it is no longer reversible [55].

The United States Environmental Protection Agency, USEPA, classifies As as a carcinogen in group A because the evidence of its adverse health effects. Exposure to 0.05 mgL^{-1} can cause 31.33 cases of skin cancer per 1,000 inhabitants and has considered lowering the maximum acceptance limit of 0.050 mgL^{-1} to that of 0.010-0.020 mgL^{-1}.

III. Origin of the Arsenic in Sources of Water for Human Consumption.

In general, the presence of As in the sources of water for human consumption is due to natural factors of geological origin produced by the dissolution of minerals, erosion and disintegration of rocks and atmospheric deposition. According to the environment conditions, As can be found in its trivalent or pentavalent forms. The oxidized form predominates in superficial water, while the reduced form is found in groundwater.

Reference [12], attributes the high content of As in various water wells to the dissolution of minerals (oxidation of arsenopyrite, dissolution of scorodite) contained in the rock through the path of water flows [2; 15; 28-29]. They also found that natural poisoning in groundwater geothermal is due to the reduction of As rich in iron oxyhydroxides. Regions such as Shullsburg and Platoro, United States [30-31], and Obuasi, Ghana [32] have suffered contamination in groundwater contamination due to the oxidation of sulphurous minerals. In Argentina, loess type material is considered the main source of As in groundwater [33]. High concentrations of As have been found in the western United States in areas bounded by acidic and intermediate volcanic rocks [34].

Nonetheless, human activities may cause arsenic pollution. As is used extensively to process glass, paper, pigments, textiles, wood preservatives, and ammunition. It is also a by-product of mining, while smelting metal refining; this is the electrolytic processes for producing high quality metals. And finally, in agriculture, it is used in organic arsenical pesticides [35]. Therefore, the anthropogenic origin is not of less concern. The land of the mines dumpsites, represents a significant threat for the environment, due to the dispersion of the byproducts derived from the extraction and processing of minerals such as gold, silver, etc. [28; 36-38]. Subsequently, due to wind and gravitational weathering processes, several particles arrive at the runoff and are transported along the streams, sometimes sedimenting. This makes part of the surface water and groundwater close to dumpsites enriched with As. The study conducted in Alaska, by reference [39], found a positive correlation between dissolved As suspended in surface runoff and sediments at the bottom of streams.

According to the reference [40], the oldest dumps deposited 60 years ago have been oxidized and are now generating leachates flowing directly into the river, while recent landfills still do not generate leachates. However, due to the deposits that do not have adequate management, the particles are dispersed by wind and gravity covering the surroundings. Reference [14] has studied the concentrations of arsenic in the groundwater of the Zimapán valley, Mexico. There As concentrations reach up to 1,097 mg/L in one of the most productive wells. This was attributed part to the minerals contained in the rocks of the area, the leachate of the waste from the mines, and the percolation of blast furnace gases.

Metals cannot be degraded by biological or anthropogenic processes; once they are found in the aquatic ecosystem, they are transformed through biogeochemical processes and distributed among various species with different physicochemical characteristics; for example, particulate matter (> 0.45 μm), colloidal (1 nm-0.45 μm), and dissolved species (≤ 1 nm) [41].

IV. The Relationship Between the Characteristics of the Area of Interest, and the Dispersion of Contaminant.

The transport and concentration in natural springs and streams is closely related to the amount of precipitation,

physiographic characteristics in the zone, the processes of erosion, disintegration, dissolution, and leaching [11].

Reference [16] studied the granulometric characteristics in the San Antonio-El Triunfo mining district in Baja California Sur, Mexico [42-44]. Their goal was to relate the distribution of As and particle size. They found that at velocities greater than 2.5 ms^{-1}, the particles containing As were moving and carrying the contaminant to the lower part of the basin. When the velocity was lower, the particles did not move and this caused the increase in concentration of As. This zone had intense rains and of short duration, which favored the drainage with respect to the infiltration of the water. They identified that the dispersion of contaminants can be divided into two zones: (i) high energy zones, where eroded waste of the mines are transported and part of the coarse fraction is deposited; and (ii) low energy zones, where the terrain has a smoother slope, and the current deposits the rest of the coarse, fine and dissolved fractions of the load [45].

The efficiency of the sediment for the accumulation and transport of inorganic pollutants is remarked by reference [46], where particles with a minor size than 0.063 mm are the main accumulators of pollutants. Similar investigations were carried out in southeastern Spain and Michigan, United States [47-48].

In 2003, several samples and analyzes were carried out in the mining sector of Santa Maria de la Paz, where the samples obtained in Cerrito Blanco showed concentrations up to 5900 μL^{-1} in systems used for irrigation and livestock [49]. In addition, it was found that the particles were transported due to heavy rainfall up to 10 km from the mine dumps.

V. Risk analysis in water supply systems.

Hazard can be defined as any biological, chemical, physical or radiological activity, threat or agent that may cause harm to humans or the environment. If this hazard can be materialized by an incident or situation, it is called a hazardous event and the probability of this dangerous event is called risk [56].

Environmental pollution is characterized by the presence of substances in the environment that cause health and well-being damage of man, or that cause ecological imbalance, this happens when the pollutants exceed certain limits considered tolerable. Ecological imbalance is a phenomena that evolves slowly in time and its effect is manifested by a progressive deterioration of the environmental conditions. This pollution could occur in air, water, and soil. And, in each case, it has its own characteristics that require specific prevention and combat measures, which are relevant to the protection sector of the environment, and are usually outside the scope of civil protection [57].

WHO [58] points out that drinking water risk depends on source quality, treatment efficiency, and adequate transport to consumers. When water comes from improved and more accessible sources of supply; people spend less time and effort to physically pick it up, which means they can be productive in other areas. It is also related to a greater personal safety, since it diminishes the need to make long and dangerous trips to get the vital liquid. Improving water supply also leads to reduced health spending, as people are less likely to become ill, to incur medical costs, and are better able to remain economically productive.

The National Research Council (NRC) divides risk analysis into two main processes: risk management and assessment. In addition to these processes, there must be a constant risk communication. A risk assessment, identifies the negative consequences that result from an action, providing valuable information on the potential impact on public health and ecology. While risk management, allows decisions to be taken to control the hazards identified in the assessment, taking into account the economic, social, legal, political, scientific, and technological aspects [59].

In order to carry out the risk management, the analysis of hazards and critical control points (HACCP) is used as a tool, which is used in drinking water supply systems (SAAP) and in the development of water safety plans (WSP) [60]. HACCP is a systematic approach to the identification, evaluation and control of hazards that focus on prevention, the system contemplates five preliminary stages: conformation of the work team, description of the product, identification of uses, elaboration of the flow diagram system and validation and hazard analysis, determination of critical control points, establishment of critical limits, establishment of a monitoring system, establishment of corrective measures, establishment of verification or validation procedures, and establishment of a system of documentation and registration [61-63].

Reference [64] described the application of HACCP in SAAP and considers the greatest microbiological hazard is contamination of sources and re-contamination during storage and distribution. At the international level, HACCP has been implemented since 1997 in Australia, France and Iceland, and since 2006, in Singapore [63; 65-66].

In Mexico, the Federal Health System (FSS) develops six strategies and 38 projects with a high impact on health [67], which are aimed at reducing morbidity and mortality rates in the population. One of these strategies focuses on providing to the population a basic coverage against risks, referring to the water chemically and physically clean and thus handle the risk generated by hydroarsenism, cancer, skin diseases, fluorosis or diarrhea [49].

The prevention strategy establishes three fundamental steps. First, know the dangers and threats; to know where, when and how they affect us [68]. Second, identify and establish at the national, state, municipal and community level, the current characteristics and levels of risk in these phenomena [69]. Finally, to design actions and programs to mitigate and reduce these risks in a timely way through the reinforcement and adaptation of infrastructure, improving standards and their application, and, finally, preparing and informing the population to know how to act before, during and after a contingency. This is where the new technologies associated with the integration of geospatial information are of great importance [70].

VI. CONCLUSIONS.

Around 450,000 inhabitants are exposed to As by drinking water in Mexico, where the most affected are the rural areas by

consuming water without any treatment. For this population, the health, environmental and sanitation authorities are required to implement water supply services and to promote and intervene in the execution of programs to prevent and control drinking water consumption with As levels above permissible levels. Programs should involve the participation of authorities, community, and local health systems.

Therefore, in order to achieve such programs, it is necessary to investigate the effects of As on the health population exposed to low concentrations in water and other routes of exposure, in order to mitigate the problem of As in hazardous areas, a source of Arsenic free water or suitable conditioning technology, study alternative sources for long-term use, monitor progress, and provide care to patients by periodically monitoring water sources and treatment effectiveness if appropriate.

ACKNOWLEDGMENT

The authors thank to the Consejo Nacional de Ciencia y Tecnología (CONACYT) the scholarship to study their postgraduate degrees. They also thank ACI for the systems that remove arsenic and pathogens, which are being installed in the mountainous region of Querétaro.

REFERENCES

[1] Bundschuh, J., Farias, B., Martin, R., Storniolo, A., Bhattacharya, P., Bonorino, G., Albouy, R., Viero, A.P., Fuentes, A. 2004. Groundwater arsenic in the Chaco-Pampean Plain, Argentina: Case study from Robles County, Santiago del Estero Province. Applied Geochemistry, 19(2), 231-243.

[2] Nickson, R., Mcarthur, J., Burgess, W., Ahmed, KM., Ravenskroft, P., Rahman, M..1998. Arsenic poisoning of Bangladesh groundwater. Nature 395: 338.

[3] Carabantes, A., y Fernicola, N. A. 2003. *Arsénico en el agua de bebida: un problema de salud pública*. Revista Brasileira de Ciências Farmacêuticas, 39(4), 365-372. https://dx.doi.org/10.1590/S1516-93322003000400003.

[4] Bocanegra, O. C., Bocanegra, E. M., Alvarez, A. A. 2002. *Arsénico en aguas subterraneas: Su impacto en la salud*. Groundwater and Human development. ISBN 987-544-063-9.

[5] Liu, J., Baoshan, Z., Aposhian, H. V., Zhou, Y., Chen, M. L., Zhang, A., Waalkes, M. P. 2002.Chronic arsenic poisoning from burning high-arsenic-containing coal in Guizhou, China. Environ. Health Perspect., Cary, v. 110, p. 119-122.

[6] Bhattacharya, P., Jacks, G., Jana, J., Sracek, A., Gustafsson, J.P., Chatterjee, D. 2001. Geochemistry of the Holocene alluvial sediments of Bengal Delta Plain from West Bengal, India: Implications on arsenic contamination in groundwater. In: Jacks G., Bhattacharya P., Khan A.A., Eds., Groundwater Arsenic Contamination in the Bengal Delta Plain of Bangladesh, Proceedings of the KTH-Dhaka University Seminar, University of Dhaka, Bangladesh. KTH publicación especial, TRITA-AMI REPORT 3084, pp. 21-40.

[7] Carrillo, A., & Drever, I. 1997. Environmental Assessment of the Potential for Arsenic Leaching into Groundwater from Mine Wastes in Baja California Sur, Mexico. Geofísica Internacional, *37*(1), 1-8.

[8] Pfeiffer, M.., Batbayar, G., Hofmann, J., Siegfried, K., Karthe, D., Hahn-Tomer, S. 2015. Investigating arsenic (As) ocurrence and sources in ground, surface, waste and drinking water in northern Mongolia. Environ Earth Sci (2015) 73: 649. doi:10.1007/s12665-013-3029-0.

[9] Smith, A. H., Goycolea, M., Haque, R., Biggs, M. L. 1998. Marked increase in bladder and lung cancer mortality in a region of northern due to arsenic in drinking water. Am. J. Epidemiol., Baltimore, v. 147, n. 7, p.660-669.

[10] Reyes, Y. C., Vergara, I., Torres, O.E., Díaz-Lagos, M., González, E. E. 2016. *Contaminación por metales pesados: Implicaciones en salud, ambiente y seguridad alimentaria.* Resivsta de Ingeniería Investigación y Desarrollo, 16 (2), pp. 66-77.

[11] Hernández, B., De Luna, F., Sánchez, J. A., Romero, F. M. 2015. *Dispersión hídrica de arsénico en el distrito minero de San Antonio-El Triunfo, Baja California Sur, México*. Tecnología y Ciencias del Agua, 6(5), 113-122.

[12] Armienta, M., Villaseñor, G., Rodriguez, R. 2001. The role of arsenic-bearing rocks in groundwater pollution at Zimapán Valley, México. Environmental Geology (2001) 40: 571. doi:10.1007/s002540000220.

[13] Nickson, R., Mcarthur, J., Burgess, W., Ahmed, K. M., Ravenskroft, P., Rahman, M. 1998. Arsenic poisoning of Bangladesh groundwater. Nature 395: 338.

[14] Armienta, M. A., Rodriguez, R., Aguayo, A., Ceniceros, N., Villaseñor, G., Cruz, O. 1997. Arsenic contamination of groundwater at Zimapán, México. Hydrogeol J 5:39–46.

[15] Korte, N. 1991. Naturally occurring arsenic in groundwaters ofthe midwestern United States. Environ Geol Water Sci 18: 137–141.

[16] Ohmoto, H., Hart, S. R., Holland, H. D., 1966. Studies in the Providencia Area Mexico. II:k-Ar and Rb-Sr ages of the intrusive rocks and hydrothermal minerals. Econ Geol 61:1205–1213.

[17] Baker, B. A., Topliff, A. R., Messing, R. B., Durkin, D., Johnson, J. S. 2005. Persisten neuropathy and hyperkeratosis from distant arsenic exposure. J Agromedicine 2005; 10:43-54.

[18] Castro, M. L. 2004. *Arsénico en el agua de bebida de América Latina y su efecto en la salud pública*. HDT - CEPIS 2004;95:1-12.

[19] Nuñez, R. 1994. *Relacion entre la biotransformacion del arsenico y el desarrollo de tolerancia a sus efectos toxicos*. Tesis de posgrado en Toxicologia. Centro de Investigación y de Estudios Avanzados del Instituto Politécnico Nacional.

[20] Gorby, M. S. 1988. Arsenic poisoning. West J Med 1988;149:308-15.

[21] Rojas, R. 2006. *Planes de seguridad del agua (PSA).* OMS/OPS/SDE/CEPIS-SB, Hojas de Divulgación Técnica, HDT –No. 100., ISSN: 1018-5119.

[22] OMS. 2004. *Relación del agua, el saneamiento y la higiene con la salud*. Hechos y cifras. en www.who.int/water_sanitation_health/publications/facts2004/es/index.html. (Accesado el 11 de mayo 2017).

[23] Avilés, M., Pardón, M. 2000. *Remoción de arsénico de agua mediante coagulación-cloculación a nivel domiciliario*. Federación Mexicana de Ingeniería Sanitaria y Ciencias del Ambiente, FEMISCA 2000., pp.1-10.

[24] Finkelman, J., Corey, G., Calderon, R. 1993. Environmental epidemiology: A project for América and The Caribbean. Metepec, ECO.

[25] NOM-127-SSA1-1994. *Salud ambiental. Agua para uso y consumo humano. Limites permisibles de calidad y tratamientos a que debe someterse el agua para su potabilizacion*. (Modificacopm del año 2000).

[26] Quaas, R. 2010. Información geoespacial y toma de decisiones: Actualidad y retos. CENAPRED.

[27] Carrillo, A. & Drever, I. 1997. Environmental Assessment of the Potential for Arsenic Leaching into Groundwater from Mine Wastes in Baja California Sur, Mexico. Geofísica Internacional, *37*(1), 1-8.

[28] Chopin, E. I. B., Alloway, B. J. 2007. Distribution and mobility of trace elements in soils and vegetation around themining and smelting areas of Tharsis, Riotinto and Huelva. Iberian PyriteBelt, SWSpain.Water Air and Soil Pollut 182:245–261. doi:10.1007/s11270-007-9336-x.

[29] Moncure, G., Jankowski, P. A., Drever, J. I. 1992. The hydrochemistry of arsenic in reservoir sediments, Milltown, Montana, USA. In: Kharaka YK Maest AS (eds) Water–rock interaction. AA Balkema, Rotterdam, pp 513–516.

[30] Gray, J. E., Coolbaugh, M. F., Plumlee, G. S., Atkinson, W. W. 1994. Environmental geology of the Summitville mine, Colorado. Econ Geol 80: 2006–2014.

[31] Toran, L. 1987. Sulfate contamination in groundwater from a carbonate-hosted mine. J Contam Hydrol 2: 1–29.

[32] Smedley, P. L., Edmunds, W. M., Pelig-Ba, K. B. 1996. Mobility of arsenic in groundwater in the Obuasi gold-mining area of Ghana: some implications for human health. In: Appleton JD, Fuge R, McCall GJH (eds) Environmental geochemistry and health. Geol Soc Special Publ, Lond 113: 163–181

[33] Nicolli, H. B., Suriano, J. M., Gomez, M. A. P., Ferpozzi, L. H., Baleani, O. A.1989. Groundwater contamination with arsenic and other trace elements in an area of the Pampa, province of Córdoba, Argentina. Environ Geol Water Sci 14:3–16.

[34] Welch, A. H., Lico, M. S., Hughes, J. L. 1988. Arsenic in ground water of the western United States. Ground Water 26: 333–347.

[35] OMS. 2016. Arsénico Nota descriptiva. http://www.who.int/mediacentre/factsheets/fs372/es/ (Accesado el 13 de Febrero 2017).

[36] Fernández-Caliani, J. C., Barba-Brioso, C., González, I., Galán, E. 2009. Heavy metal pollution in soils around the abandoned mine sites of the Iberian pyrite belt (Southwest Spain). Water Air Soil Pollut 200:211–226. doi:10.1007/s11270-008-9905-7.

[37] Ramos-Arroyo, Y. R., Prol-Ledesma, R. M., Siebe-Grabach, C. 2004. *Características geológicas y mineralógicas e historia de extracción del Distrito de Guanajuato, México.* Posibles escenarios geoquímicos para los residuos mineros.

[38] Thornton, I. 1996. Impacts of mining on the environment: some local, regional and global issues. Appl Geochem 11:355–361.

[39] Wilson, F.H. & Hawkins, D.B. 1978. Arsenic in streams, stream sediments, and groundwater, fairbanks area, Alaska. Geo (1978) 2: 195. doi:10.1007/BF02380485.

[40] Méndez, M. & Armienta MA. 2003. Arsenic phase distribution in Zimapán mine tailings, Mexico. Geof Int 4(1):131–140.

[41] Martorell, J.J. 2010. Biodisponibilidad de metales pesados en dos ecosistemas acuaticos de la costa Suratlantica andaluza afectados por contaminación difusa. Tesis Doctoral Universidad de Cádiz.

[42] SGM. 2014. *Listado de proyectos mineros*. Dirección General de Desarrollo Minero. México, DF: Servicio Geológico Mexicano, Centro de documentación de la Dirección General de Desarrollo Minero, Secretaría de Economía.

[43] COREMI. 1999. *Monografía geológico minera del estado de Baja California Sur.* México, DF: Consejo de Recursos Minerales, Secretaría de Comercio y Fomento Industrial.

[44] Mapes, E.V., Montero, Z., Godoy, G. J. 1964. *Geología y yacimientos minerales del Distrito Concepción del Oro y Avalos, Zacatecas.* Consejo de Recursos Naturales No Renovables. Publicación 10-E, México, DF.

[45] Castro-Larragoitia, J., Kramar, U., Monroy-Fernández, M.G., Viera-Décida, F., García-González E.G. 2013. Heavy metal and arsenic dispersion in copper-skarn mining district in a Mexican semi-arid environment: sources, pathways and fate. Environ Earth Sci (2013) 69: 1915. doi:10.1007/s12665-012-2024-1.

[46] Espinosa, E., Armienta, M.A., Cruz, O. 2009. Geochemical distribution of arsenic, cadmium, lead and zinc in river sediments affected by tailings in Zimapán, a historical polymetalic mining zone of México. Environ Geol (2009) 58: 1467. doi:10.1007/s00254-008-1649-6.

[47] Murray, K. S., Cauvet, D., Lybeer, M., Thomas, J. C.1999. Particle size and chemical control of heavy metals in bed sediment from the Rouge River, southeast Michigan. Environ Sci Technol 33:987–992

[48] Salomons, W. 1995. Environmental impact of metals derived from mining activities: processes, predictions, preventions. J Geochem Explor 52:5–23.

[49] Razo, I., Carrizales, L., Castr, J. 2004. Arsenic and heavy metal pollution of soil, water and sediments in semi arid climate mining area in México.Water, Air, & Soil Pollution (2004) 152:129 doi:10.1023/B:WATE.0000015350.14520.c1.

[50] The National Academy os Science. 1999. Arsenic in drinking water. National Academy Press, Washington.

[51] Frederick, P., Kenneth, B., Chien-Jen, C. 1994. Health implications of arsenic in drinking water. Journal AWWA, 88 (4), 155-167, Abr. 1996.

[52] Hall, A.,H. 2002. Chronic arsenic poisoning. Toxicol lett 2002; 128:69-72.

[53] Gehle, K., Harkins, D., Johnson D., Rosales-Guevara, L. 2000. Case studies in environmental medicine: arsenic toxicity. Atlanta, United States. Agency for Toxic Substances and Disease Registry, 2000; pp:1-42.

[54] Schoolmeester, W.L & White, D.R. 1980. Arsenic poisoning. South Med J 1980; 73:198-208.

[55] Bangladesh Centre for Advanced Studies. 1997. Arsenic special issue. BCAS, Newsletter, 8(1):1-8, Jan.-Mar. 1997.

[56] Pérez V., A. Torres L.,P., Cruz V., C.H. 2009. *Planes de seguridad del agua. Fundamentos y perspectivas de inmplementación en Colombia*. ing.inv., Volume 29, Issue 3, p. 79-85, 2009. eISSN 2248-8723. Print ISSN 0120-5609.

[57] CENAPRED 2014. *Diagnóstico de peligros e identificación de riesgos de desastres en México*.

[58] OMS. 1997. World Health Organization., Guidelines for Drinking-water Quality., Second Edition, Surveillance and Control of Community Supplies.

[59] National Academic Press. 2002. Biosolids applied to land., Advancing standards and practices, ISBN: 0-309-57036-0, Washington.

[60] EPA Environmental Protection Agency. 2006. Hazard Analysis Critical Control Point (HACCP) Strategies for Distribution System Monitoring, Hazard Assessment and Control.

[61] FAO/WHO Food and Agriculture Organization of the United Nations/World Health Organization. 2001. Codex Alimentarius - Food Hygiene - Basic Texts - Hazard Analysis and Critical Control Point (HACCP) System and Guidelines For Its Application., Second Edition, Roma.

[62] Sperber, W. 2005. HACCP and Transparency., Foof Control, Vol. 16, 2005, pp. 505-509.

[63] Damikouka, I., Katsiri, A., Tzia, C. 2007. Application of HACCP principles in drinking water treatment., Desalination, Vol. 210, 2007, pp. 138-145.

[64] Havelaar, A. 1999. Application of HACCP to drinking water supply., Food Control, Vol. 5, No. 3, 1999, pp. 145-152.

[65] Gunnarsdóttir, M., Gissurarson, L. 2008. HACCP and water safety plans in Icelandic water supply: preliminary evaluation of experience., Journal of water and health, Vol. 6, No. 3, 2008, pp. 377-382.

[66] Chit Pin, T., See, T. 2008. Water Safety Plan for water supply network in Singapore., Memorias Water Safety Plans: Global experiences and future trends., Portugal, ASPEB, IWA, OMS.

[67] SEMARNAT. 2010. *Compendio de Estadísticas Ambientales*. http://aplicaciones.semarnat.gob.mx/estadisticas/compendio2010/10.100.13.5_8080/ibi_apps/WFServlet8ca2b.html. (Accesado el 13 de Agosto de 2016).

[68] OMM. 2016. *Peligros y desastres naturales*. http://www.wmo.int/youth/es/peligros-naturales. (Accesado el 13 de Agosto de 2016).

[69] ISDR.2016. *Alto a los desastres*. http://www.stopdisastersgame.org/es/isdr.html. (Accesado el 13 de Agosto de 2016).

[70] Guevara, E., Quaas, R., Ferández, G. 2006. *Guía Básica para la elaboración de Atlas Estatales y Municipales de Peligros y Riesgos*. Conceptos Básicos sobre Peligros, Riesgos y su Representación Geográfica. (pp 11-22) México. CENAPRED.

PITS AS DRAINS IN PIG FACILITIES USING WATERPROOF CONCRETE FOR REDUCTION OF CONTAMINANT RESIDUE FILTRATIONS.

C.E. Hernández Arreguín
Maestría en ciencias, Departamento de Posgrado
Universidad Autónoma de Querétaro
Querétaro, México
carlos91_54@hotmail.com

Abstract - This research presents the problem that involves the pig facilities, since it is a sector that is increasing not only in our country, but also throughout the world. And if this growth is not done in a controlled way, it can mean a rather serious source of pollution. This research aims to develop a drainage system for the management of excreta more efficient or with new materials in the construction that benefits all sectors of production but above all that benefits the environment.

I. INTRODUCTION

By 2016, global pork production is forecast to reach 109.3 million tonnes. In Mexico, production is expected to increase, so that our country will consolidate itself as ninth producer worldwide with a share of 1.3% of the total world production of pork.

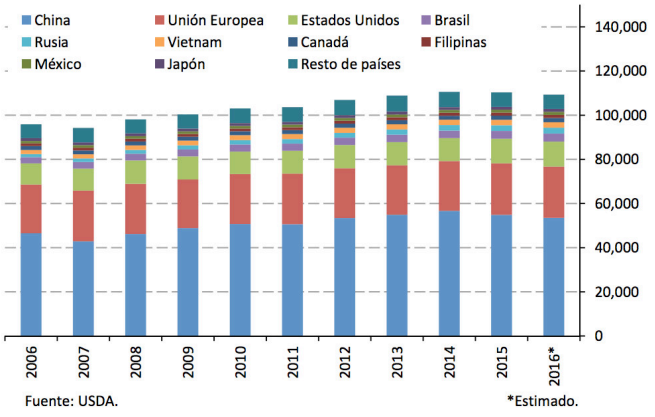

Global pork production, 2006-2016
(Thousands of tons)

During the last decade the national production of pig card has presented a continuous growth, especially from 2011. The outlook is favorable to continue with the trend of growth in the next years.

Thus, domestic production in 2016 is expected to reach 1.36 million tons, an annual growth of 3.2%. In 2015, production reached a level of 1.32 million tons of meat. And during the decade of 2006 to 2015 this product obtained an average annual growth of 2% (SAGARPA, 2015).

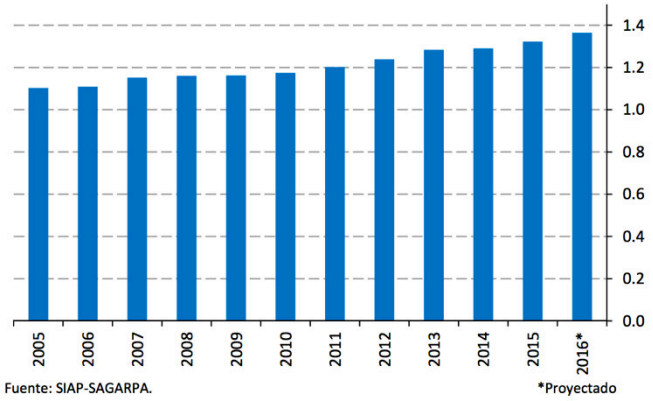

Pork production in México, 2005-2016
(Millions of tons)

Regarding meat production by federal entity, it is noted that 67.3% of the national production is concentrated in five entities. During 2015, Jalisco produced 19.5% of the national total; In Sonora, 17.3%; 12.2% in Puebla; 9.3% in Yucatan; And in Veracruz, 9.0% of the national meat production.

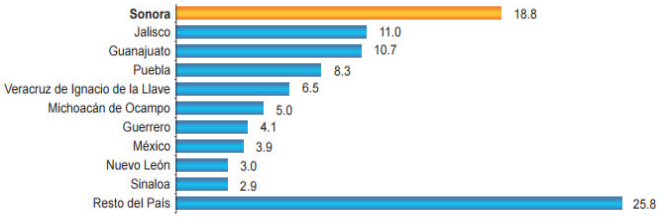

Percentage distribution of total pig stock by major producing states. Source: INEGI. VIII Censo Agrícola, Ganadero y Forestal, 2007.

This increase in production has been matched by an increase in the size of the pig farms, the INEGI through the Agricultural, Livestock and Forestry Census 2007, recorded the existence of 9, 921, 192 pigs in the country, a figure Which includes both those that are raised and exploited in production units (8, 611, 401), and those housed in backyard housing or activities (409, 791).

The increase in the size and capacity of the pig farms resulted in an increase in the contaminating capacity of these facilities, especially in regions of the country that have a high density of porcine population.

II. BACKGROUND

In Mexico there are basically three different production systems, characterized by their technological level: Technified, semitecnified and backyard system. The first two have a defined geographical distribution, on the contrary, the backyard system is presented in all the states of the country.

Technological system: It is characterized by the use of state-of-the-art technology, with particular adaptations to the climatic conditions where it is located.

The level of integration is high, allowing it to control the genetic quality of the herd and standardize the pigs produced for slaughter. They are usually companies that have advice in the formulation of rations according to the availability of inputs and productive capacity of the herd, as well as with food factory.

The states where this system is predominant and those that are free of economic diseases are practically the same, indicating their concern about the health control of the herd. The markets in which it markets its production are the main urban areas of the country and the cold meats and sausage industry. This production system has been increasing its participation in the production in the last years; It is estimated that it represents approximately 58% of the national production and is located mainly in the states of Sonora, Sinaloa and Yucatán (Lastra et al., 2000).

Semi-technological system: It is named because its main characteristic is to use modern technology along with traditional techniques of management, its productive parameters are very variable; However, generally their productivity is lower than the observed in the technified system.

This is mainly due to the fact that the infrastructure of the farms and the sanitary control of the farms are not adequate, to which is added the use of commercial foods, which are characterized to cover the nutritional requirements of a hypothetical population of pigs. It markets its products mainly in regional markets and in small urban centers; Its participation in the national market represents around 15% and its productive importance decreased by 5% in the last decade (Lastra et al, 2000).

This system is found in all the states of the republic, although it is majority in the Center (Guanajuato, Michoacán, Jalisco) and South of the country.

Backyard system: This system is practiced throughout the national territory, including urban areas, where 409, 791 are registered. An important feature of this system is that the genetic quality of the animals is low, which translates into low Yields (Lastra et al., 2000).

III. PROBLEMATIC

The main impacts of livestock on the environment come basically from two sources: greenhouse gas emissions (GHG) and ammonia emissions, it has been shown that exposure to the gases produced (ammonia, sulfur Hydrogen, methane and carbon dioxide) poses direct health risks to workers and pigs on the farm; And the management of their excreta.

We must understand that excreta are the waste of animals, their origin is in the food that is provided to animals, from which the body takes the necessary nutrients for its maintenance, production and reproduction; Is added elements of digestion not used by the metabolism, which already mixed are expelled outside the same and result in faeces and urine.

The management of excreta is of paramount importance, since they represent a high risk of contamination of the soil and groundwater mainly with nitrates and phosphates due to the probable runoff and filtration, which increases the eutrophication process of aquifers.

IV. PITS AS DRAINAGE WITHIN PORCINE FACILITIES.

To address the problem of contamination caused by animal excreta, strategies must be implemented at different levels; On the one hand, it is important that environmental legislation is currently in place and the maximum permissible values of pollutants present in wastewater, including those from animal production units, have been established. On the other hand, producers should be provided with models of treatment and use of excreta adequate to specific conditions of each farm and through the implementation of which the potential contamination of the waste is minimized. The options adopted by each farm should be the most appropriate according to their technical, economic and environmental feasibility, as well as to the availability of water and particular practices of cleaning, collection, treatment and use currently being carried out on farms.

The storage trenches under the ground are the current system used as drainage for the excretion of excreta inside the porcine warehouses; This system consists of deposits with variable capacity, generally constructed of septum or reinforced concrete, usually located under grilled soils or slat.

Storage pit used as drainage in a maternity shed for sows.

This system is quite simple but effective, so it has become the drainage system for the evacuation of excreta more used inside the porcine facilities.

The system consists of storing a mixture consisting of feces, urine, cleaning water, water poured from the drinkers and food remains; To be later emptied by means of gravity.

Cama para cerdas en maternidad colocada sobre fosa para drenaje.

The pits are nothing more than deposits of variable depth with a width of no more than 2.44 meters and a variable length, these pits must be drained every time they fill, the occasions in which the pit must be drained depends on the cycle or stage in The one that is the pig.

The emptying of pits by means of gravity is the most simple and economical method, although it is also the emptying by means of pumping, scraping or by jet of water.

V. Environmental regulation for the discharge of porcine excreta

In Mexico, contamination control by porcine excreta discharges is regulated by the following laws and regulations:

Environmental regulation

- Ley General del Equilibrio Ecológico y la Protección al Ambiente -1982
- Ley Federal de Derechos de 1991 (Parámetros: DQO, SST)
- Ley de Aguas Nacionales -1992- y su Reglamento -1994.
- Norma Oficial Mexicana NOM-001-ECOL-1996, Que establece los límites máximos permisibles de contaminantes en las descargas de aguas residuales en aguas y bienes nacionales.
- Norma Oficial Mexicana NOM-002-ECOL-1996, Que establece los límites máximos permisibles de contaminantes en las descargas de aguas residuales a los sistemas de alcantarillado urbano o municipal.

The Federal Government, through the Ministry of Finance, has implemented the application of economic instruments to companies that assist in solving environmental problems related to wastewater discharges in the field of tax policy:

- Fiscal incentive. Deduction of 100% of the amount of investments in equipment to prevent and control environmental pollution.
- Payment of a right for the discharge of wastewater to water and land owned by the nation, enshrined in the Federal Law of Rights.

VI. concrete with low permeability

To reduce the risk of contamination of soil and groundwater by the probable runoff and filtration of the mixture of feces, urine, cleaning water, water poured from the drinking fountains and food remains the use of low permeability concrete as material For the construction of these graves.

Low permeability concrete prevents the capillarity of water in contact with concrete in walls and foundations, helping to mitigate attacks by aggressive chemical agents for concrete such as sulfates and carbon dioxide dissolved in water.

Currently this type of concrete is already used in the construction of tanks, canals, decks, retaining walls and structures exposed to water.

REFERENCES

[1] SAGARPA. 2000. Programa Nacional de Normalización. Comité consultivo nacional de normalización de protección zoosanitaria. www.sagarpa.gob.mx/senasica. Accesado 28-05-2003.

[2] NOM-051-ZOO-1995. Trato humanitario en la movilización de animales.

[3] Bedoya, M. 2002. Bioseguridad en granjas porcinas.aninet pags 1-5. www.pic.com. Accesado 16-01-2003.

[4] CODEX. 1997. Límites máximos del codex para residuos de medicamentos veterinarios. http:www.apps1.fao.org. Accesado el 27 de Mayo del 2003.

[5] FAO. 1997. Código de prácticas para la alimentación adecuada de los animales, a fin de combatir los riesgos para la salud humana procedentes de la carne contaminada. Organización de la Naciones Unidas para la Agricultura y la Alimentación. Noticia. www.fao.org/noticia. Accesado 28-05-2003.

[6] NOM-127-SSA1-1994. Agua para uso y consumo humano. Límites permisibles de calidad y tratamientos a que debe someterse el agua para su potabilización.

[7] Doyle, M.E. 2001. Alternatives to antibiotic use for growth promotion in animal husbandry. FRI Briefings. 4:1-17.

[8] ASTM C 1585-04 "Standard Test Method for Measurement of Rate of Absorption of Water by Hydraulic- Cement Concretes " American Standards Testing Materials Vo. 4.02 Concrete and Aggregates, 201 ASTM International, 100 Barr Harbor Drive, PO Box C700, West Conshohocken, U.S.A.

[9] AZORÍN, F., SÁNCHEZ-CRESPO, J.L. (1986). Métodos y aplicaciones del mues- treo. Alianza Editorial.

[10] KRUPA, S. V. (2003). Effects of atmos- pheric ammonia (NH3) on terrestrial vege- tation: a review. Environmental Pollution 124, 179-221.

[11] LAINEZ, M. (1998). Caracterización técnica de la producción porcina en la Comunidad Valenciana. Tesis doctoral. Universidad Politécnica de Valencia.

[12] STEINFELD, H., GERBER, P., WASSE- NAAR, T., CASTEL, V., ROSALES, M., DE HAAN, C. (2006). Livestock' s long shadow. FAO, 377 pag.

[13] H. Taylor, "Cement Chemistry". Academic Press, London, pp. 277–315, 1990

[14] Manual del Participante. Producción de Cerdos. Colegio de Post graduados. Instituto de Enseñanza e Investigación en Ciencias Agrícolas México-Puebla-San Luis Potosí-Tabasco-Veracruz-Córdoba. Secretaría de la Reforma Agraria. Carlos G. Germán Alarcón, Julio César Camacho Ronquillo y Jaime Gallegos Sánchez. http://www.sra.gob.mx/internet/informacion_general/programas/fondo_tierras/manuales/Prod_Cerdos.pdf

[15] Secretaría de Fomento Ganadero, del Gobierno del Estado de Sonora. Ing. Eduardo Paredes Bússani, Analista Pecuario del OEIDRUS. Los datos fueron proporcionados por la fuente en mención, la interpretación es nuestra

Virtual reality bicycle simulators

State of the art

Emmanuel Alejandro Rodelas Dominguez
Department of virtual reality and immersive applications
Autonomous University of Querétaro
Santiago de Querétaro, Querétaro de Arteaga.
erodelas24@alumnos.uaq.mx

Cesar Oswaldo Mendoza Herbert
Department of virtual reality and immersive applications
Autonomous University of Querétaro
Santiago de Querétaro, Querétaro de Arteaga.
oswaldo.herbert@uaq.mx

***Abstract*—Virtual reality (VR) nowadays has become something that most of the people heard about and a small part has experienced. See a whole different place with just putting a VR headset on or feel the adrenaline of driving a car at high speed without be in a real car is a new step on computer science, image processing, control and interactive systems. This article talks about the beginning of VR, some of the main types of virtual simulators and focuses on bicycle simulators and the different research paths that these kinds of simulators have acquired nowadays.**

Keywords— Virtual, reality, technology, bicycle, type, simulator.

I. INTRODUCTION

Virtual reality is a field of study that aims to create a system that provides a synthetic experience for its users. The experience is dubbed "synthetic", "illusory" or "virtual" because the sensory stimulation to the user is generated by the "system". [1]|. What here is known as system it could be screens, projectors, head mounted displays, headphones or speakers that shows the virtual experience to a person, sensors like gyroscopes, accelerometers, buttons or cameras that detect the user actions and a computer that could process all the interactions and images to generates an output to the user. All this features or objects are part of the key elements for a virtual reality experience, that are four: a virtual world, immersion, sensory feedback (responding to user input), and interactivity [2]. The goal of this technology or field of study with these four key elements is give the user the feeling of being mentally immersed or present physically in the virtual simulation.

II. VIRTUAL REALITY BACKGROUND

The first immerse system was a stereoscopic-television apparatus for individual use patented by Morton L. Heiling in 1957, this apparatus was composed of a pair of optical units, discharge nozzles, a hollow casing and a pair of television tube units, co-acting to cause the user to comfortably see the images, hear the sound and to be sensitive to the air discharge of said nozzles [3].

After this stereoscopic apparatus Morton L. Heiling patent in 1961 a device named Sensorama Simulator, Fig. 1, described as an apparatus to stimulate the senses of an individual to simulate an actual experience realistically [4]. The main purpose of the Sensorama was immersing the viewer to a film by enclosing the head in a cabin.

Four years later in 1965 Ivan E. Sutherland talked about the ultimate display that would be a room within which the computer can control the existence of matter, where the computer could easily sense the positions of almost any of our body muscles and with appropriate programming such a display could literally be the wonderland into which Alice walked [5].

3 years later he created the first head-mounted three dimensional display a device which presented the user with a perspective image which changes as he moves [6]. This device had two methods of sensing head's position, the first one involved a mechanical head tracking using spooled retractable cables, Fig. 2, but it was heavy and the second one was a continuous wave ultrasonic head position sensor with transmitters attached to the head-mounted optical system. One of the first tests was a simple stick representation of a cyclo-hexane molecule in three dimensions and after with improved computation capability a small cube was displayed in the center of the user's operating area. The user can examine it form whatever side he desires.

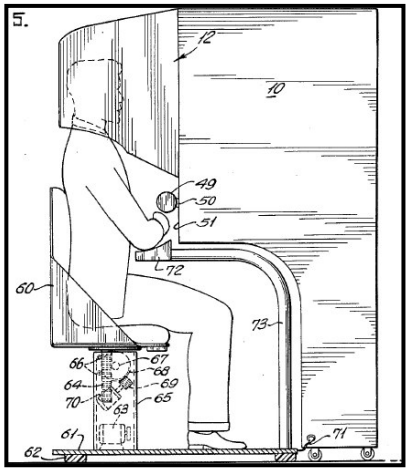

Fig. 1 Sensorama Simulator [4]

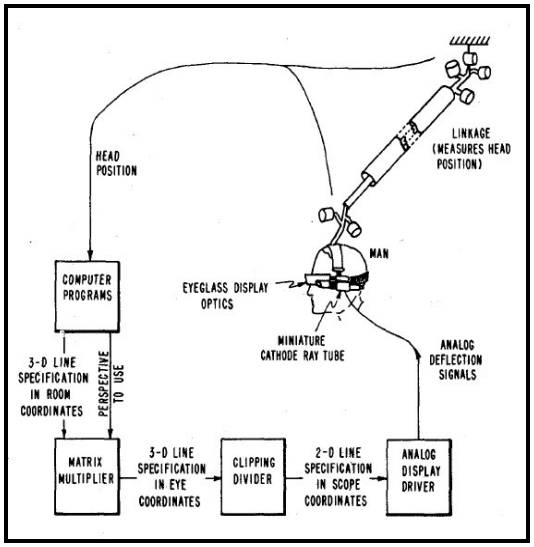

Fig. 2 Head-mounted three dimensional display [6]

After this demonstration a variety of research were born in this topic, in the university of Wisconsin in 1969 Myron Krueger, a computer researcher referred the term "Artificial Reality" while experimenting with a series of experiences and perspectives on virtual reality systems. The difference with Sutherland's work was the use of cameras to track the person's movement and the user was not encumbered by any mechanical devices or other sensors attached to their body [7].

In the same year Frederick P. Brooks puts on the table the requirement of hardware for specific application problems and the University of North Carolina, where he worked, focus on these developments generating a variety of input and output devices for haptic feedback as responsive forces, head-mounted displays and high-performance graphics engines (developing virtual reality).

In 1977 at the University of Illinois in Chicago where different types of graphical representations, input and output devices, and interaction techniques were explored, the Sayer glove was developed which consist of a glove outfitted to sense the bend of the wearer's fingers,

In 1988 Frederick P. Brooks focus his research to the construction of real-time 3-D illusions by computer graphics, make observations about interfaces to virtual worlds and the application of virtual-worlds techniques to the enhancement of scientific computing [8]. And proposed six application systems where his research takes part.

In 1987 Jaron Lainer an ex Atari worker that found in 1985 the visual programming lab (VPL Research) used the term virtual reality to define this field. The company of Jaron and Thomas G. Zimmerman was the first to sell VR goggles and gloves making a major development in the area of virtual reality haptics.

In 1992 the CAVE visual display system was announce, a walk-in virtual reality 10-foot cube with three or more of its surfaces rear-projected with stereoscopic, head-tracked, computer graphics.

In 1992 a movie named The Lawnmower familiarized the concept of virtual reality to the audience and in 1993 Sega, the video game developer and publisher, announced a headset that was seen in the Winter Consumer Electronics Show, but never saw the light because of development difficulties.

In 1995 in another attempt to introduce VR to the people Nintendo released the Virtual Boy, a 3D gaming console that could display stereoscopic 3D graphics, but the sales failed and in 1996 Nintendo ceased the distribution.

Since then the approaches in virtual reality and the hardware and software used to create it have been evolved to the point where we can experience this virtual worlds in our houses with dedicated hardware, like Oculus Rift or from our cell phones with Google Cardboard or Samsung Gear.

III. VIRTUAL SIMULATORS

An essential part of the virtual reality is the degree of immersion with the system; the user is physically immersed in a virtual world when using a VR display but not mentally, this mentally degree of immersion is influenced by the interaction within the virtual world, if the user is just watching instead of changing the virtual environment there will be a lack of immersion. To fight this passive immersion degree the simulators were created.

A simulation is the recreation of a process or a system from the real world. A virtual simulator is recreating this process in the virtual world. The simulators helped not just for increase the degree of immersion in the system but for learning tasks without the risk of failure creating learning experiences for use in real world.

Flight simulators are an early example of simulators based on interactive computer displays. This system implements the use of mechanical instruments like pedals, levers and buttons to simulate the cabin and the goal was the pilot get familiar with this system without really being on an airplane.

The VCASS, Fig. 3, was a virtual flight simulator created for military training and Thomas Furness III was one of the first that use this technology for these propose [9]. The implementation of these simulators comes at a time when aircraft systems became more complex and sophisticated requiring more hours for training to maintain the same flying proficiency.

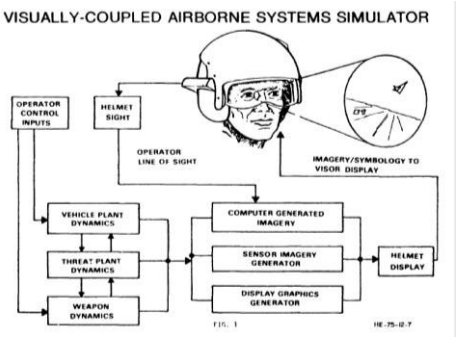

Fig. 3 Visually-Coupled Airvorne Systems Simulator [9]

BDI surgical simulator, Fig. 4, was a simulator that used force display as a degree of immersion providing the user visual and haptic information to experience what a surgeon would be with a live patient. The surgical instruments were actual medical instruments and were connected to force-feedback devices to provide haptic feedback.

Like the flight simulator, the use of these systems allows new people interested in the area to practice without the use of hospital space, human patients, animals or a constant supervision of an expert [7]. This saves time and helps people to master this skill.

Driving simulator aims to drive a car placing the user in a base car platform and the controls gave input to the VR system. Caterpillar made this type of platforms from his own equipment, Fig. 5. The prototype was created to allow design engineers to test new machine designs prior to building physical models. The preliminary usage of the system was for assessing operator visibility and allowing engineers to make corrective modifications very early in the design process [7].

These simulators gave a close approach to manage these activities but to get a better understanding of the interaction and immersion state, platforms were introduced.

A platform simulator is a system that integrates hardware and software components, like controllers, maneuvers, body tracking systems, audio input/output, displays, HMD, haptic systems, virtual environment, etc.

The advantage of a virtual reality system on a platform is in the feedback component that tries to gives the participants a real sensation of the movements of sitting in a real vehicle.

Platforms start with flight simulators; the user sits in front of a display screen and interacts with the hardware system. As feedback the platform moves giving the user an immerse feeling and the sense of what would happen in reality. Later this immersion system reached the car simulators and after that studies related to bicycle platform simulators were born. These bicycle simulators were interesting systems due its unstable natural condition and the creation of a platform that emulates these movements was a challenging approach.

Fig. 4 Surgical Simulator [7]

Fig. 5 Caterpillar driving simulator [7]

One of the first bicycle simulators was developed in the Max-Plank institute with a simple motion generation system and a visual simulator with large truncated cone-shaped projection screen.

Another of the first bicycle simulators was developed in the Korean Advanced Institute of Science and Technology, KAIST, the interactive bicycle simulator, Fig. 6, this simulator consist of a bicycle, a Stewart platform, a Magneto-Rheological handle and a pedal resistance to generate motion feelings, the real time visual simulator and the projection system, the sub-controllers and the integrating control network [10]. The main goal of this simulator was study essential issues and integration technologies in order to develop more advanced interactive simulators.

A year later a second version of this simulator was made consisting of a bicycle, a four degree of freedom (DOF) platform, a handlebar and a pedal resistance system to generate motion feelings, a real-time visual simulator, a HMD, beam projection system and a 3D sound system [11] ,with this second simulator KAIST made an interactive racing simulator system between bicycles mixing them into a network system and riding in a virtual velodrome environment.

For the multi-user system, each visual simulator communicates with a distributed server, transmits the rider's position of the other rider located somewhere in the distribute network.

Fig. 6 KAIST interactive simulator [10]

On 2005 the Shanghai Jiaotong University make its own bicycle platform simulator, Fig. 7, with the same six DOF Steward platform and two sub models, a stability sub model and a vibration sub model[12].

An innovated completed mathematical model of a bicycle was presented. The motion equations were developed based on the Lagrange's equation and also the Runge-Kutta method was selected to make numerical simulation. They make experiments to verify these models with a real instrumented bicycle and got similar results for the steering angle, tilt angle, velocity of bicycle and vibration with different road profiles.

In 2007 in the Journal of the Chinese Society of Mechanical Engineers a study of an interactive bike simulator was published. It was a two DOF platform, Fig. 8, for controlling roll and yaw angles through cable length and because the platform was driven by changing cable length by using a motor-driven reel the cost of the system could be reduced comparing the traditional hydraulic or ball-screw driven platform based on similar motion range[13].

The goal of this platform was to study an interactive bike simulator of two DOF mechanisms with dynamic platform and its application to virtual reality from the rider in the virtual environment.

In the same year the Chinese University of Hong Kong developed a cycling simulator consisting of 4 main units, a display unit, a bike platform, a sensing unit and an actuation unit [14]. This simulator was not mounted on a movable platform and its main purpose was to create a virtual cycling simulator suitable for exercise and entertainment. The simulator is capable of simulating the dynamic changes of the virtual environment including the resistance of different land profile and the decelerating/accelerating effect of the bike when going up/down hill. The display unit, (image of the virtual world) was created with 2 projectors that produce the stereoscopic effect of the virtual scene.

Fig. 7 Interactive Bicycle Simulator [12]

Fig. 8 Two degree of freedom platform [13]

Again on 2007 in the University of Applied Sciences in Germany another bicycle simulator was made. This simulator was composed of a six DOF Steward platform and a bike mounted on it. The target of the project was to develop a real bicycle simulator with the ability to represent real life traffic situations[15].

On 2014 in the Journal of NeuroEngineering and Rehabilitation a bicycle simulator was used for rehabilitation purposes. Sensorized pedals, handlebars and a heart rate monitor interfaced with a virtual biking environment were made. The system includes signals from 15 different sensors. The relevance of this system will be established when riders can modify their cycling kinetics, improve their fitness and more important transfer the benefits from training in the virtual environment to real world mobility[16].

In 2016 in the University of Missouri in Columbia the ZouSim bicycling simulator was created, Fig. 9. The simulator was developed for traffic engineering purposes. For studying facility design, including geometrics, signage, markings, and traffic control. Rider safety and mobility can be investigated using this type of simulator[17].

IV. RESEARCH PATHS IN BICYCLE SIMULATORS.

From this research made in bicycle simulators different systems can be observed. Most of the papers referred to bicycle simulators focus on 1 of this 3 oriented paths emerging for the creation and study of bicycle simulator systems.

The first is the implementation of a real bicycle simulator using equations that describe the motion of a bicycle and the implementation of these equations in a virtual world. These systems try to emulate or recreate the same forces, feelings and dynamics of ride a bicycle on the real world [10], [12], [18]–[20]. Models are different depending of the assumptions made, from simple models considering or ignoring certain variables to non linear models involving wind speed, drag forces or road conditions.

The, Nanyang University simulator, the KAIST interactive simulator [10] and the Korea Advanced Institute of Science and Technology bicycle simulator are examples of this type of research.

Fig. 9 ZouSim bicycle simulator [17]

The second path is in rehabilitation process, the virtual simulator helps measuring heart rate, sitting habits, position of the body, postural balance and factors focusing in medical research. This simulators use either screen/projector or HMD to show the virtual world to the rider. University of Korea shows a study that uses a virtual cycling system to improve postural balance[21], the VRACK (virtual reality augmented cycling kit) [16] with embedded sensors monitor physiological and biomechanical parameters for help in rehabilitation, and this are examples of this medical approach.

The third path is in bicycle road safety, a bicycling simulator can be one instrument for testing and investigation design alternatives for bicycle facilities [17]; validation of paths for cyclists, get driving patterns in roads, facility design of streets, mobility and interaction with drivers is the focus approach of this research that in the last years has increase. Fivis interactive simulator is a prototype that serve for road safety education, for prevention purposes, and for specific simulations of visual information under simultaneous physical exercise [15], in the MUARC a simulator has been developed to assess new infrastructure designs that will enhance cyclist safety when riding on-road [22].

These 3 paths are the major focuses of bicycle simulators, the big environment where bicycle simulators develop but not the unique; there are papers talking about simulators as entertainment, exercise mechanisms and for visiting places and make virtual ride tourism. Imagine going on a ride to the mountain that you like, drive the tour of France route or just riding along on a beach or a famous parade without spending hours traveling and have the feeling of really be there.

V. CONCLUSIONS.

Virtual reality systems are a relative new technology that has grown quickly; an advance technology that we use now and the future of these systems is evolving. From the first stereoscopic-television apparatus to the CAVE virtual system and the new reality systems in these days, like HMD's, the factors of the virtual systems have been the same: a virtual world, an immersion feeling, sensory feedback, and interactivity; the only that has change is the degree of evolution these components had to bring a better immersion to virtual reality systems.

Immersion feeling and interactivity evolved with the integration of platforms. The virtual reality platforms start in airplanes and scaled to four and two wheeled vehicles. Once in bicycle simulators a variety of approaches emerge to study different aspects of this type of virtual reality simulators.

The approaches of virtual reality simulators keeps expanding to different disciplines but 3 main subjects or points of views could be established for these simulators: simulate real bicycle models, help in medical research applications and improve safety of the rider in the streets.

There is no best bicycle simulator but depends of the application and the goal of the research, the truth is the better the bicycle simulators become the best the system will be to fool the rider to the point he/she doesn't feel difference between the virtual simulator and the real world.

REFERENCES

[1] J. K. Gerard, *Designing Virtual Reality Systems. The Structured Approach*. 2005.

[2] W. R. Sherman and A. B. Craig, *Understanding Virtual Reality*. 2003.

[3] M. Heilig, "Oct. 4, 1960," 1960.

[4] M. Heilig, "3,050,870 8," p. 16, 1962.

[5] B. Watson and D. Luebke, "The ultimate display: Where will all the pixels come from?," *Computer (Long. Beach. Calif).*, vol. 38, no. 8, pp. 54–61, 2005.

[6] I. E. Sutherland, "A head-mounted three dimensional display," *Proc. AFIPS '68 (Fall, part I)*, pp. 757–764, 1968.

[7] A. B. Craig, W. Sherman, and J. D. Will, *Developing Virtual Reality Applications*. 2009.

[8] F. P. Brooks, "Grasping reality through illusions - Interactive graphics serving science," p. 15, 1988.

[9] A. I. R. Force, S. Command, U. States, and A. I. R. Force, "Proceedings of the image conference," 1977.

[10] Dong-Soo Kwon *et al.*, "KAIST interactive bicycle simulator," *Proc. 2001 ICRA. IEEE Int. Conf. Robot. Autom. (Cat. No.01CH37164)*, vol. 3, pp. 2313–2318, 2001.

[11] D.-S. Kwon *et al.*, "KAIST interactive bicycle racing simulator: the 2nd version with advanced features,"

"Intelligent Robot. Syst. 2002. IEEE/RSJ Int. Conf. on," vol. 3, no. October, p. 2961, 2002.

[12] Q. He, X. Fan, and D. Ma, "Full Bicycle Dynamic Model for Interactive Bicycle Simulator," *J. Comput. Inf. Sci. Eng.*, vol. 5, no. 4, p. 373, 2005.

[13] C.-K. Chen, F.-J. Chen, J.-T. Huang, and C.-J. Huang, "Study of Interactive Bike Simulator in Application of Virtual Reality," *J. Chinese Soc. Mech. Eng.*, vol. 28, no. 6, pp. 633–640, 2007.

[14] S.-W. Yeh, J.-J. Lo, J.-J. Huang, and Z.-Y. Fan, "The development of a virtual cycling simulator," *Technol. E-Learning Digit. Entertain.*, vol. 4469, no. October 2015, pp. 829–840, 2007.

[15] O. Schulzyk, J. Bongartz, T. Bildhauer, U. Hartmann, R. Herpers, and B. Goebel, "A bicycle simulator based on a motion platform in a virtual reality environment," 2007.

[16] R. G. Ranky, M. L. Sivak, J. A. Lewis, V. K. Gade, J. E. Deutsch, and C. Mavroidis, "Modular mechatronic system for stationary bicycles interfaced with virtual environment for rehabilitation.," *J. Neuroeng. Rehabil.*, vol. 11, no. 1, p. 93, 2014.

[17] C. Sun and Z. Qing, "Design and construction of a virtual bicycle simulator for evaluating bicycle traffic control and facilities design.," pp. 1–17, 2016.

[18] S. Yin and Y. Yin, "Study on virtual force sensing and force display device for the interactive bicycle simulator," *Sensors Actuators, A Phys.*, vol. 140, no. 1, pp. 65–74, 2007.

[19] H. J. Yap *et al.*, "Design and Development of a 6-Dof System for Virtual Bicycle Simulator," vol. 5, no. 2, pp. 31–39, 2016.

[20] J. C. Shin and C. W. Lee, "Rider's net moment estimation using control force of motion system for bicycle simulator," *J. Robot. Syst.*, vol. 21, no. 11, pp. 597–607, 2004.

[21] J. Y. Kim, C. G. Song, and N. G. Kim, "A new VR bike system for balance rehabilitation training," *Proc. - 7th Int. Conf. Virtual Syst. Multimedia, VSMM 2001*, pp. 790–799, 2001.

[22] S. O'Hern, J. Oxley, and M. Stevenson, "Validation of a bicycle simulator for road safety research," *Accid. Anal. Prev.*, vol. 100, pp. 53–58, 2017.

Microstructural Study of Hydroxyapatite Nanofibers by High Temperature In Situ X-Ray Diffraction.

S. Alonso-Sierra*, L. A. Baltazar-Montoya, L. A. Rivera-Escobedo, R. Velázquez-Castillo
División de Investigación y Posgrado, Facultad de Ingeniería, Universidad Autónoma de Querétaro, Cerro de las Campanas S/N, Querétaro, Qro., México, C.P. 76010.
*alonso.susana@yahoo.com.mx

C.L. Peza-Ledesma, B.M. Millán-Malo, E.M. Rivera-Muñoz*
Centro de Física Aplicada y Tecnología Avanzada de la UNAM, Juriquilla, Apdo. Postal 1-1010, Querétaro, México.
*emrivera@fata.unam.mx

***Abstract*— Hydroxyapatite nanofibers with preferential crystalline grown were synthesized by Microwave-assisted Hydrothermal Method. The nanofibers were heated until sintering temperature and the crystalline structure was studied by high temperature in-situ X-ray diffraction. Hydroxyapatite nanofibers were also analyzed using Fourier Transform Infrared Spectroscopy and Scanning Electron Microscopy to determine chemical and morphological changes after thermal treatment. The results indicate that a new crystalline structure of calcium phosphate was formed around 850°C but preferential crystalline behavior remains despite the thermal treatment.**

Keywords*— *Hydroxyapatite nanofibers; High temperature; X-Ray Diffraction.

I. Introduction

Bone tissue represents about 18% of total weight of the human body; 70% of an inorganic phase and about 22% corresponds to an organic one. Most of the inorganic phase is made up of hydroxyapatite crystals (HAp) and the organic one is manly made of collagen [1].

Synthetic HAp has physicochemical properties similar to natural bone tissue. Microwave-Assisted Hydrothermal Method has been reported for the synthesis of HAp nanostructures. The main characteristic of this process is the possibility to control the morphology and dimensions of the obtained nanostructures by adjusting the experimental parameters, such as microwave powder, pressure, temperature, reaction time and precursor composition [2]. It has been reported that it is possible to modify the morphology of the hydroxyapatite structures by using glutamic acid [3-4].

To improve biocompatibility and mechanical properties of HAp during its period of use, the ceramic powders must be molded into some specific form. Modified Gel-Casting Process (MGCP) has been reported to obtain HAp scaffolds with diverse morphologies and micro-macro interconnected porosity [5]. In this process HAp powders are added to a polymer mixture with sacrificial porous agents, when the polymerization occurs, the frameworks are treated in thermal process to eliminate polymers and sintering ceramic particles. The sintering of HAp particles occurs at 1100°C after 2 h, as it has previously reported [6].

In this work, the physiochemical modifications of HAp nanofibers, during thermal treatment in MGCP, was studied. The ceramic powders were heated at 600°C, 800°C, 900°C, 1000°C and 1100°C, in situ into a High temperature attachment in an X-ray diffractometer to determine crystalline structure variations and/or the presence of new phases.

II. Materials and Methods

To obtain Hydroxyapatite nanofibers, Microwave -assisted Hydrothermal Method was used. In this process two different solutions are prepared; one dissolving glutamic acid [$C_5H_9NO_4 \cdot H_2O$] and calcium nitrate [$Ca(NO_3)_2 \cdot 4H_2O$] and another mixing monobasic potassium phosphate [KH_2PO_4] and potassium hydroxide [KOH]. Both solutions were dissolved in distilled water at 60°C with magnetic stirring for two hours then the solutions were mixed. The reaction conditions for the HAp synthesis were similar to those previously reported [7]. The white crystalline solid obtained was filtered and washed with ethanol and dried during 24 hours.

A. *X-Ray Diffration*

X-ray diffraction was used to determine the crystalline phases that were present in the samples by heating them from

room temperature up to 1100°C. X-ray diffractograms were obtained at room temperature, 600°C, 800°C, 900°C, 1000°C and 1100°C, with a High Temperature chamber attached to a Rigaku Ultima IV diffraction instrument operated at 40 kV, 30 mA, with Cu Kα radiation wavelength of λ= 1.5406 Å.

B. *Infrared Spectroscopy*

The chemical composition of the material was studied by FTIR spectroscopy. Infrared analysis was done, before and after thermal process, in a Perkin Elmer Spectrum Two using KBr pellet technique.

C. *Scanning Electron Microscopy*

Before and after thermal process, the samples were fixed on a copper specimen holder with carbon tape and covered with a gold thin film in a Sputter Coater EMS 550 in order to make them conductive. They were observed in a JEOL JSM 6060LV Scanning Electron Microscope, using 20kV electron acceleration voltage.

III. RESULTS

A. *X-Ray Diffration*

X-ray diffractograms of the treated samples are shown in Fig. 1. Hydroxyapatite crystalline phase was identified according JPDS-ICDD PDF file #09-0432 and principal Bragg reflections are indicated. At room temperature, the samples do not exhibit other crystalline constituent, which confirm the purity of the HAp nanostructures synthesized by this method. Moreover, the peaks are sharp and well defined, which indicates that HAp is highly crystalline. All the samples have a crystalline orientation in the [001] direction, which differ to the HAp PDF on the data base. In this file the most intense Bragg reflection corresponds to (211) planes. The (300) planes appear as the most intense signal in all temperatures, which indicates a crystalline orientation of the nanofibers in the [001] direction according to previous reports [8].

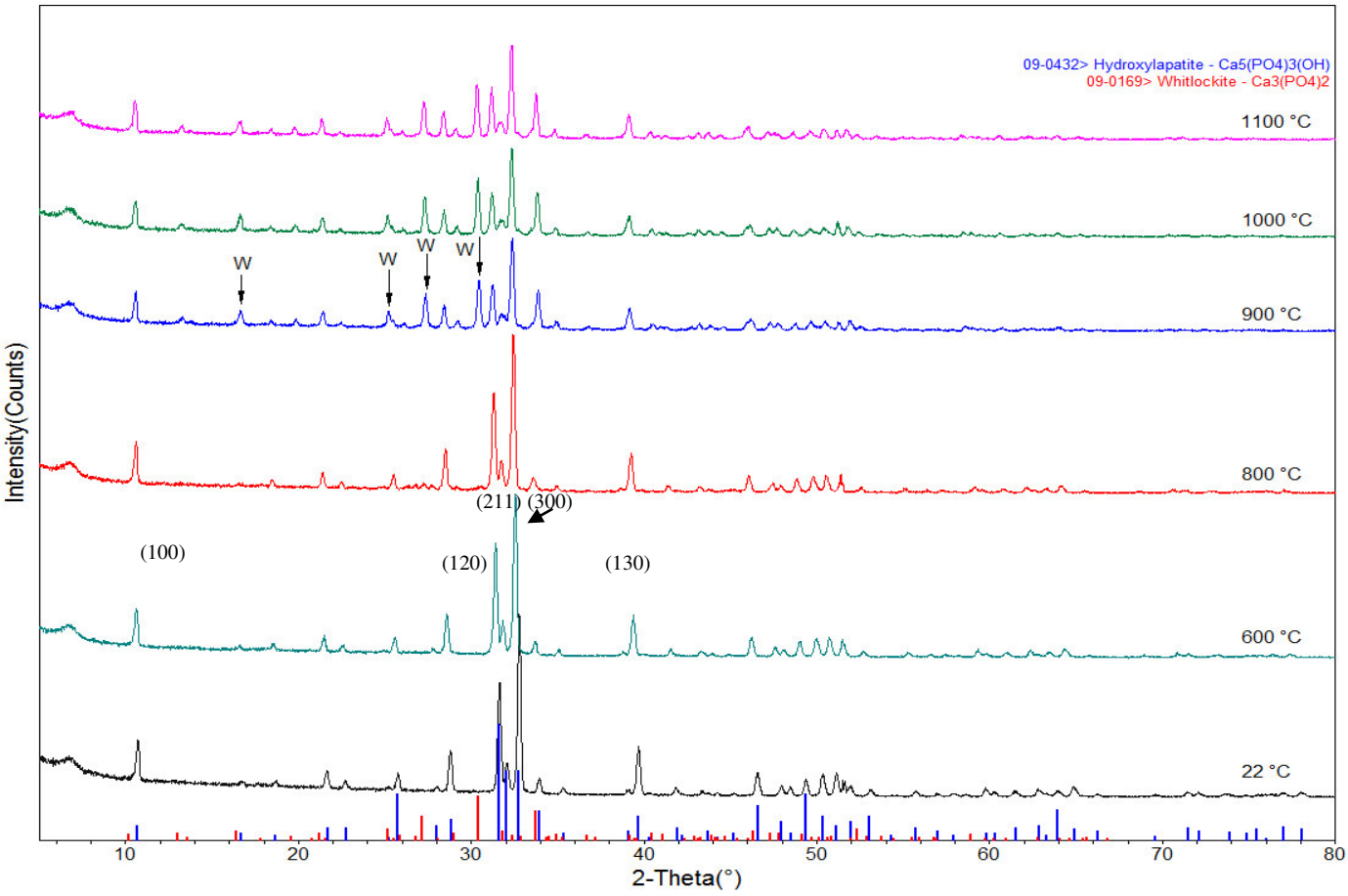

Fig. 1. High temperature in situ XRD of a sample of HAp.

Nevertheless, at 900°C, a new phase was identified according JPDS-ICDD PDF file #09-0169 that appears along with HAp. This new crystalline phase corresponds to a calcium phospahate known as Whitlockite [$Ca_3(PO_4)_2$]. This phase remains until sintering temperature but the HAp crystalline orientation remains during all the process.

Thus, MGCP do not change the crystalline structure of Hydroxyapatite nanofibers obtained by Hydrothermal-assisted Microwave method and the crystalline preferential orientation continues during all the process.

B. Infrared Spectroscopy

The FTIR analyses of synthesized nanostructures is shown in Fig. 2. The distinctive vibration bands of Hydroxyapatite are clearly visible for all samples. Two FTIR bands, located at 635 and 3568 cm^{-1} correspond to the vibration of hydroxyl ion (OH^-). The ones located around 1030 and 565 cm^{-1} are the characteristic bands of bending vibration of the phosphate group (PO_4^{-3}). Those bands at 886, 1410 and 1465 cm^{-1} are indicative of the carbonate ion substitution (CO_3^{2-}) [9].

There is no change observed in the FTIR bands after thermal treatment, which suggests that no chemical modifications occur during sintering process of HAp nanostructures in MGCP.

C. Scanning Electron Microscopy

The morphology of synthesized HAp fibers is shown in Fig. 3. SEM images revel that micro fibers were obtained and, at the same time, these micro fibers are formed by others smallest fibers, which are within the nanometric scale. The surface of the micro fibers seems to be smooth with face and edges well defined. These characteristics are indicative of highly crystalline growth, and agree with XRD results. After sintering process, the sample also was observed by SEM (Fig. 4).

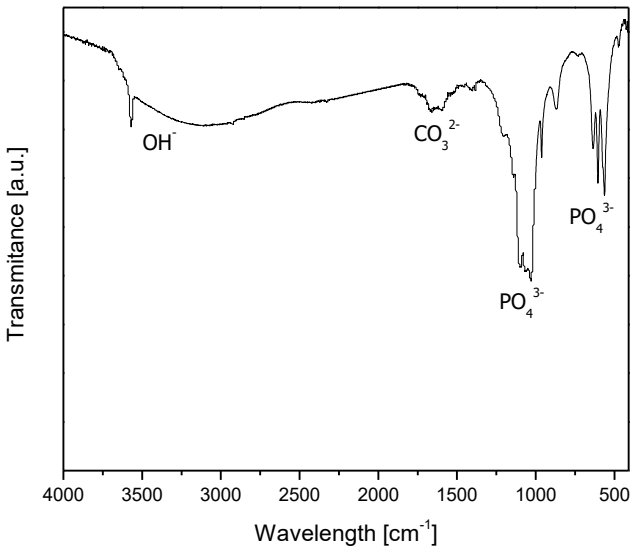

Fig. 2. Infrared spectrum of HAp synthesized.

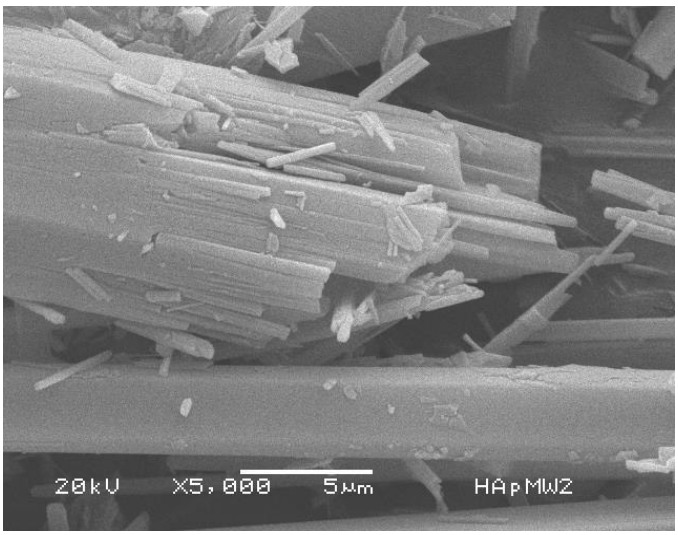

Fig. 3 SEM image of HAp fibers synthesized.

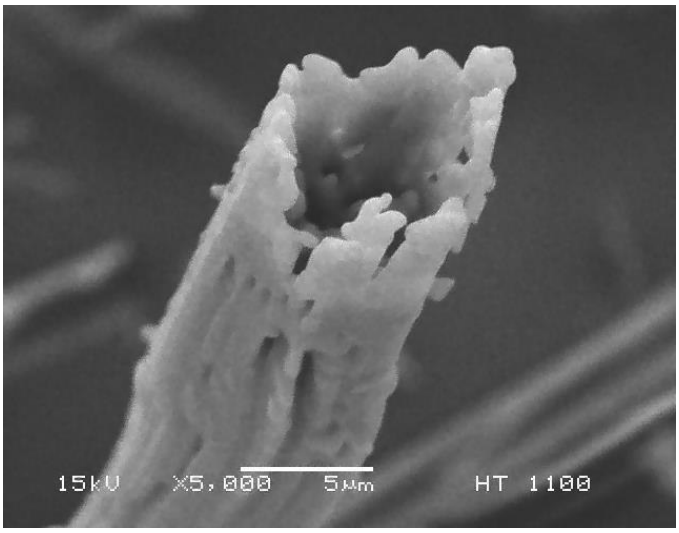

Fig. 4 SEM image of HAp fibers after sintering process.

The sintering of nanofibers can be observed but they still have the fiber form, which also agree with XRD results. Then, the last stage of MGCP may modify the form of fibers and probably affect the mechanical properties of scaffolds.

IV. Conclusion

The HAp nanofibers were grown in a preferential crystalline direction along the c axis of the HAp hexagonal crystalline structure. This structure and the crystalline orientation remain during all the thermal treatment. At 900°C a new crystal phase appears which could affect properties of biocompatibility. Spectroscopy analysis confirm that HAp was obtained. The ceramic is formed by fibers and nano-fibers well defined and this morphology is changed after sintering temperature.

REFERENCES

[1] J. Campa Molina, G. S. Ulloa Godínez, L. Bucio Galindo, I. A. Belío, R. Velazquez and E. M. Rivera Muñoz, Biomateriales. Fundamentos, técnicas y aplicaciones., Jálisco, México: Universidad de Guadalajara, 2007.

[2] J.L. Cabrera, R. Velázquez-Castillo, E. M. Rivera-Muñoz, «Synthesis of hydroxyapatite nanostructures using microwave heating» *Journal of Nanoscience and Nanotechnology* 11 (2011): 1-7.

[3] E. M. Rivera-Muñoz **,** R. Velázquez-Castillo, R. Huirache-Acuña, J.L. Cabrera-Torres and J. Arenas-Alatorre, "Synthesis and characterization of hydroxyapatite-based nanostructures: nanoparticles, nanoplates, nanofibers and nanoribbons", "*Materials Science Forum*" *Vols. 706-709 (2012) pp 589-594*

[4] E. M. Rivera-Muñoz **,** R. Velázquez and J.L. Cabrera-Torres, "Morphological analysis of hydroxyapatite particles obtained by different methods"; "*MATERIALS SCIENCE FORUM*" *Vols. 638-642,* 681-686 (2010)

[5] Alonso-Sierra, S. (2013). *Control de la macroporosidad de un material compuesto orgánico-inorgánico a base de hidroxiapatita: síntesis y caracterización. Tesis de Maestría*. Querétaro, Qro., México.

[6] E. M. Rivera-Muñoz, R. Velázquez and P. Muñoz-Álvarez, «Mechanical characterization of hydroxyapatite-based organic-inorganic composites,» *Materials Science Foroum,* Vols. %1 de %2539-543, pp. 583-588, 2007.

[7] J. R. Alanís-Gómez, E.M. Rivera-Muños, J.S. Cervantes-Medina, H. Almanza-Reyes, R. Nava-Mendoza, C. Cortes-Romero and R. Velázquez-Castillo. "Synthesis of Micro and Nano sized Hydroxyapatite fibers through the microwave assited hydrothermal method" J. NanoSci and NanoTech, Vol 16, 7557-7566, 2016.

[8] N. Méndez-Lozano, R. Velázquez-Castillo, E. M. Rivera-Muñoz, L. Bucio-Galindo, G. Mondragón-Galicia, A. Manzano-Ramirez, M. A. Ocampo, L. M. Apátiga-Castro. "Crystal Groth and structural analysis of hydroxyapatite nanofibers synthesized by the hydrothermal microwave-assisted method. Ceramics International. Vol 43, 451-457, 2017.

[9] G. Tripathi y B. Basu, «A porous hydroxyapatite scaffold for bone tissue engineering: Physico-mechanical and biological evaluations,» *Ceramics international,* vol. 38, pp. 341-349, 2012.

Fluorescence quantifier system of GFP microbial Biosensors

Raúl ROMERO GALINDO[1], Ramón Gerardo GUEVARA GONZÁLEZ[1], Isaac Vega Muñoz[1], Anna Paola PUTZU TORREZ[1], Luis Miguel CONTRERAS MEDINA [1]
Universidad Autónoma de Querétaro
[1]C.A Ingeniería de Biosistemas. División de Investigación y Posgrado, Facultad de Ingeniería
Querétaro, Querétaro
ral305@hotmail.com

Abstract: Fluorescence biosensors are an attractive target for the development of a new generation of analyte detection systems of interest since fluorescence-based methodologies are more sensitive and easier to apply than current technologies. In this work we present a quantifier fluorescence system based on an instrumentation photodiode that suggests its use for fluorescence measurement applications in *Escherichia coli* (*E. coli*) bacterial biosensors that emit fluorescence in response to an analyte of interest. This system consists of a violet light-emitting diode (LED), excitation and emission filters, convergent optical lens and an OPT301 photodiode capable of detecting photons and converting them into electrons, where the fluorescence life time can be measured in real time.

Keywords: Green Fluorescence Protein, Biosensor, Photodiode, Escherichia coli Bacteria.

I. INTRODUCTION

The use of advances in genetic engineering, allows a detection element to be fused with a reporter gene to produce a cellular biosensor [1]. When a gene for a protein is used as a transcription reporter, a cellular promoter leads to expression of the reporter gene resulting in a measurable signal that locally reflects the expression of the promoter in vivo. Typically a bioluminescent or fluorescent protein such as luciferase or GFP [1]. Commonly *E. coli* bacteria are modified to perform these genetic expressions where the luminescent intensity of the fluorescent protein is directly proportional to the concentration of the analyte of interest. The responses to this type of biosensors are being used with great sensitivity and versatility [2], with fluorescence intensity being proportional to the concentration of an analyte of interest [1]; However, they should undergo a longer preparation [2] since there are no electronic devices that make it possible to use this method of measuring in a versatile, easily accessible way for measurements in countryside. In this work we present a fluorescence quantification system based on a photodiode that suggests its use for fluorescence measurement applications in bacterial biosensors that emit fluorescence in response to an analyte of interest.

II. GREEN FLUORESCENCE PROTEIN

The *Aequorea victoria* medusa formed by a protein that has the property of emitting green light, has become a useful tool for cellular biology [3]. GFP, a protein that is made up of 238 amino acids [4], is the most studied and used, there are many other variants that have been developed from the modifications made in GFP [5]. GFP expression not only serves as a reporter indicator for some particular stress but also as an indicator of membrane integrity [6]. The promoter of interest controls the expression of GFP [7].

Many fluorescent proteins contain chromophores other than the amino acid sequence of the protein, the chromophore of the GFP is internally generated by a three amino acid reaction [8], given by spontaneous cyclization and oxidation of residues 65-66-67, corresponding to the amino acids Ser 65 - Tyr 66 - Gly 67 of the native protein, and is responsible for the emission of green lightv [3]. This chromophore has two peaks of excitation and emission, if it is exited at 395 it presents an emission peak of 508, if it is excited at 475 it has an emission peak of 503 [9].

For the formation of the chromophore of the GFP, it is necessary that there is a correct folding of the protein, if this folding is not achieved or there is a poor folding, the chromophores are not formed and therefore there is no fluorescence emission [8]. When the GFP is used as a transcription reporter, it attributes to a regulatory sequence of another gene (promoter), a promoter of interest is fused to a GFP coding region that drives the expression of the fluorescent protein, resulting in a fluorescent signal [5] that temporally and locally reflects the expression of a promoter in vivo [8].

III. BASIC PRINCIPLES FOR FLUORESCENCE MEASUREMENT

When certain molecules called fluorophores, fluorochromes, or fluorescent dyes absorb light, they increase their energy level to a finite-time excitation state [10] where the emission of photons from fluorescence is as rapid a process as absorption ($10^{-10} - 10^{-7} s$) [11]. If a fluorescent sample is irradiated with adequate energy, the molecules absorb that energy, this energy allows the displacement of a valence electron from the ground state GS0 (being an electronic singlet where the electrons have

And the net spin is 0 at a higher energy level) to an excited state [12]. After the emission of the photon, the molecule returns to its fundamental state [13]. The emission of photons accompanying the passage of the vibrational level is a spontaneous process called fluorescence [11].
Several studies have allowed the development of new fluorimeters of smaller size, and lower cost through the use of blue LEDs that excite the sample [14]. If instant measurements are taken and the current optical and processing tools are used, it is possible to take instant measurements at low cost.

IV. MATERIALS AND METHODS

A fluorescence quantification system (Fig. 1) is implemented to excite the green fluorescent protein and detect the fluorescence emission spectrum. It has an insulation chamber with the purpose of avoiding measurement errors generated by external light, inside the camera there is a violet light-emitting diode as a source of excitation, a sample container, an optical lens to concentrate the Photons emitted by fluorescence, an optical filter to let only fluorescence pass, and a photodiode that collects the fluorescent photons to be intercepted by a unit of voltage.

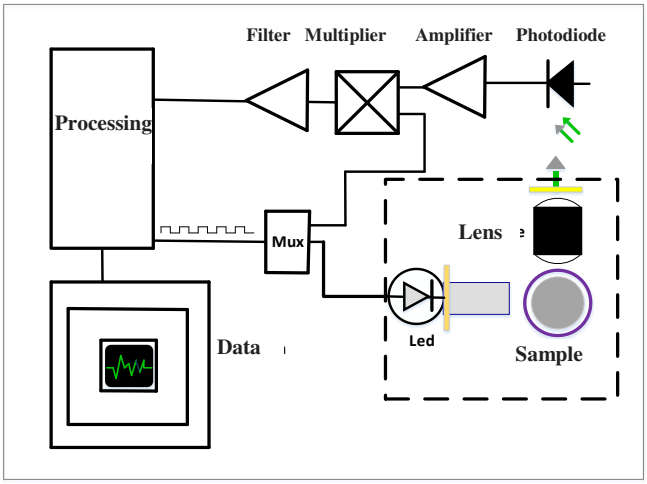

FIGURE 1 BLOCK DIAGRAM OF THE FLUORESCENCE QUANTIFIER SYSTEM.

A. *Optical and excitation system*

A 5 mm transparent LED was used, which emits ultra-bright violet light with a composition of Gallium Nitride fed with a voltage of 3.9 VDC, emitting a luminous intensity of 250 to 300 milli candle, with a current consumption of 20 mA, with length Of 420 nm wave and with 35 ° of illumination angle with respect to the horizontal, is used as an excitation source that affects the sample containing bacteria e.coli with GFP, later a convergent-positive optical lens (Fig. 2) Is placed at a distance of 3 mm from the sample to collect the fluorescent photons, this lens allows the parallel rays that are incident on it to be directed towards the same point by concentrating the photons coming from the sample into a focal plane. Placed an excitation filter of 508 nm which allows only the passage of the light that is in a range of 508 nm + -35[15].

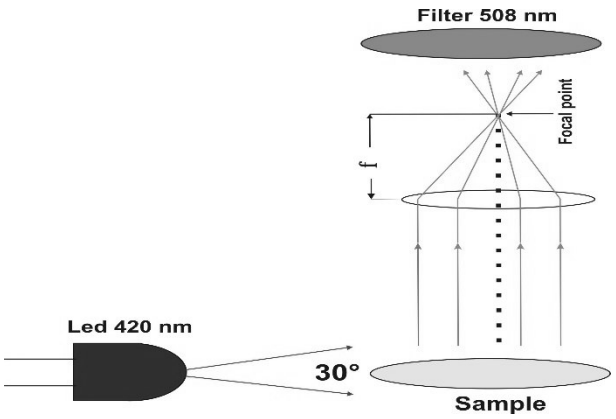

FIGURE 2 OPTICAL AND EXCITATION SYSTEM WITH CONVERGENT OPTICAL LENS.

B. *Detection system*

For the detection system an OPT301 photodiode was used, characterized by having an integrated back-impedance amplifier. The integrated amplifier consists of a FET precision input and an integrated resistor. This photodiode has excellent linearity and low current of darkness. The combination of this photodiode and the transducer amplifier in an integrated chip, eliminates the problems commonly encountered in discrete designs such as current errors, noise peaks and high current of darkness (Fig. 3-a) has a spectral responsiveness that Goes from 400 to 700 nm with a maximum output voltage of 0.5v / µw making use of the internal resistance of 1 MΩ (Fig. 3-b).

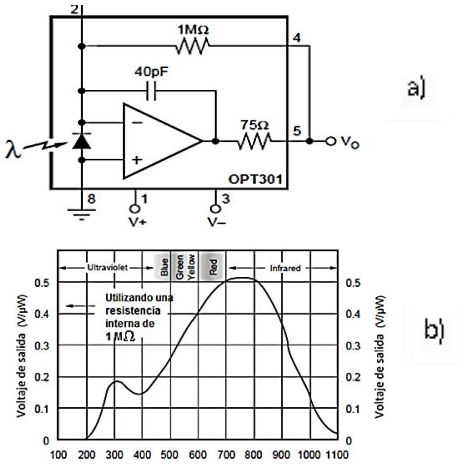

FIGURE 3 AMPLIFIER CONFIGURATION AND SPECTRAL RESPONSIBILITY OF PHOTODIODE OPT 301.

The photodiode converts the amount of photons received by fluorescence to a corresponding number of electrons. Electrons are shifted to a conducting band generating a photo-current, this photo-current was converted to a voltage by the Trans impedance amplifier internal configuration. The electronic

circuit for the amplification of the detector is shown in Fig. 4. An operational amplifier TL081 was used to be able to amplify the signal, also, a potentiometer was placed with the intention of regulating the offset and reducing the differential of voltage that is found Between the two inputs of the amplifier resulted in an inverted signal with a gain of 100 x, then an Operational Amplifier TL082- dual Bifet was used to invert the output signal with gain 1 in order to have a positive signal, as the Incidence of fluorescent photons, increases the output signal of the photodiode linearly.

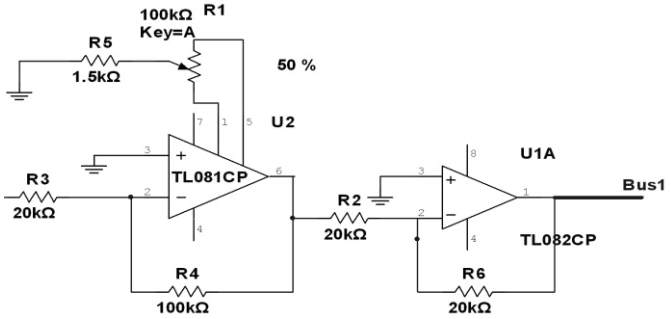

FIGURE 4 CONFIGURATION OF OPERATIONAL AMPLIFIERS, TL081 AMPLIFIES AND INVERTS WITH A GAIN OF 100X, WHILE THE TL082 ONLY INVERTS THE SIGNAL.

C. Bacterial growth with antibiotic zeonin

Cells transformed with pTracer SV40 were cultured in LB medium with Zeonine, antibiotic, according to the protocol we lowered the salt concentration from 10g to 5g, and adjusted the pH to 7.5 with NaOH1N, since the zeonine is sensitive to pH 7.0. Then, it was autoclaved, subsequently using the extraction hood without light on, Zeonin was added at a final concentration of 25 µg / mL. Zeonin was stored at -20 ° C and photosensitive, so it was protected with aluminum. Taking the medium with the antibiotic, 20-30 mL Petri dishes were poured and allowed to solidify, the transformed clones were seeded, capped The aluminum boxes were labeled and incubated at 32 ° C. The broth LB was prepared according to the manufacturer's instructions (20 g / L), the pH adjusted to 7.5 with, autoclaved, then emptied 5 mL of medium in a 15 mL conical tube and antibiotic-zeonine was added at a final concentration of 25 µg / mL. The clone was taken to grow, and this was dropped into the medium, incubated at 32 ° C. Diluted solutions or dilutions of a concentrated sample were used to determine the detections points.

D. Compilation of fluorescence data

For the generation of fluorescence data, a relation of 3 paired data was collected between the predictor variable (measured fluorescence) and the other as response variable. Three decimal dilutions of the culture sample 1: 5, 1:50, and 1: 500 were made to establish the detection points of the fluorescence system, the measurements were performed in triplicate. We considered the average of the measured data and are plotted in fig. 5.

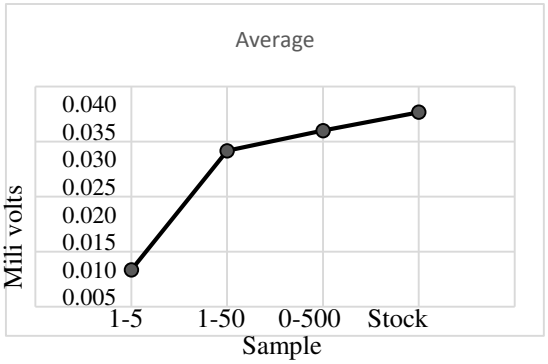

FIGURE **5** AVERAGE OF THREE DILUTIONS AND SAMPLE STOCK 1-5, 1-50, AND 1-500 OF E.COLI BACTERIA WITH PSV TRACER 40 PLASMID.

V. CONCLUSIONS

This system allows quantifying fluorescence from an array of optical elements in systems of biological interest. A wide range of applications is expected, from quantification of nucleic acids, reactive oxygen species, detection of bacteria and quantification of any analyte of interest. Finally, this work is aimed at the invention of a tool that allows its use at different scales at the laboratory level and in situ of living systems. It is important to perform a viable bacterial count to perform a linear regression analysis, determine detection limits and system resolution.

VI. REFERENCES

[1] Taylor, J. C. y otros, 2004. Construction of a whole-cell gene reporter for the Xuorescent bioassay of nitrate. *Elsevier,* pp. 60-66.

[2] Amy, C. V., & Tina K., V. D. (2004). Stress responsive bacteria: Biosensors as environmental Monitors. *Elsevier. Advances in microbial physiology, 49*, 133-163.

[3] Alicia, Franco, & Marinés, L. (2009). Aplicaciones de la proteína verde fluorescente (GFP) en la biología celular y en la visualización del sistema nervioso. *Redalyc, 1*(2), 84-96.

[4] Ormö M, Cubitt AB, Kallio K, Gross LA, Tsien RY, Remington SJ. (1996). Crystal structure of of the Aequorea victoria Green fluorescent protein,4, 1392-1395.

[5] Jin-Min, T., Ming-Chung, C., Lynn, L. H., Ching-Dong, C., Hao-Jen, H., & Ruey-Hua, L. (2014). The blue fluorescent protein from Vibrio vulnificus CKM-1 is a useful reporter for plant research. *Springer Botanical studies*, 55-79.

[6] Polizzi, M. K., & Kontoravdi, C. (2015). Genetically-encoded biosensors for monitoring cellular stress in bioprocessing. *ScienceDirect, 31*, 50-56.

[7] Bren, A., Hart, Y., Dekel, E., Koster, D., & Alon, U. (2013). The last generation of bacterial growth in limiting nutrient. *BMC- systems biology, 7*(27), 1-9.

[8] Donna, E. C., Yao-Ming, H., & Derek, J. P. (2013). GFP-Based Biosensors. *Intech*.

[9] Tsien, R. Y. (1998). The Green Fluorescent Protein. *Annual Reviews Biochemistry, 67*, 509-544.

[10] Amersham, p. b., 2000. *Fluorescence Imagin - principles and methods.* [En línea]

[11] Valeur, B., 2001. Molecular Fluorescence: Principles and Applications". Wiley-VCH. Weinheim

[12] Ishikawa-Ankerhold, H. C., Ankerhold, R. y Drummen, G. P. C., 2012. Advanced Fluorescence Microscopy Techniques—FRAP, FLIP, FLAP, FRET and FLIM. *molecules,* 17(4), pp. 4047-4132.

[13] Becker, W., 2012. Fluorescence lifetime imaging – techniques and applications. *Journal of Microscopy,* Volumen 30, pp. 119-136.
[14] Pavoni, J. F., Neves-Junior, W. F., Spiropulos, M. A., & Araúujo, D. (2014). Uma montagem experimental para a medida de fluorescencia. *Revista Brasileira de Ensino de Fisica, 36*(4), 4501
[15]
Instruments, T. (01 de 03 de 2017). *Texas Instruments.* Obtenido de www.ti.com

Natural frequencies estimation of a 4-story building using SAP2000.

Sergio Martínez-de-Jesús[1], Carlos A. Perez-Ramirez[2], Martin Valtierra-Rodriguez[2], Miguel A. Perez-Lara-y-Hernandez[1], and Juan P. Amezquita-Sanchez[2,*]

[1] Faculty of Engineering, Autonomous University of Querétaro, Querétaro, Querétaro, México.

[2] Faculty of Engineering, Autonomous University of Querétaro, Campus San Juan del Rio, San Juan del Rio, Querétaro, México.

*jamezquita@uaq.mx

***Abstract*— The estimation of the natural frequencies and damping ratios of civil structures have a great importance for structural design, since the proper use of these dynamic parameters allows the structural engineer providing a safe and comfortable structure to the final user, as it is reduced the vibration effects of the structure when subjected to excitations due to live or accidental loads. In particular, the estimation of the natural frequencies, allows knowing the structure dynamic behavior, as they are used for the seismic design. The modal parameters can be obtained using software for structural analysis. This paper presents a study case of how to develop the model of a 4-story 2x2 bay 3D steel frame structure in SAP2000 to obtain its natural frequencies.**

Keywords*— *natural frequencies; civil structure; 4-story; SAP2000.

I. INTRODUCTION

Civil structures play a fundamental role in daily life of the society, since they provide living and working places; further, they allow us to move from one place to another. Modal parameters identification from acquired dynamic signals is the process to determine dynamic characteristics of a structure, which can be used to build or update a proper model of the structure [1-6].

A very important topic for the monitoring of the structural integrity is the estimation of the modal parameters such as natural frequencies, which can be obtained using programs such as ANSYS, ABACUS or another analysis program. In this regard, SAP 2000 is a commonly used program in order to obtain the finite element model (FEM) from different structures that can be a simple small 2D static frame analysis to a large complex 3D one, which usually involves the utilization of a nonlinear dynamic analysis. Since the latter case is representative of real-life structures, it will be used to obtain the natural frequencies. It should be noticed that although papers make use of the FEM to estimate the analytical natural frequencies of the in-test structure, they do not explain the employed process that they use to obtain the aforementioned values. In this regard, this paper presents a study case that describes the required steps to build a FEM-based model to estimate the natural frequencies using SAP2000.

II. FEM USING SAP2000

This section describes the required steps to build the FEM-based model.

A. Steps required to create the FEM-based model of the structure.

Firstly, open the SAP2000 program and go to menu *File/New file* and *choose 3D frame*. This step is depicted in Fig. 1.

Once this step is performed, assign the number of stories and the bays in X and Y directions, as depicted in Fig. 2.

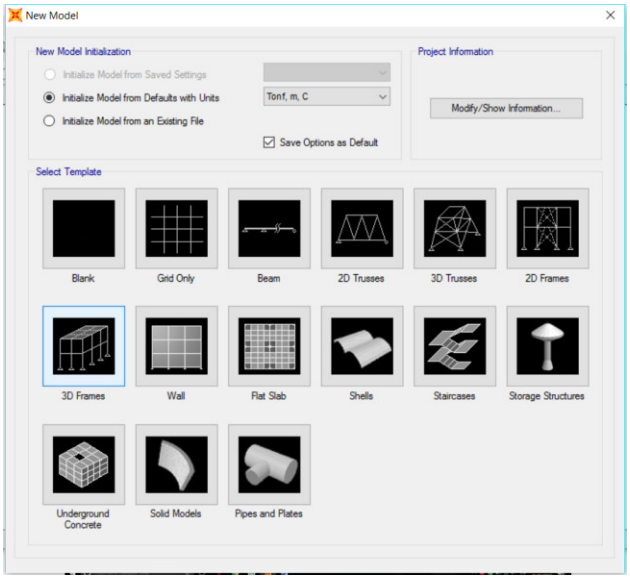

Fig. 1. Choose the template for new model (3D frames).

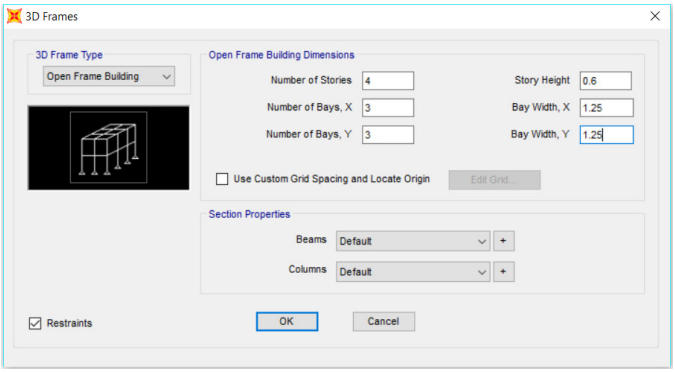

Fig. 2. Assigning Stories and bays.

B. *Definition of materials and sections*

Once the abovementioned steps are executed, the basic model is obtained. It should be noticed that the model has frame elements. Next, it is necessary to define the materials and sections used in the real-life structure. Fig. 3 shows the graphical description of the aforementioned definition.

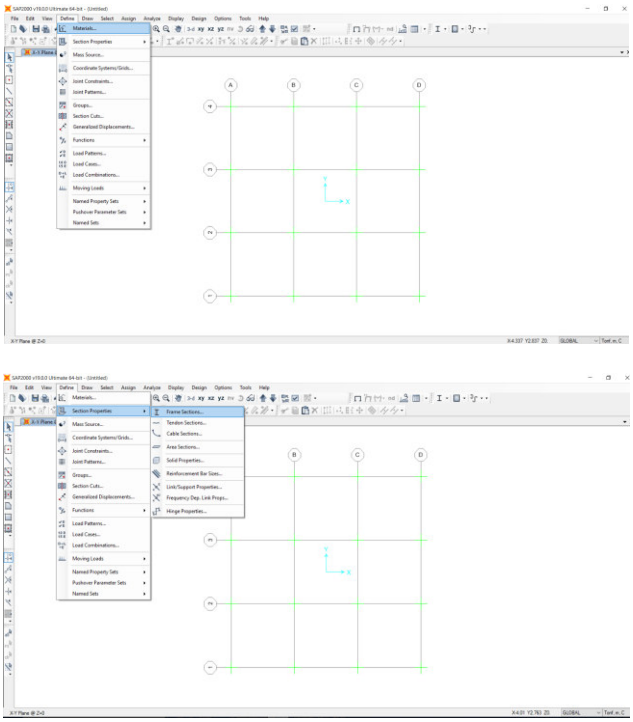

Fig. 3. Define materials and sections.

C. *Loads assignment*

Once the sections have been assigned, the loads must be assigned to the model. SAP2000 allows assigning the loads to a joint, frame, cable or area element. In this case, the load will be assigned to area as depicted in Figs. 4 and 5.

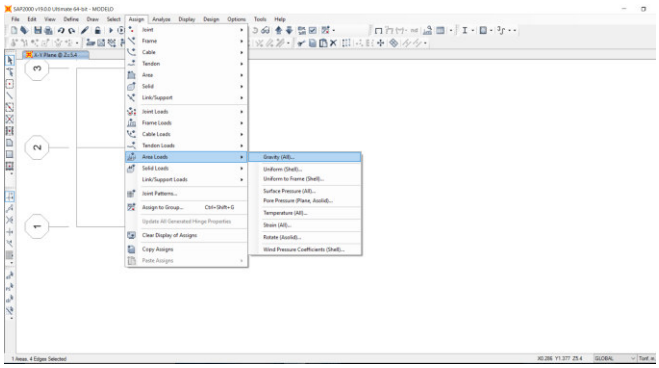

Fig. 4. Assigning loads.

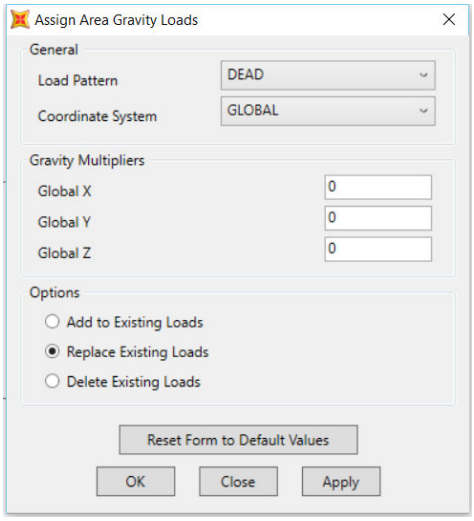

Fig. 5. Assigning area gravity loads.

D. *Modes estimation*

The last step to obtain the natural frequencies is to execute the Modal case instruction. Fig. 6 shows the graphical representation of this step.

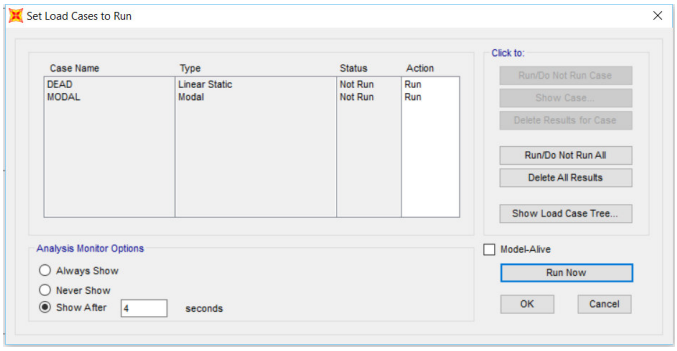

Fig. 6. Running analysis window.

III. BUILDING MODEL IN SAP2000

The tutorial described in section 2 will be applied to generate the building model of 4-story. Table 1 shows the used elements for defining the sstructure.

TABLE I. MODEL ELEMNTS

Property section	Elements of structure		
	Column	*Beams*	*Diagonals*
Area(m2)	$1.4x10^{-3}$	1.43x10-3	2.68x10-4
Iy(m4)	$1.97x10^{-6}$	1.22x10-6	0
Iz(m4)	$0.664x10^{-6}$	0.249x10-6	0
J(m4)	$8.01x10^{-9}$	38.2x10-9	0
E(Pa)	$2x10^{11}$	2x1011	2x1011
G(Pa)	E/2.6	E/2.6	E/2.6
Pieces	18	48	16

After applying the described steps, the obtained model is shown in Fig. 7.

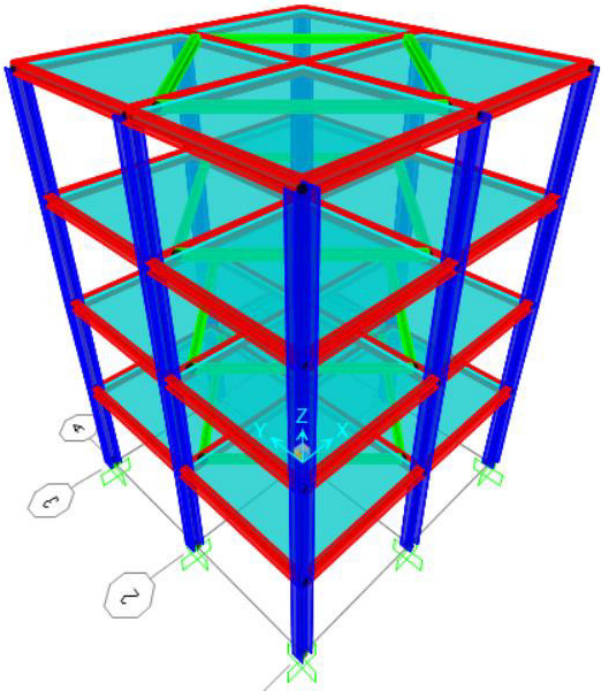

Fig. 7. Model of structure builded in SAP2000.

IV. RESULTS

After ruining the analysis step, the following results are obtained, which are depicted in Figs. 8 to 10.

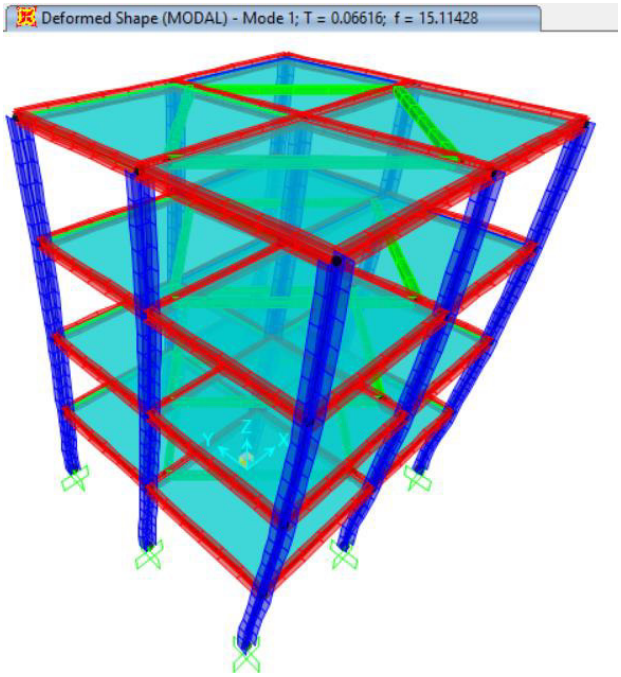

Fig. 8. Mode 1 of the structure built in SAP2000.

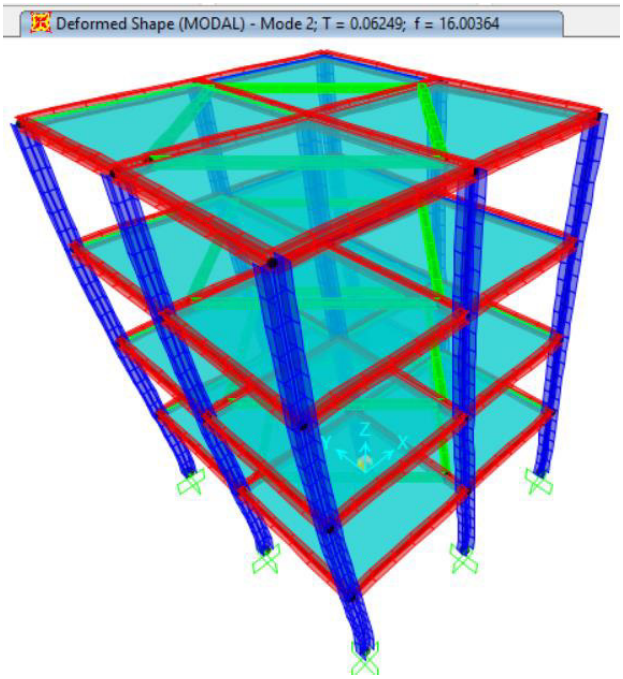

Fig. 9. Mode 2 of the structure built in SAP2000.

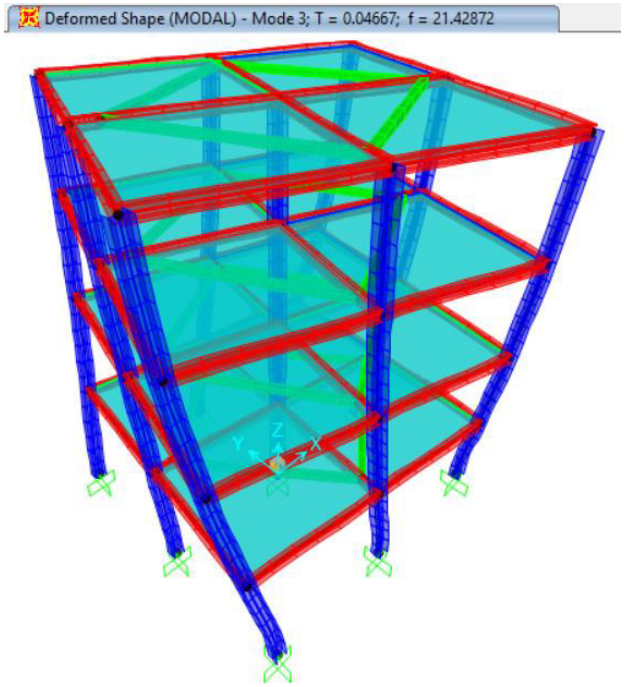

Fig. 10. Mode 3 of structure built in SAP2000.

Table 2 shows the first five modes obtained using the SAP2000.

TABLE II. MODAL PERIODS AND FREQUENCIES

Mode	*Period (s)*	*Frequency (Hz)*
1	0.0661	15.11428
2	0.0624	16.00363
3	0.0466	21.42871
4	0.0226	44.20060
5	0.0208	48.05786

V. CONCLUSIONS AND FUTURE WORK

In this work, a tutorial for modeling in SAP2000 is presented for building, analyzing, and identifying the natural frequencies of a 4-story steel structure is presented.

The SAP2000 program is very useful for performing the modal analysis and thus obtaining the natural frequencies in a fast way. As a future work, the comparison between the obtained experimental natural frequencies and the analytical ones is necessary, in order to find out the possible mistakes that are generated when it is considered an idealized model, which does not include different aspects that influence the estimation of the natural frequencies. In this regard, it will be possible to calibrate the FEM-based model in order to have an accurate and reliable model that can represent the dynamic behavior of the in-test structure.

ACKNOWLEDGMENT

I would like to thank my advisor, Dr. Juan Pablo Amézquita-Sánchez, for the support provided for the preparation of this paper. Further, this work was supported in part by the Mexican Council of Science and Technology (CONACyT) by the scholarships 595885 and 289377 and by the SEP-CONACyT CB-2015/254697 project.

REFERENCES

[1] García-Palencia,A.J.,Santini-Bell,E.,2013.Atwo-step model updating algorithm for parameter identification of linear elastic damped structures. Comput.-Aided Civil Infrastruct.Eng.28(7),509–521.

[2] Lozano-Galant, J.A., Nogal, M., Castillo, E., Turmo, J., 2013. Application of observa-bility techniques to structural-system identification. Comput.-Aided Civil Infrastruct. Eng. 28 (6), 343–450.

[3] Yuen, K.V., Mu, H.Q., 2015. Real-time system identification: analgorithm for simultaneous model class selection and parametric identification. Comput.- Aided Civil Infrastruct. Eng. 30 (10), 785–801.

[4] Zhang, J., Guo, S.L., Zhang, Q.Q., 2015. Mobile impact testing for structural flexibility identification with only a single reference. Comput.-Aided Civil Infrastruct. Eng. 30 (9), 703–714.

[5] Oh, B.K., Kim, M.S., Park, H.S., 2015. Model updating technique based on modal participation factor for beam structures. Comput.-Aided Civil Infrastruct. Eng. 30 (9), 733–747.

[6] Boscato, G., Ceravolo, R., Russo, S., Fragonara, L.Z., 2015. Global sensitivity-based model updating for heritage structures. Comput.-Aided Civil Infrastruct. Eng.30 (8), 620–635.

CONACYT
Consejo Nacional de Ciencia y Tecnología

CONCYTEQ

UNIVERSIDAD AUTÓNOMA DE QUERÉTARO
13° CONGRESO INTERNACIONAL DE INGENIERÍA
15th-19th MAY 2017

Signal Processing Techniques used in Structural Health Monitoring: a Brief Review

Diego O. W. Pacheco-Ortega, Miguel A. Perez-Lara-y-Hernandez, Aurelio Dominguez-Gonzalez
División de Investigación y Posgrado de la Facultad de Ingeniería (DIPFI)
Universidad Autónoma de Querétaro
Santiago de Querétaro, México

Juan P. Amezquita-Sanchez, Carlos A. Perez Ramirez, Martin Valtierra-Rodriguez
Facultad de Ingeniería, Universidad Autónoma de Querétaro, Campus San Juan del Rio,
Querétaro, México

***Abstract*—Civil structures frequently suffer damage during their service lives. These damages are mainly due to numerous causes such as excessive movement, high temperatures, accumulation of cracks growth, corrosion, degradation of columns, joints and beams, and the impact of external objects. The accumulation of these damages can cause a weakening of the structure and if these damages are not detected, they can produce a collapse of it. Structural Health Monitoring (SHM) is a concept used to evaluate the condition of civil structures, with the purpose of generating a monitoring system capable of detecting damages in an early stage to avoid economical and human losses. One of steps more important in SHM scheme is the signal processing technique, which must be capable of determining features used for assessing the condition of the civil structure. Therefore, the purpose of this article is to give a brief review of the different signal processing techniques used in SHM.**

Keywords—*Vibration; signal processing techniques; civil structures*

I. Introduction

Throughout the history of the humanity different constructions have been built for the service of society and benefit the people who inhabit them. With the passage of time, and especially in modern times, there is a tendency to develop and build increasingly large, high and complex civil structures, which are used as housing, offices, hospitals, etc. Therefore, to assure the good state of these constructions is necessary, since some failure in any structural element that conforms them, would cause great losses both monetary and even human.

In any construction, the detection and location damages are of vital importance in order to determine the correct state of the structure. For this reason, both analytical and experimental methods must be developed. They allow creating monitoring systems capable of evaluating the state of a civil structure, that are simple of applying and low cost, besides that they must be effective to detect damages early and for making the corresponding maintenance if it is necessary.

In the last decade, vibration-based methods have been proposed in a SHM scheme, because a damage can significantly modify the dynamic properties such as mass, stiffness and damping, which, at the same time, modify the dynamic response of the system. Generally, these methods compare the dynamic properties or the structural response of the damaged model with the properties or the response of the model without damage, to obtain the necessary information or the parameters that allow detecting, locating and quantifying the severity of damages [1]. Therefore, it is required a signal processing technique capable of estimating characteristics embedded in the vibrations that allow to assess the state of the civil structure. [2].

In this paper, a brief review of the different techniques that have been applied in a SHM scheme as well as their advantages and disadvantages of the systems developed are presented.

II. Structural Health Monitoring (SHM)

A SHM scheme is based on three steps: data acquisition, data processing (signal processing), and interpretation (diagnosis) to assess the state of a structure, as shown in Fig. 1 [3].

SHM is referred in the literature as a tool used for the detection of structural damage or deficiencies. The detection of such damages is usually defined by Phares et al. [4] in four levels:

- I. Determination of what damage is present in the structure.
- II. Determination of the location of the damage.

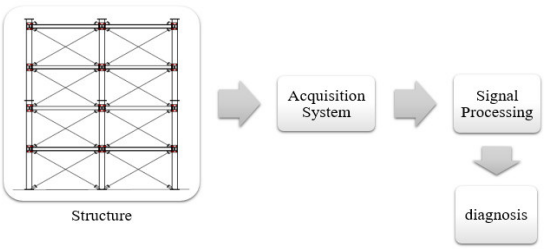

Fig. 1. Schematic of Structural Health Monitoring.

- III. Quantification of the severity of the damage.
- IV. Estimate of the remaining lifetime of the structure.

Usually, the fourth level is not included in the damage detection because the estimate of the remaining lifetime includes deeper studies related to the fault that is present [5-11].

III. Signal Processing Techniques

In recent years, new advances in SHM have led to the use of numerous signal processing techniques based on vibration analysis with the aim of detecting, locating and quantifying the severity of damage in structures [3]. The following signal processing techniques are some of the most commonly used in SHM.

A. *Fast Fourier Transform*

Fast Fourier transform (FFT) is one of the most used and oldest techniques for signal processing in SHM due to the fact that it can be applied easily and it is considered an effective method for examining stationary signals [2]. The FFT is widely applied for obtaining natural frequencies, damping factors and in some cases for the detection of faults in civil structures [12]. For example, Brincker et al. [13], Yuen and Katafygiotis [14] used the FFT to identify the modal structural parameters of a two-story 3D frame, a ten-story 2D frame, and the Mong Man Wai seven-story building located in Hong Kong subject to dynamic environmental excitations, respectively. Lee and Kim [15] used the FFT on a scaled bridge model constructed of three steel beams subjected to impact testing to calculate damage. Amezquita-Sanchez et al. [16] applied the FFT to identify modal structural parameters of a 3D truss-type structure exposed to earthquakes and forced excitation.

Although FFT can be easily implemented for generating a SHM scheme, Tang et al. [17] mention that the FFT has too many disadvantages to extract the dynamics of a structure or its application in the analysis of real structures, since the studied signals are non-linear and non-stationary, therefore, these characteristics of signal cannot be evaluated by the FFT properly. In addition, the FFT cannot represent the spectral variations (the natural frequencies contained in the signal) through time, which is essential in SHM.

B. *Short Time Fourier Transform*

The spectral analysis using FFT is adequate to analyze vibrations in steady state. This indicates that transient vibration effects are averaged in the analysis period, missing information of the nature or form of these variations. Therefore, it is necessary an analysis capable of describing transient signals, such as those monitored in civil structures. This is achieved with the Short Time Fourier Transform (STFT) [3]. This alternative was introduced by Gabor in 1946 and it provides a representation of signal in time and frequency.

STFT, which is an extension of FFT, is capable of analyzing non-stationary signals. The STFT can denote the variation of the essence of the signal frequency as the signal variations through time distributing the signal into minor time windows where each window is examined using the FFT. The STFT has been applied to calculate the modal parameters of various structures, including a seven-story frame [18], a three-story 3D steel frame [19], 3D truss-type structure [16] and beams [20].

A disadvantage of this technique is that it needs a large window to realize a good resolution, where the transient signals are not clearly distinguished, or small windows with low resolution in frequency, which does not allow detecting the transient dynamic behavior of the system properly. It also does not allow to observe two natural closed frequencies [21].

C. *Wavelet Transform*

Wavelet Transform (WT) is a processing method that provides a time-frequency description of the signal through the time and scale window functions. The advantages of WT are computational efficiency, data comprehension and noise elimination [2]. Due to these advantages, WT and its improved forms, Wavelet Packet Transform (WPT) and Continuous Wavelet Transform (CWT), have been extensively utilized as signal processing techniques in recent years. WPT is a method that discomposes a signal into consecutive components of low and high frequencies repeatedly. Consequently, the coefficients of the approximations and details are discomposed to generate a tree of frequency bands. Therefore, WPT can provide uniform frequency bands [22]. CWT is considered one of the best techniques for the analysis of non-stationary signals, since this tool can decompose to the signal in multiple frequencies, known as multi-resolution. Among its main advantages, CWT is local in time, real, orthogonal, orthonormal and compact.

In last years, WT and its improved forms, WPT and CWT, have been used to detect faults in civil structures. For example, Jian et al. [23] proposed the detection of cracks by means of WPT in a scaled building, which was excited with a mallet. Han et al. [24] applied the WPT to detect damage in a single steel beam. Hou et al. [25] use the CWT to detect damage in a spring-mass-damper system exposed to earthquakes and random excitation. Pakrashi et al. [26] and Umesha et al. [27] detected cracks in beams applying the CWT. Yan et al. [28] applied the WT to detect and locate sudden changes of rigidity in a 20-story 2D frame and a five-story 3D structure. Taha [29] used the WT to detect damages caused by lack of elements. The WT, besides being used for the detection of faults, has been used for the detection of natural frequencies in civil structures [30].

WT has received a lot of attention because it is simple, fast, and not expensive to implement. However, its algorithm presents several disadvantages such as it cannot provide the precision and reliability needed for big scale structures due to their complex behavior, the variety of material characteristics and susceptibility to noise in measurements of structural response, in addition, it has a necessity for a large sample dataset and much processing is required [31, 32].

D. Multiple Signal Classification

The multiple-signal classification algorithm (MUSIC) offerings great advantages in comparison to the aforementioned methods, since it generates a high resolution spectral estimation, even for data that is embedded in a lot of noise. Therefore, it is a very efficient tool for the monitoring of structures in real time. Jiang and Adeli [33] applied for first time the algorithm MUSIC for the monitoring of civil structures, presenting a new method of evaluation of damages based on this algorithm. This method was corroborated applying the experimental data acquired for a scaled model of a 38-story building. The results indicated that the proposed method is effective for the SHM in real time in high-rise buildings. Osornio-Ríos et al. [34] confirmed the aforementioned MUSIC system for monitoring the health of 3D truss-type structure subjected to forced excitation. The results show that the method is efficient to differentiate between a healthy structure and another with corrosion or a crack.

The MUSIC system provides the frequency representation of a signal, but the time data is gone. To keep frequency and time data, García-Pérez et al. [35] suggest a Short Time MUSIC (ST-MUSIC) where the system MUSIC is applied in a sequence during short periods of sampling. For each period, a different spectrum is acquired and the total of such spectrums indicate the time-frequency distribution. ST-MUSIC is alike to the SFFT analysis, but with a higher resolution in the time and frequency domains. As a result, ST-MUSIC is able to analyze stationary, non-linear or transient signals through time [2]. Using these advantages, Amezquita-Sanchez et al. [21] used the ST-MUSIC to detect the natural frequencies of 70-member and five cubes cantilever truss-type structure exposed to forced excitation. Therefore, the ST-MUSIC algorithm presents good results to identifying natural frequencies even when the signal is noisy, mainly for the natural closed frequencies.

Despite the good results, the algorithm MUSIC and ST-MUSIC require an a priori knowledge of the amount of frequencies in the signal to be analyzed with the purpose to select an appropriate order, also to consuming a large amount of computational resources [36, 37, 2].

E. Hilbert-Huang Transform

Huang et al. [38] presented the Hilbert-Huang Transform (HHT) as an adaptive signal processing technique capable of evaluating stationary, non-stationary and transient signals. HHT is based on two phases: an empirical mode decomposition (EMD) and the Hilbert Transform (HT). EMD discomposes time series data into a set of quasi-stationary band-limited functions, named intrinsic mode functions (IMF). Then, the HT is applied to each IMF to acquired its amplitude and phase angle.

HHT has been widely utilized to estimate the natural frequencies and damping factor of various structures, including a steel beam subjected to impact tests and a posttensioning bridge situated between Bern and Zurich, Switzerland, exposed to dynamic environmental excitation [39], a three-degree of freedom system and a scaled model of steel-concrete composite beam subjected to impact tests [40], the Nanjing Yangtze River steel bridge situated in Nanjing, Jiangsu , China, exposed to dynamic environmental vibrations [41], a five-story one-bay 3D steel frame exposed to two earthquakes [17] and Shanghai World Financial Center, placed in Shanghai, China, exposed to dynamic environmental and forced excitations [42].

The most important disadvantage of the HHT technique is the named mode mixing effect found in the EMD technique, which means that waves with the equal frequency are allocated to different IMFs in the procedure of finding the IMFs [43].

F. SHM of multiple faults

In real constructions, two or more places or kinds of damage may be existing at the same time. It has been known that one type of damage condition may affect with the detection of another type of damage, resulting in a wrong valuation of the structural condition. The identification of combined damage in structures continues to represent a challenge for SHM, because reliable identification of a combined condition is a difficult task [36].

In the literature, about the detection and location of multiple faults in structures, the following work is mentioned: Garcia-Perez et al. [36] presented a fusion of methodologies, in which WPT and EMD are combined with artificial neural networks (ANN) for the automatic and online detection and location of one or multiple combined damage in a five-cube truss-type structure. The results showed that the proposed method is very effective and reliable to detected and located the three types of damage used (joint failure, reduction of stiffness and corrosion), as well as their combinations.

Despite the good results obtained in the work mentioned above, research about SHM to identify and locate multiple faults is still very poor, so it is important to continue investigating with other processing techniques that identify multiple faults, as well as their combinations, especially in structures that present a more real behavior.

G. Fractal Dimension

A promising technique for the identification and location of multiple faults is the fractal dimension (FD), which is a concept pertaining to chaos theory [44], and it has been utilized for the analysis of stationary signals. However, in recent years its efficiency has been demonstrated for the evaluation of transient and nonlinear signals. The FD provides a measure of self-similarity and irregularities captured in a time series, which denotes to the number of times a pattern repeats itself in the signal [44], this makes the FD be a appropriate method to detect single and several combined failures in structures since a difference in the time series might be produced by variations in the physical characteristics of the structure, such as the existence of any type of damage.

The works about detection and location of multiple faults using FD has been focused mainly in machines and motors; achieving results with an accuracy of 87%. However, in recent years Amezquita-Sanchez et al. [46] presented a methodology,

combining the Katz algorithm (FD) with an ANN, for a monitoring system applied to induction motors. The results obtained show a higher overall efficiency (95%) than previous work.

In the monitoring of civil structures, FD has found its main application in simple structures such as beams [47, 48]. However, in recent years, Amézquita and Adeli [49] used the FD, with which they developed a method for the identification, location and quantification of damages in smart high-rise building structures, proving that this tool can be used to perform monitoring of damage in large-scale structures.

IV. Conclusions

In recent years, SHM, has presented great advances due to the use of new technologies, as well as in the acquisition system (sensors), in the advancement of new signal processing techniques, and in a better interpretation of the results thanks to new powerful computers. This article presented an overview of the main signal processing methods utilized in SHM.

Although different papers have been published concerning the estimation of modal parameters in civil structures, however, Pérez et al. [50], after a thorough review of the principal processing techniques used for the estimation of these parameters (WT, FFT, MUSIC and others), concluded that there is currently no technique capable of accurately estimating modal parameters. For this reason, it is necessary to continue investigating with new signal processing techniques since it would be necessary to have a method with the capability of monitoring the condition of the civil structures with more precision, that is immune to the noise, without the necessity for a complex processing, and primarily, to develop a method capable of detecting one or several faults combined in an automatic procedure.

Acknowledgment

This project was supported in part by the Mexican Council of Science and Technology (CONACyT) by the scholarships 606089 and 289377 and by the SEP-CONACyT CB-2015/254697 project.

References

[1] Hernández, G. M. R. 2004. Detección de daño a partir de cambios en las características vibracionales usando redes neuronales.

[2] Amezquita-Sanchez, J. P., and H. Adeli. 2016. Signal Processing Techniques for Vibration-Based Health Monitoring of Smart Structures. Arch. Comput. Methods Eng. 23:1–15.

[3] Amezquita Sánchez, J. P. 2012. Monitoreo de vibraciones en tiempo real para la detección de daños en estructuras (Tesis Doctoral). Universidad Autónoma de Querétaro.

[4] Phares, B. M., Wipf, T. J., Greimann, L., & Lee, Y.-S. 2005. Health Monitoring of Bridge Structures and Components Using Smart Structure Tecnology, V1 y V2. Iowa, USA: Center of Transportation Research and Education, Iowa State University.

[5] Tuzzeo, D., y F. L. di Scalea. 2002. Non-contact air-coupled ultrasonic guided waves for detection of hidden corrosion in aluminum plates. Journal of Research in Nondestructive Evaluation, 13(2):61-78.

[6] Banks, H. T., M. L. Joyner, B. Wincheski, y W. P. Winfree. 2002. Real time computational algorithms for eddy-current based damage detection. Inverse Problems, 18(3):795-823.

[7] Vossoughi, F., C. P. Ostertag, P. J. M. Monteiro, y R. D. Albert. 2007. Damage characterization of concrete panels due to impact loading by motionless Xray laminography. Journal of Materials Science, 42(9):3280-3285.

[8] Li, H., Y. Huang, W. L. Chen, M. L. Ma, D. W. Tao, y J. P. Ou. 2011. Estimation and Warning of Fatigue Damage of FRP Stay Cables Based on Acoustic Emission Techniques and Fractal Theory. Computer-Aided Civil and Infrastructure Engineering, 26:500–512.

[9] Curadelli, R. O., J. D. Riera, D. Ambrosini, y M. G. Amani. 2008. Damage detection by means of structural damping identification. Engineering Structures 30:3497-3504.

[10] Hejll, A. 2007. Civil Structural Health Monitoring-Strategies, Methods and Applications, Doctoral Thesis. Sweden: Lulea University of Technology.

[11] Talebinejad, I., C. Fischer, y F. Ansari. 2011. Numerical Evaluation of Vibration-Based Methods for Damage Assessment of Cable-Stayed Bridges. Computer-Aided Civil and Infrastructure Engineering, 26(3):239–251.

[12] Proakis, J. G., y D. K. Manolakis. 2006. Digital Signal Processing, Principles and Applications, Fourth Edition, Prentice-Hall, New Jersey, USA.

[13] Brincker R., Zhang L., Andersen P. 2001. Modal identification of output-only systems using frequency domain decomposition. SmartMater Struct 10:1–10.

[14] Yuen, K., Katafygiotis, L. 2005. Model updating using noisy response measurements without knowledge of the input spectrum. Earthq Eng Struct Dyn. 34(2):167–187.

[15] Lee J., and Kim S. 2007. Structural damage detection in the fre- quency domain using neural networks. J Intell Mater Syst Struct 18(8):785–792.

[16] Amezquita-Sanchez, J.P., Osornio-Rios, R.A., Romero-Troncoso, R.J. et. al. 2012. Hardware–software system for simulating and analyzing earthquakes applied to civil structures. Nat Hazards Earth Syst Sci 12:61–73.

[17] Tang, J. P., D. J. Chio, C. W. Chen, W. L. Chiang, W. K. Hsu, C. Y. Chen, y T. Y Liu. 2011. A case study of damage detection in benchmark buildings using a Hilbert–Huang transform-based method. Journal of Vibration and Control, 17(4): 623-636.

[18] Yinfeng, D., Yingmin, L., Mingkui, X., Ming, L. 2008. Analysis of earthquake ground motions using an improved Hilbert–Huang transform. Soil Dyn Earthq Eng. 28(1):7–19.

[19] Nagata, Y., Iwasaki, S., Hariyama, T., Fujioka, T., Obara, T., Wakatake, T. 2009. Binaural localization based on weighted wiener gain improved by incremental source attenuation. IEEE. Trans Audio Speech Lang Process. 17(1):52–65.

[20] Yesilyurt, I., and Gursoy, H. 2013. Estimation of elastic and modal parameters in composites using vibration analysis. J Vibr Control. doi:10.1177/1077546313486275.

[21] Amezquita-Sanchez, J.P., Garcia-Perez, A., Romero-Troncoso, R. J., Osornio-Rios, R. A., Herrera-Ruiz, G. 2013. High-resolution spectral–analysis for identifying the natural modes of a truss-type structure by means of vibrations. J Vib Control. 19:2347–2356.

[22] Reda, M. M., A. Noureldin, J. L. Lucero, y T. J. Baca. 2006. Wavelet transform for structural health monitoring: A compendium of uses and features. Structural Health Monitoring, 5:267-295.

[23] Jian, G., C. Yong, y S. Bing-nan. 2005. Experimental study of structural damage identification based on WPT and coupling NN. Journal of Zhejiang University SCIENCE, 6A (7):663-669.

[24] Han, J. G., Ren, W. X., Sun, Z. S. 2005. Wavelet packet based damage identification of beam structures. Int. J. Solids Struct 42(26):6610–6627.

[25] Hou, Z., Hera, A., Shinde, A. 2006. Wavelet-based structural health monitoring of earthquake excited structures. Comput Aid Civ Infrastruct Eng. 21(4):268–279.

[26] Pakrashi, V., O'Connor, A., Basu, B. 2007. A study on the effects of damage models and wavelet bases for damage identification and calibration in beams. Comput Aid Civ Infrastruct Eng 22(8):555– 569.

[27] Umesha, P. K., R. Ravichandran, y K. Sivasubramanian. 2009. Crack detection and quantification in beams using wavelets. Computer-Aided Civil and Infrastructure Engineering, 24(8):593-607.

[28] Yan, G., Duan, Z., Oua, J., DeStefano, A. 2010. Structural damage detection using residual forces based on wavelet transform. Mechanical System Signal Processing. 24(1):224–239.

[29] Taha, M. M. R. 2010. A neural-wavelet technique for damage identification in the ASCE benchmark structure using phase II experimental data. Advances in Civil Engineering, doi:10.1155/2010/675927.

[30] Xiang, J. y M. Liang. 2012. Wavelet-based detection of beam cracks using modal shape and frequency measurements. Computer-Aided Civil and Infrastructure Engineering, 27: 439-454.

[31] Zang, C., M. I. Friswell, y M. Imregun. 2004. Structural damage detection using independent component analysis. Structural Health Monitoring, 3(1):69-83.

[32] Adewuyi, A. P. y Z. Wu. 2011. Vibration-based damage localization in flexural structures using normalized modal macrostrain techniques from limited measurements. Computer-Aided Civil and Infrastructure Engineering, 26(3):154-172.

[33] Jiang, X. y H. Adeli. 2007. Pseudospectra, MUSIC, and dynamic wavelet neural network for damage detection of highrise buildings. International Journal for Numerical Methods in Engineering, 71(5):606-629.

[34] Osornio-Rios, R.A., Amezquita-Sanchez, J.P., Romero-Troncoso, R.J., Garcia-Perez, A. 2012. MUSIC-ANN analysis for locating structural damages in a truss-type structure by means of vibrations. Comput Aid Civ Infrastruct Eng. 27(9):687–698.

[35] Garcia-Perez A, R. J. Romero-Troncoso, E. Cabal-Yepez, y R. A. Osornio-Rios. 2011. Application of high-resolution spectral analysis for identifying faults in induction motors by means of sound. Journal of Vibration and Control Epub ahead of print 18 October 2011. doi: 10.1177/ 1077546311422925.

[36] Garcia-Perez, A., Amezquita-Sanchez, J. P., Dominguez-Gonzalez, A., Sedaghati, R., Osornio-Rios, R. y Romero-Troncoso, R. J. 2013. Fused empirical mode decomposition and wavelets for locating combined damage in a truss-type structure through vibration analysis. J. Zhejiang Univ. Sci. A 14:615–630.

[37] Camarena-Martinez, D., Valtierra-Rodriguez, M., Garcia-Perez, A., et al. 2014. Empirical mode decomposition and neural networks on FPGA for fault diagnosis in induction motors. The Scientific World Journal Article. ID 908140: 1–17.

[38] Huang, N. E., Shen, Z., Long, S. R., Wu, M. C., Shih, H. H., Zheng, Q., Yen, N. C., Tung, C. C., Liu, H. H. 1998. The empirical mode decomposition and Hilbert spectrum for non-linear and non-stationary time series analysis. Proc R Soc A Math Phys Eng Sci 454:903–995.

[39] Yan, B. y A. Miyamoto. 2006. A comparative study of modal parameter identification based on Wavelet and Hilbert–Huang transforms. Computer-Aided Civil and Infrastructure Engineering, 21(1):9-23.

[40] Bao, C., Hao, H., Li, Z., Zhu, X. 2009. Time-varying system identification using a newly improved HHT algorithm. Comput Struct 87(23–24):1611–1623.

[41] He, X., Hua, X., Chen, Z., Huang, F. 2011. EMD-based random decrement technique for modal parameter identification of an existing railway bridge. Eng Struct 33(4):1348–1356.

[42] Shi, W., Shan J., Lu, X. 2012. Modal identification of Shanghai World Financial Center both from free and ambient vibration response. Eng Struct 36:14–26.

[43] Wu, Z., Huang, N. 2009. Ensemble empirical mode decomposition: a noise-assisted data analysis method. AdvAdapt Data Anal 1(1):1–41.

[44] Hsu, W. Y. 2013. Single-trial motor imagery classification using asymmetry ratio, phase relation, wavelet-based fractal, and their selected combination. International journal of neural systems.

[45] He, Z., You, X., Zhou, L., Cheung, Y., & Du, J. 2010. Writer identification using fractal dimension of wavelet subbands in gabor domain. Integrated Computer-Aided Engineering.

[46] Amezquita-Sanchez, J. P., M. Valtierra-Rodriguez, D. Camarena-Martinez, D. Granados-Lieberman, R. J. Romero-Troncoso, and A. Dominguez-Gonzalez. 2015. Fractal dimension-based approach for detection of multiple combined faults on induction motors. J. Vib. Control.

[47] Cao, M., & Qiao, P. 2009. On the wavelet–fractal nonlinear damage diagnosis of mechanical systems. Smart Materials and Structures.

[48] Shi, J., Xu, X., Wang, J. and Li, G. 2010. Beam damage detection using computer vision technology. Nondestructive Test. Evaluation.

[49] Amezquita-Sanchez, J. P., & Adeli, H. 2015. Synchrosqueezed wavelet transform fractality model for locating, detecting, and quantifying damage in smart highrise building structures. Smart Materials and Structures. 24:65034.

[50] Perez-Ramirez, C. A., Amezquita-Sanchez, J. P., Adeli, H., Valtierra-Rodriguez, M., Romero-Troncoso, R. D. J., Dominguez-Gonzalez, A., & Osornio-Rios, R. A. (2016). 2113. Time-frequency techniques for modal parameters identification of civil structures from acquired dynamic signals. Journal of Vibroengineering, 18(5), pp. 3164-3185

UNIVERSIDAD AUTÓNOMA DE QUERÉTARO
13° CONGRESO INTERNACIONAL DE INGENIERÍA
15th-19th MAY 2017

Theoretical and experimental study to first principles of $Cd_{1-x}Zn_xS$ and its performance in the production of H_2

L.F. Morelos-Medina[1], R. Nava[1], R. Velazquez-Castillo[1], A. Cuan[1].

[1]Facultad de Ingeniería, Universidad Autónoma de Querétaro, Cerro de Las Campanas, s/n 76010, las campanas, Santiago de Querétaro, Qro, Mexico. E-mail: mr.morelos@gmail.com

***Abstract*—A comprehensive study of different morphologies CdS photocatalysts and $Cd_{1-x}Zn_xS$ was performed. Experimentally two different synthesis techniques were tested by co-precipitation and sonochemistry. The stoichiometric ratio is used for Zn x = 0.20 and x = 0.25. Once synthesized compounds the structural analysis was performed by various characterization techniques, such as X-ray diffraction of powders (XRD), ultraviolet-visible spectroscopy (UV-Vis), scanning electron microscopy (SEM), using the equation Scherrer, which uses the results of XRD, the crystal size was calculated, obtaining a smaller crystallite size generally with sonochemical technique (range 2.2 - 2.6 nm). While for coprecipitation technique crystallite size it was higher (2.4 - 2.7 nm). For computer modeling study of the results of XRD characterization we were used, resulting in the cubic phase at higher rates. Three models, the bulk, surface and nano-particle is studied. The models were calculated for both CdS and the composite of $Cd_{1-x}Zn_xS$. To obtain the electronic properties of the "Vienna Ab Initio Simulation Package" programs, known as VASP and Gaussian09 were used. The results show the distribution of bands, the umbrage's energy "band gap", distribution of atomic charges and the reaction coordinate for activating molecule of water for the production of H_2.**

Keywords—photocatalysis, water activation, hydrogen production.

I. Introduction

The development of these catalysts of CdS and replaced with Zn already are being synthesized in the area and in other parts of the world, however, as will be seen in the section of the statement of the problem, it is a difficult issue to address, because it is not clear how it generates the key pair hole-electron and the mechanics followed for the process of recombination of electron-hole pair.

Given the strong economic impact and the area of opportunity of this type of material as an alternative source of fuel, it is necessary to delve deeper into the basic knowledge at the level of electronic structure and investigate the parameters involved in the atomic, molecular, by effect of size and composition, which modifies the electronic properties and performance of these materials by providing various applications and industrial interest.

The conversion of solar energy into hydrogen through the process of separation of water using a catalyst of semiconductors is one of the most interesting ways to achieve clean and renewable energy. The exploration of the semiconductors with high photocatalytic activity under visible light irradiation is one of the most difficult issues at the world [1-6].

In this sense, the study and development of molecular models or surfaces using the computational chemistry tools help to understand these phenomena chemicals that are sometimes difficult to observe in an experiment, deepening and generating basic and fundamental knowledge that will help the experimental part to modify their prototypes and develop materials specific to their applications are required, as is the case of the photocatalysts of $Cd_{1-x}Zn_xS$.

More specifically in the mechanism of the formation of the electron-hole pair and its recombination in the photocatalysts of CdS and $Cd_{1-x}Zn_xS$ finding the relationship with the size and composition of these materials and relate directly to the gap or bandgap energy.

II. Methodology

A. *Experimental (synthesis of the photocatalyst)*

The samples of $Cd_{1-x}Zn_xS$ (where x = 0.25, which is the concentration of Zn). Were prepared on the basis of their precursors by precipitation of CdS and ZnS from aqueous solutions of zinc acetate di hydrated Zn $(CH_3COO)_2 \cdot 2H_2O$ and cadmium acetate di hydrated Cd $(CH_3COO)_2 \cdot 2H_2O$ at room temperature using 3.4 g of sodium sulphide nona hydrated $Na_2S \bullet 9H_2O$ as an agent of precipitation.

B. *Theoretical (modeling of the photocatalyst)*

All calculations for the model surface were made using the special code for this type of study with the name "Vienna Ab Initio Simulation Package", known as VASP [7-14]. For the description of the electronic properties [15] are used functions of the plane wave and with a projector of potential augmented plane wave, used within the formalism of the theory of density functional theory (DFT).

III. Results and Discussion

A. *Spectroscopy UV-vis*

The environment for the coordination of Cd^{2+} and Zn^{2+} ions in samples calcined was studied by UV-vis the diffuse reflectance spectroscopy. The edges of absorption of the photocatalysts $Cd_{0.75}Zn_{0.25}S$ gradually change from 640 nm to 570 nm as it increases the concentration of Zn, as shown in Figure 1.

Which is more noticeable with the change of coloration of the photocatalysts being for the CdS an orange tone and for the $Cd_{0.75}Zn_{0.25}S$ a yellow tone checking the offset of the energy levels.

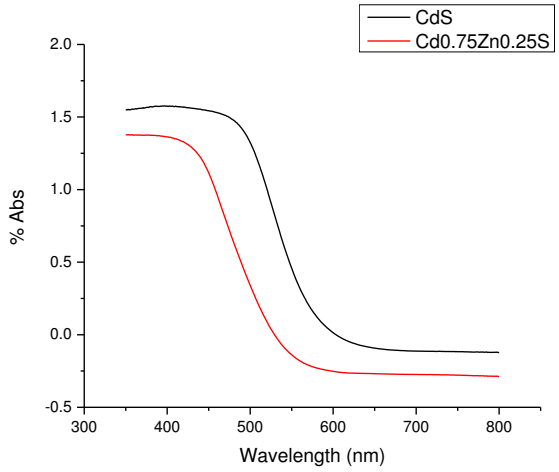

Figure 1. UV-Vis spectrum of the photocatalyst CdS vs $Cd_{0.75}Zn_{0.25}S$.

B. *X-ray diffraction (XRD)*

The data of X-ray diffraction of the photocatalysts of CdS and Cd1-xZnxS, confirmed the conservation of the phase ”hawleyite” after the addition of the metal sulfides by precipitation. All samples of CdS and Cd1-xZnxS showed profiles similar X-ray diffraction, which are discussed on an individual basis.

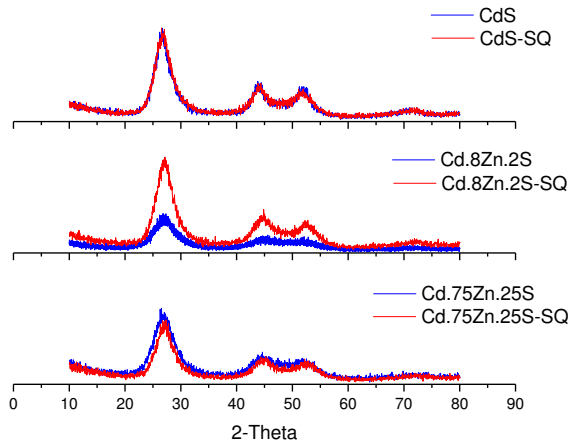

Figure 2. XRD plot of the photocatalysts of CdS and Cd0.75Zn0.25S.

In summary, as shown in Figure 2, you can appreciate a Rietveld plot similar to the case of Cd0.75Zn0.25S by precipitation and sonochemistry is observed greater interference this is due to the obtained nano particles with a size of 2.2 nm.

C. *Scanning electron microscopy (SEM)*

Through the SEM, you can observe the particle sizes and the type of morphology of the same, in the following figures we can see that there is an agglomeration of nanoparticles uniform type cauliflower with an almost spherical morphology, this is due to the processes of synthesis of nanoparticles, the method of precipitation used with the conditions used in this work, we give as a result a particle size that are in the range of 30 to 80nm.

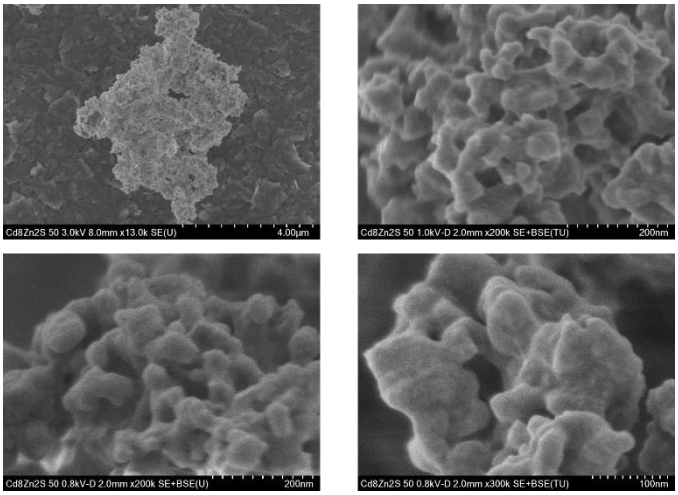

Figure 3. Electron micrographs of the photocatalyst.

D. *Calibration of the system*

In the first instance to model the structure of the CdS in order to perform the calibration of the system. Starting with the modeling of the breast of the material or lump of glass getting the cutoff energy points k and suitable for this system. In Figure 4, the model used for calibration.

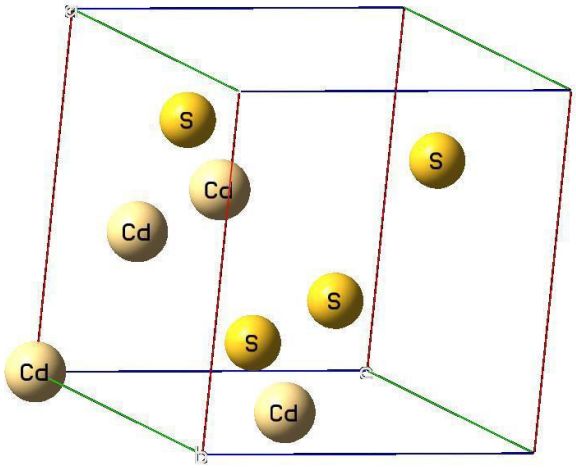

Figure 4. Schematic representation of the CdS.

E. *Determination of the plane*

A super 3x3x3 to represent better within the material and thus to be able to determine the preferential level of growth, corroborating what obtained in x-ray diffraction.

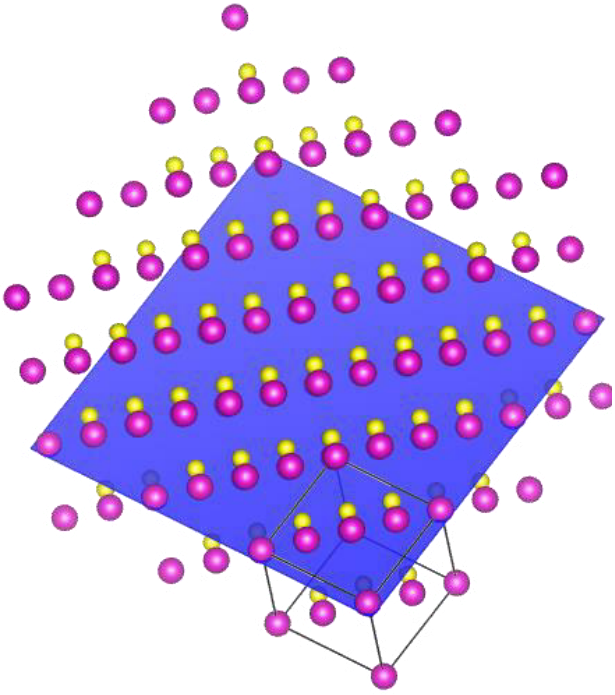

Figure 5. Super Cell 3x3x3 of the CdS, VESTA.

Once grown the super cell is determined by the atomic distribution by obtaining a preferential level (001) confirming the results of diffraction with the most abundant in our material.

F. *Surface*

For the surface took the preferential (001 level), grew 4 layers to represent our area. In this way, you will begin to perform the optimization of the surface.

G. *Density of States (DOS)*

Then with the models constructed above the electronic properties were calculated and analyzed. The total density of states (TDOS).

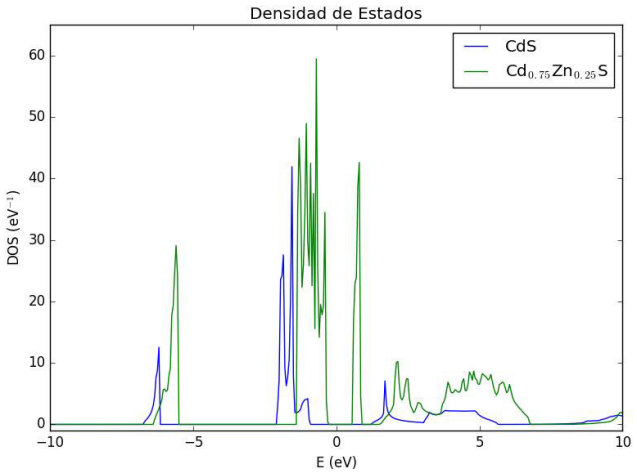

Figure 6. Total density of states of the CdS and Cd0.75Zn0.25S

The TDOS calculated for CdS and Cd0.75Zn0.25S can be observed that are modified by the presence of Zn.

H. *Reaction mechanism*

The study was conducted of the reaction mechanism of the water molecule to determine the activation energy of 1.5 eV is being that our material has a bandgap of 1.9 eV taking enough energy to activate the water molecule to produce hydrogen.

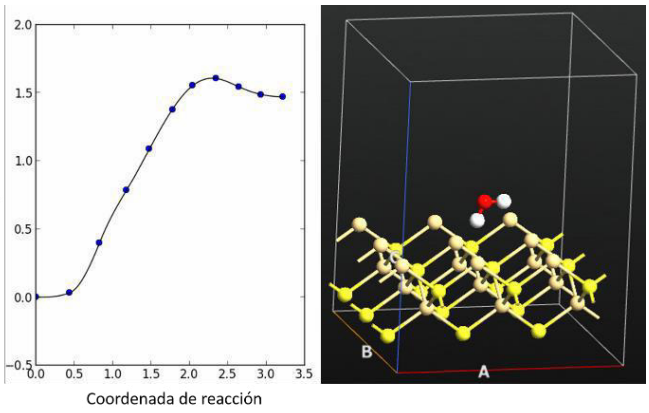

Figure 7. The reaction mechanism of the water molecule.

IV. Conclusion

In the present work, we synthesized nanoparticles of CdS and Cd1-xZnxS by the method of sonochemistry proving to be very efficient in time, energy and costs, which was achieved with the obtaining of nanoparticles under 50 nm.

For the synthesis of nanoparticles of CdS and Cd1-xZnxS by the method of co-precipitation proved to be a very effective method for obtaining nanoparticles of CdS and Cd1-xZnxS, being a very simple and relatively efficient in time, with this synthesis was achieved successfully nanoparticles of CdS and Cd1-xZnxS with particle sizes less than 50 nm.

ACKNOWLEDGMENT

We acknowledge with gratitude the support provided by the Laboratory of Supercomputing and Visualization in parallel, Cluster of UAM-YOLTLA Iztapalapa.

REFERENCES

1. Girginer B, Galli G, Chiellini E. Preparation of stable CdS nanoparticles in aqueous me- dium and their hydrogen generation efficien- cies in photolysis of water. Int J Hydrogen Energy 2009;34:1176e84.
2. Gust D, Moore TA, Moore AL. Solar fuels via artificial photosynthesis. Acc Chem Res 2009;42:1890e8.
3. Hagfeldt A, Graetzel M. Light-induced redox reactions in nanocrystalline systems. Chem Rev 1995;95:49e68.
4. Hirai T,Nanda M, Komasawa I. Dithiol-me- diated incorporation of CdS nanoparticles from reversemicellar systeminto Zndoped SBA-15mesoporous silica and their photoca- talytic properties. J Colloid Interface Sci 2003; 268:394e9.
5. Janet CM, Viswanath RP. Large scale synt- hesis of CdS nanorods and its utilization in photo-catalytic H2 production. Nanotechno- logy 2006;17:5271e7.
6. Jing DW, Guo LJ. A novel method for the pre- paration of a highly stable and active CdS photocatalyst with a special surface nanos- tructure. J Phys Chem B 2006;110:11139e45.
7. Jing DW, Guo LJ. Efficient hydrogen produc- tion by a composite CdS/mesoporous zirco- niumtitaniumphosphate photocatalyst under visible light. J Phys Chem C 2007;111:13437e41.
8. Kudo A, Miseki Y. Heterogeneous photoca- talyst materials for water splitting. Chem Soc Rev 2009;38:253e78.
9. Kumar P. Inclusion chemistry in periodic me- soporous hosts: growth of quantum-confined materials and gas separation membranes. Ph.D. dissertation. University of Cincinnati; 2007.
10. Li M, Jiang J, Guo L. Synthesis, characteri- zation, and photoelectrochemical study of Cd1-xZnxS solid solution thin films deposited by spray pyrolysis for water splitting. Int J Hydrogen Energy 2010;35:7036e42.
11. Linsebigler AL, Lu GQ, Yates JT. Photoca- talysis on TiO2 surfaces: principles, mecha- nisms, and selected results. Chem Rev 1995;95:735e58.
12. Lunawat PS, Kumar R, Gupta MN. Structure sensitivity of nano-structured CdS/SBA-15 containing Au and Pt cocatalysts for the pho- tocatalytic splitting of water. Catal Lett 2008;121:226e33.
13. Matsumura M, Furukawa S, Saho Y, Tsu- bomura H. Cadmium sulfide photocatalyzed hydrogen production from aqueous solutions of sulfite: effect of crystal structure and pre- paration method of the catalyst. J Phys Chem 1985;89:1327e9.
14. Mau AWH, Huang CB, Kakuta N, Bard AJ, Campion A, Fox MA, et al. Hydrogen photo- production by Nafion/cadmium sulfide/plati- num films in water/sulfide ion solutions. J Am Chem Soc 1984;106:6537e42.
15. Meissner D, Memming R, Kastening B. Pho- toelectrochemistry of cadmium sulfide. 1. Reanalysis of photocorrosion and flatband potential. J Phys Chem 1988;92:3476e83.

CONACYT
Consejo Nacional de Ciencia y Tecnología

CONCYTEQ

UNIVERSIDAD AUTÓNOMA DE QUERÉTARO
13° CONGRESO INTERNACIONAL DE INGENIERÍA
15th-19th MAY 2017

Development of a wireless signal acquisition system from sensors for comfort and energy quality

[1]Zamudio-Ramírez I., [2]Jaen-Cuellar A. Y., [3]Osornio-Ríos R. A.
Facultad de Ingenieria, Campus San Juan del Río
Universidad Autónoma de Querétaro
Av. Río Moctezuma 249, C.P. 76808, San Juan del Río, Querétaro, México
[1]izamudio13@alumnos.uaq.mx, [2]ayjaen@hspdigital.org, [3]raosornio@hspdigital.org

***Abstract*— The acquisition of wireless signals from sensors represents a variety of advantages over cable communication systems. This work presents a ZigBee-based signal acquisition system that takes advantage of its features to make a flexible system that can be used in different fields without the necessary use of a PC since a touchscreen and a microcontroller is used. The system stores information of all sensors of all the network created in a Micro SD and uses it to make plots, also it is possible to visualize real-time readings.**

Keywords— Touchscreen, ZigBee, Wireless Sensor Network (WSN).

I. Introduction

In recent years, the introduction of network-enabled devices into the home environment has increased at an unprecedented rate [1]. Home automation has taken the advantage of network-enabled devices. According to [2], home automation requires the introduction of technology within the home to enhance the quality of life of its occupants. In this area, there are three basic characteristics that need to be addressed: comfort, efficiency, and safety [3]. Nowadays, several devices can be found to automate homes and buildings to monitor several physical variables all the time by using wired or wireless networks. Wired networks costs are lower; however, the drawbacks in the installation usually make it the second option [4]. Moreover, wireless technologies such as Wi-Fi, Bluetooth, ZigBee have the potential for the remote control and monitoring of variables used in automation of buildings. It would be very helpful to use low power consumption devices for the automation of buildings.

Several works have been developed to automate buildings such as in [5] where a domotic embedded system for room temperature monitoring is developed with the help of a central PC and a microcontroller. Others like in [6-9] implement automation systems using wireless technologies which add a degree of simplicity when installing due to a decrease in the number of wires, but such works have in common a lower system integration, an important fact when there is a necessity to expand the number of variables to detect and the number of rooms to be automated. Furthermore, to make a more flexible system it is necessary to store, plot and manage big amount of data without utilizing a PC in the field. Besides, these systems are capable of being used in different applications making them very robust, configurable and flexible.

In this paper, a wireless building automation system is described. The proposed system can integrate new nodes to the current network according to personal necessities by updating them with the help of a software wizard developed on purpose for this task. Another feature of the proposed system is that it allows easy addition and removal of sensors with the help of Plug-and-Use sockets, making a more flexible system capable of being used with a wide variety of sensors that can be spread around different places to, in this way, take their samples at the same time and show them in the form of plots or real-time readings. The system has the power to save big amounts of data which makes it suitable for different uses and applications. Additionally, it allows the monitoring of electrical sensors by using ZigBee antennas and a microcontroller Arduino Due with a touchscreen module. The sensors can monitor information of different physical magnitudes such as temperature, luminosity, presence, gas concentration, glass breakage, among others, in order to establish a clear state of the building in real time. The wireless home network is implemented with wireless ZigBee Routers and End Devices modules that communicate centrally with a ZigBee coordinator. The proposed system is validated by implementing it in a building located in the Universidad Autonoma de Queretaro during two months. After this period of tests, it will be implemented in a building named Academic Center of Advanced and Sustainable Technologies (CATAS for its acronym in Spanish) which is under construction at this time. The obtained results demonstrate that this system can resist environmental conditions (into a building), and it works pretty well during long periods of time giving accurate records of every variable measured indicating the functionality and efficiency of the system.

II. THEORETICAL BACKGROUND

According to [10], domotic refers to a home automated or commonly called intelligent house, which is a house whose elements and devices are integrated and automated with the help of a network. Generally, a domotic system will dispose of a communication network that permits the interconnection of some equipment (detectors and sensors) in order to get all the information of a domestic environment and then, with the help of a smart central unit, process the information [11], as shown in Fig. 1.

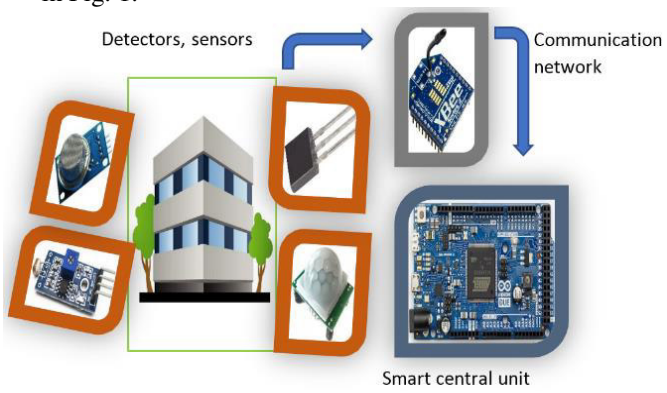

Fig. 1. Home automation and its requirements.

Smart home grids are installed using wired or wireless networks. Although wireless network costs are higher, they are easier to install. There are many wireless technologies found in the market, but the most common are free licensed like ZigBee, Bluetooth, and Wi-Fi. The cost, power consumption, and performance are the main selection criteria for wireless network nodes. The main features of these technologies are shown in Table 1.

Table 1 Main characteristics of free license wireless technologies.

Techno-logy	Data Rate	Max power consumption	Typical range
ZigBee	20 to 250 Kbps	3 mW	10-100 m
Bluetooth	1 to 3 Mbps	100 mW	2-10 m
IEEE 802.11b	1 to 11 Mbps	100 mW	30-100 m

Bluetooth technology has a low range and, from a scalability point of view, there is a strict limitation in the number of home equipment attachable to the Bluetooth master device due to the characteristics of the protocol. Although Wi-Fi has high range and big data rate, the ZigBee technology offers lower power consumption, which is an important aspect of home automation.

The interference problems between the possible standards have been investigated. For example, [12] researched the coexistence of ZigBee, Bluetooth, and Wi-Fi. The three protocols use the same 2.4 GHz ISM band. It can be concluded that ZigBee and Wi-Fi can exist together with fewer interference problems than alternative technologies currently available

ZigBee defines a set of protocols based on IEEE 802.15.4 standard and it uses three main types of devices to implement its architecture [13], as illustrated in Fig. 2.

- ZigBee Coordinator (ZC). The most complete and important device, its function is to store data and it is the coordinator of the network.
- ZigBee Router (ZR). Its main function is to interconnect devices separated and limited due to its range in the network.
- ZigBee End Device (ZED). This device can maintain communication with its father node (the node that gave it the access to the network) a ZC or a ZR but not to other devices. In this way, this node can be sleeping most of the time and have lower power consumption rates.

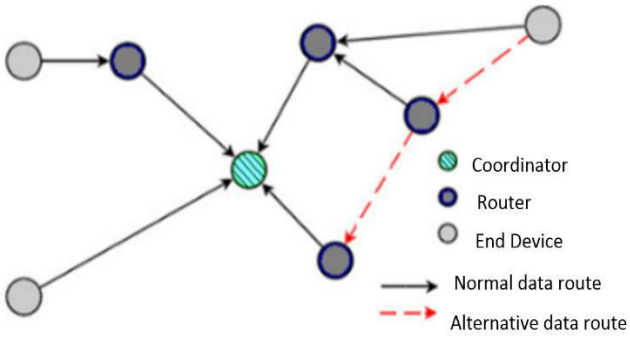

Fig. 2. General ZigBee Device Network.

Due to a lesser range among the nodes, frequently a packet must be sent repeatedly with the use of routers to increase the scope (a good feature of ZigBee), furthermore, ZigBee can send the information in two modes, API (Application Programming Interface) and AT (Application Transparent). Although AT mode (data is not created from the XBee) is simpler than API, it can not be easily implemented in a network because its main use is to send information between two devices. On the other hand, API mode is more complex but sends all the information created from the XBee in one packet, as shown in Fig. 3.

Note: MSB= most significant byte, LSB= less significant byte.

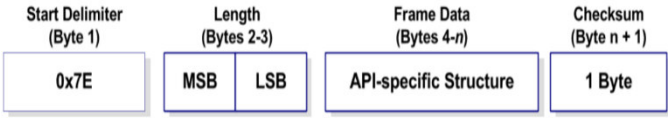

Fig. 3. API data packet.

The API-specific Structure contains all the information related to analog readings, digital readings and the device that sends the information to the coordinator.

III. METHODOLOGY

Fig. 4 shows the block diagram of how the network is implemented for the acquisition system. It can be seen that several antennas can be spread through all the building and

connected at the same time to the smart central unit. The information of different sensors can be associated with each signal monitoring card (up to four analog sensors and three digital sensors due to XBee physical constraints) and it can follow different routes to the central unit. Since the range of XBee is limited, the information can pass directly to the central unit or be resent through a ZigBee Router. Furthermore, it is possible to connect the smart central unit to a PC to interchange relevant information collected by this and add new antennas to the grid with minimal changes according to personal necessities.

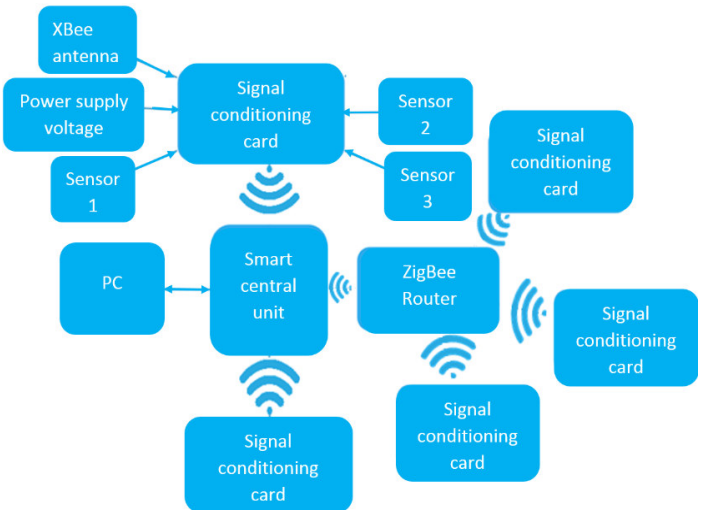

Fig. 4. Network to be implemented.

To prove the functionality of the system, it was installed in a specific case, where an acquisition signal board was mounted in a classroom, and less than 30 m away (range of XBee devices), the signal monitoring board was placed.
The developed system consists of a signal monitoring module, a signal conditioning module, a light sensor, a smoke gas sensor, a presence sensor, a glass breakage sensor and a temperature sensor. The system is depicted in Fig. 5, where a ZigBee-based home automation is implemented for the monitoring of physical signals in a wireless way.

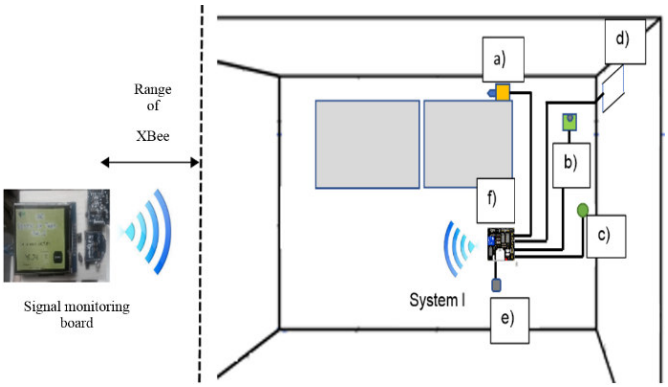

Fig. 5. Schematic diagram of installation of the proposed system in an enclosure, a) light sensor, b) smoke gas sensor, c) presence sensor, d) glass breakage sensor, e) temperature sensor, f) signal conditioning card.

To send the information, a signal conditioning module is needed because most of the sensors have a non-standardized voltage signal in the output that must be compatible with the XBee devices. Also, the conditioning module must work as the power source for the sensors. Each analog sensor used requires to adjust its voltage from 5 V to 1.2 V as maximum output voltage, so the circuit shown in Fig. 6 is used for this purpose, the same circuit is applied for each of the four analog ports included in every XBee antenna.

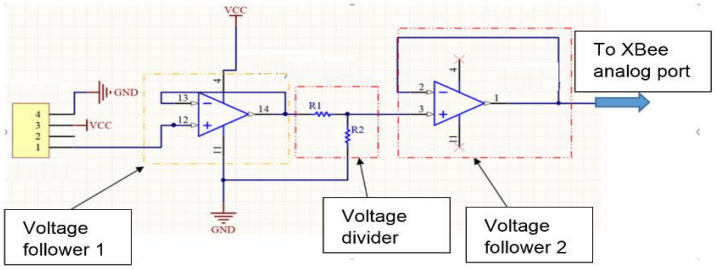

Fig. 6. Signal conditioning for every analog sensor.

The signal conditioning module includes the following items; a socket for the XBee antenna, a LED that indicates a good operation of the XBee module, a relay to operate high power devices such as motors, lamps, etc., and two pins to implement a communication with an extra microcontroller.
Once the hardware modules that fulfill the function to send the data are designed, the information of all the physical variables measured in the building are collected in one coordinator device and they must be shown in a simple and clear way to the final user, so with the help of a touchscreen and an Arduino Due board the system shows real-time readings, and creates plots from data saved in a Micro SD following the flowchart presented in Fig. 7. First, when the reset button is pressed, the program starts and initialize the components required to accomplish the functions described before which are: one digital real-time clock, one Micro SD flash memory, and one touchscreen module. Once the components are initialized, network status data must be obtained from Micro SD to show the correct parameters. After this point, the data from all the nodes must be acquired serially by the XBee coordinator, if there is no data, the touch sensor coordinates must be obtained to update the menu according to the command requested by the user. If the user doesn't touch the screen and the last request was to show real time data, the screen must show the readings specified. To end a loop cycle, the data obtained from the network must be recorded to get it ready in any time requested.

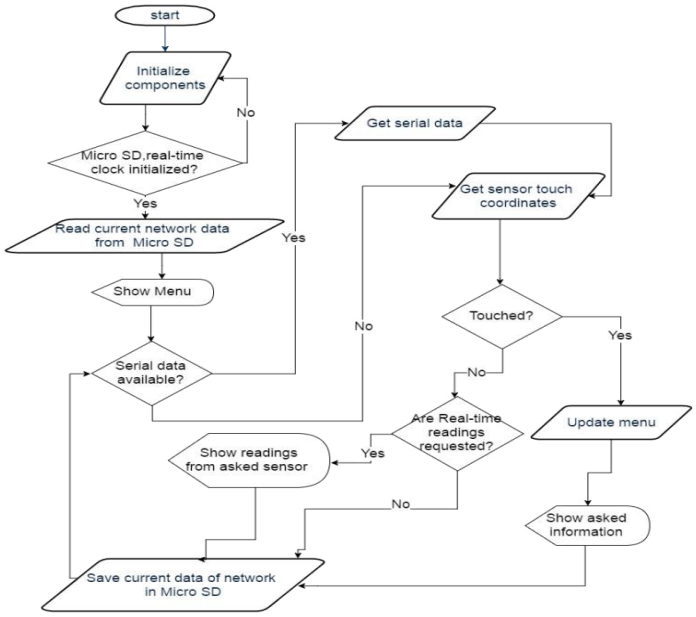

Fig. 7. Flowchart to establish a user-machine interface.

IV. RESULTS

The results are shown in the following figures. The experimental tests of the system were run over two months in a classroom of the Universidad Autonoma de Queretaro. The readings obtained from the temperature sensor with the system proposed were compared with a thermocouple multimeter.

As seen in Fig. 8, a formal signal conditioning board was designed and fabricated; such board can send data from four analog sensors and three digital sensors to the coordinator XBee. The board is capable of receiving commands from the coordinator and execute an action to drive power elements or pass information to another microcontroller. One or more of these modules can be installed in one room according to space requirements avoiding complex wired connections.

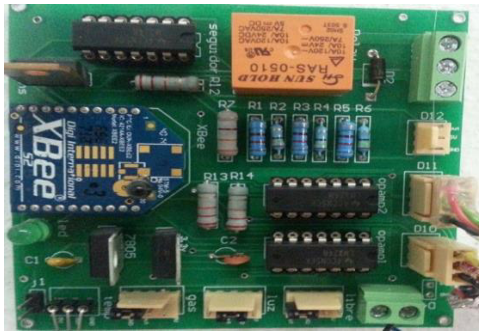

Fig. 8. Signal conditioning board.

A signal monitoring board, presented in Fig. 9, was also designed and fabricated with the purpose of working as a human-machine interface. This board includes a touchscreen which makes a robust and flexible system since a PC is not needed to monitor the signals.

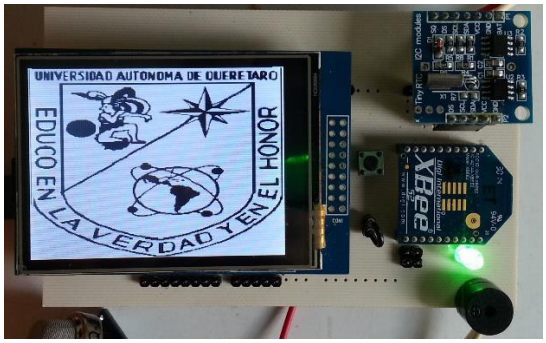

Fig. 9. Signal monitoring board.

Furthermore, to demonstrate the functionality of the system, this was installed in an enclosure as shown in Fig. 10, where all the sensors can be seen installed and connected to one signal conditioning card.

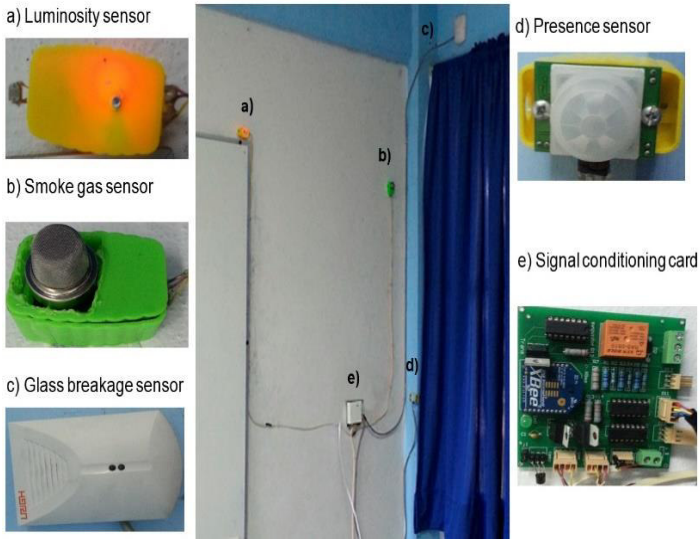

Fig. 10. Proposed system installed in a classroom.

The main functional screens of the touchscreen included in the system are shown below in Fig. *11*, a) screen menu that indicates the place where the signal monitoring board is installed, b) displays from what sensor the user wants to see the readings, c) screen of the real-time readings and d) illustrates an example of the plots that the system is capable of making. It is demonstrated that the user can observe and access to the state of all the building through real-time readings of the sensors with few touches on the screen. It is also, possible to create plots of all the variables measured and saved in the Micro SD memory flash.

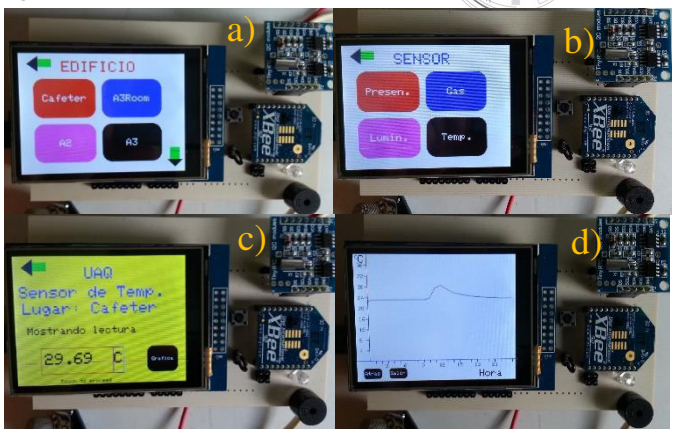

Fig. 11. Main functional screens of the system proposed, a) place of sampling, b) kind of sensor, c) real-time readings, d) Graphs.

To make a more flexible system in the number of antennas that can be spread into a building, a software wizard was developed to indicate to the signal monitoring board that a new antenna is required to add to the current network with a PC via USB port. Also, the software can trace data collected and saved for analysis indicating the current location and the serial number printed in each antenna connected. The software was developed in Visual Studio c# 2013 in a PC laptop of 1.8 Ghz with operative system Windows 8. To accomplish its functionality, the program is divided into three main functions: making graphics, sending information and receiving information from Arduino Due microcontroller. When the user wants to add a new antenna to the actual network it is necessary to fill some information asked by the program. Also, the program shows comments to specify the information required in case of mistakes, if the information is correct, then it is sent to the microcontroller via USB port.

Finally, 100 samples were taken (one sample per minute) of the temperature sensor and a digital multimeter fluke 177 with a thermocouple to compare the samples. The results obtained are the following:

-The RMS error between the used systems provides an average value of 0.301186129 °C.

-The Pearson correlation coefficient gave a 98.819% of relation between the thermocouple Fluke and the temperature sensor used with a relative error of 1.0594339%.

In general, an error below 3% is already considered as an acceptable value for a measurement system and therefore as the proposed system has an error close to 1% it can be concluded that it presents a high accuracy with respect to a commercial system.

V. Conclusions

In this work, a domotic system that uses ZigBee for the acquisition of data from sensors in a wireless way was developed having a better range than Bluetooth and less power consumption than Wi-fi. From the previous remarks, it is verified that the proposed system presents results comparable to those of commercial purpose but with a greater flexibility and lower cost.

The use of a ZigBee wireless system for the monitoring of signals from electrical sensors offers multiple advantages over a wired system:

- Ease of installation, as the final system does not require complex connections or special wiring.
- Flexibility to place the central module/display anywhere in the building, instead of being fixed.
- Possibility of integration as a node belonging to a network of sensors connected to a central home automation system.
- Possibility of acquiring and monitoring additional or different signals to the ones already used (temperature, luminosity, gas and presence) and transmit all data at the same time to the network coordinator using the same ZigBee radio transmitter.

The system created will be installed in a building of the Universidad Autonoma de Queretaro, CATAS (Academic Center of Advanced and Sustainable Technologies) to collect all the information of the state of the building and concentrate them in one central unit, with the facility to move it from place to place if needed and add new antennas to the current network.

Acknowledgment

This work was supported by FOMIX QRO-2014-C03-250269.

References

[1] M. Bromley and G. Webb, “Trends in smart home systems, connectivity, and services”, 2003.

[2] T.G. Stavropoulos, A. Tsioliaridou, G. Koutitas, D. Vrakas, and I. Vlahavas, “System architecture for a smart university building”, Diamantaras, K., Duch, W., Iliadis, L.S. (eds.) ICANN 2010, Part III. LNCS, vol. 6354, pp. 477-482. Springer, Heidelberg 2010.

[3] G. Khusvinder, Y. Shuang-Hua, Y. Fang, and L. Xin, “A zigbee-based home automation system”, IEEE Transactions on Consumer Electronics, Vol. 55, No. 2, May 2009.

[4] K. Semanur, S. İbrahim, Ş. Alper, “A low cost smart security and home automation system employing an embedded server and a wireless sensor network”, International Conference on Consumer Electronics-Berlin, 2016.

[5] L. Dobrescu, “Domotic embedded system”, 9788-1-4799-5479-7/14 IEEE., 2014.

[6] L. Eurico, V. Luis, P. Fernão, and D. Filipe, “A zigbee wireless domotic system with bluetooth interface”, 9788-1-4799-4032-5/14 IEEE, 2014.

[7] J. Brito, T. Gomes, J. Miranda, J. L. Monteiro, J. Cabral, “An intelligent home automation control system based on a novel heat pump and wireless sensor networks”, 978-1-4799-2399-5/14 IEEE, 2014.

[8] J. P. Cofré, G. Moraga, C. Rusu, I. Mercado, R. Inostroza, J. Jiménez, “Developing a touchscreen-based domotic tool for users with motor disabilities”, 978-0-7695-4654-4/12 IEEE, 2012.

[9] P. Vikram and A. Nayyar, “Real time smart home automation based on pic microcontroller”, Bluetooth, and Android Technology. 978-9-3805-4421-2/16 IEEE, 2016.

[10] D. Sánchez, “Diseño de una casa inteligente basado en la tecnología jini”. Undergraduate dissertation. Mexico, 2004.

[11] G. O'Driscoll, “The essential guide to home networking technologies”, Prentice Hall, 2000.

[12] K. Shuaib, M. Boulmalf, F. Sallabi, and A. Lakas, "Co-existence of zigbee and wlan a performance study", IFIP International Conference on Wireless and Optical Communications Networks, pp. 5, 2006.

[13] O. Maxim, “Home automation with zigbee”, Computer Science, 5174, 2008.

Concretes based on substitution of fine aggregates by plastic recyclates and their variability of resistances.

Vilchis Hernández Danae[a], Olmos Ortega Héctor[b], Gonzales Mata Fernando[c] , García Aguilera Jorge[d] , M. Trejo-Perea[e] / Universidad Autónoma de Querétaro
School of Engineering
Querétaro, Qro.
dvilchis21@alumnos.uaq.mx[a], hector_olmos_o@hotmail.com[b] , george_rosee@hotmail.com[d], mtp@uaq.mx[e].

***Abstract*— Currently, the declining economic situation of the population in general, together with the environmental impact, has encouraged engineers to seek work techniques that generate low energy consumption and at the same time increase the possibility of introducing the recycling of non-toxic waste in companies To generate a reduction of costs with the use of this waste, this situation has been reflected mainly in strategies of sustainable construction with the objective of optimizing times, costs and environmental damages.**

The needs of future generations must be met according to the development of each country. Taking into account that construction is one of the activities that contributes most to these advances, it is expected that the working methods in this area will evolve along with society. To do this, have proposed the method of assembly that reduces the time and costs of the project, in addition to allowing the reduction of pollutants such as concrete and its production of greenhouse gases through the use of recycled materials in prefabricated building blocks. This paper presents the preliminary compilation of the variation of resistance of different concrete designs that will serve as possible material for the development of prefabricated assembly blocks. For the sample designs, the fine aggregate of the concrete with 2.5% and 5% rubber was replaced, as well as 2.5%, 5% and 7.5% PET with a f'c = 250kg / cm²

***Keywords*— resistance; concrete; recycling; rubber; pet.**

I. INTRODUCTION

Nowadays the development of projects in the area of construction is increasing, so the function and the needs that must meet these, are sought through the innovation of materials, provide greater comfort with the least possible investment. This work of compilation addresses the resistance of materials, environmental protection and the optimization of resources by means of different materials used for concrete in blocks of assembly for construction. For example, in Kurukshetra, India. Work with the possibility of replacing the fine aggregate with industrial waste or by-products such as sand casting sand and bottom ash, which offer technical, economic and environmental advantages, which are of great importance in the current context of sustainability In the construction sector [1]. Some of the examples of applied innovation around the world can be applied in our country to protect the environment and improve quality by building with ecological assembly blocks.

Due to the high production of PET and rubber in our country and throughout the world, have decided to focus our research on tests containing these materials, replacing the fine aggregate in the conventional concrete sample. The high cost of labor in construction is even greater than that invested in the raw material itself. Today's constructions demand different properties, such as lower densities, without neglecting sustainable development. Must implement recycling and construction is a good area of opportunity.

According to reports from the Intergovernmental Panel on Climate Change (IPCC); One of the consequences of the construction industry is the deterioration of the environment, by the extraction of basic aggregates of concrete [4].

Some researchers have opted to substitute the fine aggregate for ground glass since in Brazil 800 thousand tons of waste are produced per year, of which only 27.6% are recycled and of which 3% of glass is discarded as garbage, inside Of these studies have been added ground glass with a particle size of between 0.075 and 1.5 mm of thickness in different percentages according to the weight of the tests. The researchers proved to meet the required strength in the compression tests and an increase in tensile strength with particle sizes of 0.15 to 0.3 mm, which makes it an optimal and viable aggregate for concrete specimens [6].

According to the Mexican Standards: NMX-E.000-SCFI-1999 and NMX-E-332-SCFI-1999, which establish the terminology of plastics recycling and symbology for the identification of the material constituting plastic-nomenclature articles , Respectively, the following materials are distinguished: PET, HDPE, PVC, LDPE, PP, PS and other plastics which are the result of the sample of the above. In the case of PET, which is polyethylene terephthalate, used in the manufacture of soft drinks and soft drinks, it is the most used

plastic material in Mexico. According to the Mexican Institute of Industrial Plastic S.C., in 1997 in Mexico the quantities of the different plastics referred to in Table 1 were used, 53% being used for the preparation of strips, monofilament, film and raffia; 32.7% to the production of bottles and containers; 11.8% for the manufacture of boxes, covers, cuvettes, cups and cases and 2.0% in the manufacture of sheets, disposable products and coatings. [7].

TABLE 1. PLASTIC QUANTITY USED IN MEXICO (1997). [7]

Plastic	Abbreviation	Thousands of tons
Low density polyethylene	PEBD	216
High density polyethylene	PEAD	186
Polyethylene terephthalate	PET	170
Polypropylene	PP	159.5

Once it has been understood why to use a material such as recycled plastic for aggregate in the elaboration of the mortar, analyze the properties that these plastics can provide to the mortar and the modifications that they make in their habitual behavior, thus it is analyzed if our Sustainable combination is feasible to generate a structural mortar element.

The properties of the mortar + plastic, which will analyze and compare in the results are the following:

Density, in this case will use the Spanish standard to interpret the results UNE EN 12390-7. [8]

Mechanical Properties, analyzed and compared according to standards on masonry mortar, such as tensile strength and compression properties UNE EN 1015-11 [9] among other properties.

The results of the density test are presented in Fig. 1 obtained in the 2016 research [2]. It was clearly shown that, in both cases, the higher the plastic content, the lower the density of the materials. There is, as expected, a correlation between density and plastic content. These figures also show the normalized density in the control mortar and concrete values. In both cases achieved the highest reduction (almost 30%) addition of polyethylene (20%) the density of polyethylene is lower than the density of PVC thus measured evolution was as expected. In civil engineering works, where the potential quantity of the necessary materials is enormous, this is an interesting reduction for the case of the own weight of the massive structures (see Fig. 2) [2].

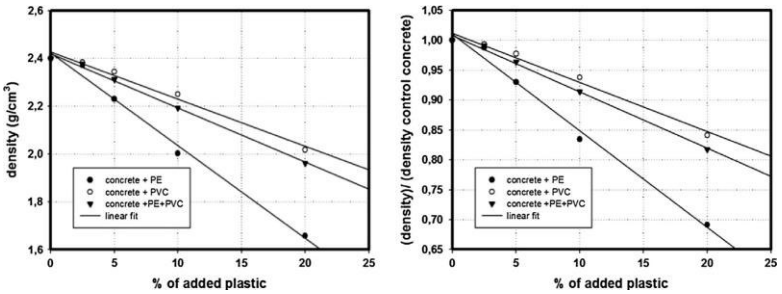

FIG. 1. DENSITY VALUES OF THE MORTAR-PLASTIC COMPOUNDS (LEFT) AND NORMALIZED VALUES (RIGHT) [2].

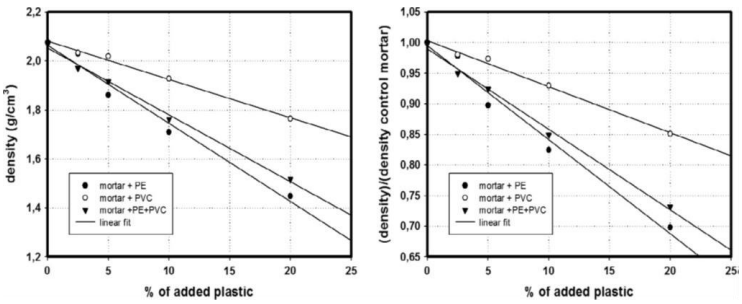

FIG.2. DENSITY VALUES OF THE MORTAR-PLASTIC COMPOUNDS (LEFT) AND NORMALIZED VALUES (RIGHT) [2].

In this same research [2], the results (Table. 2) obtained when testing concrete cylinders are tested for compression, up to a maximum period of 58 days

TABLE 2. RESULTS OBTAINED IN RESEARCH CARRIED OUT IN COMPRESSION TESTS ON CONCRETE CYLINDERS. [2]

Resistance table	Control concrete	Control concrete + 2.5% PE	Control concrete + 5% PE	Control concrete + 10% PE	Control concrete + 20% PE
Compression samples density (kg/m^3)	2399	2370	2239	2002	1658
Compresive strength 7 days (MPa)	30	25.8	19.2	8	2.1
Compressive strength 28 days (MPa)	34.6	29.9	25.4	9.2	3.4
Compressive strength 56 gays (MPa)	46	32.9	26.3	9.8	3.7

Analysis: After analyzing the results obtained from the investigation of plastic aggregates [2] can conclude that plastic (PVC, PE or PVC + PE) provides a positive lightness to the concrete, ie, it is important to analyze this aspect since With lower density, lower weight and this is of great help for the reinforcement of structures, however, it should be noted that the mechanical tests with a greater proportion (greater 2.5%) of plastic replacement their properties are getting worse until it is totally useless.

Based on the previous information, the objective of this investigation is to perform a replica of the mechanical tests to compression based on the Mexican standard NMX-C-083-ONNCCE 2002 [10] and complemented with NMX-C-109 standards -ONNCCE [11], NMX-CH-027-SCFI [12] and NMX-169 ONNCCE [13]. With the purpose of comparing our results and being able to generate our own conclusions, adding to this research the proposal of using rubber as a plastic aggregate to the concrete as well as the proposal of an intelligent design of an assembly block that allows to save the times of construction and abarate the play.

II. METHODOLOGY

Phase 1:

The sample was designed according to a resistance of 250 kg / cm2 according to the Mexican norms NMX-B-231 [14], NMX-C-030-ONNCCE [15] and NMX-C-170-ONNCCE [16] , Adding to this design the new proposal to replace 2.5% and 5% of the fine aggregate with plastic, for the recycled material of substitution rubber and PET were chosen as objects of study; Once the design proposal of the specimen was obtained, the cores were cast in 10x20 cm steel cylinders according to the regulations, the cylinders were demolded at the passage of 2 days, these were marked and taken to the setting chamber Where they remained for 28 days, on the 28th, the cores were extracted from the chamber to obtain the weights of the samples already set and dried. The densities were calculated according to the standard UNE EN ISO1015-10 [9] and UNE EN 12390-7 [8]. As a next step, the test of the cylinders was carried out to mechanical compression tests in the universal machine, located in the soil laboratory of the engineering faculty at the Autonomous University of Querétaro, according to Mexican standards for tests of NMX cylinders C-083-ONNCCE 2002 [10] and complemented with NMX-C-109-ONNCCE [11], NMX-CH-027-SCFI [12] and NMX-169 ONNCCE [13]. Once the results were obtained, it was possible to generate a discussion and comparison of the same in said debate, the conclusions of the first phase of the investigation were determined and the best plastic aggregate in the concrete was voted.

Phase 2:

At this stage it was decided which specimen shows the best properties to work with. It is necessary to propose a unique and innovative design of block of assembly that allows the saving of time of assembly and abarate the costs of construction.

After that, the assembly blocks of their own design will be cast with the objective of realizing the prototypes to perform the tests corresponding to the standard NMX-C-036-ONNCCE [14] and to be able to classify them depending on their resistance as blocks Of structural or non-structural use according to NMX-C-404-ONNCCE-2012 [15] and NMX-C-441-ONNCCE-2013 [16].

Once the blocks are classified, it will give a way to continue testing the blocks and thus obtain a complete classification according to their quality.

III. RESULTS

The cylinders were tested in compression in the universal machine with a pitch of neoprene pads to assure the uniformity of action of the load, were loaded with a constant load until resisting its maximum load and the result thrown by the universal machine was in KN. (Table 2) which had to be converted to kg / cm2.

The first results obtained were from the cylinders with rubber aggregate to the concrete, we can observe (Table 2) that three tests have been performed, an average of the resistance has been obtained for 2.5% of the aggregate and another for 5% of the plastic aggregate , Which would later work to obtain the mean value of error in the witnesses with plastic aggregates.

TABLE 3. RESULTS OF RESISTANCES OBTAINED THROUGH TESTS CARRIED OUT TO COMPRESSION IN "UNIVERSAL MACHINE" (WITNESS WITH RUBBER AS AGGREGATE).

Percentage of recycled aggregate	Maximum load KN)	Maximum resistance (Kg/cm^2)
2.50%	189.209	245.72
2.50%	177.129	230.038
2.50%	182.334	236.797
2.50%	**AVERAGE**	**237.5183**
5%	143.834	186.797
5%	148.962	193.457
5%	148.107	192.347
5%	**AVERAGE**	**190.867**

Once the results were obtained and converted, a comparative (table 3) of compression resistance of design vs resistance to compression with plastic aggregates was realized and a percentage of error in the resistance with plastic aggregates in the concrete was realized, is Say a percentage of how much was affected the plastic at the target resistance of 250 kg / cm2.

TABLE 4. PERCENT OF ERROR REGARDING THE DESIGN AND RESISTANCE OF CONVENTIONAL CONCRETE SAMPLE RESISTANCE (ACCORDING TO PERCENTAGE OF RUBBER AS AGGREGATE

AVERAGE	Average error obtained with respect to the design (percentage)
2.50%	4.99
5%	23.6532

This process was repeated for the test of the cylinders with PET aggregate to the concrete, however it is important to emphasize that in the casting of the 5% PET aggregate cylinders there were witnesses quite damaged by the presence of the plastic, which led to A great variation of results and the disqualification of some of them (table 4).

TABLE 5. RESISTANCE RESULTS OBTAINED THROUGH TESTS PERFORMED UNDER COMPRESSION IN "UNIVERSAL MACHINE" (CONTROLS WITH PET AS AN AGGREGATE).

AVERAGE	Maximum load (KN)	Maximum resistance (Kg/cm^2)
2.50%	185.012	240.305
2.50%	174.718	226.935
2.50%	189.286	245.857

2.50%	AVERAGE	237.699
5%	123.55	160.474
5%	103.816	134.843
5%	181.632	235.915
		DISCARDED
5%	AVERAGE	147.6585

Finally, a comparison (design 5) of compression strength of design vs compressive strength with plastic aggregates is now carried out on the concrete with PET aggregate to obtain the percentage with which the PET affects the objective resistance of 250 kg / cm2.

TABLE 6. PERCENTAGE OF ERROR WITH RESPECT TO THE DESIGN AND THE RESULT OF CONVENTIONAL CONCRETE SAMPLE RESISTANCES (ACCORDING TO PERCENTAGE OF PET AS AGGREGATE).

AVERAGE	**Average error obtained with respect to the design (percentages)**
2.50%	4.9204
5%	40.9366

IV. CONCLUSIONS

1. The results of resistance of the compression cores are favorable since the design has been made at 300Kg / cm2 and has been found with a 20% error in the most optimistic cases, this is considered a favorable result since in occasions The concrete design carried out with common concretes has a higher percentage of error.

2. By making a comparison of specimens, obtain quite similar results between the two aggregates at 2.5%, however, can notice that the rubber has a more stable and constant behavior in the decompensation of the resistance, and the PET when added in more quantity begins To exert greater affectations in the concrete and as could see, throws very random resistances.
3. It is extremely important that these tests can be repeated in a greater number of witnesses in order to obtain a larger database in order to choose a sample with a certainty.
4. Investigations will proceed with both specimens.

REFERENCES

[1] Yogesh Aggarwal, Rafat Siddique.: “Microstructure and properties of concrete using bottom ash and waste foundry sand as partial replacement of fine aggregates”. Rev. Construction and Building Materials, Elsevier. Vol. 54, (2014) 210-223.

[2] José Luis Ruiz-Herrero, Daniel Velasco Nieto, Alberto López-Gil, Ángel Arranz, Alfonso Fernández, Antolín Lorenzana et al.: “Mechanical and thermal performance of concrete and mortar cellular materials containing plastic waste”. Rev.Construction and Building Materials, Vol. 104, (2016) 298-310.

[3] Miguel R. E, Banda Noriega R. B.E, Barreda M. F, Monzón J.D., Sota J. D .: "Portland cement concretes with foundry sands. Bases for sustainable management ". Recycling of construction and demolition waste (RCD) and process waste (PR) PROCQMA - National Technological University, National University of the Center of the Province of Buenos Aires, (2006). ISBN 950-42-0056-7.

Miguel R. E, Banda Noriega R. B.E, Barreda M. F, Monzón J.D., Sota J. D.: “Hormigones de cemento portland con arenas de fundición. Bases para la gestión sustentable”. Reciclado de residuos de construcción y demolición (RCD) y de residuos de procesos (RP) PROCQMA - Universidad Tecnológica Nacional, Universidad Nacional del Centro de la Provincia de Buenos Aires, (2006). ISBN 950-42-0056-7.

[4] Ferrán Ballestera , Julio Díaz , José Manuel Moreno.: “Cambio climático y salud pública: escenarios después de la entrada en vigor del Protocolo de Kioto”. Unidad de Epidemiología y Estadística.Toledo. España, Rev. Ecosalud y participación social, Vol. 20, (2006) 160-174

Ferrán Ballestera, Julio Díaz, José Manuel Moreno .: "Climate change and public health: scenarios after the entry into force of the Kyoto Protocol". Unit of Epidemiology and Statistics. Spain, Rev. Ecosalud and social participation, Vol. 20, (2006) 160-174.

[5] Cempre, Consórcio Empresarial para a Reciclagem, www.cempre.org.br, Internet em 15/04/2002.

[6] D. A. R López, C. A. P. de Azevedo, E. Barbosa Neto.: “Evaluation of physical and mechanical properties of concretes produced with ground waste glass as fine aggregate”, Rev. Ceramica, Vol 51, (2005) 318-324.

[7] Instituto Nacional de Ecología y Cambio Climático (2002). Precios de los materiales recuperados a través de la pepena. Recuperado el 1 de mayo de 2016. http://www.inecc.gob.mx/descargas/dgipea/precios_mat_pepena.pdf

[8] UNE EN 12390-7: testing hardened concrete – Part 7: density of hardened concrete.

[9] UNE-EN 1015-11:2000/A1:2007: methods of test for mortar for masonry –Part 11: determination of flexural and compressive strength of hardened

[10] NMX-C-083-ONNCCE 2002

[11] NMX-C- 109-ONNCCE

[12] NMX-CH- 027-SCFI

[13] NMX-169 ONNCCE

[14] NMX-C-036-ONNCCE

[15] NMX-C-404-ONNCCE-2012

[16] NMX-C-441-ONNCCE-2013.

CONACYT
Consejo Nacional de Ciencia y Tecnología

CONCYTEQ

UNIVERSIDAD AUTÓNOMA DE QUERÉTARO

13° CONGRESO INTERNACIONAL DE INGENIERÍA

15th-19th MAY 2017

Effects of tool path deviation of industrial robots in roll hemming

Eduardo Esquivel
Facultad de Ingeniería
Universidad Autónoma de Querétaro
Querétaro, México
Email: je.esquivel@outlook.com

Carlos Jáuregui
Facultad de Ingeniería
Universidad Autónoma de Querétaro
Querétaro, México
Email: jc.jauregui@uaq.mx

Horacio Orozco
Ingeniería Mecánica
Instituto Tecnológico de Celaya
Celaya, Guanajuato
Tel: +52-1-461-61-1-7575

***Abstract*—The main idea of this paper is the proposal of two approaches to correct the path deviation of tool end effector in industrial robots. In part II, we explain the common defects of the roll hemming process and its main parameters. In part III, we describe different experiments related with defects. In part IV, we analyzed the tool path deviation defects on the tested samples. Finally, in part V we propose two main approaches to correct path deviation of the tool end effector of industrial robots justified in a deep literature research and in part VI, we conclude with the discussions of the two approaches and the future work perspective.**

Keywords: Wrinkles; path deviation; roll hemming

I. Introduction

Hemming is one of the last stamping operations for panels of the car in automotive industry. It consists in a stamping die to form the panel of the car, especifically, the edge of the door for example, with two main porpuses: to avoid razor edges and to attach the exterior panel to the interior panel. Different papers characterized the process in order to correct defects and predict the desired contour of the final part. The main issues in this technology are the expensive modifications required in the serial production. Also it takes a considerable time to change the die. Considering this, [1] presents a study of straight edge-flat surface without considering the radius flat hem. The paper focuses on determine the major process parameters in straight edge hemming and the relations between them and some forming defects with the simulations of flanging, hemming, springback. The parameters were flanging die corner radius, prehem path, prehem stroke, final hemming force. The simulations applies only to a 2D analysis and the results report the influence of each parameter, the warp and recoil appear one instead of the other. It remarks the need of more quantitative criteria for warp and recoil and a summary of observations are established in a trend line table for purposes of manufacture. [2] focused on flange and convex edge hemming aluminum killed draw quality steel. The paper investigates the influence of the contour radius and flange length on wrinkling, hem out and factor in convex edge hemming. It suggests that further investigations will focus on pure roll and warp without wrinkling and hem out. As a result, they related radius length and wrinkling hem out, the residual wrinkling must be acceptable and wrinkling must be avoided during the flange and pre-hemming operations to obtain a good quality. [3] presents the characterization of ductil damage for aluminum alloy series 6000 with different tests for the hemmed part until the fracture was produced, the gurson-tvergaard-needleman was used for the numerical simulation on flat-surface-straight-edge to investigate the influence of parameters of damage and the constraints of process. As a result, they focused on the behavior of the material and the applied deformation. These works were all intended to improve and predict the fracture and deformation of the part prior the process.

The roll hemming process is an alternative technology were a robot (handling a roller as end effector) forms the material instead of a stamping die. The process is done in different steps moving the roller all over the edge of the door of the car. There are pre-hemming steps before the final hemming step. [4] presents the experimental data for concave/convex edge curved surfaces to study the influence of the geometry and the predeformation in the roll in and to validate the numerical simulations. They established a design of experiments for the roll hemming and the classical hemming. As a result, they established the process is complex enough to set comparisons with the variation of parameters. [5] presents a study to predict

the behavior of the material for roll hemming based on elasto-plastic uniaxial tension tests on samples of the same material. They determined the required load to fracture the material and compared this value with that of the numerical simulation. The simulation results established that straight paths along hem line include a number of serrations, they associate this phenomenon with the motion of the roller. [6] studied the finite element models including flanging, pre-hemming and final hemming with abacus explicit. They consider the uniaxial tension and compression tests to decide the cyclic hardening behavior. The simulation results show that material in the bending area are strain hardened before hemming while little plastic deformation occurs in the flanging area before hemming. These papers focused on the numerical simulation of the material sample to predict the final quality. Nevertheless the robot plays an important role in the process.

II. Defects in roll hemming process

A. The geometry of the sample sheet

We wish to illustrate the main defects in the roll hemming process which cause a non uniform final part -[1] already presented the most significant defects for the hemming process-, in order to study those defects we need to observe that the different panels comprehend different geometries and different locations respect to the robot. The figure 1 illustrates the different geometries of the door as convex surface-convex edge or convex surface-concave edge, these sections vary from each other which generates different conditions and constraints for the application of the force while the roller moves over the sheet. Also the near location and the far location present different conditions and capability of the robot to apply the force all along the path.

B. The common defects of the material

In order to study the common defects of the roll hemming process we need to see the lateral face of the sample sheet to analyze the changes in the position as roller moves. [7] carried out a numerical simulation to define the main parameters of this process and analyzing this as a multi-step process. The figure 2 clarifies the lateral face of the sheet to analyze it

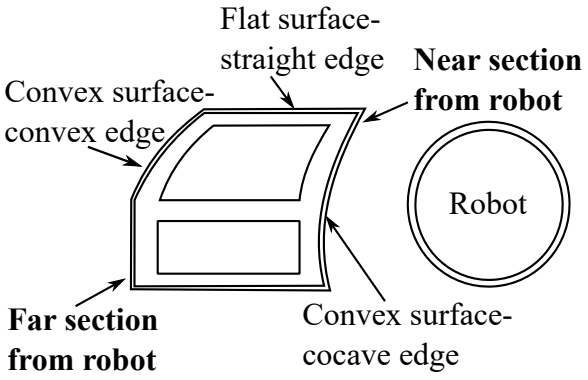

Fig. 1. Different geometries in a door and far and near positions related to the robot.

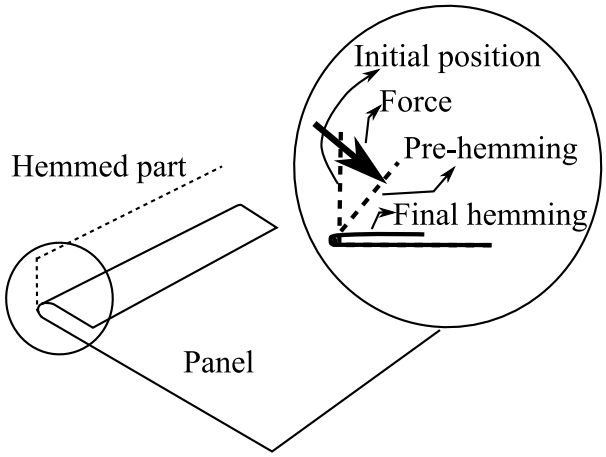

Fig. 2. A multi step process in roll hemming.

and the different pre-hemming steps, this illustrates how the flange goes from the initial position to the final hemming. The thickness and the flange length are key parameters that influence how the defects behave.

The figure 3(a) explains the roll in and roll out defect as the difference between the initial position and the final position length on the horizontal direction, the appearance of this defect is related with the value of the applied force and its direction during the pre-hemming steps. The figure 3(b) explains the warp and recoil defects which appear as a bubble or a gap in the material being the cause the internal deformation of the part as the tool is pressing over it. These are more common in the classical hemming process.

In the springback defect material recovers to its initial position as shown in the figure 4(a), this defect has a direct impact on the final quality part the desired position and this defect will lead the flange to the final position, which is different that the desired one. We call the springback as the angle between the desired and the final position during the different pre-hemming steps. For every pre-hemming steps the springback defect will increase and the final hemming will be affected by the sum of all these errors. Wrinkles are the most common defects for curved edges in classical hemming and now its being characterized for the roll hemming process (see 4(b)). Wrinkles defect are the waves formed over the sample part as roller moves over it. This fluctuation of the material

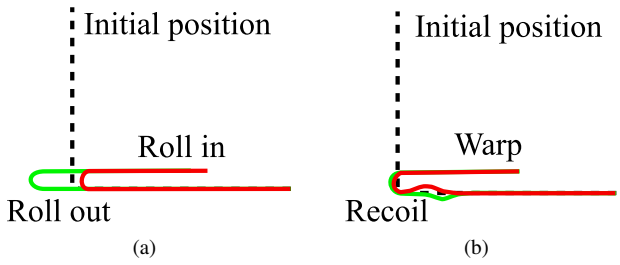

Fig. 3. Common defects on the material part. (a) Roll in and roll out in a sample sheet. (b) Warp and recoil in a roll hemming sample sheet.

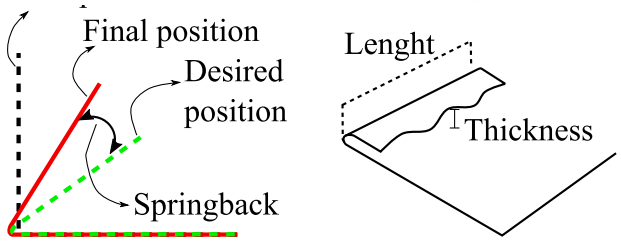

(a) (b)

Fig. 4. Related defects for elasticity of the material. (a) Springback is the recovery of material. (b) Wrinkles are waves over the sample sheet.

generates more waves and is affected by the speed of the roller and the relaxation time of the material.

C. The relation between wrinkles defect and stiffness of robots

A direct relationship exist between the wrinkles defect and the stiffness of the robot. Low stiffness could lead to a low force application (contrary to the case of the stamping die machines) and allowing the material to move and change the path direction. [8] pointed out that the stiffness of the robot matters in the roll hemming process as it is explained in the figure 5, where to different locations of the door were observed afted the final hemming step, in the figure, the position A correspond to a far location to the robot and the B corresponds to a near location to the robot, the final thickness differs for the same part.

The figure 6 shows the wrinkles formed on an aluminum sample sheet, if this defect is observed only from the interior of the panel sheet, it could be a minor problem, but when the defect is observed from the outside part, then the appearance of the car shows low quality [9].

III. Experiments related with defects

A. Measurement of springback defect

Some experiments related with defects have been carried out to determine the springback defect and the forces in the process. In [10] we developed an experiment where the workpiece deflect a determined angle θ_{max} when a flange center force is applied (see figure 7).The procedure consisted in apply a force deformation on material flange until certain angle, register the force and retrieve the applied force in order to register the springback. The force will be applied to move the aluminum sheet flange from 0° to 30° from the initial

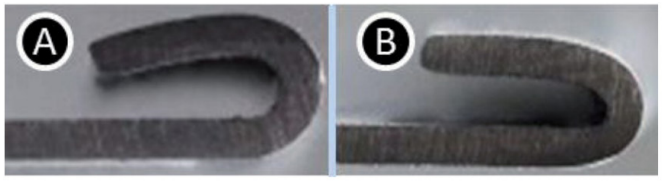

Fig. 5. Comparison of two location in sample respect to the robot base, A corresponds to a far location and B corresponds to a near location [8].

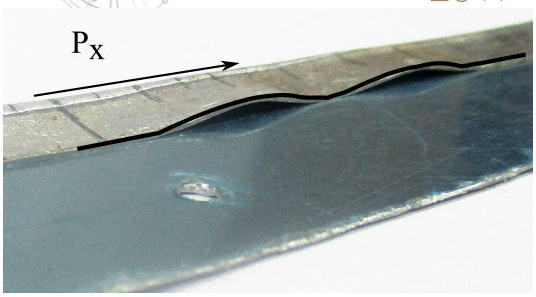

Fig. 6. Wrinkles formed on the hemmed flange [9].

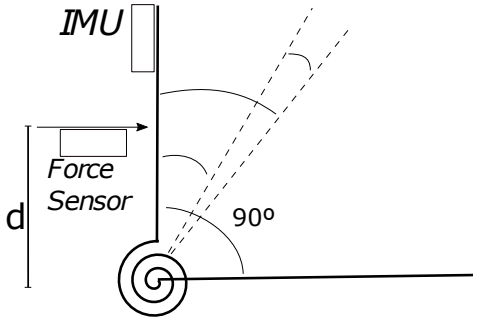

Fig. 7. A model to study the springback effect.

position. The material used is aluminum of $1mm$ thickness bended 90°. The IMU is a sensor capable of measuring angle and acceleration in x axis, according to the orientation of the position in the aluminum sheet. The Load Cell used was a S type for measuring the force, it required a Weathstone bridge connection based on the ni usb 6009 DAQ aquisition hardware, the calibration of sensor was carried by using different weights from 0 to 80N. The IMU sensor has been used to detect the inclination angle in combination with arduino data acquisition board (see figures 8(a) and 8(b)). The graph 9(a), shows the force application vs time for the first test, the graph 9(b), shows the inclination angle vs time for the first test. The springback is the difference in angle between the maximum angle and the final angle. [11] analyzed the springback effect and its efects on the material relating this defect with the 3D simulation in order to propose a springback prediction frame.

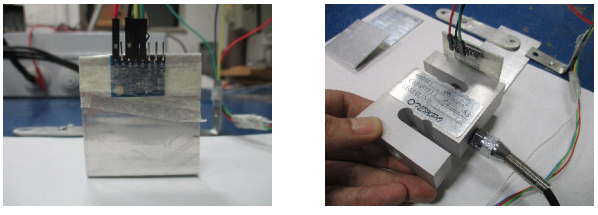

(a) (b)

Fig. 8. The sensor implementation. (a) Positioning IMU sensor. (b) Aplication of Force on sample.

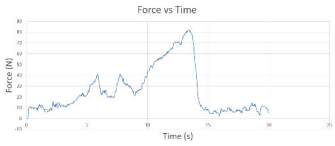

(a)

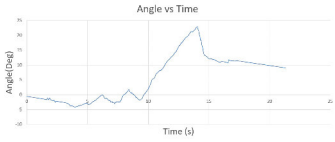

(b)

Fig. 9. Results of the experiment. (a) Force applied during pre-hemming step. (b) Angle measured during pre-hemming step.

B. Measuring of forces in sub-steps

In [9] we measured the forces involved in the process and determined the appearance of wrinkles. The layout of the experiment is shown in figures 10(a) and 10(b). The tests considered: aluminum of 6000 series and steel of standard quality for sample sheets, a part thickness of $0.5mm$ -other works reported $0.8mm$ or $1mm$ [4], [7]-, a flange length of $10mm$ -average in other works-, a flat surface, a straight edge, three hemming steps (60deg, 30deg and 0deg) and a roller radius of $20mm$. The figure 11 plots force and time for the final hemming step (0deg) for aluminum and steel parts; the force rises in the first $5s$ to $10s$; the maximum force registered was $173.28N$ for aluminum and $500.05N$ for steel; the plot shows the first $20s$, in this case aluminum values remained constants but for steel, the platform was forced and the roller leaved the trajectory.

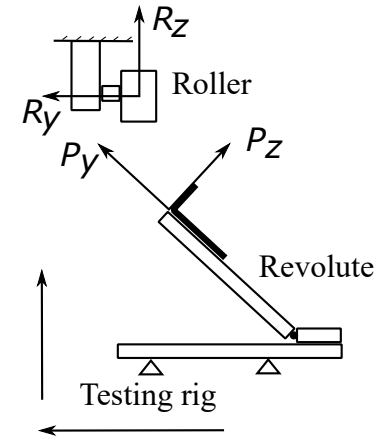

(a)

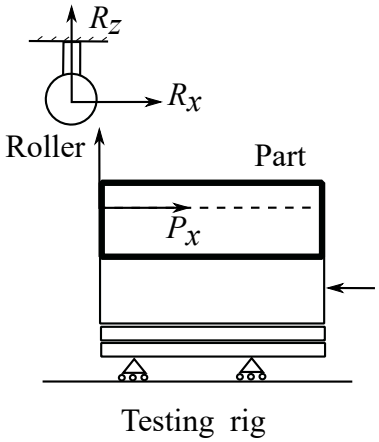

(b)

Fig. 10. Layout of the testing rig. (a) Frontal layout. (b) Side layout.

C. Measurement of thickness in samples

Every sample was marked every $5mm$ and the thickness in z direction was measured with a vernier caliper as figure 12 plots. The figure 13, plots the thickness of a desired part- a constant line of $1mm$-, the thickness of an aluminum part and the thickness of a steel part -less deformed respect to aluminum-; the maximum thickness for aluminum and steel were $2.8mm$ and $5mm$, respectively; the better shape is in the middle of the parts, is for the designed rig.

IV. Analysis of Tool Deviation

A. Study on the tested samples

We considered to analyze the path deviation in order to correct the trajectory of the roller while moving over the sheet. In the figure 14 the trajectory deviates while the roller moves over the sheet. The target path is the straight line of the pre-hemming stage and the real path is the curved trajectory highlighted by yellow color. The roller has free rotation as it moves applying force on the sheet. The figure 15, illustrates the differences between real path and target path as Δ_X causing wrinkles defect, the direction of the roller is in x direction. [12] reported that the usual stiffness of a robot is less than $1N/\mu m$ vs a CNC machine of $50N/\mu m$ being this the possible cause of the trajectory deviation. [13] measured the force in the 3 different orthogonal axis to

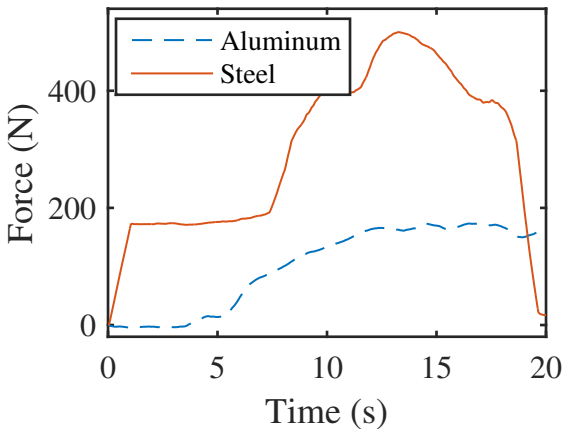

Fig. 11. Forces vs time for the final hemming (0deg) step for aluminum and steel.

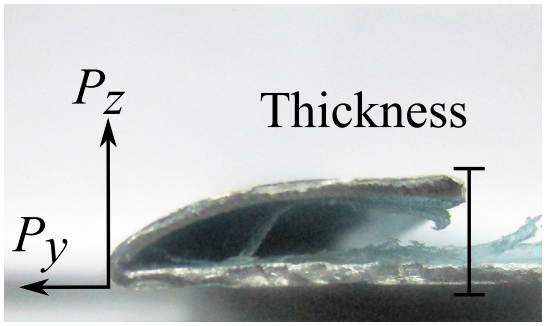

Fig. 12. Tested samples. Thickness on hemmed parts.

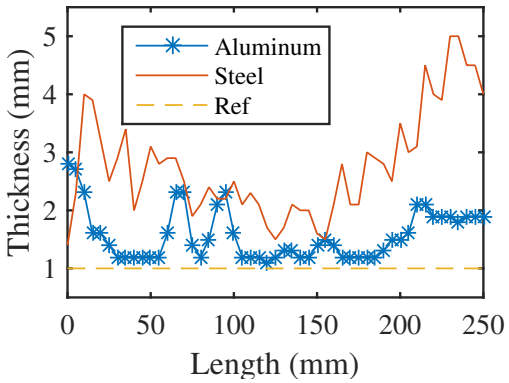

Fig. 13. Thickness vs part length.

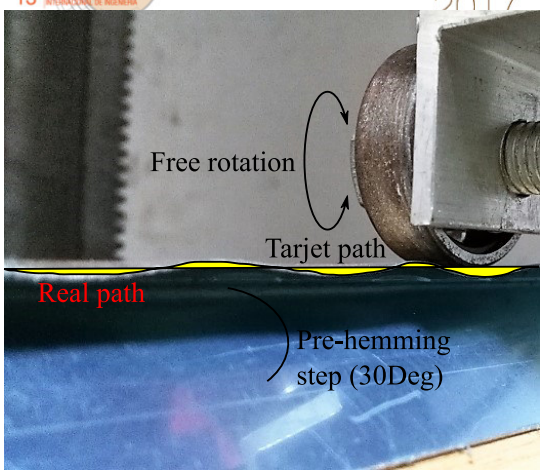

Fig. 14. Roller in contact with the sample part on a pre-hemming step.

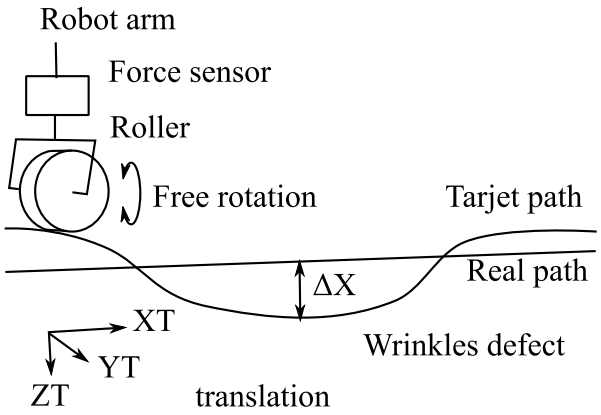

Fig. 15. Scheme of the tool path deviation.

generate a stiffness matrix with the intention of compensate the trajectory deviation, this work reported that the forces in the x and y axis is lower than the z axis of the tool end-effector for milling applications meanwhile [14] developed a compensation strategy based on finite element modeling for single point incremental forming.

V. Two approaches to correct the path deviation

A. The model based approach

We wish to propose two strategies to correct path deviation, since roll hemming is consider now a metalforming process rather than a stamping operation, different authors have worked in the tool path deviation for metalforming process, thus the models and theory of the metalforming application suits for the roll hemming process as offline compensation and online compensation. In the first model based approach the forces and path deviation are obtained from a dynamic model of the robot prior the process runs. In the second force compensation approach, the forces are used as feedback for the control loop during motion. For the first approach four stages integrate the proposed strategy as shown in figure 16. The first stage consist in setting the target path (Tp), running a FEM simulation to measure the external forces applied to the tool center point (TCP) of the robot. The second stage regards to compute the joint stiffness of the robot for the workspace concerning the process. For computing the stiffness, the more accurate, the more expensive and time consumed so, the propose should be practical and easy to implement. In the third stage, the target path, the force and the estimated joint stiffness are the input for the MBS simulation to obtain the deviation of the simulated ath respect to the target path, so a new path is adjusted until the deviation error is the minimum. For the robot, friction is not consider and links are supposed rigid. For the last stage the new path is the input for the process (without simulation) and the speed could be adjusted to reach the desired quality, this strategy relates to the strategy of [14] or [15].

B. The force compensation approach

The second strategy consists in modeling the control force loop to determine the appropriate trajectory as [13] and [12] considered in their papers. The figure 17 explains the control loop to be implemented in the robot controller. Fc is the constant force we want to apply on the sample sheet, to keep this force, a control loop established the conditions for the robot to behave. Using the force measured in the tool end effector Fi, as feedback, we may determine the increments in force ΔF, which affects the trajectory. Since $\Delta F = K\Delta X$,

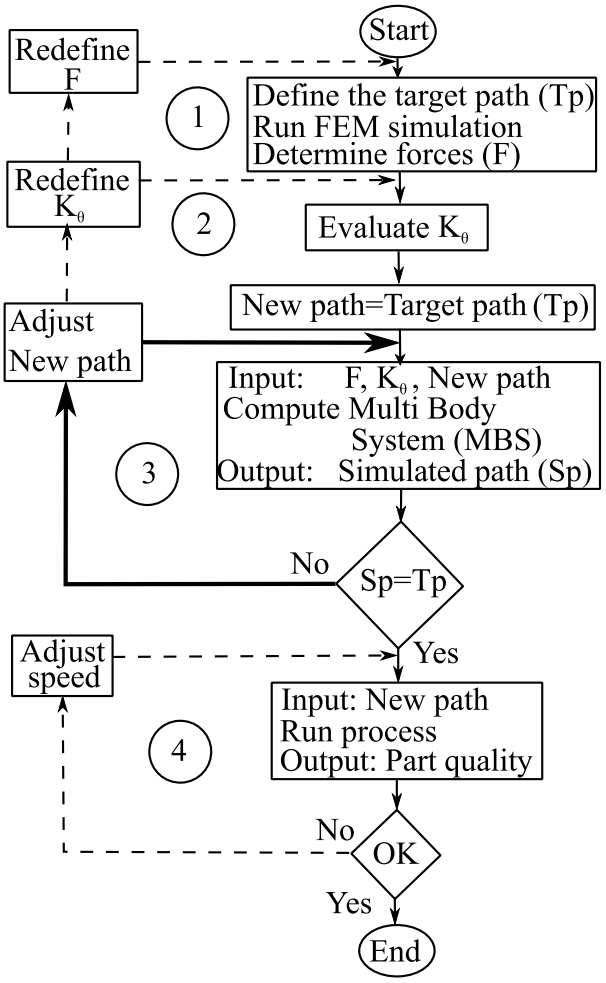

Fig. 16. The model based approach applied to roll hemming.

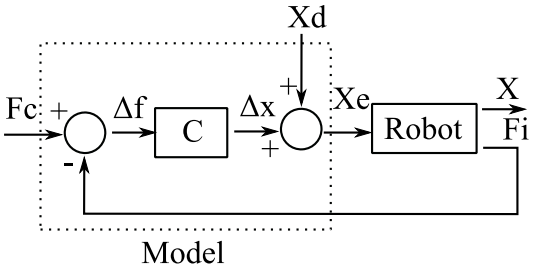

Fig. 17. The force compensation approach.

where K is the cartesian stiffness matrix, the relation between force and displacement is considered through $C = K^{-}1$. So ΔX is the increment in displacement for the trajectory. Finally, the desired trajectory Xd adds with ΔX to obtain a new trajectory Xe, which contains the information of the tool path deviation, Xe is send to the robot as the trajectory to follow. One of the issues of this strategy relays on the estimation of the cartesian stiffness matrix K, which varies for different configurations of the manipulator. Some works have been carried out to determine the values of K prior to determine the strategy, since this is a new topic of study.

VI. Discussions

In this paper we analyzed the common defects of roll hemming process, then we studied the results of different studies related with defects, which lead us to identify the main source of the tool path deviation of the robot in the process. Finally, two main approaches were proposed, an offline compensation approach and an online compensation approach, both models were proposed based on the literature research for robots in metalforming process. The first model has been applied for single point incremental forming, [14] and [15], and the second model has been applied for milling applications [12] and for stir welding [13]. So we want to remark the necesity of applying these models to the roll hemming process which lack of such a method. Probably the online compensation approach grows as a robust method than the offline approach. Also the determination of the stiffness values is a new area of study and the mapping of the stiffness requires broad experimentation and bases [16]. Future works will consider the mapping of he stiffness for the roll hemming workspace of the robot and the experimental implementation of both model approaches.

Acknowledgment

The first author wishes to gratefully acknowledge Universidad Autónoma de Querétaro through grant scholarship of Conacyt (Consejo Nacional de Ciencia y Tecnología) no. 373760/251911.

References

[1] H. Livatyali, A. Müderrisoglu, M. A. Ahmetoglu, N. Akgerman, G. L. Kinzel, T. Altan, Improvement of hem quality by optimizing flanging and pre-hemming operations using computer aided die design, Journal of Materials Processing Technology 98 (2000) 41–52. doi:10.1016/S0924-0136(99)00304-0.

[2] H. Livatyali, S. J. Larris, Experimental investigation of forming defects in flat surfaceconvex edge hemming, Journal of Materials Processing Technology 153-154 (2004) 913–919. doi:10.1016/j.jmatprotec.2004.04.425.

[3] N. Le Maoût, S. Thuillier, P. Y. Manach, Aluminum alloy damage evolution for different strain paths - Application to hemming process, Engineering Fracture Mechanics 76 (9) (2009) 1202–1214. doi:10.1016/j.engfracmech.2009.01.018.
URL http://dx.doi.org/10.1016/j.engfracmech.2009.01.018

[4] N. Le Maoût, S. Thuillier, P. Y. Manach, Classical and Roll-hemming Processes of Pre-strained Metallic Sheets, Experimental Mechanics 50 (2010) 1087–1097. doi:10.1007/s11340-009-9297-7.

[5] X. Hu, Z. Q. Lin, S. H. Li, Y. X. Zhao, Fracture limit prediction for roller hemming of aluminum alloy sheet, Materials and Design 31 (2010) 1410–1416. doi:10.1016/j.matdes.2009.08.039.

[6] S. Li, X. Hu, Y. Zhao, Z. Lin, N. Xu, Cyclic hardening behavior of roller hemming in the case of aluminum alloy sheets, Materials and Design 32 (2011) 2308–2316. doi:10.1016/j.matdes.2010.09.017.

[7] S. Thuillier, N. Le Maoût, P. Y. Manach, D. Debois, Numerical simulation of the roll hemming process, Journal of Materials Processing Technology 198 (1-3) (2008) 226–233. doi:10.1016/j.jmatprotec.2007.07.004.

[8] W.-G. Drossel, M. Pfeifer, M. Findeisen, M. Rössinger, A. Eckert, D. Barth, The influence of the robot's stiffness on roller hemming processes, in: ISR/Robotik 2014 - 45th International Symposium on Robotics, 2014, pp. 531–538.

[9] E. Esquivel, G. Carbone, D. Cafolla, M. Ceccarelli, J. Jáuregui, Forces and defects in roll hemming, Journal of Manufacturing Processes.

[10] E. Esquivel, G. Carbone, M. Ceccarelli, J. Jáuregui, Requirements and constraints for a robotized roll hemming solution, in: RAAD 2016, Springer, Belgrade, Serbia, 2017, pp. 244–251.

[11] S. El Salhi, F. Coenen, C. Dixon, M. Khan, Predicting springback using 3D surface representation techniques: A case study in sheet metal forming, Expert Systems with Applications 42 (1) (2015) 79–93. doi:10.1016/j.eswa.2014.07.041.

[12] H. Z. H. Zhang, J. W. J. Wang, G. Zhang, Z. G. Z. Gan, Z. P. Z. Pan, H. C. H. Cui, Z. Z. Z. Zhu, Machining with flexible manipulator: toward improving robotic machining performance, Proceedings, 2005 IEEE/ASME International Conference on Advanced Intelligent Mechatronics. (2005) 24–28doi:10.1109/AIM.2005.1511161.

[13] M. Guillo, L. Dubourg, Impact & improvement of tool deviation in friction stir welding: Weld quality & real-time compensation on an industrial robot, Robotics and Computer-Integrated Manufacturing 39 (2016) 22–31. doi:10.1016/j.rcim.2015.11.001.
URL http://dx.doi.org/10.1016/j.rcim.2015.11.001

[14] J. Belchior, M. Guillo, E. Courteille, P. Maurine, L. Leotoing, D. Guines, Off-line compensation of the tool path deviations on robotic machining: Application to incremental sheet forming, Robotics and Computer-Integrated Manufacturing 29 (4) (2013) 58–69. doi:10.1016/j.rcim.2012.10.008.
URL http://dx.doi.org/10.1016/j.rcim.2012.10.008

[15] H. Meier, B. Buff, R. Laurischkat, V. Smukala, Increasing the part accuracy in dieless robot-based incremental sheet metal forming, CIRP Annals - Manufacturing Technology 58 (1) (2009) 233–238. doi:10.1016/j.cirp.2009.03.056.

[16] K. Kamali, A. Joubair, I. A. Bonev, P. Bigras, Elasto-geometrical calibration of an industrial robot under multidirectional external loads using a laser tracker, in: Proceedings - IEEE International Conference on Robotics and Automation, Vol. 2016-June, 2016. doi:10.1109/ICRA.2016.7487630.

CONACYT
Consejo Nacional de Ciencia y Tecnología
CONCYTEQ

Digital image processing for plant species classification

Jaramillo-Quintanar, Severiano
Contreras-Medina, Luis Miguel
Guevara-Gonzalez, Ramon Gerardo
Torres-Pacheco, Irineo
Departamento de Investigacion y Posgrado, Facultad de Ingenieria
Universidad Autonoma de Queretaro
Queretaro, Mexico
sjaramillo10@alumnos.uaq.mx

Romero-Troncoso, Rene de Jesus
HSPdigital/CA Telematica
Division de Ingenierias Campus Irapuato - Salamanca
Universidad de Guanajuato
Salamanca, Mexico

***Abstract*—Plants are of fundamental importance to life in earth because they provide us with oxygen and food so their identification is a relevant topic. Plant leaves are present for the majority of the year and contain several characteristics that can distinguish them between different species, such characteristics cab be used to identify plants automatically. The growing interest in biodiversity and the ability to use better technologies have led to an increase in research on this topic. This work presents a novel method to extract a vector that represents the contour of a leaf, calculates its Fourier transform and uses the k-NN algorithm to classify the species of the plant. Our database consisted of 100 leaves, 25 leaves from each of the following species; tomato, radish, strawberry and cucumber. We obtained an accuracy of 88% using 75% of the leaves from the database for training and the remaining 25% for testing.**

Keywords—plant; classification; leaf; shape; contour; fft; image, k-NN.

I. INTRODUCTION

Plants are of vital importance to life in earth because they provide us with food and oxygen, among other things, so their study and understanding is necessary to improve their production, preservation and sustainability.

The traditional method to identify plant species in the field is by training taxonomy specialists who examine different plant characteristics, sometimes using guides that describe the specific characteristics of each plant species, in order to be able to determine the plant species being analyzed. This requires a specific scientific knowledge and is a big problem for most of the nature enthusiasts that want to go out and perform field studies. There is also a shortage of specialist, what is called as "taxonomic impediment" [1].

The number of plant species in the world is not known exactly. For many years botanists estimated there were from 230,000 to 270,000 plant species in the world, however recent studies [2] suggests that the number is much greater, around 421,968 plant species.

Plant leaves have been the most studied characteristic to identify plant species because they are present during a long portion of the year [3]. Other parts of the plant such as fruits and flowers are more difficult to analyze or are present for a smaller period of time [4].

Some leaf features that have been used in the past to identify plant species include different morphological features like eccentricity, aspect ratio, circularity, area, perimeter, inner distances, etc. [5]–[11]. Leaves have also been identified using Fourier descriptors [12], [13], centroid contour distance [14], [15] leaf contour [4], [16], texture [17]–[19], vein patterns [20]–[22], etc.

Among all characteristics of leaves, leaf shape is the preferred because it is the easiest characteristic to extract automatically. Also there is a great variety of techniques that can be applied to leaf shape that have already been proved to solve similar problems [23]. Leaf structure is normally preserved even if the leaf has suffered damage such as color change due to age, which would be a big problem for color based techniques.

Reference [13] uses ETF (Elliptic Fourier Transform) and suggests that 10 Fourier harmonics are enough to represent the leaf contour correctly and be able to distinguish it from other species. They used a combination of Fourier analysis and Procrustes analysis to identify species using a large database, 2420 images of leaves of 151 different species of dicotyledons collected both in Arizona, USA and Costa Rica, taken with a

flatbed scanner and reaching an accuracy of 72%. Fourier analysis was successfully combined with a radial basis probabilistic neural network (RBPNN) model to identify plant species, using a database of 1540 images of 40 different plant species the correct solution appears in the top 10 results 98.5% of the times [24].

Reference [15] realized that CCD (Centroid Contour Distance) is sensible to scaling and rotation, for that reason they normalized to tackle the first problem and applied a thinning-based method to identify consistently the beginning of the CCD points. Their algorithm was applied to 1400 samples of 140 different species of Chinese medicinal plants, reaching 75.6% of effectiveness.

Reference [4] also worked with the contour but in a different way, they draw a circle over a point in the contour to obtain a percentage of both area and perimeter of the circle that is part of the leaf. They used dataset of the 184 trees in the Northeastern United States, their system returns the 25 closer results; the correct answer appeared in the first five returned species 96.8% of the times. It is important to note that they implemented their system on an application for iOS called Leafsnap that communicates with a server where the processing takes place.

The algorithm used in [16] also worked with the contour but focused on something different, the teeth. They obtained two vectors that include information of the shape, position and quantity of leaf contour teeth and performed a series of operations to end up with only one vector that is finally the descriptor of the leaf. They understood that their algorithm was inefficient with some species but can be improved adding another descriptor that takes into account the whole leaf contour.

A combination of shape and texture features was implemented by [17]. Using a database of 3 to 10 leaves from 18 different plant species collected in the Royal Botanic Gardens, Kew, UK, they obtained a successful classification rate of 81.1%.

This work presents an algorithm to automatically classify plant species based on their contour. The database consists of 100 leaf images from 4 different species, taken with a scanner. We use only one feature vector extracted from the directions obtained from clockwise traveling the leaf contour, then apply FFT to that vector to obtain what we call leaf signature. This leaf signature is the input to the k-NN algorithm used to classify the plant species.

II. Materials

We used 100 leaf images, 25 of each of the following species; strawberry, cucumber, tomato and radish. The leafs were collected in two sessions from greenhouses located at the Campus Amazcala, from Universidad Autonoma de Queretaro. Leaves without damage were selected to improve the accuracy of the algorithm.

The images of the leaves were taken the same day the leaves were collected, to avoid damage. We used a HP scanner model ScanJet 3400C to obtain the images, removing the stalks and placing the leaves in the center of the scanner. A scanner was selected to avoid errors due to scaling, light and background noise.

The scanner resolution used was 150 DPI (Dots Per Inch) and the size of the images equal to 1062x1062 pixels.

III. Method

The proposed method for this project can be divided into four major stages, image acquisition, pre-processing, feature extraction and classification. In the pre-processing stage the image is converted from RGB to gray scale and then binarized to black and white using segmentation. The feature extraction uses segmented images to obtain a vector representing the contour of the leaf and calculates the FFT of such vector. Finally, the FFT vector became the input to the k-NN algorithm, used as classifier.

A. *Image acquisition*

The first step is the image acquisition, and if that step fails all the other steps will be useless. In this step, leaves in good conditions have to be collected, taking care of not having damage due to age, insects or any other reason. Then, the stalks of the leaves have to be carefully removed because the stalk could introduce noise to the following steps.

Once the leaves have been carefully selected and stalks cut, they are placed one by one vertically, meaning the stalk faces down, and centered over the scanner, then images of all leaves are taken and saved into a database for use in future steps.

B. *Pre-processing*

Although images were taken with a scanner, a pre-processing stage was necessary to adequate the images for the needs of the feature extraction stage.

First, to convert the images from RGB to gray scale we were using a simple average calculated using "(1)", however we noted that there was some information loss on the next step (segmentation) due to this conversion and found that taking only the value of the blue component instead of an average of the three components gave better results. This can be observed on Fig. 1.

$$P = \frac{R+G+B}{3} \tag{1}$$

were R, G and B representing the red, green and blue component colors intensities respectively of each pixel in the input image and P the value of the pixel in the gray scale output image.

The gray scale image was then converted to a binary image using the Otsu method, also called global thresholding technique [25]. This method is used to segment an image when there are two objects with remarkably different pixel intensities, the histogram of the image is calculated and the value of the valley between the two peaks is used as the segmentation threshold.

Finally, a closure operation (dilatation followed by an erosion) was used to eliminate possible dots outside the leaf caused by dust and other unwanted particles.

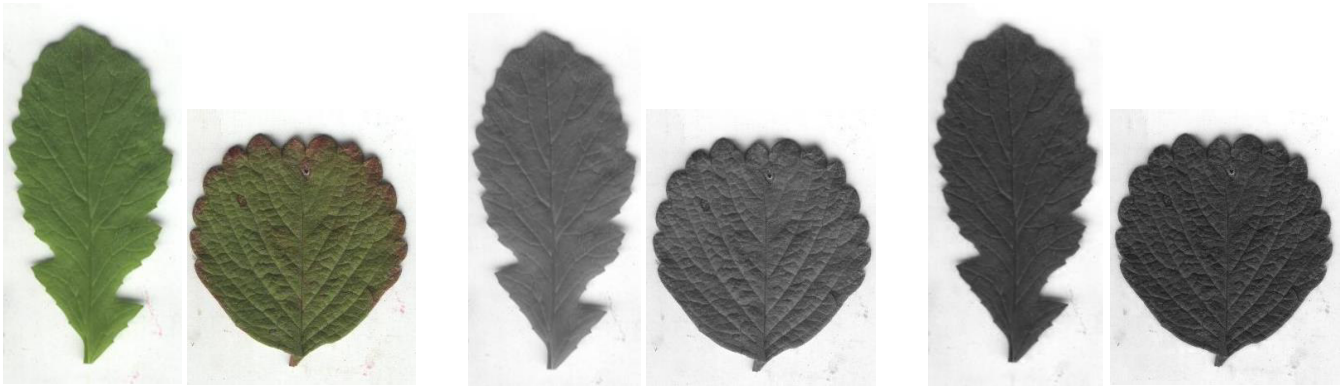

a) b) c)

Fig. 1. Example of convertion from RGB to gray with two methods. a) Original images, b) Gray scale images using intensity average of the R, G and B components, c) Gray scale images using the B component only.

C. *Feature extraction*

We proposed a novel method to extract a feature vector that represents the contour of the leaf. Our algorithm first searches the binary image until it finds a starting point on the contour's leaf. This point will be a black pixel next to a white pixel, because black points represent the leaf and white points represent the background. Once the starting point has been found, the algorithm travels the contour of the leaf in a clockwise direction until it reaches the initial point, saving into a vector the directions in which to move according to the directions diagram on Fig. 2.

Using Fig. 3 as an example for the feature vector extraction and starting on the pixel with the asterisk symbol, the next pixel in a clockwise direction is upright and according to the directions on Fig. 2 it corresponds to a value of 2, therefore 2 is saved to our feature vector. The next pixel is also upright so a value of 2 is saved, the following pixel is now to the right and a value of 3 is saved. Next pixel is downright so a value of 4 is saved. Therefore, if we start on the pixel with the red asterisk symbol and finish on the pixel with the number sign symbol the resulting vector would be [2, 2, 3, 4, 2, 4, 3, 4, 3, 4, 4, 5].

As mentioned, the algorithm described on the previous paragraph ends at the point where it started, traversing the whole contour of the leaf.

After extracting feature vectors from many leaf images, we found that none of these vectors had more than 2^12 or 4096 values, therefore we zero padded the resulting vectors to get a uniform length of 4096 values to avoid errors during the classification phase due to differences or variations in vectors' length.

Finally, the Fourier transform of the feature vector was calculated using the FFT (Fast Fourier Transform) to obtain what we call the leaf signature. The resulting FFT is normalized in amplitude to minimize errors due to different scales between different leaf signatures.

D. *Classification*

Many approaches have been used to classify plant species in previous works like radial basis probabilistic neural network [24], probabilistic neural networks [26], MMC hypersphere classifier [27], support vector machine, etc. We used the k-Nearest Neighbors algorithm because it is a simple, lightweight and easy to implement yet very efficient classifier. It is in fact the simplest machine learning classifier. We used it to test our feature extraction algorithm.

An important feature of the k-NN algorithm is that the number of neighbors (k) can be varied to find the best one according to the current application.

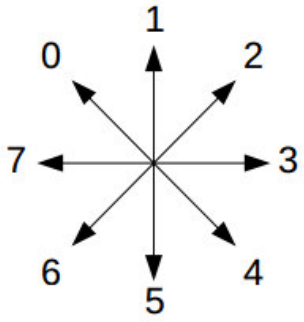

Fig. 2. Directions diagram that indicates the value to save in the feature vector, according to the direction of the next pixel in a clockwise direction.

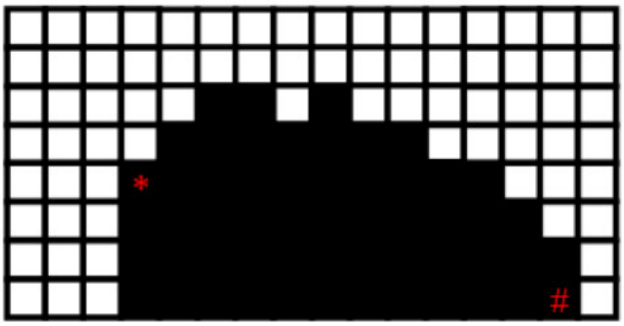

Fig. 3. Example of feature vector extraction.

Simply put, the k-NN algorithm classifies unknown data points by finding the most common class among the k-closest examples. Each data point in the k closest examples casts a vote and the category with the most votes wins [28].

IV. Results

From the total dataset of 25 leaves of four different species, totaling 100 leaves, we used 75% or 75 random images to train the algorithm and the other 25% or 25 images to test that it classifies correctly.

We did many experiments changing the number of neighbors in the classifier and the resultant accuracy can be observed on Table 1. It can be seen that the best accuracy is reached when the number of neighbors is one two or three, then the accuracy goes down to 76% for 6 neighbors. If we continue incrementing the number of neighbors the accuracy improves a little bit reaching 84% with 10 neighbors. After that, if we continue adding the number of neighbors the accuracy begins to decay again.

Although the efficiency of our algorithm is not as accurate as [4], [24] it is better than [13], [15], [17]. We think that the accuracy decreases when increasing the number of neighbors due to the great amount of variation between leaves of the same species and the similarities of leaves from different species. A very efficient way to improve the accuracy is to increase the amount of leaves on our dataset. Also, another way to increase our accuracy is to use a more robust classifier and include more features that can be obtained from the binarized leaf like perimeter, area, roundness, contour-centroid distance, etc.

V. Conclusion and Future Work

Our algorithm reached a classification accuracy of 88%, which is around the average of the best accuracies of the most recent works, using a small database for training and a fairly simple classifier, this implies that our feature extraction algorithm is a very discriminant feature between leaves of different species and we could improve the accuracy without making the procedure too complicated.

TABLE I. Number of Neighbors vs. Accuracy

Number of Neighbors [k]	Classification Accuracy
1	88%
2	88%
3	88%
4	84%
5	84%
6	76%
7	80%
8	80%
9	80%
10	84%

For future work, we are planning to extract more features from the leaf image like perimeter, area, contour-centroid distance and aspect ratio and apply more than one classifier like probabilistic neural networks and support vector machine to present a comparison between such classifiers.

We are also planning to use a different dataset, different varieties of the same species, where the leaf differences are hardly noticeable by the naked eye.

Acknowledgment

We would like to thank CONACYT for the scholarship number 4999910/574230 and the Universidad Autonoma de Queretaro for providing the infrastructure and support to perform this research.

References

[1] M. R. Carvalho *et al.*, "Taxonomic Impediment or Impediment to Taxonomy? A Commentary on Systematics and the Cybertaxonomic-Automation Paradigm," *Evol. Biol.*, vol. 34, no. 3–4, pp. 140–143, 2007.

[2] D. Bramwell, "How many plant species are there?," *Plant Talk*, vol. 28, pp. 32–34, 2002.

[3] A. Aakif and M. F. Khan, "Automatic classification of plants based on their leaves," *Biosyst. Eng.*, vol. 139, pp. 66–75, 2015.

[4] N. Kumar *et al.*, "Leafsnap: A Computer Vision System for Automatic Plant Species Identification," *Lect. Notes Comput. Sci.*, vol. 7573 LNCS, no. PART 2, pp. 502–516, 2012.

[5] R. J. Jensen, K. M. Ciofani, and L. C. Miramontes, "Lines, outlines, and landmarks: Morphometric analyses of leaves of Acer rubrum, Acer saccharinum (Aceraceae) and their hybrid," *Taxon*, vol. 51, no. 3, pp. 475–492, 2002.

[6] H. Ling and D. W. Jacobs, "Shape Classification Using the Inner-Distance," *IEEE Trans. Pattern Anal. Mach. Intell.*, vol. 29, no. 2, pp. 286–299, 2007.

[7] D. P. A. Corney, J. Y. Clark, H. Lilian Tang, and P. Wilkin, "Automatic extraction of leaf characters from herbarium specimens," *Taxon*, vol. 61, no. 1, pp. 231–244, 2012.

[8] A. Femat-Diaz, D. Vargas-Vazquez, E. Huerta-Manzanilla, E. Rico-Garcia, and G. Herrera-Ruiz, "Scanner image methodology (SIM) to measure dimensions of leaves for agronomical applications," *African J. Biotechnol.*, vol. 10, no. 10, pp. 1840–1847, 2011.

[9] L. H. Ma, Z. Q. Zhao, and J. Wang, "ApLeafis: An Android-based plant leaf identification system," in *Lecture Notes in Computer Science (including subseries Lecture Notes in Artificial Intelligence and Lecture Notes in Bioinformatics)*, 2013, vol. 7995 LNCS, pp. 106–111.

[10] C. L. Lee and S. Y. Chen, "Classification of leaf images," *Int. J. Imaging Syst. Technol.*, vol. 16, no. 1, pp. 15–23, 2006.

[11] S. M. White, D. Marino, and S. Feiner, "Designing a mobile user interface for automated species identification," *Proc. ACM CHI 2007 Conf. Hum. Factors Comput. Syst.*, vol. 1, pp. 291–294, 2007.

[12] J. C. Neto, G. E. Meyer, D. D. Jones, and A. K. Samal, "Plant species identification using Elliptic Fourier leaf shape analysis," *Comput. Electron. Agric.*, vol. 50, no. 2, pp. 121–134, 2006.

[13] D. J. Hearn, "Shape analysis for the automated identification of plants from images of leaves," *Taxon*, vol. 58, no. 3, pp. 934–954, 2009.

[14] C. Meade and J. Parnell, "Multivariate analysis of leaf shape patterns in Asian species of the Uvaria group (Annonaceae)," *Bot. J. Linn. Soc.*, vol. 143, no. 3, pp. 231–242, 2003.

[15] Z. Wang, Z. Chi, and D. Feng, "Shape based leaf image retrieval," *IEE Proceedings - Vision, Image, and Signal Processing*, vol. 150, no. 1. pp. 34–43, 2003.

[16] G. Cerutti, L. Tougne, D. Coquin, and A. Vacavant, "Leaf margins as sequences: A structural approach to leaf identification," *Pattern Recognit. Lett.*, vol. 49, pp. 177–184, 2014.

[17] T. Beghin, J. S. Cope, P. Remagnino, and S. Barman, "Shape and texture based plant leaf classification," *Adv. Concepts Intell. Vis. Syst.*, vol. 6475, pp. 345–353, 2010.

[18] Z.-Q. Zhao, L.-H. Ma, Y. Cheung, X. Wu, Y. Tang, and C. L. P. Chen, "ApLeaf: An efficient android-based plant leaf identification system," *Neurocomputing*, vol. 151, pp. 1112–1119, 2015.

[19] S. Prasad, P. Kumar, and R. C. Tripathi, "Plant leaf species identification using curvelet transform," *2011 2nd Int. Conf. Comput. Commun. Technol.*, pp. 646–652, 2011.

[20] J. Clarke *et al.*, "Venation Pattern Analysis of Leaf Images," *Lect. Notes Comput. Sci.*, vol. 4292, pp. 427–436, 2006.

[21] H. Fu and Z. Chi, "Combined thresholding and neural network approach for vein pattern extraction from leaf images," *IEE Proceedings - Vision, Image, and Signal Processing*, vol. 153, no. 6. pp. 881–892, 2006.

[22] Y. Nam, E. Hwang, and D. Kim, "A similarity-based leaf image retrieval scheme: Joining shape and venation features," *Comput. Vis. Image Underst.*, vol. 110, no. 2, pp. 245–259, 2008.

[23] J. S. Cope, D. Corney, J. Y. Clark, P. Remagnino, and P. Wilkin, "Plant species identification using digital morphometrics: A review," *Expert Syst. Appl.*, vol. 39, no. 8, pp. 7562–7573, 2012.

[24] J. Du, D. Huang, X. Wang, and X. Gu, "Shape Recognition Based on Radial Basis Probabilistic Neural Network and Application to Plant Species Identification," in *Lecture Notes in Computer Science*, 2005, vol. 3497, no. II, pp. 281–285.

[25] R. Gonzalez and R. E. Woods, *Digital image processing*, 3rd ed. Prentice Hall, 2008.

[26] S. G. Wu, F. S. Bao, E. Y. Xu, Y. Wang, Y. Chang, and Q. Xiang, "A Leaf Recognition Algorithm for Plant Classification Using Probabilistic Neural Network," *Int. Symp. Signal Process. Inf. Technol.*, pp. 11–16, 2007.

[27] J.-X. Du, X.-F. Wang, and G.-J. Zhang, "Leaf shape based plant species recognition," *Appl. Math. Comput.*, vol. 185, no. 2, pp. 883–893, 2007.

[28] A. Rosebrock, "k-NN classifier for image classification," 2016. [Online]. Available: http://www.pyimagesearch.com/2016/08/08/k-nn-classifier-for-image-classification/.

FPGA-based sensor for real-time measurement of water content of plant leaves based on turgor pressure

Alan Ríos-Romero
Dirección de Investigación y Posgrado, Facultad de Ingeniería
Universidad Autónoma de Querétaro
Santiago de Querétaro, México
alanrios88@hotmail.com

Luis Miguel Contreras-Medina
C.A Ingeniería de Biosistemas. División de Investigación y Posgrado, Facultad de Ingeniería
Universidad Autónoma de Querétaro
Santiago de Querétaro, México
mcontreras.uaq@gmail.com

***Abstract*— The water has become the most precious natural resource in many areas and the agriculture is the main consumer, so that, it is important to improve the efficiency of water use in agriculture, especially in irrigation and monitoring systems. Regulated deficit irrigation (RDI) is an irrigation strategy that is based on maintaining the water status of the plant within the limits of stress. This paper presents the information about the development of a sensor based on the most efficient method of plant monitoring, and for which a successful RDI can be satisfied.**

Keywords*— irrigation systems, plants, turgor, water.

I. INTRODUCTION

Global climate change has been predicted to increase as a result of extreme weather events such as droughts, aberrant rains, rising temperatures, heat waves and greenhouse gasses [1]. The crop will be destined to occur in safer climates, due to extreme climatic conditions and a decrease of arable land [2].

One of the main current limiting factors for crop production is the availability of water, which could be a problem in predicted scenarios of climate change and the where the human population is increasing [3], [4].

Demographic changes in the world are increasing the pressure on the use of water resources. In 1950, the world population was 2.534 million people, while for 2005 it had increased to 6.515 million. The United Nations (UN) estimates that in the next 20 years, the world's population will increase by approximately 2 billion people, which will live predominantly in urban areas of developing countries. As a result of this trend, the UN estimates that in the next 20 years 60 percent more water will be required to be used for agricultural purposes to feed the entire world population.

According to the United Nations, agriculture uses three-quarters of the water consumed globally, people to produce the food requires different amounts of water. For example, to produce one kilogram of maize requires 900 liters of water; For one kilogram of wheat 1,300 liters of water and for one kilogram of rice 3,400 liters of water. On the other hand, 15,500 liters of water are needed to produce one kilogram of beef, which includes the water that drinks the beef throughout its life and the water required to grow the grains that serve as food.

The water use is distributed disproportionately, as agricultural activity consumes more water. According to INEGI, in Mexico 77% of the water is used for agriculture, 14% for public supply, 5% is used to produce electricity (thermoelectric) and 4% in industry. It is estimated that to produce a potato (about 100 g) 25 L is needed, to produce a tomato (about 70 g) requires 13 L and to produce an apple are required (100 g) 70 L [5].

In Mexico and around the world it is essential to continue improving the efficiency of water use in agriculture, as well as to promote its use in a sustainable way [6]. It is also essential to expand the coverage of technology-based irrigation systems to achieve more productivity principally to rural communities [7].

Several works manage the term regulated deficit irrigation (RDI), that depends on accurate monitoring of soil moisture and water stress in plants, and requires the ability to water "little and frequent" on demand [8]. If the plant is maintained in ranges according to RDI the efficiency of use of the water in agriculture will increase, so that, it is necessary to develop systems that allow knowing precisely the water status of the plant, as this would allow being closer to the RDI.

II. WATER STRESS IN PLANTS

Stress is described as a significant deviation from the optimum conditions for life [9], there is several kind os stress of plants, One of the most important is water stress, which causes a

decrease of crop yield [10]. Water stress is caused by many factors, one of them occurs when demand for water exceeds the available, and it is also important to the proper distribution of water resources in crops [11].

Other important point during the plant development is to provide water to the plant during critical periods for limiting the duration of water stress, it is also necessary to provide, depending on the area in which it is only the water required in the specific areas of cultivation, avoiding wastage water and reducing the risk of disease due to excess water accumulated. In conclusion, we can say that plants are more sensitive to drought stress during certain periods of growth, so that water use not only depends on the total water used at the end of the crop cycle, but the water used for different growth stages [12].

On the other hand, has been shown to have an irrigation system allows a higher evapotranspiration, as this makes the plants are not too get stressed with rainwater, in the case of crops in the open, scarce or poorly distributed, which is another problem in Mexico, since often the irrigation is done by time, which, due to the irregularity of the soil makes in certain areas water accumulates and other areas quickly filtered.

III. Regulated Deficit Irrigation (RDI).

Agriculture needs performance strategies that maximize water efficiency, maintaining as far as possible, acceptable levels of production and harvest quality. Under this scenario, it is of great interest to know the response of crops to drought stress. Regulated deficit irrigation (RDI) has been consolidated as a strategy that promotes water-saving. It is based on reducing water inputs in those phenological periods in which a deficit does not affect production or quality, covering the water needs of the plant during the rest of the crop cycle [13].

The RDI, besides achieving a certain water saving, can improve fruit quality [14], [15]. However, the effect of RDI on post-harvest conservation is unknown.

The main objectives of RDI are to maximize water productivity [16], [17] and to stabilize production [12].

The RDI is based on the idea of reducing or even suppressing when rains provide a certain amount of moisture in the soil [18]. RDI is generally applied in those stages of the crop cycle where the reproductive growth is relatively slow and vegetative growth and other plant processes can be affected, often resulting in improved fruit quality [19].

Numerous authors have confirmed that RDI improves the physical and chemical characteristics of the fruit in a large number of fruit species, such as mandarin [20], lemon [13], mango tree [21], apple tree [22], peach [23], olive [24], and many others.

However, it also presents some limitations that may condition its success, such as: requiring a precise knowledge of crop response to water deficit [25]; The need to dispose of the necessary water both in critical periods and during the rest of the cycle, which is not always possible during periods of water scarcity [12], [17], [18].

It should also be noted that these types of strategies are not advisable in young trees since the main objective in this type of plantations is to maximize the growth so that the trees reach the adult state as soon as possible, which implies avoiding any water deficit at any time [19], [26].

IV. Methods of measuring water content

A. *Evapotranspiration*

Evapo transpiration is known as the combination of two separate processes by which water is lost through the surface of the soil, by evaporation and on the other hand by transpiration of the crop [27]. Therefore the calculation of evapotranspiration is used to know the water that plants need for their proper development, [27][28].

Plants for their growth need water and other nutrients they take from the soil through the roots, carbon dioxide (CO2) they take from the air through their leaves and a source of energy that is sunlight. The two sources of water used by plants are rain and irrigation, to get CO2 from the atmosphere; plants open their stomata, microscopic pores on the surface of the leaves. Once water and CO2 are available for plants, photosynthesis is produced on leaves by which plants synthesize glucose from water, CO2 and sunlight. Liquid water that evaporates from the leaf surface and from the soil surface requires a lot of energy [27].

Water vapor occurs at the contact surface between water and air producing vapor around the surface. Evapotranspiration is continuous as long as the three conditions mentioned above are maintained [29]. Although evapotranspiration can be measured using measuring devices such as lysimeters, the measurement process is long and costly, so its estimation is much more frequent based on empirical and analytical equations [30].

The climate, the characteristics of the crop, the management and the means of development are factors that affect evaporation and perspiration.

B. *Photosynthesis*

The most used method for measuring photosynthesis is based on the measurement of the gas exchange (CO2 - O2) that occurs during the process and the measurement is performed on one of the two gasses [31].

According to [32], there are different methods to measure photosynthesis, which are described as destructive and non-destructive, among the destructive ones is the dry matter method and the isotopic method, which cause the partial or total destruction of the leaf that is measuring. In non-destructive methods, we have electrochemical, acoustic and chlorophyll measurement methods.

C. Soil Moisture and Matric Potential

When a plant grows, it uses water around the roots of the plant and a method to calculate the hydric status of water around it, is by measuring or estimating soil moisture.

There are many methods of measuring soil moisture, which are divided into direct and indirect, among the direct we have the gravimetric method, this method takes direct samples of the soil however it has a long response time, high cost and destruction of the plant. We also have Time domain reflectometry (TDR) and neutron sprinklers that, like the previous one, are good but they are very expensive measuring instruments [33].

Among the indirect methods for the measurement of soil moisture, we have tensiometers, resistance blocks and the thermocouple psychrometer, which have a slow response of the measurement [33]. Matric potential is the one that generates the mechanisms of retention of the water of the soil, denominated mechanisms of adhesion and cohesion[34].

When more dry is the substrate, greater pressure to be applied to extract the nutrient solution and therefore more energy the plant has to use to extract it. Research from [35] mentions that an automatic irrigation system based on soil moisture and metric potential are a good combination to save water.

D. Turgor

The measuring principle turgidity, consists of a magnetic probe [36] is quite simple and is little used as a "compartment of artificial detection" to measure relative changes turgor pressure throughout the leaf tissue. Detection is accomplished by holding an intact leaf between two flat circular pads (metal or plastic). The pads are composed by two magnets but this is not an indispensable requirement. A pad contains a receptacle which is integrated into the pressure sensor chip coated with a polymeric substance-stained blue dye. The magnet anti-pad contains an internal thread which could be moved along a threaded rod. Varying the distance between the mobile magnets allows adjusting the applied magnetic force.

The ZIM-probes are connected by cable to a transmitter, environmental data is sent by the wireless transmitter over a distance of up to 1500 m to a controller. The controller contains a GPRS modem that is linked to an Internet server via the local mobile phone network. From the server data, they can be downloaded by smartphones, tablets or laptops. Therefore, the water status of the leaves is available to the user in real time and the manager can make decisions culture adequate irrigation, based on the needs of the plant [37].

However, this kind of devices are principally applied to trees or plant that majorly contains flat leaves. The system is difucult to be adapted to a plant with venation, per example the poinsetia, or vegetables such as rabbit and pepper, etc.

V. Material and Methods

According to the previous information, it was determined that the measurements with the turgor sensor is the most efficient method to determine the amount of water in the plants, because of its rapid response, as well as being efficient to control the RDI of the plants.

A. Turgor Measurements

The results presented demonstrate that the LPCP probe is an accurate, non-invasive and robust technique for online monitoring of changes in leaf water status [38]. The high-resolution LPCP probes can also be seen from the rapid response of pressure values to exposure to the wind [39].

The previous findings highlight that the probe LPCP is a powerful tool for the management and improvement of irrigation. The remote determination of the water supply of the leaves in optimum conditions in real time, obviously, opens the great possibility of an application of a system of irrigation to the greenhouse.

TABLE I. TECHNICAL DATA OF MS5803-14BA

Sensor Performances (V_{DD} = 3 V)				
Pressure	**Min**	**Typ**	**Max**	**Unit**
Range	0		14	bar
ADC		24		bit
Resolution (1)		1 / 0.6 / 0.4 / 0.3 / 0.2		mbar
Accuracy 0°C to +40°C, 0 to 6 bar (2)	-20		+20	mbar
Accuracy -40°C to + 85°C 0 to 6 bar (2)	-40		+40	mbar
Response time		0.5 / 1.1 / 2.1 / 4.1 / 8.22		ms
Long term stability		-20		mbar/yr
Temperature	**Min**	**Typ**	**Max**	**Unit**
Range	-40		+85	°C
Resolution		<0.01		°C
Accuracy	-0.8		+0.8	°C
Notes: (1) Oversampling Ratio: 256 / 512 / 1024 / 2048 / 4096 (2) With autozero at one pressure point				

B. Plant Material

The experiment was carried out on specimens of *Euphorbia pulcherrima* commonly known in Mexico as a Noche Buena. The sensor was placed on the leaves of the plant that had the same size and height in the stem between 10.00 and 16.00 h (central Mexico time). The sensor was placed at 2cm from the tip of the leaf near the main vein.

C. Turgor Sensor

The sensor allows to make pressure measurements up to 14 bars (1400 kPa), the technical data is shown in table 1. The

sensor used is the MS5803-14BA in its miniature version and can be seen in figure 1, the MS5803-14BA consist in a piezo-resistive sensor, in addition, it should be emphasized that any other device can operate in the same way. The pressure sensor is mounted on one end of a press forged in industrial steel to hold the blade. The press forged in industrial steel consists of a screw that presses on itself, and the pressure exerted on the blade can be varied depending on the screw.

The sensor is embedded inside a plastic cylinder for further fixation and a sticking sponge is placed to prevent mistreatment of the blade.

The calibration of the pressure sensors was carried out by means of a pressurizing inside a pressure chamber equipped with a pressure pattern

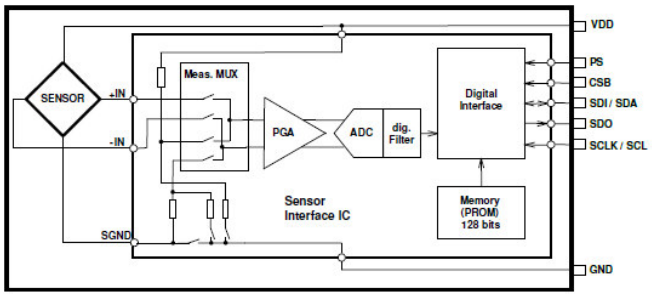

Fig. 1. Block Diagram of MS5803-14BA.

In figure 2 we can see the flow diagram of the pressure sensor, this consists of six variables to measure the pressure and temperature.

The pressure sensor signal with the forged press transmits the sensor data via serial communication to a personal computer for the analysis and storage of files.

D. Experiment Setup

In this section we will configure the experiment, as already mentioned, the sensor was placed 2cm from the tip of the leaf near the main vein at a pressure of approximately 900 mbar for a certain time, after a couple of hours, the plant was placed water to see the pressure change in the leaves of the plant. The sensor works by means of an SPI communication protocol that is generated in an FPGA, it takes the data and sends it to a computer approximately every 2 sec, in order to be able to see if there is a rapid change in the pressure of the leaves.

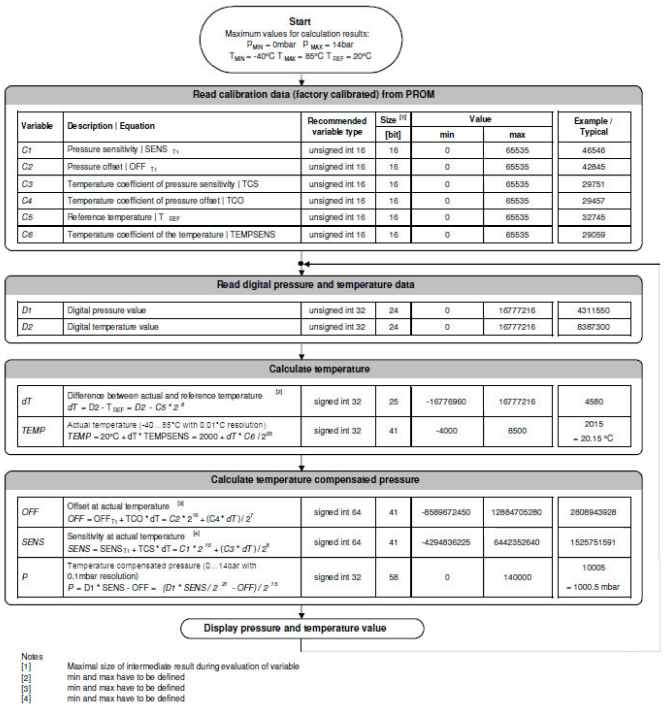

Fig. 2. Flow chart for pressure and temperature reading and software compensation.

VI. Results and Discussion

According to the results obtained in figure 3, the pressure at the beginning of the experiment is shown high but over time this pressure decreases until it is almost at a stable point, at which point water was placed at the plant at night Good. The red part of the graph shows how the pressure increases because of water, eventually, the pressure drops back down to a stability point.

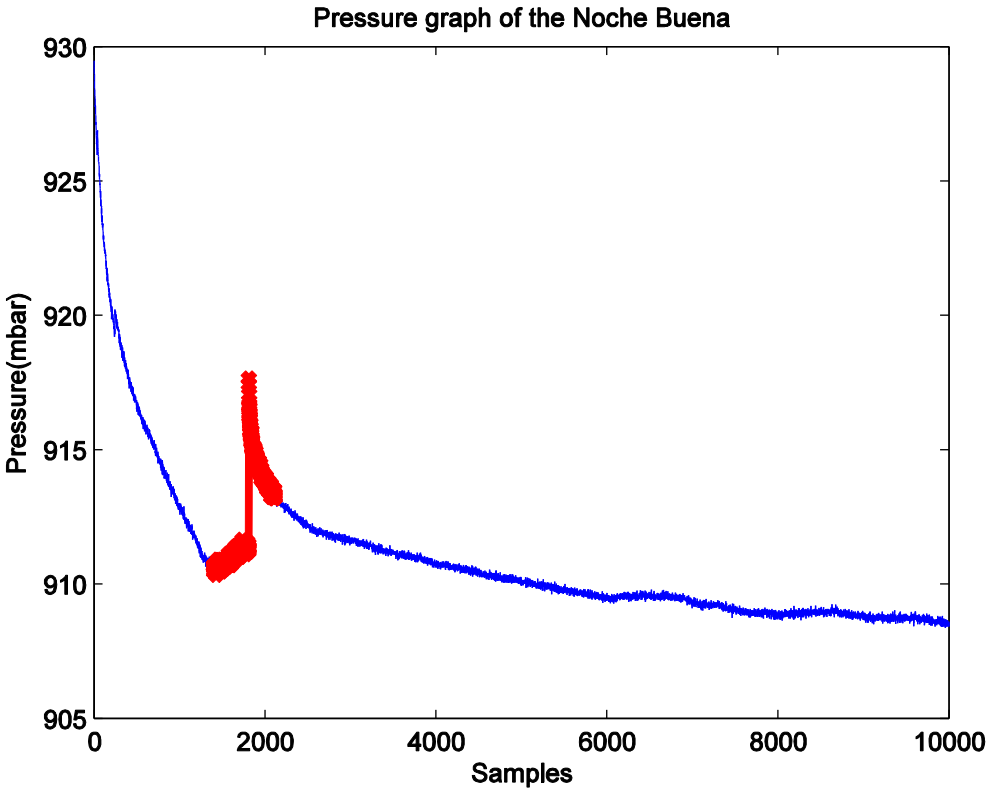

Fig. 3. Pressure grapg of the Noche Buena.

VII. Conclusion

The results show that the device is a sensitive tool and easy to use to monitor the plant. The device is always in an initial pressure condition, which causes the measured data to be those of the pressure change in the leaf. With this, we can monitor any crop with the least amount of water to obtain a higher yield in the final production.

The result is important because the device meets the requirements of a good RDI, which was to monitor the amount of water in the plants constantly. In addition, this device is inexpensive and easy to use, without mentioning that a smooth surface is not necessary in the leaf to make the measurements thanks to the adhesive sponge that we place to the sensor.

Although more work is needed on this device, the results showed that it is a promising and interesting device to be able to implement a suitable irrigation to any plant under the RDI concepts.

Acknowledgment

Special acknowledgment to CONACYT (Consejo Nacional de Ciencia y Tecnología), for the economic and technical support, also to the Engineering Faculty of Universidad Autónoma de Querétaro, México.

References

[1] C. Rosenzweig, A. Iglesius, P. R. Epstein, and E. Chivian, “Climate change and extreme weather events - Implications for food production , plant diseases , and pests,” *Glob. Chang. Hum. Heal.*, vol. 2, no. 2, pp. 90–104, 2001.

[2] J. Schmidhuber and F. N. Tubiello, “Global food security under climate change.,” *Proc. Natl. Acad. Sci. U. S. A.*, vol. 104, no. 50, pp. 19703–19708, 2007.

[3] D. Tilman, K. G. Cassman, P. A. Matson, R. Naylor, and S. Polasky, “Agricultural sustainability and intensive production practices.,” *Nature*, vol. 418, no. 6898, pp. 671–7, 2002.

[4] H. C. J. Godfray, J. R. Beddington, I. R. Crute, L. Haddad, D. Lawrence, J. F. Muir, J. Pretty, S. Robinson, S. M. Thomas, and C. Toulmin, “Food Security: The Challenge of Feeding 9 Billion People,” *Science (80-.).*, vol. 327, no. 5967, pp. 812–818, 2010.

[5] INEGI, "Usos del agua en México." [Online]. Available: http://cuentame.inegi.org.mx/territorio/agua/usos.aspx?tema=T. [Accessed: 28-Feb-2017].

[6] M. Westhoff, R. Reuss, D. Zimmermann, Y. Netzer, A. Gessner, P. Geßner, G. Zimmermann, L. H. Wegner, E. Bamberg, A. Schwartz, and U. Zimmermann, "A non-invasive probe for online-monitoring of turgor pressure changes under field conditions," *Plant Biol.*, vol. 11, no. 5, pp. 701–712, 2009.

[7] H. G. Jones, "Irrigation scheduling: Advantages and pitfalls of plant-based methods," *J. Exp. Bot.*, vol. 55, no. 407, pp. 2427–2436, 2004.

[8] Dry Peter, "Estrategias para el manejo del déficit de riego de forma de maximizar el uso del agua y la calidad del vino en Australia." 2009.

[9] M. Basurto Sotelo, a. Núñez Barrios, R. Pérez Leal, and O. a. Hernández Rodríguez, "Fisiología del Estrés ambiental en plantas," *Synthesis (Stuttg).*, pp. 1–5, 2008.

[10] M. Florido and L. Bao, "Revisión bibliográfica TOLERANCIA A ESTRÉS POR DÉFICIT HÍDRICO EN TOMATE (Solanum lycopersicum L .) Review Water stress tolerance in tomato (Solanum lycopersicum L .)," vol. 35, no. 3, pp. 70–88, 2014.

[11] G. Monforte and P. Cantú, "//Recursos Hídricos," no. 30, pp. 31–40, 2009.

[12] H. Zhang and T. Oweis, "Water-yield relations and optimal irrigation scheduling of wheat in the Mediterranean region," *Agric. Water Manag.*, vol. 38, no. 3, pp. 195–211, 1999.

[13] A. Domingo, R., Ruiz-Sánchez, M.C., Sánchez-Blanco, M.J. y Torrecillas, "Water relations, growth and yield of Fino lemon trees under regulated deficit irrigation," *Irrig. Sci.*, 1996.

[14] P. G.-A. y J. R. Castel, "Riego Deficitario Controlado en Clementina de Nules y Navel Lane Late : Producción y calidad de la fruta .," *Spanish J. Agric. Res.*, vol. 1, pp. 198–202, 2003.

[15] J. G. Pérez-Pérez, J. M. Robles, and P. Botía, "Influence of deficit irrigation in phase III of fruit growth on fruit quality in 'lane late' sweet orange," *Agric. Water Manag.*, vol. 96, no. 6, pp. 969–974, 2009.

[16] E. Fereres and R. G. Evans, "Irrigation of fruit trees and vines: An introduction," *Irrig. Sci.*, vol. 24, no. 2, pp. 55–57, 2006.

[17] E. Fereres and M. A. Soriano, "Deficit irrigation for reducing agricultural water use," *J. Exp. Bot.*, vol. 58, no. 2, pp. 147–159, 2007.

[18] S. Geerts and D. Raes, "Deficit irrigation as an on-farm strategy to maximize crop water productivity in dry areas," *Agric. Water Manag.*, vol. 96, no. 9, pp. 1275–1284, 2009.

[19] M. C. Ruiz-Sanchez, R. Domingo, and J. R. Castel, "Review. Deficit irrigation in fruit trees and vines in Spain," *Spanish J. Agric. Res.*, vol. 8, no. S2, p. 5, 2010.

[20] J. S. Verreynne, E. Rabe, and K. I. Theron, "The effect of combined deficit irrigation and summer trunk girdling on the internal fruit quality of 'Marisol' Clementines," *Sci. Hortic. (Amsterdam).*, vol. 91, no. 1–2, pp. 25–37, 2001.

[21] W. Spreer, M. Nagle, S. Neidhart, R. Carle, S. Ongprasert, and J. Müller, "Effect of regulated deficit irrigation and partial rootzone drying on the quality of mango fruits (Mangifera indica L., cv. 'Chok Anan')," *Agric. Water Manag.*, vol. 88, no. 1–3, pp. 173–180, 2007.

[22] R. C. Ebel, E. L. Proebsting, and M. E. Patterson, "Regulated Deficit Irrigation May Alter Apple Maturity, Quality, and Storage Life," *HortScience*, vol. 28, no. 2, pp. 141–143, 1993.

[23] M. Gelly, I. Recasens, M. Mata, A. Arbones, J. Rufat, J. Girona, and J. Marsal, "Effects of water deficit during stage II of peach fruit development and postharvest on fruit quality and ethylene production," *J. Hortic. Sci. Biotechnol.*, vol. 78, no. 3, pp. 324–330, 2003.

[24] F. Iniesta, L. Testi, F. Orgaz, and F. J. Villalobos, "The effects of regulated and continuous deficit irrigation on the water use, growth and yield of olive trees," *Eur. J. Agron.*, vol. 30, no. 4, pp. 258–265, 2009.

[25] T. C. Hsiao, "Plant responses to water stress," 1973.

[26] P. A. Nortes, A. Pérez-Pastor, G. Egea, W. Conejero, and R. Domingo, "Comparison of changes in stem diameter and water potential values for detecting water stress in young almond trees," *Agric. Water Manag.*, vol. 77, no. 1–3, pp. 296–307, 2005.

[27] R. G. Allen, L. S. Pereira, D. Raes, and M. Smith, *Evapotranspiración del cultivo Guías para la determinación de los requerimientos de agua de los cultivos*. 2006.

[28] R. López-Urrea, A. Montoro, P. López-Fuster, and E. Fereres, "Evapotranspiration and responses to irrigation of broccoli," *Agric. Water Manag.*, vol. 96, no. 7, pp. 1155–1161, 2009.

[29] P. Droogers, W. W. Immerzeel, and I. J. Lorite, "Estimating actual irrigation application by remotely sensed evapotranspiration observations," *Agric. Water Manag.*, vol. 97, no. 9, pp. 1351–1359, 2010.

[30] G. Çamoğlu, "The effects of water stress on evapotranspiration and leaf temperatures of two olive (Olea europaea L.) cultivars," *Zemdirbyste-Agriculture*, vol. 100, no. 1, pp. 91–98, 2013.

[31] V. Hernandez-Santana, J. E. Fernández, M. V. Cuevas, A. Perez-Martin, and A. Diaz-Espejo, "Photosynthetic limitations by water deficit: Effect on fruit and olive oil yield, leaf area and trunk diameter and its potential use to control vegetative growth of super-high density olive orchards," *Agric. Water Manag.*, vol. 184, pp. 9–18, 2017.

[32] J. R. Millan-Almaraz, I. Torres-Pacheco, C. Duarte-Galvan, R. G. Guevara-Gonzalez, L. M. Contreras-Medina, R. de J. Romero-Troncoso, and J. R. Rivera-Guillen, "FPGA-based wireless smart sensor for real-time photosynthesis monitoring," *Comput. Electron. Agric.*, vol. 95, pp. 58–69, 2013.

[33] E. C. Martin, "Métodos para medir la Humedad del suelo para la programación del Riego.," *Univ. Arizona*, vol. 1, no. 1, pp. 1–8, 2010.

[34] G. Létourneau, J. Caron, L. Anderson, and J. Cormier, "Matric potential-based irrigation management of field-grown strawberry: Effects on yield and water use efficiency," *Agric. Water Manag.*, vol. 161, pp. 102–113, 2015.

[35] F. F. Montesano, F. Serio, C. Mininni, A. Signore, A. Parente, and P. Santamaria, "Tensiometer-Based Irrigation Management of Subirrigated Soilless Tomato: Effects of Substrate Matric Potential Control on Crop Performance," *Front. Plant Sci.*, vol. 6, no. December, pp. 1–11, 2015.

[36] S. RÜGER, Y. NETZER, M. WESTHOFF, D. ZIMMERMANN, R. REUSS, S. OVADIYA, P. GESSNER, G. ZIMMERMANN, A. SCHWARTZ, and U. ZIMMERMANN, "Remote monitoring of leaf turgor pressure of grapevines subjected to different irrigation treatments using the leaf patch clamp pressure probe," *Aust. J. Grape Wine Res.*, vol. 16, no. 3, pp. 405–412, 2010.

[37] U. Zimmermann, R. Bitter, P. E. R. Marchiori, S. Rüger, W. Ehrenberger, V. L. Sukhorukov, A. Schüttler, and R. V. Ribeiro, "A non-invasive plant-based probe for continuous monitoring of water stress in real time: a new tool for irrigation scheduling and deeper insight into drought and salinity stress physiology," *Theor. Exp. Plant Physiol.*, vol. 25, no. 1, pp. 2–11, 2013.

[38] D. Zimmermann, R. Reuss, M. Westhoff, P. Gessner, W. Bauer, E.

Bamberg, F.-W. Bentrup, and U. Zimmermann, "A novel, non-invasive, online-monitoring, versatile and easy plant-based probe for measuring leaf water status," *J. Exp. Bot.*, vol. 59, no. 11, pp. 3157–3167, 2008.

[39] U. Zimmermann, S. Rüger, O. Shapira, M. Westhoff, L. H. Wegner, R. Reuss, P. Gessner, G. Zimmermann, Y. Israeli, A. Zhou, A. Schwartz, E. Bamberg, and D. Zimmermann, "Effects of environmental parameters and irrigation on the turgor pressure of banana plants measured using the non-invasive, online monitoring leaf patch clamp pressure probe," *Plant Biol.*, vol. 12, no. 3, pp. 424–436, 2010.

CONACYT
Consejo Nacional de Ciencia y Tecnología
CONCYTEQ

UNIVERSIDAD AUTÓNOMA DE QUERÉTARO
13° CONGRESO INTERNACIONAL DE INGENIERÍA
15th-19th MAY 2017

Development of a Fluidized-Bed Plasma Reactor to Modify Granulated Media monitored with a Laser Light Scattering Signals

E. Augusto G-Guerrero, Martin Nieto-Pérez, Jorge A. Huerta-Ruelas.
Alternative Energies Department
CICATA-Instituto Politécnico Nacional Querétaro
Cerro Blanco #141 Colinas del Cimatario. Postal Code: 76090
Querétaro, Querétaro, México
eaggro@gmail.com, m.nieto@ieee.org, jhuertar@ipn.mx

***Abstract* — The project consists of the construction and operation of a plasma granulated media treatment system and its characterization with scattered light from solid particles obtaining the fluidized bed with and without the presence of an electric discharge in the volume of the fluidized bed. Main purpose, is to assure the homogeneity of fluidization throughout the column of the bed. The general system is divided into three parts: fluidization system, plasma generation and optical characterization by scattered light. The fluidization system consists of a fluidized-bed reactor and adapted for cohesive powders. The plasma production is obtained by the Coaxial Dielectric Barrier Discharge (Coaxial DBD) generation technique, with 12 KVpp and 25 KHz frequency. The optical system is composed of 16 LEDs light emitters, assembled on a straight line plate. In front of the emitting plate and at 90 degrees, there are two plates with 16 photodetectors each, also assembled in a straight line. The receiving boards are connected to an NI MyRio card from National Instruments and sending the data to a Virtual Instruments instrument created in Labview for data analysis. This work presents project advances which are: the operation of the fluidization system and the results of obtaining fluidization with and without the presence of plasma, construction of the optical system based on light scattering. General objective of this project is to have an instrument for the surface modification of granules by plasma treatment.**

Keywords — fluidization; Coaxial-DBD; Plasma Physics; Cohesive-Powders; Light Scattering.

I. INTRODUCTION

A. *Fluidization*

Fluidization occurs when there are solid particles in a container; with a fluid in a continuously and ascending flow, the solid particles are suspended through the fluid, acquiring a behavior similar to the fluid (Figure 1), [1, 2].

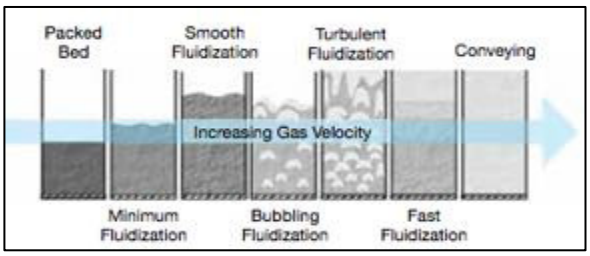

Fig. 1) *As the gas velocity through the bed increases, the type of fluidization shifts. [3]*

B. *Cohesive Powders*

According to the Geldart's Classification of fluidized-bed behavior of powders, the powders less than 30μm, are very difficult to fluidize and almost always experience the formation of a channel of fast moving bubbles that bypass most of the bed during fluidization (Figure 2). Small particles tend to behave more as particle clusters than independent particles. This kind of particles enter in the C group type on the Geldart's classification (Figure 3), and are called cohesive powders. For achieving fluidization on this type of powders, it is needed the aid of baffles, microjets, mechanical vibration, etc. [1 - 3]

Fig. 2) *Cohesive Powders tend to stick to walls and agglomerate.*

CONACYT Consejo Nacional de Ciencia y Tecnología
CONCYTEQ

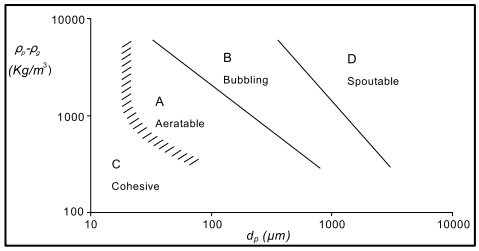

Fig. 3) *Geldart's Diagram for the types of behavior of powders fluidized by dry air at ambient conditions based on the difference between particle and gas density (vertical axis) and particle size (horizontal axis) . [1]*

C. Plasma generation technique: Coaxial DBD

The discharge is generated between two parallel electrodes and a dielectric surface before the ground electrode. This method is used for obtaining cold plasmas in no equilibrium at atmospheric pressure, Dielectric Barrier Discharge (DBD) [4]. For this project, the dielectric is a crystal quartz cylinder and the positive electrode is positioned in the center of the container. This arrange is known as coaxial DBD. As shown on Fig.4).

D. Plasma surface modification

Low pressure plasmas are universal tools for surface treatment. Because of their elementary processes with high activation energies of several electron volts, without elevated gas temperatures. Depending on the process parameters and the process gas material loss or material deposition can predominate. In the intermediate case a shallow surface layer is modified with respect to its chemical and physical properties. An extremely wide range of surface modifications can be obtained with different low pressure plasmas. Electrical gas discharges are used for plasma generation on a laboratory scale [6].

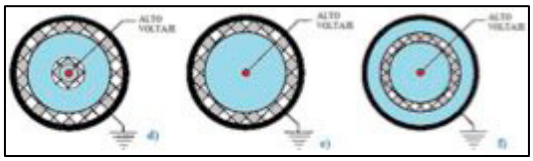

Fig. 4) *Basic Coaxial DBD configurations. [5]*

In the case of this work, the excitation frequencies are in the radio frequency range (RF). Examples of experimental observations of plasma surface modification are: simultaneous formation of different functional groups which can migrate to the subsurface, or graphitization of a polymer surface affecting its electrical conductivity. [6]

II. Experimental Set-up

A. Fluidization Column

For the proper surface treatment of the granules, a fluidized-bed is needed. To achieve this, a fluidization column with distributors were build. The fluidization column is shown in the Figure 5.

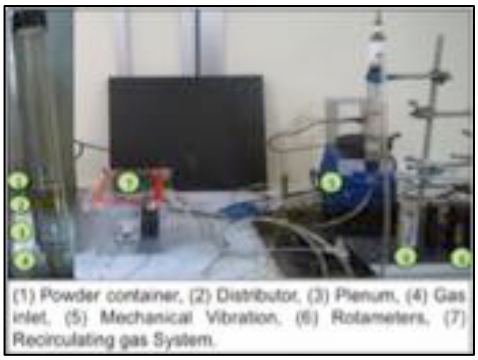

Fig. 5) *Fluidization column used for the project, designed and built at CICATA-IPN Querétaro.*

B. Plasma Generation System

For the plasma generation, it was used a high voltage power source with a RF. Configuration for the discharge, is coaxial DBD (Figure 6).

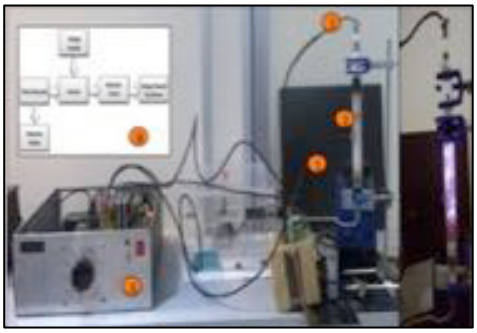

Fig. 6) *Plasma Generation System used for the project. The numbers are indicating: 1.- Electrodes, 2.- Dielectric, 3.- Power Supply, 4.- Power Supply Diagram. Developed at CICATA-IPN Querétaro.*

C. Optical Arrangement

For the scattered light analysis, an optical arrangement that covered the external area of the fluidized-bed plasma reactor was needed. As shown in (Figure 7c).

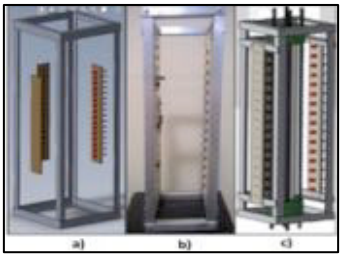

Fig. 7) *Optical device used for the project. In the image: a) Represents the design in SolidWorks. b) The device build. c) The design of the integrated device into the fluidized-bed plasma reactor. Designed and developed at CICATA-IPN Querétaro.*

In (Figure 8) is shown how the fluidized-bed plasma reactor and the optical arrangement work when integrated. The optic system working with a fluidized-bed of granules (Figure 8a). The analysis consists of measuring the homogeneous distribution among the reactor, and then with plasma treatment and the comparison of before and after the discharge. For the data analysis, the optical arrangement will be connected to a control card: NI-MyRio 1900 and then connected to a computer with a virtual instrument of Labview for the data acquisition and analysis.

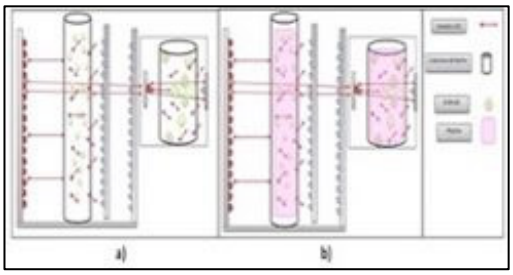

FIG. 8) *Working description diagram of the project. a) Shows the optical arrangement working only with the fluidization column. And in b) the optical arrangement is working with the fluidized-bed plasma reactor.*

D. Project Connection Diagram

The pipeline connection diagram of the project is shown in (Figure 9). Two gas sources are needed for the proper treatment of the granules with plasma. Needle valves are needed for the proper flow control of the gas before the plasma generation.

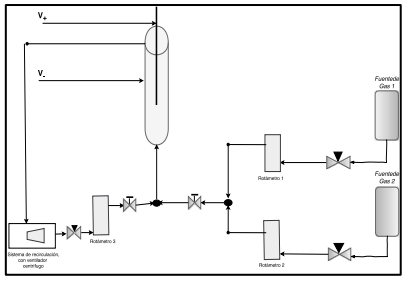

FIG. 9) Pipe line connection diagram.

A general project diagram is shown in (Figure 10). The working description diagram shown in (Figure 8) is represented now but including the integration of the: fluidization, plasma generation, optical and data acquisition systems.

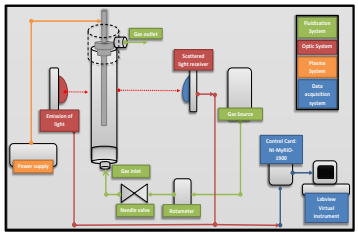

FIG. 10) *Project Diagram.*

III. CONCLUSION

The Project involves the design and development of a Fluidized-bed Plasma Reactor for the appropriate plasma treatment of granules be effective. This reactor is an instrument for the Research Center, for future research collaborations among national and international research centers and universities; also taking in consideration the advantage of the industrial growth the city of Querétaro, México is having, it is an opportunity to offer a service to the industry in the various Industrial Parks the city has and for the different industries that are coming. The surface treatment of powders with atmospheric plasma, for example with the powder TiO_2, the relevance of the surface study after the treatment of the TiO_2 relies on the actual needs for the paint industry. And will open an opportunity to offer an analysis service to the industry in the city. Another example, the relevance of the surface study after the treatment of the corn starch is to contribute to the artificial polymers substitution. With the reactor, the possibilities of surface modification of other granules are going to be possible. Specially for cohesive powders, for example starches.

REFERENCES

[1] Ortega Rivas E., "Unit Operations of Particulate Solids: Theory and Practice". Boca Raton, Florida, USA. CRC Press. 2012

[2] Valverde Millán J. "Fluidization of Fine Particles". University of Sevilla. Sevilla, Spain. Particle Technology Series. Volume 23 No. 1. 2013.

[3] Cocco R., Karri-Reddy S., Knowlton T. "Introduction to Fluidization" in CEP, American Institute of Chemical Engineers (AlChE), November 2014.

[4] Kogelschatz U. "Dielectric barrier Discharges: Their history, discharge physics and industrial applications." In Plasma Chemistry and Plasma Processing. Vol 23 No. 1 2003

[5] Soto-Ruvalcaba L. "Developmnet of a system for plasma generation based on a coplanar dielectric barrier discharge". Translated from: Desarrollo de un Sistema para Generación de Plasma basado en una descarga de barrera dieléctrica coplanar. Master's Dissertation Thesis in Advanced Technology, Instituto Politécnico Nacional-CICATA Qro. Querétaro, Querétaro, México. 2014

[6] Nitschke M. "Plasma Modification of Polymer Surfaces and Plasma Polymerization" in Polymer Surfaces and Interfaces: Characterization, Modification and Applications. 1st Edition, Chapter 10. Springer. Germany. 2008

[7] Melik D.H., Fogler H.S. "Turbidimetric Determination of Particle Size Distributions of colloidal Systems" in Journal of Colloid and Interface Science. Vol. 92, No.1. Academic Press. 1982.

UNIVERSIDAD AUTÓNOMA DE QUERÉTARO
13° CONGRESO INTERNACIONAL DE INGENIERÍA
15th-19th MAY 2017

IIR Digital Filter Design Implemented on FPGA for Myoelectric Signals

Toledo-Pérez Diana Carolina
División de Posgrado, Facultad de Informática
Universidad Autónoma de Querétaro
Querétaro, México
dtoledo56@alumnos.uaq.mx

Márquez-Gutiérrez Miguel Ángel
Facultad de Ingeniería
Universidad Autónoma de Querétaro
Querétaro, México
ar2di2@live.com.mx

[1]Martínez-Prado Miguel Ángel

[2]Rodríguez-Reséndiz Juvenal
División de Posgrado, Facultad de Ingeniería
Universidad Autónoma de Querétaro
Querétaro, México
[1]miguel.prado@.uaq.mx
[2]juvenal@uaq.edu.mx

***Abstract*—In order to attenuate the added noise by electric network used by myoelectric signals acquisition equipment, in this research work, it is developed an IIR digital filter implemented on FPGA. This filter removes a specific spectra frequencies without adding noise to the signal, which allows a better performance in the usage that is given to the signals. The filter coefficients are taken and proved from MATLAB functions. Then, those are transferred to the filter design in the FPGA. For this purpose, it was used a Basys 3 of Xilinx Artix-7 family and the design was implemented in Vivado Design Suite. The filtered signal does not present additional noise and it was eliminated the desired frequency.**

Keywords*—*IIR filter, EMG-signals filter, FPGA, digital filter design, filtering algorithms.

I. INTRODUCTION

Digital filters have been an important matter in the biomedical signals pre-processing, such is the case of myoelectric signals; from which their usage has been increased in different areas, mostly in device control, like prosthesis of different body parts, mechanical arms, movements within an interface, and so on.

On the other hand, Field Programmable Gate Array (FPGA) based technology has been introduced in different areas of industry, such as are the automotive, home appliances, and areas requiring high computational performance. This due to FPGAs offers an effective alternative in digital systems design of short response time in filter develop and its implementation on the real-time prototype [1]. The parallel processing capacity of the FPGA logic slices makes the system robust. Consequently, it is obtained a high-performance filter and a quick operation [2].

In an FPGA, the width of the data can be defined by the developer, according to his convenience, for each section of the logic that is implemented, while in a processor, this function is limited by the maker.

Infinite Impulse Response (IIR) filters have been implemented to filtering data coming from 2D and 3D images [1], [3], [4], temperature sensors [2] or biomedical signals as the electroencephalogram (EEG) like [5], using average and median filters, [6] also implemented an IIR filter. Besides, it uses a high level description of Xilinx System Generator. On the other hand, [7] filters electrocardiogram (ECG) signals, but it describes a technique to reduce the root mean square error, similarly to [8], in which it is described an adaptive filter LMS (Leas Mean Square) to fit the coefficients in order to reduce mean square error , i. e. the cost function.

The idea of using an FPGA in the pre-processing stage is to reduce the executed process by the microprocessor during the signals treatment. Besides, using a card like the Basys 3 (with a Xilinx IP core and a microprocessor) allows to perform different usages of the MESs without the necessity of a PC.

The aim of this work is to present a design of a discrete time infinite impulse response Notch filter, capable of diminishing a brief frequency interval of electric signals around a specific value, implemented by an IIR digital filter in FPGA. For this purpose, the filter coefficients are taken

from MATLAB functions. This filter was designed in order to make faster and proper treatment of electromyographic signals in the preprocessing step. The filter was designed and programmed on Vivado Design Suit 2016-3. Then, the filter was implemented in a Basys-3 to compare the results with those obtained from MATLAB.

II. THEORETICAL BACKGROUND

A. Conditioning of Myoelectric Signals

The superficial MyoElectric Signals (sMESs) are those signals extracted from the muscles and measured from the surface of the skin; these signals contain important information related to the amount of participation of each muscle that intervenes in the different body movements. Besides, they can be used to recognize activities in a non-invasive way.

An sMES is formed by overlapping individual action potentials, these are generated from irregular discharges of active motor units in the muscle fiber [9]. Due to the fact that an sMES could be considered as a stochastic signal, non-stationary, it has an average approximated to zero and a variable variance.

The sMESs are corrupted during acquisition. Since commonly they include noise coming from different sources, in which the 50 Hz frequency predominates due the Power Line Interference (PLI) for Europe and 60 Hz of America. Due to this, it is necessary to implement a Notch filter to eliminate PLI.

The conditioning process allows having a MES with the least amount of external and intrinsic noise possible. This can be achieved by integrating analog filters during signal acquisition or by adding a pre-processing stage with digital filters.

B. Digital Filters

A digital filter is a system which receive and produce discrete time signals, it is implemented as an algorithm that modifies input signal and produces an output in a different version; by removing or attenuating unwanted frequencies or noise from the original signal.

Digital filters offer some advantages over analog ones, such as: high accuracy, fidelity, and the immunity to environmental noise. They are classified into: recursives, non-recursives, fan, adaptatives, multi-dimensionals, multi-ranges, finite-duration impulse response (FIR) and infinite-duration impulse response (IIR) filters. Besides, these can be implemented in hardware or software [10].

The frequency-domain behavior of a filter is described mathematically regarding its Transfer Function (TF) or network function. This function corresponds to the ratio of Laplace transforms of its input and output signals. The transfer function defines the response of the filter to any arbitrary input signal, where the magnitude of TF and the Frequency Function (FF) has the same importance.

C. Infinite Impulse Response Filter

IIR filter is a recursive filter, which operates with current and previous values of both inputs and outputs. In theory, the filter's impulse response does not go to zero because its infinite. The coefficients of the multiplier in the structures are exactly those of the transfer function [11].

As a result, it has characteristics of low order with high performance, which make the usage of the hardware logic slices more effective, contributing to a higher performance of the filter as well as a fast operation [2].

D. IIR Filter Design

For computation of the coefficients, where N is the number of poles and M of the zeros, there are two well-known methods [11]. In the first one, the system function is divided into two parts connecting sequentially. The first part is formulated with zeros while the second one with poles, as it is shown in the next equation, where a_i and b_i are the filter coefficients corresponding to the calculated polos and zeros, $x(n)$ the input signal and $y(n)$ the output signal:

$$w(n) = \sum_{i=0}^{M} b_i x(n-i) \quad (1)$$

$$y(n) = \sum_{i=0}^{N} a_i y(n-i) + w(n) \quad (2)$$

On the other hand, the second method, poles are calculated at the beginning and zeros later. The transfer function becomes in two product transfer functions:

$$u(n) = \sum_{i=0}^{N} a_i u(n-i) + x(n) \quad (3)$$

$$y(n) = \sum_{i=0}^{M} b_i u(n-i) \quad (4)$$

III. HARDWARE DESIGN OF THE FILTER

The implementation of a digital filter on configurable logic involves the explanation of the algorithm with a hardware description language such as the Very-high speed Hardware Description Language (VHDL). There are several advantages of the hardware description such as the modularity and the interoperability of written modules. Above allows using the same source files to implement different type of filters [6].

In order to validate the implemented filter it is required to setup an experimental platform. The signals were acquired using a MATLAB interface. Then, signals are filtered in the FPGA, after that, those were returned to the MATLAB interface. This process is shown in Fig. 1.

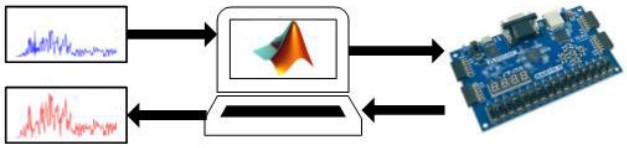

Fig. 1. General system block diagram.

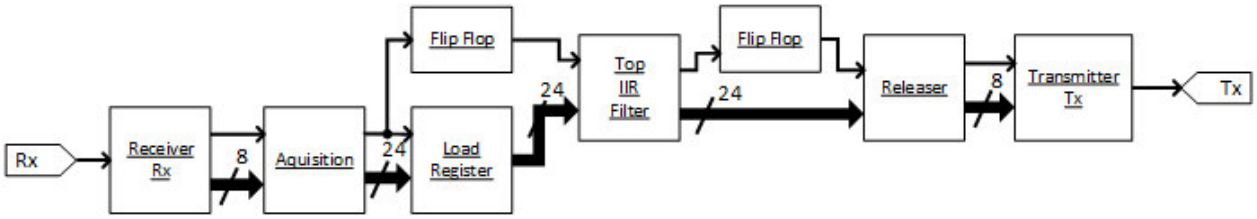

Fig. 2. Design top level diagram.

A. *Hardware description*

The filter is implemented on the FPGA block. The design top level diagram that it is implemented is in Fig. 2. Besides, it is displayed the sequence and the interaction between the signals in all blocks.

The diagram in Fig. 3 shows the design inside of *Top IIR Filter* block, where the bus signal YK0 is the feedback source to the system. The delay blocks have been made up of *Load Registers (LRs)*, which store the value from the input signal (XIN) every time the EN signal is active. In such way, that signal becomes the sample time. The *LRs* blocks amount depends on the number of values inside the *ROM*_Q block. This one contains the coefficients calculated for the filter.

The *Bus Target Counter* block is responsible for counting the received data whose value has been forced to "1000". It implies that the count begins from zero and the first stored value is multiplied with the first value inside the ROM and so on to the last value in the ROM. All the input and output signals are stored.

First, the Finite State Machine (FSM) detects the enable signal from EN and it starts to let pass 10 latency clocks. Thus the Multiplier Adder can yield the result that will be stored in an *LR* of which its output bus signal is going to be returned to the C input of the Multiplier Adder. Then, then *SB FSM* gives an impulse to the *Bus Target Counter* for increase its count and, at the same time, it changes the output bus signal so it deploys the next signals pair that is multiplied. In the end, the *Bus Target Counter* stores the coefficient in other *LR* which carry this value until the previous value is computed. The final value cannot be 50-bits length, so it pass through a *Saturation Block* which verifies if the signal does not achieve the limit values and if it does, then just chop the bus for the output signal have the same format of the input signal. Also, it can be returned to the line of delays corresponding to $a_n x(k-n)$.

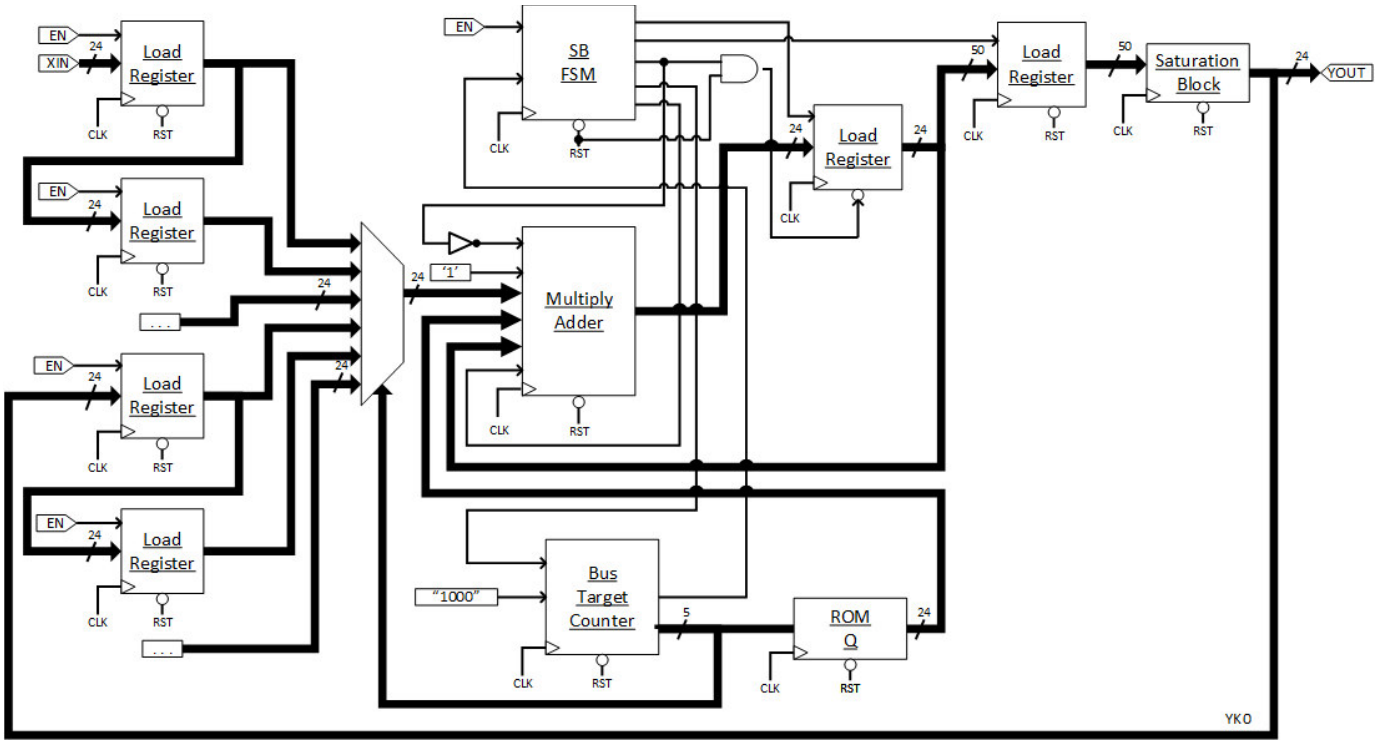

Fig. 3. Top level diagram of the IIR filter.

The signal names for the core symbol are shown in Fig. 4. Herein, the *Multiplier Adder* is described, it takes into account two different latency paths; one from A and B inputs to the P output, and the other from the C/PCIN input to the PCOUT output. These latencies are defined as A:B – P Latency and shown schematically in Fig. 5.

All inputs are right-justified when passed to the operators inside the core. In the *Multiply Adder*, there is no truncation or rounding of the multiplier output; it is a full precision result. The C input is added to the product LSB-to-LSB. MSB and LSB positions can be chosen to extract the desired "slice" of output data. The pinouts of *Multiply Adder Block* are in Table I.

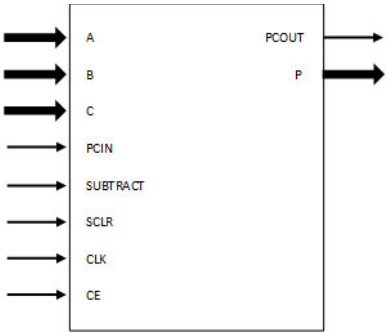

Fig. 4. Core Symbol [12].

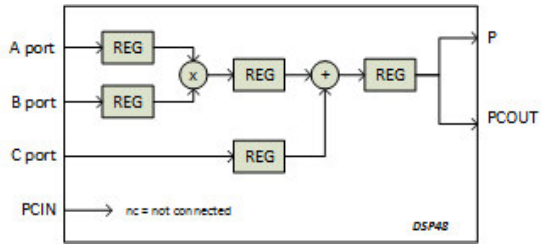

Fig. 5. Multiply adder single extreme DSP implementation optimal pipelining (USE_PCIN=0) [12].

TABLE I. CORE SIGNAL PINOUT.

Name	Description
A[24:0]	A Input bus (multiplier operand 1)
B[26:0]	B Input bus (multiplier operand 2)
C[55:0]	C Input bus (operand 1 of add/sub operation)
PCIN	Cascade Input
SUBTRACT	Controls Add (High) / Subtract (Low) operation
CE	Clock Enable (Active-High)
CLK	Clock (Rising edge)
SCLR	Synchronous Clear (Active-High)
PCOUT[47:0]	Cascade Output
P[54:0]	Output bus

Finally, the Fig. 6 shows the diagram used to co-simulate the VHDL design using ModelSim® and Matlab® and Fig. 7 shows the graphs obtained.

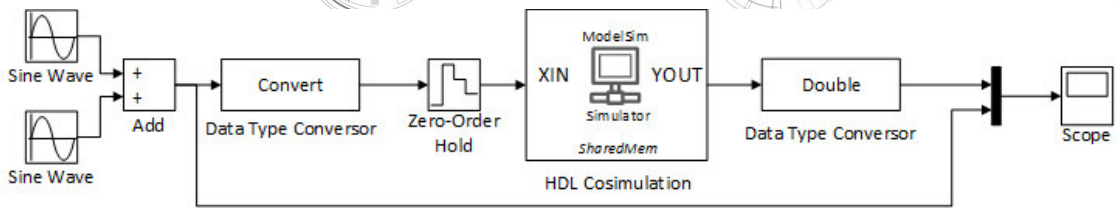

Fig. 6. Simulink diagram to the HDL co-simulation using Modelsim®.

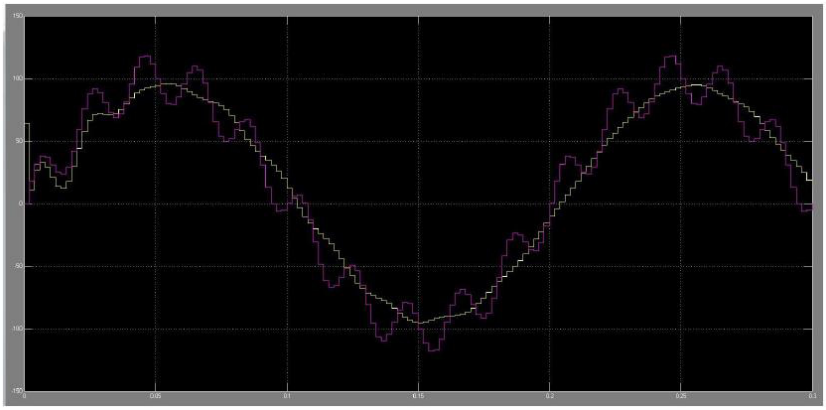

Fig. 7. Scope from the simulation in Simulink and Modelsim®.

IV. RESULTS

The filter is implemented within a Basys 3 Artix-7 FPGA Trainer Board, of Xilinx family, with 33,280 logic cells in 5200 slices (each slice contains four 6-input LUTs and 8 flip-flops) and 90 DSP slices. The implementation on a Basys 3 requires of Vivado Design Suite.

Starting from the resulting filter it is possible to determinate in a precise way the gain in decibels in passing and rejection bands, as well as variation and attenuation in both bands. For such reason and in contrast with other tools was chosen the elliptical digital filter, grade nine, which is implemented with MATLAB. For this purpose, it is utilized an 'ellipord' function with the filter specifications; and 'ellip' function calculates the a_n and b_n coefficients. Finally, input signals were filtered using 'filter' function. The input vector is composed of extracted values from a MES, with a sampling frequency of 500 Hz. The frequency to be attenuated is 50 Hz, which corresponds to noise introduced in the signal by the measuring instrument. The filter specifications are in Table II while the coefficients are listed in Table III.

TABLE II. FILTER SPECIFICATIONS.

fp_1 (Hz)	fs_1 (Hz)	Rp (db)	fp_2 (Hz)	fs_2 (Hz)
45	48	0.5	48	50

TABLE III. ELLIPTIC FILTER COEFFICIENTS.

i	a_i	b_i
1	1	0.8067
2	-6.2237	-5.2292
3	18.2184	15.9365
4	-32.3191	-29.4156
5	37.8494	35.8196
6	-29.9151	-29.4156
7	15.6103	15.9365
8	-4.9374	-5.2292
9	0.7347	0.8067

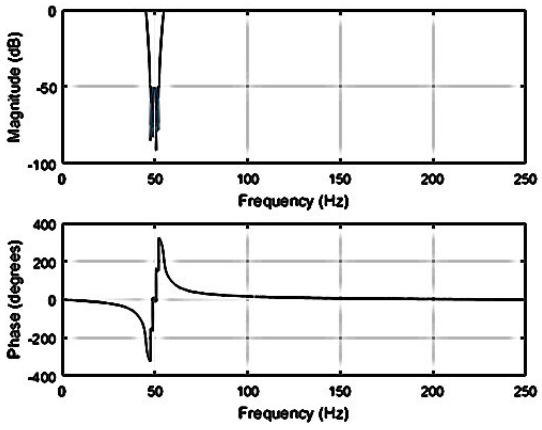

Fig. 8. Magnitude and phase response of the filter.

For a better understanding of the filter, in Fig. 8 it is shown the magnitude and phase response, where it is seen that the magnitude in 50 Hz value is decreasing until -100 dB. In the same place, the phase ranges from almost -400 to almost 400 degrees, so that frequency (50 Hz) it is going to be attenuated from the original signal.

In the co-simulation environment, the input signals used to confirm the expected behavior present an undesired frequency of 50 Hz. Therefore, it is expected that the output signal shows a similar wave-form as the first one.

In the other hand, due to that it is only possible to send 8-bit data one by one through USB port from MATLAB to FPGA, a function was developed to split the data in three continuous bytes and another to receive and join them. Besides, the FPGA performs the same operation, an acquisition block to receive data in 8-bit blocks.

In the Fig. 9, it is shown an input signal, which is filtered using the 'filter' function of MATLAB. In this, it can be seen that the original signal does not exhibit major changes, nevertheless, in the frequency spectrum showed in the Fig. 10, it is remarkable that the desired value (50 Hz) has been removed.

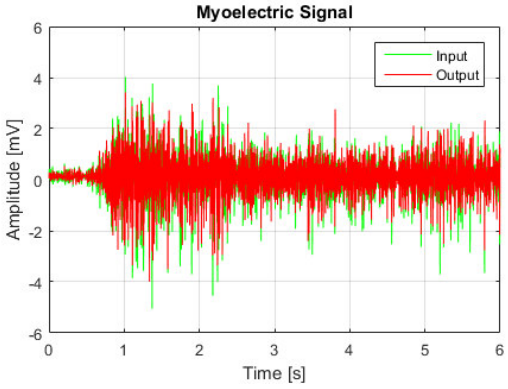

Fig. 9. Filtered myoelectric signal in MATLAB.

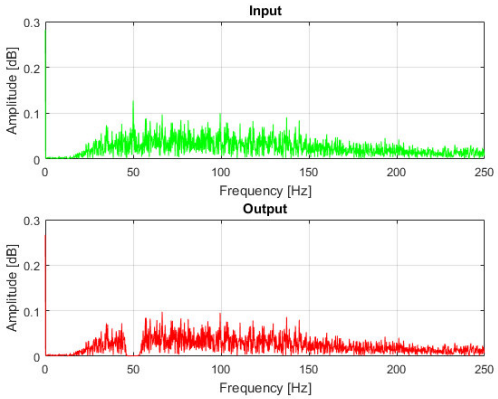

Fig. 10. The frequency spectrum of filtered myoelectric signal.

Also, it was made an analysis to know the relation between the signal and the noise, using *snr* function in MATLAB. For the input signal, the obtained value was -15.1763 dB and for the output signal was -14.8943 dB.

The results obtained from the synthesis and implementation in the FPGA, regarding resource consumption are shown in Table IV.

TABLE IV. TABLE 1. RESOURCE RESUME.

Resource	Post-Synthesis			Post-Implementation		
	Available	*Used*	*%*	*Available*	*Used*	*%*
LUT	20800	330	2	20800	329	1.58
FF	41600	718	2	41600	879	2.11
IO	106	4	4	90	4	4.44
BUFG	32	1	3	106	4	3.77
DSP	-	-	-	32	1	3.13

V. CONCLUSIONS

The usage of digital filters as pre-processing tool for EMG signals guaranties the attenuation of not desired frequencies while the introduced noise is negligible. The relation between the signal and the noise clearly presents an improvement in applying *snr* analysis, due to there is a difference of +0.2820 dB between the input and the output.

The exposed methodology in this research work describes the implementation of an IIR filter on an FPGA by utilizing the Xilinx IP Core for multiplication (Multipler-Adder) and thus, obtaining a shorter processing time and a successful noise rejection. FPGA utilization resources consumed are around 4% leaving the remaining to be used for describing the application for those signals.

To the proposed structure for the filter implementation, take it around 10 clock cycles to calculate the output signal after taking the sample. Therefore, it is possible, depending the oscillator crystal used to elevate the sample frequency until one tenth of the crystal frequency. In contrast with the implementations in software as MATLAB, that although the use decimal point of double precision, the processing time depends of the processor speed and the number of tasks that it is doing. This time could be using to performance the subsequent operations, such as signal classifications, control and any other required task.

Acknowledgments

To Faculty of Engineering, graduate division of Universidad Autónoma de Querétaro by allowing me to study phD and CONACYT for making it possible.

REFERENCES

[1] A. Madanayake, L. Bruton, y C. Comis, "FPGA architectures for real-time 2D/3D FIR/IIR plane wave filters", en *2004 IEEE International Symposium on Circuits and Systems*, 2004, vol. 3, pp. 613–616.

[2] C. Zhao y Z. Zhang, "Digital filter design and performance analysis of dynamic temperature signal denoise based on FPGA", en *2016*

10th International Conference on Sensing Technology (ICST), 2016, pp. 1–7.

[3] S. Wang y T. Maruyama, "An implementation method of the box filter on FPGA", en *2016 26th International Conference on Field Programmable Logic and Applications (FPL)*, 2016, pp. 1–8.

[4] D. Mukherjee, S. Mukhopadhyay, y G. P. Biswas, "FPGA based parallel implementation of morphological filters", en *2016 International Conference on Microelectronics, Computing and Communications (MicroCom)*, 2016, pp. 1–6.

[5] K. Sundaram, Marichamy, y Pradeepa, "FPGA based filters for EEG pre-processing", en *2016 Second International Conference on Science Technology Engineering and Management (ICONSTEM)*, 2016, pp. 572–576.

[6] D. Costa y C. S. Páez, "A comparative analysis of hardware techniques for implementation of IIR digital filter on FPGA", en *2015 XVI Workshop on Information Processing and Control (RPIC)*, 2015, pp. 1–6.

[7] H. K. Jayant, K. P. S. Rana, V. Kumar, S. S. Nair, y P. Mishra, "Efficient IIR notch filter design using Minimax optimization for 50Hz noise suppression in ECG", en *2015 International Conference on Signal Processing, Computing and Control (ISPCC)*, 2015, pp. 290–295.

[8] D. Sharma y R. Kaur, "Performance analysis of adaptive IIR filter using sign algorithm in LabVIEW", en *2015 2nd International Conference on Computing for Sustainable Global Development (INDIACom)*, 2015, pp. 1510–1513.

[9] J. M. Fernández, R. C. Acevedo, y C. B. Tabernig, "Influencia de la fatiga muscular en la señal electromiográfica de músculos estimulados eléctricamente", *Rev. EIA*, núm. 7, pp. 111–119, jun. 2007.

[10] A. Antoniou, *Digital Signal Processing: Signal Systems and filters.*, 1a ed., vol. 1, 1 vols. USA: McGraw-Hill, 2006.

[11] A. Paul, T. Z. Khan, P. Podder, M. M. Hasan, y T. Ahmed, "Reconfigurable architecture design of FIR and IIR in FPGA", en *2015 2nd International Conference on Signal Processing and Integrated Networks (SPIN)*, 2015, pp. 958–963.

[12] Xilinx, Inc., "LogiCore IP Multiply Adder v2.0". 01-mar-2011.

Technique for synchronizing a single-phase inverter to the mains

Samir Cabello Romero
Facultad de Ingeniería de la Universidad
Autónoma de Querétaro
Queretaro, Mexico
Samir.cabello74@gmail.com

Abstract— **The injection of energy into the grid by investors is a recent and attractive issue due to the new energy reforms that have been made in recent years, which is why it is necessary to use, research and develop Systems interconnected to the electric grid with a control scheme such as the one proposed in this work Due to the dynamics in the mathematical model of the inverter, there are constant variations in the parameters of the plant, therefore, to apply a control scheme that works robustly requires a control with a system able to adapt to these variations in the time. It is therefore necessary to use two types of control primarily in the design of an inverter, one in charge of maintaining good voltage regulation at the output and another, a control loop that is able to follow the frequency and phase of the low network Conditions of distortion in the wave.**

For correct operation of inverter control, it is necessary that the inverter is properly synchronized with the mains. This is achievable by using a PLL. A PLL scheme used in three-phase systems is based on the use of a synchronous frame of reference (SRF). For single-phase systems, the direct application of an SRF, It is possible, but it is possible to generate a quadrature component with the voltage sign and to be able to apply the inverse Park transform. One way of producing quadrature components is implementing a delay, which is responsible for introducing a phase shift of 90º with respect to the fundamental frequency of the Input signal.

I. INTRODUCTION

In the design of an inverter connected to the grid to inject energy, it is crucial to design a control loop[1] that made me measure the frequency and phase of the electric grid to make the inverter follow this instruction.

The latter, a control loop called the PLL phase tracking loop, is responsible for executing this task.

Phase, amplitude and frequency of the utility voltage are critical information for the operation of the grid-connected systems. The grid voltage monitoring is used to ensure that the performance of a grid-connected system comply with the standard requirements for operation under comon utility distortions In such applications, an accurate and fast detection of the phase angle of the utility voltage is essential to assure the correct generation of the reference signals. Thus, phaselocked loop topologies must handle distorted utility voltages if they are intented to applications that required the tracking of the utility voltage vector. The Phase-Locked Loop (PLL) structure is a feedback control system that automatically adjusts the phase of a locally generated signal to match the phase of an input signal.

With the increasing demands for high-quality power sources, a pulse-width modulated (PWM) inverter has been used as a key element for a high-performance power conversion system for critical loads such as computers, medical equipment and communication systems. A single-phase PWM inverter is generally used in low-power applications. To obtain a high-quality output, the PWM inverter should provide tight output voltage regulation, low total harmonic distortion (THD) and low output impedance against load variations. Moreover, an accurate reference tracking capability is also important because modern power conversion systems are connected to the utility and are operated in parallel for increasing usability and reliability

II. PLLCONCEPTS BASICS

The PLL circuit is a feedback system whose purpose Principal principle in the generation of an output signal with fixed amplitude and frequency coincident with that of Input, within a certain range

The PLL technique has been used as a common way of recovering the phase and frequency information in electrical

systems. In the area of power electronics, the PLL technique has been adopted for the speed control of electric motors. This is also available for generating the current references synchronised with the utility voltages in the power conversion system[2]. A simple method of obtaining the phase information is to detect the zero crossing points of the utility voltages. However, since the zero crossing points can be detected only at every half-cycle of the utility frequency (i.e. 120 times per second), the phase tracking action is impossible between the detecting points, and fast tracking performance cannot be achieved. Another method is the technique using the quadrature of the input waveform shifted by 90 degrees[3].

An electronic inverter or DC / AC converter as its name indicates a circuit where a direct current voltage is input to the input and an alternating current voltage of variable magnitude and frequency.

It consists primarily of electronic power devices, which act as cut-and-saturation switches operating in an appropriate sequence to obtain three symmetrical and balanced output voltages. The controller is another fundamental component in the constitution of the converter, it is the one that generates the signals of on and off of the semiconductor devices and guarantees its good behavior. Any type of inverter (single phase and three phase) or controlled activation and deactivation devices (BJT, MOSFET, IGBT, MCT, SIT, GTO) or forced switching thyristors, according to the application as we can see in the figure 1.

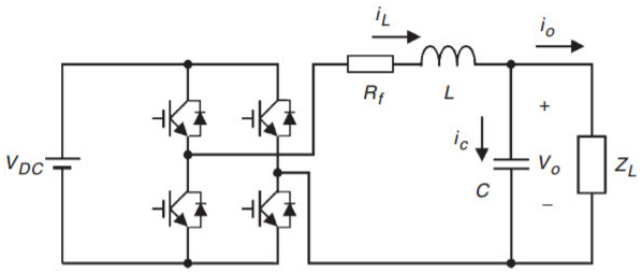

Fig. 1 Basic circuit of an inverter.

Maintaining the Integrity of the Specifications

When the PLL is out of sync, a very high or very low input signal frequency, the output voltage adopts the center pulse (ωco)[4]. There is a frequency band (locking range, lock range) between which the PLL is in the tuning, characterized by ωi = ω0, and another between which the circuit is capable of tuning (ΔωC capture range, range Of the catch). The catch margin is always lower than the catch margin and both are centered with respect to the central push.

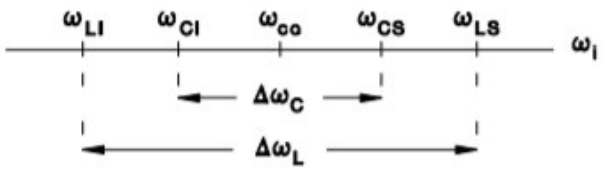

Fig. 2. Frequency band.

$$V_D = K_m V_{iM} V_{oM} sen(\omega_i t + \theta_i) sen(\omega_0 t + \theta_0) = \quad (1)$$

$$= K_d \begin{bmatrix} cos(\omega_0 t - \omega_i t + \theta_0 - \theta_i) \\ -cos(\omega_0 t + \omega_i t + \theta_0 + \theta_i) \end{bmatrix} \quad (2)$$

$$K_d = K_m \frac{V_{iM}\, V_{oM}}{2} \qquad \omega i = 2\pi f_i \quad \omega o = 2\pi f_0$$

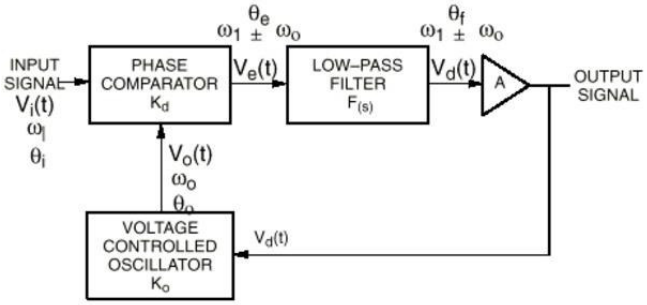

Fig. 3. Phase locked loop.

When there is no signal applied to the system input, the voltage Vd (t) controlling the VCO has a value of zero. The VCO oscillates at a frequency, f0 (or what is equivalent in Wo radians) which is known as free oscillation frequency. When a signal is applied to the system input, the phase detector compares the phase and frequency of that signal with the VCO frequency and generates an error voltage Ve (t) which is proportional to the phase and frequency difference between The two of signals[1]. This error voltage is then filtered, extended, and applied to the control input of the VCO. In this way, the control voltage Vd (t) forces the oscillation frequency of the VCO to vary so as to reduce the frequency difference between f0 and the input signal fi. If the input frequency fi is sufficiently close to that of f0, the nature of the PLL feedback causes the VCO oscillator to synchronize and engage the incoming signal. Once hooked up, the VCO frequency is identical to that of the input signal except for a finite phase difference.

Is the phase difference needed to generate the correcting error voltage Vd to achieve the free frequency offset of the VCO to match the frequency fi of the input signal and thus keep the PLL engaged[5]. This system autocorrection capability also allows the PLL to "route" the frequency changes with the input signal once it has been engaged. The range of

Identify applicable sponsor/s here. If no sponsors, delete this text box (*sponsors*).

frequencies on which the PLL can maintain the engagement with an input signal is defined as the "clutch range" of the system[1]. The band frequencies on which the PLL can hook with an input signal known as the "capture range" of the system and is never greater than the range of hooking.

Another means of describing the operation of the PLL is in observing that the phase comparator is actually a multiplier circuit that mixes the input signal with the VCO signal[6]. This mix produces a range of frequencies which are sums and frequency differences

$$(f_i + f_0)\ y\ (f_i - f_0) \qquad (3)$$

When the loop is hooked

$$(f_i = f_0; then\ f_i + f_0 = 2f_i\ and\ f_i - f_0) \qquad (4)$$

Hence, at the output of the phase comparator we only have a DC component. The lowpass filter overrides the frequency component sum by being (fi + fo) out of its bandwidth but lets pass the DC that is then amplified and attacks the VCO[7]. Note that when the loop is engaged, the frequency difference component is always DC, such that the engagement range is independent of the flank of the low pass filter bandwidth

III. PLL COMPENSATOR

Before you begin to format your paper, first write and save the content as a separate text file. Keep your text and graphic files separate until after the text has been formatted and styled. Do not use hard tabs, and limit use of hard returns to only one return at the end of a paragraph. Do not add any kind of pagination anywhere in the paper. Do not number text heads-the template will do that for you.

A phase-locked loop is a feedback system combining a voltage controlled oscillator (VCO) and a phase comparator so connected that the oscillator maintains a constant phase angle relative to a reference signal. Phase-locked loops can be used, for example, to generate stable output high frequency signals from a fixed low-frequency signal.

Figure 4A shows the basic model for a PLL. The PLL can be analyzed as a negative feedback system using Laplace Transform theory with a forward gain term, G(s), and a feedback term, H(s), as shown in Figure 4B. The usual equations for a negative feedback system apply.

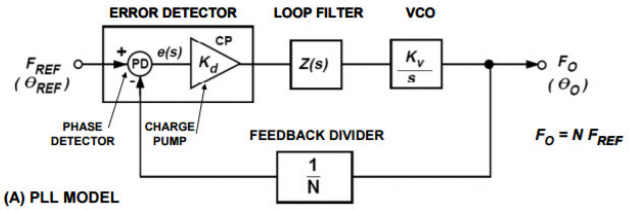

Fig. 4. Basic model for a PLL.

The basic blocks of the PLL are the Error Detector (composed of a phase frequency detector and a charge pump), Loop Filter, VCO, and a Feedback Divider. Negative feedback forces the error signal, e(s), to approach zero at which point the feedback divider output and the reference frequency are in phase and frequency lock, and FO = NFREF.

Referring to Figure 4, a system for using a PLL to generate higher frequencies than the input, the VCO oscillates at an angular frequency of ωO. A portion of this signal is fed back to the error detector, via a frequency divider with a ratio 1/N. This divided down frequency is fed to one input of the error detector. The other input in this example is a fixed reference signal. The error detector compares the signals at both inputs. When the two signal inputs are equal in phase and frequency, the error will be constant and the loop is said to be in a "locked" condition.

A. *Phase frequency detector (PFD)*

Figure 5 shows a popular implementation of a Phase Frequency Detector (PFD), basically consisting of two D-type flip flops. One Q output enables a positive current source; and the other Q output enables a negative current source. Assuming that, in this design, the D-type flip flop is positive-edge triggered, the possible states are shown in the logic table.

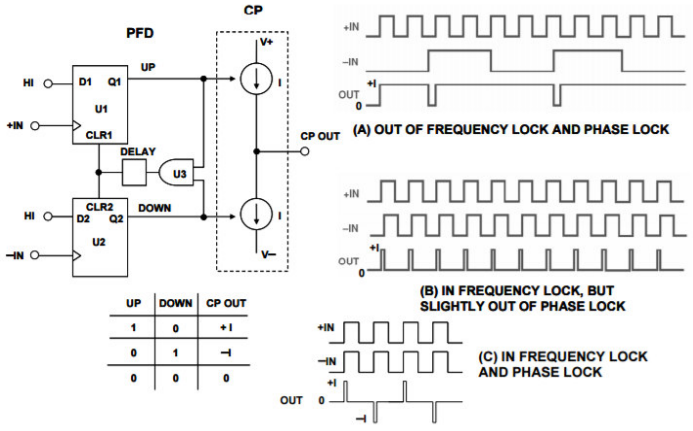

Fig. 5. Popular implementation of a Phase Frequency Detector (PFD).

Consider now how the circuit behaves if the system is out of lock and the frequency at +IN is much higher than the frequency at –IN, as shown in Figure 5A. Since the frequency at +IN is much higher than that at –IN, the UP output spends most of its time in the high state. The first rising edge on +IN sends the output high and this is maintained until the first rising edge occurs on –IN. In a practical system this means that the output, and thus the input to the VCO, is driven higher, resulting in an increase in frequency at –IN. This is exactly what is desired. If the frequency on +IN were much lower than on –IN, the opposite effect would occur. The output at OUT would spend most of its time in the low condition. This would have the effect of driving the VCO in the negative direction and again bring the frequency at –IN much closer to that at +IN, to approach the locked condition.

Figure 5B shows the waveforms when the inputs are frequency-locked and close to phase-lock. Since +IN is leading –IN, the output is a series of positive current pulses. These pulses will tend to drive the VCO so that the –IN signal become phase-aligned with that on +IN. When this occurs, if there were no delay element between U3 and the CLR inputs of U1 and U2, it would be possible for the output to be in high-impedance mode, producing neither positive nor negative current pulses. This would not be a good situation.

The VCO would drift until a significant phase error developed and started producing either positive or negative current pulses once again. Over a relatively long period of time, the effect of this cycling would be for the output of the charge pump to be modulated by a signal that is a subharmonic of the PFD input reference frequency[8]. Since this could be a low frequency signal, it would not be attenuated by the loop filter and would result in very significant spurs in the VCO output spectrum, a phenomenon known as the "backlash" or "dead zone" effect. The delay element between the output of U3 and the CLR inputs of U1 and U2 ensures that it does not happen. With the delay element, even when the +IN and –IN are perfectly phasealigned, there will still be a current pulse generated at the charge pump output as shown in Figure 5C. The duration of this delay is equal to the delay inserted at the output of U3 and is known as the anti-backlash pulse width. Note that if the +IN frequency is lower than the −IN frequency and/or the +IN phase lags the −IN phase, then the output of the charge pump will be a series of negative current pulses—the reverse of the condition shown in (A) and (B) in Figure 5.

B. Preescalers

state the units for each quantity that you use in an equation.

In the classical Integer-N synthesizer, the resolution of the output frequency is determined by the reference frequency applied to the phase detector. So, for example, if 200 kHz spacing is required (as in GSM phones), then the reference frequency must be 200 kHz. However, getting a stable 200 kHz frequency source is not easy. A sensible approach is to take a good crystal-based high frequency source and divide it down. For example, the desired frequency spacing could be achieved by starting with a 10 MHz frequency reference and dividing it down by 50.

REFERENCES

[1] K. J. Lee, B. G. Park, R. Y. Kim, and D. S. Hyun, “Robust predictive current controller based on a disturbance estimator in a three-phase grid-connected inverter,” *IEEE Trans. Power Electron.*, vol. 27, no. 1, pp. 276–283, 2012.

[2] P. M. Bhagwat and V. R. Stefanovic, “Generalized Structure of a Multilevel PWM Inverter,” *IEEE Trans. Ind. Appl.*, vol. IA-19, no. 6, pp. 1057–1069, 1983.

[3] C. A. T. P, I. Electricista, and M. Sc, “DISEÑO Y CONSTRUCCIÓN DE UN INVERSOR TRIFÁSICO Design and Construction of a Three-phase inverter,” no. 40, pp. 37–42, 2008.

[4] J. A. Houldsworth and D. A. Grant, “The Use of Harmonic Distortion to Increase the Output Voltage of a Three-Phase PWM Inverter,” *IEEE Trans. Ind. Appl.*, vol. IA-20, no. 5, pp. 1224–1228, 1984.

[5] J. Holtz and B. Beyer, “Optimal synchronous pulsewidth modulation with a trajectory-tracking scheme for high-dynamic performance,” *IEEE Trans. Ind. Appl.*, vol. 29, no. 6, pp. 1098–1105, 1993.

[6] “Vikram Kaura,” vol. 33, no. 1, pp. 58–63, 1997.

[7] D. G. Holmes, R. Davoodnezhad, and B. P. McGrath, “An improved three-phase variable-band hysteresis current regulator,” *IEEE Trans. Power Electron.*, vol. 28, no. 1, pp. 441–450, 2013.

[8] G. Pfaff, A. Weschta, and A. F. Wick, “Design and Experimental Results of a Brushless AC Servo Drive,” *IEEE Trans. Ind. Appl.*, vol. IA-20, no. 4, pp. 814–821, 1984.

Hexavalent Chromium Removal from water by using SBA-15 functionalized with different weight ratios of Ferric Oxide.

José Isaac Aguilar-Clemente

Facultad de Química
Universidad Autónoma de Querétaro (UAQ)
Querétaro, Querétaro, México.
(jaguilar63@alumnos.uaq.mx)

Rodrigo R. Velázquez-Castillo

Facultad de Ingeniería
Universidad Autónoma de Querétaro (UAQ)
Querétaro, Querétaro, México.
(rodrigo.velazquez@uaq.mx)

Abstract— **The present study focuses on the SBA-15 substrates functionalized with Ferric Oxide for Hexavalent Chromium (Cr^{+6}) removal from water. The removal was tested by ICP-MS. The sorbents were characterized by Nitrogen SBET, BJH techniques, powder XRD, FTIR and UV-Vis Spectroscopies and Thermo gravimetric analysis (TGA).**

Keywords— SBA-15; Ferric Oxide; Hexavalent Chromium; Water Treatment.

I. INTRODUCTION

According to the World Health Organization guide for drinking water quality, the pollution of water can be classified in four major categories. One of the most important is about chemical pollution which includes metals in aqueous solution [1].

The development of chemical industry had polluted environment with metals such as Chromium [2]. The problem is worse in developing countries, due to the increase of industrial facilities, which lack of control for pollutants [3].

Chromium is an essential and trace element that joins in the fats metabolism, the aforementioned when chromium is in a (III) oxidation state form.

Alike chromium (III), chromium at basal state is innocuous.

However chromium (VI) is particularly lingering in the environment, due to the difficulty of assimilation-excretion by living organisms, and an oxidation/reduction behavior in presence of DNA or RNA, for this reason Chromium is considered a toxic element.

Chromium (VI) is a carcinogen, teratogenic, and mutagenic agent, toxic even at low concentrations, this toxicity and recalcitrance are the main reasons for its uses as a biocide in cooling water for industrial devices. Other industrial uses of this transition metal are electroplating, tanning and textile dying [4].

Due to the toxicity associated with chromium, Mexico has established techniques or a combination of them for the removal of Chromium in water [5]. Some removal methods are considered of high efficiency however, its cost, difficulty of reagents selection, the use of lots of raw materials and long operation time, represents operating disadvantages for the removal of this metal [6].

An Alternative to the techniques mentioned for Mexican Regulation NOM-127-1994 was studied in the present work, this alternative is a mesoporous silica substrate called SBA-15 which was functionalized with magnetite nanoparticles. In **Table 1 and 2** advantages of the developed magnetite functionalized material are shown by comparing it to the Mexican Regulated methods.

TABLE 1. CHARACTERISTICS OF METHODS FOR CHROMIUM REMOVAL FROM WATER.

Reference	Removal Method	Unit Cost	Efficiency	Reagent Quantity	Material Reuse Possibility
NOM-127	Flocculation	L	L	L	NO
	Ionic Exchange	H	H	L	YES
	Reverse Osmosis	H	H	H	NO

*H and L means High and Low levels respectively.

TABLE 2. CHARACTERISTICS OF PROPOSED METHOD FOR CHROMIUM REMOVAL FROM WATER.

Reference	Removal Method	Unit Cost	Efficiency	Reagent Quantity	Material Reuse Possibility
Present Work	Mesoporous Material SBA-15	L	–	L	YES

*H and L means High and Low levels respectively.

In the **tables 1 and 2**, can be observed that mesoporous materials have two main advantages from other removal methods mentioned by NOM-127. In the present work the efficiency of chromium removal from water was quantified in order to define the convenience of use mesoporous materials for the treatment of polluted water.

II. Materials and Methods

For this work SBA-15 was functionalized with ferric oxide at 5, 10 and 20 weight percent related to the weight of substrate [7]. The functionalization process was carried out by the impregnation method using ferric chloride solutions as a precursor, the ferric chloride solution was added to the mesoporous materials drop wise while mixing until the calculated amount of Ferric ions was reached [8]. Later, the material was dried at room temperature, pre-heated and dried at 110 °C.

Finally a calcination process was performed at 500°C to produce the ferric oxide nanoparticles by oxidation of ferric chloride. These nanostructures are directly involved in the chromium ions adsorption.

In order to assurance the quality of sorbents, all the substrates were characterized after Synthesis, functionalization and sorption processes.

The textural properties were evaluated by Nitrogen absorption-desorption isotherms [9]. X-Ray diffraction, XRD, by powder at low and conventional angles were carried out to determine the crystal structure. FTIR and Uv-Vis spectroscopies were carried out to elucidate the existing chemical functional groups [10], to observe the morphology of all materials a Scanning Electron Microscopy, SEM, was used [11], and to determine the thermal stability of the material, a Thermo gravimetric Analysis, TGA, was used [12].

The Chromium removal capacity was evaluated by batch reaction using mechanical agitation at 120 rpm and the same adsorption-reaction time, 1 hour for all the treatments.

For all the experiments and repetition 0.275 g of the functionalized SBA-15 was put into contact with 50 mL of 10 and 100 mg/L aqueous solutions of hexavalent chromium salt, $(NH_4)_2Cr_2O_7$ Ammonium Dichromate. Afterward, the treated dissolutions were sealed and preserved by refrigeration for a posterior analysis by Inductively Coupled Plasma-Mass Spectrometry, ICP-MS, for the quantification of Chromium in the certified laboratory of the Centro de Investigación y Desarrollo Tecnológico en Electroquímica, CIDETEQ.

The adsorption experiments were carried out at three different pH values of 2, 7, and 10. The temperature of the adsorption system was varied at two different values, 25 and 35 °C.

In addition, a time versus adsorption capacity and saturation experiments were carried out for the higher concentration of Chromium, 100 mg/L.

III. Findings and Results

For the mesoporous material synthesis, an efficiency of 99.37±0.012% was obtained. This synthesis efficiency is high and expected for the Sol-Gel synthesis process for the SBA-15 substrates.

The functionalization of SBA-15 was carried out by the aforementioned technique, all the sorbents were characterized by the techniques mentioned in Material and Methods.

The presence of SBA-15 and the functionalization of the mesoporous material were confirmed by characterization methods, the next figures presents the techniques mentioned above. In **Figure 1** adsorption-desorption isotherms are presented

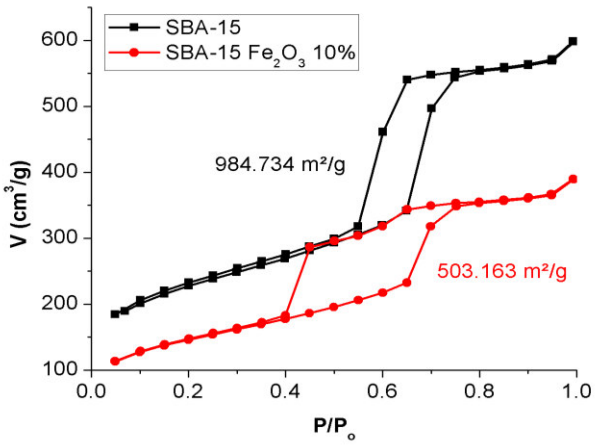

FIGURE 1. ADSORPTION-DESORPTION ISOTHERMS OF FUNCTIONALIZATED AND PURE SBA-15.

In **Figure 1** the nitrogen isotherms show that functionalized SBA-15 has less surface area than pure SBA-15. In **Figure 2 and 3** XRD diffractograms for low angle are shown.

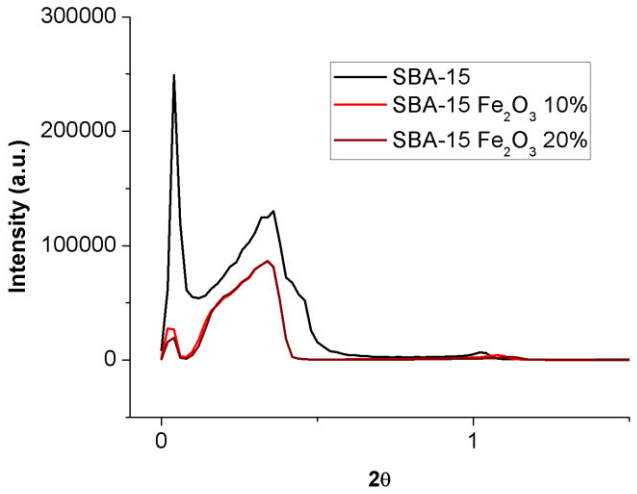

FIGURE 2. LOW ANGLES DIFFRACTION PATTERNS OF FUNCTIONALIZED AND PURE SBA-15.

In addition to SBET results the Low angles X-Ray diffraction shows that functionalized SBA-15 had a lower quantity of pores, fact that suggest the formation of nanoparticles of ferric material inside the silica pores, for wide angles **Figure 3** shows X-ray diffraction pattern.

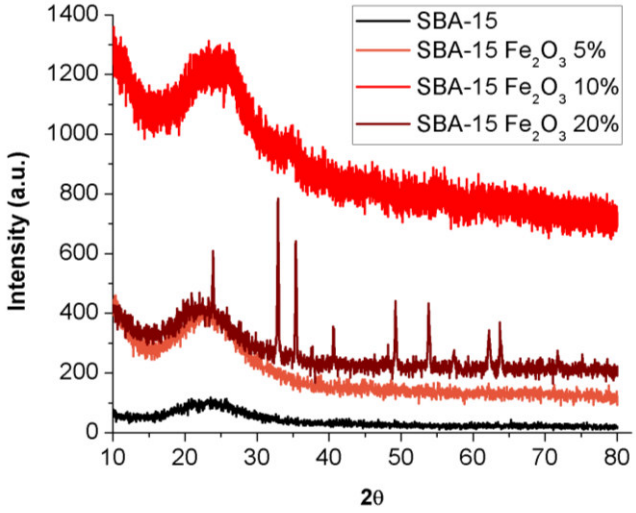

FIGURE 3. CONVENTIONAL ANGLES DIFFRACTION PATTERNS OF FUNCTIONALIZED AND PURE SBA-15.

For conventional X-ray diffractogram it can be observed that the added ferric oxide particles change diffraction pattern for the material. A confirmation of the presence of ferric oxide can be found on **Figure 4 and 5** which present FTIR and Uv-Vis spectrogram respectively.

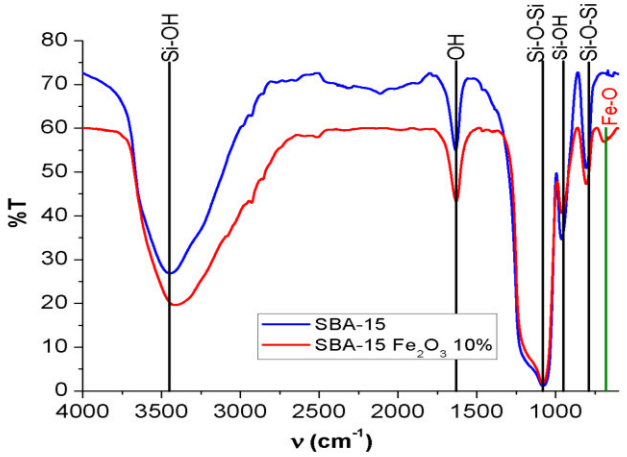

FIGURE 4. FTIR SPECTOGRAMS OF FUNCTIONALIZED AND PURE SBA-15.

Figure 4 shows the intensity decrease in functional groups corresponding to Si-OH at 3450 and 960 cm^{-1}, OH at 1650 cm^{-1}, and the appearance of a peak in 680 cm^{-1} corresponding to Fe-O bonds. Uv-Vis spectrogram is shown in **Figure 5**.

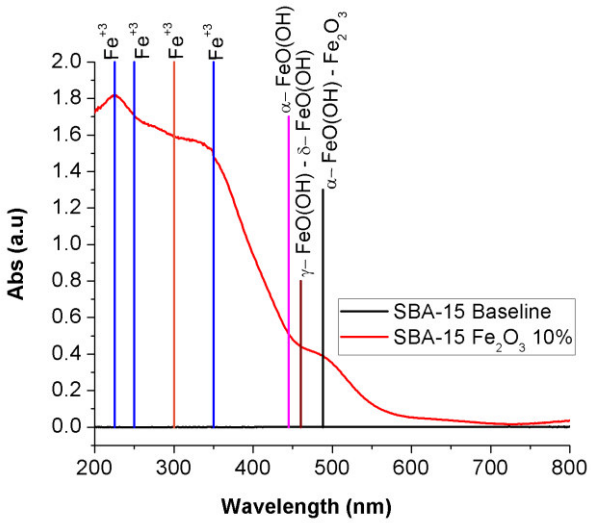

FIGURE 5. UV-VIS SPECTOGRAM OF FUNCTIONALIZED SBA-15, PURE SBA-15 LINE.

In **Figure 5** the Uv-Vis spectrogram shows a SBA-15/functionalized absorption no similar to the baseline set by pure SBA-15, for literature and reported Uv-Vis Ferric compound spectra or pattern, can be concluded that the signals comes from Fe^{+3} ions, and α,γ and δferric Oxy-hydroxides with magnetite or ferric oxide.

Finally the SEM micrographs showed in **Figures 6 and 7** shows micrographs of Pure SBA-15 and functionalized SBA-15 respectively.

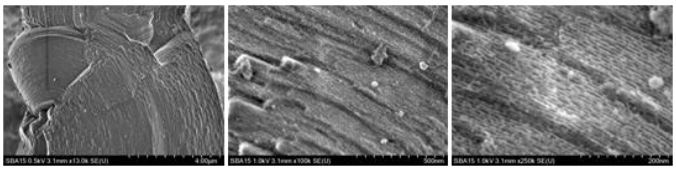

FIGURE 6. HRSEM MICROGRAPHS OF PURE SBA-15.

In **Figure 6** the expected morphology of SBA-15 was observed, with no appearance of material with different composition to SiO_2. However in **Figure 7** the micrograph of ferric oxide functionalized SBA-15 is shown.

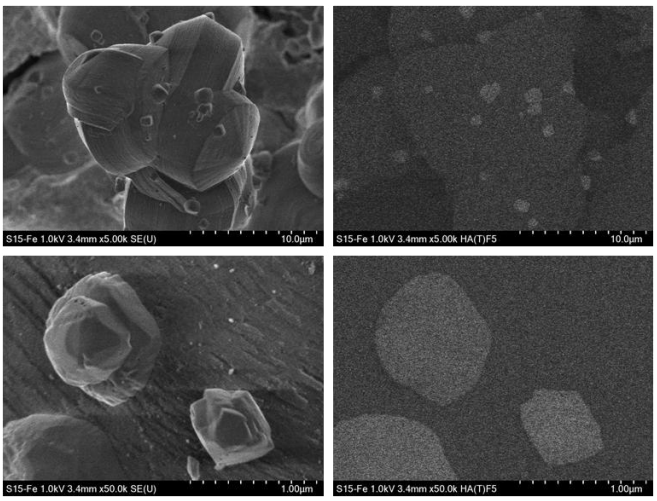

FIGURE 7. HRSEM MICROGRAPHS WITH BSE FOR FERRIC OXIDE FUNCTIONALIZED SBA-15.

In **Figure 7** the morphology of SBA-15 remains intact, except for the appearance of crystal with a greater atomic weight than Si or O on pure SBA-15, confirmed by Back Scattered Electron technique, fact that visually confirms the formation of ferric oxide nanoparticles in the SBA-15.

Different characterization methods are pointing out a successful functionalization process for SBA-15.

Once the synthesis and functionalization take place as expected, the evaluation of chromium sorption capacity was evaluated in order to prove the hypothesis.

The 10% ferric oxide functionalized SBA-15, had showed a removal efficiency of about 80% for 10 mg/L experiments (actually in the repeatability and reproducibility process), while 100 mg/L experiments had 8.55 ±1.31%, which remains constant to pH changes, or Chromium salt nature. In **Figure 8** the box plots of the Chromium removal due to the treatments are shown for a pH range varying from 2 to 10.5.

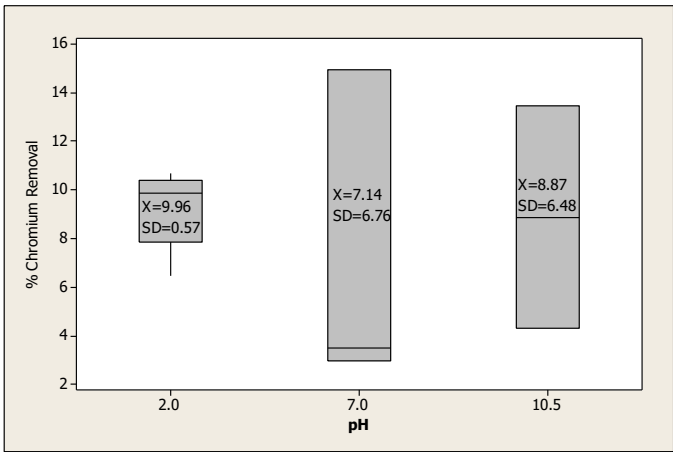

FIGURE 8. BOX PLOT OF CHROMIUM REMOVAL RELATED TO PH CHANGE IN A RANGE FROM 2 TO 10.5 FOR TREATMENTS WITH SORBENTS.

It can be observed from **Figure 8** that pH does not affect the chromium removal from water; this was proved by an ANOVA at a 95 % of significance. Additionally, it was found that oxidation state and chemical compound for the chromium content in water does not affect the chromium removal.

The series time experiments, realized with 10% ferric oxide functionalized SBA-15, showed that the equilibrium of the reaction is reached at times shorter than one hour, and the saturation concentration is between 10 and 60 mg/L.

All the ICP-MS quantification was corroborated and reproduced by the certified Chemical analysis laboratory of CIDETEQ.

Although chromium removal from water was proved by the ICP-MS technique, the assurance of Chromium content in sorbent was determined in order to confirm the removal of this metal. **Figure 9** shows the FTIR spectrogram of a Fe_2O_3/SBA-15 sorbent after the treatment of chromium polluted water.

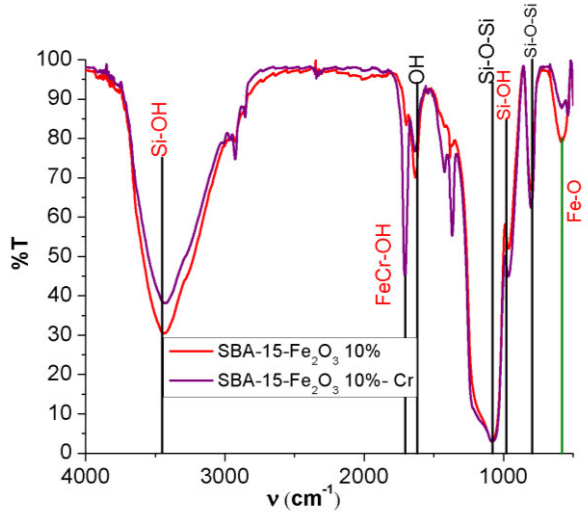

FIGURE 9.FTIR SPECTOGRAM OF FERRIC OXIDEFUNCTIONALIZED SBA-15 POLLUTED WITH CHROMIUM REMOVED FROM WATER.

Figure 9 shows a decrease of Si-OH groups at 3450, 1650 and 960 cm^{-1}, and a Fe-O bonds decrease in 680 cm^{-1}, while a strong adsorption was observed in a band that appears at 1705 to 1630 cm^{-1}, the band corresponds to a reported signal of ferric-chromium oxide/hydroxide.

The removal of chromium from water and the decrease of OH and Fe-O active sites in functionalized SBA-15, and the appearance of Fe-O-Cr bonds, strongly suggest the removal of chromium in water is due to the ferric oxide functionalized mesoporous material.

Results with 5 and 20% of ferric oxide content are in process. Other pending characterization techniques are X-ray photo electron spectroscopy, XPS, Raman spectroscopy and X-ray fluorescence spectroscopy, XRF are in process in order to achieve a better understanding of the sorption phenomena in the experiments performed in this work.

ACKNOWLEDGMENT

We like to acknowledge to the Centro de Física Aplicada y Tecnología Avanzada, CFATA, for counseling, performing and interpretation of Scanning Electron Microscopy, SEM, and the FTIR Spectroscopy performing for the substrates.

Also we acknowledge to the Universidad Autónoma de Querétaro, UAQ, for the FOFI project with number 20501195091 of the Engineering Faculty.

We appreciate the CONACYT research grant given to student CVU number 710307. And we acknowledge the budget dedicated to science and research for enable the teamwork with CIDETEQ.

We acknowledge CIDETEQ for the ICP-MS analysis, especially to the coworker's team, Georgina Navarro-Castro, Ma. Guadalupe Olvera-Torres, Ma. Vanessa Paz-González.

REFERENCES

[1] Organización Mundial de la Salud, "Guías para la calidad del agua potable", Vol. 1, 3ra Ed., 2006.

[2] H.Z. Torres, T.M. Helí, "Planeación y control, una visión integral de la administración", Grupo editorial Patria, P. 90-151. D.F., 2014.

[3] F. Bautista-Zúñiga, "Introducción al estudio de la contaminación del suelo por metales pesados", Facultad de medicina veterinaria y zootecnia. Universidad Autónoma de Yucatán. P. 17-31, 1999.

[4] D. Park, Y.S. Yun, J.J. Hye, J.M. Park, "Mechanism of hexavalent chromium removal by dead fungal biomass of Aspergilius niger". Water Research Journal, 39 P. 533-540, 2005.

[5] Secretaría de Salud, "NOM-127-SSAI-1994", Norma oficial mexicana, 2000.

[6] M.I. Aguilar, J. Sáez, M. Lloréns, A. Soler, J.F. Ortuño, "Tratamiento físico-químico de aguas residuales, coagulación-floculación". Universidad de Murcia, 2002.

[7] R. Nava-Mendoza , V. Hernandez-Morales , Y. J. Acosta-Silva , S. A. Macías-Sanchez , J. J. Perez-Bueno, B. Pawelec , "Adsortption of lead (II) on SBA-15 mesoporous sieve functionalized with NH2 groups", Journal of Microporous and mesoporous Materials, Vol. 160, pp. 133-142, 2014.

[8] Balu, "Nanopartículas soportadas sobre materiales porosos para la síntesis de productos de alto valor añadido". Universidad de Córdoba, 2012.

[9] F. Rouquerol , J. Rouquerol , K.S.W. Sing, P. Llewellyn , G. Maurin , "Adsorption by Powders and Porous Solids, principles, methodology and applications", Elsevier, pp. 22-58, 2014.

[10] Arellano N., Pérez J., Caribay S., López C., (2008) Síntesis de sílice mesoporosa tipo SBA-15 a partir de un silicato de sodio de Venezuela. Caracas, Venezuela.

[11] Ojeda-Bosch, F. Sánchez-Rojas, "Process analytical chemistry: applications of ultraviolet/visible spectrometry in enviromental analysis: an overview", Applied Spectroscopy Journal, Vol. 44 (3), pp. 245-265, 2009.

[12] Y. Xi, Z. Ding, H. He, R. L. Frost, "Structure of organoclays – an X-Ray diffraction and thermo gravimetric analysis study", Journal of Colloid and Interface Science, Vol. 277 (1), pp. 1-256, 2004.

Synthesis and characterization of CNT-Zn as an anticorrosive coating.

Rogelio Abraham Gómez Figueroa, Julio César Cruz Argüello, Danna Lizeth Trejo Arroyo, Alberto Yeladaqui Tello*
División y Estudio de Posgrado e Investigación
Instituto Tecnológico de Chetumal
Chetumal, Quintan Roo.
jcruz@itchetumal.edu.mx

Juan Francisco Pérez Robles
Departamento de Nanomateriales
Centro de Investigación y Estudios Avanzados del Instituto Politécnico Nacional Unidad Querétaro, Cinvestav.
Querétaro, Querétaro.

***Abstract*—Since the origin of corrosion studies and his problematics has been inquired about the way how to optimize the useful life of the anticorrosive system, whether given by cathodic protection or the isolation and surface recover. In the present investigation was synthetize and characterized a composite of Multiwalled Carbon Nanotubes (MWCNT) and Zinc nanoparticles for further conducting a painting coating with efficiency improvements against corrosion problems.**

The synthesize process of MWCNT was made by Chemical Vapor Deposition (CVD), the precursor used was acetylene (C_2H_2) and the catalyst employed was a proportional mix of iron(Fe) and Cobalt (Co); for the functionalization/reduction of the CNT-Zn the precursor employed of Zinc was Chloride Zinc and borohydride sodium $NaBH_4$ as reducing agent.

Keywords: Multiwalled Carbon Nanotubes; Corrosion; Zn-composite coating; Chemical Vapor Deposition.

I. INTRODUCTION

Construction is today a preponderant form, a fundamental piece in the development of any country, the economic pumping that generates the progress of the entire urban settlement, so they always seek to implement a durable and optimal infrastructure for the needs of man, since its cost is generally very high. Over time, different methods have been implemented to extend the useful life of concrete structures such as reinforcing steels with coatings (galvanized paints, epoxy or alkyds, stainless steels), corrosion inhibitors (NO_3, arsenic compounds or antimony or of both) and cathodic Protection (sacrificial anodes and data protection systems by the printing press), [1].

At present the development of modern cathodic protection methods have adapted the development of anticorrosive coatings with the use of Carbon Nanotubes (NTC) to improve the efficiency of the same impulses. The corrosion inhibitor improves its performance by reduced pore size and higher density, as well as features such as functionality, conductivity, reinforcement capacity and dispersion capability in large areas using chemical deposition techniques, among other things NTC is an excellent material to use as a multifunctional coating, [2].

In 2007 B.M. Praveen and his team of collaborators made a coating a base of carbon nanotubes-zinc applied with an electrodeposition with the sulfate bath in which the carbon nanotubes are dispersed in a solution and are co-deposited together with the zinc. Electrochemical studies revealed increased resistance of composite coatings to corrosion and the delayed formation of white oxide revealed a better shelf life of NTC-Zn composites, [3].

In 2014, SungMo Park y MinYoung Shon researchers studied the effects of multi-walled carbon nanotubes (MWCNT) on corrosion protection with an applied zinc-rich epoxy resin coating. It was observed that coatings with higher MWCNT content generated an increase in conductivity and strength of adhesion compared to coatings containing only zinc, [4].

Regionally in the Yucatán Peninsula, the Instituto Tecnológico de Chetumal ITCH and the Instituto Tecnológico de Cancun ITC have carried out joint studies to achieve the development of carbon nanotubes incorporated in commercial epoxy coatings for the control of corrosion, a recurrent problem in the locality and thus increasing the cathodic protection efficiency in exposed reinforcing steel in an alkaline environment. The synthesis of the NTC was carried out by means of a chemical vapor deposition reactor (CVD) which were applied as a solute were dissolved in an epoxy paint that was subsequently applied to blanks (6 cm carbon steel corrugated rods) to be subjected to accelerated corrosion tests using a Potentiostat kit and the creation of an electrochemical cell; the results showed an improvement in about 500 cycles

greater than that of a coating based on a conventional epoxy paint, [5].

II. EXPERIMENTAL

Synthesis of CNT carbon nanotubes.

The process of the synthesis of the carbon nanotubes was carried out by CVD process (Chemical Vapor Deposition) on an equipment Thermolyne brand, model 79400 Tube Furnace; the carbon precursor used was Acetylene (C2H2) the below cost of production that have the nanotubes created from this precursor make the acetylene is in comparison much cheaper than other precursors and the low energy consumption that derives from this precursor in the reactor CVD, since the temperatures in the reactor usually are not higher to the 700ºC during the whole process of synthesis different to other syntheses where the temperature of the CVD usually reaches up to 1600 ºC.

The catalysts used with the precursor due to their reactive properties were Iron (Fe) and Cobalt (Co) in a concentration of 75% -25% respectively, on general terms, the CVD synthesis process takes approximately two hours:

The first synthesis stage of the multiwall carbon nanotubes "MWCNT's" consist in doping the substrate whit catalysts Iron (Fe) and Cobalt (Co), for consequently inserted the substrate in The CVD reactor.

The second process stage consist in doping the reactor with Nitrogen (N) once reaches the required ideal temperature (700 ° C), after the pure Nitrogen valve closes and a CVD reactor is doping with a mixture of Nitrogen (N) and Hydrogen (H) in a concentration of 90% -10% respectively, to eliminate all the oxidized residue in the CVD reactor, this process lasts approximately 20 minutes.

The third process stage consists in doping the CVD reactor with a precursor of carbon nanotubes in this case Acetylene (C2H2), as well as of inert gas (Nitrogen N) for a time of approximately 30 minutes at a constant temperature of 700ºC, once finished the growth process of the Multiwalled Carbon Nanotubes (MWCNT) shuts off the reactor so that the temperature drops to ambient temperature in this case around 20 ° C.

Finally, the newly synthesized carbon Nanotubes are subjected to a purification process, to remove any residual impurity of Iron (Fe) and Cobalt (Co) or amorphous carboxyls in the newly synthesized composite.

The purification of NTC is performed in three stages:

Firstly, the CNT's are carried an ultrasonic bath for about two minutes in 2% hydrofluoric acid in the sufficient amount that covers the entire composite, later with the use of deionized water, the impurities are decanted.

The second stage consists of an ultrasonic bath for fifteen minutes in hydrochloric acid and its subsequent decanting with the use of deionized water.

Finally, the multilayer NTC composite is placed in a muffle for about 24 hours at a temperature of 110 ° C.

CNT Functionalization.

The process of laying the carbon nanotubes in an oxidation process with the nitric acid HNO_3 and the sulfide H_2SO_4 in a ratio of 1:3, the CNT are placed in a Magnetic stirring grill with the nitric acid for 10 minutes, then the sulfuric acid is slowly poured for 3:30 hours to an internal temperature of 70 ° C and 80 ° C external, at the end the solution is neutralized with deionized water and begins its filtration process.

Reduction.

The Reduction of the CNT-Zn was carried out for three different concentrations: CNT-Zn 20:80, CNT-Zn 50:50, CNT-Zn 80:20 in a Sonochemical reactor; the approximate process time is 15 Minutes per reduction, the main reactants for this process were Sodium Borohydride $NaBH_4$ and Citric acid $C_6H_8O_7$, together with the appropriate ratio of carbon nanotubes, Zn precursor reagent (Zinc chloride, $ZnCl_2$) and 30 ml of deionized water, at the end of the reduction The CNT-Zn samples were calcined in a muffle at 110 ° C for a time of 24 hours.

III. RESULTS

Characterization NTC-Zn

SEM Microscopy.

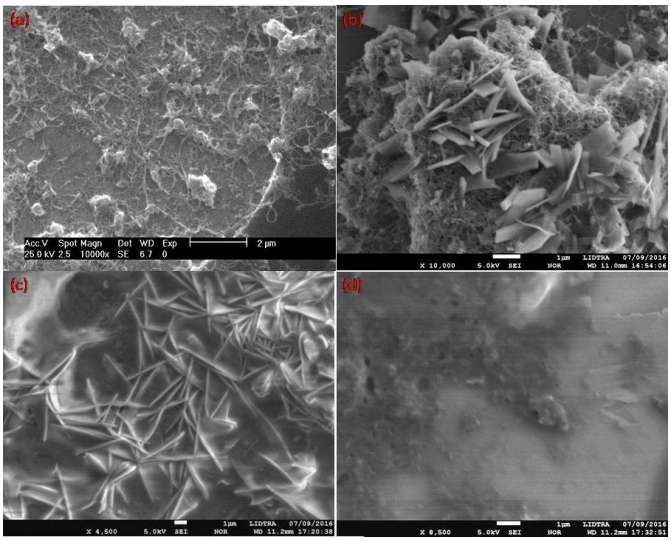

FIG. 1.- SEM images of the NTC-Zn composites in the relationships 80-20 (a), 50-50 (b) and 20-80 (c and d).

The study by scanning electron microscopy shows the differences between the various proportions of carbon nanotubes (CNT's), and the metallic Zinc, figure 1.
1a image shows the material with 20% of Zinc and the rest of carbon nanotubes, where the tubular structure of the carbon base material can be observed with agglomerations of Zinc particles dispersed in the network. Image 1b shows the composite with a 50-50 ratio of CNT and zinc, where you can see that nanotubes surround large agglomerations and structures of zinc laminates. It is possible to observe a good dispersion of the CNT on these structures, wrapping them completely. The material with the amount of zinc, (more 80%) is shown in Figure 1c where it is observed that practically the CNT disappears a simple view, the material being mostly composed by the Zinc laminar structures. To confirm the presence of the CNT in this composite the edges of the material, image 1d, were analyzed, where the tubular structure embedded within the Zinc is appreciated.

RAMAN Spectroscopy

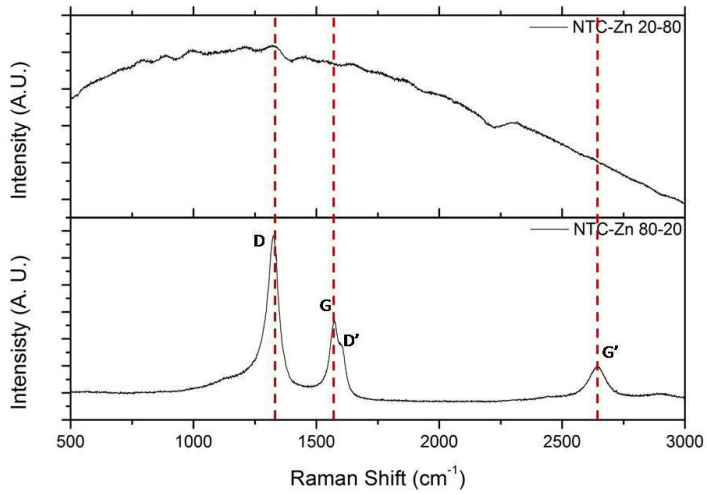

FIG. 2.- Raman analysis of the composites of CNT-Zn with the ratios of 20 and 80% of Zinc.

Figure 2 shows the Raman spectra of the CNT-Zn samples at the 80-20 (bottom) and 20-80 (upper image) ratios. In the 80-20 material spectrum, the characteristic peaks of carbon nanotubes of the multiple wall, D, G and G ', can be clearly seen in 1320, 1570 and 2700 cm-1 approximately [6-8]. The relationship between the bands D and G is used regularly to calculate a purity of the nanotubes obtained, the lower this value is the purer the nanotube [9,10]. In our case the band D is of greater intensity, almost that it arrives at double of the value of the band G, by one that the CNT went through an oxidation process to generate active sites for its union to the zinc. Similarly, a fourth band at the 1600 cm-1 position is called D', this band is related to the defects in the graphic material walls due to the oxidation process or the intercalation of the dopant ions, generating behaviors Metals in the sample, I.E. more electron conductors, [11,12]. Finally, the spectrum corresponded to the sample h 80% of Zinc did not show the appearance of CNT signals, because the large amount of Zinc which, like any pure metal, no peaks of presentation in the Raman spectra capped the Signal coming from the nanotubes.

XRD STUDY
Graphics:

NTC-Zn 20:80

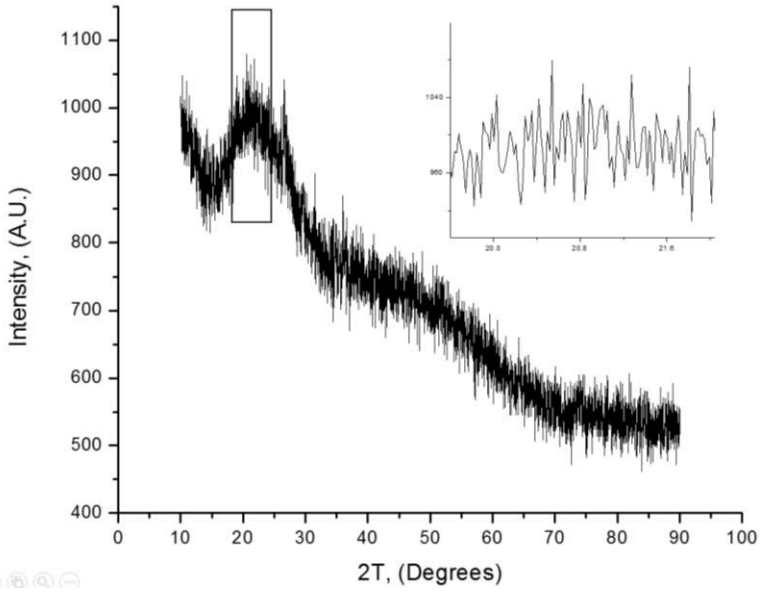

FIG. 3.- XRD patterns of the composite NTC-Zn 20:80.

NTC-Zn 50:50

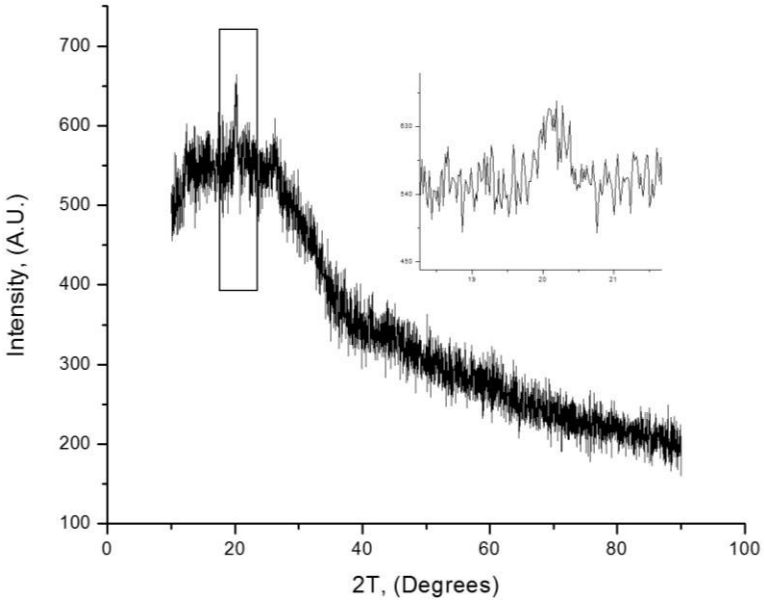

FIG. 4.- XRD patterns of the composite NTC-Zn 50:50.

NTC-Zn 80:20

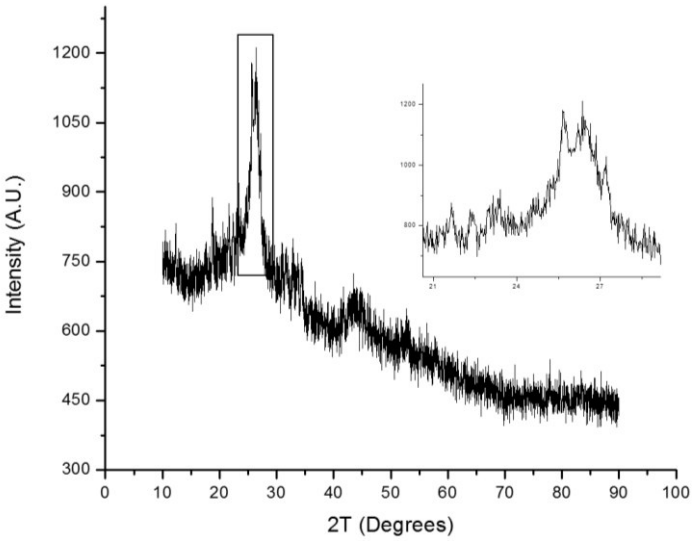

FIG. 5.- XRD patterns of the composite NTC-Zn 80:20.

The XRD patterns presents on figures 3, 4 and 5 show the behavior of deposits of zinc on the substrate of the functionalized NTC on each concentration determined (NTC-Zn 20:80; NTC-Zn 50:50; NTC-Zn 80:20), respectively.

The crystallite size of the coatings was calculated from the XRD data using Debye- Scherrer equation and was found to be creasing with increase in deposition Zn on the substrate of CNT: 29.5nm (CNT-Zn,80:20), 180nm (CNT-Zn, 50:50) and a maximum of 352nm (CNT-Zn, 20:80).

As is apparent, the behavior the concentration NTC-Zn 80:20 presents better crystallite size and if could be inferred that will to present better coating properties.

Electrochemical Analysis

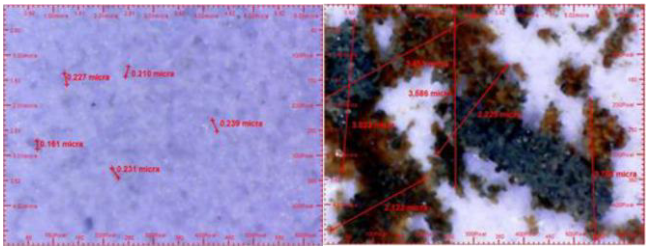

FIG. 6.- Micrograph 400x coating CNT-commercial paint at 10 and 1600 CV.

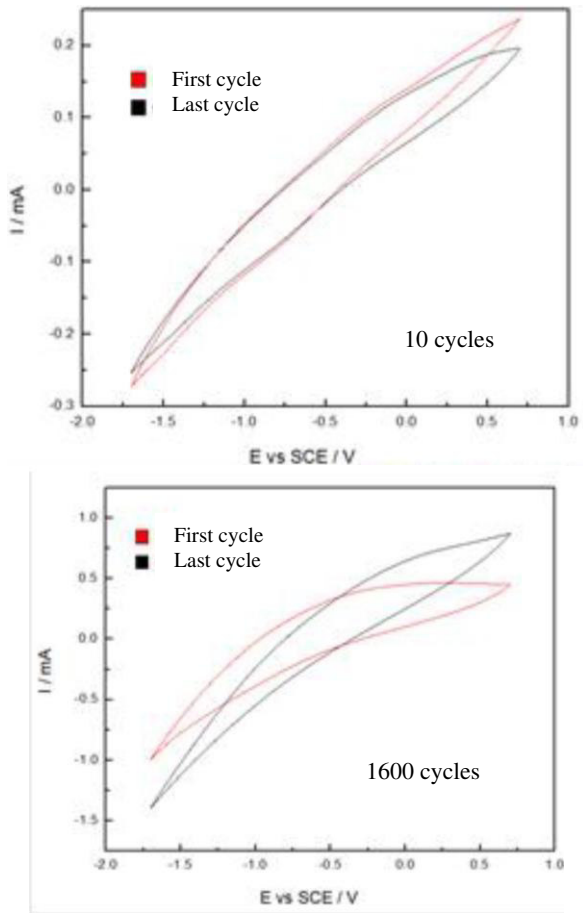

FIG. 7.- Cyclic voltammetry at 10 and 1600 CV of a coating CNT-Commercial anticorrosive coating.

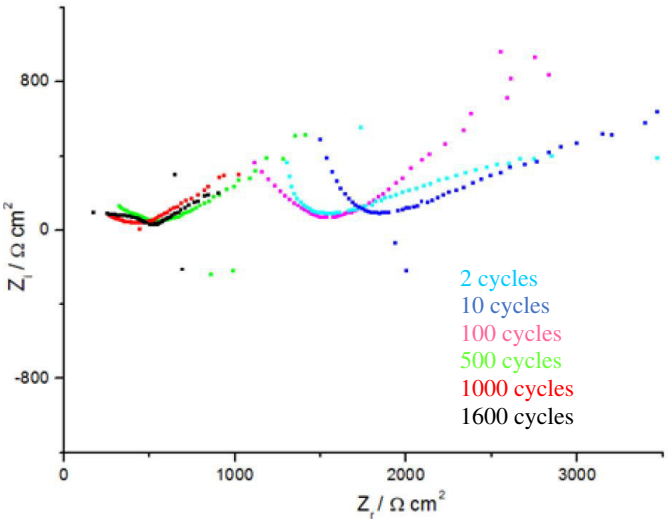

FIG. 8.- Electrochemical Impedance Spectroscopy at a coating CNT-Commercial anticorrosive coating.

Figures 7 and 8 shows some of the electrochemical tests (Cyclic Voltammetry, Electrochemical Impedance Spectroscopy) performed in a previous investigation of an anticorrosive coating composed of multiple wall carbon nanotubes (MWCNT's) and commercial anticorrosive paint, the study analyzed the possibility of an improved efficiency and lifetime in a commercial coating by adding and diluting the carbon nanotubes in the base paint or substrate.

The results showed that the properties of conductivity (cathodic protection), dispersion capacity and reduction in the pore size of CNTs enhanced in 100 cycles of voltammetry (cv), coating life of 1500 CV at 1600 CV before to produce corrosion residues.

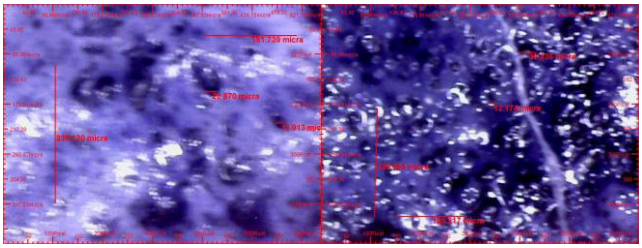

FIG. 9.- Micrograph 800x coating CNT-Zn 50:50 anticorrosive coating at 10 and 1700CV.

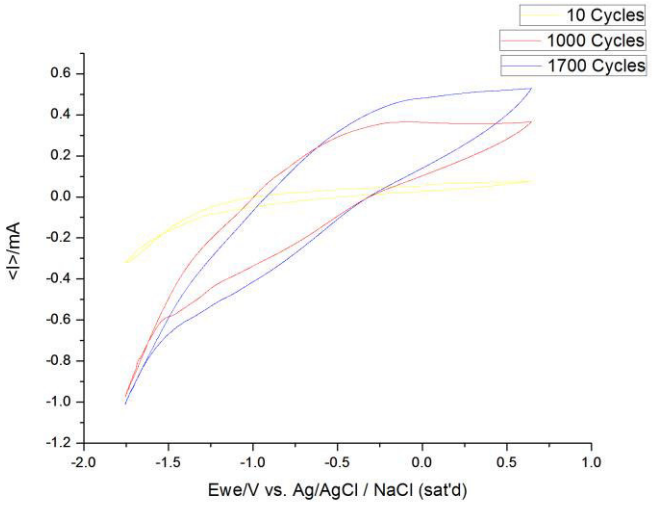

FIG. 10.- Cyclic voltammetry at 10, 1000 and 1700 CV of a coating CNT-Zn 50:50 anticorrosive coating.

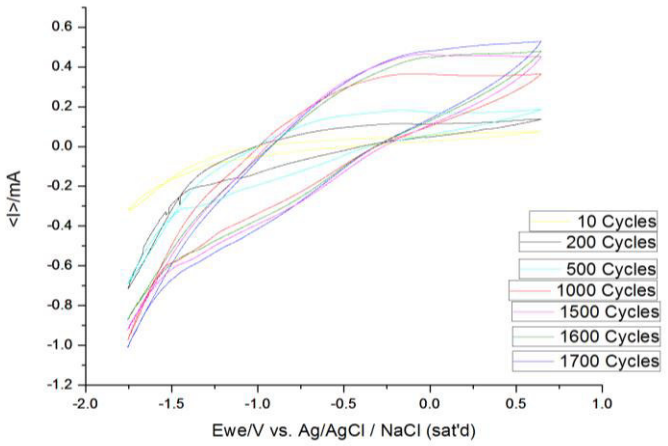

FIG. 11.- Cyclic voltammetry at 10, 200, 500, 1000, 1500, 1600 and 1700 CV of a coating CNT-Zn 50:50 anticorrosive coating.

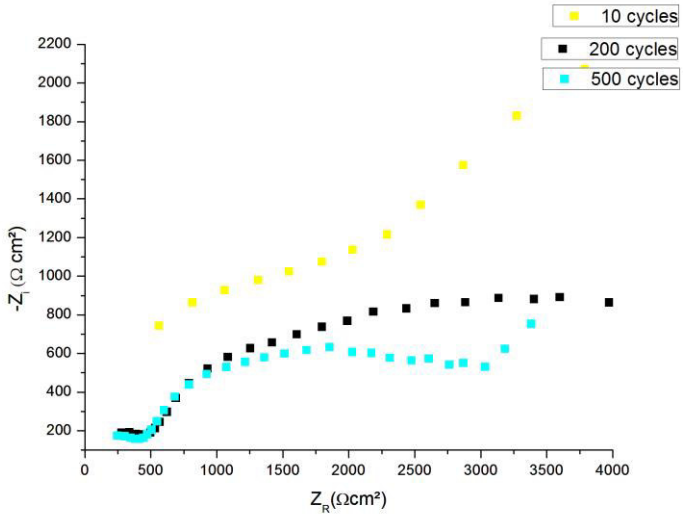

FIG. 12.-Electrochemical Impedance Spectroscopy at a coating CNT-Zn 50:50 anticorrosive coating at 10, 200 and 500 CV.

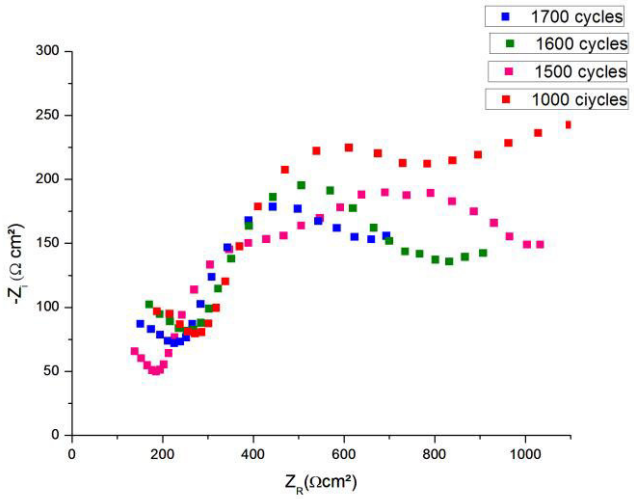

FIG. 13.- Electrochemical Impedance Spectroscopy at a coating CNT-Zn 50:50 anticorrosive coating at 1000, 1500, 1600 and 1700CV.

Figures 10, 11, 12 and 13 shows some of the electrochemical tests (cyclic voltammetry, electrochemical impedance spectroscopy) made to the compound CNT-Zn in 50:50 concentration achieving at least 1700 CV without showing any presence of corrosion in their micrographs, nevertheless is easy infer on the figures 12 and 13 that resistance to pass of electrons is decreasing in function of amount de number of cycles of Voltammetry.

IV CONCLUSION

Preliminarily it has been shown that the efficiency of the CNT-Zn compounds as anticorrosive coatings has proved to be superior to commercial paint coatings and CNT or simple anticorrosive commercial coating; the study shown here was suspended due to time issues for the presentation at this congress, the expected expectation is at least reach the 2000 CV with any of the three concentrations of CNT-Zn and fully know the scope of this compound.
Note: A 0.036gr coat of 50:50 CNT-Zn compound was used as a coating for a work area of 0.71cm².

V ACKNOWLEDGES

The authors acknowledge CONACYT (Conacyt,Cátedras 266483 and Ciencia Básica 235848) for the financial support and Instituto Tecnológico de Cancun for the technical support and CINVESTAV Queretaro for the technical support.

VI REFERENCES

[1] Torres-Acosta; Valle-Moreno; Pérez-Quiroz; Camacho-Hurtado, Martínez-Madrid; *El uso de una pintura rica en Zinc como sistema de Protección Catódica en concreto*. Instituto Mexicano del Transporte (IMT), (2002), ISSN 0188-7297, p. 17-18.

[2] F. L. De Volder; H. Tawfick; H. Baughman; A. Hart. Carbon Nanotubes: Present and Future Commercial Applications. *Sicence 339*, DOI: 10.1126/science.1222453, (2013) , p. 535-538

[3] B.M. Praveen, T.V. Venkatesha, Y. Arthoba Naik, K. Prashantha. Corrosion studies of carbon nanotubes–Zn composite coating; *Surface & Coatings Technology, 201,* (2007); p. 5836-5838.

[4] SungMo Park, MinYoung Shon. Effects of multi-walled carbon nano tubes on corrosion protection of zinc rich epoxy resin coating; *Journal of Industrial and Engineering Chemistry,* 21 (2014), P. 1258-1260.

[5] Moises Perez; Aplicación de Nanotubos de Carbono Multipared como protector catódico de la corrosión en acero de refuerzo. *Tesis de grado Maestro en construcción ITCH*.(2016).

[6] Dresselhaus, M. S., Dresselhaus, G., Saito, R. & Jorio, a. Raman spectroscopy of carbon nanotubes. Phys. Rep. 409, 47–99 (2005).

[7] Costa, S. Raman Study on Doped Multiwalled Carbon Nanotubes. Acta Phys. Pol. A 116, (2009). p.32–35.

[8] Costa, S., Borowiak-Palen, E., Kruszyńska, M., Bachmatiuk, a & Kaleńczuk, R. J. Characterization of carbon nanotubes by Raman spectroscopy. Mater. Sci. 26, (2008) p.433–441

[9] DiLeo, R. a., Landi, B. J. & Raffaelle, R. P. Purity assessment of multiwalled carbon nanotubes by Raman spectroscopy. J. Appl. Phys. 101, (2007) p. 64307.

[10] Hou, P. X., Liu, C. & Cheng, H. M. Purification of carbon nanotubes. Carbon N. Y. 46, (2008) p.2003–2025.

[11] Osswald, S., Havel, M. & Gogotsi, Y. Monitoring oxidation of multiwalled carbon nanotubes by Raman spectroscopy. J. Raman Spectrosc. 38, (2007) p.728–736.

[12] Zhao, X. et al. Multiple splitting of G-band modes from individual multiwalled carbon nanotubes. Appl. Phys. Lett. 81, (2002) p. 2550–2552.

CONACYT
Consejo Nacional de Ciencia y Tecnología

CONCYTEQ

Analysis of physical and mechanical properties of Concrete Blocks using seawater for manufacturing

José Antonio SANDOVAL MORFIN[1]
Engineering Faculty
Universidad Autónoma de Querétaro
Santiago de Querétaro, Querétaro, Mexico
Chesm_19@hotmail.com

Rubén RAMIREZ JIMÉNEZ[2]
Engineering Faculty
Universidad Autónoma de Querétaro
Santiago de Querétaro, Querétaro, Mexico
Ruraji@uaq.mx

***Abstract*— The use of seawater in the construction industry is quite small, this is mainly due to corrosion effects it has on the steel, it is necessary to use additives to resist chlorides and sulfates when it comes to concrete, various researchers have studied for years the effects of seawater in reinforced concrete. On the other hand the field of masonry elements has been left behind, these materials are not reinforced with steel and often have non-structural use. In Mexico consumed around 748,078m3 of drinking water for making concrete blocks and bricks, it is estimated that by 2020 water consumption in this industry reach 1,496,156 m3, enough to supply populations for months. In this project the effects of seawater will be analyzed to make masonry elements, evaluating their impact on the characteristic properties of these materials following the regulations of Mexico, an optimized mixing design was proposed to use seawater to obtain suitable properties of concrete blocks.**

Keywords*— *concrete blocks, corrosion, seawater, drinking water.

I. INTRODUCTION (*HEADING 1*)

Masonry is one of the most commonly used building systems for erecting walls or foundations at the global level. It consists of orderly joining elements such as rocks, partitions or prefabricated blocks of concrete by means of a cementing compound such as mortar, adobe, cement, etc. In Mexico, 95% of the homes under construction in the country are made of masonry, for which the annual demand for bricks and blocks is estimated at 2,618,181 thousand [16].

The economic crisis, inflation, devaluation, etc. have caused that the materials used for the manufacture of prefabricated blocks are increased, generating with this that the public and private works diminish. The builder has sought ways to do more with less, that is, he uses materials and systems that reduce the price without sacrificing the integrity of the work. Looking for sustainable products that do not raise their prices over time would be ideal, however, construction materials are practically certified so as not to jeopardize people's safety, which implies a complex validation process.

For centuries water has been a key factor for quality in construction, it is used to manufacture all concrete structures, masonry and in the vast majority of finishes. Its quality is regulated by NMX-C-122-05, where one of the most important factors is the content of salts, such as chlorides and sulfates. The water used is usually potable as our homes, with a maximum of 4 grams of salt per liter, compared to sea water, it has an average of 35 grams per liter. The problem lies in the corrosion, the higher the salt content, the greater corrosion.

Reinforced concrete is a material used to create continuous structures where the elements are cast in monolithic form, if corrosion attacks an area of the structure it is likely that over the years it will spread throughout it, steel bars become Thinner to present the fault, is similar to a cancer, this spreads throughout the body weakening gradually all our defenses to death, on the other hand the structures of masonry come to present corrosion in its outer layer however not type Structural, because they are not elements that contain steel, its interior is not weakened, only have efflorescence and in extreme cases external collapses.

The behavior of masonry elements is very similar to that of simple concrete, due to its composition, both are composed of cement, aggregates and water, but the proportions of the mixtures are very different.

The prefabricated blocks are not intended to be very resistant on their own, but for this reason the minimum compressive strength of a partition is 30 kg / cm2, but since the concrete is used for structural purposes must have resistance to the Compression ratio of 100 kg / cm2 and commonly in the housing resistance of 250 kg / cm2 for structural use. The

regulations for concrete and masonry structures in Mexico are very strict since the earthquake of 85, it can be said that the safety factors are high, however these standards are focused on the design and construction, the standards for the manufacture of materials is In charge of the ONNCCE, this body determined as valid the use of sea water to manufacture elements that do not contain reinforcing steel.

Around the world, different studies have been carried out on the impact of sea water on concrete, most of them focused on the analysis of the effects of weathering on marine climate, may be without contact or contact with sea water, researchers Have focused on the chemical analysis of the salts on the reinforcing steel and the strength of the structures since these aspects represent reasons for failure in the structure. Because it is inevitable to build near coastal areas, the chemical deterioration of concrete when subjected to seawater has been a topic of interest to researchers for decades, and the findings have revealed some very important facts but still require further study [1].

The main chemical components of sea water are chloride, sodium, magnesium, calcium and potassium ions. However, sodium chloride (NaCl) with an approximate 35 g / l, which represents 88% of dissolved salts in seawater, predominates [2]. PH values for sea water vary between 7.4 and 8.4. The corrosion of the reinforcing steel occurs below a PH of 11. Therefore, in cases where the concrete is subjected to a severe environment such as sea water, the cement must provide alkalinity with some additive [3]

The chemical reactions of seawater with concrete are mainly due to attack by magnesium sulphate (MgSO4), which attacks by crystallization, which reacts with the calcium hydroxide Ca (OH) 2, which is present in the cement, this Reaction generates the formation of soluble magnesium hydroxide (Mg (OH) 2) which in turn forces the reaction to form gypsum which leaves a weak concrete where the adhesion of calcium (Ca II) particles is not concretized leaving pores In the microstructure, chloride ions penetrate and cause accelerated corrosion in steel reinforcement [4].

Several solutions have been found for the attack of the sulfates in the concrete with years of experimentation, a Portland cement that is resistant to sulphates (CRS) has been created and is currently used in all types of structures near the sea, as well as the creation of Additives that prevent corrosion of the steel, creating protective layers where the oxidation fails to penetrate.

There are several studies that have demonstrated the effects of mixing and curing of cement and sand mortars, as well as concrete with sea water focusing mainly on compression. Some research indicates that seawater is not suitable for mixing and curing of reinforced concrete under marine conditions [5]. However, concrete made with seawater may have an initial above-normal strength of concrete with potable water and the reduction of strength with age can be compensated with the water-cement ratio. Naghoj and Abdel-Rahmna (2005) reported that the addition of Loam (a type of sedimentary soil with a balanced proportion of sand, silt and clay particles) in a concrete mix can increase the compressive strength under normal conditions and improve Performance to withstand the aggressive means of seawater. Binci et al. (2008) reported that the use of steel slag or steel sand (GBS) as well as pumice ground (GBP) have a beneficial effect on the compressive strength loss due to seawater attack and abrasion.

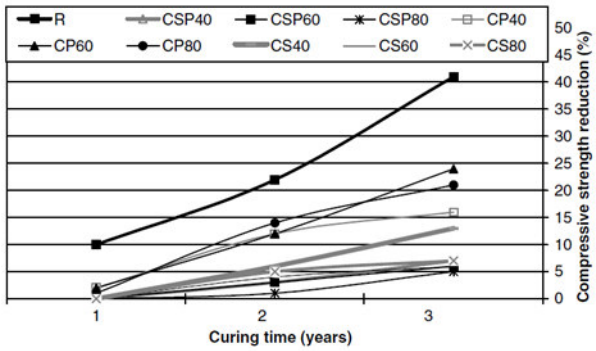

Fig.1 Graphic of the Reduction of the Compression of elements in Agua de Mar [7]

In Fig. 1 it can be seen that the effects of seawater after 3 years can be very harmful or negligible depending on the type of mixture, the addition of GBS in the mixture seems to present better results than the addition of GBP, on the other Side without the addition of these materials present the worst results in a standard mixture (R), the elements with better results presented a decrease of the resistance of 5% (CSP60 and CS80), those that had worse performance showed a reduction of the 25% - 40%, it is important to consider that an element immersed in seawater is in an overly adverse condition [7]. The characteristics of the mixtures with the best results and the worst ones are presented in Table 1.

Table 1 Properties of the mixtures [7]

Mix ID	CSP60	CS80	R	CP60
Cement (kg/m3)	300	300	300	300
GBP (kg/m3)	165	-	-	330
GBP (%)	30	-	-	60
GBS (kg/m3)	165	440	-	-
GBS (%)	30	80	-	-
Water (kg/m3)	165	159	135	159
Sand (kg/m3)	385	330	550	385
Gravel (kg/m3)	1200	1200	1200	1200
Air Content (%)	4	3.8	4	3.8
Temperature (°C)	29	29	28	30
Strength Loss (%)	5	7.5	40	25

Binci et al (2008) worked with constant cement and aggregate proportions, the amount of water and fine aggregate were the factors that varied, as well as the addition of GBS and GBP.

The great majority of studies agree that in order to mitigate the aggressive effects of sulfates in seawater, low water-

cement ratios must be worked, resulting in better workability to the mixture, as well as improved Cement bonding together with crystallization occurs as a result of a loss of resistance at early ages [8]. For this reason it is necessary to mitigate the reaction of the sulfates with the cement in the possible way.

Tébar and Sagrera (1991) reported effects very similar to those of Binci, made mortar specimens by adding steel slag in blast furnaces, fly ash and siliceous sand. These specimens were immersed in potable water, sea water and a proposal for artificial sea water with a composition very similar to that of the Autonomous Port of Huelva, Spain, where the study was carried out. The best results show a minimal change in the resistance of elements immersed in sea water against the elements immersed in filtered drinking water, this variation tends to be equal with time, this change is due to the effect of the salts for an initial period, It should be noted that for 3 years the decrease was less than 5%.

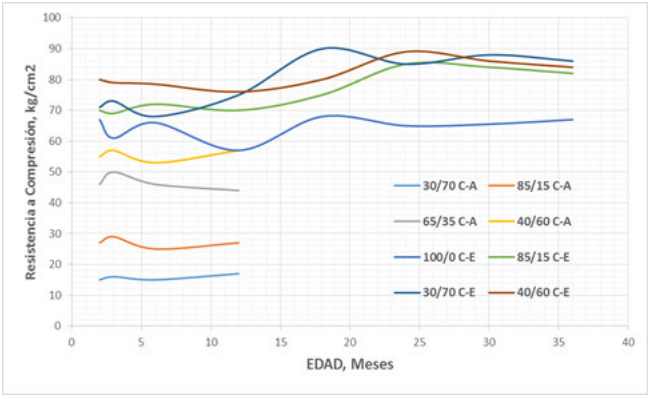

Fig. 2 Evolution of the mechanical resistances, to flexo-tensile. Elements in Drinking Water with different relations Cement / Siliceous Sand or Slag (C-A, C-E) [9]

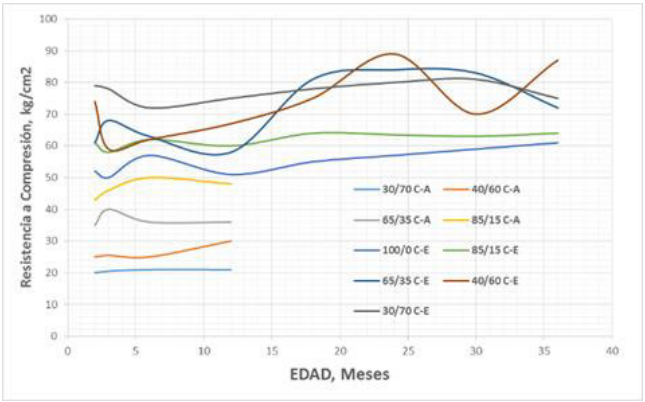

Fig.3 Evolution of the mechanical resistance, to flexo-traction. Elements in Sea Water with different relationships Cement / Siliceous Sand or Slag (C-A, C-E) [9]

In Fig. 2 and 3 we can see a comparison between the elements submerged in drinking water and the elements submerged in sea water, the resistance calculated for the mixtures is 90 kg / cm2, in both graphs it can be noticed that the mixtures Tend to reach the resistance, however in the elements with sea water the fall of resistance is more pronounced in some mixtures.

Tébar and Sagrera (1991) agree with Binci et al. (2008), in which the GBS addiction can mitigate resistance reduction to a great extent, obtaining very favorable results with low resistance losses.

Regarding sea water in curing and mixing of concrete, Wegian (2010) performed tests on cubic specimens, comparing the effects of CRS against Traditional Portland Cement (TC) on concrete mixtures with and without seawater. The results with CRS were not as good as expected, using simple variations in the water-cement ratio yielded better results.

More recent studies recommend adding Metakaolin (MK) when using seawater in the mixing of concrete [11]. The MK is a supplementary cementic material with high pozzolanic activity, the concrete application of which dates back to 1960 during the construction of the Jupiá dam in Brazil. The MK is made by heating Kaolin to temperatures of 650-800 ° C, at this point the long-range structure of the silicon-aluminum layer deteriorates with a deformation in the structure due to the loss of the intermediate layer of water and OH [12]. By the addition of MK in concrete mixtures, the compressive strength of the concrete was improved, the porosity and permeability reduced and the pore structures were refined due to the filling effect [13]. Fernández et al. (2011) evaluated mortar specimens where the cementitious material were mixtures of CT and different types of annealed clay.

Table 2 Properties of mortars [13]

Mix ID	Clay Type	Activation Temperature (C°)	% Substitution	%CT	Water/Cement
K600	Caolín	600	30	70	0.4/0.5
K800	Caolín	800	30	70	0.4/0.5
I600	Illita	600	30	70	0.4/0.5
I800	Illita	800	30	70	0.4/0.5
M600	Montmorilonita	600	30	70	0.4/0.5
M800	Montmorilonita	800	30	70	0.4/0.5
CT	----------	---------	0	100	0.4/0.5

The results showed that the best pozzolanic properties of a clay after being subjected to a calcination process have the kaolin, when being combined with the CT an increase in the small compressive strength is obtained comparing with the TC without being mixed, respect To the other clays the difference is too great.

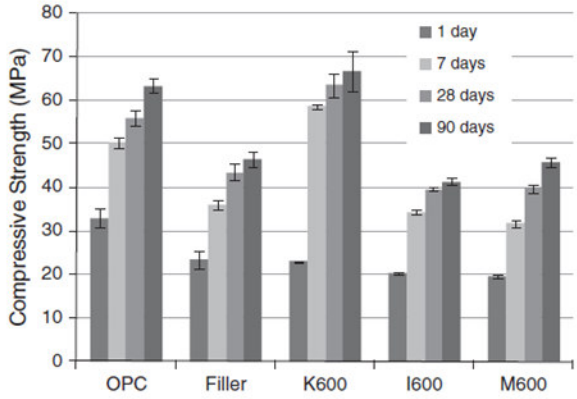

Fig.4 Evolution of compressive strength of calcined clay - cement mortar [13]

The previously mentioned study by Q. Li et al. (2015) evaluated different mixtures of concrete mixed and cured with sea water and potable water but unlike Wegian (2010) added different% of MK. Their mixtures contained percentages of 8-25% MK. The resistance of the elements mixed and cured with sea water and 21% of MK, presented the highest resistance of all.

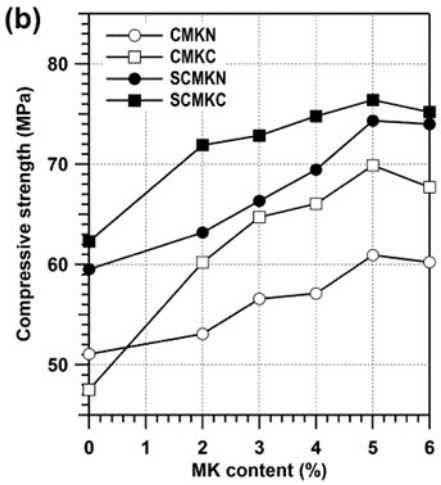

Fig.5 Development of concrete compression strengths varying% MK [11]

The CMK elements are those mixed with potable water, the SCMK are those mixed with sea water, the last letter means the water with which it was cured N or C, N is drinking water and C sea water. As mentioned above SCMKC type concrete reported a better performance against the effects that sea water usually develops on concrete.

II. METHODOLOGY

This research aims to:

"Analyze the effects of Sea Water on the manufacture of Concrete Blocks, comparing their properties with those made with Drinking Water, to validate the safety of the use of Sea Water in this industry."

To meet this goal, it will be necessary to take into consideration 2 key points:

- Adhere to the Norms
- Facing the salinity of sea water with the help of previous research

A. *Identify Variables*

The difference between the concrete and a block lies mainly in the proportions and type of aggregates and the amount of cement used. The main components and adjustable variables of the partition are:

I. Cement

II. Sand

III. Gravel

   a. Jal

   b. Tepojal

   c. Confitillo

IV. Water

V. Water-Cement Ratio

VI. Additives

In response to the variation of these parameters we expect a change in the following properties:

1. Compressive strength
2. Absorption
3. Shrinkage by drying
4. Specific weight
5. Efflorescence

In the NMX-C-441 we find all the characteristics that the elements of masonry present, their dimensions, the technical specifications that they must comply and the different methods of tests that must be done to a sample of the production. The elements of masonry are classified first by their dimensions, the biggest ones enter the branch of Concrete Blocks, and the small ones in Bricks and Partitions.

Table. 3 Classification of pieces according to their dimensions [20]

Piece	width (cm)	height (cm)	Long (cm)
Cement Blocks	10 to 30	10 to 30	Over 30
Bricks and other annealing blocks	10 to 30	until 15	until 30

The minimum compressive strength for partitions is 35 kg / cm2 and the maximum average water absorption is 25% for 24hrs [20]

B. Mix Desing

The great majority of the sewage manufacturers make the mixtures without keeping a detailed record of the quantities in which the ingredients are incorporated, with the exception of cement, which, being the highest cost ingredient, is strictly controlled. Very basic proportions are used which may vary depending on the industry and the type of block to be worked, the mixtures may differ between a hollow block and a solid block, these are generally based on the manufacturer's experience.

We will work with mixtures used in the state of Querétaro, the manufacturers gave us the following proportions to make wallboard:

The shape of the mixture is Cement-Sand-Gravel.

a) 1:2:5
b) 1:5:2
c) 1:5:3
d) 1:2:7

Water is added about 20% less than cement. For each mixture the amounts of material are different. The procedure is as follows. For the proportioning a) 1: 2: 5

Volumetric Weights (Meli, 1985)

- PV Sand = 1580 kg/m3
- PV Gravel (Tepojal) = 733 kg/m3
- PV Cement CT= 1510 kg/m3

Taking into consideration that the dimensions of the Block are 10x14x28 (Block used in construction) we get its volume:

$$V = 0.1 * 0.14 * 0.28 = 0.00392\ m3$$

We will consider that 10 specimens are made in each mix to advance faster. It is important to remember that waste is always generated in this case we take 10%.

$$Vtotal = 10 * .00392 * 1.1 = 0.04312 m3$$

Considering for the mixture a) 1: 2: 5 a total of 8 parts, divide the volume by 8 to obtain the volume of each part.

V per part = 0.04312/ 8 = 0.00539 m3

This quantity is multiplied by the number of parts of each aggregate involved in the mixture and by its PV of the aggregate to obtain the quantities per unit weight of each aggregate.

*Sand Weight = 0.00539*2*1580 = 17.03 kg*

*Gravel Weight = 0.00539*5*733 = 19.75 kg*

*Cement Weight = 0.00539*1*1510 = 8.19 kg*

To these quantities we add 30% due to the arrangement of the particles by the vibration and compacted to which the specimens are subjected, at this weight we will call it Real Weight (RW).

RW Sand = 22.14 kg

RW Gravel = 25.67 kg

RW Cement = 10.65 kg

In this way the proportioning is performed for each mixture.

Table. 4 Proportions of Materials to make 10 Blocks.

Mix ID	Sand (kg)	Gravel (kg)	Cement (kg)	Water (Lt)
A	22.14	25.67	10.65	8.5
B	42.58	7.90	10.65	8.5
C	37.84	7.00	7.23	6.5
D	15.90	25.8	7.60	7.0

In the event that the tests are deficient, mixtures will be made by replacing 21% of the cement with MK as performed by Q. Li et al. (2015) for each type of mixture, we will need the following amounts of MK.

Table. 5 Quantity of Cement and MK to make 10 Blocks.

Mix ID	Cement (kg)	MK (kg)
A	8.52	2.13
B	8.52	2.13
C	5.78	1.44
D	6.10	1.52

C. Desing of Experiment

For this experiment the compressive strength of specimens with different proportions will be evaluated in their mix design and at three different test ages, which are 7, 14 and 28 days, being the result of resistance to 28 days the most solid data. All these specimens will be made with sea water in their mixing and those with sea water will be bought in the factories.

Table. 6 Experimental Matrix for compressive strength of Specimens.

Mix ID	Compressive Strength kg/cm2		
	Test Age (days)		
	7	14	28
A	X1	Y1	Z1
B	X2	Y2	Z2

C	X3	Y3	Z3
D	X4	Y4	Z4

In order to obtain the total number of specimens with which the experiment was carried out, the factorial experiment was calculated taking into account the factors that intervene in the following way:

a) Mixtures No. = 4

b) Test Age = 3

c) Water Type = 2

d) No. of specimens by mix, age, water = 5

Total of Blocks = 4 * 3 * 2 * 3 = 102

D. Manufacture of Blocks

In all productive process of masonry elements, a series of activities are carried out which are closely related to each other; The quality of the final product will depend on the fact that the different processes are carried out in compliance with the technical requirements. In the same way, in each process from the initial activities to the end, they must be organized in concatenated and clearly defined stages, which conclude in the elaboration of the product. In this case the final product is the partition, the following is the sequence of the activities to manufacture partitions:

A) Selection of Materials

• Thin and coarse aggregate

• Cement (Brand, Type, etc.)

• Water Selection

• Will you add additives?

B) Equipment Availability

• Mixing Equipment

• Molding Equipment

• Vibrating Equipment

C) Dosing and Mixing

• It is metered according to the type of mixture cement, sand and gravel.

• Mix with dry equipment.

• Add water slowly until desired texture is obtained.

• The mixing can be manual or with equipment type spinning.

D) Molded and Molded

• Fill the mold in layers as it vibrates.

• Vibration is maintained until a water film is observed on the surface.

• The demolding must be done with care on a flat surface, avoiding to hit the unit.

• Avoid manipulation of blocks.

E) Cured

• Specimens should be covered with clear plastic to avoid losing moisture and being watered for at least 7 days.

F) Stored

• Walls should be kept dry and protected from moisture.

E. Sampling and Quality Control

In order to evaluate the quality of the elements manufactured, the NMX-C-441 marks a sample of 3-5 elements for each mixture, it will be necessary to do 3 main tests:

i. Compressive Strength: On the NMX-C-036 we will obtain the characteristics of the test to measure Compression Resistance. The test is very basic, it consists of exerting vertical pressure on the faces of the element until it reaches its fault, for this a universal machine will be necessary.

ii. Total Absorption in 24 hours: In the NMX-C-037 we will obtain the characteristics of the test to measure Absorption. This test involves moistening the elements over a defined period of time and weighing the amount of water that was absorbed by the element, is very similar to a moisture test.

iii. Visual Inspection: The NMX-C-441 indicates that a visual inspection of the elements must be made for the following defects:

• Cracks

• Ampoules

• Fractures

• Disaggregation

• Efflorescence

III. Expected Results and Disscussion

The effects of sea water on concrete have been analyzed by too many researchers, some studies differ from others, for example Akinkurolere et al., (2007) recommend not to use sea water in concrete mixing, it is noteworthy that specifies that in concrete Reinforced with steel, which is very important because it was remarked from the beginning that the salts of the sea water attack mainly the steel.

On the other hand Binci et al., (2008) provides a solution to combat the effects of chloride ions and sulfates that alter the pozzolanic performance of cement. The article by Q. Li et al., (2015) gives us a very effective choice to work with sea water in concrete mixtures, MK seems to be an inhibitor of salt attack in simple concrete, its results are too encouraging, Although something that Q.Li et al., Did not mention is if it could be used for reinforced concrete, surely the results would be very different.

Finally, it is necessary to comment that none of the articles mentioned in this work is focused on elements of masonry, however the blocks are very similar to concrete, much weaker in resistance but in composition almost equal, so it is probable that the results of these studies apply very similar to blocks and partitions.

It is probable that the resistances of the mixtures with sea water and without MK can diminish but as it is demonstrated will not go over 5%, if after this decrease the standards are not met it will be necessary to add a % MK to the mixture hoping that this cover the specified technical requirements.

REFERENCES

[1] Kumar, S., 2000. Influence of water quality on the strength of plain and blended cement concretes in marine environments. Cement and Concrete Research, 30 (3), 345–350.

[2] McCoy, W.J., 1996. Mixing and curing water for concrete. Significance of tests and properties of concrete and concrete making materials, STP 169-A. Philadelphia, PA: American Society for Testing and Materials, 515–521.

[3] Gani, M.S.J., 1997. Cement and concrete. 1st ed. England: Chapman and Hills, 49–169.

[4] Swamy, R.N., 1991. The alkali-silica reaction in concrete. London: Spon Press.

[5] Akinkurolere, O.O., Jiang, C., and Shobola, O.M., 2007. The influence of salt water on the compressive strength of concrete. Journal of Engineering Applied Science, 2(2), 412–415.

[6] Naghoj, N.M. and Abdel-Rahmna, N., 2005. Enhancing the performance of concrete subjected to salty seawater. In: Admixtures – enhancing concrete performance, the international conference, Dundee, Scotland, UK. London: Thomas Telford, 35–40.

[7] Binici,H., et al., 2008. Performance of ground blast furnace and ground basaltic pumice concrete against seawater attack. Construction and Building Materials, 22 (7), 1515–1526. Building Code Requirements for Structural Concrete (318–99) and Commentary (318 R-99) (1999). Farmington Hills, MI: American Concrete Institute.

[8] Zaher, K. and Shihada, S., 2003. Effect of Gaza seawater on concrete strength for different exposures. Journal of the Islamic University of Gaza, 11 (20), 156–172.

[9] Gaspar Tebar, J. L. Sagrera Moreno, M. Aguanell Garcia, and V. Gonzalez Vila, “Durabilidad del hormigón: Influencia de la adición de escoria a un cemento Portland resistente a los sulfatos. Acción del agua de mar y de una disolución saturada de yeso,” Mater. construcción., vol. 40, no. 217, pp. 53–67, 1990.

[10] F. M. Wegian, “Effect of seawater for mixing and curing on structural concrete,” IES J. Part A Civ. Struct. Eng., vol. 3, no. 4, pp. 235–243, 2010.

[11] Q. Li, H. Geng, Y. Huang, and Z. Shui, “Chloride resistance of concrete with metakaolin addition and seawater mixing: A comparative study,” Constr. Build. Mater., vol. 101, pp. 184–192, 2015.

[12] M. Murat, C. Comel, Hydration reaction and hardening of calcined clays and related minerals III. Influence of calcination process of kaolinite on mechanical strengths of hardened metakaolinite, Cem. Concr. Res. 13 (5) (1983) 631–637.

[13] R. Fernandez, F. Martirena, K.L. Scrivener, The origin of the pozzolanic activity of calcined clay minerals: a comparison between kaolinite, illite and montmorillonite, Cem. Concr. Res. 41 (1) (2011) 113–122.

[14] Meli R. 1985, “Diseño Estructural”. 1ra Ed. Editorial Limusa, México DF.

[15] CONAGUA, “Situación de los recursos hídricos” en Estadísticas del agua en México, Ed. 2014, México D.F., CONAGUA, 2014, pp. 23¬-55.

[16] INEGI, Censos Económicos, 2010.

[17] Norma Mexicana NMX-C-036-ONNCCE-2004. Diario Oficial de la Federación. Publicada 27/07/2004.

[18] Norma Mexicana NMX-C-037-ONNCCE-2005. Diario Oficial de la Federación. Publicada 25/04/2005.

[19] Norma Mexicana NMX-C-038-ONNCCE-2005. Diario Oficial de la Federación. Publicada 25/04/2005.

[20] Norma Mexicana NMX-C-441-ONNCCE-2005. Diario Oficial de la Federación. Publicada 25/04/2005.

Lighting and thermal confort in Intelligent buildings

Review

Emiliano Ponce López
Department of civil engineer
Faculty of engineer UAQ, Cerro de las Campanas S/N
Querétaro, México
emiliano.ponce.lopez@gmail.com

Omar Chavez Alegría
Department of civil engineer
Faculty of engineer UAQ, Cerro de las Campanas S/N
Querétaro, México

Juan Román Sánchez Gómez
Department of civil engineer
Faculty of engineer UAQ, Cerro de las Campanas S/N
Querétaro, México

José Gabriel Ríos Moreno
Department of civil engineer
Faculty of engineer UAQ, Cerro de las Campanas S/N
Querétaro, México
riosg@uaq.mx

Bruno Azael Lazarini de la Fuente
Department of civil engineer
Faculty of engineer UAQ, Cerro de las Campanas S/N
Querétaro, México

Mario Trejo Perea
Department of civil engineer
Faculty of engineer UAQ, Cerro de las Campanas S/N
Querétaro, México
mtp@uaq.mx

***Abstract*—** *In this review we look for the technological and practical advances destined to the thermal and light control that in our opinion are applicable to our situation in Mexico, for this we looked for in different sources, we analyze which require less investment, political, social or economic development and to see which have already been carried out, we hope to find sustainable technologies for the environment and to contribute to our research in thermal and light comfort, some of the techniques and technologies applied today should have already been overcome or at least improved since as civilization we have been able to adapt the environment in any type of climate.*

***Keywords*—** *Termo-confort, Smart-bulding, Eco-desing.*

I. INTRODUCTION

In recent decades climate change has become a fact, pollution is present in almost every major city in the world, clear examples of which are China with surprising levels of pollution (1), that is why we should choose to use the Less natural resources, and electricity consumption. To date, almost 45% of electric energy is consumed by offices in lighting and climate control (2), with the correct management and control systems could be reduced by 60% this consumption (3).

This only indicates that they do not have a correct control both light and thermal in these buildings, if this is extrapolated to the living room consumption is equally alarming, for these reasons should be invested in thermal comfort and sustainable light.

II. LIGHTING CONFORT

A. Lighting needs

Currently it is required to illuminate the most similar to natural light as it presents greater benefits to physical and psychological health (5), however this does not necessarily generate the highest levels of comfort, since this is changing respect for the geographical area, Climate, whether it is day or night, and what activity is performing (6).

Currently, to carry out any activity, a minimum of 20 lux is required, which is the average luminosity of an overnight parking lot, and a maximum of 2000 lux for very precise activity.

B. Technological development in the field of lighting

To date there are four main lamps for lighting in any type of construction, which are incandescent, halogen, electric arc

and fluorescent lamps, although there are also different types of light control and consumption of electric energy spent in lighting in this review We are important to highlight the technological advances as well as in control systems to achieve the greatest electric saving since in the end the user is who he considers to be more comfortable for him.

As far as light development is concerned one of the most remarkable achievements is the creation of natural blue light in leds (7), created by Isamu Akasaki Nobel Prize winner in physics. This allows us to generate a certain degree of comfort depending on the users, since the comfort

Apart from this, after several investigations, LED spotlights have been placed as the most economical lighting equipment, however, a process of analysis must be continued to produce better LEDs that are more environmentally friendly and with production costs (8).

Completing other research in the area of electrical energy saving from lighting, Tongji University led by Leu Xu, designed a system that detected the presence of users, the natural light that entered the room and calculated how much light should provide System to maintain an electric saving and a balanced light comfort, with this they achieved a 30% saving with the pure sensor that detected the presence of users and 23% with the natural light detector (9).

Similarly, H. Burak Gunay experimented in a series of offices with the use of blinds and artificial lighting, so that after a time of gathering data they managed to create an algorithm that predicted the users' needs by saving electric energy (10)

On the other hand, the ability of passive lighting with bio-luminescent elements, which are able to illuminate zones in moments of complete obscurity, is already ignored. This has already been studied by several researchers who have found from fungi to elemental self-chargeable by energy Solar (11), these elements can be adapted to the construction, either in concrete or in mosaics, saving electricity at night when one requires the use of low illumination.

All this we have thought of meeting the needs of low illumination, which are in itself those of household although there is a demand that could well be adaptable to other needs, for example in Table 3 the different demands are observed

III. THERMAL CONFORT

Thermal comfort is defined as "that condition of the mind that provides satisfaction with the thermal environment" (12). In order to decide which is the ideal temperature to which the users are, it is necessary to analyze the environmental conditions, the production of heat per user, the apparent humidity, among other factors for this reason different researchers have developed their own systems to standardize, measure and Manipulate these variables.

A. Thermal Comfort Techniques

One of the most complete algorithms found in this research were those performed by Fanger, who from a mathematical and practical analysis develops his own system to define the ideal temperature of an enclosure depending on a series of factors such as relative humidity , Heat production, type of clothing, ambient temperature and relative air velocity. These data are used in one of the diagrams that appear as Fig. 1 and Fig. 2. In this case the author mentions that Fig. 1 is applicable in the conditions of sedentary activities, with a dress of 0 to 1 clo and a humidity Relative to 50% and Fig. 2 is applicable for 0- and sedentary activities. (12)

TABLE I. CLO VALUES

Clothing	*Clo*
Naked	0
Bikini	0.05
Short	0.1
Ordinary tropical chlothing	0.3
Light tropical suit	0.8
Typical business suit	1
Polar clothing	3-4

1 Clo= 0.155m^2 ºC/W (0.18 m^2h ºC/kcal), Standard values in Table 1. (12)

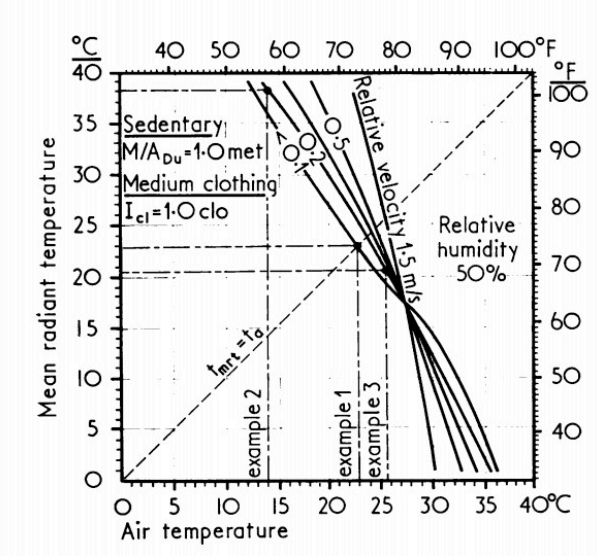

Fig. 1. Comfort diagram showing the combined influence of mean radiant temperature. And air temperature. The confort lines corresponding to five different velocities are curves through diferent combinations of mean radiant temperature and air temperature which will provide optimal thermal comfort.

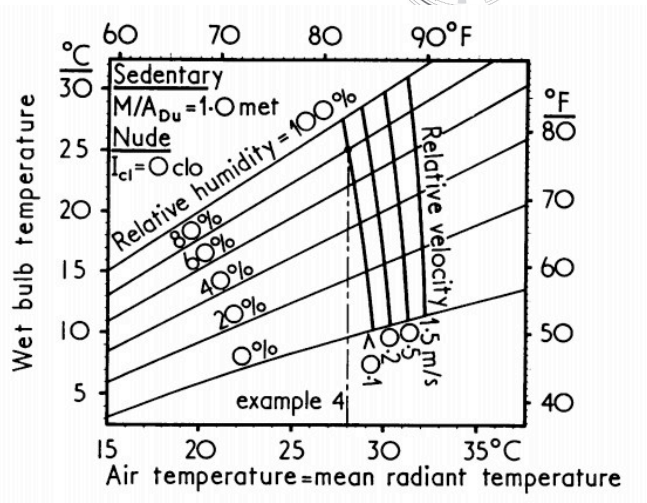

Fig. 2. Comfort diagram showing the combined influence of humidity and ambient temperature. The confort lines correspondig to four different velocities are curves through different combinations of ambient temperature and humidity which will provide optimal thermal comfort.

TABLE II. PMV

Clothing	*Clo*
3	Very Hot
2	Hot
1	Slightly hot
0	Thermal neutrality
-1	Fresh
2	Cold
-3	Very cold

Fig. 3. At the end of the predictive system was obtained the Predictive Mean Vote (PMV) obtained from Table 2, the idea of this qualification was to achieve that the thermal quality was equal to 0, usually presented a 5% of dissatisfaction . (12) Now with these data attached to other parameters, we proceed to make a series of calculations which by their length is recommended to read the full article 12.

The solar cooling is a technique for obtaining cold water which is injected into the ventilation system of a building, currently in the laboratories of the University of Seville is cooled in this way. (13) To obtain this cold water a Series of solar collectors are channeled to two boilers of hot water which inject this hot water to a machine which by a pressure system and cool a container with water, which proceeds to be introduced to the cooling system.

TABLE III. LIGTHING DEMAND

Area	*Lighting level*
Domestic	Hall and bedroom(50-150 lux), bathroom (150 lux), Toilet (100 lux).
Hotel	Reception (300 lux), room (100 lux)
Bookstore	General bookstore (300 lux), book shelves (150 lux)
Office	General and coference zones (500 lux)

This method despite being very strange of a that works with heat is very efficient, nevertheless there is always a backup system. (13) (15)

B. Technological advances in thermal comfort

One of the places in the world where the technology and techniques of thermal comfort, lighting comfort, and quality of air are applied, CDdI-CIESOL-ARFRISOL maintains a series of control systems, which are divided into four large groups, The measures of the interior of the building, the measurements of the ventilated façade, the measurements of the sensors extracted from the meteo-radiometric station, and the measurements of the sensors of the solar cooling system (14) very similar to those previously mentioned (13). All this construction is based mainly on a correct design of bioclimatic architecture and a network of sensors. Its main source of control is solar cooling, which consists of a field of solar collectors, a hot water storage system, a boiler and an absorption machine for producing solar cooling, which we explained earlier.

This research and technological advances are based on several investigations by other authors so that for reasons of shortening it is recommended to read the article that explains in detail how this technology works together (15).

Another practical technological advance that was very interesting is the use of Phase Change Material (PCM) which are applied in the construction of households in North America which are very light so they lose very easy thermal stability since there is no Body that slows the flow of heat in hot places, or maintains them in case of low temperatures. These PCMs are applicable in various parts of the world (16) and our team seems to be an alternative for low-income households, since they do not have a well-constructed housing with poor quality materials or materials that do not conform to the region. These can also be applied to quickly-built households for military, post-catastrophe support.

As the most economical developments in this area, Andrea Invidiata investigated the use of different window shading

systems, in which EnergyPlus software estimated the use of air conditioning for a year in different rooms with different shading systems, perforated concrete, blinds Double sliding aluminum, PVC roller shutters and double wooden shutters. In his results, he discovered that the use of wooden shutters and roller shutters made of PVC are the most appropriate solutions, not only in energy saving but also in their investment.

IV. Conclusion and discussion

A household with all the comforts of a smart home is completely possible if you are implemented with the right techniques and technologies, such as a system that maintains perpetual light control, constant analysis of air quality, and in a very important way a control of Thermal comfort. And all this we can see the research previously seen, which despite the fact that they are still expensive technologies over time can be cheap or plan from the beginning passive systems with a correct bio-architecture, with a correct analysis of the air circulation, a good Window design. In Mexico the architectural design of many buildings is nil, and in the case of existing it is only aesthetic rarely real solutions are presented to problems that are applied to a general solution and this solution does not always respond to that problem. As we could see throughout this review have to consider many variables to be able to make a correct thermal analysis and also a light, and although we do not venture into the issue of "air quality", we do not doubt that it is just as complex and relevant for construction.

All deserve a decent home, responsible with the environment and with its community, and one of the best options is a smart home with the adaptations according to the region.

And lastly a smart home is not necessarily a house full of sensors and computers, it is a house adaptable to the needs of the user at minimum cost and with the minimum subsidy of nature.

In the same way we consider that this type of housing is extrapolated to all types of construction, in which it is necessary to use systems that adapt the internal environment, in order to reduce electricity consumption and natural resources, since Indirectly the use of these equipment even if it possesses a power plant generating zero emissions does not absolve an air conditioning system to use natural resources and social resources for its craft. For this reason, must be developed every day in new systems responsible with the environment and society.

References

[1] Shuiping Cheng, “Heavy metal pollution in China: Origin, pattern and control”, Chinese Journals , vol. 10, pp. 192–198, March 2003.

[2] Hüseyin Kurt, Kemal Atik, Mehmet Özkaymak, Ziyaddin Recebli, “Thermal performance parameters estimation of hot box type solar cooker by using artificial neural network”, International Journal of Thermal Sciences, vol. 47, pp. 192-200, March 2007.

[3] Christel de Bakker, Myriam Aries, Helianthe Kort, Alexander Rosemannm, “Occupancy-based lighting control in open-plan office spaces: A state-of-the-art review ”, Bulding and Environment, vol. 112, pp. 308-321, November 2016

[4] Official Mexican Standard ,Norma Oficial Mexicana NOM-025-STPS-2008) 30/12/2008

[5] Rizki A. Mangkuto, Mardliyahtur Rohmah, Anindya Dian Asri, “Desing optimisation for window size, orientation, and wall reflectance with regarg to various daylight metrics and lighting energy demand: A case study of buildings in the tropics”, Applied Energy, vol. 164, pp. 211-219, November 2015.

[6] Gül Koclar oral, Köknel Yener, Nurgün Tamer Bayazit, “Building envelope desing with the objective to ensure thermal, visual and acustic confort conditions”,Building and Environment, vol. 39, pp. 281-287, June 2003

[7] Isamu Akasaki, “Key inventions in the history of nitide-based blue LED and LD”, Journal of crystal growth, vol. 300, pp. 2-10, February 2007.

[8] Bang, You-Young; Lee, Dae Sung; Lim, Seong-Rin, “Identification of Principal Design Features to Develop Environmental Friendly Light-Emitting Diode (LED) Bulbs”, Journal of Nanoelectronics and Optoelectronics, vol. 12, pp. 625-630, June 2017

[9] Lei Xu, Yiqun Pan, Yuan Yao, Dandan Cai, Zhizhong Huang, Norber Linder, “Lighting energy efficiency in offices under different control strategies”, Energy and Buildings, vol. 138, pp. 127-139, March 2017

[10] H. Burak Gunay, William O’Brien, Ian Beausoleil-Morrison, Sara Gilani, “Development and implementation of an adaptive lighting and blinds control algorithm”, Building and Environment, vol. 113, pp. 185-199, February 2017

[11] Thérèse Wilson, “Comments on the mechanisms of chemi-and bioluminescence”, Photochemisty and Photobiologu, vol. 62, pp. 601-606, May 1995

[12] P.O. Fanger, “Assessment of man’s thermal comfort in practice”, British Journal of Industrial Medicine, vol. 30, pp. 313-324, May 1973.

[13] Darine Zmbrano, Carlos Bordons, Winston García-Gabín, Eduardo F. Camacho, “A solar cooling plant: a cenchmark for hybrud systems control”, Unpublished.

[14] M.Castilla, J.D. Álvarez, M. Berenguel, M.Pérez, F. Rodríguez, J.L. Guzmán, Iberoamerican magazine of automatic and industrial information, Revista Iberoamericana de automática e informacion industual, “Comfort control techniques in buildings”, “Técnicas de control del confort en edificios”, vol. 7, pp. 5-24.

[15] Darine Zmbrano, Carlos Bordons, Winston Garcia-Gabin, Eduardo F. Camacho, “Model development and validation of solar cooling plant”, vol. 31, pp. 315-327, May 2007

[16] Barilelo Nghana, “Phase change material’s (PCM) impacts on the energy performance and thermal comfort of buildings in a mild climate”, Building and Environment, vol. 99, pp. 221-238, April 2016

[17] Andrea Invidiata, Enedir Ghisi, “Life-cycle energy and cost analyses of window shading used to improve the thermal perfomance of houses”, Journal of Cleaner Production, vol. 133, pp. 1371-1383, October 2016.

CONACYT
Consejo Nacional de Ciencia y Tecnología

CONCYTEQ

Geometric optimization of PET fibers to improve the flexural strength in mortars.

Ing. María Isabel Arteaga Capistrán
Universidad Autónoma de Querétaro
Facultad de Ingeniería
Querétaro, México.
E-mail: m.i.artega.capistran@gmail.com

Dr. Juan Bosco Hernández Zaragoza
Universidad Autónoma de Querétaro
Facultad de Ingeniería
Querétaro, México.
E-mail: bosco@uaq.mx

***Abstract*— This study investigated the utilization of polyethylene terephthalate (PET) fibers recycled as reinforced mortar. The fibers were obtained by simple mechanical cutting from bottles. Investigation was carried out on cement-lime 1:3 mortar samples. Different volumes of fibers, 0, 0.5, 1.0 and 1.5 percent, were introduced in dry mortar mixes. Specifically, the mechanical properties as flexure, compressive strengths and mortar toughness were measured. The results indicate that the incorporation of PET fibers significantly improve the flexural strength of mortars.**

***Keywords*— Flexural strength, Geometry, Mortar, PET fibers.**

I. Introduction

The 21st century has involved an almost unlimited use of plastics; the products made with these materials are present in everyday life as part of objects such as furniture, toys, car parts, pens, clothes and food containers, just to name a few [1].

Over the last two decades, plastic materials have been widely investigated and experimented as concrete and mortar components, such as, e.g., aggregates, reinforcing fibers and binders. Commercially available construction materials usually include virgin plastic elements, while recycled plastic is receiving growing interest in the scientific community, since researches conducted in recent years have shown that several construction materials incorporating waste plastics combine remarkable thermo mechanical properties with economic and environmental benefits [2].

A. Composite Materials

The composites are formed of two more materials than the joined or connected phases to obtain a combination of properties that cannot otherwise be achieved. The volumetric fraction and the connectivity of the material phases in a composite material as well as the nature of the interface between the dispersed phase and the matrix are very important for the determination of the properties [3].

B. Fiber Reinforced Compound Materials

Fiber reinforced composite materials provide improvements in strength, stiffness or performance at high temperatures in metals and polymers and toughness in ceramic materials. The fibers are usually of low density, which gives them a high resistance and specific modulus, but they are usually very fragile. The fibers may be continuous or discontinuous [3].

The fibers are introduced into a matrix with a variety of orientations. Random orientations and isotropic behavior are obtained using discontinuous fibers; the unidirectional aligned fibers produce composite materials with anisotropic behavior, with great improvements in strength and stiffness in the direction parallel to the fibers. To meet the imposed loads, properties can be adjusted by orienting the fibers in many directions [3].

C. Types of Fibers

The fibers are mainly used as reinforcement; there are many types available in the form of continuous filaments, fabrics, mats, or as ground fiber. The fibers are used for filament winding, lamination and molding [4].

- Inorganic fibers
- Synthetic organic fibers
- Natural organic fibers

D. Fiber Mortars

Recycled nylon fibers obtained from waste fishing nets, focusing our attention on the use of recycled nylon fibers as tensile reinforcement of cementations mortars. We deal with compression and bending tests on cementations mortars reinforced with recycled nylon fibers, and establish comparisons with the experimental behavior of the unreinforced material and with results given in existing literature. In our analysis of different weight fractions and

aspect ratios of the reinforcing fibers, we observe marked increases in the tensile strength (up to + 35%) and toughness (up to 13 times greater) of the reinforced nylon mortar, as compared with the unreinforced material [5].

The dynamic characteristics and the constitutive relationship, of polypropylene fiber reinforced mortar (PFRM) materials, were investigated under compressive impact loading. The compressive strength, the dynamic elastic modulus, the toughness as well as the ductility of PFRM were analyzed. Experimental results show that the dynamic performance of PFRM materials is significantly affected by strain rates. Nevertheless, the strain rate effect decreases as the strength of mortar increases. Polypropylene fibers are able to improve the impact toughness [6].

E. Polyethylene Terephthalate (PET) Fibers in Construction

The recycled polyethylene terephthalate (PET) plastic waste was depolymerized through glycolysis to produce unsaturated polyester resin (UPER). The UPER so produced was then used as a binding agent to produce polymer mortar (PM) and polymer concrete (PC). Eight different sets of PM and PC were produced by varying PET to glycol ratio, dibasic acids and initiator promoter combinations. The PET to glycol ratio used in the present study was 1:1 and 2:1. The initiator promoter combinations taken were Methyl ethyl ketone peroxide (MEKP) and cobalt naphthanate (CoNp) in one group of sets while Benzoil peroxide (BPO) and N, N-diethyl aniline (NNDA) in other group of sets. For each set, microscopic studies were conducted on neat resin and polymer mortar. [7].

As part of the research on fiber-reinforced concrete, the results of some tests for an approach to a broader testing on the possibility of using fibers from polyethylene terephthalate (PET) bottles to increase the ductility of the concrete are reported. The fibers are simply cut from waste plastic bottles reducing, in this way, the manufacturing costs of recycled PET fiber-reinforced concrete [8].

An experimental study of thermal conductivity, compressive strength, first crack strength and ductility indices of recycled PET fiber-reinforced concrete (RPETFRC). It was examined PET filaments industrially extruded from recycled PET bottle flakes with different mechanical properties and profiles. On considering a volumetric fiber dosage at 1%, it was observed marked improvements in thermal resistance, mechanical strengths and ductility of RPETFRC, as compared to plain concrete. A comparative study with earlier literature results indicates that RPETFRC is also highly competitive over polypropylene- fiber-reinforced concrete in terms of compressive strength and fracture toughness [9].

The fibers have been obtained by simply cutting the bottles; the fibers are then added to the mix concrete or they are used as discrete reinforcement of specimens and little beams in substitution of steel bars. The tests are to be considered as an approach to a more extensive investigation on the use of PET as a reinforcing material for concrete and masonry structures. The results that have been obtained are very interesting, especially regarding the adherence between PET and concrete, suggesting a possible use of this material in the form of flat or round bars, or networks for structural reinforcement [10].

In the case of Portland cement, the use of plastic materials in the Portland cement industry has been investigated. To die Parameters investigated include fiber content and fiber length and tests performed include flexure and plastic shrinkage tests. Experimental results showed a substantial increase in flexural Toughness, about 26 to 61 times, and a considerable increase in flexural strength ranging from 6% to 84% of mortars reinforced with RPFibers compared to plain mortar. Test results also showed the meaning Reduction in width, and total area of plastic shrinkage cracks of slabs reinforced with an increased Amount of RPFs compared to control slabs without fibers. No plastic shrinkage cracks were observed. On the surface of mortar slabs reinforced with 1.5% (by volume) of 50 mm long, RP fibers. Additionally,

Reducing the cost of plastic waste disposal, this investigation recommends adding about 1.5% of locally Produced; 50 mm long recycled plastic fibers to ordinary cement mortar for improving the ductility And crack arresting mechanism of the mortar matrix [11].

II. MATERIALS AND METHODS

A. Materials

The cement used in the elaboration of the mortar for structural use, must comply with the characteristics and specifications described in the Mexican standard NMX-C-414-ONNCCE. The cement must be stored in the work in a dry place, protected from the weather that can cause the hydration.

The aggregate (sand) must comply with the specifications of Mexican standard NMX-C-111-ONNCCE. For some specific uses, such as fine finishes, or when mortar workability requires it, the producer can sift the aggregate in order to have a mortar paste with finer particles, as long as the resulting mortar complies with other established requirements in this draft standard.

The water for the mixing of the mortar must comply with the specifications of the Mexican standard NMX-122-ONNCCE. It must be stored in clean and covered tanks.

The examined fibers are obtained through hand cutting of PET bottles with different capacity, 0.5mm thickness, and flat surface. It was begun the hand cutting process by removing the neck and the base of the PET bottles through ordinary scissors. It was then longitudinally cut the lateral surface of the bottles obtaining PET fibers with 3 mm width and 45 mm length, other with 2 mm width and 30 mm length and finally PET fibers with 1 mm width and 15 mm length as are presented in the Fig. 1.

Fig. 1. Fibers of PET used in this investigation.

B. Experimental program

This investigation was designed to study the effects of recycled plastic waste fibers on the flexural behavior and plastic shrinkage of Portland cement mortar. Fibers were used in two different lengths (15 mm, 30 mm and 45 mm) and three different fiber volume fractions (0.5%, 1.0%, and 1.5%).

C. Preparation of mortar specimens

The compressive strength of the hardened mortar is obtained using cubic specimens, processed, cured and tested according to the Mexican standard NMX-C-061-ONNCCE, with the exception of the storage of the specimens. Or, in the case of mortar of filling, it is possible to determine with cylinders elaborated, cured and tested in accordance with the Mexican norms NMX-C-160-ONNCCE and NMX-C-083-ONNCCE. For the flexural test prisms of 40 mm x 40 mm x 160 mm were designed, as shown in Fig. 2.

The cube and prism specimens were cast in two layers following procedures. The RP fibers were added gradually during casting to avoid fiber lumping and ensure homogeneous distribution of the fibers within the mix. All the specimens were compacted using external vibration and covered with moist burlap and polyethylene sheets for 24 h. They were then demolded and cured for 28 days in water.

The wet curing treatment of the specimens prepared for resistance evaluation must comply with the Mexican standard NMX-C-148-ONNCCE.

Fig. 2. Preparation of mortar specimens.

D. Compressive strength

This test method as shown in Fig. 4 provides a means of determining the compressive strength of hydraulic cement and other mortars and results may be used to determine compliance with specifications. Further, this test method is referenced by numerous other specifications and test methods. Caution must be exercised in using the results of this test method to predict the strength of concretes.

Record the total maximum load indicated by the testing machine, and calculates the compressive strength as follows:

$$fm = P / A \tag{1}$$

Where:

fm = Compressive strength in psi or (MPa)

P = Total maximum load in lbf or (N)

A = area of loaded surface in^2 or (mm^2)

Either 2-in or [50-mm] cube specimens may be used for the determination of compressive strength, whether inch-pound or SI units are used, as shown in Fig. 3. However, consistent units for load and area must be used to calculate strength in the units selected. If the cross-sectional area of a specimen varies more than 1.5 % from the nominal, use the actual area for the calculation of the compressive strength. The compressive strength of all acceptable test specimens made from the same sample and tested at the same period shall be averaged and reported to the nearest 10 psi [0.1 MPa].

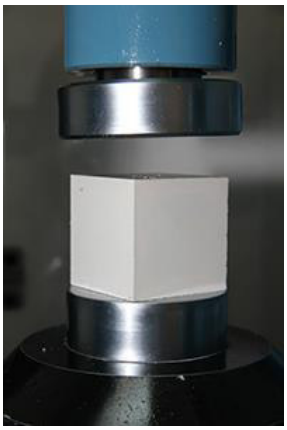

Fig. 3. Loading configuration for compressive testing.

E. Flexural strength

Flexural test is the application of a force in the center of a bar supported at each of its ends, to determine the strength of the material at a static or applied load slowly. It is typically used in the case of brittle materials.

Calculate flexural yield strength (F_y) as follows:

$$F_y = P_y L / bd^2 \tag{2}$$

Where:

F_y = Flexural yield strength psi (or MPa)

P_y = Force at the point on the force-deflection curve where the curve deviates from linearity, lbf (or N)

L = Major support span, in. (or mm)

b = Width of specimen, in. (or mm)

d = Depth of specimen, in

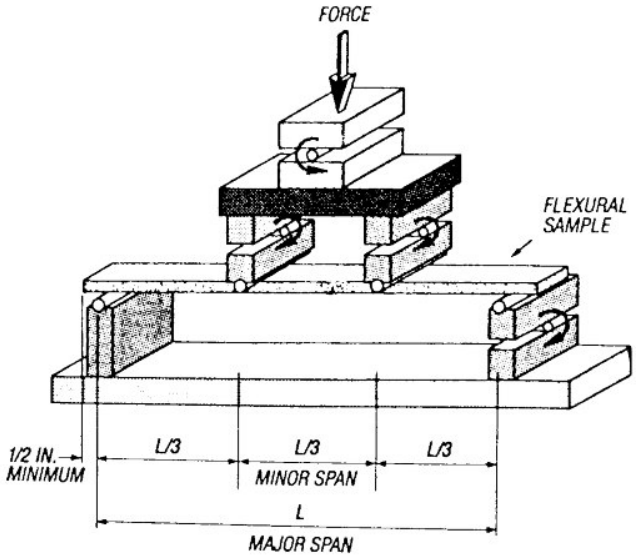

Fig. 4. Loading configuration for flexural testing.

III. RESULTS AND DISCUSSION

A. *Compressive strength*

From recycled fibers obtained by simple mechanical cutting of disposable containers of Polyethylene Terephthalate (PET) of different lengths, thicknesses and shapes, a recycled material is obtained in which PET fibers are bonded in a cement-based mortar Hydraulic system to which mechanical and adhesion tests are performed to obtain the best behavior of a base mortar with advantages in terms of ecological, economic benefits and an increase in the mechanical resistance of the product.

Recycling of Polyethylene Terephthalate (PET) has three main ecological consequences: the reduction of the volume of waste (and therefore of the pollution generated), the preservation of natural resources (since recycled plastic is reused) and the reduction of Costs associated with the production of new goods. The PET offers extraordinary advantages that facilitate its recycling by the fact of being a plastic of high cost of production among those of massive consumption. This is mainly due to the increase in raw materials due to the increase in oil prices. In addition, the quality of recycled PET may be higher than virgin material, depending on the intended use.

REFERENCES

[1] G Martínez, G., & Hernández, J. B. (2015). Materiales Sustentables y Reciclados en la Construcción. https://doi.org/http://dx.doi.org/10.3926/oms.211

[2] Fraternali, F., Farina, I., Polzone, C., Pagliuca, E., & Feo, L. (2013). Composites : Part B On the use of R-PET strips for the reinforcement of cement mortars. Composites Part B, 46, 207–210. https://doi.org/10.1016/j.compositesb.2012.09.070

[3] Askeland, D., y Phulé, P. (1997). Ciencia e Ingeniería de los Materile. México: Editorial Thomson.

[4] Salgado, R. (2003). Compósitos poliméricos reforzados con cascarilla de arroz modificada en su superficie. Tesis de Doctorado en Ingeniería no publicada. Universidad Autónoma de Querétaro, Facultad de Ingeniería, Querétaro, México.

[5] Spadea, S., Farina, I., Carrafiello, A., & Fraternali, F. (2015). Recycled nylon fibers as cement mortar reinforcement. Construction and Building Materials, 80, 200–209. https://doi.org/10.1016/j.conbuildmat.2015.01.075

[6] Zhang, H., Liu, Y., Sun, H., & Wu, S. (2016). Transient dynamic behavior of polypropylene fiber reinforced mortar under compressive impact loading. Construction and Building Materials, 111, 30–42. https://doi.org/10.1016/j.conbuildmat.2016.02.049

[7] Mahdi F, Abbas H, Khan AA. (2009). Strength characteristics of polymer mortar and concrete using different compositions of resins derived from post-consumer PET bottles. Constr Build Mater 2010;24:25–36

[8] Foti, D. (2011). Preliminary analysis of concrete reinforced with waste bottles PET fibers. Construction and Building Materials, 25(4), 1906–1915. https://doi.org/10.1016/j.conbuildmat.2010.11.066

[9] Fraternali, F., Ciancia, V., Chechile, R., Rizzano, G., Feo, L., & Incarnato, L. (2011). Experimental study of the thermo-mechanical properties of recycled PET fiber-reinforced concrete. Composite Structures, 93(9), 2368–2374. https://doi.org/10.1016/j.compstruct.2011.03.025

[10] Foti, D. (2013). Use of recycled waste pet bottles fibers for the reinforcement of concrete. Composite Structures, 96, 396–404. https://doi.org/10.1016/j.compstruct.2012.09.019

[11] Tonet, K. G., & Gorninski, J. P. (2013). Polymer concrete with recycled PET: The influence of the addition of industrial waste on flammability. Construction and Building Materials, 40, 378–389. https://doi.org/10.1016/j.conbuildmat.2012.09.

CdS-nanocrystalline thin films doped with Mn grown on flexible PET-substrates by Chemical Bath Deposition

K. Rodríguez-Rosales, F. de Moure-Flores
Departamento de Materiales- Energía
Facultad de Química, Universidad Autónoma de Querétaro, UAQ
Querétaro, Qro., México
karen.uaq@outlook.com
fcomoure@hotmail.com

J.G. Quiñones-Galván
Departamento de Física, Centro Universitario de Ciencias Exactas e Ingenierías,
Universidad de Guadalajara, UDG
Guadalajara, Jalisco, México
erk_183@hotmail.com

***Abstract*— CdS thin films doped with Mn were grown on flexible polyethylene terephthalate (PET) substrates with In_2O_3:Sn by chemical bath deposition. For the CdS: Mn films the effect of growth time (was 1.0, 1.5, 2.0, 2.5 and 3.0 hours) at a growth temperatures of 70 and 80 ° C were studied, for the Mn contamination a 1.56 µM solution of manganese acetate. The structural characterization (TEM) indicates that the CdS films obtained by chemical deposition are of polycrystalline nature, presenting the hexagonal phase of the CdS; In addition, indicate the presence of nanoparticles. A strong green photoluminescence emission was observed in all the samples; this emission is associated to near band edge transitions for CdS. The calculated bandgap values by UV-Vis are in excellent agreement with PL emission, the values are from 2.22-2.31 eV. The structural and optical characterization of the CdS films indicates that the semiconductor films obtained in the present work have the physical properties suitable for use in the processing of solar cells.**

Keywords—CdS films, flexible substrates, PET substrates, doped, Mn, chemical bath deposition, photoluminescence

I. INTRODUCTION

Cadmium sulfide is a semiconductor of group II-VI and has great potential for modern technology with applications in optoelectronic and microelectronic devices, some examples are: photosensors, radiation filters, solar cells (like optical window), etc. [1]. Cadmium sulfide (CdS) thin film deposition has attracted increased attention to materials research scientists due to a predicted efficiency of 30% in the CdS/CdTe solar cell system [2]. CdS is a wide bandgap *n*-type semiconductor with value 0f 2.42 eV, it crystallizes in hexagonal and cubic phases, being the wurtzite hexagonal the stable phase. Developments of different deposition techniques to enhance optoelectronic properties and reduce fabrication costs have been intensively studied. Although there exist reports on physical vapor deposition techniques such as: pulsed laser deposition, vapor transport and sputtering and Chemical Bath Deposition (CBD) The CBD is very attractive due to its feasibility to produce large-area thin films at low cost [3].

There are different mechanisms in CBD, one of the best known and best represents the formation of thin films is the ion-ion mechanism, using CdS common thiourea deposition as an example, this is[4]:

$$Cd(NH_3)_4^{+2} \leftrightarrow Cd^{+2} + 4NH_3 \quad (1)$$

(Dissociation of the complex with free ions Cd^{+2})

$$(NH_2)_2CS + 2OH^- \rightarrow S^{2-} + CN_2H_2 + 2H_2O \quad (2)$$

(Formation of the sulfur ion)

$$Cd^{2+} + S^{2-} \rightarrow CdS \quad (3)$$

(Formation of CdS by ionic reaction)

The CdS films deposited by CBD have high resistivity (107-1012 Ωcm) [5]. It is known that a negative factor in materials with high resistivity is the Joule effect, and represents one of the challenges in the field of the manufacture of devices. To solve this problem, some research groups submit their CdS

films to some heat treatments or add impurities to those films. In the last three decades studies have been carried out on the doping of CdS deposited by CBD, some of the elements used are: Na, Ni, Li, Al, Cu, I, Cl, B, Zn, Cr, F, Sn, Mn And In [6]. Therefore, in this work we intend to impurify the CdS with Mn, because the Mn has been found in the working group to improve the optoelectronic properties [7].

Over the last years, flexible substrates have demonstrated a great potential to be used as flexible solar cells, flexible displays among other applications [8]. Particularly, polyethylene terephthalate (PET) substrate has been used for photovoltaic devices because it provides higher electrical conductivity, light weight, transmittance in visible range, low cost and good flexibility . In this work, CdS-nanocrystals films doped with manganese were grown on flexible PET-substrates by CBD at different growth times. The physical properties were analyzed as a function of temperature and growth time.

II. EXPERIMENTAL DETAILS

ll.1 Grown of CdS:Mn films

All the chemicals used in this work were analytical reagent. CdS-nanocrystals thin films doped with Mn where grown on flexible PET/In_2O_3:Sn substrates by CBD. Before depositing, the PET/ In_2O_3:Sn substrates (1.5 cm by 2.5 cm) have been cleaned successively with a solution of neutral soap, deionized water and ethanol in ultrasonic bath. The reaction solution was prepared mixing 0.025 M $CdCl_2$, 0.05 M $(NH_2)_2CS$, NH_4Cl and 1.56E^{-4} M $Mn(C_2H_3O_3)_2$. Then the pH value of the solution was adjusted to 11 with ammonium hydroxide (NH_4OH). The CdS deposits were made at atmospheric pressure and using constant concentrations and volumes of precursor solutions, the solutions were prepared with deionized water. $CdCl_2$, $(NH_2)_2CS$ and $Mn(C_2H_3O_3)_2$ were employed as cadmium, sulfur and manganese sources respectively. The other components had the function of complexing the reaction process. The growth temperatures were 70 and 80°C and the temperature was controlled with a hot plate equipped with a magnetic stirrer. Deposition times set were 1.0, 1.5, 2.0, 2.5 and 3.0 hours.

ll.2 Samples characterization

Samples were structurally characterized high resolution transmission electron microscopy (HR-TEM) using a JEOL JEM 2010 microscope with a lanthanum hexaboride filament at an acceleration voltage of 200 kV. The optical properties were determined by UV-Vis and room temperature Photoluminescence (RT PL) spectroscopies. The UV-Vis spectra were obtained with a Perkin-Elmer Lambda-2 spectrophotometer. Photoluminescence (PL) spectra were obtained at room temperature using an Omnichrome-Series56 He-Cd laser with the 325 nm line.

III. RESULTS AND DISCUSSION

HR-TEM micrographs were recorded in order to know the crystalline structure of CdS films. Figure 1 presents the TEM images corresponding to the samples grown at 70 and 80 ° C, respectively. At a temperature of growth of 70 ° C shows the plane (101) corresponding to the hexagonal phase, at a temperature of 80 °C there is a mixture of phases, the planes (210) of the cubic phase and the plane (101) of the hexagonal phase. The structural characterization indicates that the formation of CdS doped with Mn on substrates of PET is of nanocrystalline nature.

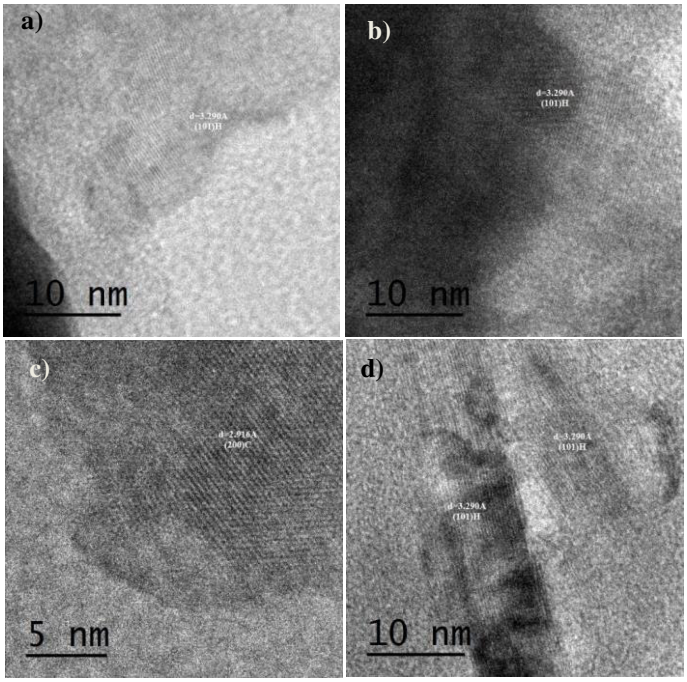

Fig. 1 High resolution TEM images for samples deposited on PET substrates for deposition times of a) 1.0 h, b) 3.0 h min at the 70 ºC and c) 1.0 h, d) 3.0 h at 80 ºC.

Optical properties of CdS:Mn films were analyzed by UV-Vis spectroscopy, UV-Vis spectra are presented in Fig.2 with edges of absorption around 560 nm, presenting a maximum rate of 80% of the transmittance. Using the transmittance measurements (optical density) and the Tauc method [14], the bandgap values were calculated. Fig. 3 shows the plot of $(O.D.*hv)^2$ vs. hv for CdS films deposited on PET substrates by CBD. In Table 1 we present the wide band gap for the films of CdS:Mn, all the values obtained are close to 2.3 eV. The values of E_g to the films doped with manganese decrease with respect to the values reported in the literature (2.42 eV), this is due to

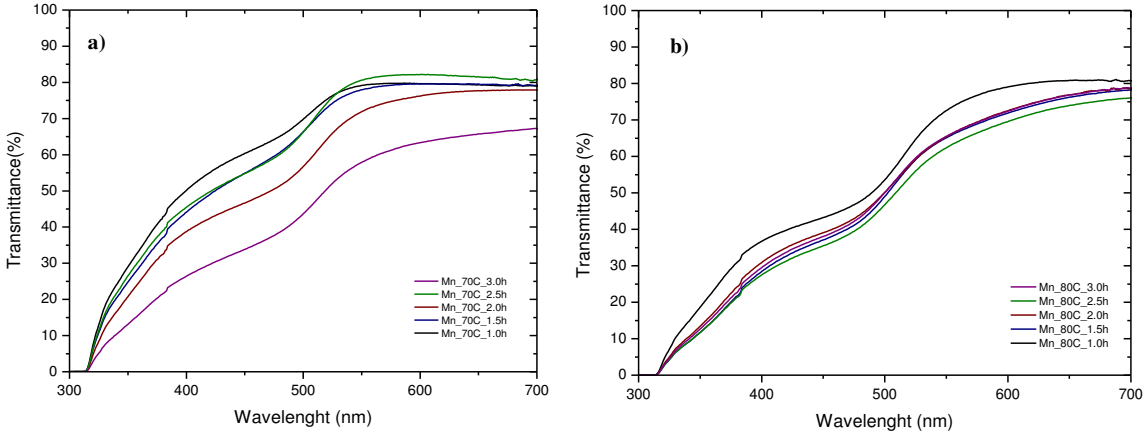

Fig. 2. Transmittance spectra for CdS:Mn films grown on PET/In_2O_3:Sn substrates at different deposition times a) CdS:Mn to 70°C a b) CdS:Mn to 80°C.

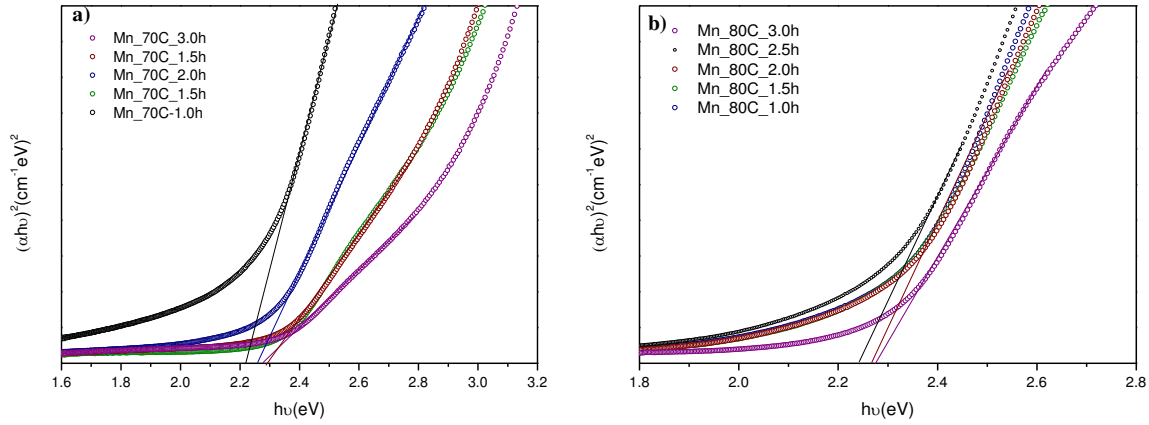

Fig. 3. Tauc Plots for CdS films grown on PET/In_2O_3:Sn substrates at different deposition times. a) CdS:Mn to 70°C a b) CdS:Mn to 80°C.

Table 1. Estimate of the width of band gap for thin films of CdS:Mn

Temperature (°C)	Time (h)	E_g (eV)
70	1.0	2.27
	1.5	2.31
	2.0	2.26
	2.5	2.31
	3.0	2.22
80	1.0	2.28
	1.5	2.29
	2.0	2.27
	2.5	2.23
	3.0	2.29

the fact that the atoms donors cause energy levels within the band gap of the CdS by extending the conduction band and reducing the edge of energy of the samples.

As part of the optical characterization photoluminescence measurements were made, Fig. 4. It is noted that all spectra are two wide bands centered at 2.3 eV and 2.8 eV, the first signal corresponds to the emissions of the CdS and the second is the signal transmitted by the substrate, PET/In_2O_3:Sn. The first signal observed at short wavelengths, referred to as green band, can be found in the literature focusing on positions in the energy range of 2.27 eV to 2.40 eV in single crystals and polycrystalline thin films. The green band has its origin in transitions due to the vacancies of sulfur near the bottom of the conduction band to the top of the band of valencia, the recombination between donor-acceptor pairs always occurs and when there are vacancies of sulfur in the second state of ionization, and as seen above the films of CdS grow with deficiencies of sulfur.

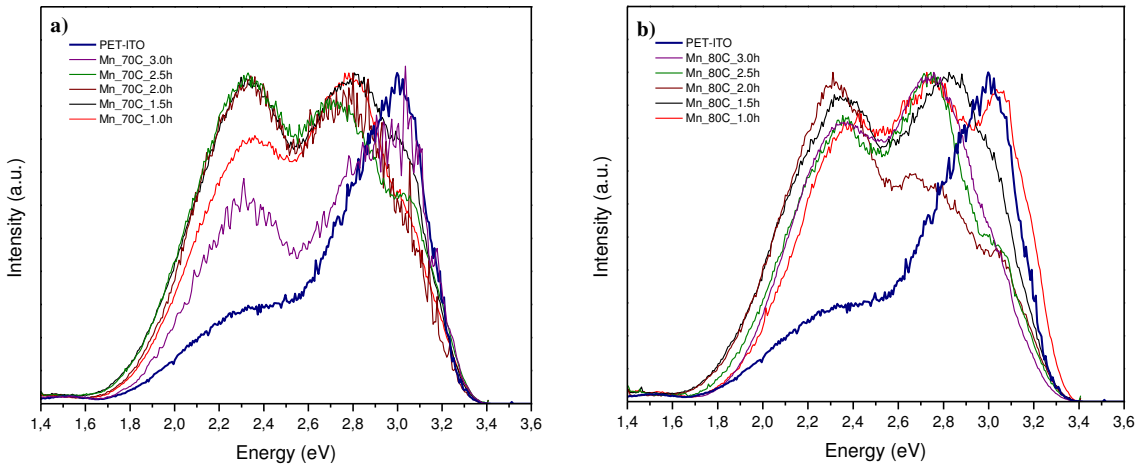

Fig. 4. Photoluminescence spectra for the films of CdS:Mn deposited at different times to a)70°c and b)80 ºC.

IV. CONCLUSIONS

CdS:Mn-nanocrystalline thin films have been grown by chemical bath deposition on flexible PET/In_2O_3:Sn substrates. The structural analysis indicates that the CdS films are composed of crystalline material. The contribution of crystalline material has the hexagonal phase of the CdS at the 70 ºC and mixture phases of at 80 ºC. UV-Vis spectra and photoluminescence showed that the addition of manganese to the CdS promotes the decrease in the value of the width of band gap of the films, taking approximate values to 2.2 eV against 2.4 eV is the value reported in the literature. The thickness of the films is a function of the time of growth, it is noted that at times of higher deposit value of transmittance. The bandgap values of CdS films are in the range 2.22-2.31 eV. Room temperature photoluminescence measurements reveal the green signal at 2.22-2.31 eV, which suggested sulfur vacancies in CdS films. The structural and optical and characterization indicates that the semiconductor films potentially useful for flexible photovoltaic devices.

ACKNOWLEDGMENT

The authors acknowledge financial support for this work from FONDO SECTORIAL CONACYT-SENER-SUSTENTABILIDAD ENERGÉTICA through CeMIE-sol, within of the strategic project number 37; “Development of new photovoltaic devices and semi-superconductor materials”.

REFERENCES

[1] Lee, T. Y., I. H. Lee, S. H. Jung, and C. W. Chung. Characteristics of CdS thin films deposited on glass and Cu(In,Ga) Se2 layer using chemical bath deposition. Thin Solid Films. Vol. 548, pp 64–68, 2013.

[2] O. Vigil-Galán, A. Arias-Carbajal, R. Mendoza-Pérez, G. Santana-Rodríguez, J. Sastre-Hernández, J. C. Alonso, E. Moreno-García, G. Contreras-Puente and A. Morales-Acevedo, “Improving the efficiency of CdS/CdTe solar cells by varying the thiourea/$CdCl_2$ ratio in the CdS chemical bath”, Semicond. Sci. Technol, vol. 20, pp 819-822, 2005.

[3] F. de Moure-Flores, K.E. Nieto-Zepeda, A. Guillén-Cervantes, S. Gallardo, J.G. Quiñones-Galván, A. Hernández-Hernández, M. de la L. Olvera, M. Zapata-Torres, Yu Kundriavtsev, M. Meléndez-Lira, “Effect of the immersion in $CdCl_2$ and annealing on physical properties of CdS:F films grown by CBD”, J. Phys. Chem. Solids. Vol. 74, pp 611-615, 2013.

[4] Hodes, G. Chemical Solution Deposition of Semiconductor Films. Marcel Dakker, Inc., New York, New York, 2002.

[5] de Melo O., Hernández L., Zelaya-Angel O., Lozada-Morales R., Becerril M., Low resistivity cubic phase CdS films by chemical bath deposition technique, Appl Phys Lett. Vol. 65, pp 1278, 1994.

[6] Santos Cruz J., Castanedo Pérez R., Torres Delgado G., Zelaya Angel O., CdS thin films doped with metal-organic salts using chemical bath deposition, Thin Solid Films. vol. 518, pp 1791, 2010.

[7] Venkata-Haritha M., Chandu V.V.M. Gopi, Chebrolu Ventaka Thulasi-Varma, Soo-Kyoung Kim, Hee-Je Kim, “Influence of Mn+2 incorporation in CdSe quantum dots for high performance of CdS-CdSe quantum dot sensitized solar cells”. J Photochem Photobiol A, vol. 315, pp. 34– 41, 2015.

[8] T. Guo, G. Dong, F. Gao, Y. Xiao, Q. Chen, and X. Diao, “High performance ZnO:Al films deposited on PET substrates using facing target sputtering” , Appl. Surf. Sci. vol. 282, pp 467–471, 2013.

UNIVERSIDAD AUTÓNOMA DE QUERÉTARO
Fi
13° CONGRESO INTERNACIONAL DE INGENIERÍA
15th-19th MAY 2017

Development of a measuring instrument to identify areas for improvement in the educational model in STEM disciplines

Ramirez – Vazquez Juan Pablo
Posgrado Facultad de Ingenieria
Universidad Autonoma de Queretaro
Santiago de Queretaro, Mexico
jpramvaz@gmail.com

Huerta – Manzanilla Eric Leonardo
Posgrado Facultad de Ingenieria
Universidad Autonoma de Queretaro
Santiago de Queretaro, Mexico
eric.huerta@uaq.mx

***Abstract*— The present research work it intends have an integrated instrument that allows through learning styles, identify areas of opportunity for improvement in the teaching process of the educational programs of engineering level degree and postgraduate of UAQ. The different theories of learning clearly state not only the disparity of approaches, but above all, the existence of different types of learning, so it is assumed that learning is reflected by reality on the part of the subject and as such it occurs in the activity that develops each individual in his contact with objects and uses different strategies to learn. The approaches and styles of learning constitute a contemporary problem of education, which has not yet arrived at concrete solutions, appreciating that both factors and variables involved in a teaching - learning process must be taken into account. Institutions if higher education require a quality education, so analyze it several research conducted in this decade oriented at that topic.**

Keywords—learning styles; education; teaching- learning process; integrated instrument.

I. INTRODUCTION (*HEADING 1*)

Admission to university constitutes a critical trauma that significantly influences the trajectories that students deploy in the course of academic training and, therefore, can be considered an indicator to analyze student dropout [3, 19, 21]. The teachers of the subjects of the first semester are not the obstacles that the students face in their university studies. For students it is a moment of change, of insertion in a new culture, of adaptation to the university world and a new way of studying scientific knowledge. However, the research on first-year university students, the obstacles they face and how the impact on learning is a field in construction in Latin America [18], which currently seeks greater degrees of consolidation on a theoretical scale -methodological. In Latin America, the most used questionnaire as a measurement instrument is the Honey-Alonso, [11, 1] on Learning Styles and consists of eighty questions, twenty items referring to each of the four styles, which must be answered by agreeing or disagreeing (Likert´s Scales). In 1992 [1] took advantage of the theories, contributions and experiences in the business environment of Honey and Mumford and carried out a questionnaire of Learning Styles for the academic field and in the Spanish language.

The term style was defined by [10] as "a set of aptitudes, preferences, tendencies and attitudes that a person has to do something and that manifests itself through a behavioral pattern and of different skills that make distinction of the others under one single label in the way they are driving, dress, talk, think, learn, know and teach". It is important that engineering teachers have the necessary psycho-pedagogical resources to know the characteristics of students, learning styles for programmatic power, effective training activities for the whole group [2, 15, 17], covering both the individual characteristics like the collective patterns of their students.

In the last decade, the styles that differ from the learning styles of university students are defined: the type of career [7], the cycle within a single career, the predominant teaching methods of their teachers [9], among others the study of learning styles has been added as an indicator of the individual differences of students in the way they perceive, represent, process and understand the conceptual contents taught by teachers [5, 6, 16]). Each student has a set of rules, notions, behaviors and ideas that give meaning to practice. To understand the meaning of practice it is necessary to analyze the student's learning style, that is, how to receive and process the information. A style of adaptive education is an integrated

diagnostic-intervention process in the classroom that assumes that learning is not the result of the individual characteristics of the student or the choice of an effective method, but the ability of the environment Instructive of adapting to the cognitive differences of each student [4, 13, 14]. This entails the search for and improvement of the adjustment of the student's individual student education in regular school contexts [12]. In recent years, this field has been added the study of learning styles as an indicator of individual differences of students in how to perceive, represent, process and understand the conceptual contents taught by teachers. Various theories speak of human behavior, theories about learning processes try to explain the internal processes when we learn, for example, the acquisition of intellectual skills, the acquisition of information or concepts, cognitive strategies, motor skills or attitudes.

The National Science Foundation (NSF) began using the term STEM to refer to Science, Technology, Engineering and Mathematics. It began as an educational approach that has worked well as strengthening teamwork. Implementing or improving the education of STEM disciplines should be a primary goal for nations that want to become or remain competitive, as it has been shown to favor the development of skills such as critical thinking, work in equipment, problem-solving skills and can develop essential skills so that everyone has more opportunities to contribute to the development and application of scientific and technological advances.

Currently, the promotion of initiatives in these disciplines has become one of the fundamental objectives of educational planning not only in countries such as the United States, the United Kingdom or Finland, but also in the European Union as a whole and in various international organizations. Even leading companies in various sectors, but in general closely linked to the technological field, have joined forces with public administrations to develop programs or initiatives to promote technological vocations among young people. Therefore, it is urgent to encourage in Mexico the young people of the upper middle level of the country, to pursue careers in areas related to STEM disciplines.

II. METHODOLOGY *(HEADING 2)*

In the present work, a measurement instrument will be developed that summarizes the three models of learning styles most related to STEM disciplines, according to the literature review of the thirteen most relevant learning models in Europe. Subsequently, for the three models of selected learning styles, a single questionnaire (designed with Likert´s Scales) will be integrated, which will be tested through a sampling plan and will be applied twice to each undergraduate and graduate student. The latter, in order to measure the internal reliability and to verify the consistency in the collection of the data obtained from the questionnaire, with the aid of statistical analysis. The results of the reagents obtained through quantitative measurements will then be compared; for each of the three previously selected models and the validation of the implemented measuring instrument will be carried out, through the internal reliability and the obtained longitudinal consistency. Finally recommendations and proposals will be proposed for the different programs sampled (degree and postgraduate) in the FI-UAQ.

There are several ways to know the learning styles, so a questionnaire will be carried out (on two occasions by each participant of the FI-UAQ), integrating the three styles of selected and related learning To the STEM areas. Regularly the educational models are evaluated qualitatively, so it is proposed that by reviewing in the literature the thirteen most relevant learning models in Europe, develop an integrated questionnaire based on three models of learning style most related to the disciplines of STEM.

The learning style questionnaire will be used as a basis for developing an assessment in Spanish and adapted to the culture of which the reagents are valid with $\alpha_{Cronbach} > 70\%$.

Figure 1 shows the flow diagram of the research work.

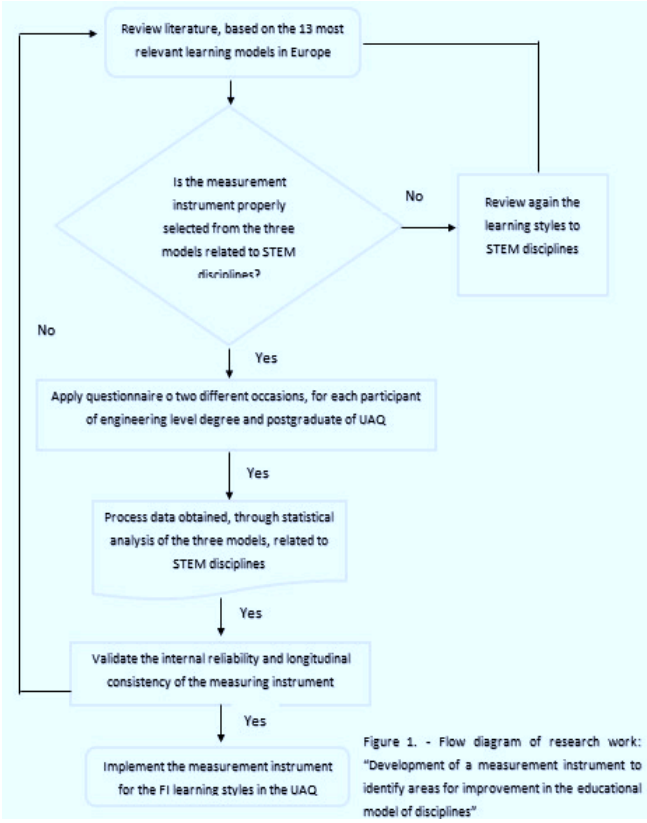

Figure 1. - Flow diagram of research work: "Development of a measurement instrument to identify areas for improvement in the educational model of disciplines"

Table 1 shows the model of Felder and Silverman, from which the model proposed in the present work is generated and the learning styles are classified from three dimensions. The styles are located in the second column, the description of each of them in the third column and are related to the answers that can be obtained from the questions that are shown in the first column.

Table 1- Classification of Learning Styles

Question	Dimension of learning and styles	Description of the styles
What kind of information do students prefer?	Dimension relative to type of information: Sensitive - Intuitive	Basically, students perceive the types of information: External information or sensitivity to sight, hearing to physical sensations and internal or intuitive information through memories, ideas, readings, etc.
With what type of information organization is the student more comfortable in working?	Dimension relative to the type of preferential stimulus: Visual - verbal	With regard to external information, students basically receive it in visual formats through tables, diagrams, graphs, demonstrations or in verbal formats through sounds, oral and written expression, formulas, symbols, etc.
With what type of information organization is the student more comfortable in working?	Dimension relating to the way information is organized: Inductive - deductive	Students feel at comfortable and better understand information if it is organized inductively where facts and observations are given and principles are inferred or deductively principles are revealed and consequences are deduced.

Source: Perea Robayo M. (2003). Study material in Learning Styles of the University of Rosario (Colombia)

Kolb's learning styles were included within his model by experience and defined as "some learning abilities that stand out above others" as a result of the inherited apparatus of one's own life experiences and of the demands of the environment The optimal learning, which is referred to in Figure 2, is the result of working the information in four phases.

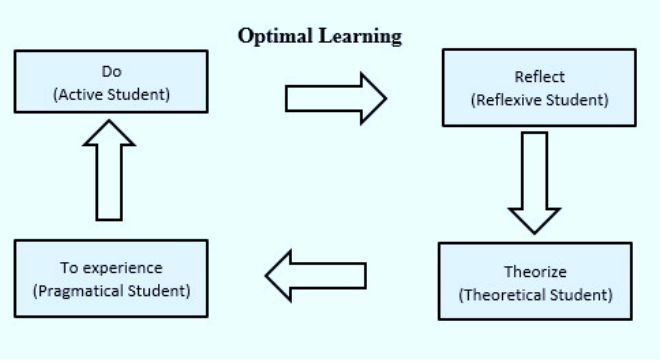

Figure 2.- Representation of the optimal learning of a person. Source. Self-elaboration based on an optimal learning approach according to Kolb, 1984.

The three learning styles that were selected, through literature review and related to the SMET disciplines, are described below.

1) Vermunt Learning Styles Inventory (ILS)

The Vermunt inventory was developed in 1998, following a style of learning that can be safely used in higher education and in the disciplines of STEM, to evaluate approaches to learning in a reliable and valid way. In turn, also to discuss with students the changes in learning and teaching. For this reason, he investigated learning theories, combining cognitive and emotional aspects, emphasizing teaching - learning environments rather than individual differences. He identified 4 Learning Styles and each affecting 5 dimensions, which are "cognitive processing", "learning orientation" (motivation), "affective processes" (feelings about learning), "mental learning models" Learning regulation ". To identify learning styles he constructed a questionnaire of 120 questions divided into two parts.

- Part A: Study activities with 55 items to be evaluated in 5 levels;
- Part B: Motives and opinions regarding the study in two sections: First: Study reasons with 25 items to be evaluated in 5 different levels; And the second: Opinions on the study of 40 questions to be evaluated in 5 levels

2) Kolb Learning Styles Inventory (LSI)

In 1984 Kolb developed an inventory to measure people's strengths and weaknesses, asking them to rank four words that related to the four capacities in a hierarchical way. The sample consisted only of adults, most of whom had completed their professional studies.

3) Herrmann's Brain Dominance Instrument (HBDI)

Hermann's model proposes the existence of four styles of thinking which he termed quadrants (A, B, C and D). Quadrants constitute four autonomous modalities of differential information processing, which can be deployed individually or in combination, both sequentially and simultaneously, in the different processes of brain functioning. This model can be represented as follows.

- Quadrant A (logical, critical, quantitative, analytical and realistic)
- Quadrant B (administrator, sequential, retailer, planner and conservator)
- Quadrant C (communicative, expressive, musical, expential and emphatic)
- Quadrant D (intuitive, simultaneous, integrative and imaginative).

A measurement instrument was developed by Herrmann and consists of 120 questions that identify the 4 categories of mental preferences or styles of thought. The HBDI application detects the quadrant

combination profile, which shows how many and which quadrants are dominant.

Cronbach's alpha and internal consistency of the items of a measuring instrument

The internal consistency method based on Cronbach's alpha allows to estimate the reliability of a measurement instrument through a set of items, which are expected to measure the same construct. In this sense, the degree of relationship between the items that make up the scale are of fundamental importance and are determined statistically as a correlation matrix between the items.

The validity of an instrument refers to the degree to which the instrument measures what it intends to measure. The reliability of the internal consistency of the instrument can be estimated with Cronbach's alpha. Measurement of reliability using the Cronbach's alpha assumes that the items (measured on the Likert scale) measure the same construct and are highly correlated. The closer the value of the alpha to 1 is, the greater the consistency of the items analyzed. The reliability of the scale must always be obtained with the data of each sample, to guarantee the reliable measurement of the construct in the concrete research sample.

Longitudinal Consistency

It is obtained by evaluating the individual, from asking the same questions in a different period of time. The measuring instruments of the constructs have to demonstrate that they possess the psychometric properties of validity and reliability. These properties must be calculated with each of the samples in which it is applied since it is not an inherent property of the instrument and could be reliable and valid with a sample of participants but not with another sample. If in the longitudinal consistency the field work is taken care of and the non-response rate is minimized; Therefore it might be possible to generate level estimators with adequate statistical accuracy.

Notice of Confidentiality and Privacy of Data Collected

The questionnaire will contain appropriate indications for the management of the information collected in a confidential way, as well as the contents of the questionnaire will be explained in detail to the interviewees, before requesting their participation. Finally, consent will be requested to create a commitment in your participation. The measuring instrument used will not request or share personal data of participants, in order to preserve the confidentiality of the student. The appropriate use of a reliable measuring instrument of learning styles in Spanish and that can be used in educational programs at the undergraduate and postgraduate levels of the FI-UAQ will be validated.

III. RESULTS EXPECTED *(HEADING 3)*

1.- Obtain a measurement instrument that brings together, through an integrated questionnaire (with Likert´s scales) the three learning styles to the disciplines of STEM, from the most relevant learning models in Europe.

2.- Validate that the measurement instrument implemented, present a high internal reliability, by obtaining a Cronbach alpha greater than 0.7

3.- A longitudinal consistency of the implemented measurement instrument is expected for the learning styles sampled in the research work.

4.- Obtain reliable results, through the quantitative measurements by the implemented measurement instrument.

ACKNOWLEDGMENT *(HEADING 5)*

I am grateful to CONACYT and the UAQ for their unconditional support for the completion of the work: Development of a measurement instrument to identify areas for improvement in the educational model of the disciplines ".

REFERENCES

[1] Alonso, C. 1992. Analisis y Diagnostico de los Estilos de Aprendizaje en Estudiantes Universitarios. Tesis Doctoral.

[2] Caglitary, N.E. 2008. Using learning styles theory in engineering education. European Journal of Engineering Education 33:415-424.

[3] Crissman, J., and U. Lee. 2005. The keys to first-year student persistence. Challenging and supporting the First-Year student. A handbook for improving the First-Year of college 27-46.

[4] Cronbach, L., and R. Snow. 1975. Aptitudes and instructional methods. A handbook for research on interactions.

[5] Díaz, C. 2013. Mapas mentales y estilos de aprendizaje. Aportes a la enseñanza-aprendizaje en un espacio formativo en ingeniería. Revista Educación en Ingeniería 8:45-52.

[6] Evans, C., and E. Cools. 2011. Applying styles research to educational practice. Learning and Individual Differences 21:249-254.

[7] Felder, R. M., and R. Brent. 2005. Understanding Student Differences. Journal of Engineering Education 94:57-72.

[8] Felder, R. M., and J. Spurlin. 2005. Reliability and validity of the Index of Learning Styles: A meta-analysis. International Journal of Engineering Education 21:103-112.

[9] Felder, R. M., and L. Silverman. 2002. Learning and teaching styles in engineering education. Journal of Engineering Education 78:674-681.

[10] Garcia, J. 2006. Los Estilos de Aprendizaje y las Tecnologias de la Informacion y la Comunicacion en la Formacion del Profesorado. Tesis Doctoral. Universidad Nacional de Educación.

[11] Honey, P. 1988. Improve your people skills. Institute of Personal Management.

[12] Isoc D., and T. Isoc. 2010. A new adaptive teaching method for engineering school. Journal Plus Education 6:124–131.

[13] Kostolányová, K. 2013. Theoretic principles of the adaptive teaching process. New Educational Review 34:208-219.

[14] Kostolányová K., J. Šarmanová, and O. Takács. 2011. Classification of learning styles for Adaptive Education. New Educational Review 23:199-212.

[15] Lowery, C. 2009. Adapting to student learning styles in a First-Year electrical-electronic engineering degree module. Engineering Education 4:52-60.

[16] Paz, H. 2014. Aprendizaje autónomo y estilo cognitivo: diseño didáctico, metodología y evaluación. Revista Educación en Ingeniería 9:53–65.

[17] Poitras, G., and E. Poitras. 2011. A cognitive apprenticeship approach to engineering education: The role of learning styles. Engineering Education 6:62-72.

[18] Silva, M. 2011. El primer año universitario. Un tramo critico para el exito academico. Perfiles Educativos 33:102-114.

[19] Seabi, J., and J. Payne. 2013. Effects of identity processing styles on academic achievement of First-Year university students. International Journal of Educational Management 27:311-322.

[20] Solis, R., and C. Arcudia 2010. Estilos de aprendizaje de los estudiantes de ingenierIa civil. Revista Educacion en Ingenieria 5:24-36.

[21] Tinto, V. 2007. Research and practice of student retention: What is next?. Journal College Student Retention 8:1-19.

Binary Cementitious Blends with Natural Zeolite Addition: A Review

E.D. Perez-Diaz
Master in Science, Postgrad Department
Universidad Autónoma de Querétaro
Querétaro, México.
edgarperezd@hotmail.com

L.C. Sandoval-Herazo
Doctorate in science of the engineer, Postgrad Depart.
Instituto Tecnológico de Orizaba
Orizaba, México.
lcsandovalh@gmail.com

***Abstract*— In this paper a review is presented about recent studies involving the fundamental properties of mixtures based on Portland cement with partial replacement of natural zeolite. Reviewed reports include properties in fresh state of binary mixtures, such as heat of hydration, set times, among other properties, and in hardened state, such as compressive and flexural strength, permeability, resistivity, among others. This article demonstrates that replacing Portland cement with natural zeolite as a pozzolanic material improves the properties of a cementitious mixture (pastes, mortars and concretes) with the durability of a concrete benefiting. The mechanical strength as a fundamental property of a concrete increases with the incorporation of natural zeolite, within the percentages with better mechanical behavior is a range between 10% and 20% of natural zeolite with respect to the weight of the cement, however between 20% and 40% (perhaps a little more) are generated concrete with adequate mechanical resistance. Researchers compare natural zeolite with commercial pozzolanic materials such as silica fume and fly ash, highlighting the characteristics they provide to a concrete. Also, the methodologies used by some authors are highlighted, with the objective of giving a more comparative experimental panorama to the researchers.**

Keywords—Portland Cement; Partial Replacement; Zeolite; Hydration; Clinker; Fly ash; Silica fume; Pozzolanic material; Reactivity Pozzolanic; Concrete; Mortars

I. INTRODUCTION

Approximately at the beginning of the 20th century, in order to reduce the amount of Portland Cement (PC), pozzolans have been used for the production of cement mixtures, in pozzolanic cements where the role of volcanic material is to react Portlandite, to produce the additional hydrated calcium silicate, thus improving the strength of the hardened mortar [1]. Fly ash, silica fume and activated clay (e.g. metakaolin), have been other components that have cement as the Pozzolanic Material (PM) that have been discovered over the past century. The zeolite tuffs resulting from the reaction of volcanic ash deposited in salt lakes are considered as a natural material with pozzolanic characteristics [3]. The International Concrete Association [4] defines natural pozzolans as a material composed of silica and aluminum, which in themselves do not have binder properties, but with a process of obtaining finer particles and with addition of water can obtain a material with mechanical properties beneficial to the PC, which helps to obtain compressive strengths greater than those of conventional hydraulic concrete [5].

Natural Zeolite (NZ) as PM for the partial substitution of PC has been studied in the last years, becoming a subject of considerable interest for the technological application of materials in different disciplines, industries and in the environment [6]. In the cement industry, the NZ has been accepted as an excellent supplementary cementitious mixture. Mixing NZ with cement by the high amount of silica and reactive alumina in the zeolite is chemically combined with the calcium hydroxide which is produced by the hydration of the cement to form CSH (Calcium Silicate Hydrated) gel and additional aluminates [7]. The reduction of the pore content with the improvement of the transition zone between the mixed zeolite in a cement paste and aggregates of the hardened concrete produce improvements in the concrete structure [8].

The zeolites, from a geological point of view, are minerals of volcanic origin, generated from the accumulation of Volcanic Ash (VA) in surface water bodies of alkaline content. The interaction of the VA with the salts present in the water gives rise to the different zeolites [9]. The zeolites are a type of natural mineral economical and its mining is very accessible [10], they are chemically composed of porous crystalline

aluminosilicates of the group of tectosilicates that have micro-cavities of well-defined molecular dimensions. In the pores, we find metallic cations and water molecules which are derived from zeolites by increasing the temperature [6, 11, 12]. Zeolites are known in different industries for the ability to lose and gain water by 30% with respect to their dry weight [7]; as a pozzolanic material contains reactive SiO_2 and Al_2O_3, reacting with important hydration products of PC [6, 11], improving mechanical properties, resistance of chemical agents such as sulphate attacks, increased material durability and reduced costs [13, 14].

The last edition of the atlas of zeolite framework types [12], exposes 176 unique types of zeolite, of which about 40 are natural [15] and the rest have been designed and obtained in the laboratory for use in different industries. Regarding concrete technology in construction, the types of zeolites most used are found in zeolitic sedimentary tuffs dispersed throughout the world. Among the most common are those of type clinoptilolite, mordenite, phillipsite and chabazite [16].

The territory of Mexico, in an approximate proportion of 50%, is formed by volcanic sequences of the pliocene type [17], which germinate in different states of the country. In the north-west the states of Sonora, Sinaloa, Chihuahua and Durango; in the west Jalisco and Nayarit; at the center Zacatecas, Guanajuato, San Luis Potosi, Queretaro, Puebla and Hidalgo; and in the south Guerrero and Oaxaca [18]. Currently presenting 30 NZ deposits, predominating zeolite type Clinoptilolite [19], being cataloged as one of the main exporting countries of zeolite in America, after Cuba [20]. However, in Mexico, research on the NZ directed to the productions of cementitious mixes, involving the construction industry, has not been sufficiently strong and relevant to achieve the objective of being applied and added as alternative cementing material in the PC in an indispensable manner in the preparation of mixtures, such as, pastes, mortars and concretes. Hence the importance of developing robust research that leaves in a precise and clear way the functionality, profitability and sustainability of applying an optimal partial substitution of NZ per PC in cementitious mixtures.

The trend of construction materials technology is due to the investigation of new elements, methods, techniques and materials that contribute to greater efficiency and performance to the construction and in turn to prevent, compensate and mitigate the damages caused to the environment. This following the policy that establishes to reduce the amount of cement required in a concrete mix, since its production is environmentally unpleasant due to high energy consumption and concomitant atmospheric CO_2 emissions [21]. The atmosphere and the environment in general, in the installations of the cement industries, is subject to a heavy polluting load caused by the emission of particles and pollutants, due to the different operations and methods that are implemented [22]. PC production consumes a high amount of energy and raw materials, this industry is responsible for the large amounts of CO_2 emitted every year, approximately 7% of the total caused by man [6].

The aim of this paper is to give a brief overview of the current state of research in the last decade on the implementation of NZ for the production of binary cementitious mixtures, highlighting the characteristics of the final product compared to the conventional product. The report is structured into four additional sections, section II provides specific information about the characteristics obtained in the evaluation of PC pastes that are altered by a partial substitution with NZ. Section III presents a summary of the investigations carried out on mortars (fundamental matrix of a concrete composed of sand, cement and water) with the addition of NZ. Section IV is related to the information obtained on concrete with the partial replacement of PC by NZ. Finally, Section V summarizes the conclusions and discussions for future research.

II. Portland Cement Pastes With Natural Zeolite

When a cementitious material comes into contact with water, chemical reactions are produced in order to provide mechanical properties and durability to the final product. Due to this it is necessary, first, to characterize the behavior of a PC paste with zeolite in its fresh state. After that, we present the different investigations carried out on a paste of PC with zeolite.

Bohac [11] performs an investigation to understand the behavior and properties of a PC paste, with partial substitution of NZ, during the hydration stages. The substitution is carried out in different percentages of zeolite (0%, 5%, 10% and 15% with respect to the weight). The PC used in this research is type I with a water / cement ratio of 0.5. The influence of the heat of hydration and the behavior of the first stages of hydration and setting are analyzed.

The study is carried out by applying the rheology of materials, a method that allows to accurately measure the heat developed from a flow in time, for a cementitious material in fresh state. The main objective is to measure the exothermic reaction related to hydration and analyze the properties of the mixture as the modulus of elasticity.

From the obtained results, the heat of hydration developed by the cementitious mixtures in their different percentages of zeolite is compared, the calorimetric curve obtained in this study presents four exothermic peaks. The first reaction develops during the first few minutes upon contact with water, producing a rapid release of energy produced by the immediate reaction of C_3A and Clinker sulfates [23, 24, 25]. The high content of Al_2O_3 (reactive alumina) in the zeolite influences the acceleration of hydration (**Fig. 1**), causing a high exothermic heat development in the cement mixture in the first minutes, besides the formation of ettringite Crystalline) is formed in this stage promoted by the reactive alumina of the zeolite.

In the nucleation and growth stage of CSH and CH (Ca $(OH)_2$) hydrates, the heat evolution decreases with increasing zeolite content (**Fig. 2**), allowing a better formation of crystals and a hardened more compact mixture [26].

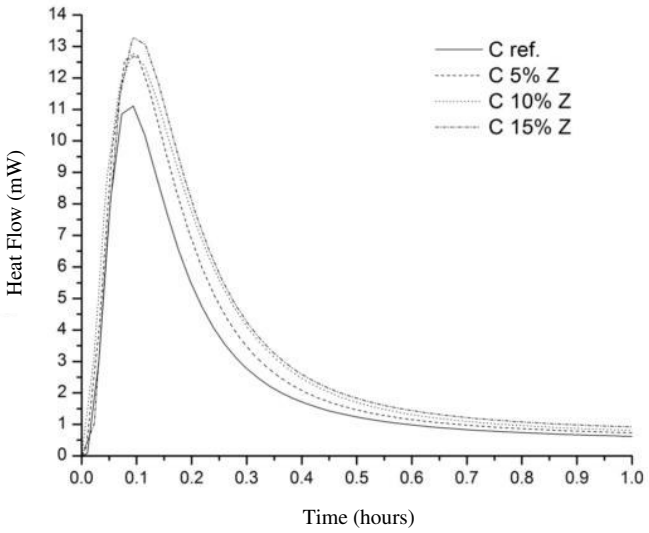

Fig. 1. Initial peak of cement

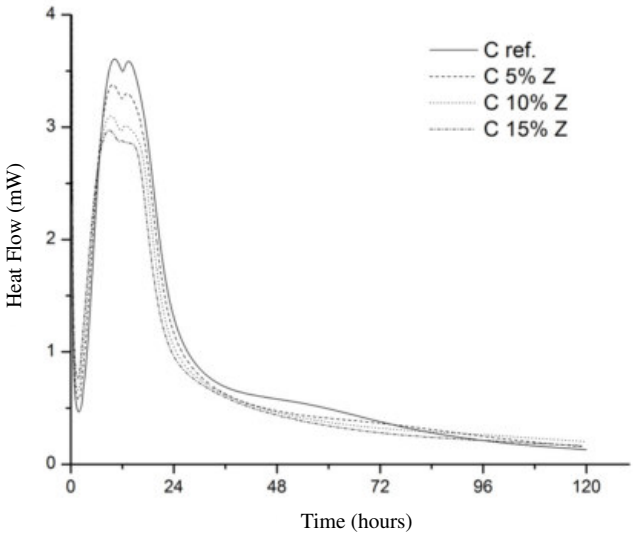

Fig. 2. Heat flow development.

The total heat developed over a period of 120 hours (**Fig. 3**) confirmed that at a higher zeolite content the heat release would be lower than in a Cement Mixing Conventional (CMC) from the second hydration stage. The presence of zeolite in the cement mixtures promotes the formation of ettringite, which increases the elasticity of the cement paste at the beginning of the hydration process. The amount of ettringite formed and its morphology is influenced by the dissolution rate of CH and gypsum in the liquid phase [27], there is an increase in ettringite formation when the liquid phase of CH is saturated due to the presence of zeolite [28].

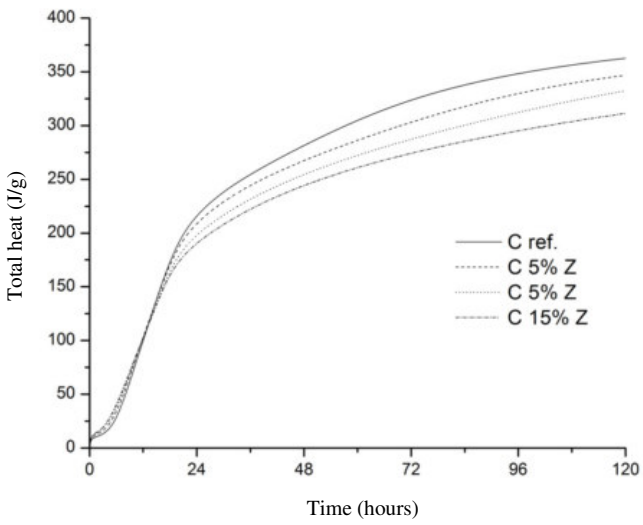

Fig. 3. Total heat development

The mechanical behavior of cement mixtures with zeolite depends on the type and purity of NZ. There is research registered with data lower mechanical resistance than a conventional cementitious mixture. Vélez and Perugachi [29] with the purpose of studying the mechanical behavior of a binary cementitious mixture based on PC type I and NZ from Ecuador, performs a research adding 0%, 5%, 10%, 15%, 20% and 25% of zeolite by means of air curing. the adding of this zeolite Ecuadorian in the PC produced a decrease on the resistance compressive maximum of a cement pastes for proportions 10% to 20%, while for 5% of NZ produced an increase on this property mechanical about 10 MPa with respect control mixing with cement type IV.

In a cement mixture with the addition of natural zeolite in an amount greater than 30%, it is necessary to use a superplasticizer additive due to a high decrease in workability. The cements mixed with high volume of NZ showed a different behavior compared to the cements mixed with a low amount of NZ reported in the literature [30]. A substitution of 55% of ZN is reported [31], affecting the fresh state of a cement mixture, Uzal emphasizes in his research that the initial and final setting times may be shorter than ordinary cement mixtures, although normally it is expected that the replacement of the PC by mineral additives causes a delay in the setting time of the cement system due to a lower proportion of PC [31]. The researcher points out that the number of pores in the cement paste is reduced with the NZ content, which is beneficial for mechanical strength and permeability. The author reports that some particles in the amount of substitution of 55% of NZ in cement pastes do not react at 28 days of age, especially the larger particles, these particles present a pozzolanic reaction of clinoptilolite on the surface of with a higher amount of calcium and less silicon content compared to the inner part.

The effect of replace cement for clinoptilolite is an increase in the water requirement necessary for maintaining an ideal consistency as compared with CMC [32, 33]. A content of NZ about 55% increase the water demand around a 40% and 60% higher than CMC, this range of water demand depend of

particle size, to the large (internal and external) surface areas, chemical composition, irregular shape with rough surface and honeycomb structure which has large voids [31, 33, 34].

As an important point in the Uzal's research, the mechanical strength obtained at the age of 28 days of curing with a replacement of 55% of NZ was similar to the results of control specimens with values near to 50 MPa and at the 180 days of curing with values near to 70 MPa (**fig. 4**), highlight that a superplasticizer was used.

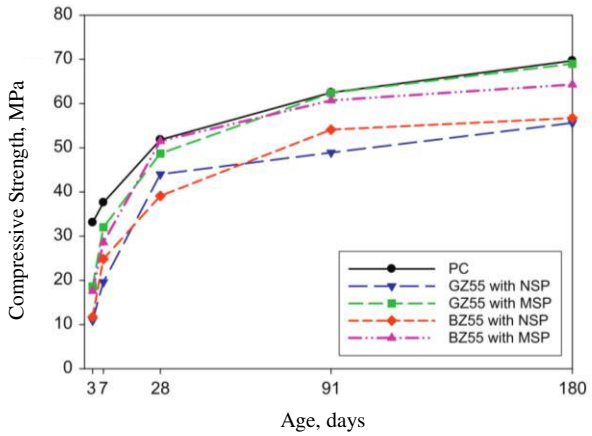

Fig. 4. Compressive strength development of the cement mortars prepared with two types of superplasticizer (NSP and MSP). GZ (Gordes, Turkey) and BZ (Bigadic, Turkey).

III. Portland Cement Mortars With Natural Zeolite

Phillipsite, Phillipsite-chabazite, Clinoptilolite and Erionite are the most common zeolitic tuffs in the world, each with different characteristics that influence pozzolanic behavior, e.g. reactive silica (r-SiO_2), chemical composition, Cation Exchange Capacity (CEC) is some of them [6]. it is compare some physicochemical and mechanical characteristics of mortars mixtures combined with this type of zeolitic tuffs, with the purpose of distinguishing the type of zeolite that develops a better mechanical behavior. **Table I** shows the types tuff zeolitic and their source.

TABLE I. Types of Naturals Zeolites

Zeolitic tuff in research		
Zeolitic tuff	***Abbreviation***	***Source***
Phillipsite	PHT	Naples, Italy
Phillipsite-chabazite	CHT	Naples, Italy
Clinoptilolite	CLT	Anatolia, Turkey
Erionite	ERT	Sonora, Mexico

With regard the most influential characteristics on the pozzolanic behavior, it emphasizes the major contains of r-SiO_2 between the four tuff zeolitic, the CLT zeolite with a value of 67% and ERT zeolite with a very similar value of 64%. At higher fineness or surface area (m 2 / g) of the zeolite particles it allows to have a better performance and pozzolanic behavior [36], the zeolite ERT is well above the other types of zeolite with a surface area of 271.2 (CHT with 129.1, CLT with 13.9 and PHT with 25.5). The evaluation of the pozzolan reactivity of zeolitic tuffs determined that for CLT and CHT substituted cementitious mixtures, more than 10% of zeolite is required to be active as pozzolanic material; For PHT the presence of pozzolanic activity was detected with a 40% substitution of this type of zeolite; The best performance in this sense was obtained by ERT, since with an amount of 10% it was enough to have a behavior of pozzolanic material, **fig. 5** represents a boxplot that reports the solubility curve, the points below the curve indicate the presence of pozzolanic activity for each type zeolitic tuff [6].

In the same way, for mechanical characterization was necessary evaluate the mechanical strength of mortars with zeolite and mortars with OPC (Ordinary Portland Cement), evaluated by resistance to compression with the proportions of 10%, 20% and 40% with respect to the weight of the cement, the best behavior at the age of 28 days of curing was presented by the mixture with ERT.

Having a higher amount of reactive silica causes a cement mixture with better properties at a longer time [37] than is the case presented by the zeolite type CLT, for the zeolite ERT is not the highest in r-SiO_2, but the percentage that has an optimal threshold, in addition to this has a much greater surface area than the other type of zeolites thus allowing better mechanical characteristics. In zeolitic tuffs in this study that has a higher or very approximate behavior to a CMC are the zeolites CHT, CLT and ERT, replacing the PC in percentages of 10%, 20% and 10% respectively.

It should be noted with reference to the above mentioned that with a quantity of 40% zeolite the hardening of the binary mixture is much longer compared to lower substitution percentages, it should be tested with an age greater than 28 days to identify the final strength of the mortar and to have a better mechanical characterization.

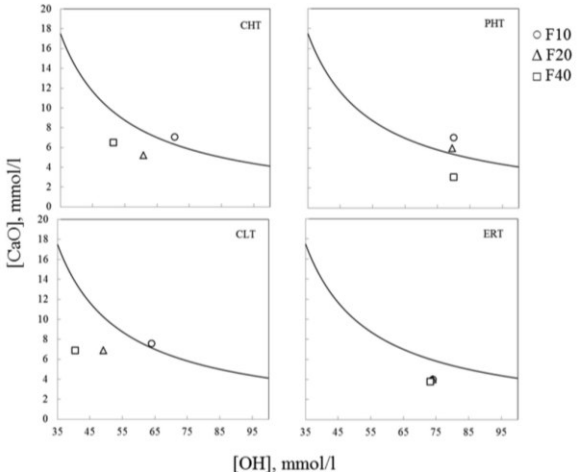

Fig. 5. Fratini's test (data after 8 days of curing): evaluation of the pozzolanic character of each zeolitized tuff for F10, F20 and F40 blends.

In Mersin University, Turkey, [32] it reports a study of some important properties of cement mortars with partial replacement of clinoptilolite type NZ in the proportions 0%,

5%, 10%, 15%, 20% and 30%. Within the mechanical properties, the compressive and flexural strengths were determined. For compression, all percentages of substitution were higher than the results obtained in the control specimens, with the best performance being the amount of 20% of NZ; with respect to flexion the control resulted with lower resistance compared to mixtures with NZ substitution, the amount of 10% and 20% of NZ performed better than the others. Other characteristics found in this research such as the dry unit weight of the mortar are affected with the incorporation of NZ, this decreases with the substituted amount of natural PM. Water absorption and porosity decreased with the increase in the amount of NZ.

Bacteria-induced corrosion in concrete pipes is a common problem for owners and operators of wastewater transport systems, the coating protector is one of the most common solutions, providing a barrier between wastewater and concrete. Other common applications that were used as a coating protector for concrete substrates are polyvinyl chloride (PVC), 100% solid polyurethane, polymers and coal [38, 39]. Zeolites functionalized with heavy metals exhibit both antimicrobial characteristics and resistance to biologically produced sulphuric acid attack. Hence, processed or natural zeolites can be used as protective coating materials from bacterial-induced corrosion in concrete and mortars. Their chemical and thermal stability, micropore structure and antimicrobial characteristics, make zeolites valuable product for many industrial applications [40].

As mentioned, PC production leads to high environmental pollution, the search for alternative cement is a solution that helps mitigate the damages caused by the cement industry. As mentioned, PC production leads to high environmental pollution, the search for alternative cement is a solution that helps mitigate the damages caused by the cement industry. A mortar made with PC total replacement by NZ using an alkali activator (NaOH) instead of water (H2O), thus, it becomes in a new cement construction material using zeolite and an alkali activator. The zeolite cement mortar created in a mix proportions of 180 g of cement, 171 g of NaOH (50%) and 565 g of aggregate provides the highest strength mechanical obtaining a value 42.3 MPa, also, the 7-day compressive strength was 90% equivalent to the 28-day, which means the strength develops dramatically in the early stage [41].

IV. Portland Cement Concretes With Natural Zeolite

After studying the different reactions of the PC combined with NZ and analyzing the fundamental matrix of a concrete, which is the mortar, we present the different studies carried out in recent years on concrete mixtures that have been replaced with NZ to determine and understand the different characteristics that these binary concretes provide. In this way, Ahmadi in Iran [7], performs a peculiar investigation comparing NZ with the most commercial pozzolans, which are, silica fume (SF) and fly ash (FA) for the production of pozzolanic concretes. The experimental methodology consists of determining the pozzolanic reactivity of the NZ by comparing it with SF. From previous studies, it is considered that the pozzolanic reactivity of NZ lies between SF and FA [42], but in terms of improvement in compression strength NZ is better than AF but lower than SF [43].

The production of concrete specimens is made for the partial replacement of PC by NZ on the basis of 5%, 10%, 15% and 20% with respect to the weight of the cement; while SF takes 5%, 10% and 12.5% by weight of the cement. The origin of the zeolite was from the mines of northern Semnan in Iran and was of the type clinoptilolite, **table II** presents some characteristics of the PM. The amount of SiO_2, Al_2O_3 and Fe_2O_3 is slightly more than 80% according to XRD results.

TABLE II. Physical characteristics of PM

Specific gravity and surface area of PM used		
Natural Pozzolanic material	***Specific gravity***	***Surface area (m^2/kg)***
Zeolite	2.2	320
Fly ash	2.22	410
Silice fume	2.2	20,000

From the results obtained by Ahmadi, the following stand out:

- The initial pozzolanic reactivity in NZ was lower compared to that of SF, however from 28 days of age the NZ exhibit a high rate of lime consumption (100%) as well as SF, that is, the pozzolanic reactivity of the NZ is slower in comparison to that of SF and at the end of 28 days they maintain the same reactivity.
- The workability of the mixtures in the fresh state were not affected by the NZ, however a superfluidificant was used to obtain the desired slump in the highest contents of zeolite.
- The absorption of water decreases in concrete with partial substitution of NZ or SF. With respect to NZ the water absorption does not vary with the zeolite content (NZ about 2% of absorption with respect to the weight), a greater discrepancy in the increase of SF is observed (2.25% of absorption for 5% of SF and 1.75% for a 12.5% SF).
- In regard to permeability, there is a threshold in the NZ content, for a 5% and 10% substitution it was much lower than the control specimens. However for the percentages of 15% and 20% it was much higher than the control, a reason to this is the amount of particles of NZ that does not reach to react, allowing the permeability of the oxygen by the porous structure of the NZ [7]. For SF, the oxygen permeability is proportional to SF content, with a better performance, the substitution of 12.5% SF with respect to NZ and control.
- The electrical resistivity increases with the substitution of NZ and SF in comparison to the control; the resistivity for concrete mixtures, at all curing ages, with the NZ substitution is lower than those obtained with concrete mixtures with SF.

Meanwhile, partialy replacing 15% of NZ in a concrete improves the resistance and durability of it. The chloride

penetration and the corrosion rate of the concrete was reduced, also contractions were lower and it did not demand too much superplasticizer [44]. Vejmelková [45] achieved a binary cementitious mixture (20% NZ) with slightly lower values of mechanical strength (compression, bending and fracture) compared to a CMC, however, resistance to frost, de-icing salt and agents chemical in general is greater in the binary mixture than in the conventional one, therefore, a material with greater durability and a mechanical resistance in the tolerance range is obtained. Also, Nagrockiene and Girskas [46] found that the properties of the modified concrete replacing PC by NZ (2.5%, 5%, 7.5% and 10%) were improved, increasing compressive strength by 15% the absorption of water up to 2.3 times.

Chan and Ji [43] have concluded, after a number of investigations and reviews, that zeolite is more effective than fly ash but silica fume is better at compressive strength than zeolite. A number of studies show that the proportion or amount of zeolite in a binary cement mixture depends on the characteristics and chemical-environmental conditions of zeolitic tuff, considering an intermediate threshold of 10% of zeolite according to the literature consulted. Likewise, Najimi [44] inferred that concrete with partial addition of zeolite is characterized by the reduction of the heat of hydration and consequently of thermal cracking and improved durability properties such as penetration of chloride ions, corrosion rate, contraction by drying and penetration of water.

V. DISCUSSION

It has been presented a critical review of the literature concerning the partial substitution of PC by the NZ for the production of pastes, mortars and concretes. This review proves that mechanical strength, as a functional property of concrete, is improved with the replacement of cement by zeolite and the quantities are realted with the type of zeolite used, each type of zeolite has a different reactive silica, responsible of providing greater mechanical resistance compared to conventional concrete. Assuming the zeolite type is clinoptilolite, the most suitable proportions based on this report are between 20% and 40%, 55% of zeolite in a concrete is reported with a similar strength to a OPC using a superplasticizer. It should be mentioned that for some countries it is not obligatory to acquire a mechanical resistance greater than or equal to that of a conventional concrete, while it is within the limit established by the standard that governs the mechanical resistance to the compression of pozzolanic cements (in some countries of Europe they do not usually exceed 32.5 MPa [6]). In this sense, the percentages to the redistor of 40% are of great interest, the main objective is to reduce the production of cement, in this way to mitigate the damages caused by the emissions generated in its production.

If it is desired to obtain a slightly higher resistances than that of a OPC, the partial substitution between 10% and 20% will be the most adequate, depending on the pozzolanic reactivity of the zeolite and the percentage of reactive silica (approximately 65% and 80%), a major and determinant factor is the surface area of the zeolite particles, the higher the surface area (the finer the zeolite grains) the greater the pozzolanic reaction, allowing higher mechanical resistance, but with a greater demand for water.

A zeolite concrete can be used perfectly in any field of civil engineering, zeolite is an economical material in comparison to other pozzolanic materials (for countries rich in this mineral, for example in Colombia it has not yet been exploited because of the lack of research, this pozzolanic material is acquired by importation [20]). In coastal areas or areas with high chemical content, zeolite-based binary mixtures would be very useful, the low permeability of these concretes would considerably increase the durability of the structural members. Karakurt [47] verifies that the incorporation of natural zeolite in cementitious mixtures increases the resistance to attacks produced by sulphates. In general this type of binary concrete can be used in the same way as conventional concretes with a slight reduction in cost and improvements in their properties.

VI. CONCLUSION

This paper summarizes the present research of the incorporation of natural zeolite in cementitious mixtures based on PC, highlighting the fundamental properties that this material acquires by the substitution. The latest carried out research agrees that the use of natural zeolite for the production of concrete and its derivatives is 100% recommended for its high mechanical performance and for the increase of the durability of the members made with this binary material. The implementation of natural zeolite as a pozzolanic material should not be a second option but a fact, a study of the technical-budget processes of production of binary cement based on natural zeolite should be done with the aim of changing the construction paradigms and start using alternative materials to help mitigate environmental damage.

ACKNOWLEDGMENT

The authors wish to express their appreciation to the researcher Mario Trejo Perea for his helpful advice and his kind help during the writing process.

REFERENCES

[1] H. Taylor, “Cement Chemistry”. Academic Press, London, pp. 277–315, 1990

[2] F. Massazza, “Pozzolanic Cement”. Cem. Concr. Compos, Vol. 15, pp. 185–214, 1993

[3] M. Rosell, R. Galloso and B. Calvo, “Zeolita como aditivo mineral activo en hormigones de altas prestaciones”. Boletín Geológico y Minero, vol. 117 (4), pp. 783-792, 2006.

[4] American Concrete Institute (ACI), “Terminología del cemento y del concreto. ACI 116-R-00”. Instituto Mexicano Del Cemento Y Del Concreto, A.C., 2002, pp. 88.

[5] J. Costafreda, B. Calvo and J. Parra, “Contribución de la zeolita natural a las resistencias mecánicas de cementos, morteros y hormigones”, IX Jornadas Iberoamericanas de Materiales de Construcción, Madrid, España, 2011.

[6] B. Leguori, F. Lucolano, B. Gennaro, M. Marroccoli and D. Caputo, “Zeolitized tuff in environmental friendly production of cementitious material: Chemical and mechanical characterization”. Construction and Building Materials journal, vol. 99, pp. 272-278, 2015.

[7] B. Ahmadi and M. Shekarchi, “Use of natural zeolite as a supplementary cementitious material”, Cement & Concrete Composites, vol. 32, pp. 134–141, 2010, Aviable in: http://dx.doi.org/10.1016/j.cemconcomp.2009.10.006

[8] N. Feng, H. Yang and L. Zu, "The strength effect of mineral admixture on cement concrete", Cem Concr Res, vol 18(3), pp. 464–72, 1988.

[9] A. Calleja, "la importancia de las zeolitas", Universidad de Salamanca, España, CT, vol. 1, pp- 211-227, 2009.

[10] R. Wang and G. Wang, "Influence and mechanism of zeolite on the setting and hardening process of styrene-acrylic ester/cement composite cementitious materials". Construction and Building Materials, vol. 125, pp. 757–765, 2016.

[11] M. Bohác, D. Kubátová, R. Necas, A. Zezulová, A. Masárová and R. Novotný, "Properties of cement pastes with zeolite during early stage of hydration", International Conference on Ecology and new Building materials and products, ICEBMP, vol. 151, pp. 2-9, 2016.

[12] Ch. Baerlocher, L.B. McCusker and D.H. Olson, atlas of zeolite framework types. 6th ed., vol. 1. Elsevier, published on behalf of the structure Commission of the international Zeolite Association, 2007, pp. 398.

[13] I. Janotka and L. Krajci, "Sulfate resistance and passivation ability of the mortar made from pozzolan cement with zeolite", J. Therm. Anal. Calorim, Vol. 94, pp. 7–14, 2008.

[14] M. Valipour, F. Pargar, M. Shekarchi and S. Khani, "Comparing a natural pozzolan, zeolite, to metakaolin and silica fume in terms of their effect on the durability characteristics of concrete: a laboratory study", Constr. Build. Mater. Vol. 41, pp. 879–88, 2013.

[15] R. Tschernich, "zeolites of the world". Geoscience Press, Inc., Phoenix, pp. 563, 1992.

[16] C. Colella, M. de' Gennaro and R. Aiello, "Use of zeolitic tuff in the building industry", in: D.L. Bish, D.W. Ming (Eds.), Natural Zeolites: Mineralogy, Occurrence, Properties, Applications, Reviews in Mineralogy & Geochemistry, vol. 45, Mineralogical Society of America, Washington, D.C., pp. 551–587, 2001.

[17] M. Jiménez, "Caracterización de minerales zeolíticos mexicanos", tesis de pregrado. Universidad Autónoma Del Estado De México. Toluca, México. 2004.

[18] L.E. Ortiz, "Criterios y especificaciones concernientes a la exploración y valoración de minerales en la República Mexicana". Dirección de Recursos Minerales. Gerencia de Recursos Mineros. 2001.

[19] Unión Puebla. Zeolitas, los asombrosos minerales de Puebla. El universal. (2015, junio, 01). Aviable in: http://archivo.unionpuebla.mx/articulo/2015/06/01/ciencia/zeolitas-los-asombroso-minerales-de-puebla.

[20] Escobar M. Zeolita, mineral promisorio que el país podría explotar, UN Periódico, Impreso No. 172, (2013, noviembre, 09), aviable in: http://www.unperiodico.unal.edu.co/dper/article/zeolita-mineral-promisorio-que-el-pais-podria-explotar.html.

[21] G.P. Gerilla, K. Teknomo and K. Hokao, "An environmental assessment of wood and steel reinforced concrete housing construction", Building and Environment, Vol. 42, pp. 2778–2784, 2007.

[22] H. Ricardo and j. Romero, "mejoras en los impactos ambientales de cementos Cienfuegos S.A.", Revista Universidad y Sociedad, Vol. 4 (1), pp. 1-8, 2012.

[23] K.L. Scrivener and P.L. Pratt, "Microstructural studies of the hydration of C3A and C4 AF independently and in cement paste", in: F.P. Glasser (Ed.), Brit. Ceram. Proc. 35, Stoke-on-Trent, British Ceramic Society, pp.207–219, 1984.

[24] H.N. Stein and J.M. Stevels, "Influence of silica on the hydration of 3CaO, SiO2", J. Appl. Chem. Vol. 14, pp. 338–346, 1964.

[25] J.W. Bullard, "A determination of hydration mechanisms for tricalcium silicate using a kinetic cellular automaton model", J. Am. Ceram. Soc., Vol. 91, pp. 2088–2097, 2008.

[26] W. Lerch, "The influence of gypsum on the hydration reactions of portland cement", Proc. ASTM 46, 1946, pp. 1252–1292.

[27] H. Uchikawa, S. Uchida and K. Ogawa, "Influence of fly ash characteristics on the rheological properties of fresh fly ash cement paste", Proc. Ann. Meet. Mater. Soc., Boston 1982, Concrete Rheology, pp. 203–214.

[28] P.K. Mehta, "Effect of lime on hydration of pastes containing gypsum and calcium aluminates or calcium sulfoaluminate", J. Am. Ceram. Soc., Vol. 56, pp. 315–319, 1973.

[29] R. Vélez and R. Perugachi, "Estudio y Simulación del Comportamiento del Cemento Pórtland Tipo I con la Adición de 10% de Zeolita Ecuatoriana Mediante el Curado al Aire". Escuela Superior Politécnica Del Litoral, Guayaquil, Ecuador. 2008.

[30] T. Perraki, E. Kontori, S. Tsivilis, G. Kakali, "The effect of zeolite on the properties and hydration of blended cements". Cement & Concrete Composites. Vol 34, pp. 128–33, 2010.

[31] B. Uzal, L. Turanli, "Blended cements containing high volume of natural zeolites: Properties, hydration and paste microstructure", Cement & Concrete Composites, Vol. 34, pp. 101–109, 2012.

[32] C. Bilim, "Properties of cement mortars containing clinoptilolite as a supplementary cementitious material" Construction and Building Materials Vol. 25, pp. 3175–3180, 2011.

[33] C. Shon, Y. Klim, "Evaluation of West Texas natural zeolite as an alternative of ASTM Class F fly ash", Construction and Building Materials, Vol. 47, pp. 389-396, 2013.

[34] Y. Kocak, E. Tasci, U. Kaya, "The effect of using natural zeolite on the properties and hydration characteristics of blended cements", Construction and Building Materials, Vol. 47, pp. 720-727.

[35] L. Turanli, B. Uzal and F. Bektas, "Effect of material characteristics on the properties of blended cements containing high volumes of natural pozzolans", Cem Concr Res, Vol. 34, pp. 2277–82, 2004.

[36] D. Caputo, B. Liguori and C. Colella, "Some advances in understanding the pozzolanic activity of zeolites: the effect of zeolite structure". Cement & Concrete Composites, Vol 34, pp. 455–462, 2008.

[37] G. Mertens, R. Snellings, K. Van Balen, B. BicerSimsir, P. Verlooy, J, "Pozzolanic reactions of common natural zeolites with lime and parameters affecting their reactivity". Cem. Concr. Res., Vol.40, pp. 398–404. Elsen 2010.

[38] A. Beeldens, J. Monteny, E. Vincke, N. De Belie, D. Van Gemert, L. Taerwe, W. Verstraete, "Resistance of biogenic sulphuric acid corrosion of polymer-modified mortars", Cement and Concrete Composites, Vol. 23, pp. 47–56. 2001.

[39] N. De Belie, J. Monteny, A. Beeldens, E. Vincke, D. Van Gemert, W. Vestraete, "Experimental research and prediction of the effect of chemical and biogenic sulphuric acid on different types of commercially produced concrete sewer pipes", Cement and Concrete Research vol. 34, pp. 2223–2236. 2004.

[40] T. Haile, G. Nakhla, E. Allouche, "Evaluation of the resistance of mortars coated with silver bearing zeolite to bacterial-induced corrosion", Corrosion Science, Vol. 50, pp. 713-720. 2008.

[41] B. Jo, J. Choi, K. Yoon, J. Park, "Material characteristics of zeolite cement mortar", Construction and Building Materials, Vol. 36, pp. 1059-1065, 2012.

[42] C.S. Poon, L. Lam, S.C. Kou and Z.S. Lin, "A study on the hydration rate of natural zeolite blended cement pastes". Constr Build Mater, Vol. 13(8), pp. 427–32, 1999.

[43] SYN. Chan, X. Ji, "Comparative study of initial surface absorption and chloride diffusion of high performance zeolite, silica fume and PFA concretes". Construction and Building Materials, Vol. 25, pp. 293–300, 1999.

[44] M. Najimi, J. Sobhani, B. Ahmadi and M. Shekarchi, "An experimental study on durability properties of concrete containing zeolite as a highly reactive natural pozzolan", Construction and Building Materials, vol. 35, pp. 1023-1033, 2012.

[45] E. Vejmelková, D. Koňáková, T. Kulovaná, M. Keppert, J. Žumár, P. Rovnaníková, Z. Keršner, M. Sedlmajer and R. Černý, "Engineering properties of concrete containing natural zeolite as supplementary cementitious material: Strength, toughness, durability, and hygrothermal performance", Cement and Concrete Composites, vol. 55, pp. 259-267. 2015.

[46] C. Karakurt, I. Topcu, "Effect of blended cements produced with natural zeolite and industrial by-products on alkali-silica reaction and sulfate resistance of concrete", Construction and Building Materials, Vol. 25, pp. 1789-1795, 2011.

[47] D. Nagrockiene and G. Girskas, "Research into the properties of concrete modified with natural zeolite addition", Construction and Building Materials, vol. 113, pp. 964-969, 2016.


CONACYT
Consejo Nacional de Ciencia y Tecnología


CONCYTEQ

Transportation networks in virtual cities

Queretaro city downtown as a case study

Madera-Madera, Miguel A.
School of Informatics
Autonomous University of Queretaro
Queretaro, QRO, Mexico
miguelmadera50@gmail.com

Gonzalez-Gutierrez, Fidel; Gonzalez-Gutierrez, Arturo
Diaz-Delgado, Guillermo
School of Engineering
Autonomous University of Queretaro
Queretaro, QRO, Mexico
{fglez, aglez, gdiaz}@uaq.mx

Abstract

Recently, the growth of the human population has created the need to modernize the way public transportation networks are designed. Traditional methods for approaching this problem fail when the geometry of the given road network of a city is irregular. This problem can also be viewed as a graph problem where the goal is to connect all the regions of a planar graph with the minimum total path length possible. This is known as the Minimum Length Corridor Problem, which has been proved to be an NP-Complete problem. The aim of this study is to design and implement heuristics to efficiently solve instances of the MLCP. These heuristics are applied as a case study to simulate one of the major roads of the city of Queretaro, in order to discover viable routes for public transportation. They are also applied to a series of square $n \times n$ meshes for which an optimal result is known. We show that for the mesh instances of odd size n, there exists an algorithm, which produces optimal solutions in quadratic time. Also, we present an algorithm with approximation ratio less than 2 for mesh instances in polynomial time. We use these heuristics to solve our case study regarding the public transportation network for the city of Queretaro.

Keywords

Algorithms, Optimization, Graph Theory, Software Engineering

I. INTRODUCTION

In the last few decades, there has been an exponential growth of the global population that has created the need to modernize public transportation systems [1]. The central problem of this research is the theoretical improvement of public transportation networks using graph theory techniques and computational optimization, specifically reconsidering the public transportation problem as an instance of the Minimum Length Corridor Problem (MLCP).

The traditional methods of designing public transportation networks (radial designs, dispersed grids) fail when the geometry of cities ceases to be regular. Currently, most research related to the design of public transportation networks focuses on mathematical optimization and scheduling algorithms [2]. The abstractions of graph theory provide the basis for solving this problem in a generalized way. When major city roads are represented as a planar graph it is possible to establish the necessary heuristics to represent a public transportation network as a solution to the MLCP.

A. *Objective*

The main objective of this investigation is the implementation of several heuristics to solve instances of the MLCP in representations of the city of Queretaro (QRO) relatively efficiently. This includes the use of metrics to quantitatively compare the solutions generated in the virtual models. The software that was used to generate, visualize and evaluate the results presented in this work has the capacity to be expanded for future work.

B. *Minimum Length Corridor Problem*

The minimum length corridor problem is a modern routing problem that was initially proposed during the 13th Canadian Conference on Computational Geometry. Gonzalez-Gutierrez A. and Gonzalez T. proved that the MLCP is NP-complete [3]. The problem can be established as follows: Given a rectangular boundary partitioned into rectilinear polygons, the objective is to generate a corridor of least total length. A corridor is a set of line segments where each segment must lie along the line segments that form the rectangular boundary

This material is based upon work supported by a grant FOFI-UAQ 2015 from the Autonomous University of Queretaro.

and/or the boundary of the rectilinear polygons. The corridor is a tree, and must include at least one point from the rectangular boundary and at least one point from the boundary of each of the rectilinear polygons. For the purposes of this work, we are going to allow that the corridor does not include a vertex from the boundary.

C. Input Data / Graphs

The initial data for the graphs of QRO were obtained from Google Maps using specialized software that isolates the necessary roads and generates custom maps. The graphs were tested on a desktop computer. The specifications of that computer are listed in *Table I*. The following criteria were used to create the base images of the default maps:

- All text was deleted from the map.
- Every geographic feature of the map was deleted.
- Every road (of any size) was set to the color black.
- The background of the map is set to white.

With these maps it was possible to extract (using image editing software) the crucial geographic data to generate the data structures used by the simulation software. In addition, a small sample graph was manually generated to test the functions and heuristics of the simulation software. The sample graph and the graphs derived from the maps fulfill the following characteristics:

- The connections between the roads ensure that there is a path between any pair of vertices. There are no isolated vertices.
- All relevant neighborhoods in the geographic region are represented on the map.
- Small roads only exist on the map if they serve as a connection between two larger roads (The size of the roads is according to Google Maps).
- Each edge has a unique weight; the Euclidean distance between 2 intersections of a road is unique.

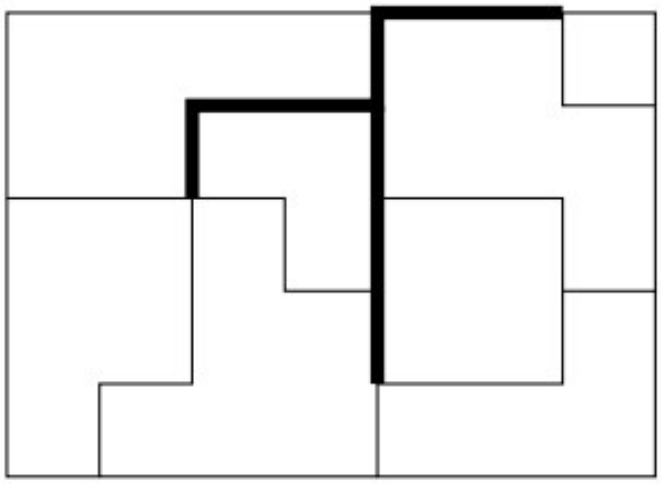

Fig. I: The optimal solution to the MLCP [4]

TABLE I. CHARACTERISTICS OF THE TEST ENVIRONMENT

Operating System	Windows 8.1
Processor	Inter Core i7 (3.40 GHz)
RAM	8 GB
System Type	X64 (64-bit)

II. ALGORITHMS TO SOLVE THE MLCP

A. Greedy Search Heuristic (GSH)

The greedy strategy implemented in the simulation software seeks to find an approximate solution to the MLCP. The algorithm first obtains a root vertex. After adding the polygons adjacent to the root, the path with the shortest distance to the nearest polygon is added to the solution. This greedy search is repeated, adding to the tree until all the polygons have been considered. Although the resulting tree is a valid solution to MLCP, this heuristic does not guarantee an optimal solution. This strategy works for both directed and non-directed graphs. To improve the execution time of this algorithm, the concept of *borders* is used. That is, the algorithm limits the search space to only the vertices at the intersection between the polygons of the solution and those of the base graph in order to reduce the time complexity of the algorithm. Searching only borders reduces execution time by magnitudes, although it is still executed in polynomial time, specifically $\boldsymbol{O(n^4)}$. The algorithm works as follows:

1. **for** all vertices of the graph **do** steps a-c
    a. Set the vertex as the root or starting point of the solution.
    b. **while** there exist unmarked polygons **do** steps i-iii
        i. Mark all the polygons that include vertices in the current solution.
        ii. Find the path with the lowest weight to the nearest polygon.
        iii. Add to the current solution the vertices and edges of the new path.
    c. Keep the solution with minimum total weight.

B. Shared Vertex Heuristic (SVH)

The shared vertex strategy is not based on polygon searches or crucial edges. This heuristic looks for the most common vertices from an ordered list of polygons. This strategy does not depend on a root vertex, improving its efficiency. Because the search space is reduced to a simple list of polygons and vertices, this heuristic is executed in quadratic time complexity $\boldsymbol{O(n^2)}$. This algorithm works as follows:

1. Select the first of an ordered list of polygons. The polygons are ordered by geographic position.

2. **while** the ordered list of polygons is not empty **do** steps a-c
    a. **if** the polygon shares vertices with other polygons from the ordered list **do**
        i. Select the vertex that is included in the largest amount of polygons from the list and append it to a list of vertices.
    b. **else do**
        i. Select the vertex that is included in the largest amount of polygons from the base graph and append it to a list of vertices.
    c. Remove all polygons that include the selected vertex from the list of ordered polygons.
3. Connect each of the shared vertices using Prim's algorithm, generating a minimum cost spanning tree.

III. Modeling Queretaro as a Graph

A. *Graph: Queretaro Downtown*

The first map of the city of Querétaro consists of only the downtown area of the city bounded by the following roads: Avenida Universidad, Avenida 5 de Febrero, Calle Ignacio Zaragoza, and Calle Corregidora. In this graph the roads are modified to only include the most important according to the following criteria:

- Every *important* neighborhood (according to Google Maps) of the area is considered in the final graph.
- Large roads and roads that connect them remain in the base graph.
- Additional roads are included so that there is always a valid path between every two vertices.

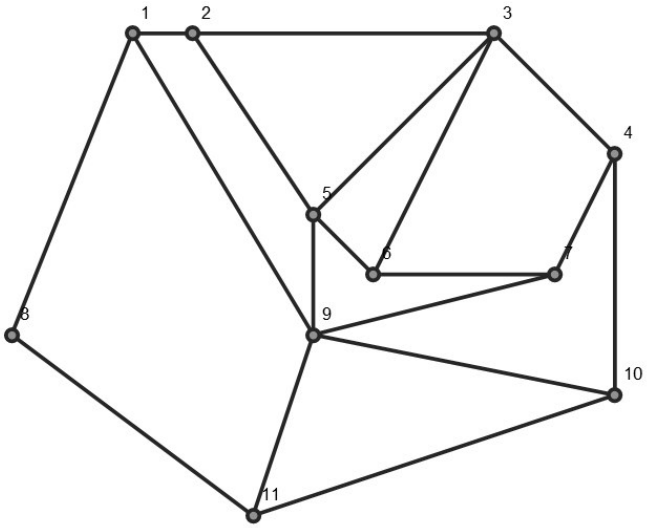

Fig. II: The sample graph for the simulation software.

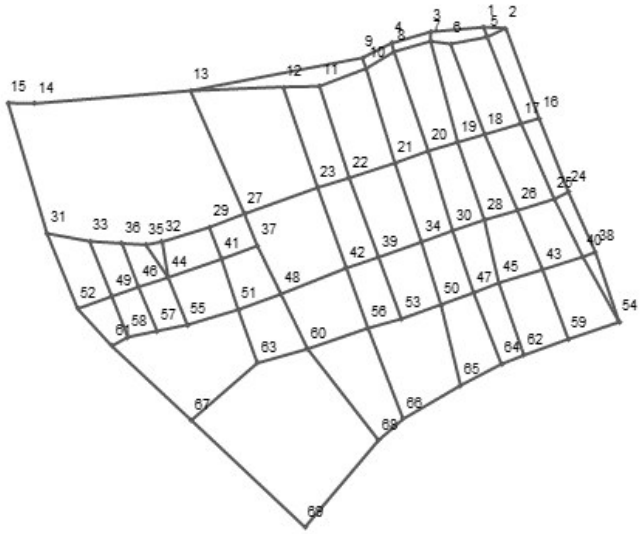

Fig. III: Queretaro Downtown Graph

B. *Graph: Queretaro Urban Zone*

The second map of the city of Querétaro consists of what is known as the *urban zone* bounded by the following roads: Avenida 5 de Febrero, Carretera México - Querétaro and Blvd. Bernardo Quintana. Although this section of the city encompasses a larger area, it follows the same characteristics of the Querétaro Downtown graph.

C. *Graph: Meshes*

Square meshes of various sizes are used to evaluate the heuristics with a consistent metric. For a square of size $n \times n$ partitioned into unit squares, Gonzalez-Gutierrez A. and Gonzalez T. have found a proved formula, given in (1), to calculate the total weight of the optimal solution f^* of this restricted instance version of the MLCP [5].

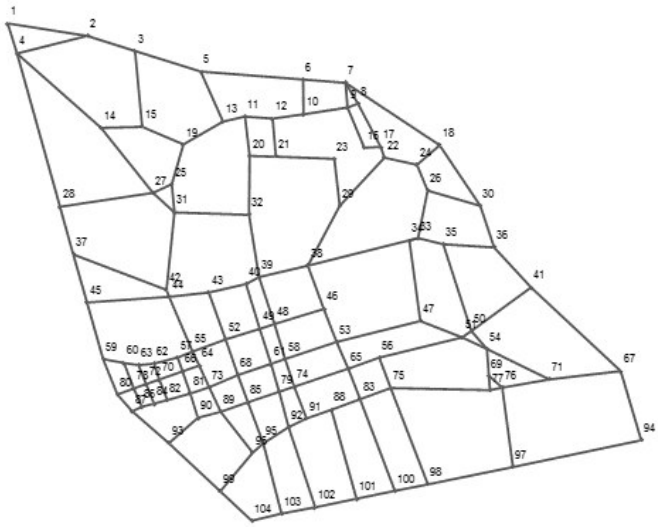

Fig. IV: Queretaro Urban Zone Graph

$$f^* = \left\lceil \frac{n^2}{2} \right\rceil - 2 \qquad (1)$$

IV. Results

A. Mesh Graphs: Total Distances

Due to the regular nature of the graphs, all of the heuristics tested aligned to a quadratic regression. In some cases the resulting quadratic equation is exact, in others, it is a close approximation. The equations for the GSH, SVH, and optimal distances are noted in *Table II*.

B. Map Graphs: Total Distances

Comparisons for the map graphs is difficult because it is not feasible to calculate the optimal solutions to MLCP using brute force with the resources available. The polynomial time complexity of this task is beyond the scope of this investigation. The weights (measured in meters) are taken from *Mathematica*'s online geographic database. *Table III* compares the total weight of the base graphs with those of the MLCP solutions produced by the heuristics.

TABLE II. Regression of Mesh Distances

Heuristic	Equation
Optimal	$f^* = \left\lceil \frac{n^2}{2} \right\rceil - 2$
GSH	$n^2 - 1$
SVH	${}^3/_5\, n^2 - n$

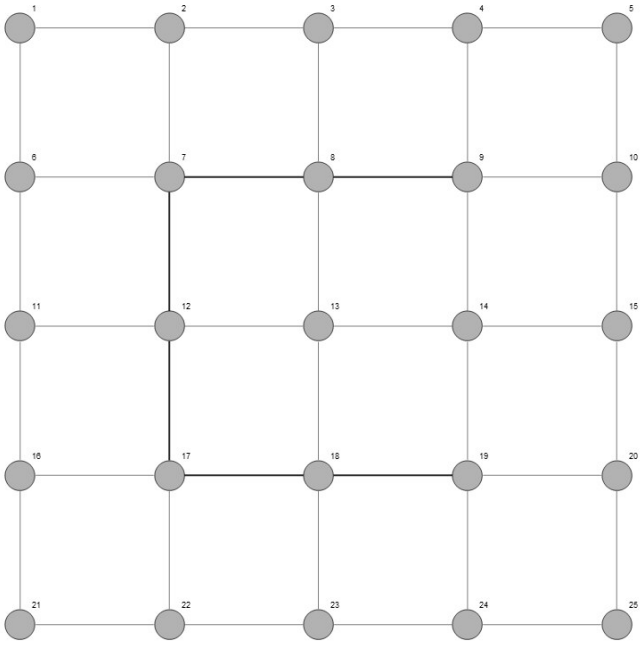

Fig. V: The optimal solution to a 5x5 mesh.

TABLE III. Total Map Graph Distances

Heuristic	Sample Graph	QRO Downtown Graph	QRO Urban Zone Graph
Base	68.72	31, 299 m	78,337 m
GSH	3.41	5,337 m	15,694 m
SVH	6.24	5,395 m	15,723 m

C. Timing Comparisons

The Mathematica built-in function *Timing* is used to compare the exact time taken by each algorithm. This function calculates time slots using processor clock cycles. Here it is possible to visualize the actual constraints between the algorithms when they are applied to real data with a multitude of vertices, edges and polygons. It is necessary to take note of the challenges in time measurements in any traditional computer system; this measurement should only be a general value for relative execution time.

TABLE IV. Average Runtime on Map Graphs

Heuristic	Sample Graph	QRO Downtown Graph	QRO Urban Zone Graph
GSH	0.03 s	138.62 s	907.9 s
SVH	0.00 s	0.3 s	1.75 s

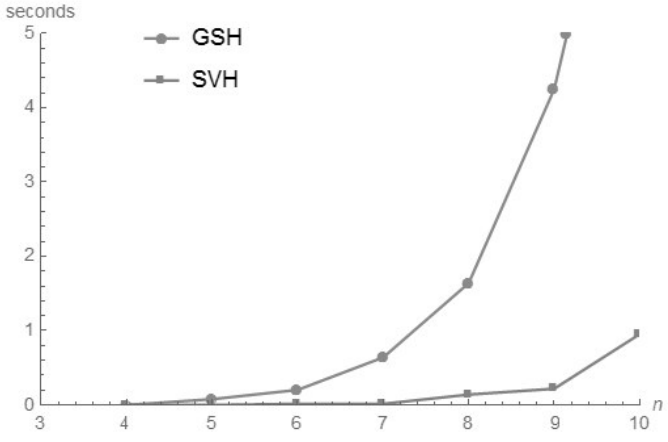

Fig. VI: Average runtime on mesh graphs.

V. Conclusions

The data generated in the previous section clearly show that the best strategy (when applied to meshes and real geographic networks) is the shared vertex heuristic. Its time complexity and efficiency arise due to the fact that it does not continually compare the distances of the edges to create a path. Instead, it simply reduces a list of polygons that decrease in size by each iteration. Geographic data will almost always contain more edges than vertices, thus favoring the shared vertex strategy over those that require iteration and constant comparison of paths. When applied to meshes, this heuristic reaches the optimal solution in cases where n is odd. In some cases (specifically where the graph tends to be more irregular), the best strategy in terms of development time and versatility is the simple greedy search heuristic. By simply modifying how the path (and the underlying data structure) grows, it is possible to obtain a path, a tree, or a cycle from this implementation. Although it is generally much slower than the shared vertex strategy, it is functional in a wider range of related problems. Figs. VII, VIII, IX and X visualize the generated MLCP solutions.

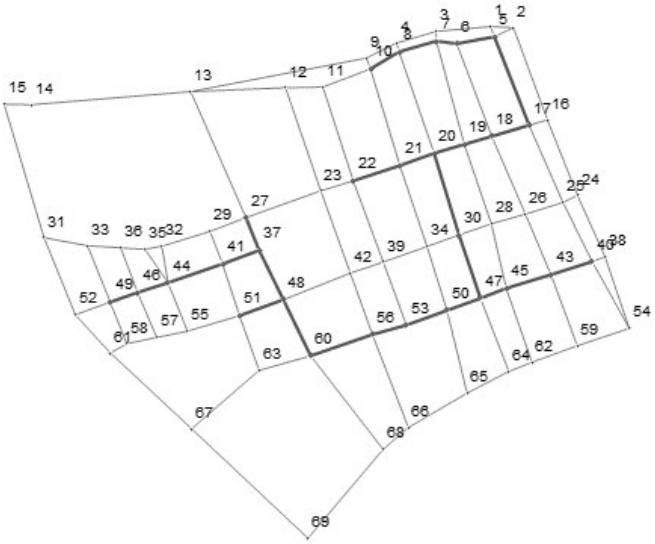

Fig. VIII: SVH solution for the QRO Downtown Graph

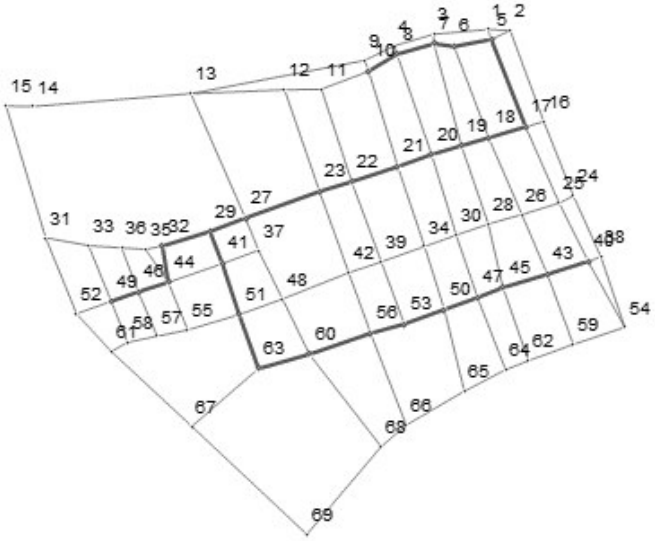

Fig. VII: GSH solution for the QRO Downtown Graph

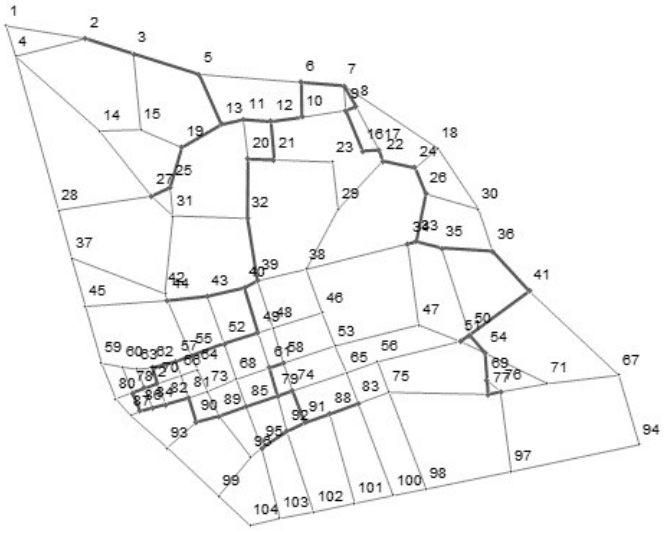

Fig. IX: GSH solution for the QRO Urban Zone Graph

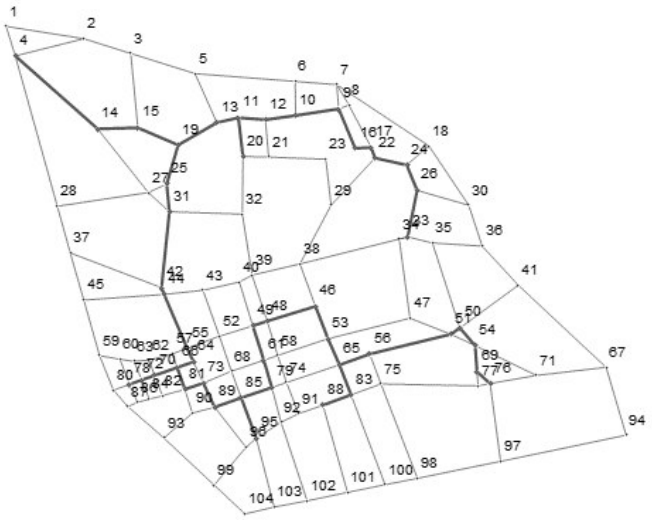

Fig. X: SVH solution for the QRO Urban Zone Graph

REFERENCES

[1] Nielsen, G. & Lange, T. (2008). Network design for public transport success–theory and examples. Norwegian Ministry of Transport and Communications, Oslo.

[2] Jago Dodson, J. S., Paul Mees & Matthew, B. (2011, March). The principles of public transport network planning: a review of the emerging literature with select examples. Griffith University: Urban Resarch Program, (15).

[3] Gonzalez-Gutierrez, A., & Gonzalez, T. F. (2007). Complexity of the minimum-length corridor problem. Computational Geometry, 37(2), 72-103.

[4] Chicago O'Rourke, E. D. D. ˜J. (August 13–15, 2001). "open problems from cccg 2000. Proceedings of the 13th Canadian Conference on Computational Geometry (CCCG 2001).

[5] Gonzalez-Gutierrez, A. & Gonzalez, T. F. (Paper in Progress). Experimental analysis of lp-based algorithms for the minimum length corridor problem.

CONACYT
Consejo Nacional de Ciencia y Tecnología

CONCYTEQ

Research of bioclimatic benefits in the development of prefabricated joists with recycled PET plastic material.

Ing. Elvick Alejandro Noguera Dávila
Facultad de Ingeniería
Universidad Autónoma de Querétaro
Querétaro, México
elvick.end@gmail.com

Dr. José Luis Reyes Araiza
Facultad de Ingeniería
Universidad Autónoma de Querétaro
Querétaro, México

***Abstract*— The purpose of this research is to characterize the physical and mechanical properties of a prefabricated joist with the inclusion of recycled PET material. The inclusion of this PET material in the concrete of the joist is intended to lighten the weight of the joist itself, as well as work as a thermal insulation and thus improve the thermal comfort of the construction.**

Keywords*— *Plastic PET, Concrete, Open core joist, Thermal comfort, Recycling

I. INTRODUCTION

Concrete is the main material used in construction because of its high mechanical strength and low cost of placement, however, currently the culture of environmental sustainability is making more and more echo in society, so it has opened a gap for the recycling and reuse of certain materials, an issue that could not be ruled out of the engineering field, that is why research and developments have been carried out on how to adapt these materials to the field of construction, in this particular case, the PET.

One way to mitigate the damage caused to the environment by the waste and disposal of this material is to implement it in the development of prefabricated elements for use in construction.

Mexico is the second largest consumer of PET resin for the production of bottles. Since it is the second largest consumer of soft drinks. That is why in our country there is a latent environmental need to give secondary use to this material.

PET is the most easily obtained plastic, handling and recycling, so it is not difficult to create a gap in the engineering field for its study, development and use in construction, in order to create social awareness and a sustainable future .

Type of plastic	Quantity (1000 tons)
Polyethylene terephthalate (PET)	1700
High density polyethylene (HDPE)	4120
Low density polyethylene (LDPE)	5010
Polypropylene (PP)	2580
Polystyrene (PS)	1990
Other	3130

Table 1. Types and quantities of plastics in Municipal Solid Waste in the U.S.

Plastics can be separated into two types. The first type is thermoplastic, which can be melted for recycling in the plastic industry. These plastics are polyethylene, polypropylene, polyamide, polyoxymethylene, polytetrafluoroethylene and polyethylene terephthalate. The second type is thermoset plastic. This plastic can not be melted by heating because the molecular chains are tightly joined with mesh cross-links. These types of plastic are known as phenolic, melamine, unsaturated polyester, epoxy resin, silicone and polyurethane. At present, these plastic wastes are disposed of by burning or burying. However, these processes are costly.

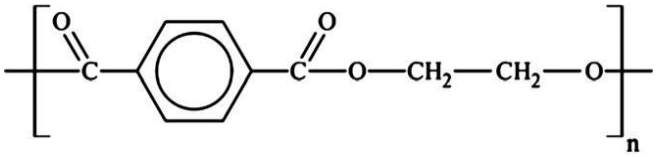

Fig. 1. Chemical structure of PET

Choi [1] investigated the effects of aggregate PET bottle residues on concrete properties. The waste plastic could reduce the weight of 2-6% of the normal weight concrete. However, the compressive strength was reduced up to 33% compared to normal concrete.

Recently, Marzouk [2] also studied the effects of PET residues on density and compressive strength of concrete. It was found that density and compressive strength decreased when PET aggregates exceeded 50% by volume of sand.

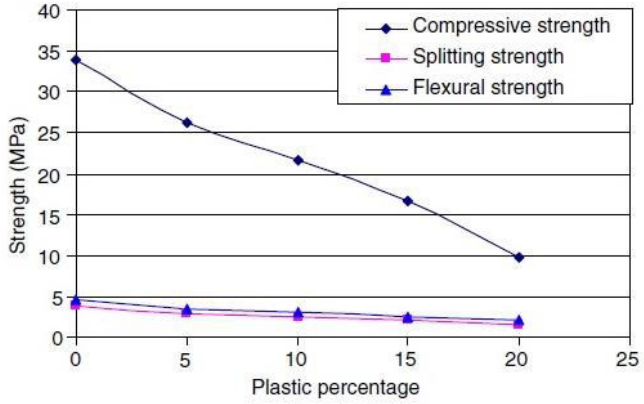

Table 2. Relation between the compressive strength and the percentage of plastic content [2]

Ochi [3] describes methods for making reinforcing fibers from recycled PET bottles and evaluates their beneficial effects in terms of ductility, flexure and compressive strength of concrete specimens. In the study by Kim [4], PET fibers with different geometries (embossed, straight, and crimp) are used to control shrinkage of plastic against composite-based cement cracking. Silva [5] analyzed the durability of recycled PET fibers embedded in cement-based materials. Kim [6] examined the reinforcement of concrete with recycled PET fibers produced in the laboratory at different volume fractions (0.5%, 0.75% and 1.0%). The PET fibers examined by these authors are manufactured through cutting and deformation machines, from rolls produced from waste PET bottles.

Jo [7] investigated the mechanical properties such as the compressive strength and the flexural strength of the polymer concrete using an unsaturated polyester resin based on recycled PET, which contributes to reduce the cost of the material and save energy.

The study shows that plastic bottles crushed into particles of PET small can be successfully used as aggregate replacement of sand in compounds of cement concrete, which seems to offer an attractive low-cost material with consistent properties and help solve some of the problems of solid waste created by the production of plastics.

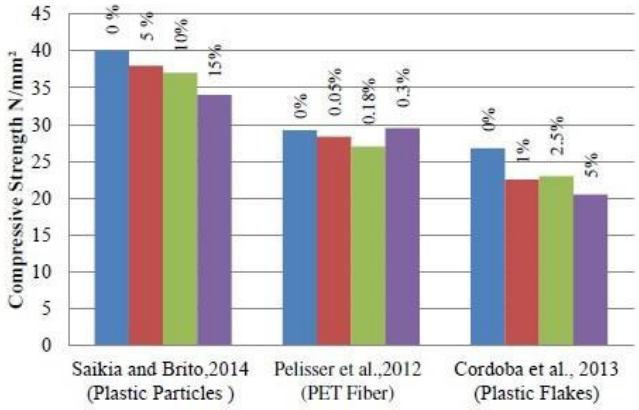

Table 3. Effect of the addition of different forms of plastic in compression tests [8]

Normativity and Regulation

In Mexico the joist and girder system is governed by the regulations of local constructions and several Mexican norms. The Mexican norms applicable to the girder and girder system are mentioned:

- NMX-C-406-ONNCCE-2013.
- NMX-C-463-ONNCCE-2009.
- NMX-C-460-ONNCCE-2009.

Currently NMX-C-406-1997-ONNCCE, whose name is: "Construction industry - joist and girder systems and similar prefabricated components for slabs - Specifications and test methods" is the current NMX standard, which governs joist and girder systems.

II. Methodology

A. *First Stage: Material bank*

There will be a collection of PET material, which can be containers, bottles, boxes, etc. of different shapes and sizes, which does not represent any potential difference in the

expected results, since this material will be fused by heat. In other words, its state of matter will change from solid to liquid.

B. *Second Stage: Preparation of the material*

The collected PET material will undergo a grinding process in order to obtain a small sample of said material. This is so that at the time of heating it can pass to the liquid state more easily, thus having an emulsion of PET material ready to be poured into a mold for its solidification.

C. *Third Stage: Joist manufacturing*

Once the PET emulsion is obtained, or the PET in the liquid state, it will be poured into a mold with the technical specifications and regulatory measures of an open-type joist joist, in turn attaching the steel reinforcement.

Once this is done, it will be cooled to its solidification and subsequent detachment from the mold in which it took its shape.

D. *Fourth Stage: Tests*

The newly prefabricated joist will not need a certain time of curing days, since once cooled it will take the shape of the joist and hardness.

Subsequently, the relevant tests will be carried out to characterize its physical and mechanical properties, such as its compressive strength, tension, its thermal and acoustic properties, in order to compare its differences with the open-core joists and calculate Its viability in a scenario in which the type joists are replaced by these new prefabricated with recycled PET material.

III. Expected Results

In the practice of this project it is expected that all the above objectives will be fulfilled. It depends on the fact that the prefabricated joist with the new recycled PET material is viable for use in the field of construction.

It is expected that the physical characteristics are at least 90% similar to those of an open core type joist, because of being smaller we would be talking about a failure at the moment of its application in the construction.

Likewise, its mechanical characteristics must comply with the aforementioned standards, as this new material is expected to be feasible for the construction of social housing.

Its thermal and acoustic insulation properties are expected to be 10-15% higher than those of pre-fabricated open-core joists, since the new joist to be implemented is made of PET plastic material, which has insulating properties.

IV. Conclusions

This project seeks an adaptation in the construction field in which it is feasible to replace prefabricated concrete structures with a material that abounds in the world in a negative way for the environment, giving it a second useful life, having a cleaner planet and a sustainable practice.

If positive results are obtained with respect to the substitution of these materials, a new branch would be created in which some of the solid waste produced in the world could be used again, thus generating an improvement in the environment, and beneficial conditions for The flora and fauna that surrounds us, decreasing the danger of extinction of hundreds of species threatened by the contamination of the product made with the PET material.

References

[1] Choi, Y.W., Moon, D.J., Chung, J.S., Cho, S.K., 2005. Effects of waste PET bottles aggregate on the properties of concrete. Cement and Concrete Research 35, 776–781.

[2] Marzouk, O.Y., Dheilly, R.M., Queneudec, M., 2007. Valorization of post-consumer waste plastic in cementitious concrete composites. Waste Management 27, 310–318.

[3] Ochi T, Okubo S, Fukui K. Development of recycled PET fiber and its application as concrete-reinforcing fiber. Cem Concr Compos 2007;29:448–55.

[4] Kim JJ, Park CG, Lee SiW, Lee SaW, Won JP. Effects of the geometry of recycled PET fiber reinforcement on shrinkage cracking of cement-based composites. Composites Part B: Eng 2007;39:442–50.

[5] Silva DA, Betioli AM, Gleize PJP, Roman HR, Gómez LA, Ribeiro JLD. Degradation of recycled PET fibers in Portland cement-based materials. Cem Concr Res 2004;35:1741–6.

[6] Kim SB, Yi NH, Kim HY, Kim J, Song Y. Material and structural performance evaluation of recycled PET fiber reinforced concrete. Cem Concr Compos 2010;32:232–40.

[7] Jo, B.W., Park, S.K., Kim, C.H., 2006. Mechanical properties of polyester polymer concrete using recycled polyethylene terephthalate. ACI Structural Journal 103, 219–225.

[8] Raju, Sharma (March 2015). Use of different forms of waste plastic in concrete. Journal of Cleaner Production, 473 – 482.

Greenhouse climate management as a strategy to improve tomato yield

Jhonam Clemente Arellano-Beltrán, Enrique Rico-García, César Iván Hernández-Pérez
School of Engineering
Autonomous University of Queretaro
Queretaro, Mexico
arbejh@gmail.com

***Abstract*—Climate inside a greenhouse is very important for the proper development of plants, therefore the efficient management of environmental conditions leads to an increase in production, improves fruit quality and phytosanitary control, which translates into greater profitability and plant health. In this review the objective was to summarize information about relationships between greenhouse tomato crop and environmental conditions such as solar radiation, temperature, relative humidity and CO_2 concentration. We also expose the values of each climate variable already obtained in previous research for the correct physiological functioning of crop to achieve tomato yield. In addition, new strategies implemented in greenhouses to control these climate variables and photosynthetic rate that can improve quality and biomass production, are also described. Finally, this review shows new developments in scientific research related to the climate management in greenhouses to enhance tomato production.**

Keywords—tomato, climate, greenhouse, CO_2, photosynthesis.

I. IMPORTANCE OF THE TOMATO CROP

Tomato (*Solanum lycopersicum L.*) is the most popular crop and the most cultivated vegetable worldwide (4.7 Million ha) [1]. It is cultivated on more than one hundred countries for industry process and fresh consumption. The ten most important producer countries (China, U.S., India, Egypt, Turkey, Italy, Iran, Spain, Brazil and Mexico) have more than 80% of total production, and the first three trendsetting and global consumer price [2]. The importance of this vegetable is due to its high yield potential and nutritional and commercial value [3]. Tomato is one of the most consumed vegetables in the world and is rich in dietary nutrients and antioxidants. It is a good source of bioactive compounds, including carotenes (lycopene, β-carotene), ascorbic acid, and phenolic compounds. High amount of ascorbic acid has been reported. [4].

Tomato is one of the most studied fleshy fruits because it is easy to grow, so requirements and environmental conditions for an adequate growth and production has been very well studied [1]. The most studied environmental conditions to improve tomato yield are: temperature, relative humidity, light and CO_2 concentration. These variables are well controlled in high technology greenhouses but not in open field. So, in greenhouses, that are a semi-closed or closed system, is profitable to control environmental conditions, and this makes their study important to improve tomato yield..

II. CLIMATE IN GREENHOUSES

Compared with traditional agriculture, greenhouse horticulture can take advantage of the controllability of environmental conditions [5], as well, greenhouse horticulture has been developed to protect crops from unfavorable environmental conditions, thereby extending the growing season, at the cost of a high-energy demand. Over the last decades, greenhouse concepts were developed aiming at reducing the energy consumption. In these concepts, cooling by window ventilation was replaced by mechanical cooling. The excess solar energy was then collected and stored, to be reused to heat the greenhouse in winter. The greenhouse with reduced or no window opening were named as semi-closed or closed greenhouses. Further advantages of the semi-closed greenhouse are the reduction of CO_2 emission and improvement of crop and pest management [6].

In general, greenhouses facilitate the control of environmental conditions and provide protection against heavy rain and excess irradiation. Therefore, in tropical latitudes high value vegetables are increasingly produced under protected cultivation. It is becoming a common practice to cover ventilation openings with insect proof screens, thus enabling growers to reduce the frequency of pesticide application; however, this also decreases wind velocities and air exchange. Therefore, in the tropics, the microclimatic conditions inside greenhouses may temporarily be less favorable as compared to unprotected cultivation [7].

The primary climate variables that can be controlled in a greenhouse include temperature, humidity, CO_2 concentration, and light intensity at the plant level. Many studies have investigated available technologies for controlling greenhouse climate variables that are important for greenhouse crop production. The actuators for greenhouse climate control are usually controlled by the greenhouse process control computer, those control systems are developed rather detached from general building control and are a domain on their own. The majority of control rules in the process control computer are heuristic rules based on the experience of the growers and suppliers. Growers define and adapt these settings in the process control computer based on their observations of the crop status, and based on their experience; in addition, growers use weather predictions, specific crop knowledge, production planning and product price forecasts [8].

Nonetheless, energy saving climate strategies are rarely applied in Central European and North American greenhouses. The value of the product on the market is high compared to the prices of fossil fuels, which continue to be relatively moderate, and growers are concerned about a potential decline in yield and quality [9]. A worldwide shift in policy is currently forcing most industries and governments to reduce greenhouse gas emissions and reduce their dependence on fossil fuels. In northern climates, the horticulture industry has not been spared of these changes due to their high energy consumption. Greenhouse operators must address this issue by balancing energy efficiency through structural or fuel saving techniques, while keeping growing conditions optimal in order to compete with an international market for commodities. Specifically, heating requires improvements [10].

Increasing international competition puts pressure on tomato growers to reduce the costs of production by, among other, economizing on resource use. To this end, new growing techniques are required, including use of new varieties, climate control, and extension of the growing period. Growth of tomato plants in a greenhouse is a complex process, governed by the interactions between plant genetic properties and environmental conditions, as modified by climate control inside greenhouses. It is therefore difficult to predict intuitively, the management measures necessary to create crop growing conditions that will lead to optimal resource. Dynamic crop growth models in which insights in plant physiological processes and their dependence on environmental conditions are combined, may provide a practical aid in management decision making, so that the effects of alternative management strategies can be examined [11].

The lack of climate control in many greenhouses of Mediterranean countries results in an inadequate microclimate that negatively affects yield components and input-use efficiency. A better control of the greenhouse aerial environment can improve marketable yield and quality, and extend the growing season [12].

III. HOW TO IMPROVE YIELD IN TOMATO GREENHOUSES WITH CLIMATE-MANAGEMENT?

Climate in greenhouses can be studied by experimentation and simulation; with the latter method, can be characterized more quickly, at lower cost and flexible and repeatable [13].

Photosynthesis is the primary physiological process that drives plant growth and crop productivity and influences many other plant processes. It is also strongly affected by environmental stresses [14].

In general, net photosynthetic rate increases with increasing CO_2 concentration in a range between 0 and 1,000 ppm. Thus, the CO_2 concentration in greenhouses is often increased in the daytime up to about 1,000 ppm to promote photosynthesis and plant growth in greenhouses with the vents closed. On the other hand, roof and or side vents need to be opened (natural ventilation) or fans need to be turned on (forced ventilation) in the daytime to keep the air temperature or water vapor pressure deficit (VPD) at optimal values in the greenhouse when solar radiation and or air temperature inside are high. Recently, however, there have been some reports on controlling the air temperature and VPD in the greenhouse by descending fog technology, which are useful to reduce the need for natural ventilation also, thus allowing for higher CO_2 concentrations to be maintained in the greenhouse [15].

Leaf gas exchange rates depend on environmental conditions such as light, temperature, CO_2 concentration and humidity. These rates also vary among leaves even within an individual plant depending upon the leaf ontogeny and growth environments [16].

Leaves are photosynthetic organs that absorb light and convert the photon energy of light to chemical energy for use in CO_2 assimilation. Here we review how CO_2 assimilation rates vary, depending on environmental factors and among leaves. Net CO_2 assimilation is a balance between the carboxylation of ribulose 1,5-bisphosphate (RuBP) catalyzed by ribulose-1,5-bisphosphate carboxylase/oxygenase (Rubisco) and the release of CO_2 by photorespiration and mitochondrial respiration. The steady-state biochemical model of CO_2 assimilation considers photosynthetic metabolism as a composite of two processes, namely, RuBP carboxylation and regeneration. The former, modeled based on the Rubisco kinetics, is limited mainly by CO_2 supply, whereas the latter is assumed to be limited by the rate of photon absorption at low light and by its use in electron transport at high light. CO_2 concentration at the assimilation sites in chloroplasts depends on the stomatal and mesophyll conductances for CO_2 diffusion. Both conductances are sensitive to environmental variables, but no mechanistic models of environmental responses for these conductances are available. Various empirical models have been developed and combined with the biochemical photosynthesis model allowing for expression of CO_2 assimilation rates as a function of environmental variables [16].

IV. TEMPERATURE EFFECT ON TOMATO YIELD

Tomato yield is affected by temperature, this is so because temperature is directly related with physiologic process that

can be favorable or unfavorable for development and growth of tomato plants; for example, many reports describe the effects of low temperatures on the growth and development of young tomato plants: leaf and truss initiation rates decrease linearly with decreasing temperature [9]. Mean daily temperatures in the range of 21– 27 °C have been reported to be optimal for tomatoes [7].

Photosynthetic capacity of tomato leaves is strongly affected by temperature. However, the dependence of each photosynthesis-limiting process on temperature is not necessarily the same. With short-term (minutes to hours) temperature changes, some key components of the photosynthetic apparatus seem to be more affected than others. For example, PSII (photosystem II) is often thought to be the most labile and easily damaged component of photosynthesis during heat stress. Export of photoassimilates is another metabolic process that is sensitive to inhibition by high temperature. There is evidence that inactivation of Rubisco is an early event in the inhibition of photosynthesis by elevated temperature and that inhibition of Rubisco activase may be a key regulatory process affected by high temperature stress. However, other reports have concluded that the primary site of high temperature damage is associated with a component of the thylakoid membranes [17].

The effects of a vertical temperature gradient on crop photosynthesis will probably be small, since the temperature of the upper part of the canopy is not substantially affected. Consequently, the vertical temperature gradient did not affect total dry matter production in tomato [18].

Temperature-CO_2 interactions affecting crop photosynthesis, Heuvelink, 2009 [19], found that photosynthetic rate enhances with an increment of temperature and CO_2 enrichment.

A decline in growth-dependent sink demands and a reduced translocation of assimilates to sink organs can be expected at decreasing temperature. This in turn could result in the accumulation of sugars and starch in the leaf. However, when the storage capacity for carbohydrates in leaves in the form of sugars and starch is saturated, an increasing fraction of the assimilated car- bon may be used to synthesize other substances. These substances, which cannot be remobilized for growth, are summarized in the following under the term ‘structural dry matter’. Several studies have investigated the response of tomato leaves to very low temperatures. Although some data is available on the effect of low temperatures ranging from 12 to 16◦C on contents of leaf dry matter and non-structural carbohydrates of thermophile greenhouse-grown fruit vegetables, there is still much uncertainty regarding the maximum storage capacity of sugars and starch in tomato [20].

Agricultural greenhouses need input energy to maintain a satisfactory temperature for the plant growth, especially in winter, and the energy savings is an important issue of greenhouse control. Over the last decades, many efforts have been made to replace energy sources of fossil fuels with renewable energy or to improve energy efficiency for greenhouse heating [21].

V. HUMIDITY RELATIVE EFFECT ON TOMATO YIELD

The effect of air humidity on photosynthesis is limited, as long as the VPD ranges between 0.2 – 1.0 kPa. Humidity affects leaf photosynthetic rates only via the extent of opening of the stomata, which close at a lower humidity. Particularly under Mediterranean conditions, fogging may help to prevent stomatal closure which may occur on sunny days, thereby maintaining levels of photosynthesis. However, in moderate climates, the effect of fogging will be less, due to lower VPD levels. Doubling the VPD from 1.1 to 2.2 kPa at 25ºC and 700 ppm, decreased stomatal conductance by 50%, whereas the rate of photosynthesis was hardly affected [18].

Around 60% relative humidity has been reported to be optimal for tomatoes [7]. Forced air movement was reported to result in higher rates of photosynthesis, due to a reduction in the resistance of the leaf boundary layer. Research on tomato seedlings in climate chambers showed that photosynthesis increased by approx. 60% when air circulation increased from 0.3 to 1.0 m s^{-1}. Whether air circulation affected crop photosynthesis and transpiration depended on the structure of the canopy. In a low canopy, in a small climate chamber, increasing the air velocity from 0.1 to 1.0 m s–1 increased the net rate of photosynthesis two-fold. However, in closed greenhouses, forced air circulation via tubes, with air velocities of 0.2 – 1.0 m s^{-1} close to the tubes, did not affect the rates of photosynthesis or growth in tomato. This might be due to the fact that the air velocity in the upper part of the dense canopy was not affected [18].

In winter, in Asian countries, especially in Japan, the temperature in closed greenhouses often exceed 30◦C during midday period of sunny days. Growers usually open the roof windows during this period to reduce the temperature inside the greenhouse. However, due to the air exchange between outside and inside of a greenhouse, VPD conditions could be found because of high VPD outside greenhouse in winter season. High VPD could be responsible for the decrease in yield and quality for any crops in the greenhouse. The most adverse effect of high VPD on plants would be to induce leaf water stress. VPD beyond the optimal for plant growth also inhibited stomatal conductance and photosynthesis. An increase in VPD from 1.0 to 1.8 kPa causes major reductions in plant growth on several crops, which could be due to the depression of photosynthesis. Many studies have found that atmospheric drought, or a high VPD, induced midday depression in stomatal conductance for CO_2 diffusion, which led to a decline in net photosynthetic rate. A long-term adaptation to depressed photosynthesis in response to atmospheric drought inside the greenhouse can limit plant growth, dry matter accumulation, and hence decrease yield. Therefore, alleviating the adverse effects of midday atmospheric drought during the winter can translate to better plant growth and higher yield in greenhouses crop production. An experiment using tomato to observe the effect of a fog system on photosynthetic rate, it was found that plants with fog system increased photosynthetic rate [22].

Extreme high atmospheric evaporative demand results in plant water deficit situations, which are often accompanied by a depression in stomatal conductance. By regulating stomatal

aperture and hence the transpiration water loss, plant can attempt to minimize water deficit. This regulation has an adaptive significance in protecting plant vascular systems from dysfunction, but the reduction in stomatal aperture is also accompanied by depressing effects on stomatal conductance for CO_2 diffusion, leading to a sharp decline in photosynthesis rate. Inhibition of photosynthesis caused by the high temperature and low humidity (high vapor pressure deficit) can limit plant growth and dry matter accumulation, and hence reduce yield, which already became a major constrain for the sustainable greenhouses vegetable production in northern China during summer season. Several methods have been applied to reduce heat stress and leaf dehydration in greenhouses. Fog systems are one of the most efficient methods to maintain favourable leaf water status during periods of strong evaporative demand and improve plant growth and yield [23].

The VPD in greenhouse could be effectively controlled by the fogging systems and a long term fogging application resulted in significant alterations in leaf structure with higher stomatal density and faster leaf expansion rates. These promoted an increase in stomatal conductance and net photosynthetic rate, resulting in a simultaneous improvement in tomato plant biomass and tomato fruit production. Application of fogging system based on VPD regulation is an effective strategy to regulate greenhouse environment in order to improve tomato production during winter. Thus, economic profit can be realized when a proper application of fogging system is used in commercial greenhouse production [22].

The yield of tomato is reported to be increased by higher relative humidity. Thus, establishing a CO_2 concentration control technique combined with an air humidity control is the key to achieve high yield and productivity in greenhouse tomato production [24].

The role of a proposed microfog system in regulating greenhouse environments and enhancing productivity during summer season was studied by [23], this study show that a high relative humidity can improve the net assimilation rate of tomato leaves.

VI. LIGTH EFFECT ON TOMATO YIELD

Photosynthesis is known to be a monotonically increasing function of radiation, specifically photosynthetic photon flux density (PPDF), this has been demonstrated by experiments in which tomato plants are growing in chamber with different constraints of PPDF, found an increment of photosynthesis [25].

Typically, high light intensities coincide with increased levels of CO_2 and controlled temperatures in closed greenhouses, leading to higher rates of photosynthesis. An experiment with tomatoes grown in open and closed greenhouses showed that fresh weight (FW) production was increased by 10 – 15% in closed or semi-closed greenhouses, compared to an open greenhouse with an annual production of 55.2 kg m^{-2}. In the South of France, an increase in production of 34% from April – August was reported for a tomato crop in a closed greenhouse compared to an open greenhouse with a production level of 24.4 kg m^{-2}. However, closed greenhouse consume 15-times more CO_2 for CO_2 enrichment than the open greenhouse [18].

Growth light intensities can also determine the extent of photosynthesis and growth stimulation by high CO_2: the stimulating effects of high CO_2 tend to decrease and may even become negative as growth light intensities increase [26]. Also, there is found that combination of high CO_2 and high PPF in spring leads to a down-regulation of photosynthesis in greenhouse tomato plants [27].

Greenhouses with sophisticated environmental control systems, or so-called plant factories with solar light, enable growers to achieve high yields of produce with desirable qualities. In a greenhouse crop with high planting density, low photosynthetic photon flux density PPFD at the lower leaves tends to limit plant growth, especially in the winter when the solar altitude and PPFD at the canopy are low and day length is shorter than in summer. Therefore, providing supplemental lighting to the lower canopy can increase year-round productivity. However, supplemental lighting can be expensive. In some places, the cost of electricity is lower at night, but the effect of using supplemental light at night has not yet been examined [28].

The growth environment plays a pivotal role in determining the source–sink balance. Under non-stressing conditions, irradiance becomes particularly important as it is the driving force for photosynthesis. Supplementary lighting is commonly applied in greenhouses in order to improve crop photosynthesis and thus production. The beneficial effect of supplementary lighting is determined by the balance between assimilate production in source leaves and the overall capacity of the plants to use these assimilates. This implies that it is important to identify the plant source–sink balance in order to efficiently utilize supplementary lighting [29].

VII. CO_2 CONCENTRATION EFFECT ON TOMATO YIELD

Plant responses to elevated CO_2 are strongly influenced by environmental factors. For instance, sufficient supply of nutrients, especially nitrogen, is required for the formation of new sink organs in order to maintain the source sink equilibrium and thereby sustain stimulation of photosynthesis and plant growth under elevated CO_2 levels [26]. Air CO_2 concentration is a relevant climate variable to be controlled in greenhouses as it has a marked effect on plant CO_2 assimilation. The atmospheric level limits the potential photosynthesis of most plant species and their productivity [12].

CO_2 is one of the most important nutrients to green plant growth. Research results showed that the CO_2 concentrate in air is not enough for plant growth under some conditions, especially in a sunny day. Supplying CO_2 has become an important solution to improve yield and quality in greenhouses. CO_2 supply could improve the photosynthetic rate, fruit quality and yield of the crop [5].

Yield increases are observed in C3 plants whether it is through larger total dry mass, bigger and more numerous fruits,

larger leaves and flowers, as well as earlier flowering time and reduced overall production time. On average, greenhouse crops benefit from concentrations between 700 and 1000 ppm, which produces yield increases from 21 to 61% in dry mass [10].

Carbon dioxide is routinely used to enrich the greenhouse environment in tomato production to enhance photosynthesis and hence increase crop yield and grower income. This practice has been shown to provide a marked increase in yield. However, its economic benefit depends on the margin between the increase in crop value and the cost of providing the CO_2 gas [30].

Attempting to establish the optimal concentration by experiment is not feasible because the economic value of enrichment is not constant but varies with solar radiation through photosynthesis rate, and with greenhouse ventilation rate through loss of CO_2. The optimal CO_2 set point depends on several influences: the effect of CO_2 on the photosynthetic assimilation rate, the partitioning to fruit and to vegetative structure, the distribution of photosynthate in subsequent harvests, and the price of fruit at those harvests, as well as the amount of CO_2 used, greenhouse ventilation rate and the price of CO_2. The effects of these factors can be described, individually, using mathematical models. These models can then be combined to produce a calculation procedure to determine the optimum CO_2 concentration [30]. The optimal set point, that which would give the maximal rate of net cash return, is where the slopes are parallel and would be at a CO_2 concentration of 717 ppm [31].

At increased levels of CO_2, the net rate of carboxylation is stimulated because increased CO_2 competes with O_2 at the active site of Rubisco. Photorespiration, the O_2 inhibition of photosynthesis, increases with increasing temperature. Therefore, the largest effect of increased CO_2 levels on photosynthesis will be at high temperatures, at an irradiance of 1,200 µmol m^{-2} s^{-1} and a CO_2 concentration of 1,000 ppm, the optimum temperature for maximum tomato crop photosynthesis was 29.0ºC, compared to 27.1ºC at 400 ppm. This 1.9ºC increase was much lower than that reported for individual leaves, due to the fact that leaves deeper in the canopy were not at saturating light levels and therefore responded less to temperature [18].

Over the short term, a rise in CO_2 concentration enhances photosynthesis of C3 plants by stimulating carboxylation of Rubisco and carbohydrate synthesis, thereby increasing plant growth. Over the long term, the beneficial effects of elevated CO_2 concentration are determined by the balance between carbohydrate production in source leaves and the overall capacity of the plant to use photoassimilates in sink organs. In sink limited plants, a loss of photosynthetic efficiency may be caused by a biochemical limitation of inorganic phosphate (Pi) and/or Ribulose 1,5-bisphosphate (RuBP) regeneration, and eventually by a down regulation of photosynthesis involving a cascade of reactions that repress the expression of genes, thylakoid proteins, Rubisco, and Rubisco activase proteins [27].

The reduced window ventilation in the (semi) closed greenhouses results in a continuously high air CO_2 concentration of about 800–1000 ppm throughout the year, while now a day in conventional modern greenhouses the CO_2 concentration in summer is 400–600 ppm. In the short-term, elevated CO_2 concentration enhances photosynthesis. However, in the long-term, plants grown at an elevated CO_2 concentration may have a lower photosynthesis rate at a given CO_2 concentration than plants grown at a lower CO_2 concentration [6].

The changes in physiology, phenology, growth, and the yield of crops lead to changes in quality of the produce or products. In general, high CO_2 has been reported to influence the fruit quality by affecting content of antioxidants, ascorbic acid, and sugars. High ascorbic acid and sugar contents in tomato fruits were reported when elevated concentrations were used at different maturity stages. However, some of the studies reported that enhancements in antioxidant substance contents were very low in tomato under high CO_2 concentrations [4]. Also, CO_2 enrichment in greenhouses has effect on yield increase, enhanced resistance to diseases/pests, and advanced maturity period [32]. Photosynthetic rate can increase on tomato plants with CO_2 supply from 0 to 1400 ppm [33]; but it can decrease over this limit [29].

VIII. Other Factors Affecting Tomato Yield

Crop growth is the most important process and is mainly influenced by surrounding environmental climatic variables (Photosynthetically Active Radiation—PAR, temperature, humidity, and CO_2 concentration of the inside air), the amount of water and fertilizers supplied by irrigation, pests and diseases, and culture labors such as pruning and pesticide treatments, among others. A greenhouse is ideal for crop growing since it constitutes a closed environment in which climate and fertigation can be controlled (with different control problems and objectives). Empirically, the water and nutrients requirements of the different crop species are known and, in fact, the first automated systems were those that control these variables. On the other hand, the market price fluctuations and the environmental rules to improve water-use efficiency or to reduce fertilizer residues in the soil (such as the nitrate contents) are other aspects to be taken into account [34].

In conditions where the rate of photosynthetic CO_2 assimilation exceeds the capacity of sink organs, there is an accumulation of high levels of carbohydrates in leaves which triggers a down-regulation of photosynthesis involving a repression of several photosynthetic genes, namely Rubisco and thylakoid proteins [27].

IX. Conclusion

The patterns of changes in climate and the mechanisms driving plant responses to such changes are important for the development of agricultural practices and crops that are better adapted to future growing conditions. It is predicted that atmospheric CO_2 concentration will rise globally to 550 ppm in the middle of the present century. On the other hand, the short and long-term projected changes in temperature and precipitation patterns show a great regional and sometimes

seasonal variability [35]. In tropical lowlands both air temperature and relative humidity exceed the optima for tomato almost throughout the year [7].

It should be important to assessing the impact of climate change on agro-ecosystem function and this exploring opportunities for bio-based energy production. Therefore, mechanistic quantification of photosynthesis deserves further attention in dynamic simulation models of crop growth [14].

In modern greenhouses there are a number of alternative systems that can be deployed to control the climate, and the choice what to use and when is not easy for the grower. A novel management system is proposed, consisting of an energy input minimizing module, and a module to realize the determined input with the available equipment [36].

ACKNOWLEDGMENT

This Research was supported by the Mexican Council of Science (CONACYT).

REFERENCES

[1] D. Schwarz, A. J. Thompson, and H.-P. Kläring, "Guidelines to use tomato in experiments with a controlled environment.," *Front. Plant Sci.*, vol. 5, no. November, p. 625, 2014.

[2] E. Hernández-Leal, R. Lobato-Ortiz, J. J. García-Zavala, D. Reyes-López, A. Méndez-López, and A. Hernández-bautista, Olga Bonilla-Barrientos, "COMPORTAMIENTO AGRONÓMICO DE POBLACIONES F 2 DE HÍBRIDOS DE TOMATE (Solanum lycopersicum L .) AGRONOMIC PERFORMANCE OF F 2 POPULATIONS FROM TOMATO HYBRIDS (Solanum lycopersicum L .)," *Rev. Fitotec. Mex.*, vol. 36, no. 3, pp. 209–215, 2013.

[3] M. Kanechi, Y. Hikosaka, and Y. Uno, "Application of sugarbeet pure and crude extracts containing glycinebetaine affects root growth, yield, and photosynthesis of tomato grown during summer," *Sci. Hortic. (Amsterdam).*, vol. 152, pp. 9–15, 2013.

[4] H. Mamatha, N. K. Srinivasa Rao, R. H. Laxman, K. S. Shivashankara, R. M. Bhatt, and K. C. Pavithra, "Impact of elevated CO2 on growth, physiology, yield, and quality of tomato (Lycopersicon esculentum Mill) cv. Arka Ashish," *Photosynthetica*, vol. 52, no. 4, pp. 519–528, 2014.

[5] Y. Q. Jiang, T. Li, M. Zhang, S. Sha, and Y. H. Ji, "WSN-based Control System of Co $_2$ Concentration in Greenhouse," *Intell. Autom. Soft Comput.*, vol. 21, no. 3, pp. 285–294, 2015.

[6] T. Qian, J. A. Dieleman, A. Elings, and L. F. M. Marcelis, "Leaf photosynthetic and morphological responses to elevated CO 2 concentration and altered fruit number in the semi-closed greenhouse," *Sci. Hortic. (Amsterdam).*, vol. 145, pp. 1–9, 2012.

[7] J. F. J. Max, W. J. Horst, U. N. Mutwiwa, and H.-J. Tantau, "Effects of greenhouse cooling method on growth, fruit yield and quality of tomato (Solanum lycopersicum L.) in a tropical climate," *Sci. Hortic. (Amsterdam).*, vol. 122, no. 2, pp. 179–186, 2009.

[8] P. J. M. van Beveren, J. Bontsema, G. van Straten, and E. J. van Henten, "Optimal control of greenhouse climate using minimal energy and grower defined bounds," *Appl. Energy*, vol. 159, pp. 509–519, 2015.

[9] H.-P. Kläring, Y. Klopotek, A. Krumbein, and D. Schwarz, "The effect of reducing the heating set point on the photosynthesis, growth, yield and fruit quality in greenhouse tomato production," *Agric. For. Meteorol.*, vol. 214–215, pp. 178–188, 2015.

[10] L. M. Dion, M. Lefsrud, and V. Orsat, "Review of CO2 recovery methods from the exhaust gas of biomass heating systems for safe enrichment in greenhouses," *Biomass and Bioenergy*, vol. 35, no. 8, pp. 3422–3432, 2011.

[11] E. Dayan, H. van Keulen, J. W. Jones, I. Zipori, D. Shmuel, and H. Challa, "Development, calibration and validation of a greenhouse tomato growth model: I. Description of the model," *Agric. Syst.*, vol. 43, no. 2, pp. 145–163, 1993.

[12] M. C. Sánchez-Guerrero, P. Lorenzo, E. Medrano, N. Castilla, T. Soriano, and A. Baille, "Effect of variable CO2 enrichment on greenhouse production in mild winter climates," *Agric. For. Meteorol.*, vol. 132, no. 3–4, pp. 244–252, 2005.

[13] L. Y. Briceño-Medina1* and R. E. J.-A. , Manuel V. Ávila-Marroquín2, "SIMICROC: MODELO DE SIMULACIÓN DEL MICROCLIMA DE UN INVERNADERO," 2011.

[14] X. Yin and P. C. Struik, "C3 and C4 photosynthesis models: An overview from the perspective of crop modelling," *NJAS - Wageningen J. Life Sci.*, vol. 57, no. 1, pp. 27–38, 2009.

[15] P. Thongbai, T. Kozai, and K. Ohyama, "CO2 and air circulation effects on photosynthesis and transpiration of tomato seedlings," *Sci. Hortic. (Amsterdam).*, vol. 126, no. 3, pp. 338–344, 2010.

[16] N. P. R. A. E. Kouki Hikosaka, Ülo Niinemets, *Canopy Photosynthesis: From Basics to Applications*, vol. 42. 2016.

[17] D. Camejo, J. J. Alarcón, W. Torres, P. Rodríguez, and J. M. D. Amico, "CHANGES INDUCED BY HIGH TEMPERATURES IN PHOTOSYNTHESIS AND ANTIOXIDANT RESPONSE ON TWO GENOTYPES OF TOMATO (Lycopersicon esculentum)," vol. 23, no. 4, pp. 33–37, 2002.

[18] A. De Gelder, J. A. Dieleman, G. P. A. Bot, and L. F. M. Marcelis, "An overview of climate and crop yield in closed greenhouses," *J. Hortic. Sci. Biotechnol.*, vol. 87, no. 3, pp. 193–202, 2012.

[19] E. Heuvelink, Q. Niu, H. Supply, and C. Group, "Quantification of temperature, CO 2 , and light effects on crop photosynthesis as a basis for model-based greenhouse climate control," vol. 84, no. January, pp. 233–239, 2009.

[20] Y. Klopotek and H.-P. Kläring, "Accumulation and

remobilisation of sugar and starch in the leaves of young tomato plants in response to temperature," *Sci. Hortic. (Amsterdam).*, vol. 180, pp. 262–267, 2014.

[21] J. Chen, F. Xu, D. Tan, Z. Shen, L. Zhang, and Q. Ai, "A control method for agricultural greenhouses heating based on computational fluid dynamics and energy prediction model," *Appl. Energy*, vol. 141, no. 1, pp. 106–118, 2015.

[22] N. Lu, T. Nukaya, T. Kamimura, D. Zhang, I. Kurimoto, M. Takagaki, T. Maruo, T. Kozai, and W. Yamori, "Control of vapor pressure deficit (VPD) in greenhouse enhanced tomato growth and productivity during the winter season," *Sci. Hortic. (Amsterdam).*, vol. 197, pp. 17–23, 2015.

[23] D. Zhang, Z. Zhang, J. Li, Y. Chang, Q. Du, and T. Pan, "Regulation of Vapor Pressure Deficit by Greenhouse Micro-Fog Systems Improved Growth and Productivity of Tomato via Enhancing Photosynthesis during Summer Season," *PLoS One*, vol. 10, no. 7, p. e0133919, 2015.

[24] M. Suzuki, H. Umeda, S. Matsuo, Y. Kawasaki, D. Ahn, H. Hamamoto, and Y. Iwasaki, "Effects of relative humidity and nutrient supply on growth and nutrient uptake in greenhouse tomato production," *Sci. Hortic. (Amsterdam).*, vol. 187, pp. 44–49, 2015.

[25] H.-P. Kläring and a. Krumbein, "The Effect of Constraining the Intensity of Solar Radiation on the Photosynthesis, Growth, Yield and Product Quality of Tomato," *J. Agron. Crop Sci.*, vol. 199, no. 5, pp. 351–359, 2013.

[26] O. Ayari, M. Dorais, and A. Gosselin, "Daily Variations of Photosynthetic Efficiency of Greenhouse Tomato Plants during Winter and Spring," *J. Am. Soc. Hortic. Sci.*, vol. 125(2), no. June 1995, pp. 235–241, 2000.

[27] O. Ayari, G. Samson, M. Dorais, R. Boulanger, and A. Gosselin, "Stomatal limitation of photosynthesis in winter production of greenhouse tomato plants," *Physiol. Plant.*, vol. 110, no. 4, pp. 558–564, 2000.

[28] F. T. Tewolde, N. Lu, K. Shiina, T. Maruo, M. Takagaki, T. Kozai, and W. Yamori, "Nighttime Supplemental LED Inter-lighting Improves Growth and Yield of Single-Truss Tomatoes by Enhancing Photosynthesis in Both Winter and Summer," *Front. Plant Sci.*, vol. 7, no. April, pp. 1–10, 2016.

[29] T. Li, M. Zhang, Y. H. Ji, S. Sha, Y. Q. Jiang, and M. Z. Li, "Management of CO<inf>2</inf> in a tomato greenhouse using WSN and BPNN techniques," *Int. J. Agric. Biol. Eng.*, vol. 8, no. 4, pp. 43–51, 2015.

[30] T. H. Misselbrook, K. A. Smith, R. A. Johnson, and B. F. Pain, "SE—Structures and Environment," *Biosyst. Eng.*, vol. 81, no. 3, pp. 313–321, 2002.

[31] D. P. Aikman, "A Procedure for Optimizing Carbon Dioxide Enrichment of a Glasshouse Tomato Crop," *J . agric . Engng Res .*, vol. 63, pp. 171–183, 1996.

[32] M. Xin, L. Shuang, L. Yue, and G. Qinzhu, "Effectiveness of gaseous CO2 fertilizer application in China's greenhouses between 1982 and 2010," *J. CO2 Util.*, vol. 11, pp. 63–66, 2015.

[33] J. Yuhan, J. Yiqiong, L. Ting, Z. Man, S. Sha, and L. Minzan, "An improved method for prediction of tomato photosynthetic rate based on WSN in greenhouse," vol. 9, no. 1, pp. 146–152, 2016.

[34] F. Rodríguez, A. Ramírez-arias, J. L. Guzmán, and A. Ramírez-Arias, *Advances in Industrial Control Modeling and Control of Greenhouse Crop Growth*. 2015.

[35] P. T. Pazzagli, J. Weiner, and F. Liu, "Effects of CO2 elevation and irrigation regimes on leaf gas exchange, plant water relations, and water use efficiency of two tomato cultivars," *Agric. Water Manag.*, vol. 169, pp. 26–33, 2016.

[36] P. J. M. Van Beveren, J. Bontsema, G. Van Straten, and E. J. Van Henten, "Minimal heating and cooling in a modern rose greenhouse," *Appl. Energy*, vol. 137, pp. 97–109, 2015.

General ground motion attenuation relation in the Mexican Volcanic Belt (MVB)

Pérez-Moreno, L.F.[1], Arroyo, M.[1] & Zúñiga, F.R.[2]
[1]Facultad de Ingeniería UAQ, Centro Universitario, 76010 Querétaro, Qro. lfcopm@hotmail.com, marroyoc@uaq.mx
[2]Centro de Geociencias UNAM, Campus Juriquilla, 76230 Querétaro, Qro. ramon@geociencias.unam.mx

***Abstract*— When dealing with seismicity in cities that are located in the central part of México, it is often considered a low seismic risk. Nevertheless there are historical records on major seismic events with consequences in the area. In this paper the most important antecedents related to seismicity in the Mexican Volcanic Belt are mentioned. A research proposal is presented to obtain a general attenuation relation of the earthquakes occurred in the area using a Bayesian linear regression technique and comparing the results with those obtained by using a least squares approach. The research is still in progress, so that the results presented in this article are only preliminary.**

Keywords—ground motion, attenuation relation, Mexican Volcanic Belt

I. INTRODUCTION

In addressing the issue of seismicity in México, it is very common to remember catastrophes such as occurred on September 19, 1985 in México City. Events like this are a consequence of the earthquakes originated by the subduction of the Cocos plate below the North American plate in the Pacific zone. However, when referring to cities that are located in the central zone of the country, it is common to consider a low seismic risk, because there is no history of significant damage to the populations of the area due to earthquakes.

In addition to the above, there is the fact that the frequency of occurrence of subduction earthquakes and their dimensions are generally greater than those of cortical earthquakes [1]. However, the central zone of the country is crossed by several regional fault systems, being the most relevant the Taxco – San Miguel de Allende system and the Chapala – Tula system, on which evidence has been found to be potentially active [2]-[4] [1].

Therefore, although the Mexican Volcanic Belt is an area where the frequency of occurrence of earthquakes is not as high as those areas affected by events originated in the subduction zone of the Pacific coast, it should not be ignored the possibility that it may have significant damage due to an earthquake of considerable magnitude related to the fault systems located in the region [5], since there is a history of major events occurred in the area [1] [5]-[8]. For the above reasons, it is important to consider the risks to which cities within the Mexican Volcanic Belt may be exposed. Nowadays, the problem of seismic attenuation is a crucial issue in the development of seismic engineering, being fundamental its research and understanding for any risk study oriented to the prevention of damage, human and material, in view of the possible occurrence of an earthquake of great magnitude [9].

II. BACKGROUND

A. Seismicity in the Mexican Volcanic Belt

The Mexican Volcanic Belt is a seismic zone of volcanic activity located in central México with an E-W orientation, extending from the Pacific Ocean to the Gulf of México. The central and eastern parts of this area are characterized by surface seismicity that is not directly related to the subduction in the Pacific coast [10].

In the database of the National Seismological Service (SSN), the United States Geological Survey (USGS) and the International Center of Seismology (ISC), there are data on earthquakes occurred in the Mexican Volcanic Belt region (Fig. 1).

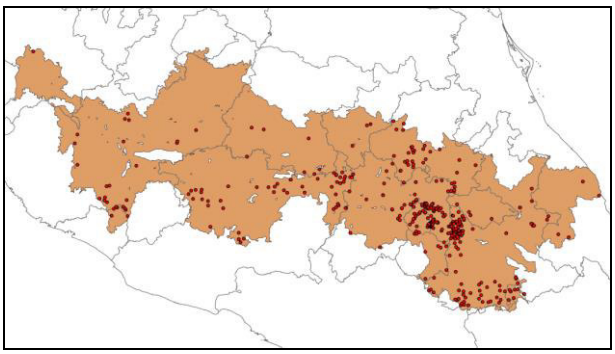

Fig. 1. Seismicity in the Mexican Volcanic Belt between 1922 and 2016.

In the Mexican Volcanic Belt there is a low seismicity compared to other regions of the country, according to SSN data during 2016, there were 15 460 seismic events in México, of which 75% occurred in the states of Guerrero, Oaxaca and Chiapas (Fig. 2), which are frequently affected by earthquakes caused by the subduction of the Cocos plate below the North American plate in the Pacific coast. However, there is a history of earthquakes of considerable magnitude occurred in the area and which is important to consider.

On December 27, 1568 an earthquake occurred at the southeast of Guadalajara city, to which it has been estimated a magnitude between 7.5 and 7.8, being the greater known earthquake associated to the Mexican Volcanic Belt [11]. Another earthquake occurred on February 11, 1875 also in Jalisco, with a magnitude of 7.1 [1].

In 1887, two earthquakes occurred in Pinal de Amoles, on May 8 [5] and November 26 [5] [10] [12]. The event of November 26 has been estimated with a maximum intensity of VII in the vicinity of the epicentral area, where some houses were damaged. The event was perceived in Jalisco, Veracruz, Hidalgo, Michoacán and San Luis Potosí [10] and had a magnitude of 5.3 [12].

On November 19 1912, an earthquake of magnitude 6.9 occurred in Acambay and was perceived in San Luis Potosí, Guerrero, Jalisco and Puebla [10]. The event was strongly felt in Querétaro City, causing fractures in some masonry structures [1] [6].

An earthquake occurred in Jalapa, Veracruz on January 3 1920 of magnitude 6.4 (mb). The event caused damage in a wide region of Puebla and Veracruz, it is estimated that 650 people died [13].

Later, on February 22 1979, an earthquake occurred at the Venta de Bravo fault in Michoacán, with magnitude Mw = 6.1 [10]. The main effects occurred in Michoacán, but it was felt slightly in the municipality of Amealco and in Querétaro City [5], [7]. In the state of Querétaro it can mentioned the earthquake of September 10 1989 (mb = 3.8) in Landa de Matamoros, with effects in Querétaro, Guanajuato and Hidalgo [8]. It has been determined that some areas near Querétaro City reached an intensity of VIII in the Mercalli modified scale, which implies damages to constructions with weak materials, as well as ground cracking [1] [5].

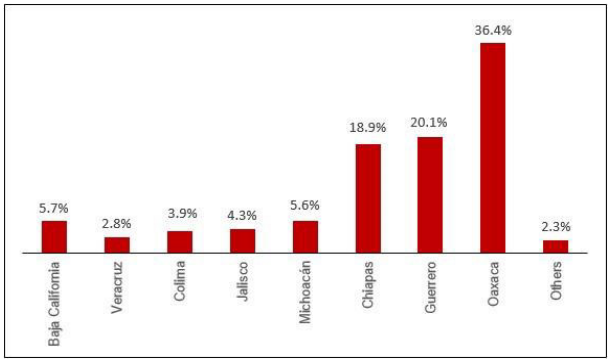

Fig. 2. Seismicity in México during 2016.

In addition to the above mentioned, there are the antecedents of the earthquakes occurred on March 10 1950 in Ixmiquilpan (mb = 4.9), on March 25, 1976 in Cardonal (mb = 5.3) and on January 27 1987 (mb = 4.1) in Actopan [1] [10] [14]. The 1976 event had a maximum intensity estimated between VIII and IX, the most severe damages occurred in the Villagrán community, with 70 houses damaged and 50% destroyed [10].

More recently, there are the records of seismic events of low magnitude in Sanfandila, Pedro Escobedo, between January and February during 1998, in Huimilpan (2001) and Arroyo Seco between December 2001 and March 2002 [1] [5] [15] [16].

The most important seismic events occurred in the central region of México are summarized in Table 1.

Despite the history of seismic events in the Mexican Volcanic Belt, few studies have been published about it [10] [11] [15] [17]-[19], due to the lack of data and the low seismic risk usually considered for this area, however, the possibility of an earthquake of considerable magnitude related to fault systems located in the region should not be ignored [2] [4] [20] [21].

The behavior of seismic waves in Mexico City has been the main object of study of the research that have been performed on seismic attenuation in the Mexican Volcanic Belt [22]-[25], mainly focused on the amplification of the movement of the earth with respect to earthquakes originated in the zone of subduction of the Pacific coast. On the other hand, it has been observed that the seismic waves that propagate from the coast are amplified when entering the Mexican Volcanic Belt [22] [26].

In recent years, the influence of site effects in the Mexican Volcanic Belt on the attenuation of seismic waves has been studied in relation to seismic events occurred within the same zone [19], finding variations in amplification levels between different regions.

Table 1. Important seismic events occurred in central México.

DATE	LOCATION	MAGNITUDE
December 27th, 1568	Jalisco	7.5 - 7.8
February 11th, 1875	Jalisco	7.1
November 26th, 1887	Querétaro	5.3
November 19th, 1912	Estado de México	6.9
January 3rd, 1920	Veracruz	6.4 (mb)
March 10th, 1950	Hidalgo	4.9 (mb)
March 25th, 1976	Hidalgo	5.3 (mb)
February 22nd, 1979	Michoacán	6.1
January 27th, 1987	Hidalgo	4.1 (mb)
September 10th, 1989	Querétaro	3.8 (mb)

B. Ground-motion attenuation relations

The objective of seismic design in civil engineering is to provide each structure with the characteristics that allow it to have an optimal behavior when subjected to the movements of the ground resulting from earthquakes that occur throughout its useful life. It is not possible to predict the history and characteristics of earthquakes that will affect a structure, so that what is sought is to reduce their probability of failure by the stresses generated by earthquakes that occur in a specific time interval.

The amplitude of seismic waves decreases with distance, this phenomenon is known as attenuation and it depends on different factors such as the characteristics of the earthquake and the medium crossed by the waves. The methods used for the calculation of the seismic attenuation are usually empirical, so they are quite simple both in their conception and application as in the theoretical and physical-mathematical basis [9].

To assess the seismic risk of a site, it is necessary to estimate the expected ground motion, the most used way in engineering is through an attenuation relationship, which is a mathematical expression with which a specific parameter of the expected ground motion is associated with one or more earthquake parameters, which qualitatively characterize the seismic source, the propagation pattern of the waves and the geological characteristics of the site [27].

To achieve this goal, regressions of the available data are made [9]. In general, the procedure used to derive an attenuation law consists of adjusting curves to the data of the ground motion at a site, so that the relationships obtained reflect the particular geotechnical characteristics of the area. However, a sufficient number of records often do not exist for a given region, which requires the use of statistical data from other regions with similar geotechnical characteristics or to search for theoretical models that estimate the ground motion [28]-[30].

Due to the importance of the seismic attenuation phenomenon in the seismic resistant design of civil constructions, in México different research have been realized to develop attenuation laws, most of them focused on interplate seismicity [31]-[38].

C. Ground motion attenuation relation for the Guerrero – Querétaro trajectory

With respect to the state of Querétaro, in recent times an attenuation law has been proposed to estimate the maximum acceleration of the ground based on multiple linear regressions using the random effects method [39] [40], analyzing six earthquakes occurred in the Pacific subduction zone in Guerrero, recorded by stations located on the path to Querétaro.

From the results obtained with the proposed expression (valid for the Guerrero - Querétaro trajectory, for earthquakes at depths between 5 and 30 km) a slow decay of the seismic waves was observed in the trajectory, but not an amplification of the signal [40].

III. RESEARCH PROPOSAL: GROUND MOTION ATTENUATION RELATIONS OF THE MEXICAN VOLCANIC BELT

When dealing with seismicity in the cities within the Mexican Volcanic Belt, it is often considered a low seismic risk, due to the scarcity of records on significant damages due to earthquakes in the area, so that there is no updated technical regulation for seismic design of structures. For this reason, the procedure usually used is based on the Complementary Technical Standards of the Construction Regulation of México City (NTC-RCDF-2004) and the Manual of Seismic Design of The Federal Electricity Commission (CFE-2008).

In the CFE manual, a seismic regionalization of Mexico is considered, delimiting four zones (A, B, C and D), in decreasing order of seismic risk. This classification is based essentially on the distance to the subduction zone on the Pacific coast, where there is the largest generation of earthquakes of great magnitude.

However, when considering the tectonic situation the background is different, since a large part of the Mexican Volcanic Belt is located in an area in which there are several systems of geological faults. Although the activity potential of these systems is low, considering the frequency of occurrence of events, the possibility of future episodes of seismic activity should not be discarded since the period of recurrence of each fault segment is unknown [5].

For the above reasons, it is necessary a study of the seismic risk considering the particular geotechnical characteristics of the zone, being the first step to make an estimate of the expected ground motion through attenuation relations for different paths based on the available records of earthquakes originated in nearby regions within the Mexican Volcanic Belt.

Usually, the occurrence of earthquakes whose intensity at a site is greater than a given value has been represented as a Poisson process, although it has been seen that the number of earthquakes generated in an area of the earth's crust is not strictly a process of this nature [41] [42]. However, this hypothesis has been maintained in order to simplify the problem and because the behavior of structures during an earthquake is more sensitive to the number of events than to their distribution over time [41].

The parameters used in this probability distribution are considered to be fixed and are estimated from frequencies in the historical records of the data. This implies that these parameters are based only on observed frequencies and that there is no possibility that they can have other values, however, there is uncertainty in the estimation of these parameters and therefore, they should be treated as random variables [42].

In order to deal with the uncertainty aspect involved in the process, it is possible to use the principles of Bayesian theory,

considering seismic parameters not as constants but as random variables [43].

The application of Bayesian theory in the determination of the seismic risk has been treated by several authors [25] [28] [44]-[47], this procedure allows to obtain solutions more rational than those obtained with the conventional methods [25], its fundamental characteristic is that it provides a method to include information not derived directly from the data, but from other sources that reflect the state of knowledge about the coefficients to be determined [30]. The application of this method is especially useful when there is a lack of information or there is a lot of uncertainty in the data [28] [29].

The records of instrumental measurements that are currently available regarding the seismicity in the Mexican Volcanic Belt are scarce, so the theoretical basis of this research will be based on the use of probabilistic models based on Bayesian theory.

A. *Data*

During this research, 39 records of 23 earthquakes occurred in the Mexican Volcanic Belt (see Table 2) will be used to obtain ground motion attenuation relations in the area. This research is limited to crustal earthquakes, so only the earthquakes with depths smaller than 30 km were considered. The locations of earthquakes are shown in Fig. 3.

The records of ground accelerations were collected from databases of Engineering Institute (IIUNAM), the National Agency for Disasters Management (CENAPRED) and Instrumentation and Seismic Recording Center (CIRES), which have an extensive network of seismic recording stations.

Each station records the ground acceleration in three orthogonal directions, two horizontal and one vertical. For each record the two horizontal components of the acceleration were considered, so that the quadratic mean horizontal component was calculated for each of them.

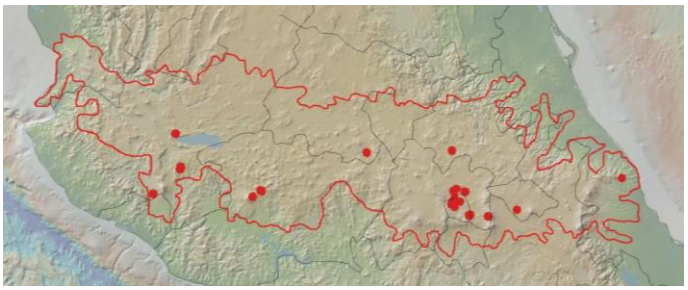

Fig. 3. Location of epicenters in Table 2.

Table 2. Earthquakes analyzed in this research.

DATE	LATITUDE (°N)	LONGITUDE (°W)	H (km)	M
August 18th, 1991	19.33	99.24	1	3.8
March 3rd, 1998	20.10	99.23	5	4.3
November 15th, 2001	19.55	99.16	3	3.5
February 1st, 2002	19.52	99.21	2	2.6
May 9th, 2002	19.51	99.03	26	3.7
November 16th, 2002	19.16	98.68	1	3.9
November 16th, 2003	19.18	98.95	5	3.8
September 13th, 2004	19.37	99.11	10	3.1
October 16th, 2005	19.29	99.19	10	3.5
September 28th, 2011	19.71	96.65	17	4.1
May 18th, 2012	20.34	103.42	15	4.5
October 5th, 2012	19.44	102.25	16	4.2
February 8th, 2013	20.07	100.52	6	3.8
June 21st, 2013	18.60	98.72	20	4
December 24th, 2013	19.48	103.76	10	3.6
July 19th, 2014	19.17	98.97	8	3.5
October 2nd, 2014	19.83	103.35	10	3.5
October 3rd, 2014	19.87	103.34	7	3.7
December, 1st, 2014	19.37	99.23	5	3.4
August 9th, 2015	19.25	98.24	5	3.8
October 24th, 2015	19.42	99.19	2	1.9
December 26th, 2015	19.53	102.13	5	4
December 27th, 2015	19.52	102.11	5	3.8

H = Depth
M = Magnitude

B. *Methodology*

As mentioned previously, due to the lack of instrumental data, the Bayesian linear regression technique will be applied for deriving the ground motion attenuation relations, making a comparison with the results obtained by the LS method.

The adopted functional form for the regression is:

$$ln\, A = \theta_0 + \theta_1 M + \theta_2 ln\, R + \theta_3 R + \varepsilon \qquad (1)$$

where A is the quadratic mean horizontal component of acceleration in centimeters per second squared, M is the moment magnitude, R is the hypocentral distance, θ_i, $i = 0, \ldots 3$ are the unknown coefficients of the linear model and ε is a random error. We assume $\varepsilon \sim N(0, \tau^{-1}I_n)$, where $\tau^{-1}I_n$ is the precision matrix of ε, which has a covariance matrix $\sigma^2 I_n$ and $\sigma^2 = \tau^{-1}$ is unknown.

Equation (1) can be expressed in the following form:

$$Y = X\,\theta + \varepsilon \tag{2}$$

where:

$$Y = (\ ln\,A_1,\ ln\,A_2,\ \ldots\ ,\ ln\,A_n\ )^T \tag{3}$$

$$\theta = (\ \theta_0,\ \theta_1,\ \theta_2,\ \theta_3\ )^T \tag{4}$$

$$\varepsilon = (\ \varepsilon_1,\ \varepsilon_2,\ \ldots\ ,\ \varepsilon_n\ )^T \tag{5}$$

$$X = \begin{pmatrix} 1 & M_1 & \ln R_1 & R_1 \\ 1 & M_2 & \ln R_2 & R_2 \\ . & . & . & . \\ 1 & M_n & \ln R_n & R_n \end{pmatrix} \tag{6}$$

Equation (3) is the vector of observed values on *ln A*, (4) is the vector of the regression parameters, (5) is the vector of observed errors and (6) is the matrix of observed values of variables *M* and *R*.

Considering that the previous knowledge about the unknown parameters θ is represented by a density function $\xi(\theta,\tau)$, it is possible to combine this information with that contained in the observed data, which can be included by means of a conditional density known as likelihood function $L(\theta,\tau|s)$.

The Bayes theorem allows obtaining a posterior conditional density $\xi(\theta,\tau|s)$ which represent the knowledge of θ and τ after getting a set of observed data *s*:

$$\xi(\theta,\tau|s) = K{\cdot}L(\theta,\tau|s)\xi(\theta,\tau) \tag{7}$$

where:

$$L(\theta,\tau|s) \propto \tau^{n/2}\, exp[-\tau/2(Y - X\theta)^T(Y - X\theta)] \tag{8}$$

and K is a normalization constant given by:

$$K^{-1} = \int_0^{\infty}\int_{\Re^p} L(\theta,\tau \mid s)\xi(\theta,\tau)\,d\theta\,d\tau \tag{9}$$

The previous information can be considered as a normal-gamma density [48] expressed by the following equation:

$$\xi(\theta,\tau) = \xi_1(\theta,\tau)\xi_2(\tau) \tag{10}$$

where:

$$\xi_1(\theta,\tau) \propto \tau^{p/2}\, exp[-\tau/2(Y - X\theta)^T\, P\, (Y - X\theta)] \tag{11}$$

$\xi_1(\theta,\tau)$ is the conditional density function of θ given τ and is a normal multivariate distribution with a *p*-dimensional mean vector $\mu = E(\theta,\tau)$ and precision matrix τP positive-definite of size $p\ x\ p$. p is the dimension of the vector of unknown parameters θ, in this case 4.

The prior function density of τ is a gamma density [48]:

$$\xi_2(\tau) \propto \tau^{\alpha-1}\, exp(-\tau\beta) \tag{12}$$

Applying the Bayes theorem (7) with equations (8) and (10), the posterior density of θ and τ is:

$$\xi(\theta,\tau|s) \propto \tau^{\varphi}\, exp(\lambda) \tag{13}$$

where:

$$\varphi = \frac{n+2\alpha+p}{2} - 1 \tag{14}$$

$$\lambda = -\tau/2\ [2\beta + (\theta - \mu)^T P(\theta - \mu) + (Y - X\theta)^T(Y - X\theta)] \tag{15}$$

The posterior marginal density of θ is found by integrating in τ and yields a *p*-dimensional t density with $n + 2\alpha$ degrees of freedom.

$$\xi(\theta|s) \propto \{2\beta + Y^TY - (X^TY+P\mu)^T\mu^* + [\theta-\mu^*]^T(X^TX+P)[\theta-\mu^*]\}^{\omega} \tag{16}$$

where:

$$\mu^* = (X^TX+P)^{-1}(X^TY+P\mu) \tag{17}$$

$$\omega = -\frac{n+2\alpha+p}{2} \tag{18}$$

In general, it could be said that the prior information about the parameters is not sufficiently justified, because of the lack of instrumental information, so it is important to assign prior uncertainties to θ_i. As mentioned in a previous research [25], it can be adopted as the most likely region for each parameter the one that includes 90% of the total area under the prior density function, that is, the mean plus minus 1.7 the standard deviation, i.e. it will be considered $SD[\theta_i] = E[\theta_i]/1.7$.

The parameter θ_1 is related with the magnitude and its influence on the amplitude of the expected ground motion, in this case it will be taken a previous value of 0.3.

θ_2 represents the effect of the geometric expansion of wave front, and it has a theoretical value of -1 or -0.5, depending on the wave front characteristics [9] [27]. All the records considered in this research have a hypocentral depth less than 100 km, so it can be considered a spherical wave front. For this reason, it will be assigned a previous value of -0.5.

The available prior information about parameters θ_0 and θ_3 is more vague than for the others. θ_0 considers site effects and θ_3 is related to the elastic energy that is absorbed by the medium in the form of heat by friction (intrinsic attenuation). We will use values of 3 and -0.005, based on the results obtained in previous research [25] [47].

The previous expected value of σ will be adopted as 0.7, based on the fact that attenuation relations obtained in previous research show this as a typical value [25].

Finally, it is necessary to fix the matrix P, in which is considered the covariance of the parameters. The previous knowledge is not enough to estimate the joint variation degree of the parameters, so it can be considered that P has the form of a diagonal matrix.

IV. RESULTS

Table 3 shows a comparison between the parameters obtained by a least squares approach and the preliminary Bayesian linear regression.

Table 3. Bayesian (BAY) and least squares (LS) results.

COEFFICIENT	BAY	LS
θ_0	2.97	2.23
θ_1	-0.03	0.25
θ_2	-0.92	-1.02
θ_3	0.01	0.01

In the case of the Bayesian approach it can be observed that the prior values assigned to the parameters differ from those finally obtained. This is because the previous information that was initially considered, was updated with the information contained in the observed data.

As the Fig. 4 shows, the least squares approach has the major disadvantage of being an unconstrained process, because of this, a small variation in the data produces instability in results.

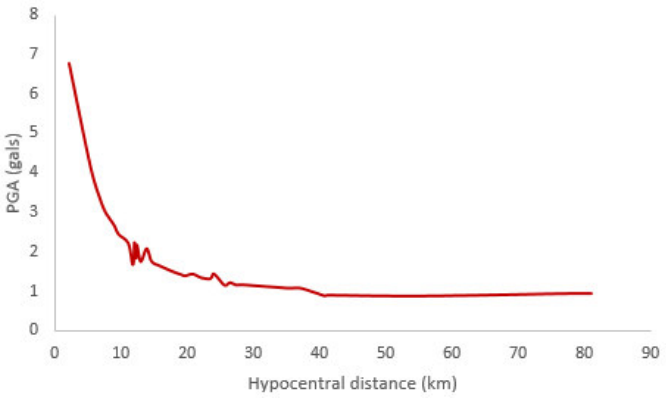

Fig. 4. Attenuation curve obtained with the least squares approach.

On the other hand, as shown in Fig. 5, the prior information included in the Bayesian linear regression makes the process very stable, and it can be considered as corrections to the LS solution.

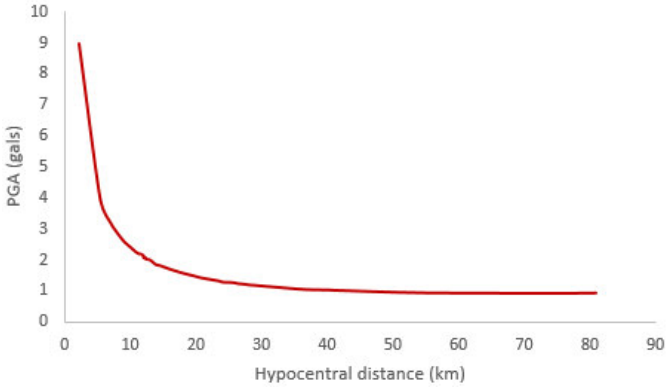

Fig. 5. Attenuation curve obtained with the Bayesian analysis.

V. CONCLUSION

The Mexican Volcanic Belt is a zone in which the seismic risk has been considered as low because the occurrence of earthquakes doesn´t have the same frequency as those cities located near the Pacific coast. However there are historical records about events of considerable magnitude associated with the geological faults in the area.

In this article a summary of these events was made, emphasizing the importance of making a seismic risk research in the area, being the first step the estimation of the expected peak ground motion due to the earthquakes occurred within the Mexican Volcanic Belt.

A first proposal was made using a Bayesian linear regression technique and a least squares approach, however it is necessary to compare the attenuation between different paths to observe the variations due to the particular geological conditions in the area.

REFERENCES

[1] F. R. Zúñiga. 2010. El otro riesgo sísmico: los sismos en el centro de México. In: XI Simposio Nacional de Ingeniería Sísmica.

[2] M. Suter, G. Aguirre, C. Siebe, O. Quintero, and J. C. Komorowski. 1991. Volcanism and active faulting in the central part of the Trans-Mexican Volcanic Belt, Mexico. Geol. excursions South. Calif. Mex. Guideb. 1991 Annu. Meet. Geol. Soc. Am.:224–243.

[3] G. J. Aguirre-Díaz, F. R. Zúñiga-Dávila Madrid, F. Pacheco, M. Guzmán-Speziale, and J. Nieto-Obregón. 2000. El graben de Querétaro, México. Observaciones de fallamiento activo. GEOS 20:2–7.

[4] M. Suter. 2002. Active faults in the central part of the Transmexican Volcanic Belt, Mexico.

[5] F. R. Zúñiga, J. M. Gómez, and M. Guzmán. 2009. La sismicidad de Querétaro. In: El valle de Querétaro y su geoentorno. CONCYTEQ/UNAM/UAQ. p. 17–26.

[6] M. Suter, M. Carrillo, and O. Quintero. 2014a. Intensity data points for the 1912 Acambay earthquake.

[7] M. Suter, M. Carrillo, and O. Quintero. 2014b. Macroseismic intensity data for the 1979 Maravatío earthquake.

[8] M. Suter, M. Carrillo, and O. Quintero. 2014c. Macroseismic intensity data for the 1989 Landa earthquake.

[9] D. García. 2001. Atenuación sísmica. Aplicación a terremotos intraplaca en México central.

[10] M. Suter, M. Carrillo-Martínez, and O. Quintero-Legorreta. 1996. Macroseismic study of shallow earthquakes in the central and eastern parts of the trans-Mexican volcanic belt, Mexico. Bull. Seismol. Soc. Am. 86:1952–1963.

[11] G. Suárez, V. García-Acosta, and R. Gaulon. 1994. Active crustal deformation in the Jalisco block, Mexico: evidence for a great historical earthquake in the 16th century. Tectonophysics 234:117–127.

[12] M. Suter, M. Carrillo, and O. Quintero. 2014d. Intensity data points for the 1887 Pinal de Amoles earthquake.

[13] G. Suárez. 1992. El sismo de Jalapa del 3 de enero de 1912. Rev. Soc. Mex. Ing. Sísmica:3–15.

[14] M. Suter, M. Carrillo, and O. Quintero. 2014e. Macroseismic intensity data for the 1987 Actopan earthquake.

[15] F. R. Zúñiga, J. F. Pacheco, M. Guzmán-Speziale, G. J. Aguirre-Díaz, V. H. Espíndola, and E. Nava. 2003. The Sanfandila earthquake sequence of 1998, Queretaro, Mexico: Activation of an undocumemted fault in the northern edge of central Trans-Mexican Volcanic Belt. Tectonophysics 361:229–238.

[16] G. J. Aguirre-Díaz, J. Nieto-Obregón, and F. R. Zúniga. 2005. Seismogenic basin and range and intra-arc normal faulting in the central Mexican Volcanic Belt, Querétaro, México. Geol. J. 40:215–243.

[17] N. M. Shapiro, M. Campillo, A. Paul, S. K. Singh, D. Jongmans, and F. J. Sánchez-Sesma. 1997. Surface-wave propagation across the Mexican Volcanic Belt and the origin of the long-period seismic-wave amplification in the Valley of Mexico. Geophys. J. Int.:151–166.

[18] A. Clemente-Chavez, A. Figueroa-Soto, F. R. Zúñiga, M. Arroyo, M. Montiel, and O. Chavez. 2013. Seismicity at the northeast edge of the Mexican Volcanic Belt (MVB) and activation of an undocumented fault: The Peñamiller earthquake sequence of 2010-2011, Queretaro, Mexico. Nat. Hazards Earth Syst. Sci. 13:2521–2531.

[19] A. Clemente, F. R. Zúñiga, J. Lermo, A. Figueroa-Soto, C. Valdés, M. Montiel, O. Chavez, and M. Arroyo. 2014. On the behavior of site effects in central Mexico (the Mexican volcanic belt - MVB), based on records of shallow earthquakes that occurred in the zone between 1998 and 2011. Nat. Hazards Earth Syst. Sci. 14:1391–1406.

[20] A. Demant. 1978. Caracteristicas del Eje Neovolcánico Transmexicano y sus problemas de interpretación. Univ. Nal. Autón. México, Inst. Geol. Rev. 2:172–187.

[21] C. A. Johnson, and C. G. A. Harrison. 1990. Neotectonics in central Mexico. Phys. Earth Planet. Inter. 64:187–210.

[22] S. K. Singh, E. Mena, and R. Castro. 1988. Some aspects fo source characteristics of the 19 september 1985 Michoacan earthquake and ground motion amplification in and near Mexico City from strong motion data. 78:451–477.

[23] S. K. Singh, and M. Ordaz. 1993. Strong motion seismology in Mexico. Tectonophysics 218:43–57.

[24] F. J. Chávez-García, F. J. Sánchez-Sesma, M. Campillo, and P. Bard. 1994. El terremoto de Michoacán de septiembre de 1985 : efectos de fuente, trayecto y sitio. Física la Tierra 6:157–200.

[25] M. Ordaz, S. K. Singh, and a. Arciniega. 1994. Bayesian Attenuation Regressions: an Application to Mexico City. Geophys. J. Int. 117:335–344.

[26] S. K. Singh, A. Iglesias, D. García, J. F. Pacheco, and M. Ordaz. 2007. Q of Lg waves in the central Mexican volcanic belt. Bull. Seismol. Soc. Am. 97:1259–1266.

[27] K. W. Campbell. 2003. Strong-Motion Attenuation Relations. In: International Handbook of Earthquake and Engineering Seismology. Academic Press. p. 1003–1012.

[28] A. M. Hasofer, and L. Esteva. 1985. Empirical Bayes estimation of seismicity parameters. 2:199–205.

[29] E. Rosenblueth, and M. Ordaz. 1987. Use of seismic data from similar regions. Earthq. Eng. Struct. Dyn. 15:619–634.

[30] D. García. 2006. Estimación del movimiento fuerte del suelo para terremotos interplaca e intraslab en México central. Universidad Complutense de Madrid.

[31] L. Esteva, and E. Rosenblueth. 1964. Espectros de temblores a distancias moderadas y grandes. Boletín Soc. Mex. Ing. Sísmica II:1–18.

[32] L. Esteva. 1970. Consideraciones prácticas en la estimación bayesiana de riesgo sísmico. Inst. Ing. 248:209–228.

[33] M. Mahdyiar, S. K. Singh, and R. P. Meyer. 1986. Moment magnitude scale for local earthquakes in the Petatlan region, Mexico, based on recorded peak horizontal velocity. Bull. Seismol. Soc. Am. 5:1225–1239.

[34] M. Ordaz, J. M. Jara, and S. K. Singh. 1989. Riesgo sísmico y espectros de diseño en el estado de Guerrero. In: VIII Congreso Nacional de Ingeniería Sísmica.

[35] S. K. Singh, M. Ordaz, J. F. Pacheco, R. Quaas, L. Alcántara, S. Alcocer, C. Gutiérrez, R. Meli, and E. Ovando. 1999. A preliminary report on the Tehuacan, Mexico earthquake of June 15, 1999 (Mw=7). Seism. Res. Lett. 70:489–504.

[36] S. K. Singh, A. Iglesias, J. F. Pacheco, and M. Ordaz. 2001. A source and wave propagation study of the Copalillo Mexico earthquake of July 21, 2000 (Mw=5.9). Bull. Seismol. Soc. Am.

[37] C. Gómez-Soberón, M. Ordaz, and A. Tena-Colunga. 2005. Leyes de atenuación en desplazamiento y aceleración para el diseño sísmico de estructuras con aislamiento en la costa del Pacífico. In: XV Congreso Nacional de Ingeniería Sísmica.

[38] D. García, S. K. Singh, M. Herraíz, M. Ordaz, and J. F. Pacheco. 2005. Inslab earthquakes of Central Mexico: Peak ground-motion parameters and response spectra. Bull. Seismol. Soc. Am. 95:2272–2282.

[39] A. Clemente. 2010. Ley de atenuación de aceleración (PGA) y escalamiento de forma espectral sísmica para Querétaro, deducidos por análisis de trayectorias: aplicada a Guerrero-Querétaro. Universidad Autónoma de Querétaro.

[40] A. Clemente, M. Arroyo, F. R. Zúñiga, A. Figueroa-Soto, M. Pérez, and C. S. López. 2012. Relación de atenuación del movimiento del suelo para la aceleración máxima (PGA) sobre el Cinturón Volcánico Mexicano (MVB); análisis por trayectoria: Guerrero-Querétaro. Rev. Ing. Sísmica 93:67–93.

[41] L. Esteva. 1969. Seismic risk and seismic design decisions. In: MIT Seminar on the Earthquake Resistant Design of Nuclear Reactors. Cambridge, Massachussets. p. 142–181.

[42] W. Dong, H. C. Shah, and A. Bao. 1984. Utilization of geophysical information in Bayesian seismic hazard model. Soil Dyn. Earthq. Eng. 3:103–112.

[43] D. Muñoz. 1989. Conceptos básicos en riesgo sísmico. Fis. la tierra:199–215.

[44] L. Esteva. 1968. Bases para la formulación de desiciones de diseño sísmico. Universidad Nacional Autónoma de México.

[45] D. Arroyo, and M. Ordaz. 2010a. Multivariate bayesian regression analysis applied to ground-motion prediction equations, part 1: Theory and synthetic example. Bull. Seismol. Soc. Am. 100:1551–1567.

[46] D. Arroyo, and M. Ordaz. 2010b. Multivariate bayesian regression analysis applied to ground-motion prediction equations, part 2: Numerical example with actual data. Bull. Seismol. Soc. Am. 100:1568–1577.

[47] M. A. Jaimes, A. Ramirez-gaytán, and E. Reinoso. 2015. Ground-Motion Prediction Model From Intermediate-Depth Intraslab Earthquakes at the Hill and Lake-Bed Zones of Mexico City Ground-Motion Prediction Model From Intermediate-Depth Intraslab Earthquakes at the Hill and Lake-Bed Zones of Mexico City. J. Earthq. Eng. 19:1260–1278.

[48] L. D. Broemeling. 1985. Bayesian analysis of linear models. Marcel Dekker Inc. New York.

Super Critical CO_2 Power Cycle Modeling

C. S. Lora Pérez
Facultad de Ingeniería, Universidad Autónoma de Querétaro, UAQ
Santiago de Querétaro, México
cslperez@hotmail.com

J. C. Jauregui
Facultad de Ingeniería, Universidad Autónoma de Querétaro, UAQ
Santiago de Querétaro, México
juancarlosjauregui2007@gmail.com

Abstract **At present, the use of reliable alternative sources of energy has gained much importance due to the reduction in fossil fuel reserves. The supercritical CO_2 power cycle has recently gained a lot of attention from researchers for use in energy applications with heat sources including renewables such as the solar thermal. In this paper, the introduction of the development of a power cycle model that uses supercritical CO_2 as a working fluid combined with solar energy as an energy source will be explained.**

Keywords—power cycle; supercritical CO_2; Brayton cycle; solar; thermal.

I. INTRODUCTION

At present, the use of reliable alternative sources of energy has gained much importance due to the reduction in fossil fuel reserves. In this sense, solar energy is projected as a source of alternative energy because the sun´s potential is virtually inexhaustible. Every hour, the sun throws more energy into the Earth in the form of light and heat to satisfy the global needs of a full year. In order to use solar energy in the most efficient way posible, many technologies have been explored over the last few decades [1]. The Brayton cycle with Super Critical CO_2 working fluid has recently gained a lot of attention from researchers for its use in energy applications with heat sources including renewables such as the solar thermal. The advantages of the super-critical CO_2 cycle are high efficiencies and more compact turbo machinery. The CO_2 critical point condition is 30.98 ° C and 7.38 MPa which is achievable with less compression work because of its low compressibility factor which is one of its advantages. The super-critical CO_2 cycle can potentially improve the economy of renewable energy systems significantly [2].

TABLE I. COMPARISON DATA FOR THE CO_2 AND STEAM

Critical Point		*CO_2*	*Steam*
Critical	Temperature (K)	304.13	647.1
	Pressure (bar)	73.77	220.64

Dynamic simulation of thermodynamic systems is required to evaluate and optimize their responses over time or to define, implement and evaluate control strategies. The simulation consists in subjecting the cycle to transient conditions such as those produced by the variation of solar radiation [3].

II. SUPER CRITICAL CO_2 POWER CYCLE REVIEW

Super Critical Carbon Dioxide (S-CO_2) is currently being used for many applications because of its special characteristics. Reference [4] proposed a first research paper comparing the efficiency of a steam cycle with one based on CO_2 in an application with nuclear heat source. His original work focused on the condensation cycle for applications in two temperature ranges, one low temperature between 450 ° C and 550 ° C, and the other high temperature range between 650 ° C and 800 ° C [2]. A power cycle fully operating above the critical area of CO_2 was proposed by [5].

From these early works, numerous variations have been proposed to the Brayton power cycle using S-CO_2 as working fluid. However, most of the research is being conducted in applications with nuclear heat sources.

Reference [6] regained power cycle for nuclear applications and designed the recompression cycle with an inlet temperature to the turbine between 550 ° C - 750 ° C.

After the work of [6] several investigations have been made with S-CO2 including solar power concentrator systems, fuel cells, systems with heat recovery output of gas turbines among other alternative Power conversion systems [2].

Reference [7] investigated the possibility of using S-CO2 as working fluid in a nuclear plant comparing several designs.

Reference [8] compared several cycle designs with S-CO_2 which could maximize the output power from the turbine output gases.

Research in Brayton power cycles with S-CO_2 is still in laboratorial stages. Several tests have been carried out by different institutes such as the Sandia National Laboratory (SNL, Nuevo México, USA), Knolls Atomic Power Lab (KAPL, Nueva York, USA) and the Institute of Applied Energy (IAE, Kyoto, Japan). The SNL built a recompression cycle with 2 TAC type turbomachinery (turbine-alternator-compressor) for nuclear applications. KAPL built a simple cycle recovered with 2 turbines (one turbine generator and one

to move the compressor) that was also used for nuclear applications. IAE built a small-scale S-CO_2 cycle to evaluate performance. According to the experimental results of these tests, it can be concluded that the efficiency of the cycle increases when the compressor input temperature approaches the critical point, consequently, it is necessary to maintain very precise control loops to preserve the cycle operational stability [2].

III. MODELING PROCESS

In general, the power cycles are modeled during its steady state; as a result, it is assumed that the system operates continuously without changes in its base load [9]. This kind of performance is reachable when the energy source is someway controllable, but for solar source systems a transient model is necessary.

The modeling process is based on the balance equations of energy and mass and their complexity depends on whether or not the system is considered working in steady state, quasy-steady or dynamic. For steady state, the time derivatives are not taken into account, contrary to dynamic simulation. The steady and dynamic behavior can be represented by many approaches depending on flow phase, single or a 2 phase flow. Nevertheless, some approaches present a high difficulty because of their mathematical complexity. But, a lumped parameter model is likely when a simplified description of the process is required. The great advantage is the reduced computational time. This kind of modeling process consists in describing the thermal system as an equivalent thermal network formed by resistors and capacitors [9].

A lumped thermal mass model was used to simulate the heat transfer process of heat exchangers without phase transitions and the results indicate that the developed lumped model is robust and computationally efficient [3].

A. *Process Components*

An ideal Recuperated Brayton Power Cycle consists of a solar Collector, Compressor, Turbine, Recuperator and Condenser (Fig. 1).

1-2 Compressor
2-3 Recuperator (Cold Side)
3-4 Solar Collector
4-5 Turbine
5-6 Recuperator (Hot Side)
6-1 Condenser

The absorbed energy in Solar Collector will be transferred to working fluid (s-CO_2) through radiation and convection. Then the fluid will suffer an expansion in the turbine producing mechanical energy which is converted through a generator into electrical energy. After the turbine, the working fluid will still transfer energy through a recuperator to the compressor outlet fluid. Then the working fluid will transfer waste heat to environment before passing through the compressor.

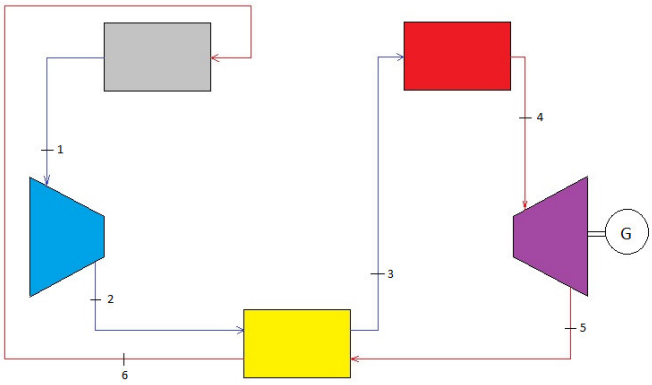

Fig. 1. Simple Recuperated Brayton Cycle layout [2].

In literature several layouts have been proposed and they are a combination of commonly used processes like intercooling, reheating and recuperation.

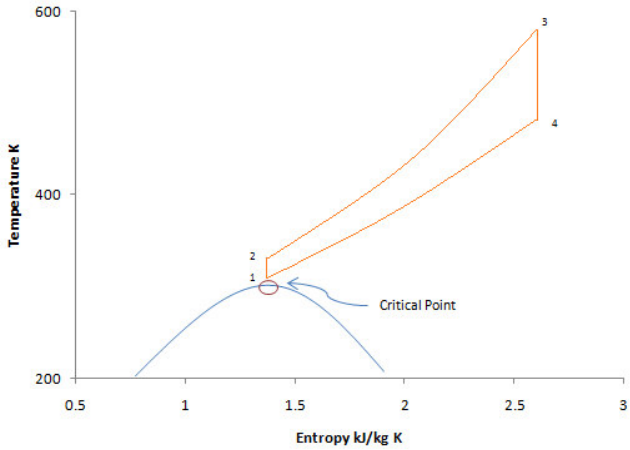

Fig. 2. T-S diagram of s-CO_2 simple Brayton Cycle.

Fig. 2 demonstrates the cycle operating near the CO_2 critical point, which in spite of its advantages makes the system susceptible to unstable behavior.

It is important to understand the effects of oscillation in solar energy and meteorological inputs to propose possible control strategies.

To build the whole cycle model it is necessary a thermodynamic, heat transfer and momentum analysis in each component in order to obtain a model for each component.

- *Solar Collector:* To model this component, it will be assumed as one unit (One-Node Capacitance). The effects of thermal capacitance will be included so the intermittent energy incident [10].

$$C_a \frac{dT_m}{dt} = F'[S - U_L(T_m - T_{amb})] - \frac{Q_u}{A}$$

C_a = Lumped capacitance
T_m = Mean fluid temperature
F' = Overall efficiency factor
S = Solar radiation
U_L = Overall loss coefficient
T_{amb} = Ambient temperature
Q_u = Total useful energy gain

- *Compressor:* This component will increase the pressure of the CO_2. This model will have one inlet and one outlet flow. The important input data for the compressor model will be dimensions, pressure and temperature before component, ratio pressure and efficiency[9].

$$\dot{m}_{in} = \dot{m}_{out}$$

Energy balance:

$$\dot{m}_{in}\, h_{in} = \dot{m}_{out}\, h_{out} + P$$

m_{in} = Inlet flow
m_{out} = Outlet flow
h_{in} = Inlet enthalpy
h_{out} = Outlet enthalpy
P = Pressure energy

- *Turbine:* During the expansion in this component, enthalpy is transformed into mechanical energy. The model will calculate the working fluid output enthalpy with inlet enthalpy, pressure change and efficiency[9].

$$\Delta h = (h_{in} - h_{ref}) - (h_{out} - h_{ref})$$

- *Heat Exchanger:* Basically, the proposed cycle will have 2 heat exchangers, recuperator and condenser. The equations will describe the heat flow from the hot side to the tube wall and then from the tube wall to cold side of the working fluid (through convection).

The main purpose for this work is to analyze the behavior of the cycle under the dynamic nature of the heat source in order to pose possible control strategies and obtain predictable power.

IV. EXPECTED RESULTS

It is expected to develop a thermo solar power plant thermodynamic model operating in a Brayton cycle under environmental conditions of the State of Queretaro for control purposes. This knowledge will contribute to develop new projects in Mexico using solar energy to achieve the proposed goals in the Energy Transition Law.

REFERENCES

[1] B. K. Naik, A. Varshney, P. Muthukumar, and C. Somayaji, "Modelling and Performance Analysis of U Type Evacuated Tube Solar Collector Using Different Working Fluids," *Energy Procedia*, vol. 90, no. December 2015, pp. 227–237, 2016.

[2] Y. Ahn *et al.*, "Review of supercritical CO2 power cycle technology and current status of research and development," *Nucl. Eng. Technol.*, vol. 47, no. 6, pp. 647–661, 2015.

[3] Q. A. Buch, R. Dickes, A. Desideri, V. Lemort, and S. Quoilin, "Dynamic modeling of thermal systems using a semi-empirical approach and the ThermoCycle Modelica Library," *28Th Int. Conf. Effic. Cost, Optim. Simul. Environ. Impact Energy Syst.*, 2015.

[4] G. Angelino, "Carbon Dioxide Condensation Cycles for Power Production," *ASME J. Eng. Power*, vol. 90, no. 3, pp. 287–296, 1968.

[5] E. G. Feher, "The Supercritical Thermodynamic Power Cycle," *Energy Convers.*, vol. 8, pp. 85–90, 1968.

[6] V. Dostal, M. J. Driscoll, and P. Hejzlar, "A supercritical carbon dioxide cycle for next generation nuclear reactors," *Massachusetts Inst. Technol. Dept. Nucl. Eng. Cambridge, MA, Pap. No. MIT-ANP-TR-100*, 2004.

[7] D. Vitale Di Maio, A. Boccitto, and G. Caruso, "Supercritical carbon dioxide applications for energy conversion systems," *Energy Procedia*, vol. 82, pp. 819–824, 2015.

[8] G. Kimzey, "Development of a Brayton Bottoming Cycle using Supercritical Carbon Dioxide as the Working Fluid," 2012.

[9] F. Alobaid, N. Mertens, R. Starkloff, T. Lanz, C. Heinze, and B. Epple, "Progress in dynamic simulation of thermal power plants," *Prog. Energy Combust. Sci.*, vol. 59, pp. 79–162, 2017.

[10] S. a. Klein, J. a. Duffie, and W. a. Beckman, "Transient Considerations of Flat-Plate Solar Collectors," *J. Eng. Power*, vol. 96, no. 2, p. 109, 1974.

Temperature effect on growth of freshwater prawn *Macrobrachium tenellum* in recirculating aquaculture system

Sánchez-Velázquez J. Peña-Herrejón G.H. Aguirre-Becerra H. García-Trejo J.F.

Laboratorio de Bioingeniería Acuícola. Facultad de Ingeniería
Universidad Autónoma de Querétaro
Amazcala, El Marqués, Querétaro, México.
julietasanvel@gmail.com

***Abstract*— *Macrobrachium tenellum* is one of the mexican species of freshwater prawns that has lately been considered as a strong candidate for aquaculture because is considered a fancy dish in some places of Mexico and other parts of the world, its cost achieves $300 mexican pesos per kilogram. Generally, this organism is extracted by fishing, so that there are few studies about its production under intensive culture as recirculating aquaculture systems in which temperature culture is a critical issue for this organism due to its growth natural conditions. The aim of this study was to evaluate growth (size and weight) at two freshwater prawns (*M. tenellum*) densities (10 and 20 organisms/m^2) with (W T) and without (O T) regulation on temperature in a recirculating aquaculture system at experimental level. Dissolved oxygen, pH, nitrites and nitrates did not differ significantly (P>0.05) to each treatment just ammonia. Mean weight and mean size increased in both densities with regulation on temperature (W T) but there had been a significant difference (P>0.05) between W T and O T at 20 organisms/m^2 for weight. Size increased for W T treatments but did not show difference at any density. This work suggests that physical conditions as temperature must be maintained at optimal levels in recirculating aquaculture systems in order to achieve market size and weight and try to maintain at least 50% of survivor.**

Keywords*— *Aquaculture, density, Macrobrachium spp, optimal temperature and productivity.

I. Introduction

Aquaculture production systems can be extensive, semi-intensive or intensive depending on the number of organisms grown by volume of water, supply and source of water. The culture in ponds is extensive, the cage culture is semi-intensive, and the aquaculture recirculation system (RAS) is an intensive system. Conventional methods such as ponds and cages, both open pit, always have the risk of being contaminated by water and air, in addition water quality control is more difficult in these systems and the number of organisms that could maintain is limited [18].

RAS are based on the continuous circulation of water through mechanical and biological filters to achieve the removal of nitrogenous solids and waste. These systems do not need to be replaced because water quality is stable enough to ensure good conditions for the crop in question [14]. In addition, under-cover RAS are viable and infinitely expandable, environmentally compatible and guarantee both the safety and quality of production [18], because of they begin with drinking water there is less likelihood of diseases for the crop, and if any organism introduced is ill, in addition the invasion of aquatic organisms to wild environments is limited, they use less than 90-99% of water from those conventional aquaculture systems [15].

The critical parameters of water quality that must be considered in a RAS are dissolved oxygen, temperature, pH, suspended solids, ammonia, nitrite and carbon dioxide. These parameters are interrelated with reactions at the physical, biological and chemical levels. Monitoring and adjusting systems to maintain the levels of these parameters in acceptable ranges is very important to achieve the viability of the whole system [18].

The crustaceans are poikilothermic animals, those that cannot regulate their temperature and is quite similar to that of their environment, the production of metabolic heat is relatively low and their thermal conductivity is high, they are ectothermic, the crustaceans make adjustments and present a compensatory response to the different external temperatures, using specific homeostatic mechanisms [19]. The temperature allows all aspects like growth, health, and nutritional requirement, of an organism grown in aquaculture. Under

natural conditions, aquatic animals are rarely exposed to sudden temperature changes and have not developed mechanisms to address this situation, however, some aquatic organisms can adapt to temperature changes in their tolerance ranges, but very slowly [19].

The crustaceans *Macrobrachium* sp are freshwater prawns that have a great economic value because of its flavor and protein content [1], also is considered as luxury food [2][4]. *Macrobrachium tenellum* from Mexico does not show any work about their production in recirculating aquaculture systems [8] under different conditions of temperature. The principal studies are about their biology, environmental function and taxonomy, natural population [7][8][9][10][11][12][13]. In addition, *M. tenellum* is produced by earth-ponds, and its intensive production has not been established yet [3][5][6].

The economic importance of *M. tenellum* lead us to investigate its growth at different temperature conditions to know if is recommendable their production in recirculating aquaculture systems.

II. Materials and Methods

The experiment took place at the Engineering Department of the University of Queretaro in Amazcala that belongs to the Marques, Querétaro. It was carried out in a multitunel greenhouse of 504 m^2, with galvanized structural steel, covered by polyethylene plastic and mesh windows, without heating and passive ventilation system. The experimental units were tanks of 1.43 m length, 0.55 m height, 1.01 m width with 500 L of volume. The recirculation aquaculture system water filtered with a Canister Filter UV of 8 000 L/h model EFU-15000 BOYU using a water pump 10 000 L/h model PQF-10 000 BOYU. The experimental design has a Latin square, there are two temperatures (optimal and environmental) and tow stocking densities (10 and 20 organisms/m^2) by triplicated with a total of 12 treatments. The assay will last 40 days.

Organisms were obtained from Acuicola S.A. farmer from Manzanillo, Col. Once they obtained in laboratory were acclimatized by 7 previous days to the assay, after that they were place in the experimental units. The animals fed with Camaronina M.R. Purina 35%, at 13:00 hours only once at the day. Ratio food at 10% initial biomass [20].

It was used a datalogger Watchdog serie 1000 trough sensors Spectrum Technologies, Inc to obtain water temperature (^oC) throughout the experiment. Oxygen dissolved (DO_2) (mg/L) determined by multiparameter Hach serie HQ40d and pH measured with a pH-measure Hanna twice per week. Element concentration Nitrates (NO^{-3}) nitrites (NO^{-2}) and ammonia (NH_4^+) measured twice per week according to the methodology of spectrophotometer DR/6000 Hach. Initial and final weight were determined with a balance Sartorius de 300g (D.S. 0.001 g) and initial and final size were determined with Vernier Mitutoyo model CD-6”PSX respectively.

Variations in environmental, physics, chemistry conditions, growth and size data were tested using analysis of variance. Significant results were further tested using Statgraphics Centurion XV version 15.2.06.

III. Results and Discusion

The concentration of Nitrogen compounds is shown in table 1. There was not difference between treatments, only for ammonia.

Table 1. Conditions of water (mean±sd) were determined in treatment with regulation on temperature (W T) and without regulation temperature (O T) during 40 days of the experiment.

Condition	W T	O T	Optimal
Nitrates mg/L	1.69±0.68a	1.33±0.56a	-
Nitrites mg/L	0.08±0.01a	0.003±0.00b	0.1-0.7
Ammonia mg/L	0.15±0.08a	0.05±0.04b	0.1-0.5
Oxygen mg/L	6.87±0.56a	6.36±079a	> 4
pH	9.80±0.12a	9.50±0.41a	7-8.5

Lower case means statistically significant difference (P<0.05)

Temperature variation is shown in table 2, there was not difference between treatments.

Dissolved oxygen, pH, nitrites and nitrates did not differ significantly (P>0.05) to each treatment only ammonia (Table 1).

Table 2. Temperature (mean±sd) in each treatment with regulation on temperature (W T) and without regulation temperature (O T) during 40 days of the experiment.

Temperature	W T	O T	Optimal
Mean	25.59±2.50a	29.34±1.48a	28
Min	21.8	26	25
Max	29.5	32	30
Rang	8	6	5

Lower case means statistically significant difference (P<0.05)

Mean weight and mean size increased in treatments W T, not matters if there would be different density (Figure 2, A y B).

The temperature had an effect on shrimp survival, showing a significant difference between treatments with T (W T) and without T (O T). The conditions provided during this experiment for the W T treatments allowed a 50% survival, reported by experts as acceptable for these organisms.

A)

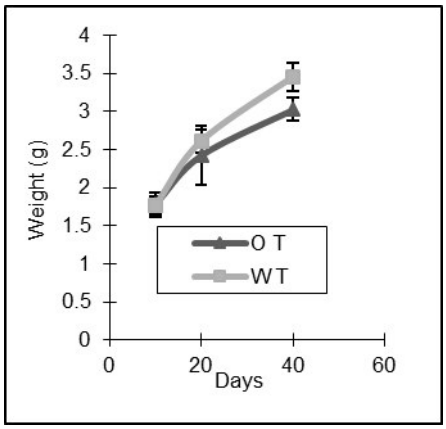

B)

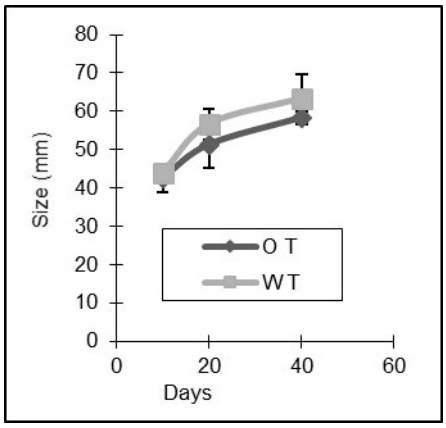

Figure 1. Mean weight (A) and mean size (B) of 10 org/m^2 in treatments without regulation on temperature (OT) and with regulation on temperature (WT).

The preferred temperature for *M. tenellum* is 28 °C with margins of 27 to 30 °C [20]. Hernández-Sandoval, 2008 [21] observed that *M. occidentale* tolerates a wide temperature range as it can develop from 20 °C to above 31 °C, this coincides with the intervals reported for *M. acanthurus* by Díaz et al., 2002 11 °C to 34.2 °C [22], and Manush et al., 2004 [23] report for *M. rosenbergii* 14.9 °C and 40.7 ° C, however Lagerspetz and Vainio (2006) [19] discuss the concept of euritermity since specimens of the same species and population can change their tolerability depending on various factors, age, physiological condition, sex, height, diet and reproduction.

The temperature inside the greenhouse was affected by the opening and closing of windows, as the highest peaks of 50 ° C were reached at 16:00 hours. The day after the windows were open and we had a drastic fall of the temperature affecting growing conditions. It is suggested that, for future studies, avoid the loss of energy and use it to raise the temperature throughout the crop and take advantage of the greenhouse.

IV. Conclusions

This work suggests that temperature had direct effect on growth, there was an increased in size and weight in those treatments that had higher values of temperature. It must be mentioned that 10 organisms/m^2 had better size and weight and it could be used as stocky density to begin new approach in order to develop operation strategies.

V. Acknowledgment

We thank the Engineering Department of the University of Queretaro and the National Science and Technology Council (CONACYT) for giving us the opportunity to develop technology for the use and benefit of Mexico.

V. References

[1] FAO, Global capture production statistics dataset 1950-2009 and Global Aquaculture Production Stastitics dataset (Quantity and Value) 1950-2009, Roma, FAO <www. fao.org/fishery/statistics/software/fishtat/en>, 2011

[2] FAO, The state of world fishieries and aquaculture, Roma, FAO < http://www.fao.org/3/a-i3720e.pdf > , 2014.

[3] García M., Becerril F. Vega F. Y Espinosa D. Langostinos del género Macrobrachium con importancia económica y pesquera en América Latina: conocimiento acutal, rol ecológico y conservación. Lat. Am. J. Aquat. Res., 41(4): 651-675., 2013.

[4] Kent, G. Aquaculture and food security. Proceedings of the PACON Conference on Sustainable Aquaculture June, Honolulu, Hawaii, USA. Honolulu: Pacific Congress on Marine Science and Technology, 95: 11-14, 1995

[5] Benitez M. and Ponce J. Biología, Ecología e Investigación sobre el langostino de Río Macrobrachium carcinus. Lennaeus, 1758. Estados Unidos de América, 2012

[6] Iñiguez J. and Díaz E. Diagnóstico y Potencial Pesquero en las Microcuentas Ayutla y Concá. Facultad de Ciencias Naturales. Universidad Autónoma de Querétaro, 2006

[7] Guzman A. Cabrera J. Kensler C. Notes on *Macrobrachium* species in México. In. J. A, Hanson y H.L Goodwin (eds.). Shrimp and prawn farming in the western Hemisphere. Dowden Hatchinson y Ross, Pennsylvania, 315-316, 1977

[8] Mejía L. Alvarez F. Román R. y Viccon J. Fecundity and distribution of freshwater prawns of the genus *Macrobrachium* in the Huitzilapan River. Veracruz, México. Crustaceana, 74(1):69-77, 2001.

[9] Murphy N. Austin C. Phylogenetic relationships of the globally distributed freswater prawn gen *Macrobrachium* (Crustacea: Decapoda: Palaemonidae): biogeography, taxonomy, and the convergent evolution of abbreviated larval development. Zool. Scr. 34(2):187-197, 2005.

[10] Hernández, L. Murugan G. Ruiz G. Meada A. Freshwater shrimp of the genus *Macrobrachium* (Decapoda Paleamonidae) from the Baja California Península, México. J. Crust. Biol., 27(2):351-359, 2007.

[11] Barba E. Juárez J. Estrada F. Abundance and distributionof crustaceans in wetlands of Tabasco. Rev. Mex. Biodivers., 81: 153-163, 2010.

[12] Islam M. Rahman M. Tanaka M. Stocking density positively influences the yield and farm profitability in cage aquaculture of sutchi catfish, *Pagasius sutchi*. J. Appl. Ichthyol, 22:441-44, 2005.

[13] Montero D. Izquierdo M.S, Tort L. Robaina L. Vergara J.M. High stocking density produces crowding stress altering some physiological and biochemical parameters in gilthead seabream *Sparus aurata*, juveniles. Fish physiology and biochemistry, 20(1): 53-60, 1999

[14] New M. Farming freswater prawns: a manual for the culture of the giant river prawn *Macrobrachium rosenbergii* . FAO (Food and Agriculture Organization) Fisheries Technical Paper 428. Marlow, United Kingdom, 2010.

[15] Tidwell 1994 .

[16] La FAO 2014

[17] Timmons, M.B., and J.M. Ebeling. Aquaculture *Recirculating Aquaculture*, 2010

[18] Tidwell, James H. World Aquaculture Society *Aquaculture Production Systems*, 2012.

[19] Lagerspetz, Kari Y H, and Liisa A Vainio. "Thermal Behaviour of Crustaceans." *Biological Reviews* 81(2): 237–58, 2006 http://www.blackwellsynergy.com/doi/abs/10.1017/S1464793105006998

[20] Vega F. Martínez E. Espinosa L. Cortés M, Nolasco H. Crecimiento y supervivencia del langostino *Macrobrachium tenellum* en cultivos experimentales de verano y otoño en la costa tropical del pacífico mexicano. Tropical and Subtropical Agroecosystems 14:581-588, 2011.

[21] Hernandez Sandoval, P. Efecto de la temperatura en el crecimiento y sobrevivencia del langostino Macrobrachium occidentale y del acocil Cherax quadicarinatus. Tesis de Maestría en Ciencias (Recursos Natruales y Medio Ambiente). Departamento de Acuicultura, Centro Interdisciplinario de Investigación para el desarrollo interal regional, IPN. Sinaloa, México.60p.2008.

[22] Díaz, F., Sierra, E., Denisse, A., & Rodríguez, L. Behavioural thermoregulation and critical thermal limits of *Macrobrachium acanthurus* (Wiegman). K. Thermal Biol., 27(5):423-428. 2002.

[23] Manush, S.A., Pal, A.K., Chatterjee, N., Das, T. & Mukherjee, S.C. Thermal tolerance and oxygen consumption of Macrobrachium rosenbergii acclimated to three temperatures. J. Thermal Biol. 29,15-19, 2004.

CONACYT
Consejo Nacional de Ciencia y Tecnología

CONCYTEQ

A Review of Optimal Truss Structures with real-world costs.

Case: Genetic Algorithms

A. Vera Murillo
División de Investigación y Posgrado de la Facultad de Ingeniería
Universidad Autónoma de Querétaro
Santiago de Querétaro, Qro., México
avera2718@gmail.com

J. M. Horta Rangel
División de Investigación y Posgrado de la Facultad de Ingeniería
Universidad Autónoma de Querétaro
Santiago de Querétaro, Qro., México
horta@uaq.mx

***Abstract*—The structural engineering is closely related with the optimization of the design elements, in order to obtain their minimum cost. The optimal design of a 3D truss structure can be classified in three topics: sizing, configuration and a topology optimization; the obtaining cross area members, the location of the nodes and the connectivity of the members in different configurations respectively. The real-world cost is not a linear relationship between weight and costs, also is needed to take into account the extra cost for choosing many different sections and a complicated constructed topology. The review done in this paper has considered the different proposal of truss's optimizations with Genetic Algorithms (GA's), a point of view of their advantages between themselves and how they consider the real-world costs.**

Keywords—optimizing; truss; genetic algorithm; real-world cost; 3D truss.

I. INTRODUCTION

Engineering is always evolving, and the use of mathematical finite element model's (FEM) is a necessity of all structure's designers nowadays. The efforts used in the improving of the ways of design also, and no less important, seek the optimization in cost of the structures, for this paper only the optimization of truss structures is mentioned.

The primary objective of this investigation is to show the different ways to optimized a truss structure and their efficiency to obtain a minimum cost with real design and constructive situations.

The main discussion is about how the different search made in many papers determine different ways to reduce the cost of the truss structures and how implement their optimizations with real-world costs.

II. OPTIMIZING OF TRUSS STRUCTURES

The Genetic Algorithms are adaptive methods that can be used to solve searching and optimizing problems [1]. Its foundation is in the behavior of the genetic process of the living beings. All the populations, through the time, evolved in the nature according of the principals of natural selection and the surviving of the fittest [2]. Using the last behavior, the GA are available to create solutions that adapt to the problems of the real world.

Since the last decades of the past century, the engineers have used the GA's as a powerful tool for optimum design of structures. There are various techniques to optimizing truss structures, most of them can be classified into three main categories: sizing, configuration, and topology optimization.

In sizing, the cross-section area is a variable to optimize. In configuration, the position of the nodes can be changed in order to obtain the best option. In topology optimization, the connectivity of the members is determined searching an efficient truss, meaning, the algorithm will search the best arrangement of the elements.

In order to optimize the structures with GA, there's the need of associate the objective function (and its parameters) with the state equations, which are the sum of the considerations such as maximum displacements, maximum stress values, slenderness problems, frequencies and dynamic behavior.

For optimizing truss structures, one of the options, for simplicity, is to use as an optimization parameter only the cross-sectional areas of the members [3]. In this study the optimizing of the weight of the truss depends only of one discrete variable (cross-section area member), this one can attain any value from a specified range. For this case, the problem can be simplified for the next equation:

$$Minimize\left\{W(A)=\sum_{i=1}^{Ni}\rho_i L_i A_i\right\} \quad (1)$$

where ρ_i is the density of the material, A_i is the cross-sectional area, and L_i is the length of the ith element. There're two types of constraint conditions, the strength (stress) and the serviceability (deflection). The constraints are an implicit function of the design variables, to overcome the problem, a GA is not enough to solve it, the develop of a hybrid is necessary. For solving the constraint functions, these ones are compute in (FEM), and later, use the results for solving the problem as variables in a conventional GA.

The problem is being optimizing with the consideration of a linear relation between weight and cost. Without considering an extra cost of using different sections, the complexity in the construction-time and the advantages of the hyper-static truss designs.

Considering the truss optimization with the three previous mentioned factors (sizing, configuration and topology optimization) simultaneously is another efficient way to solve the problem [4]. In this way, the problem become one of multi-level one, first is performed a topology optimization, later, member areas and the truss configuration are conduct to an optimization process. These two problems are not linearly separable and don't provide the globally best design. Now the problem need to be solved with a GA applied to three variables in a multi-level solution. The constraints are involved in stress, deflection, and static stability considerations in order to find functionally useful trusses.

In this method, there is an emphasis on the basic nodes, the ones whose must exist in any feasible design, and the use of non-basic nodes whose are added to share the loads and are optional in the design. The important nodes are defining by the designer at the beginning. The goal of the present work is to find which of non-basic nodes are necessary in a truss and its coordinates in order to obtain the minimum truss's weight.

To each member, the algorithm assign it a cross-sectional area, if its area is smaller than a predefine value ξ, that member is assumed to be absent the final truss. The method provides an optimize solution of the problem, a better one that considers only two out of three factors, but has same limit consideration of a linear relation between weight and cost, and the omission of the advantages of a hyper-static truss.

With the purpose of obtain structures at a minimum cost, there're other considerations that imply that there is no lineal relation between cost and truss's weight [5]. These considerations are: the cost on the number of products types used in the design and the addition of the cost of its cross-section to the cost of the weight of the section.

III. REAL COST OF QUANTITY OF DIFFERENT SECTIONS

A real-world cost function is created in a hybrid algorithm

in order to obtain an optimize truss. The method uses the optimization of cross-section area and node's position in a constant topology. In order to use the real-world, cost functions are joined to the hybrid algorithm using a clustering approach, identifying groups of similar sized members and defining all members of the group with a single cross-section area. This method is an addition to other existing techniques of optimizing.

Explicit costs in real-world also depends of the number of different products used in the design. The fabrication cost can be included with the next functions:

$$Total\ cost, T_C = C_m + C_p n_p \quad (2)$$

where np is the number of products and Cp is the cost per product. Cm is the total material cost, evaluated as follows:

$$C_m = n_t \sum_{i=1}^{n} c(p_i) l_i \quad (3)$$

the number of trusses in the structure is named as nt, li it's the length of the member, the numbers of members are defined as n. c(pi) is the cost per unit length of the product pi of the ith member. The calculation of c(pi) is:

$$c(p) = \rho(m_p) A_p c_w(m_p, s_p) \quad (4)$$

where mp represents the material type of product p, p(mp) gives the material density for mp, the cross-section area of product p is Ap, and the cost per unit weigh of the product p is cw(mp,sp). Finding a simple solution of the problem, the use of clustering minimizes the number of products np in the truss.

This method includes some considerations of real-world costs, but doesn't have an algorithm of some restraint of the number of clustering groups. Also, doesn't include a topology optimization and other considerations in order to obtain a truss with a minimum cost.

The applying of optimizing methods can be generalized in various kinds of trusses. An example of this, there are reticular structures forming domes. Domes are defined as structural systems that consist of one or two layers of bar elements which are arched in all directions [6]. In this case, the three main categories are used; sizing, shape (or geometry) and topology optimization.

Optimizing sizing, geometry and topology in a truss structure with some algorithm, the number of resources used in the obtaining of the problem solution can be greater than the one that designer wants to or could afford. For this case Rahami [7] explains a method where the processing time is minimum.

The improve is based on force method to reduce the input variables to make easier and get a considerable help in handling the problem. The formulation of the problem in terms of energy concepts allows the efficient use of an optimization with a GA. With this method, the generation with the GA are reduced with the computational time and the convergence time.

The resources applied in this method could be minimum in comparison with a classic GA method, but don't include the problem of real-world cost, the method just include a minimum cost with a linear relation between cost and weight.

Wang and Ohmori [8] in order to obtain an optimized structure also use GA, but their structures not only resist the

ultimate design forces under ordinary load conditions, also avoid collapse under accidental load conditions such as an extremely large earthquake. In this method first the collapse structure is need to be calculate with an elasto-plastic behavior.

The initial configuration has a ratio of collapse load factor, it is calculated through a elasto-plastic behavior of its elements, considering those members have reached yield stress or buckling stress. The ratio of collapse load factor will be adding to the factor of accidental loads, and with the load combinations increased by the factor of the accidental loads the optimization of the truss can be begun.

The method shown is a general solution of truss structures, with the advantage of having a behavior that can resist a bigger ratio than structures design only for ordinary loads. This consideration result in an expensive design, cause there´s no certain knowledge that the accidental load conditions could be as bigger as the necessary loads to make the structure have a collapse. The use of elasto-plastic analysis in this problem can be changed if the designer use accidental load factors of corresponding structures regulation. But the elasto-plastic behavior is one of the advantages of an hyper-static structure.

Many designers and researchers have optimized the truss structures with GA, using different combinations of three general considerations of optimization (sizing, position of nodes and topology). Jin and De-yu [9] determines topology optimization as a higher-level optimization method as compared with size and shape optimization, and the constraints he uses to solve the topology of truss structures are fundamental frequency, displacement and acceleration responses and the frequency domain, with a minimization of weight as the objective function.

To introduce the objective function, the minimization of (1) is the principal equation. To consider the dynamic behavior, the structural vibration equation based on finite element method can be formulated as follows:

$$[M]\{\ddot{x}(t)\} + [C]\{\dot{x}(t)\} + [K]\{x(t)\} = \{f(t)\} \qquad (5)$$

where [M]: Mass Matrix NxN, [C]: Damping Matrix, [K]: Stiffness Matrix; [N]: Number of degrees of fredom; {f(t)}: Excitation Force Vector, x: Displacement Vector; Derivated x: Velocity Vector; Double derivated x: Acceleration Vector. The excitation Force Vector is the sum of all the forces which are affecting the structure, as wind forces, dead forces, live forces, snow forces, among others.

In the topology optimization, the cross-section areas of removed elements still have a value, a tinny value ξ. But those members with tinny area affect the number and magnitude of natural frequencies. For solving this problem the general structure need to be renumbered and analyzed with the new configuration without the members with tinny areas.

The method can obtain an approach to an optimized truss, but forget the optimization of area section and the position of nodes. With this method, the final product is a truss structure with an excellent dynamic behavior, knowing that may exist a truss structure with a lower weight but worst dynamic behavior. In order to solve this criterion, is need to determine when, or in what relation, the dynamic behavior is better than a lower weight. The method does not consider the real-world costs.

IV. LATTICE TOWER

As a particular case of truss structure's optimization, there is the lattice towers. The lattice tower is a three-dimensional truss structure used in daily life [10]. This towers are commonly used as transmission, wind turbine or communication towers, civil engineering structures, mechanical parts, towers in heliostats fields, among others.

In order to solve the problem of achieving simultaneous topology, shape and sizing optimization of lattice towers, Noilublao and Bureerat [10] use a restricted topology, limited by ground finite elements of a particular tower level, using in each level 8 nodal points and 16 ground elements. The length of elements and the position of the nodes are variables of the optimization process.

With these considerations, the use of efforts to obtain a final structure are less than when topology optimization is not restricted. But the consideration produce the general problem of hasn't a limit of the number of different elements neither a consideration of a practical design. These problems are traduced in mayor structure's cost.

Lattice towers have a hyperstability behavior, because of this behavior, the tower has a mayor global security additional factor for its elasto-plastic material (steel) [11].

These additional factors provide a mayor security of the tower against accidental forces, not having the need of increase the design factors, which result in a better economic final cost.

The common elements for been used in lattice towers are the angles [12], because of its weight and the facilities of their connections. The use of angles has the problem of its three-dimensional behavior buckling, principally when the deformations are big and when the tower has inelastic behaviors. The problems of using angles could increase the maintenance costs.

One of the best advantages of the use of reticular trusses as tower's structures is the behavior of only axial forces in their elements [13]. This behavior provides the optimization of the tower be easier than ones that have flexure bending moments. The problem when the elements of the tower works only with internal axial forces is the effective length of buckling, cause this one affects the compression resistance of the element.

One solution is to add secondary elements to reduce the effective length of buckling. With these secondary elements, the weight of the tower can be reduced, making an optimized structure in weight.

V. CONCLUTIONS

The optimization of the truss structures considering real cost is an important issue in the modern civil engineering, because is essential to take the experimental and theoretical technological advances to use them in the practical field for obtaining lower costs.

The theoretical advances provide truss structures optimized in weight, but if we need to use these configurations in real world, the costs will increase because of the variation of the different sections and the difficulties of build that structures.

There is a need of including real costs factors in the optimization of trusses in order to decrease not only the weight of the structure, either the costs of the construction process.

ACKNOWLEDGMENT

The authors wish to thank to División de Investigación y Posgrado de la Facultad de Ingeniería, Universidad Autónoma de Querétaro, because without its support, this paper could not be possible. And CONACYT (Consejo Nacional de Ciencia y Tecnología) for its support to the Programa Nacional de Posgrados de Calidad.

REFERENCES

[1] Moujahid, A., and I. Inza. 2008. Algoritmos genéticos. Metod. Mat. en Ciencias la Comput. 1–34.

[2] Darwin, C. 1859. El Origen De Las Especies. Uruguayeduca.Edu.Uy. 1–463.

[3] Cheng, J. 2010. Optimum design of steel truss arch bridges using a hybrid genetic algorithm. J. Constr. Steel Res. 66:1011–1017. doi:10.1016/j.jcsr.2010.03.007.

[4] Deb, K., and S. Gulati. 2011. Design of Truss-Structures for Minimum Weight using Genetic Algorithms. Elsevier Sci. Volume 37:Pages 447–465.

[5] Kripakaran, P., A. Gupta, and J. W. Baugh. 2007. A novel optimization approach for minimum cost design of trusses. Comput. Struct. 85:1782–1794. doi:10.1016/j.compstruc.2007.04.006.

[6] Babaei, M., and M. Sheidaii. 2013. Optimal design of double layer scallop domes using genetic algorithm. Appl. Math. Model. 37:2127–2138. doi:10.1016/j.apm.2012.04.053.

[7] Rahami, H., A. Kaveh, and Y. Gholipour. 2008. Sizing, geometry and topology optimization of trusses via force method and genetic algorithm. Eng. Struct. 30:2360–2369. doi:10.1016/j.engstruct.2008.01.012.

[8] Wang, H., and H. Ohmori. 2013. Elasto-plastic analysis based truss optimization using Genetic Algorithm. Eng. Struct. 50:1–12. doi:10.1016/j.engstruct.2013.01.010.

[9] Jin, P., and W. De-yu. 2006. Topology optimization of truss structure with fundamental frequency and frequency domain dynamic response constraints. Acta Mech. Solida Sin. 19:231–240. doi:10.1007/s10338-006-0628-2.

[10] Noilublao, N., and S. Bureerat. 2011. Simultaneous topology, shape and sizing optimisation of a three-dimensional slender truss tower using multiobjective evolutionary algorithms. Comput. Struct. 89:2531–2538. doi:10.1016/j.compstruc.2011.08.010.

[11] Asgarian, B., S. Dadras Eslamlou, A. E Zaghi, and M. Mehr. 2016. Progressive collapse analysis of power transmission towers. J. Constr. Steel Res. 123:31–40. doi:10.1016/j.jcsr.2016.04.021.

[12] Lee, P. S., and G. McClure. 2007. Elastoplastic large deformation analysis of a lattice steel tower structure and comparison with full-scale tests. J. Constr. Steel Res. 63:709–717. doi:10.1016/j.jcsr.2006.06.041.

[13] Prasad Rao, N., and V. Kalyanaraman. 2001. Non-linear behaviour of lattice panel of angle towers. J. Constr. Steel Res. 57:1337–1357. doi:10.1016/S0143-974X(01)00054-2.

CONACYT
Consejo Nacional de Ciencia y Tecnología

CONCYTEQ

Modeling for water transfer and chromium transport through a loamy soil.

Physic-chemistry, hydraulic characteristic and experimental water transfer in column .

Samantha de Jesús Rivero Montejo
Deparment of Chemistry
UAQ
Queretaro, Mexico
Rivermon2014@gmail.com

Carlos Alberto Chavez García
Deparment of Engineer
UAQ
Queretaro, Mexico
chagcarlos@uaq.mx

***Abstract*—The present work describes the effects of the physicochemical (texture, structure, pH, bulk density and porous networks) and hydraulic properties (hydraulic conductivity and moisture retention curve) of a soil matrix on water transfer. The modeling of water flow and chromium transport will be carried out with infiltration experiments applying Richards's equation and advection- dispersion equation. This study examined the relationship between the infiltration experiments in columns packed with a loamy soil during various periods of time of 3.5, 9.45 and 12.30 hr. The aim of this research was to determine the hydraulic properties for the inverse method performing infiltration tests.**

Keywords—physicochemical properties, hydraulic properties, modeling, infiltration experiments

I. INTRODUCTION

Soil is a matrix that performs functions of great importance such as food production, part of the cycle of the formation of elements on the surface of the earth, minimizes the environmental impact, acts in the degradation of components of anthropological waste, and as a sustenance for the living organisms. It also carries out anthropological functions such as physical support (housing, industry, roads), recreational, agricultural and forestry activities [1] [11].

The soil has the ability to cushion or deactivate natural pollutants, filters, stores, degrades, neutralizes and immobilizes toxic organic and inorganic substances, preventing them from reaching groundwater and air or entering the food chain [7]. When toxic substances exceed the adsorption capacity of the soil, contamination is generally caused by pesticides, fertilizers and heavy metals such as cadmium, lead as well as chromium [9]. This properties are very important in the attenuation of heavy metals in the environment [8]. Their mobility and subsequent leaching towards groundwater, depends on the physical or chemical characteristics such as texture, organic matter content, inorganic matter, cation exchange capacity, pH and humidity, which determine the interactions with the metal [3][10].

The ability to predict the movement of water and solutes through soil horizons requires the integration of variables, as well as the description and analysis to determine parameters such as the retention time of a pollutant in the soil, conversion potential Biochemistry and the risk of contaminating the underground water [12]. Due to this, the infiltration of the water, its direction and transport time in the profile of the matrix in the saturated zone has been the reason for the analysis of transfer phenomena and transport processes. For the above, we have applied, on a macro scale, mathematical models that use differential equations of balance in a time and space not located, in which the porous medium is considered a continuous medium and using variables and parameters representative of these properties [2][4]

In the study of water movement rational equations have been used to describe soil surface movement and infiltration. The infiltration is modeled with numerical or analytical solutions from the Richards equation. These solutions are obtained by assuming a semi-infinite column of soil with a constant initial moisture content throughout [5].

For modeling water movement, it is of great importance to take into account hydraulic properties such as the hydraulic conductivity and the moister retention curve. The hydraulic conductivity (K) is a fundamental characteristic in the modeling of water flow and contaminant transport in soil and sediment which is easy measurable from parameters such as bulk density, porosity, particle diameter, texture, etc. and can be affected not only by—these parameters but also by the sample dimension and the experimental parameters [6]. Therefore the aim of this preliminary study was to determine

the physicochemical and hydraulic properties of the soil collected from San Juan del Rio, Queretaro for the estimation of the parameters that would be use at the modeling of the water flow and chromium transport in soil.

II. Materials and methods

This study was performed considering the physicochemical and hydraulic properties (Hydraulic conductivity) in the packed soil columns for a loamy soil which will be used in the modeling of water flow and chromium transport in soil.

A. Description of the study site

The study was conducted using soil from San Juan del Río, Querétaro, Mexico. The studied soil comes from an agriculture site with a mild semi-dry climate. For this study a sample of 20 kg of soil was collected and dried at room temperature for approximately two days. Later the dried soil was sieved with a 2mm sieve.

B. Physicochemical properties

Physicochemical analyzes were conducted to determine pH, electrical conductivity, organic matter content, bulk density, cation exchange capacity (ECC) and soil texture according to the NOM-021-SEMARNAT-2000 for soil.

To determine the pH of the soil, the supernatant suspension obtained by mixing soil and water in a 1: 2 ratio was examined using an electrode for pH. The texture of the soil was determined by granulometric analysis with Bouyoucos hydrometer, where the percentage of clay, silt and sand present in the mineral fraction of the soil were obtained. The moisture content was determined by the gravimetric method. The bulk density of the soil was performed by the AS-03 method according by the NOM-021-SEMARNAT-2000.

The amount of organic matter (MO) was determined by the Walkeley and Black method. The determination of the electrical conductivity was performed using a saturation extract of soil. The cation exchange capacity was determined using ammonium acetate to saturate.

The determination of the texture and granulometric curve was obtained by the procedure of Bouyucos through the method AS-09 following the norm NOM-021-SEMARNAT-2000.

C. Column experimentation

For the infiltration experiments a 200 ppm chromium solution was used (Hycel standard with tridestilade water). During the experiment, the infiltration time was registered after each 0.5 cm of volume was filtered through the soil.

Columns experiments were performed in acrylic columns with a 5.8 cm of diameter, 14 cm height divided in four sections (three sections of 2 cm and one section at 8 cm height). Each section was taped and wax at the interior of the cylindrical column. The feed was supplied in manual form using an initial volume of 123.1 ml that is equal to 5 cm of chromium solution at 200 ppm. The study used three columns packed with 269.9 g the bulk density (Table 1) to the 8 cm height.

The infiltration experiment was performed following the time of the first column, duplicated the time for the second column and triplicate the time for the constant regimen. After finishing the constant regimen, a variable regimen was applied.

III. Results

Physicochemical properties, hydraulic conductivity and de infiltration experimental presented has been conducted with the purpose of modeling the water transfer and chromium transport in soil.

A. Soil properties

Physicochemical characteristics for a loamy soil (Table 1) can describe some qualities of the chromium transport. This properties can be used for the modeling as they can modify the transport. The chromium transport can be affected by the pH. While an acid pH accelerate the transport a basic pH decreases it. The texture and organic matter content can provide other important factors due the clay-solute complexation.

TABLE I. Physical-chemistry properties of a loamy soil

Physicochemical characteristics		
Characteristics	***value***	***United***
pH	6.38	
Texture	Loamy	
Gravimetric moisture content	0.0034	%
Bulk density	1.37	gcm^{-3}
Organic matter content	1.87	%
Cation exchange capacity (ICC)	11.18	meg $100g^{-1}$
Electric conductivity	0.12	dS m^{-1}

B. Granulometric curve

Figure 1 shows the results obtained from the granulometric test, from which the experimental data was applied to the Fuentes (1992) equation for large pore, neutral pore and a geometric mean. For the modeling the geometric mean will be used. From the gravimetric test were obtained the parameters D_d, m and n (Table 2) used in the simulations for water flow and solute transport were obtained

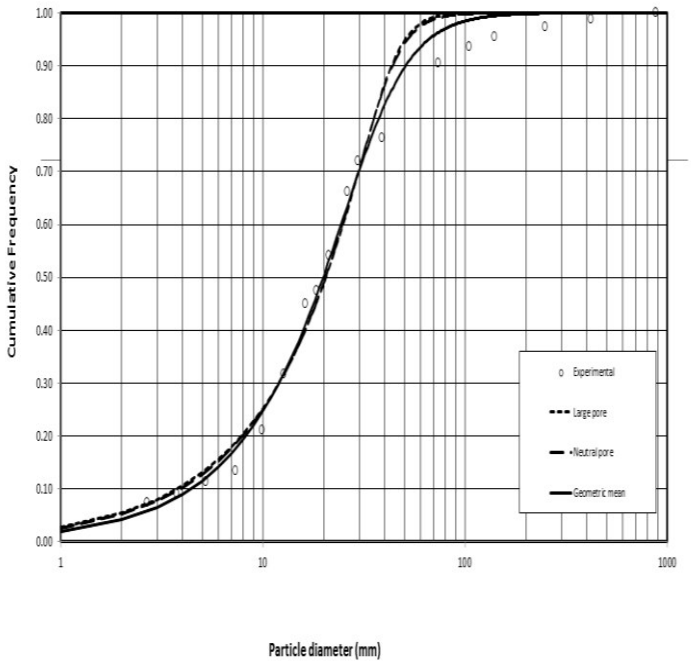

Fig. 1. Granulometric curve : experimental, large pore, nuetral pore and geometrical mean

The equation realized by Fuentes (1992), applied to porous for describing a fractal equation, can be used to obtained the parameters mention D_d and m and n

TABLE II. FORM PARAMETERS

particle characteristics			
Parameters	***Experimental***	***neutral***	***Geometrical mean***
D_d	42.389 µm	41.348 µm	35.086 µm
m	0.1646	0.1896	0.3692
n	3.5754	3.1788	1.8540

The granulometric curve was used to determine the soil texture and the percentage of clay, sand and silt (Table 3) and the percent that conform the texture soil according to the USDA classification

TABLE III. TEXTURE SOIL

Texture characteristics	
Clay and silt	77.6667 %
Sand	22.3333 %
Clay	8 %
Silt	69.6667 %

This information provided the interaction between the soil and the chromium and the mechanism that occurs with the clay present in the soil and the pollutant.

C. Columns experiments

The columns infiltration experiments were conducted by the first column infiltration time and was the double time of the first column for the second column and the triple time for the third column resulting in the Fig 2, Fig 3 and Fig 4

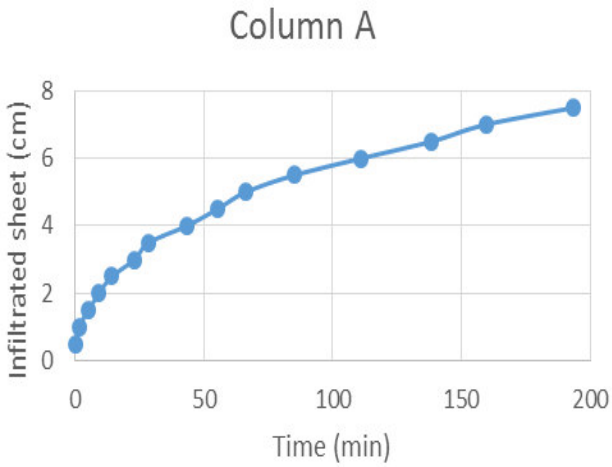

Fig. 2. Infiltration curve: column A (First column)

In the Fig. 2 is represented the infiltrated sheet accumulated in the infiltration experimental and this column determined the time for the infiltration for the second and third column being the time of 196 minutes of infiltration approximately.

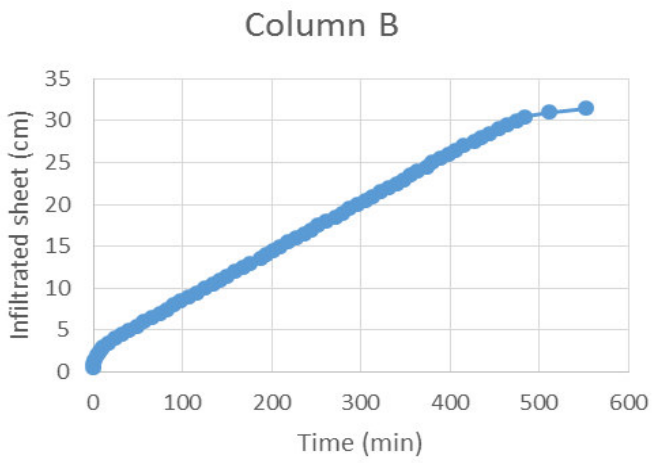

Fig. 3. Infiltration curve: column B (Second column)

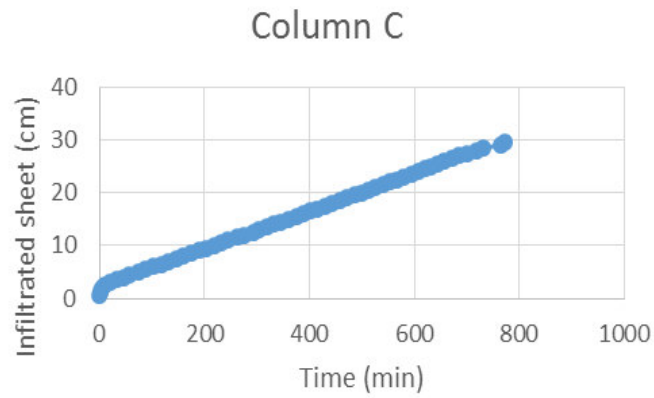

Fig. 4. Infiltration curve: column C (Tird column)

Using the information obtained by experimental infiltration, the water flow model will be made. This infiltration experiment proportioned data to estimate the hydraulic conductivity and the quadratic error using the infiltrated sheet and the infiltration time. Also this information will be applied to the inverse method using Richards' s equation.

IV. Conclusion

In this study the physicochemical properties of a loamy soil and the possible interactions with the chromium were investigated using as reference bibliography and the information obtained.

The infiltration experiments were used to obtain the characteristic presión (ψ_d) and the hydraulic conductivity (Ks) applied to an inverse method for Richard´s that have been previous programed. Also this experiment will be used in the simulation of the advection-dispersion for chromium.

The inverse method applied to the water transference will performance using a Dirichlet as upper border and the Newmann as the lower border.

Acknowledgment

We are grateful to the students in the master's degree in Environmental Science and Technology and express our gratitude to Gabriela Robles, Alejandra Contreras and Isaac Aguilar Clemente for providing support in this study. We would also like to express our acknowledgment to the Autonomous University of Queretaro, Campus Airport for the facilities provided during the experimental study and the CONACYT institution for the graded support.

References

[1] Bohn, Hinrich L.; Myer, Rick A.; O'connor, George A. *Soil chemistry*. John Wiley & Sons, 2002. Tird edition. Pp 17, 26-27, 29, 54-56, 59.

[2] Davit, Yohan, et al. Correspondence between one-and two-equation models for solute transport in two-region heterogeneous porous media. *Transport in porous media*, 2012, vol. 95, no 1, p. 213-238.

[3] De Jonge, Lis Wollesen; Moldrup, Per; Schjønning, Per. Soil Infrastructure, Interfaces & Translocation Processes in Inner Space (" Soil-it-is"): towards a road map for the constraints and crossroads of soil architecture and biophysical processes. *Hydrology and Earth System Sciences*, 2009, vol. 13, no 8, p. 1485-1502

[4] Du, Y.-J., et al. Impacts of presence of lead contamination in clayey soil–calcium bentonite cutoff wall backfills. *Applied Clay Science*, 2015, vol. 108, p. 111-122.

[5] Fuentes, Carlos; Chávez, Carlos; Zataráin, Feline. Una solución analítica de la infiltración en un suelo con manto freático somero: aplicación al riego por gravedad. *Tecnología y ciencias del agua*, 2010, vol. 1, no 3, p. 39-49.

[6] Ghanbarian, Behzad; Taslimitehrani, Vahid; Pachepsky, Yakov A. Accuracy of sample dimension-dependent pedotransfer functions in estimation of soil saturated hydraulic conductivity. *CATENA*, 2017, vol. 149, p. 374-380.

[7] Ortiz-Bernad, Irene, et al. Resistance of solid-phase U (VI) to microbial reduction during in situ bioremediation of uranium-contaminated groundwater. *Applied and environmental microbiology*, 2004, vol. 70, no 12, p. 7558-7560.

[8] Sherene, T. Mobility and transport of heavy metals in polluted soil environment. En *Biological Forum—An International Journal*. 2010. p. 112-121

[9] Sparks, Donald L. *Environmental soil chemistry*. Academic press, 2003. USA. Second edition. Pp 3-4, 13-16.

[10] US Department of Health and Human Services, et al. Agency for Toxic Substances and Disease Registry. 2007. *Case Studies in Envionmental medicin-Lead*

toxicity. ATSDR Publication ATSDR-HE-CS-2001-0001, 2007

[11] Volke, S.T., Velasco, T.J.A., de la Rosa, P.D. Suelos contaminados por metales pesados y metaloides: muestreo y alternativas para su remediación, 2005. Instituto Nacional de Ecología. SEMARNAT. México, 1a edition D.F. Pp 80-88,120, 144

[12] Zerihun, D., et al. Coupled Surface–Subsurface Solute Transport Model for Irrigation Borders and Basins. I. Model Development. *Journal of irrigation and drainage engineering*, 2005, vol. 131, no 5, p. 396-406

CONACYT
Consejo Nacional de Ciencia y Tecnología

CONCYTEQ

UNIVERSIDAD AUTÓNOMA DE QUERÉTARO
13° CONGRESO INTERNACIONAL DE INGENIERÍA
15th-19th MAY 2017

SHM Vibration-Based Damage Identification Methods using Frequency Response Function

Juan Bernardo Martinez
Facultad de Ingeniería
Universidad Autónoma de Querétaro
Santiago de Querétaro, México
Jmartinez217@alumnos.uaq.mx

Suresh Thenozhi
Facultad de Ingeniería
Universidad Autónoma de Querétaro
Santiago de Querétaro, México
Sureshtalr@gmail.com

***Abstract*— Damage Identification using Frequency Response Function (FRF) has been proved to be an excellent resource for damage estimation and identification, new methods and techniques had been developed from the last 10 years which hasn't been reviewed, we summarizes the most recent methods for feature extraction on the FRF and the Tools used for damage identification, focusing in FRF from vibration-based measured or simulated values of a Linear Model.**

Keywords*— *Damage Detection Methods, Techniques, Structural Integrity, Structure Health Monitoring, SHM, Vibration-Based Methods, Frequency Response Function, Frequency Domain

I. Introduction

Structural Health Monitoring (SHM) diagnosis of the state of materials, different elements and of the full assembly or these parts constituting the structure as a whole. The state of the structure must remain as specified in the design, although this can be altered by normal aging due to usage. By the action of the environment, and by accidental events. SHM is an improved way to make a Non Destructive Evaluation. These technologies are currently becoming more and more common. SHM refers to the broad concept of assessing the ongoing, in structures using a variety of measurement techniques. The SHM process involves a good amount of Techniques and methods to carry out the process of SHM one kind. In the actuality there has been plenty of researchers working in this subject which shows the great interest among the researchers in developing new techniques and methods for damage detection in SHM in order to improve and get better approximation and precision for damage detecting, still there is a lack of recent reviews in this matter most of the reviews cover from before 10 years from now [1]–[3] recollecting the most recent work regarding in Damage Detection using FRF.

II. SHM Based On Frequency Response Function

A. *Frequency Response Function.*

The FRF is a transfer function, expressed in the frequency-domain. FRFs are complex functions. They may be represented in terms of magnitude and/or phase. A FRF can be formed from either measured data or analytical functions. A FRF expresses the systems response to an applied force as a function of frequency. The response may be given in terms of acceleration, velocity or displacement. The FRF it expressed mathematically in (1):

$$\{X(\omega)\} = [H(\omega)]\{F(\omega)\} \tag{1}$$

Where $\{X(\omega)\}$ is the Output if the System, $[H(\omega)]$ is the FRF Matrix and $\{F(\omega)\}$ is the input force in the frequency domain, The FRF matrix represents the system frequency response characteristic[4].

The presence of structural damage leads to the changes in dynamic characteristics of the structure itself such as the vibration responses, natural frequencies, mode shapes. Therefore, the changes in dynamic characteristics of a structure can be used in turn to detect, locate and quantify the structural damage [5]–[7].1 In the literature, there have been appeared a variety of structural damage identification methods. Some of these methods uses the FRF of the Structure, using measured FRFs may have certain advantages over using modal data. For example, the FRFs are less contaminated because they are directly measured from structure, the FRFs can provide much more information on damage in a desired frequency range than modal data are extracted from a very limited number of FRF data around resonance [9]. Thus the use of FRFs which are usually the most compact form of data obtained from vibration test seems very promising for damage detection [10]

B. Vibration-based methods

Vibration-based methods are perhaps the most common methods used for damage detection, they represent the actual measured data from the structure from which we can obtain the FRFs to estimate the changes in the system's modal properties [11]–[13]. The basic concept of the vibration based damage identification methods is that the dynamic behavior of a structure can change if damage occurs. Damage in a structure can alter the structural integrity, and therefore, the physical properties like stiffness, mass and/or damping may change. The dynamic behavior of a structure is a function of these physical properties and will, therefore, directly be affected by the damage. The changes in these parameters (or properties derived from these parameters) are used as indicators of damage, if there is any change in the material of the structure[14]. For instance if there is any addition in mass to the structure it will vibrate differently, the motion equation of the structure can be defined with a multiple-degree-of-freedom (DOF) systems as shown in equation (2) in where $\boldsymbol{M}$ represents Mass, $\boldsymbol{C}$ the damping, $\boldsymbol{K}$ the stiffness of the structure and $\boldsymbol{f}(t)$ is an input force.

$$\boldsymbol{M}\ddot{\boldsymbol{x}}(t) + \boldsymbol{C}\dot{\boldsymbol{x}}(t) + \boldsymbol{K}\dot{\boldsymbol{x}}(t) = \boldsymbol{f}(t) \tag{2}$$

There are techniques in which knowing the FRF it can be determined if there's any changes in any of these parameters[15].which are translated to damage in certain elements of the structure according to the magnitude and location. Vibrations Based testing has become a very common test to obtain data of a structure due to its efficiency and it low cost implementation.

III. Vibration-based FRF Damage detection Methoods

There are many methods and techniques regarding the damage detection using FRF, using Vibration-Based test, these FRF can be easily acquired using accelerometers or other sensor this data it used for creating the FRF, regarding the measure it's the method for to be used. The principal root behind structural damage detection techniques is in the vibration response of the structure for example, the modal properties or the FRF data are sensitive indicators of structural integrity[9]. However the feasibility of using FRF changes is limited due to these reasons. (i) Damage in the structure which create small changes in the FRF and consequently will requires very precise instruments to be detected or measured, There are a large number of studies regarding the development of new sensors and sensing systems for SHM application. In particular there are significantly more studies on the use of fiber optic sensors [16] and wireless acquisition systems [17]. (ii) Significant damage may cause very small changes in the FRF, particularly for large structures, therefore theses change may be undetected due to measurement errors (iii) inability to distinguish damage at symmetrical locations in a symmetric structure and (iv) natural frequencies are easily affected by the environment, changes such as temperature of humidity fluctuations. Hence the use of natural frequencies alone in damage can lead to unrealistic predictions [14], [18]

A. Frequency Shift

Some authors measure the frequency shift in the systems or structures to determine the existence of damage in their corresponding structures in [19] measures the FRF and detects the shifts of frequency to identify damage in a railway depending of the magnitude of the shift it can be determined what kind of damage is, also determines the location of the damage, there are some other authors who also uses the frequency shift for other structures[20], [21].

B. Using Transmissibility Matrix

A damage identification approach based on dynamic response reconstruction in the frequency domain is proposed with numerical and experimental verifications. The response reconstruction is based on transforming the measured responses into responses at other nodes or locations of the structure using the transmissibility matrix, damage identification is achieved by minimizing the difference between a measured response vector and the reconstructed response vector with these it can be determined in which node the exist such damage [4], [22], [23].

C. Mode Shape and Mode Curvature.

Changes in mode shapes are much more sensitive to local damage when compared to changes in natural frequencies [24]. An alternative to mode shapes is to use mode-shape derivatives, such as curvature. Mode-shape curvatures can be computed by numerically differentiating the identified mode-shape vectors twice to obtain an estimate of the curvature. These methods are motivated by the fact that the second derivative of the mode shape will be much more sensitive to changes in the system than the mode shape itself, also in certain structures this mode-shape curvatures can be defined as changes in strain energy which has been known to be a sensitive indicator of damage [25], [26]

IV. Damage Detection tools

In the SHM systems exist many tools used for the analysis of the data gathered in order to determine if there is or not a damage in certain structure, some of these are mention in past reviews [27] some of the recent work embraces metaheuristic algorithms such as Artificial Neural networks (ANNs), this kind of tools have been of great interest among the researches due to its high performance in computational efficiency [28], Some of the ANN applied in Vibration-Based Damage detection or SHM are mention in past reviews [29]

A. Artificial Neural Network

One of the soft computing techniques existing, are neural networks which have been utilized increasingly for damage identification due to their excellent pattern recognition[30], the FRFs are introduced in a train neural network to determine the damage in the structure [10] There are author which combine methods and techniques for obtaining more precise damage detections such as probabilistic theorems in cases when it can be obtained a whole set of data [31]. There are also other type of Neural Networks to obtain more precise damage detection like feed-forward neural network or convolutional neural network (CNN) [32].

B. Correlation

Many authors uses correlation and their variants to determine the existence of damage, Cross Correlation is used in is a measure of linear relationship between two waveforms, while a time-lag function is applied to one of them. One can potentially see a drop in correlation magnitude between the data sets as well as a lag or lead in the position of the largest magnitude correlation. in [33] uses Autocorrelation to determine the existence of crack in a beam type structure it is available to determine the size of the crack by using the autocorrelation function, other variant Cross Correlation which is a measure of linear relationship between two waveforms in its applied to the FRF and compared with a baseline to detect damage in wind turbine blades. Exist methods which uses the Correlation as based to create Damage Location Assurance Criteria (DLAC) which is a correlation based approach between vectors of experimental natural frequency change ratios with vectors of analytical natural frequency change ratios these are correlated for damage detection in [34] The relative change system response before and after damage occurs in the structure is adopted as the damage index to show the damage location.

C. Wavelet Transformation.

Other powerful tool for signal analysis used in damage detection on the FRFs measurements is the Continuous Wavelet transformation known as CWT authors use these tool to determine the existence of damage in structures [35], [36] other authors uses variation of the Wavelet Transformation like the Cauchy Wavelet Transformation. [37]. Or the discrete Wavelet transformation (DWT) these tools shown a promising in damage detection, hardly they are very sensitive to noise.

D. Principal Component Analysis.

The measurement of the FRF directly from the structures leads to polluted signals with noise, still with modern sensors the noise is inevitable. An important aspect of damage detection research is how to distinguish the abnormal response variation due to damage from the normal response. Difference between the baseline of the intact structure and the response of the damaged structure will be used as an indicator for damage occurrence, the principal component analysis (PCA)[6], [38] for simultaneous de-noising and feature extraction has been applied for SHM process. First the baseline responses of an intact structure are recorded. Then, PCA is employed to find the principal components (PCs) of the baseline. Usually, only a few PCs are needed to establish the feature space to characterize the variation in baseline responses, these components are the baseline of the intact structure. The reconstructed FRF of an intact structure, which features are the same as those of the baseline, will show high degrees of similarity with the baseline. On the other hand, the FRF principal components of a damaged structure, whose characteristic had been changed due to the damage will lead to a high degree of discrepancy between the baseline of the intact structure, in [39] this method is highly measured to be analyzed.

V. Conclusions

SHM has been briefly reviewed in this paper, we can observe that this subject is the center of attention of many researcher efforts, it has been studied since the 80's to our actual time, and still can be improved in the accuracy of the methods, these methods and techniques are applied to linear models, or lineal approximation there still research regarding to the Non Linear Characteristics of the Model, as we know damping is a Highly Non Linearity in the Structures, matters like these suggest that analyzing the responses of these parameter may conclude with damage detection more precisely.

References

[1] C. Study, "Vibration-based Damage Identification Methods: A Review and Comparative Study," *Struct. Heal. Monit.*, vol. 10, no. 1, pp. 83–111, 2010.

[2] E. P. Carden, "Vibration Based Condition Monitoring: A Review," *Struct. Heal. Monit.*, vol. 3, no. 4, pp. 355–377, 2004.

[3] H. Sohn, C. R. Farrar, F. Hemez, and J. Czarnecki, "A Review of Structural Health Monitoring Literature 1996 – 2001," *Third World Conf. Struct. Control*, no. DECEMBER, pp. 1–7, 2002.

[4] S. S. Law, J. Li, and Y. Ding, "Structural response reconstruction with transmissibility concept in frequency domain," *Mech. Syst. Signal Process.*, vol. 25, no. 3, pp. 952–968, 2011.

[5] H. Y. Hwang, "Identification Techniques of Structure Connection Parameters Using Frequency Response Functions," *J. Sound Vib.*, vol. 212, no. 3, pp. 469–479, 1998.

[6] R. P. Bandara, T. H. T. Chan, and D. P. Thambiratnam, "Frequency response function based damage identification using principal component analysis and pattern recognition technique," *Eng. Struct.*, vol. 66, pp. 116–128, 2014.

[7] U. Lee and J. Shin, "A frequency response function-based structural damage identification method," *Comput. Struct.*, vol. 80, no. 2, pp. 117–132, 2002.

[8] S. W. Doebling, C. R. Farrar, M. B. Prime, and D. W. Shevitz,

"Damage Identification and Health Monitoring of Structural and Mechanical Systems from Changes in Their Vibration Characteristics: A Literature Review," *Library (Lond).*, no. February 2017, 1996.

[9] Z. Wang, R. M. Lin, and M. K. Lim, "Structural damage detection using measured FRF data," *Comput. Methods Appl. Mech. Eng.*, vol. 147, no. 1, pp. 187–197, 1997.

[10] R. P. Bandara, T. H. T. Chan, and D. P. Thambiratnam, "Frequency response function based damage identification using principal component analysis and pattern recognition technique," *Eng. Struct.*, vol. 66, pp. 116–128, 2014.

[11] B. J. Schwarz and M. H. Richardson, "Experimental Modal Analysis," *CSI Reliab. Week*, vol. 35, no. 1, pp. 1–12, 1999.

[12] H. Packard, "The fundamentals of modal testing," *Methods*, pp. 1–56, 1997.

[13] J. He and Z.-F. Fu, "Modal Analysis," *Modal Anal.*, vol. 117, no. 10, p. 291, 2001.

[14] A. Zare Hosseinzadeh, G. Ghodrati Amiri, S. A. Seyed Razzaghi, K. Y. Koo, and S. H. Sung, "Structural damage detection using sparse sensors installation by optimization procedure based on the modal flexibility matrix," *J. Sound Vib.*, vol. 381, pp. 65–82, 2016.

[15] M. Salavati, "Approximation of structural damping and input excitation force," *Front. Struct. Civ. Eng.*, 2017.

[16] H. Guo, G. Xiao, N. Mrad, and J. Yao, "Fiber optic sensors for structural health monitoring of air platforms," *Sensors*, vol. 11, no. 4. pp. 3687–3705, 2011.

[17] J. P. Lynch, "An overview of wireless structural health monitoring for civil structures.," *Philos. Trans. A. Math. Phys. Eng. Sci.*, vol. 365, no. 1851, pp. 345–72, 2007.

[18] L. Wang, X. Zhou, H. Liu, and W. Yan, "Damage detection of RC beams based on experiment and analysis of nonlinear dynamic characteristics," *Constr. Build. Mater.*, vol. 29, pp. 420–427, 2012.

[19] L. Wang, Y. Zhang, and S. T. Lie, "Detection of damaged supports under railway track based on frequency shift," *J. Sound Vib.*, vol. 392, pp. 142–153, 2016.

[20] L. Wang, S. T. Lie, and Y. Zhang, "Damage detection using frequency shift path," *Mech. Syst. Signal Process.*, vol. 66–67, pp. 298–313, 2016.

[21] R. P. C. Sampaio, N. M. M. Maia, R. A. B. Almeida, and A. P. V Urgueira, "A simple damage detection indicator using operational de fl ection shapes," *Mech. Syst. Signal Process.*, vol. 72–73, pp. 629–641, 2016.

[22] J. Li, S. S. Law, and Y. Ding, "Substructure damage identification based on response reconstruction in frequency domain and model updating," *Eng. Struct.*, vol. 41, pp. 270–284, 2012.

[23] R. de Medeiros, M. Sartorato, D. Vandepitte, and V. Tita, "A comparative assessment of different frequency based damage detection in unidirectional composite plates using MFC sensors," *J. Sound Vib.*, vol. 383, pp. 171–190, 2016.

[24] X. Liu, N. A. J. Lieven, and P. J. Escamilla-Ambrosio, "Frequency response function shape-based methods for structural damage localisation," *Mech. Syst. Signal Process.*, vol. 23, no. 4, pp. 1243–1259, 2009.

[25] C. R. Farrar, S. W. Doebling, and D. A. Nix, "Vibration-based structural damage identification," *Philos. Trans. R. Soc. A.*, vol. 359, pp. 131–149, 2001.

[26] J. T. Kim, Y. S. Ryu, H. M. Cho, and N. Stubbs, "Damage identification in beam-type structures: Frequency-based method vs mode-shape-based method," *Eng. Struct.*, vol. 25, no. 1, pp. 57–67, 2003.

[27] C. Farrar and M. B. Prime, "A Summary Review of Vibration-Based Damage Identification Methods," no. February 2017.

[28] U. Dackermann, J. Li, and B. Samali, "Identification of member connectivity and mass changes on a two-storey framed structure using frequency response functions and artificial neural networks," *J. Sound Vib.*, vol. 332, no. 16, pp. 3636–3653, 2013.

[29] S. Hossain, O. Zhi, Z. Ismail, and S. Noroozi, "Artificial neural networks for vibration based inverse parametric identifications : A review," *Appl. Soft Comput. J.*, vol. 52, pp. 203–219, 2017.

[30] L. Niu and L. Ye, "Use of Neural Networks in Damage Detection of Strutures," *2009 Int. Conf. Electron. Comput. Technol.*, pp. 258–261, 2009.

[31] K. H. Padil, N. Bakhary, and H. Hao, "The use of a non-probabilistic artificial neural network to consider uncertainties in vibration-based-damage detection," *Mech. Syst. Signal Process.*, vol. 83, pp. 194–209, 2017.

[32] O. Abdeljaber, O. Avci, S. Kiranyaz, M. Gabbouj, and D. J. Inman, "Real-time vibration-based structural damage detection using one-dimensional convolutional neural networks," *J. Sound Vib.*, vol. 388, pp. 154–170, 2017.

[33] L. Montanari, A. Spagnoli, B. Basu, and B. Broderick, "On the effect of spatial sampling in damage detection of cracked beams by continuous wavelet transform," *J. Sound Vib.*, vol. 345, pp. 233–249, 2015.

[34] V. Mohan, S. Parivallal, K. Kesavan, B. Arunsundaram, A. K. F. Ahmed, and K. Ravisankar, "Studies on Damage Detection Using Frequency Change Correlation Approach for Health Assessment," *Procedia Eng.*, vol. 86, pp. 503–510, 2014.

[35] J. Xiang and M. Liang, "Wavelet-Based Detection of Beam Cracks Using Modal Shape and Frequency Measurements," *Comput. Civ. Infrastruct. Eng.*, vol. 27, no. 6, pp. 439–454, 2012.

[36] V. Shahsavari, L. Chouinard, and J. Bastien, "Wavelet-based analysis of mode shapes for statistical detection and localization of damage in beams using likelihood ratio test," *Eng. Struct.*, vol. 132, pp. 494–507, 2017.

[37] C. S. Huang, C. Y. Liu, and W. C. Su, "Application of Cauchy wavelet transformation to identify time-variant modal parameters of structures," *Mech. Syst. Signal Process.*, vol. 80, pp. 302–323, 2016.

[38] J. Li, U. Dackermann, Y. Xu, and B. Samali, "Damage identification in civil engineering structures utilizing PCA-compressed residual frequency response functions and neural network ensembles," no. December 2009, pp. 207–226, 2011.

[39] J. Tang, "Frequency response based damage detection using principal component analysis," *2005 IEEE Int. Conf. Inf. Acquis.*, pp. 407–412, 2005.

UNIVERSIDAD AUTÓNOMA DE QUERÉTARO

13° CONGRESO INTERNACIONAL DE INGENIERÍA

15th-19th MAY 2017

CONACYT
Consejo Nacional de Ciencia y Tecnología

CONCYTEQ

Energy analysis in a non-stable state of a solar receiver provided by solar energy to vaporize water

A. K. Vega Rodríguez, C. S. Lora Pérez
Facultad de Ingeniería, Universidad Autónoma de Querétaro; UAQ.
Santiago de Quéretaro, México
e-mail: a.karen.vr@gmail.com

J. C. Jáuregui Correa
Facultad de Ingeniería, Universidad Autónoma de Querétaro; UAQ.
Santiago de Quéretaro, México
e-mail: jc.jauregi@uaq.mx

***Abstract*— The losses of energy in a solar receiver are variants. Throughout the day's and throughout the year, is common, that in the thermosolar systems are useded support systems for heating. However it's possible to perform an analysis that allows us to know the behavior of the fluid along its passage by the receiver, as a function of time, of the insidious radiation in the receiver, the wind speed and the ambient temperature, with the aim of minimizing the amount of fossil energy used for the auxiliary heating of the fluid. To carry out this analysis it is necessary to contemplate all possible losses (however minimal there are) within the receiver. The expressions obtained in this study allow us to know the thermal behavior of the solar receiver and of the fluid flowing in it.**

Keywords—non-stable; solar; receiver, energy; analysis.

I. INTRODUCTION

A solar receiver is often defined as a heat exchanger that takes advantage of solar radiation (direct, diffuse or from a concentrator), with the purpose of converting it into thermal energy, which will be exploited by a fluid that circulates inside the receiver. The main applications of the fluid depend on the temperature range that can reach its passage through the receiver. If the temperature is less than 373K [1], its main applications are the heating of water and air for domestic use, or drying processes for agricultural and industrial use; If the temperature has a value between 373K and 573K, its applications are in processes that demand thermal energy, or rather heat; Finally, if the fluid reaches temperatures higher than 573K, it will be used for the generation of electric energy.

The operation of the solar receiver depends on the amount of solar radiation that affects it; therefore, the operation of the solar receiver is affected by environmental conditions and is limited to those hours where it is possible to take advantage of solar radiation [2]. Here are some factors that limit the use of solar radiation:

- Time of the day
- Day of the year
- Environmental temperature
- Wind speed
- Cloud Cover
- Angle of incidence of solar radiation

II. MATHEMATICAL MODEL FOR THE RECEIVER

The mathematical model proposed is based on energy balances for each component of a flat rectangular receiver (Fig. 1). The solar receiver consists of an absorption plate, which receives solar radiation, a part of the energy it receives is lost by convection and radiation from the plate to the environment, the rest of the energy it receives is transferred by conduction and convection from the upper surface of the absorber plate to the fluid circulating inside the solar receiver. The fluid gives a certain amount of energy to the internal surface of the plate in the background, this energy is transferred by conduction to the outer surface of the plate and to avoid losses of energy from the plate in the background with the environment is used a thermal insulation.

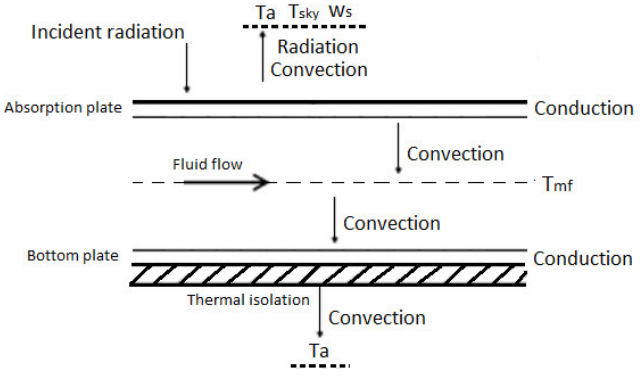

Fig. 1. Schematic design for the balance of energy in the receiver.

Conditions for model:

- Non-stable state.
- Heat conduction is considered through the walls of the manifold.
- The plate in the bottom is thermally insulated.
- The upper plate receives diffuse and direct radiation from the heliostats.
- They are considered lost by mixed convection and emission.
- The lateral sides of the collector are considered adiabatic

Figure 2 shows the resistance to the passage of energy, from a region of the environment, covering the upper surface of the absorber plate, to the thermal insulation on the outer surface of the plate in the bottom.

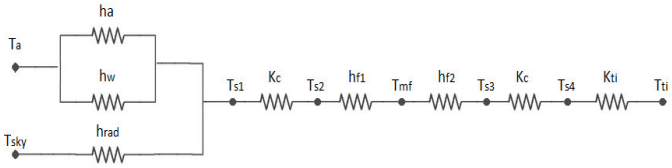

Fig. 2. The resistance analogue illustrating the recipe model.

The fluid circulating inside the receiver is confined between two plates at different temperatures, as shown in Figure 3. This temperature difference (between the internal surfaces of the plates and the fluid) generates a thermal boundary layer, in addition to a thermal condition is not developed because the energy flow entering the receiver is not constant and may not be enough just to be carried evaporation of the fluid also may present an unstable flow condition (cell fluid flow), [3].

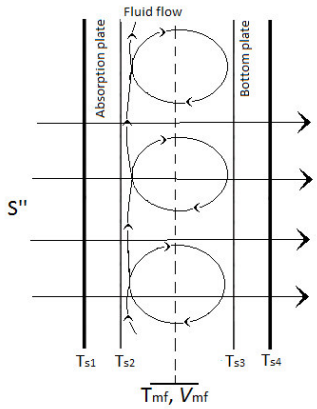

Fig. 3. Cell fluid flow.

The properties of the fluid (pressure, temperature and mass flow) are known at the receiver's input, however, as the fluid circulates inside the receiver its properties change, this is due to the heat flow (solar energy) entering the receiver perpendicular to the direction of flow direction. The fluid uses this energy in the form of latent heat and sensible heat, which causes that at the outlet of the receiver the fluid not only has a higher temperature, but also, the fluid will have changed phase or would be in a mixture of phases Energía incidente en el receptor.

The energy incident on a receiver comes from a solar concentrator such as heliostats, parabolic trough concentrators, parabolic cylinder, among others; however this work is to take to the incident energy as the sum of direct and diffuse solar radiation. Then, the energy incident on the receiver is given by [4]:

$$S'' = \alpha_s G_s + \alpha_{sky}\sigma T_{sky}^4 \tag{1}$$

where

$$G_s = 1368\frac{W}{m^2} * \left[1 + 0.034\cos\left(\frac{360\,N}{365}\right)\right] * (\sin\delta\sin\phi + \cos\delta\cos\phi\cos w) \tag{2}$$

also

$$\delta = 23.5\sin\left[(284 + N)\frac{360}{365}\right] \tag{3}$$

$$T_{sky} = 0.0552 T_a^{1.5} \tag{4}$$

$$w = \begin{cases} 0°, & at\ noon\ solar \\ 0° - \left(\frac{15°}{h} * hour\ solar\right), & morning\ negative \\ 0° + \left(\frac{15°}{h} * hour\ solar\right), & afternoon\ positive \end{cases} \tag{5}$$

$$N: Day\ of\ the\ year$$

A. *Thermal resistance*

The energy that reaches the absorber plate of the receiver is not the same amount of energy that can take advantage of the fluid; this is because the components of the receiver are resistance to the passage of energy. Thus, the receiver is represented in Figure 2 as a composite wall system, where each wall has a resistance or a set of resistors in parallel, then the one-dimensional transient heat transfer for the system is expressed as:

$$Q_R = \rho_c c_{P_c}\frac{\partial T_c}{\partial t} + UA(T_a - T_c) \tag{6}$$

Where

$$UA = \frac{1}{R_{tot}} = \frac{1}{\frac{1}{h_w + h_{rad}}} \tag{7}$$

The fluid represents a resistance to the passage of energy from the absorber plate to the thermal insulation; however, it is required to know the available energy to be taken advantage of by the fluid, which is given by:

$$Q_u = h_{f1}A(T_{s2} - T_{mf}) + h_{f2}A(T_{s2} - T_{mf}) = \rho c_P \frac{\partial T_f}{\partial t} \tag{8}$$

also

$$Q_u = h_{conv}A(T_c - T_f) \tag{9}$$

B. *Heat transfer coefficients*

The conductive, convective and radiative heat transfer coefficients are [3,7,8,9]:

$$2 < h_a < 25 \tag{10}$$

$$h_{f,i} = \begin{cases} \text{Developed flow,} \quad = \frac{N_u K_f}{d_h} \rightarrow \begin{cases} N_u = 0.023 R_e^{4/5} P_r^{\,n} \rightarrow \begin{cases} n = 0.4, & heating \\ n = 0.3, & cooling \end{cases} \\ R_e = \frac{\rho U_m D}{\mu} \geq 10{,}000 \rightarrow \begin{cases} U_m = -\frac{r^2}{8\mu}\frac{dP}{dx} \\ D = \frac{4A_t}{P_m} \\ \rho = \rho(x,t) \end{cases} \\ 0.7 \leq P_r \leq 160, \quad P_r = \frac{\mu c_P}{k} \end{cases} \\ \text{Unstable circulation,} \begin{cases} = 0.22\left(\frac{P_r R_a}{0.2+P_r}\right)^{0.28}\left(\frac{H}{L}\right)^{-1/4} \rightarrow \begin{cases} 10^3 \leq R_a \leq 10^{10} \\ P_r < 10^5 \\ 2 < \frac{H}{L} < 10 \end{cases} \\ = 0.18\left(\frac{P_r R_a}{0.2+P_r}\right)^{0.29} \rightarrow \begin{cases} 10^3 < \frac{P_r R_a}{0.2+P_r} \\ 10^3 < P_r < 10^5 \\ 1 < \frac{H}{L} < 2 \end{cases} \end{cases} \end{cases} \tag{11}$$

$$h_w = \begin{cases} 5.7 + 3.8 v_{ws}, & v_{ws} < 5\,m/s \\ 6.47 v_{ws}^{\,0.78}, & v_{ws} > 5\,m/s \end{cases} \tag{12}$$

$$h_{rad} = \varepsilon\sigma\left(\frac{T_{s1}^{\,4} - T_{sky}^{\,4}}{T_{s1} - T_a}\right) \tag{13}$$

$$0.068 < k_{ti} < 0.098 \tag{14}$$

$$k_c = 73.982 - 0.0437 T_{s1} \tag{15}$$

III. Local Conditions

The city of Santiago de Querétaro, Querétaro is located to the West of the entity, between the 20º 31 'to 20º 56' of latitude North and of the 100º 19 'to 100º 36' of West length; so:

$$\phi = 20.435 \tag{16}$$

For the mathematical model, local environmental data are required, such as: ambient temperature and wind speed, from the CENAM database [6], the following information is obtained for February 17, 2017 (Fig. 4).

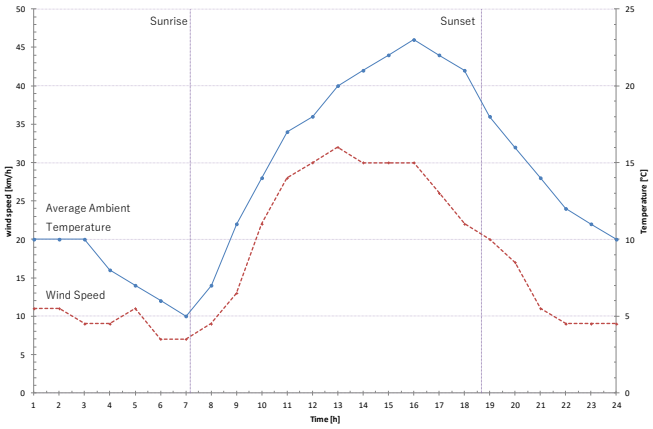

Fig. 4. Average ambient temperature and wind speed for February 17, 2010 in the city of Santiago de Querétaro.

From Figure 4, we obtain:

$$T_a = 5.3915 + 7.2127t - 3.1822t^2 + 0.5037t^3 - 0.0344t^4 + 0.0011t^5 \tag{17}$$

$$v_{ws} = 15.117t - 6.3099t^2 + 1.0235t^3 - 0.0732t^4 + 0.0024t^5 - 0.000003t^6 \tag{18}$$

IV. Results

When performing an energy balance

$$S'' = Q_u + Q_R \tag{19}$$

$$\alpha_s G_s + \alpha_{sky}\sigma T_{sky}^4 = \rho c_P \frac{\partial T_f}{\partial t} + \rho_c c_{P_c}\frac{\partial T_c}{\partial t} + UA(T_a - T_c) \tag{20}$$

Of the above, the temperature of the fluid inside the receiver can be calculated as follows:

$$\frac{\partial T_f}{\partial t} = S'' - \frac{\rho_c c_{P_c}}{\rho c_P}\frac{\partial T_c}{\partial t} + \left[\frac{\rho c_P}{h_w + h_{rad}}\right]^{-1}(T_a - T_c) \tag{21}$$

V. CONCLUSIONS

The model obtained from the analysis performed is in the verification phase.

A programming is carried out to be able to validate it, using a software tool.

REFERENCES

[1] K. Altfeld, W. Leiner, M. Fiebig. Second Law Optimization of Flat Plate Air Heaters. Solar Energy, vol. 41 (número 4), pp. 127-132, 1988.

[2] A. Lammardo, M Barrito. Mathematical model for describe the thermal behavior of a flat plate solar collector for air heating. Revista Ingeniería UC., vol. 17 (número 3), pp. 19-27, Diciembre 2010.

[3] F. Incropera, D. DeWitt. Fundamentals of heat transfer. Person Education, 4th ed.

[4] J. Duffie, W. Beckman. Solar Engineering of Thermal Processes. John Wiley & Sons, Inc. 3rd ed.

[5] Descubre Querétaro. (2017 marzo 10). http://www.queretaro.gob.mx/municipios.aspx?q=RrRbGx+QAUgDLhK1VcwWPw==

[6] CENAM. (2017 marzo 10). https://www.gob.mx/cenam/

[7] J. Bracamonte, M. Barrito. Irreversibility Analysis of Non Isothermal Flat Plate Solar Collectors for Air Heating with a Dimensionless Model. Ingeniería Investigación y Tecnología, vol. XIV (número 2), pp. 237-247, Jun 2013

[8] J. Dara, K. Ikebudo, N. Ubani,C. Chinwuko, O. Ubachukwu. Evaluation of a Passive Flat-Plate Solar Collector. International Journal of Advancements in Research & Technology, vol. 2, Issue 1, January 2013.

[9] S. Klein, J. Duffie, W. Beckman. Transient Considerations of Flat–Plate Solar Collectors. Journal of Engineering for Power, April 1974.

UNIVERSIDAD AUTÓNOMA DE QUERÉTARO